UNIVERSITY OF CALIFORNIA, SAN DIEGO

Partition Wall Subsystem Modeling and Effect on the Coupled Building System Response

A dissertation submitted in partial satisfaction of the requirements for the degree of

Doctor of Philosophy
in
Structural Engineering

by
Richard Lee Wood

Committee in charge:

Professor Tara C. Hutchinson, Chair
Professor Joel Conte
Professor Yuri Fialko
Professor Peter Shearer
Professor P. Benson Shing

2012

The Dissertation of Richard Lee Wood is approved, and it is acceptable in quality and form for publication on microfilm and electronically:

Chair

University of California, San Diego

2012

DEDICATION

To my parents and my late grandma, for their constant support and motivation.

EPIGRAPH

I can't believe it! Reading and writing actually paid off!

-Homer Simpson

TABLE OF CONTENTS

Signature Page iii
Dedication iv
Epigraph v
Table of Contents vi
List of Figures x
List of Tables xxi
Nomenclature xxii
Acknowledgements xxvi
Vita xxx
Abstract of the Dissertation xxxiii
Chapter 1 Introduction 1
1.1 Motivation 1
1.2 Partition Wall (PW) Subsystems 4
1.2.1 Example of Observed PW Behavior in a Full-Scale Building Test Program 4
1.2.2 PW Damage Observed in Post-Earthquake Reconnaissance 10
1.3 Scope of Research 14
1.4 Organization of Dissertation 15
1.5 Acknowledgement 16
Chapter 2 Partition Wall Modeling 17
2.1 Introduction 17
2.2 Previous PW Studies 17
2.2.1 Previous Experimental Studies 18
2.2.2 NEES-GC Partition Wall Tests at SUNY-Buffalo 25
2.2.3 Comparison of most recent Experimental Data Available 32
2.2.4 Previous Numerical Modeling Efforts 34
2.3 Numerical Modeling Methodology 41
2.3.1 Platform 41
2.3.2 Model Verification 43
2.3.3 PW Backbone Characterization 44
2.3.4 PW Unloading and Reloading Behavior 44
2.4 Developed PW Models 46

2.4.1 Subgroup Models 46
2.4.2 Subgroup Model Discussion 52
2.4.3 Normalized Models Introduction 53
2.4.4 Force Normalization for Normalized Models 54
2.4.5 Normalized Model Calibration 57
2.4.6 Normalized Model Discussion 61
2.5 Comparison of Developed PW Models 62
2.6 Summary Remarks 64
2.7 Acknowledgement 64
Chapter 3 Error Metric and Assessment of Developed Partition Wall Models 65
3.1 Introduction 65
3.2 Average Error in Maximum Force 65
3.3 Total Half-Cycle Hysteretic Energy 68
3.4 Use of Error Metrics to Assess all Models 71
3.5 Summary Remarks 75
3.6 Acknowledgement 76
Chapter 4 Coupled System: Building and Partition Wall Model 77
4.1 Introduction 77
4.1.1 Overview 77
4.1.2 Design of Concrete Buildings 78
4.1.3 Design of Steel Buildings 81
4.1.4 Model Discretization 88
4.1.5 Building Model Summary 93
4.2 Implementation of the PW into the Prototypical Building Models 95
4.2.1 Scaling Rules and Recommended Wall Lengths 97
4.3 Effect of PW on Building Modal Properties 100
4.3.1 Eigenvalue Analysis – Modal Periods and Mass Participation 100
4.3.2 Eigenvalue Analysis - Mode Shapes 110
4.3.3 Effect of PWs on Building Nonlinear Static “Pushover” Behavior 119
4.4 Summary Remarks 131
4.5 Acknowledgement 132
Chapter 5 Effects of Ground Motion Scaling on Building Response 133
5.1 Introduction 133
5.2 Motion Scaling Strategies 133

5.3 Building Design and Modeling 136
5.4 Dynamic Characteristics of the Considered Buildings 136
5.5 Site Location and Hazard 137
5.6 Ground Motion Scaling Methods 142
5.6.1 Linear Scaling 142
5.6.2 Frequency Scaling and Defining Baseline Ground Motions 146
5.7 Nonlinear Time History Response Results 146
5.7.1 Maximum Floor Acceleration Distribution 147
5.7.2 Acceleration Amplification Ratio Distribution 149
5.7.3 Baseline Normalized Acceleration Distribution 150
5.7.4 Baseline Normalized Interstory Drift Distribution 151
5.7.5 Curvature Ductility Distributions 153
5.7.6 Evaluating Robustness of Spectrally Matched Motions as a Baseline 156
5.8 Summary Remarks 161
5.9 Acknowledgement 163
Chapter 6 Coupled Building-Partition Wall System: Nonlinear Time History Analyses 164
6.1 Introduction 164
6.2 Selected Ground Motions 164
6.3 Analysis Procedure 168
6.3.1 Numerical Strategy 168
6.3.2 Time History Response 169
6.3.3 Example IDA Results 178
6.3.4 Analysis Cases 182
6.3.5 Synthesis of IDA results 184
6.3.6 Converting to Spectral Quantities 187
6.4 Effect of PW Inclusion on IDA results 200
6.4.1 RC-8 Model: Effect of Wall Length 200
6.4.2 RC-8 Model: Effect of PW Strength 211
6.4.3 RC-8 Model: Effect of Post-Yield Degradation 217
6.4.4 RC-8 Model: Effect of Wall Placement 227
6.4.5 RC-20 Model: Effect of PW 232
6.4.6 S-3H Model: Effect of Wall Length 237
6.4.7 S-9 Model: Effect of PW 240
6.5 Period Elongation of the Building-PW System 245

6.5.1 Introduction 245
6.5.2 RC-8 Model: Effect of Wall Length 246
6.5.3 RC-8 Model: Effect of PW Strength 247
6.5.4 RC-8 Model: Effect of Post-Yield Degradation 250
6.5.5 RC-8 Model: Effect of Wall Placement 252
6.5.6 RC-20 Model: Effect of PW 253
6.5.7 S-3H Model: Effect of Wall Length 254
6.5.8 S-9 Model: Effect of PW 255
6.6 Effect on Fragility Curves 256
6.6.1 Introduction to the Concept of Seismic Fragility Curves 256
6.6.2 Typical Fragility Approach 257
6.6.3 Bayesian Fragilities 259
6.6.4 Example Bayesian Fragility of PWs within Building Models 261
6.7 Concluding Remarks 262
6.8 Acknowledgement 264
Chapter 7 Conclusions and Recommendations 265
7.1 Motivation and Scope 265
7.2 Key Results 266
7.3 Impacts on Analysis Techniques 267
7.4 Recommendations for Future Work 268
References 269
Appendix A Partition Wall Model 274
Appendix B Nonlinear Time History Analysis Summary 292
Appendix C Summary on the Effect of Partition Walls 418

LIST OF FIGURES

Figure 1.1 Examples of nonstructural failures from the 2010 Baja California Earthquake (Mw=7.2). Partition wall (a) and pipe failures (b) at El Centro Regional Medical Center; and, ceiling fallout (c) and HVAC system failure (d) at Universidad Autónoma de Baja California (UABC) in Mexicali, BC. 2

Figure 1.2 Cost breakdown of typical office, hotel and hospital buildings. 3

Figure 1.3 Elevation view of the south side of the five-story building test (BNCS) conducted at the University of California, San Diego. 5

Figure 1.4 Spherical panorama of the second floor of the BNCS building just prior to testing. 6

Figure 1.5 Detailing of the PW installation within the BNCS project. 7

Figure 1.6 Overview of PW installation within the BNCS project. 7

Figure 1.7 Spherical panorama of the third floor after earthquake and fire test sequences. 8

Figure 1.8 Typical PW failure modes observed during the BNCS test project at UCSD: (a) screw pull-through, (b) crushing in corner and along return wall, (c) tape flaking/cracks along panel boundaries, (d) gap and damage concentrated at intersection of wall boundary, and (e) detachment of panel. 10

Figure 1.9 2010 Eureka California (M_w=6.5): interior PW damage. 11

Figure 1.10 2010 Maule (Chile) Earthquake (M_w = 8.8): interior PW damage from Felix Bulnes Hospital in Santiago demonstrating a collapsed out-of-plane wall. 12

Figure 1.11 2010 Maule (Chile) Earthquake (M_w = 8.8): interior PW damage from Main Santiago Hospital : (a) in-plane damage and (b) damage imposed from attached television monitor. 12

Figure 1.12 2010 Maule (Chile) Earthquake (M_w = 8.8): PW wall damage from Hospital Clinica Herminda Martin, Chillán, Chile: (a) PW cracks in surgical room and (b) widespread PW cracks within a hallway. 13

Figure 1.13 2010 El Mayor - Cucapah (Baja California) Earthquake (M_w = 7.2): nonstructural damage at the Facultad de Ciencias Administrativas of UABC Mexicali: (a) PW damage and (b) PW, suspended ceiling and hvac system damage. 13

Figure 1.14 2011 Tōhoku (M_w=9.0): temporarily shored damaged interior PW within a gymnasium within the Ibaraki prefecture, Japan. 14

Figure 1.15 2012 Emilia Earthquakes (M_w=6.1): interior PW damage within a hospital in Bondeno, Italy. 14

Figure 2.1 NAHB shear wall configurations: (a) details and (b) force-displacement results. .. 20

Figure 2.2 Damage state fragility functions for Bersofsky's experiment. 22

Figure 2.3 Plan view of test specimen for Lang's experiment. 23

Figure 2.4 Testing protocols used in Lang's experiment. 24

Figure 2.5 (a) Hysteretic behavior of specimen 1 and (b) damage cost estimate versus story drift. 25

Figure 2.6 Typical in-plane PW experimental setup. 27
Figure 2.7 Quasi-static drift sensitive protocol utilized in the tests of Davies (2009). 27
Figure 2.8 Sheathing and framing connectivity details: (a-b) bottom and top track connections for partially connected specimens (slip track), (c-d) bottom and top track connections for fully connected specimens, (e) wall intersection details for commercial construction practices and (f) wall intersection details for institutional construction practices. 31
Figure 2.9 Single hysteretic loop comparison for experimental result against theoretical result demonstrating the pinching effect. 35
Figure 2.10 Pinching hysteretic model shown for basic model rules. 36
Figure 2.11 Model performance assessment for an example woodframe specimen considering a pinching model. 36
Figure 2.12 CASHEW model developed for woodframe shear walls. 37
Figure 2.13 Shear wall backbone curve. 39
Figure 2.14 Wayne-Stewart hysteretic model with strength degradation. 40
Figure 2.15 Proposed empirical backbone for gypsum board on light-gauge steel stud PWs. 41
Figure 2.16 *Pinching4* material model. 43
Figure 2.17 Force-Displacement backbone for specimen 20 and the selected backbone points. 44
Figure 2.18 Experimental and numerical model comparison for specimen 20: (a) hysteretic behavior and (b) hysteretic area. 46
Figure 2.19 Subgroup 1a experimental hysteretic behavior showing identified backbone and average subgroup backbone. 48
Figure 2.20 Subgroup 1b experimental hysteretic behavior showing identified backbone and average subgroup backbone. 49
Figure 2.21 Subgroup 2a experimental hysteretic behavior showing identified backbone and average subgroup backbone. 50
Figure 2.22 Subgroup 2b experimental hysteretic behavior showing identified backbone and average subgroup backbone. 51
Figure 2.23 Overlay of each subgroup backbones shown demonstrating a large variability. 53
Figure 2.24 PW backbones (force-displacement relations) for subgroups 1b and 2b. 55
Figure 2.25 Absolute valued normalized backbones showing the mean, mean plus one standard deviation and mean minus one standard deviation. 56
Figure 2.26 Hysteretic energy for subgroups 1b and 2b for each of the specimens considered along with their respective subgroup averages. 56
Figure 2.27 Normalized hysteretic energy for subgroups 1b and 2b. 57
Figure 2.28 Selection of the mean response behavior of the PW model. Top shows normalized absolute valued hysteretic backbone while the bottom demonstrates the tangent stiffness of this backbone. 58

Figure 2.29 Hysteretic area of the mean model versus the target mean hysteretic area. 59
Figure 2.30 Hysteretic behavior of the mean response shown with specimen 4 as an example. 60
Figure 2.31 Hysteretic area of the mean model with specimen 4 as an example. 60
Figure 2.32 Overlay of each of the normalized model backbones. 61
Figure 2.33 Comparison of developed models to the proposed model by Restrepo and Lang (2011): (a) subgroup models, and (b) normalized models, where the length of the partition walls were taken as 12 feet as tested in the NEES-GC project. 63
Figure 3.1 Hysteretic overlap comparison between specimen 23 and the 2b subgroup model. 66
Figure 3.2 Captured maximum force envelope curve for specimen 23 and the 2b subgroup model. 67
Figure 3.3 Difference in maximum attained force level when comparing specimen 23 and the 2b subgroup model. 68
Figure 3.4 Hysteretic energy (area) comparison between specimen 23 and the 2b subgroup model. 69
Figure 3.5 Hysteretic energy (area) per half cycle comparison between specimen 23 and the 2b subgroup model shown against maximum achieved drift level. 70
Figure 3.6 Difference in hysteretic energy (area) per half cycle comparison for specimen 23. 71
Figure 3.7 Average force residual comparing the experimental to the developed models by damage states: a) $DS<DS_1$, b) $DS_1 \leq DS<DS_2$, c) $DS_2 \leq DS<DS_3$ and d) $DS \geq DS_3$. ... 72
Figure 3.8 Average force residual comparing the experimental to the developed models by damage states: a) $DS<DS_1$, b) $DS_1 \leq DS<DS_2$, c) $DS_2 \leq DS<DS_3$ and d) $DS \geq DS_3$. ... 73
Figure 3.9 Overall residual in half-cycle hysteretic energy comparing the experimental to the developed models by damage states: (a) $DS<DS_1$, (b) $DS_1 \leq DS<DS_2$, (c) $DS_2 \leq DS<DS_3$ and (d) $DS \geq DS_3$. 74
Figure 3.10 Overall residual in half-cycle hysteretic energy comparing the experimental to the developed models by damage states: (a) $DS<DS_1$, (b) $DS_1 \leq DS<DS_2$, (c) $DS_2 \leq DS<DS_3$ and (d) $DS \geq DS_3$. 75
Figure 4.1 Prototype Building Plan View illustrated for concrete buildings. 78
Figure 4.2 Typical beam - refer to Table 4.1 for specific details. 80
Figure 4.3 SMRF building designs for RC-20, RC-12, RC-8, RC-4 and RC-2. 80
Figure 4.4 Plan (a) and elevation view (b) for the three story SAC building, denoted as S-3. . 83
Figure 4.5 Plan (a) and elevation view (b) for the three story hospital building, denoted as S-3H. 84
Figure 4.6 Plan (a) and elevation view (b) for the nine story SAC building, denoted as S-9. .. 85
Figure 4.7 Plan (a) and elevation view (b) for the twenty story SAC building, denoted as S-20. 86
Figure 4.8 BeamWithHinges element diagram. 89
Figure 4.9 Linear tension strength concrete model. 90

Figure 4.10 Steel model used for the reinforcing steel of the wall elements in the dual wall-frame building models. 92
Figure 4.11 Summary statistics of the bare building (no PW): (a) first and second mode periods and (b) first and second mode mass participations. 95
Figure 4.12 Partition wall implementation between two adjacent story levels. 96
Figure 4.13 Normalized PW model (monotonic behavior) as implemented in OpenSees. 97
Figure 4.14 Example of PW scaling when the target wall is twice the length of the original wall with twice the number of vertical studs in the lateral direction. 99
Figure 4.15 Normalized plots demonstrating period and mass participations sensitivities for RC-2. 106
Figure 4.16 Normalized plots demonstrating period and mass participations sensitivities for RC-4. 106
Figure 4.17 Normalized plots demonstrating period and mass participations sensitivities for RC-8. 107
Figure 4.18 Normalized plots demonstrating period and mass participations sensitivities for RC-12. 107
Figure 4.19 Normalized plots demonstrating period and mass participations sensitivities for RC-20. 108
Figure 4.20 Normalized plots demonstrating period and mass participations sensitivities for S-3. 108
Figure 4.21 Normalized plots demonstrating period and mass participations sensitivities for S-3H. 109
Figure 4.22 Normalized plots demonstrating period and mass participations sensitivities for S-9. 109
Figure 4.23 Normalized plots demonstrating period and mass participations sensitivities for S-20. 110
Figure 4.24 Mode shapes for the first two modes shown for building RC-2. 111
Figure 4.25 Mode shapes for the first four modes shown for building RC-4. 112
Figure 4.26 Mode shapes for the first four modes shown for building RC-8. 113
Figure 4.27 Mode shapes for the first four modes shown for building RC-12. 114
Figure 4.28 Mode shapes for the first four modes shown for building RC-20. 115
Figure 4.29 Mode shapes for the first three modes shown for building S-3. 116
Figure 4.30 Mode shapes for the first three modes shown for building S-3H. 117
Figure 4.31 Mode shapes for the first four modes shown for building S-9. 118
Figure 4.32 Mode shapes for the first four modes shown for building S-20. 119
Figure 4.33 Normalized pushover response illustrated for RC-2 demonstrating effect of included PWs. 121

Figure 4.34 Normalized pushover response illustrated for RC-4 demonstrating effect of included PWs. 122

Figure 4.35 Normalized pushover response illustrated for RC-8 demonstrating effect of included PWs. 123

Figure 4.36 Normalized pushover response illustrated for RC-12 demonstrating effect of included PWs. 124

Figure 4.37 Normalized pushover response illustrated for RC-20 demonstrating effect of included PWs. 125

Figure 4.38 Normalized pushover response illustrated for S-3 demonstrating effect of included PWs. 126

Figure 4.39 Normalized pushover response illustrated for S-3H demonstrating effect of included PWs. 127

Figure 4.40 Normalized pushover response illustrated for S-9 demonstrating effect of included PWs. 128

Figure 4.41 Normalized pushover response illustrated for S-20 demonstrating effect of included PWs. 129

Figure 4.42 Summary of normalized base shear values for roof drifts of 1 and 3%, shown by building model. 131

Figure 5.1 Probabilistic Seismic Hazard Deaggregation generated using the 2002 USGS interactive deaggregation tools. 138

Figure 5.2 Elastic 5% damped spectral acceleration curves showing for all buildings (a) the target design spectrum and unscaled motions, (b) *sweep*, (c) *range*, (d) *fundamental*, (e) *code* scaling approaches, and (f) the average baseline (SM= spectrally matched) response and the individual spectrally matched records responses. 144

Figure 5.3 Average maximum absolute floor acceleration by building type for (a) RC-8, (b) RC-12, and (c) RC-20 buildings. (y-axis unitless). 148

Figure 5.4 Average uncorrelated acceleration amplification ratio Ω by building type for (a) RC-8, (b) RC-12, and (c) RC-20 buildings. (x- and y-axes unitless). 150

Figure 5.5 Average maximum acceleration distribution normalized by the baseline response by building type for (a) RC-8, (b) RC-12, and (c) RC-20 buildings. (x- and y-axes unitless). 151

Figure 5.6 Average maximum average interstory drift (γ_{is}) distributions response by building type for (a) RC-8, (b) RC-12, and (c) RC-20 buildings. (x- and y-axes unitless). 152

Figure 5.7 Average maximum average interstory drift (γ_{is}) distributions normalized by *baseline* response by building type for (a) RC-8, (b) RC-12, and (c) RC-20 buildings. (x- and y-axes unitless). 153

Figure 5.8 Average maximum plastic curvature induced from time history analyses. From left to right: eight, twelve and twenty story buildings scaled according to the follow methods: (a) *code*, (b) *fundamental*, (c) *range*, (d) *sweep* and (e) *baseline (BL)*. . 155

Figure 5.9 68% confidence interval plots identifying: (a) acceleration, (b) uncorrelated acceleration amplification, and (c) interstory drift dispersion along the height of the building for RC-8. (BL = baseline or spectrally matched case). 158

Figure 5.10 68% confidence interval plots identifying: (a) acceleration, (b) uncorrelated acceleration amplification, and (c) interstory drift dispersion along the height of the building for RC-12. (BL = baseline or spectrally matched case). 159

Figure 5.11 68% confidence interval plots identifying: (a) acceleration, (b) uncorrelated acceleration amplification, and (c) interstory drift dispersion along the height of the building for RC-20. (BL = baseline or spectrally matched case). 160

Figure 5.12 Dispersion comparison of the building response (left to right: RC-8, RC-12, and RC-20) by scaling method: (a) standard deviation of the maximum acceleration and (b) standard deviation of the maximum interstory drift values..... 161

Figure 6.1 Elastic 5% Damped Spectral acceleration curves for entire ground motion suite (unscaled) for the ATC-63 Far-Field Record Set. 167

Figure 6.2 Elastic 5% Damped Spectral displacement curves for entire ground motion suite (unscaled) for the ATC-63 Far-Field Record Set. 167

Figure 6.3 Interstory drift time history example illustrated by floor: RC-8 with PW assuming the minimum wall case ($L_{w,min}$) and the mean PW model under record #1 (Northridge) scaled to a PGA of 0.40 g. 171

Figure 6.4 Maximum interstory drift envelope curve for RC-8 for no wall, $L_{w,min}$, and $L_{w,max}$ consider the mean PW model under record #1 scaled to a PGA of 0.40 g. 172

Figure 6.5 Elastic 5% damped spectral displacement for a scaled record #1 (Northridge, PGA=0.4 g) where the vertical lines identify the fundamental periods (initial and final) of the uncoupled and coupled cases. 172

Figure 6.6 Annotated elastic 5% damped spectral displacement curve for a scaled record #1 (Northridge, PGA=0.4 g) where the vertical lines identify the fundamental periods (initial and final) of the uncoupled and coupled cases..... 173

Figure 6.7 Acceleration time history example illustrated by floor RC-8 with PW assuming the minimum wall case ($L_{w,min}$) and the mean PW model under record #1 (Northridge) scaled to a PGA of 0.40 g. 176

Figure 6.8 Maximum floor acceleration envelope curve for RC-8 for no wall, $L_{w,min}$, and $L_{w,max}$ consider the mean PW model under record #1 (Northridge) scaled to a PGA of 0.40 g. 177

Figure 6.9 Elastic 5% damped spectral acceleration for a scaled record #1 (Northridge, PGA=0.4 g) where the vertical lines identify the fundamental periods (initial and final) of the uncoupled and coupled cases. 177

Figure 6.10 Annotated elastic 5% damped spectral acceleration curve for a scaled record #1 (Northridge, PGA=0.4 g) where the vertical lines identify the fundamental periods (initial and final) of the uncoupled and coupled cases..... 178

Figure 6.11 IDA results for RC-8 with PW assuming the minimum wall case ($L_{w,min}$) and the mean PW model: maximum interstory drift demands at each floor versus peak ground acceleration (PGA). 180

Figure 6.12 IDA results for RC-8 with PW assuming the minimum wall case ($L_{w,min}$) and the mean PW model: maximum interstory drift demands at each floor versus elastic 5% damped spectral acceleration at the fundamental period (T_1). 181

Figure 6.13 IDA results for RC-8 with PW assuming the minimum wall case ($L_{w,min}$) and the mean PW model: maximum interstory drift demands at each floor versus elastic 5% damped spectral displacement at the fundamental period (T_1). 182

Figure 6.14 IDA results for RC-8 bare building (no wall case): peak ground acceleration (PGA) against maximum interstory drift. 185

Figure 6.15 IDA results for RC-8 bare building (no wall case): peak ground acceleration (PGA) against maximum floor acceleration. 186

Figure 6.16 Elastic 5% damped spectral acceleration for record 1 (Northridge) with example ΔT_1 overlaid: a) overall view and b) zoomed in view with $S_a(T_1^{initial})$ and median, mean and maximum spectral acceleration over ΔT_1 ($Sa(\Delta T_1)$) values. 189

Figure 6.17 Elastic 5% damped spectral displacement for record 1 (Northridge) with example ΔT_1 overlaid: a) overall view and b) zoomed in view with $S_a(T_1^{initial})$ and median, mean and maximum spectral displacement over ΔT_1 ($Sa(\Delta T_1)$) values. 190

Figure 6.18 Elastic 5% damped spectral acceleration for all records scaled to a PGA = 0.4 g with overall mean shown. 191

Figure 6.19 Elastic 5% damped spectral acceleration for all records scaled to a PGA = 0.4 g with overall mean shown with overlaid period ranges: (a) RC-8, (b) S-3H, (c) S-9, and (d) RC-20. 192

Figure 6.20 Elastic 5% damped spectral displacement for all records scaled to a PGA = 0.4 g with overall mean shown. 193

Figure 6.21 Elastic 5% damped spectral displacement for all records scaled to a PGA = 0.4 g with overall mean shown with overlaid period ranges: (a) RC-8, (b) S-3H, (c) S-9, and (d) RC-20. 194

Figure 6.22 IDA results for RC-8 (no wall): maximum interstory drift against spectral acceleration at $T_1^{initial}$. 195

Figure 6.23 IDA results for RC-8 (no wall): maximum interstory drift against spectral displacement at $T_1^{initial}$. 195

Figure 6.24 IDA results for RC-8 (no wall): maximum interstory drift against median spectral acceleration over ΔT_1. 196

Figure 6.25 IDA results for RC-8 (no wall): maximum interstory drift against median spectral displacement over ΔT_1. 196

Figure 6.26 IDA results for RC-8 (no wall): maximum interstory drift against mean spectral acceleration over ΔT_1. 197

Figure 6.27 IDA results for RC-8 (no wall): maximum interstory drift against mean spectral displacement over ΔT_1. 197

Figure 6.28 IDA results for RC-8 (no wall): maximum interstory drift against maximum spectral acceleration over ΔT_1. 198

Figure 6.29 IDA results for RC-8 (no wall): maximum interstory drift against maximum spectral displacement over ΔT_1. 198

Figure 6.30 IDA results for RC-8 (no wall): maximum floor acceleration against median spectral acceleration over ΔT_1. 199

Figure 6.31 IDA results for RC-8 (no wall): maximum floor acceleration drift against median spectral displacement over ΔT_1. 199

Figure 6.32 Maximum interstory drift moving average curves for RC-8 with cases of no wall, minimum wall length, and maximum wall length considering mean model parameters against median spectral acceleration over ΔT_1. 203

Figure 6.33 Maximum interstory drift moving average curves for RC-8 with cases of no wall, minimum wall length, and maximum wall length considering mean model parameters against median spectral displacement over ΔT_1. 204

Figure 6.34 Normalized maximum interstory drift moving average curves for RC-8 with cases of no wall, minimum wall length, and maximum wall length considering mean model parameters against median spectral acceleration over ΔT_1. 205

Figure 6.35 Normalized maximum interstory drift moving average curves for RC-8 with cases of no wall, minimum wall length, and maximum wall length considering mean model parameters against median spectral displacement over ΔT_1. 206

Figure 6.36 Maximum floor acceleration moving average curves for RC-8 with cases of no wall, minimum wall length, and maximum wall length considering mean model parameters against median spectral acceleration over ΔT_1. 207

Figure 6.37 Maximum floor acceleration moving average curves for RC-8 with cases of no wall, minimum wall length, and maximum wall length considering mean model parameters against median spectral displacement over ΔT_1. 208

Figure 6.38 Normalized maximum floor acceleration moving average curves for RC-8 with cases of no wall, minimum wall length, and maximum wall length considering mean model parameters against median spectral acceleration over ΔT_1. 209

Figure 6.39 Normalized maximum floor acceleration moving average curves for RC-8 with cases of no wall, minimum wall length, and maximum wall length considering mean model parameters against median spectral displacement over ΔT_1. 210

Figure 6.40 Normalized maximum interstory drift moving average curves for RC-8 with cases of no wall and the minimum wall length considering mean (μ), mean minus standard deviation ($\mu-\sigma$), and mean plus standard deviation ($\mu+\sigma$) model parameters against median spectral acceleration over ΔT_1. 213

Figure 6.41 Normalized maximum interstory drift moving average curves for RC-8 with cases of no wall and the minimum wall length considering mean (μ), mean minus standard deviation ($\mu-\sigma$), and mean plus standard deviation ($\mu+\sigma$) model parameters against median spectral displacement over ΔT_1. 214

Figure 6.42 Normalized maximum floor acceleration moving average curves for RC-8 with cases of no wall and the minimum wall length considering mean (μ), mean minus standard deviation ($\mu-\sigma$), and mean plus standard deviation ($\mu+\sigma$) model parameters against median spectral acceleration over ΔT_1. 215

Figure 6.43 Normalized maximum floor acceleration drift moving average curves for RC-8 with cases of no wall and the minimum wall length considering mean (μ), mean minus standard deviation (μ–σ), and mean plus standard deviation (μ+σ) model parameters against median spectral displacement over ΔT_1. 216

Figure 6.44 PW model backbones: μ (mean) model and μ model with degrading branch. 217

Figure 6.45 Normalized maximum interstory drift moving average curves for RC-8 with cases of no wall and the minimum wall length considering post-peak hardening and a degrading model against median spectral accelerations over ΔT_1. 219

Figure 6.46 Normalized maximum interstory drift moving average curves for RC-8 with cases of no wall and the maximum wall length considering post-peak hardening and a degrading model against median spectral accelerations over ΔT_1. 220

Figure 6.47 Normalized maximum interstory drift moving average curves for RC-8 with cases of no wall and the minimum wall length considering post-peak hardening and a degrading model against median spectral displacement over ΔT_1. 221

Figure 6.48 Normalized maximum interstory drift moving average curves for RC-8 with cases of no wall and the maximum wall length considering post-peak hardening and a degrading model against median spectral displacement over ΔT_1. 222

Figure 6.49 Normalized maximum floor acceleration moving average curves for RC-8 with cases of no wall and the minimum wall length considering post-peak hardening and a degrading model against median spectral acceleration over ΔT_1. 223

Figure 6.50 Normalized maximum floor acceleration moving average curves for RC-8 with cases of no wall and the maximum wall length considering post-peak hardening and a degrading model against median spectral acceleration over ΔT_1. 224

Figure 6.51 Normalized maximum floor acceleration moving average curves for RC-8 with cases of no wall and the minimum wall length considering post-peak hardening and a degrading model against median spectral displacement over ΔT_1. 225

Figure 6.52 Normalized maximum floor acceleration moving average curves for RC-8 with cases of no wall and the maximum wall length considering post-peak hardening and a degrading model against median spectral displacements over ΔT_1. 226

Figure 6.53 Normalized maximum interstory drift moving average curves for RC-8 considering the cases of wall placement: no wall, minimum wall length (all floors), no wall first floor, and no wall on top level against median spectral acceleration over ΔT_1. 228

Figure 6.54 Normalized maximum interstory drift moving average curves for RC-8 considering the cases of wall placement: no wall, minimum wall length (all floors), no wall first floor, and no wall on top level against median spectral displacement over ΔT_1. .. 229

Figure 6.55 Normalized maximum floor acceleration moving average curves for RC-8 considering the cases of wall placement: no wall, minimum wall length (all floors), no wall first floor, and no wall on top level against median spectral acceleration over ΔT_1. 230

Figure 6.56 Normalized maximum floor acceleration moving average curves for RC-8 considering the cases of wall placement: no wall, minimum wall length (all floors),

no wall first floor, and no wall on top level against median spectral displacement over ΔT_1. 231

Figure 6.57 Normalized maximum interstory drift moving average curves for RC-20 with cases of no wall and minimum wall length considering mean model parameters against median spectral acceleration over ΔT_1. 233

Figure 6.58 Normalized maximum interstory drift moving average curves for RC-20 with cases of no wall and minimum wall length considering mean model parameters against median spectral displacement over ΔT_1. 234

Figure 6.59 Normalized maximum floor acceleration moving average curves for RC-20 with cases of no wall and minimum wall length considering mean model parameters against median spectral acceleration over ΔT_1. 235

Figure 6.60 Normalized maximum floor acceleration moving average curves for RC-20 with cases of no wall and minimum wall length considering mean model parameters against median spectral displacement over ΔT_1. 236

Figure 6.61 Normalized maximum interstory drift moving average curves for S-3H with cases of no wall, minimum wall length, and maximum wall length considering mean model parameters against median spectral acceleration over ΔT_1. 238

Figure 6.62 Normalized maximum interstory drift moving average curves for S-3H with cases of no wall, minimum wall length, and maximum wall length considering mean model parameters against median spectral displacement over ΔT_1. 238

Figure 6.63 Normalized maximum floor acceleration drift moving average curves for S-3H with cases of no wall, minimum wall length, and maximum wall length considering mean model parameters against median spectral acceleration over ΔT_1. 239

Figure 6.64 Normalized maximum floor acceleration drift moving average curves for S-3H with cases of no wall, minimum wall length, and maximum wall length considering mean model parameters against median spectral acceleration over ΔT_1. 239

Figure 6.65 Normalized maximum interstory drift moving average curves for S-9 with cases of no wall and minimum wall length considering mean model parameters against median spectral acceleration over ΔT_1. 241

Figure 6.66 Normalized maximum interstory drift moving average curves for S-9 with cases of no wall and minimum wall length considering mean model parameters against median spectral displacement over ΔT_1. 242

Figure 6.67 Normalized maximum floor acceleration moving average curves for S-9 with cases of no wall and minimum wall length considering mean model parameters against median spectral acceleration over ΔT_1. 243

Figure 6.68 Normalized maximum floor acceleration moving average curves for S-9 with cases of no wall and minimum wall length considering mean model parameters against median spectral displacement over ΔT_1. 244

Figure 6.69 IDA results for RC-8 with the minimum length wall considering the mean model parameters: period elongation against spectral displacement over ΔT_1. 246

Figure 6.70 Period elongation moving average curves for RC-8 with cases of no wall, minimum wall length, and maximum wall length considering mean model parameters against median spectral displacement over ΔT_1. 247

Figure 6.71 Period elongation moving average curves for RC-8 with cases of no wall and the minimum wall length considering mean (μ), mean minus standard deviation ($\mu-\sigma$), and mean plus standard deviation ($\mu+\sigma$) model parameters against median spectral displacement over ΔT_1. 249

Figure 6.72 Period elongation moving average curves for RC-8 with cases of no wall and the minimum wall length considering post-peak hardening and a degrading model against median spectral displacement over ΔT_1..... 250

Figure 6.73 Period elongation moving average curves for RC-8 with cases of no wall and the maximum wall length considering post-peak hardening and a degrading model against median spectral displacement over ΔT_1..... 251

Figure 6.74 Period elongation moving average curves for RC-8 considering the cases of wall placement: no wall, minimum wall length (all floors), no wall first floor, and no wall on top level against median spectral displacement over the range of T_1. 252

Figure 6.75 Period elongation moving average curves for RC-20 considering the cases of no wall and minimum wall length against median spectral displacement over the range of T_1. 253

Figure 6.76 Period elongation moving average curves for S-3H with cases of no wall, minimum wall length, and maximum wall length considering mean model parameters against median spectral displacement over ΔT_1. 254

Figure 6.77 Period elongation moving average curves for S-9 with cases of no wall and minimum wall length considering mean model parameters against median spectral displacement over ΔT_1. 255

Figure 6.78 Example ATC-58 fragility curves for all in-plane PWs from the NEES-Nonstructural Project. 259

Figure 6.79 Comparison of fragilities for simulation data in RC-8 group for state-independent shape parameters, where: (a) DS_0 (no damage), (b) DS_1, (c) DS_2 and (d) DS_3. 262

LIST OF TABLES

Table 2.1 Experimental configurations for Bersofsky's experiment. 21

Table 2.2 PW specimen damage state and modeling consideration (specimen data per tests by Davies, 2009). 29

Table 2.3 PW classification by subgroup. Only subgroups with full height specimens are considered. 30

Table 2.4 PW detailing. 30

Table 2.5 Comparison of experimental test setups. 33

Table 2.6 Parameters for the subgroup models. 52

Table 2.7 Parameters for the normalized PW model. 62

Table 4.1 SMRF building design summary (refer to Figure 1.3) 81

Table 4.2 Steel building design summary. 87

Table 4.3 Confined concrete properties for concrete buildings. 91

Table 4.4 Summary of building suite considered. 94

Table 4.5 PW configuration combinations by building. 99

Table 4.6 Modal periods and mass participation sensitivity for RC-2. 102

Table 4.7 Modal periods and mass participation sensitivity for RC-4. 102

Table 4.8 Modal periods and mass participation sensitivity for RC-8. 103

Table 4.9 Modal periods and mass participation sensitivity for RC-12. 103

Table 4.10 Modal periods and mass participation sensitivity for RC-20. 104

Table 4.11 Modal periods and mass participation sensitivity for S-3. 104

Table 4.12 Modal periods and mass participation sensitivity for S-3H. 104

Table 4.13 Modal periods and mass participation sensitivity for S-9. 105

Table 4.14 Modal periods and mass participation sensitivity for S-20. 105

Table 4.15 Summary of base shear values for roof drifts of 1 and 3%. 130

Table 4.16 Summary of normalized base shear values for roof drifts of 1 and 3%. 130

Table 5.1 Building eigenvalue analysis. 137

Table 5.2 Deaggregation bin details (% hazard). 138

Table 5.3 Selected ground motions (seed records) details (PEER-NGA, 2009). 141

Table 5.4 Scale factors for each ground motion record and summary statistics. 145

Table 5.5 Average and normalized maximum curvature ductility (μ_ϕ) demands. 156

Table 6.1 Selected ground motions from the ATC-63 Far-Field Record Set. 166

NOMENCLATURE

The following section defines the variables used in this dissertation. Note: F denotes force, L denotes length, and T denotes time.

Symbol	Description	Units
$\lvert\ddot{u}\rvert_{max}$	Average maximum absolute floor acceleration	L/T^2
$\overline{F_{res}}$	Average residual force	F
$\lvert a\rvert_{max}$	Maximum acceleration	L/T^2
a	Scale factor for geometric mean method	unitless
a_1, a_2, a_3, a_4	Isotropic hardening parameters	unitless
A_{TRIB}	Tributary area	L^2
b	Width of concrete member	L
cR_1, cR_2	Parameters for Bauschinger effect	unitless
d_b	Diameter of reinforcing steel	L
DS_1, DS_2, DS_3	Damage state one; etc.	unitless
E_c	Elastic modulus of concrete	F/L^2
EDP	Engineering demand parameters	varies
E_H	Hysteretic energy (area)	$F{\cdot}L$
E_s	Elastic modulus of steel	F/L^2
E_{sh}	Post-peak modulus of steel	F/L^2
EM_1	Error metric #1, denoting force residual	F
EM_2	Error metric #2, denoting hysteretic energy residual	F•L
f'_c	28-day compressive strength of concrete	F/L^2
f'_{cc}	Compression strength of confined concrete	F/L^2
f'_{ccu}	Compression strength at ultimate strain for confined concrete	F/L^2
f_{su}	Peak stress of steel	F/L^2
f_y	Yield strength of longitudinal reinforcing steel	F/L^2
h	Height of concrete member	L
h^*	Normalized height of building	unitless
h_i	Height of floor level i	L

Symbol	Description	Units
k_c	Effects of confinement ratio	unitless
l_p	Length of plastic hinge	L
L_w	Length of partition wall	L
L_x, L_y	Length of bay in x (or y) direction	L
M	Magnitude	unitless
MP^*_i	Normalized mass participation quantity	unitless
MP_i	Mass participation factor for the i^{th} mode	unitless
MP_i^{bare}	Mass participation of bare structure (no wall) for the i^{th} mode	unitless
MP_i^n	Mass participation of n-method for the i^{th} mode	unitless
M_w	Moment magnitude	unitless
n_x, n_y	Number of bays in x (or y) direction	unitless
P	Probability	Unitless
PGA	Peak ground acceleration	L/T^2
PI	Partition index	1/L
R	Distance	L
R_0	Parameter for Bauschinger effect	unitless
RC-12	Twelve story reinforced concrete special moment frame building	unitless
RC-2	Two story reinforced concrete special moment frame building	unitless
RC-20	Twenty story reinforced concrete special moment frame building	unitless
RC-4	Four story reinforced concrete special moment frame building	unitless
RC-8	Eight story reinforced concrete special moment frame building	unitless
s	Spacing of transverse stirrups	L
S_1	Spectral acceleration at 1.0 second	T
S-20	Twenty story steel special moment frame building	unitless
S-3	Three story steel special moment frame building	unitless
S-3H	Three story steel special moment frame building representing a hospital	unitless
S-9	Nine story steel special moment frame building	unitless

Symbol	Description	Units
S_a	Spectral acceleration	L/T^2
$S_a(\Delta T_1)$	Spectral acceleration over the range of ΔT_1	L/T^2
S_d	Spectral displacement	L
$S_d(T_1)$	Spectral displacement over the range of ΔT_1	L
S_{D1}	Design spectral acceleration at period of 1.0 sec	L/T^2
S_{DS}	Design spectral acceleration at short periods	L/T^2
Ss	Spectral acceleration at short periods	T
T^*_i	Normalized period quantity	unitless
T_1	Fundamental period	T
T_1^{final}	Final fundamental period	T
$T_1^{initial}$	Initial (uncracked) fundamental period	T
T_i^{bare}	Period of bare structure (no wall) for the i^{th} mode	T
T_i^n	Period of n-method for the i^{th} mode	T
T_L	Lower bound period associated with effective mass of 90%	T
V_{base}	Base shear	F
y_i	Spectral acceleration at period i	L/T^2
y_i^t	Target spectral acceleration at period i	L/T^2
ε_{cc}	Strain at peak strength for confined concrete	unitless
ε_{ccu}	Ultimate compression strain for confined concrete	unitless
ε_{cu}	Strain at maximum concrete strength	unitless
ε_{sh}	Post yield strain of steel	unitless
ε_{su}	Strain at peak stress of steel	unitless
ρ_l	Longitudinal reinforcing steel ratio	unitless
ΣE_H	Total half cycle hysteretic energy	F·L
Ω_i	Uncorrelated acceleration amplification ratio	unitless
Δ_i	Displacement at floor level i	L
ΔT_1	Range of fundamental period	T
Σt_{stud}	Total thickness of wall studs in lateral direction	L
β	Logarithmic standard deviation	varies
β_r	Random variability observed in test data	varies
β_u	Random variability due to uncertainty	varies

Symbol	Description	Units
γ_{IS}	Interstory drift	unitless
μ	Mean	unitless
μ_{ϕ}	Curvature ductility	unitless
θ	Median demand of the EDP	varies
σ	Standard deviation	unitless

ACKNOWLEDGEMENTS

First and foremost, I would like to thank my advisor, Professor Tara C. Hutchinson, for allowing me the opportunity to pursue my research interests as outlined in this dissertation. With her assistance, I have transitioned from a recently graduated undergraduate student to a diverse researcher within earthquake engineering and its many explored areas, so far in my career. I would also wish to express my gratitude to my doctoral committee members: Professors Joel Conte, Yuri Fialko, Peter Shearer, and P. Benson Shing for their time, support, and excellent suggestions. In addition, Professors Conte and Shing of Structural Engineering have greatly expanded my knowledge in structural and earthquake engineering through their dedication to students both in class and through an open door policy, greatly facilitating my education and research. Professors Shearer and Fialko assisted in my knowledge through classes and discussions related to both geophysics and seismology which provided extensive background relevant to earthquake engineering and my research.

Within my graduate career, I have been lucky to be surrounded by many graduate students who have supported me in both idea-sharing, critique of work, and general friendship and support. I would particularly like to thank: Dr. Barbara Chang, Dr. Philipp Mahrenhotlz, Professor Andrè Barbosa, Dr. Derrick Watkins, Ms. Sue-Hsien Lin, Mr. Eduardo Velazquez, Ms. Christine Wittich, Mr. Weian Liu, Mr. Xiang Wang, Mr. Saurabh Prasad, and Mr. Li Ge. Additional thanks go to those who have assisted me in the proofreading of this work, particularly Christine Wittich and Patrick Shaw.

There have also been others who have helped me on my current career path and encouraged me to pursue graduate school. A strong desire to pursue earthquake engineering developed within the National Science Foundation's Research Experience for Undergraduate where I spent the summer of 2005 at SUNY Buffalo under the guidance of Professors Gilberto

Mosqueda, André Filiatrault, and then current graduate student Dr. Rodrigo Retamales. Additional support and encouragement came from Dr. William P. Garvey, a mentor since elementary school and formerly at Mercyhurst College, and Dr. Kerop D. Janoyan at Clarkson University.

Lastly, I would like to thank the generous and loving support of my family and friends particularly, my parents John and Barbara, late grandma Mary Bronakoski, sister Cynthia Fetzner, cousin Caroline Honour, and close friend Patrick Shaw. Their constant encouragement and support provided motivation to continue my graduate studies throughout the years.

Chapters 1, 2 and 3 contain material that was published in the following technical report, in which the author of this dissertation was the primary author:

Wood, R.L. and Hutchinson, T.C. (2012). A Numerical Model for Capturing the In-Plane Seismic Response of Interior Metal Stud Partition Walls. NEES-Nonstructural Technical Report. MCEER 12-0007. University at Buffalo, State University of New York (SUNY).

Chapter 4 and Section 6.6 contain material that was published in the following technical report, in which the author of this dissertation was the primary author:

Wood, R.L., Hutchinson, T.C., Lee, C., and Grigoriu, M.D. (2012). Fragility Function Development for Nonstructural Component Systems. NEES-Nonstructural Technical Report. MCEER 12-00XX. University at Buffalo, State University of New York (SUNY) (In preparation).

Chapter 5 contains material that was published in the following journal paper in which the author of this dissertation was the primary author:

Wood, R.L. and Hutchinson, T.C. (201X) “Ground Motion Effects on Nonlinear Higher Mode Building Response.” Earthquakes and Structures. (Accepted-In press).

This research opportunity would not have been possible without the support from numerous funding agencies. My initial research opportunity was supported by the Hilti Corporation through the *Hilti Seismic Project*: *Simulation and Testing to Support Seismic Design of Anchorage*, involving the University of California San Diego, San Diego State University, and the Universität Stuttgart. Dr. Matthew Hoehler was the research director, where technical oversight was provided by Dean Frieder Seible, Dr. Ulrich Bourgund, Mr. Rainer Hüttenberger, and Mr. John Silva, and core technical group members included Professors Robert Dowell and Rolf Eligehausen.

My second research opportunity was supported by the NEES-Nonstructural project under National Science Foundation Award #CMMI-0721399, “NEESR-Grand Challenge: Simulation of the Seismic Performance of Nonstructural Systems”. Dean Manos Maragakis (University of Nevada, Reno) is the principle investigator of this project where co-principle investigators include Professor André Filiatrault (SUNY Buffalo), Professor Tara Hutchinson, Professor Steven French (Georgia Tech), Mr. William Holmes, and Mr. Bob Reitherman (CUREE). Key interactions within this project for the success of my research include, Professors Mircea Grigoriu and Gilberto Mosqueda, Dr. Rodrigo Retamales, Mr. Changhoon Lee, Mr. Joseph Wieser, and Mr. Ryan Davies. The author particularly thanks the SUNY Buffalo team for providing a comprehensive and readily useable set of experimental data on partition wall behavior. In addition, the use of a 3-story hospital numerical building model provided by Joseph Wieser of the University of Nevada-Reno, is greatly appreciated.

Lastly my research career has been augmented in a new way through an interdisciplinary and collaborative project under IGERT Award #DGE-0966375, "Training, Research and Education in Engineering for Cultural Heritage Diagnostics”. In this project, I have had the opportunity to examine the structural and earthquake engineering aspects related to cultural

heritage. This provided for a great learning opportunity in beautiful Florence, Italy, with the assistance of Professor Falko Kuester, Alexandra Hubenko, and Maurizio Seracini.

Fellowships augmenting my academic career include a Powell Fellowship, Regents Fellowship, and a Structural Engineering Dissertation Fellowship. Opinions, findings, and conclusions are those of the author and do not reflect those of any of the sponsoring agencies.

VITA

EDUCATION

2006	B.S. with Greater Distinction, Civil Engineering (Structural Engineering Concentration), Clarkson University, Potsdam, New York
2009	M.S., Structural Engineering, University of California, San Diego
2012	Ph.D., Structural Engineering, University of California, San Diego

AWARDS & FELLOWSHIPS

2003	Living the Mission Service Award for Excellence, Compassion, Creativity and Service to Others, Mercyhurst College, Erie, PA
2006	Charles Martin Clark Prize for Outstanding Character and Scholarship, Clarkson University
2006-2009	Powell Fellowship Recipient
2007-2008	Regents Fellowship Recipient
2011-2012	IGERT Fellowship Recipient
2012	Dissertation Fellowship Recipient

PUBLICATIONS

Journal Papers

Wood, R.L. and Hutchinson, T.C. (201X). "Crack Protocols for Anchored Components and Systems." ACI Structural Journal. (Accepted-In press).

Wood, R.L. and Hutchinson, T.C. (201X). "Ground Motion Effects on Nonlinear Higher Mode Building Response." Earthquakes and Structures. (Accepted-In press).

Hutchinson, T.C., and **Wood, R.L.** (201X). "Cyclic Load Protocol for Anchored Nonstructural Components and Systems." Earthquake Spectra. (Accepted-In press).

Wood, R.L. and Hutchinson, T.C. (201X). "Lumped Model for Capturing the In-Plane Seismic Response of Partition Walls." ASCE Journal of Structural Engineering. (In review).

Technical Reports

Wood, R.L., Hutchinson, T.C., Lee, C., and Grigoriu, M.D. (2012). Fragility Function Development for Nonstructural Component Systems. NEES-Nonstructural Technical Report 12-00XX. University at Buffalo, State University of New York (SUNY) (In preparation).

Wittich, C.E., Hutchinson, T.C., **Wood, R.L.**, Kuester, F., and Seracini, M. (2012). Survey and Characterization of Culturally Important Statues in Florence Italy. Structural Systems Research Project Report Series. SSRP 12/XX. Department of Structural Engineering, University of California, San Diego. La Jolla, California (In preparation).

Wood, R.L. and Hutchinson, T.C. (2012). A Numerical Model for Capturing the In-Plane Seismic Response of Interior Metal Stud Partition Walls. NEES-Nonstructural Technical Report 12-0007. University at Buffalo, State University of New York (SUNY).

Wood, R.L., Hutchinson, T.C., and Hoehler, M.S. (2009). Cyclic Load and Crack Protocols for Anchored Nonstructural Components and Systems. Structural Systems Research Project Report Series. SSRP 09/12. Department of Structural Engineering, University of California, San Diego. La Jolla, California.

Conference Proceedings (Refereed)

Wood, R.L., Hutchinson, T.C., Wittich, C.E., and Kuester, F. (2012). "Characterizing Cracks in the Frescoes of Sala degli Elementi within Florence's Palazzo Vecchio." 4th Euro-Mediterranean Conference. Lemesos, Cyprus, October.

Wittich, C.E., Hutchinson, T.C., **Wood, R.L.**, and Kuester, F. (2012). "A Method for an Integrative Documentation and Characterization of Culturally Important Statues for Seismic Analysis." 4th Euro-Mediterranean Conference. Lemesos, Cyprus, October.

Wood, R.L. and Hutchinson, T.C. (2012). "A Numerical Model for Capturing the In-Plane Seismic Response of Interior Metal Stud Partition Walls: Preliminary Coupled Analysis" 15th World Conference on Earthquake Engineering, Lisbon, Portugal, September.

Wood, R. and Hutchinson, T. (2010). "Effects of Ground Motion Scaling on Nonlinear Higher Mode Response" 9th U.S. National and 10th Canadian Conference on Earthquake Engineering Proceedings, Toronto, Ontario. July.

Grigoriu, M., Gupta, A., Hutchinson, T., Reinhorn, A., and **Wood, R.** (2010). "A Methodology for Constructing Seismic Fragilities Based on Experimental and Mechanical Models" 9th U.S. National and 10th Canadian Conference on Earthquake Engineering Proceedings, Toronto, Ontario. July.

Contributing Author

Delta Seismic Loading Project (2012). Fragility Evaluation of Mechanical and Electrical Equipment under Seismic Loading. Department of Water Resources (In preparation).

Meneses, J. (ed). (2010). El Mayor-Cucapah, Baja California Earthquake April 4, 2010. An EERI Reconnaissance Report. Earthquake Engineering Research Institute, Oakland, California.

Stewart, J.P. and Bradenberg, S.J. (lead) (2010). Preliminary Report on Seismological and Geotechnical Engineering Aspects of the April 4, 2010 Mw 7.2 El Mayor-Cucapah (Mexico) Earthquake. Version 1. Report to the NSF-GEER Team.

ABSTRACT OF THE DISSERTATION

Partition Wall Subsystem Modeling and Effect on the Coupled Building System Response

by

Richard Lee Wood

Doctor of Philosophy in Structural Engineering

University of California, San Diego, 2012

Professor Tara C. Hutchinson, Chair

The cost of earthquake-induced damage to nonstructural components and systems (NCSs) has greatly exceeded the cost of structural damage. Although, numerous types of NCSs exist and contribute to this damage, one of the most prevalent is the light-weight (metal or wood stud) interior partition wall. The interior partition wall (PW) is a complex system with multiple attachments between floors, structural walls, or columns. Although these systems are not anticipated to interact with the building significantly; to date, few studies have been conducted to comprehensively evaluate if they influence the response of the building. What is known is that PWs are subjected to the dynamic environment of the building and continue to observe damage at much lower amplitude seismic demands than that of the structural system. As a result, building designers would benefit from numerical tools for predicting the impact of PW subsystems on the

overall building response and evaluating the PW behavior itself. To this end, a numerical model is developed that captures the in-plane seismic response of full-height cold-formed steel framed PWs. This behavior is lumped into a nonlinear zero-length spring for ease of implementation in beam-column type finite element analyses. Experimental data is used to calibrate the model by representing the force-displacement and the dissipated energy relationships. Two different error metrics are used to illustrate the model's robustness with particular attention to the prediction of experimental behavior.

To evaluate the effects of the PW on the building response, a suite of nine building models with a wide fundamental period distribution is selected. Eigenvalue, nonlinear pushover, and nonlinear time history analyses are used to examine the effects on the interstory drift and floor acceleration. Analyses indicate that the fundamental period can decrease up to 15%, due to the added stiffness of the partition wall. If the PW is neglected in the building analysis, the peak interstory drift and floor acceleration can be underestimated by approximately 50%. By tracking the period of the coupled (building-partition wall) system, the PW is shown to soften before the structural system. This softening confirms the vulnerability of the PW system at lower spectral demands, which is consistent with earthquake reconnaissance and experimental observations.

Chapter 1 Introduction

1.1 Motivation

Nonstructural components and systems (NCSs) are elements within a building, either attached to the floors or walls, which are not designed nor anticipated to contributing to the primary load bearing system of the building. Nonetheless, they will be subjected to the dynamic environment of the building undergoing seismic loading. Three broad categories of nonstructural components and systems are: 1) architectural elements, such as partition walls, suspended ceilings and lighting systems; 2) mechanical and electrical equipment, such as piping systems, fire protection systems, storage tanks, computer and data equipment, and power transformers; and 3) building contents, such as bookshelves, file cabinets and other furniture (BSSC 2000; Villaverde 2009). In recent earthquakes, it has been noted that the damage to building NCSs has not only been widespread, but significantly exceeds the damage to the structure itself. Therefore, study of their response under seismic excitation has seen more attention in recent years.

NCSs support the building's functionality and as such their damage or loss of use can be more economically significant than that associated with structural damage. Secondary effects associated with failure of NCSs have proven highly disruptive to businesses, their functionality, and revenue. Some examples of failures in the past include water damage caused by failure of sprinkler systems for fire protection, lack of emergency power, failure of suspended ceilings and partition walls (Figure 1.1). While many of these failures usually only affect the building performance after a seismic event. However, they are capable of causing serious injuries or loss of life (Filiatrault et al., 2002; EERI, 2010a). Regardless, damage to a building's NCSs resulted in operations being halted at airports, hospitals, emergency call centers, and water distribution centers. For example, during the 2010 Maule (Chile) Earthquake, 83% of hospitals in the region

affected by the earthquake had reduced or total loss of functionality due to nonstructural failures even though no noticeable structural damage occurred (EERI, 2010b).

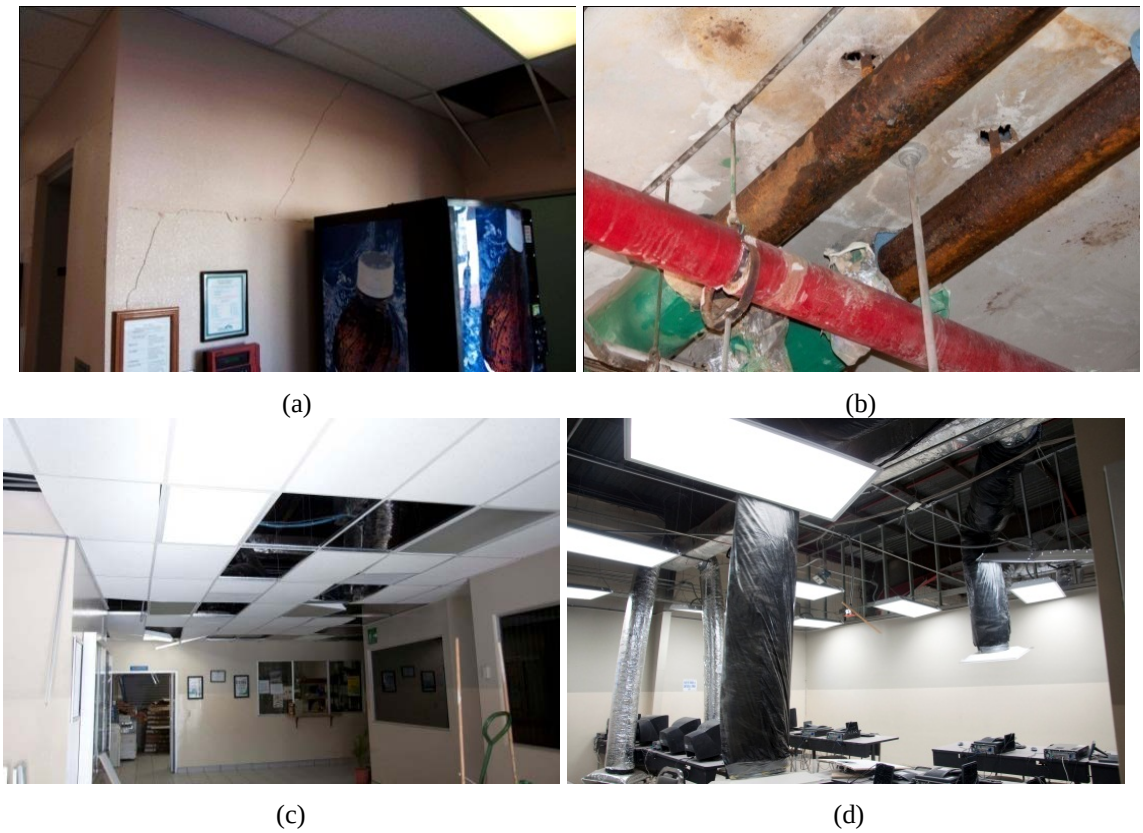

(a) (b)

(c) (d)

Figure 1.1 Examples of nonstructural failures from the 2010 Baja California Earthquake (Mw=7.2). Partition wall (a) and pipe failures (b) at El Centro Regional Medical Center; and, ceiling fallout (c) and HVAC system failure (d) at Universidad Autónoma de Baja California (UABC) in Mexicali, BC.

NCSs within buildings often have complicated configurations and connections to a building making them susceptible to earthquake damage. The majority of NCSs are placed or distributed throughout a building, and therefore not subjected to the ground motion generated by the earthquake, but rather to an amplified and filtered motion transmitted by the building. In addition, the response of the NCS depends on its location within the structure, since the demands vary by floor and location. The mass, stiffness and damping characteristics of the NCSs are usually small when compared to the structure itself. However, when the frequency of the NCSs and the building are similar, the NCS is capable of experiencing severe resonance. When the NCS

is stiff and heavy enough, it may modify the response of the building structure. The NCSs may be connected or attached to multiple locations within the building inducing differential movements on the component such as this case with distributed piping systems or partition walls. As a result, the NCS and the building structure should be considered as a combined system when analyzing the NCS or building response for effective prediction (Villaverde, 2009).

Considering the many complexities of NCSs, it is also unfortunate that the largest investment in the construction of buildings is associated with nonstructural components and systems. Studies of the cost breakdown of typical buildings have shown that NCSs are the largest investment for offices, hotels and hospitals, shown in Figure 1.2 (Taghavi and Miranda, 2003). The percent cost of the building for nonstructural components vary from 48% in hospitals to 70% in hotels. While the building contents, which are greatly influenced by the performance of the nonstructural systems, range from 17% to 44% of the total building.

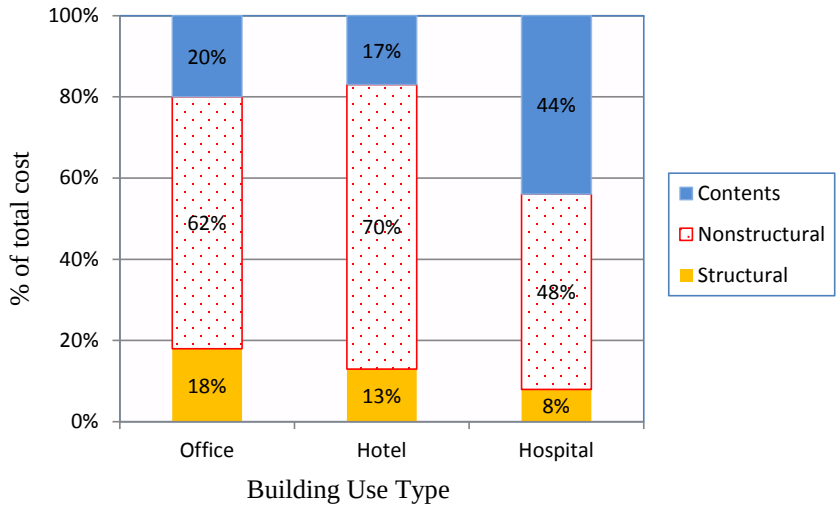

Figure 1.2 Cost breakdown of typical office, hotel and hospital buildings. (after Taghavi and Miranda, 2003)

1.2 Partition Wall (PW) Subsystems

One common NCS within nearly all buildings is a partition wall. Partition walls (PW) are intended to be non-load bearing walls used within the interior of a building to divide the space into its occupancy or use needs. Within office buildings, a greater percentage of PWs within the floor plan might be observed due to the need to create nominal sized office spaces for the occupants. From a construction point of view, PWs are a complex system attached at multiple locations within the building, either floors, columns, or structural walls. Like other NCSs however, they are subject to the dynamic environment of a building's filtered seismic motions. Typically, the seismic response of in-plane PWs are controlled by the interstory drift (floor-to-floor differential displacements). However, the PW response can also be influenced by acceleration demands in the case of attached masses such as bookshelves, televisions, etc.

1.2.1 Example of Observed PW Behavior in a Full-Scale Building Test Program

In an experimental study conducted at the University of California, San Diego, PWs were placed within a full scale test specimen simulating a fully operational building on a full-scale outdoor shake table (Figure 1.3)[1]. The building nonstructural component and systems (BNCS) specimen was a 70 foot tall, five story building, with a range of occupancies at each floor level, including office, hospital, and residential spaces (Figure 1.4). The PWs distributed throughout this building are typical of modern construction practice; that is gypsum board on light gauge steel studs. Typical construction details include: c-channel bottom tracks, slotted c-channel top tracks, and vertical c-channel studs, each installed using metal screws (Figure 1.5). An overview of the pre-test specimen is illustrated in Figure 1.6, where this spherical panorama image

[1] Full-Scale Structural and Nonstructural Building System Performance during Earthquakes & Post-Earthquake Fire (http://bncs.ucsd.edu).

illustrates nearly a 360 x 180 degree field of view. The test sequence for this project involved subjecting the specimen to a series of seven earthquake motions while the building was supported on high damping rubber isolators, and six earthquake motions while the building was fixed to the shake table. Finally, live fire tests were conducted on the third level of the building simulating post-earthquake fire. Figure 1.7 illustrates the final state of the PWs at level 3 following seismic and fire testing. Note various cracks, crushing locations, and detached PWs that dramatically reduced the fire rating of the PWs at this floor.

Figure 1.3 Elevation view of the south side of the five-story building test (BNCS) conducted at the University of California, San Diego. (http://bncs.ucsd.edu)

Figure 1.4 Spherical panorama of the second floor of the BNCS building just prior to testing.

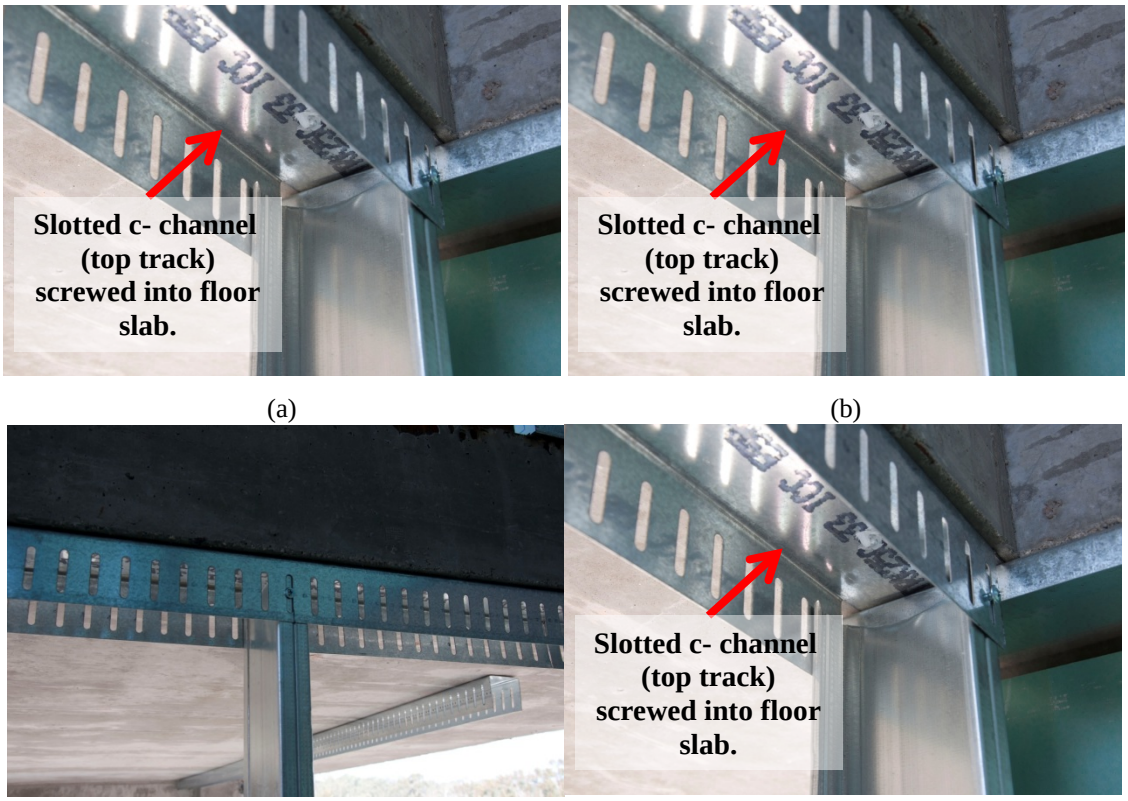

(a) (b)

(c) (d)

Figure 1.5 Detailing of the PW installation within the BNCS project.

Figure 1.6 Overview of PW installation within the BNCS project.

Figure 1.7 Spherical panorama of the third floor after earthquake and fire test sequences.

After each phase of seismic testing of the BNCS project, damage of the PWs was documented. The damage to the PWs initiated in the early stages of testing before any damage to the primary or structural system occurred. This observation is highly consistent with field reconnaissance and other testing reports. Damage to the PWs was witnessed even while the building was base-isolated, where little to no damage occurred to other nonstructural components. Interstory drifts in this case were less than 0.5% (maximum). The types of damage modes noted within the PWs for these tests include (Figure 1.8):

- Screw pull-through (a): where the screw no longer restrains the PW (out of plane) as screw head had no bearing on the panel. Note the “blue 4” refers to the initiation of this damage state during the base-isolated configuration.
- Crushing (b): localized damage on the PW primarily along the boundary formed by the return wall (perpendicular) or floor slabs. Note the blue hatched region occurred during the base-isolated state, while the red hatched region of more detailed crushing occurred during the fixed base configuration.

- Tape flaking/cracks along panel boundaries (c): along the boundaries of each gypsum panels, cracks develop first followed by tape flaking. Note the blue line initially marked cracks developed initially during the base-isolated phase, while the red arrow signifies the tape flaking off and a small gap opening up during the fixed based configuration.
- Gap at boundaries (d): as damage accumulates along the wall boundaries and permanent displacement offsets the PW, gaps develop at the boundaries. This type of damage is characterized by larger interstory drift demands which were developed in the fixed based configuration. Gaps also develop due to the pounding of perpendicular walls at corners.
- Detachment (e): with significant screw pull-through, the panels become loose with a potential for collapse. This damage state was rare in the experiment and developed when excessive interstory drift demands (> 5%) occurred as a result of a localized soft story mechanism in the primary system. This damage state can cause significant bodily injuries and possibly death.

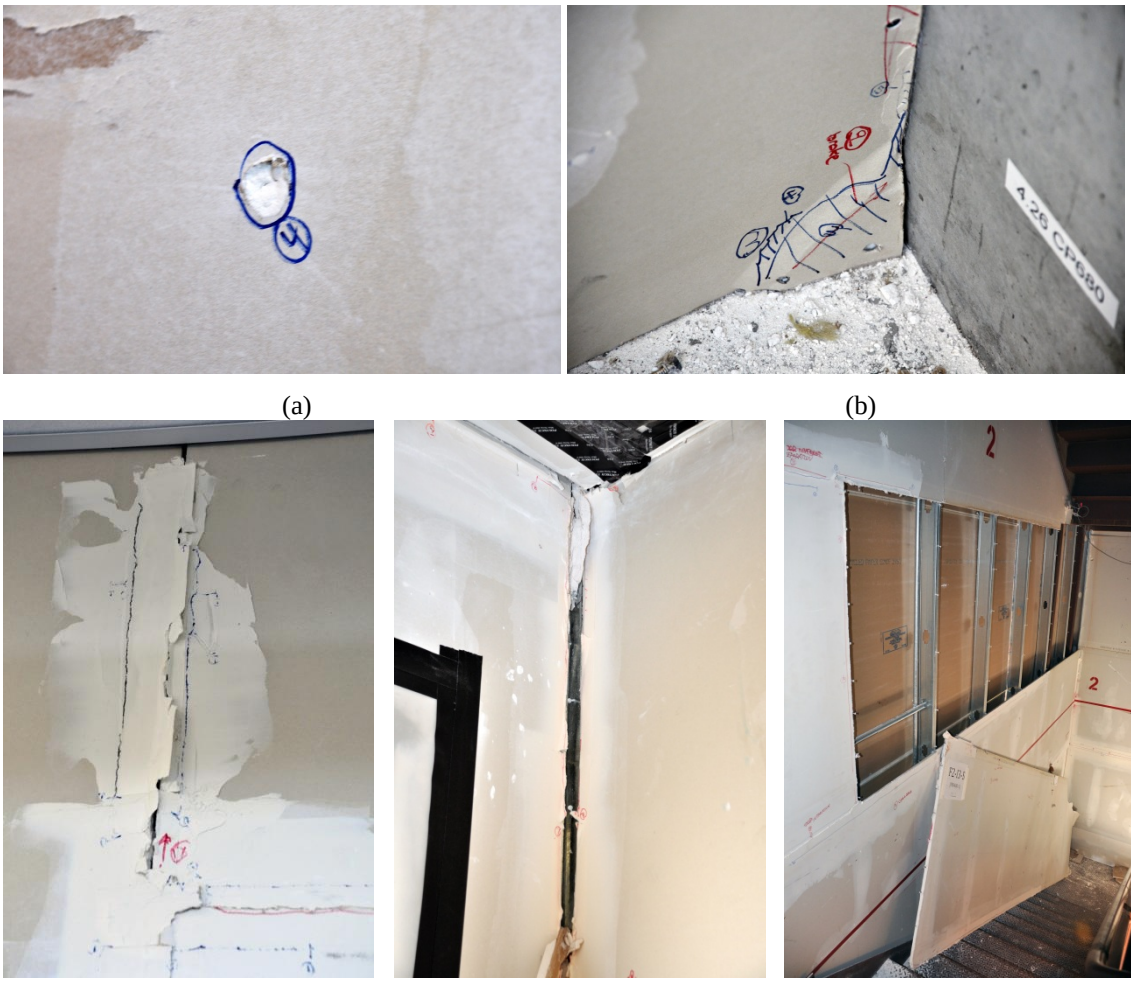

(a) (b)

(c) (d) (e)

Figure 1.8 Typical PW failure modes observed during the BNCS test project at UCSD: (a) screw pull-through, (b) crushing in corner and along return wall, (c) tape flaking/cracks along panel boundaries, (d) gap and damage concentrated at intersection of wall boundary, and (e) detachment of panel.

1.2.2 PW Damage Observed in Post-Earthquake Reconnaissance

The same failure modes for PWs simulated during the BNCS test have been observed following many past earthquakes, for seismic events of varying magnitude in many diverse geographical regions. Figures 1.9 through 1.15 highlight select field-observed PW damage from the 2010 Eureka, 2010 Maule (Chile), 2010 El Mayor – Cucapah (Baja California), 2011 Tōhoku, and the 2012 Emilia earthquakes. The moderate earthquakes of Eureka and Emilia significantly

damaged PWs while there was no evidence of damage to the primary structure (Figure 1.9; Figure 1.15). More moderate PW damage is noted through extensive cracking in remaining photographs. Figure 1.11 illustrates how PWs can compromise the cleanliness standard of a surgical room as was the case after the Chilean earthquake. Figure 1.10 and Figure 1.14 demonstrate the collapse potential of PWs and the possibility of a life-threatening hazard, as observed following the Chilean and Tōhoku events.

Figure 1.9 2010 Eureka California (M_w=6.5): interior PW damage.
(From Eureka Earthquake Clearinghouse, 2010)

Figure 1.10 2010 Maule (Chile) Earthquake (M_w = 8.8): interior PW damage from Felix Bulnes Hospital in Santiago demonstrating a collapsed out-of-plane wall. (Photo from: G. Mosqueda)

(a) (b)

Figure 1.11 2010 Maule (Chile) Earthquake (M_w = 8.8): interior PW damage from Main Santiago Hospital : (a) in-plane damage and (b) damage imposed from attached television monitor. (Photos from G. Pekcan)

(a) (b)

Figure 1.12 2010 Maule (Chile) Earthquake (M_w = 8.8): PW wall damage from Hospital Clinica Herminda Martin, Chillán, Chile: (a) PW cracks in surgical room and (b) widespread PW cracks within a hallway.
(Photos from: G. Mosqueda)

(a) (b)

Figure 1.13 2010 El Mayor - Cucapah (Baja California) Earthquake (M_w = 7.2): nonstructural damage at the Facultad de Ciencias Administrativas of UABC Mexicali: (a) PW damage and (b) PW, suspended ceiling and hvac system damage.

Figure 1.14 2011 Tōhoku (M_w=9.0): temporarily shored damaged interior PW within a gymnasium within the Ibaraki prefecture, Japan.
(From NILIM, 2011)

(a) (b)

Figure 1.15 2012 Emilia Earthquakes (M_w=6.1): interior PW damage within a hospital in Bondeno, Italy.
(From Magenes et al., 2012)

1.3 Scope of Research

The research presented herein focuses on numerical modeling of the PW to facilitate assessment of its response under seismic loading particularly during building design. First, a simple lumped PW model is needed. This model should be developed using knowledge gained

from experiments conducted on the PW as a component. Herein, a design oriented lumped PW model is developed. The motivation for the lumped model is primarily simplification, whereby a single zero-length one degree-of-freedom element captures the PW behavior without greatly increasing the degrees-of-freedom and additional computational resources. The calibration of the model uses experimental data to characterize the force-displacement relationship and the dissipated energy. Error metrics associated with average residual force and half-cycle hysteretic energy illustrate the model's robustness with particular attention to how successful the models are in prediction of experimental behavior.

Subsequently, an analyst needs to assess if the PW element is needed in the building model. Although traditionally it is believed that the PW stiffness is negligible, compared to that of the building with a greater percentage of PW utilized in modern buildings, which are becoming more flexible, it is unclear how the PW will affect the dynamic response of modern buildings. Therefore, the second step of this research was to conducted coupled (building-partition wall) analyses. The effect of the PW on the building response is quantified through eigenvalue, nonlinear pushover, and nonlinear time history analyses. In particular, interstory drift and floor accelerations are examined when the coupled system is subject to a suite of realistic earthquake motions.

1.4 Organization of Dissertation

This dissertation consists of seven chapters. Chapter 1 describes the motivation for the work, defines the problem, and summarizes the scope of the dissertation. Chapter 2 presents a brief literature review regarding prior experiments conducted on PWs, as well as, development of numerical lumped models to characterize the PWs. Chapter 2 also presents the PW model developed in this work, which was implemented in the OpenSEES platform (Mazzoni et al., 2011). Chapter 3 describes the error metrics used to demonstrate the robustness of the developed

model. Chapter 4 provides the necessary background to assess the coupled building-partition wall system including the selection of a suite of buildings, implementation of the PW, and analysis procedures. Chapter 5 examines the effect of ground motion scaling and the resulting effect on a suite of buildings in terms of best representing the interstory drift and floor acceleration distributions. Chapter 6 analyzes the nonlinear time history response of the coupled system and summarizes the effect that the PW has on this system. Chapter 7 provides conclusions of this dissertation and recommends future research topics. Appendix A presents the developed PW model script and an example placement into a building model . Appendix B includes detailed results of the nonlinear time history analyses and intermediary steps of post-processing. Appendix C contains the details outlining the effect of the building-partition wall system.

1.5 Acknowledgement

Section 1.1 of this dissertation is based on the NEES-Nonstructural Report, *A Numerical Model for Capturing the In-Plane Seismic Response of Interior Metal Stud Partition Walls,* published at the State University of New York, University of Buffalo. The co-author of this report is Tara C. Hutchinson, while the dissertation author is the primary author and investigator.

Chapter 2 Partition Wall Modeling

2.1 Introduction

To develop a simple partition wall (PW) model, robust performance is sought and it is key to have a broad database of experiments to guide selection of model parameters and validate its performance. In this work, the numerical platform OpenSees (Mazzoni et al., 2011) is utilized with the PWs in-plane response realized using a lumped model, which is discretized via a zero-length element coupled with the *pinching4* material, used in a parallel configuration. The *pinching4* material, which will be described later, provides flexibility to create a general force-displacement hysteric response, and therefore capture the subtle nuances of the PW. Development of a numerical model will allow for the evaluation of the PW performance under realistic loading, demonstrate its effect on larger building models, and later serve as a possible basis for design-oriented modeling techniques.

Prior to outlining the model methodology, a literature review is conducted demonstrating the knowledge gathered from previous experimental testing and numerical studies. Subsequently, the lumped model methodology is descried. Specifically, the calibration procedure and formulation of two sets of models are discussed. The first set of models characterizes the installation technique as dictated by building occupancy (or use). A second set characterizes fully connected wall specimens with the goal of evaluating dispersion within the experimental data.

2.2 Previous PW Studies

The following two subsections focus on detailing pertinent previous experimental studies and comparing the findings and shortcomings between them. Additional details regarding the

literature review pertaining to both the experimental studies and developing lumped numerical models are found in the report by Wood and Hutchinson (2012).

2.2.1 Previous Experimental Studies

The following discusses past efforts relevant to studying the performance of gypsum PWs. This literature review covers only the basics of previously tested gypsum PWs on both light-gauge steel and wood studs. Particular focus is directed towards the behavior of the gypsum PWs and key findings from each study.

Serrette et al. (1997) tested thirteen full-size walls of 8.0 feet by 8.0 feet constructed of light-gauge cold-formed steel stud walls, with the objective of studying the contribution of flat strap tension x-bracing, gypsum sheathing, and gypsum wall board to the in-plane shear resistance. For the frame setup, 20 gauge studs (30 mil) were placed at 24 inches on center with drywall screws at 6 inches on center in the perimeter and 12 inches on center in the field. The specimens were then loaded in plane incrementally to 25%, 50% and 75% of the estimated maximum load and then to failure. The general failure mechanism was breakage of the paper cover of the gypsum sheathing and the underlying gypsum. Prior to failure, the drywall screws rotated and pulled through the surface of the gypsum. Notable observations included: each of the gypsum panels behaved independently of each other, the shear strength of the wall decreased when the edges of the panel broke at the screw locations, and the screw edge distance did not have a significant effect on shear strength. The main strength of the wall was suggested to be governed by the penetration of the screw head.

In the follow up study, Serrette et al. tested twenty small-scale tests of 2 feet by 2 feet walls to assess the shear behavior of screw connections along the edge of the panels for plywood, oriented strand board, gypsum wallboard and FiberBond wallboard. These smaller panels were loaded in tension until failure occurred. The normalized shear strength of these walls was

comparable to the full-scale specimens, demonstrating that small scale tests provide a simple method for estimating the shear resistance.

A research program developed at the National Association of Home Builders (NAHB, 1997) Research Center was set up to assess the shear behavior of 40 foot long, cold-formed steel walls with openings. Four 8.0 feet by 40 feet shear wall specimens with 20 gauge (30-mil) studs at 24 inches on center were tested. Oriented strand board (OSB) (7/16” thick) was placed on the exterior and 1/2 inch gypsum was oriented vertically in the interior with screws at 7 inches on center along the perimeter with 10 inches on center in the field. The test frame for their study is shown in Figure 2.1. Variations explored in the study, included: openings due to doors and windows, percent sheathing, anchor bolt spacing and hold downs. The specimens were loaded monotonically until failure. The observations from the test sequence included: initial loading was linear until screw pull- through occurred which reduced the stiffness, and near the ultimate capacity the OSB experienced cracking in the perimeter screw connections and typically top track tearing. Additionally weak axis bending of the studs approximately 12 inches from the top of the specimen was observed, and was followed by OSB tear-out around the screw connections at the top of the wall.

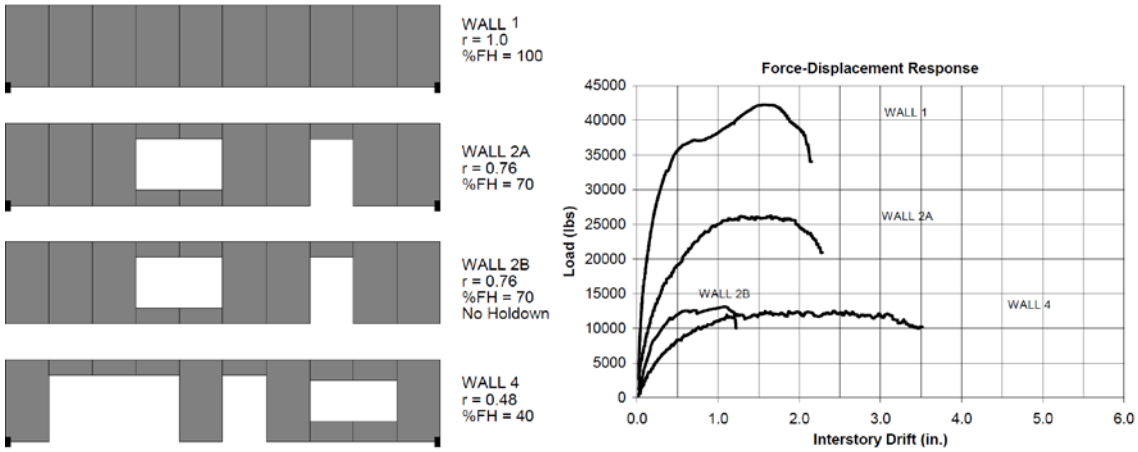

(a) (b)

Figure 2.1 NAHB shear wall configurations: (a) details and (b) force-displacement results. (from NAHB, 1997)

Arnold et al. (2003) tested 12 walls for the California Earthquake Authority (CEA)/Consortium of Universities for Research in Earthquake Engineering (CUREE) Woodframe Wall Testing Project. The first four walls (phase I) correspond to walls within the first level of a two-story structure; and, the remaining eight walls (phase II) represents single-story structure. The wall specimens were approximately 8.0 feet by 16.0 feet long with either two window openings or one window and one door opening using 1/2 inch gypsum, on wood studs. The loading protocol was the CUREE Abbreviated Loading History for Ordinary Ground Motions developed by Krawinkler et al. (2000) for the testing of woodframe structures. This protocol was applied to the testing frame in one stage (no repair to the damaged wall specimens) and in a staged approach to allow for the repair of the structure between the testing sequence. A key observation from the experimental program included the observation that the wall strength of the single story structures (phase II) was approximately 25% less than the two-story structure idealization tested in phase I, indicating that the boundary conditions were significant.

In the experimental program by Restrepo and Bersofsky (Bersofsky, 2004; Restrepo et al., 2010) 16 walls were built to determine the seismic fragility of gypsum wallboard partitions on steel studs. The specimens were 8.0 feet by 16.0 feet long and considered different connector

spacing, gypsum heights (full height vs. partial height), track connections, gypsum thickness, stud gauge and stud spacing (Table 2.1). These wall specimens were set up to simulate the interstory drift experienced during a seismic event for a typical office building, using the loading protocol selected based on the CUREE Abbreviated Loading History for Ordinary Ground Motions. This protocol was originally developed for the testing of woodframe structures (Krawinkler et al., 2000). To develop seismic fragility curves, three damage states were defined (Figure 2.2). Damage state 1 (DS_1) was minimal damage repairable by mud, tape and paint. Damage state 2 (DS_2) was characterized by superficial damage requiring replacement of gypsum sections and damage state 3 (DS_3) required full replacement of the wall. One key finding was that damage state 2 was not always obtained, as some specimens progressed directly from DS_1 to DS_3.

Table 2.1 Experimental configurations for Bersofsky's experiment. (after Bersofsky, 2004)

Test No.	Door	Connector Spacing (in)	Gypsum Height (ft)	Slip Track	Gypsum Thickness (in)	Stud Thickness (mil)	Stud Spacing (in)
1	Y	8.0	8.0	N	5/8	18	24
2	Y	8.0	8.0	N	5/8	18	24
3	**N**	8.0	8.0	N	5/8	18	24
4	Y	**12.0**	8.0	N	5/8	18	24
5	Y	8.0	**6.5**	N	5/8	18	24
6	Y	8.0	8.0	**Y**	5/8	18	24
7	Y	8.0	8.0	N	**1/2**	18	24
8	Y	8.0	8.0	N	5/8	**30**	**16**

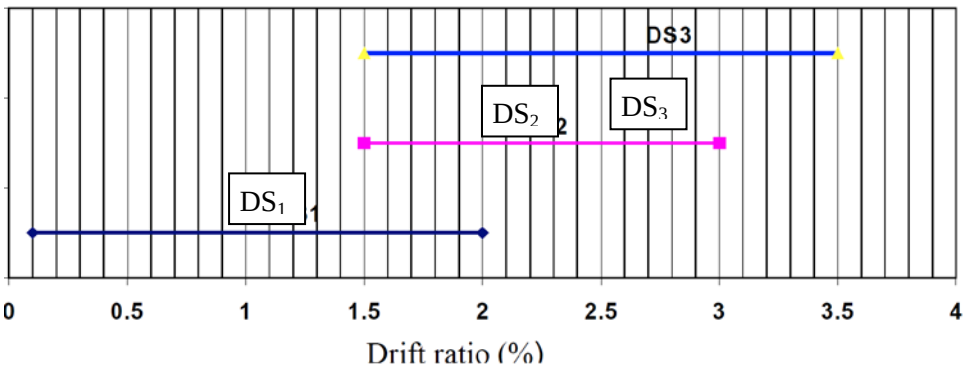

Figure 2.2 Damage state fragility functions for Bersofsky's experiment. (from Bersofsky, 2004)

Continuing the work of Bersofsky et al. (2004), Lang and Restrepo (2007) constructed two identical specimens with light-gauge steel stud gypsum wallboard to represent a typical office room (Figure 2.3). Both rooms had dimensions of 12 feet by 15 feet with additional features of a utility cutout, two t-wall (cantilever) configurations and a column wrap. The specimens were constructed using 20 gauge studs 3-5/8 inch at 24 inches on center, and a gypsum thickness of 5/8 inch. Specimen 1 used the recommended loading protocol from ATC-58 and specimen two used a modified version, which reduced the low amplitude cycles while increasing the amplitude rate (Figure 2.4). This study revealed that the seismic performance of light gauge metal stud construction is sensitive to loading protocol.

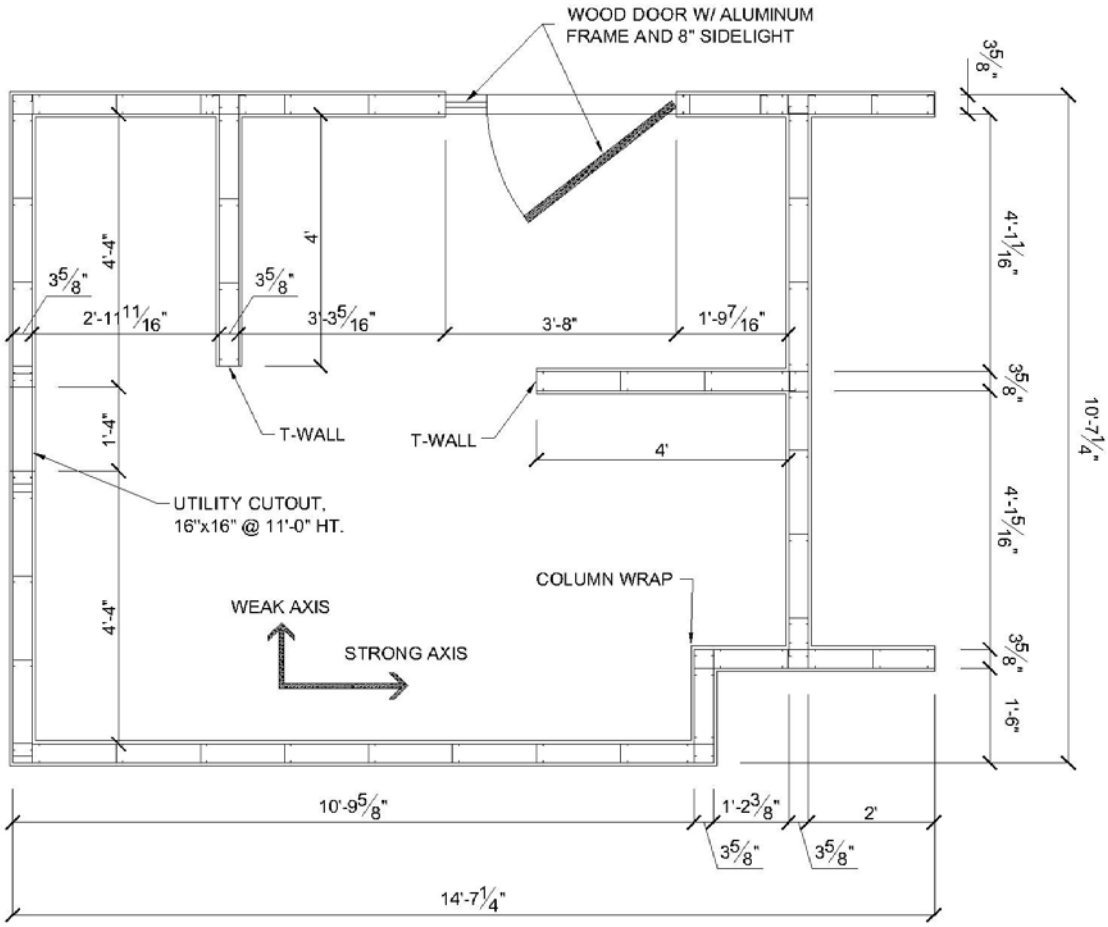

Figure 2.3 Plan view of test specimen for Lang's experiment.
(from Lang and Restrepo, 2007)

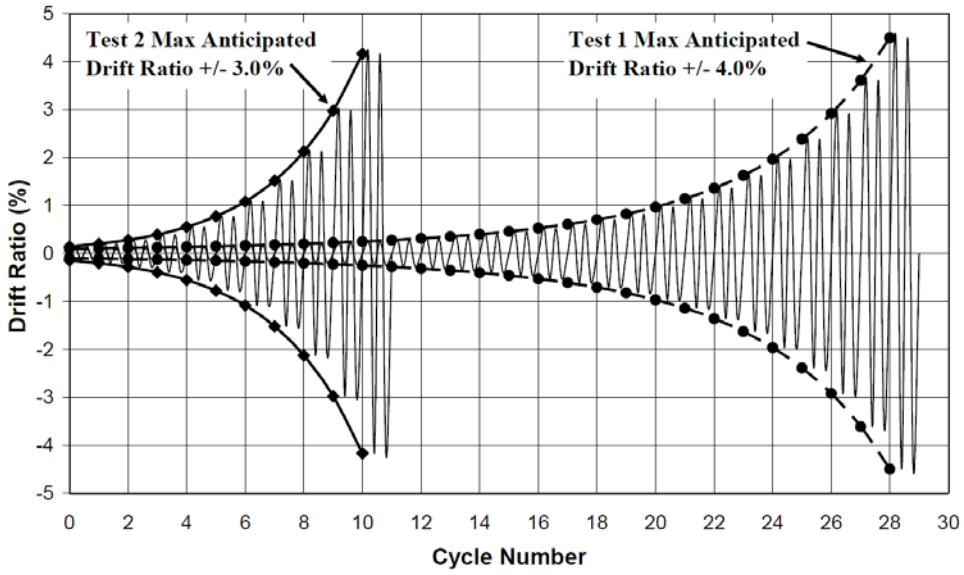

Figure 2.4 Testing protocols used in Lang's experiment.
(from Lang and Restrepo, 2007)

Lee et al. (2007) tested four light gauge steel framed walls with gypsum board to assess the performance and the repair costs associated with seismic demand of typical Japanese buildings. Three similar specimens (approximately 9 feet by 13 feet long) and a fourth specimen of 9 feet by 9.75 feet, were constructed with typical installation techniques to assess the sensitivity of quasi-static verses dynamic loading protocols and the effect of a window cutout. A common installation technique, which is different from US practice, is the provision for a vertical gap of 0.39 – 0.59 inches (10-15 mm) at the partition and return wall connection. This gap is provided to reduce the damage of the partition, since the partition is unrestrained by a return wall or column for small deformations. The walls saw no damage initially due to the gap at the partition ends, however when the PW beared on the boundary element (return walls), the PW sustained damage along the perimeter (Figure 2.5). When comparing the two load protocols, the dynamic loading effect was noted to be negligible. The resistance of these tested walls was

approximately 20% of the structural resistance of a steel moment frame, a value that is significant for design and analysis.

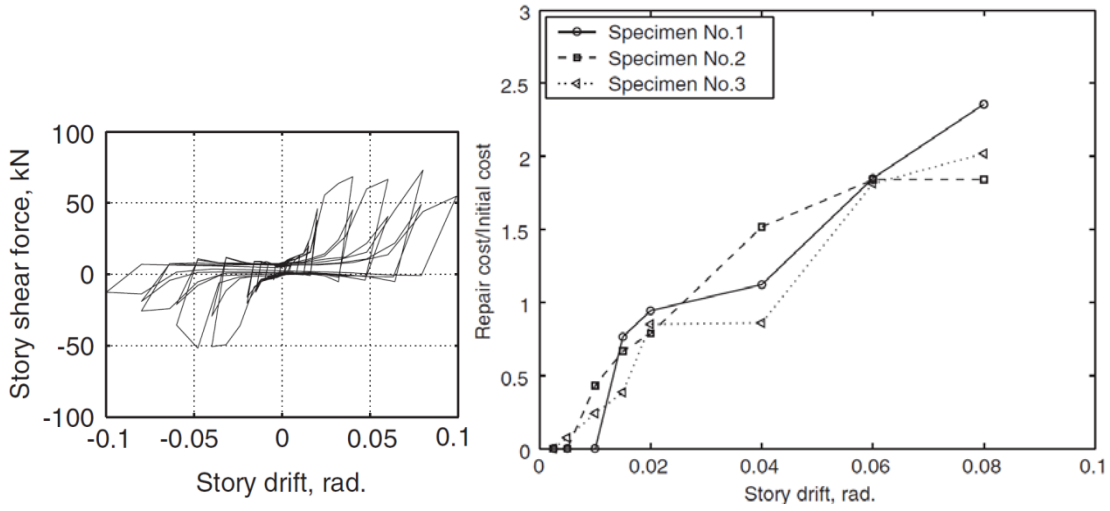

(a) (b)

Figure 2.5 (a) Hysteretic behavior of specimen 1 and (b) damage cost estimate versus story drift.
(from Lee et al., 2007)

2.2.2 NEES-GC Partition Wall Tests at SUNY-Buffalo

As part of the NSF-NEES[2] Grand Challenge (NEES-GC) Nonstructural Project[3], a larger series of PW experiments were conducted at the State University of New York, University at Buffalo (SUNY-Buffalo). The NEES-GC Nonstructural overall focused on the ceiling-piping-partition (CPP) system. This system consists of several subsystems having complex geometries and boundary conditions, which interact with each other. In addition, multiple support attachments throughout the building impose acceleration and deformation demands to the various subsystems, which are dependent on their placement location. Due to a lack of system-level

[2] NSF-NEES is the National Science Foundation-Network of Earthquake Engineering Simulation (NEES Nonstructural, 2012).

[3] NEES-Nonstructural Project (http://nees-nonstructural.org/).

research on the CPP system, the NSF-NEES Grand Challenge (GC) project was initiated by researchers across the United States. This project was led by the University of Nevada, Reno and included large scale testing at NEES sites and complimentary numerical simulations. A key goal of the project is to understand the seismic performance economic losses, loss of functionality and injury potential within a building. The work described herein contributes to this effort, with the focus on developing and calibrating a numerical model, for use in capturing the in-plane seismic response of PWs, a key subsystem within the CPP.

2.2.2.1 Overview of the NEES-GC PW Tests

Fifty wall specimens were tested at the SUNY-Buffalo with details defined by a group of industry practitioners familiar with common design configurations. These PWs were approximately 11.5 feet tall by 12 feet long with return walls (perpendicular to the loading direction) of either 2.0 feet or 4.0 feet (Davies, 2009). The wall specimens were placed in the upper level of the Nonstructural Component Simulator (UB-NCS), shown in Figure 2.6, which is a full scale two story frame loading system capable of reproducing motions between adjacent floors (Mosqueda et al., 2009). The subset variables considered in the various tested wall configurations, which were also parameters used in the numerical modeling included: connectivity of the sheathing and studs to the top and bottom tracks (slip track or full connection), spacing of the track-concrete fasteners (12 or 24 inches on center), wall intersection detailing, stud and track thickness (18 or 30 mil (0.0188 or 0.0312 inches in thickness), and spacing of the steel studs (16 or 24 inches) (Davies, 2009). To evaluate the drift sensitive PWs in the test program, a quasi-static protocol was selected as illustrated in Figure 2.7 (Retamales et al., 2011).

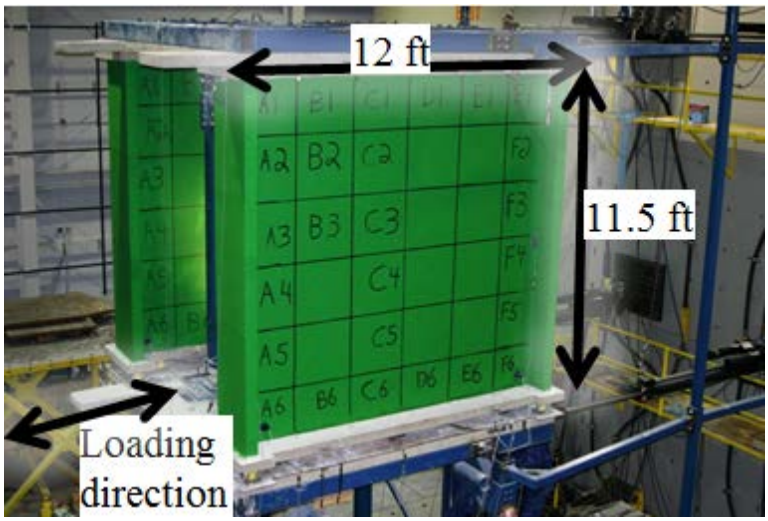

Figure 2.6 Typical in-plane PW experimental setup.
(photo courtesy of SUNY-Buffalo Experimental team)

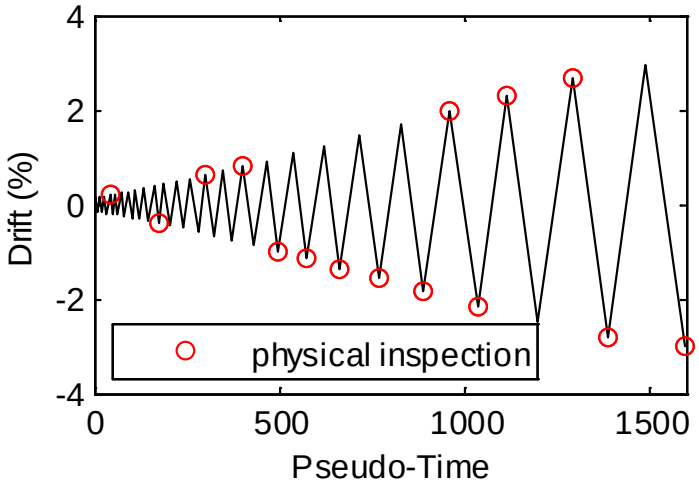

Figure 2.7 Quasi-static drift sensitive protocol utilized in the tests of Davies (2009).

2.2.2.2 Damage State Identification

Damage states (DS) were defined and adopted by SUNY-Buffalo (Davies, 2009) to describe the physically observed damage. To some extent these were delineated via the envisioned repair techniques. In the damage classification, three damage states were proposed: DS_1 as light damage, DS_2 as moderate damage and DS_3 as complete or severe damage (summary of the specimens in Table 2.2). DS_1 is characterized by primarily superficial damage, such as small cracks and/or screw popout. Damage within DS_1 can be repaired such that the wall appears new. DS_2 is more moderate damage, whereby the damage is localized and progressed. Physical examples include crushing in the wall corners, out of plane bending of the wallboard at wall intersections, or damaged boundary studs. DS_2 can be repaired in local damaged regions with gypsum and boundary stud replacement. DS_3 is the most severe damage, characterized by track damage or hinging of the studs. Walls reaching this state would require full replacement. It is noted that similar damage state classifications have been identified by others (e.g. Bersofsky, 2004; Restrepo and Lang, 2011). Table 2.2 indicates that the onset of DS_1 generally occurred between 0.2 and 0.4% drift, DS_2 between 0.4 and 1.0% drift, and DS_3 beyond 1% drift. The onset of a damage state is complicated by the limited observation points during testing (Figure 2.7; Davies, 2009). Importantly, however, the drift ratios at a given DS are most sensitive to the type of wall (commercial versus institutional) and its connection type (full versus partial).

Table 2.2 PW specimen damage state and modeling consideration (specimen data per tests by Davies, 2009).

Specimen No.	Subgroup	Construction Grade	Connection Type	Damage State (drift ratio, %)			Normalized Model
				DS_1	DS_2	DS_3	
1	1a	Commercial	Partial	0.20	0.62	0.62	
2	1a	Commercial	Partial	0.20	0.62	1.00	
3	1a	Commercial	Partial	0.40	0.62	0.62	
4	1b	Commercial	Full	0.40	0.62	1.16	X
5	1b	Commercial	Full	0.20	0.40	2.32	X
6	1b	Commercial	Full	0.40	0.62	2.66	
7	1b	Commercial	Full	0.20	0.62	1.00	
8	1b	Commercial	Full	0.40	1.00	1.00	X
9	1b	Commercial	Full	0.20	0.40	0.62	
10	1b	Commercial	Full	0.20	0.81	0.81	
20	2a	Institutional	Partial	0.20	1.00	2.32	
21	2a	Institutional	Partial	0.40	0.81	--	
22	2a	Institutional	Partial	0.62	0.62	1.00	
23	2b	Institutional	Full	0.40	0.81	1.00	X
24	2b	Institutional	Full	0.40	0.40	1.16	X
25	2b	Institutional	Full	0.40	0.40	0.62	X
26	2b	Institutional	Full	0.40	1.00	1.00	X
27	2b	Institutional	Full	0.40	0.62	0.81	X
28	2b	Institutional	Full	0.40	0.81	0.81	X

Note: rows in gray were identified as outliers in Section 1.5.

2.2.2.3 PW Types

Building occupancy will certainly affect the materials and details used for its PWs. For example, commercial grade PWs have thinner gauge studs, spaced at larger intervals, when compared with PWs installed in institutional buildings (Table 2.3). Likewise, stronger connections are required for the institutional configuration (Table 2.4). In this case gypsum board and vertical studs are screwed directly into the top track. Details in the connectivity of the specimens are illustrated in Figure 2.8. Consequently four types of PWs were identified as predominant, namely: 1) commercial, 2) institutional, 3) partial height and 4) remedial design (Davies, 2009). In the work presented herein, numerical models were developed for the subgroups 1a (commercial partially connected), 1b (commercial fully connected), 2a (institutional

partially connected) and 2b (institutional fully connected). Groups 3 and 4 were not selected for modeling. Group 3 refers to partial height specimens, in which the failure mechanism was governed by brace buckling. Due to the buckling nature of the braces, the unrestrained length of the studs is critical and to reasonably capture this, one needs to explicitly model the brace. These details may vary substantially in practice. Nonetheless, knowledge of the brace characteristics would allow for modification of the developed models herein by altering the top boundary condition. Group 4, remedial designs, was also not considered, since these are not typical construction practices.

Table 2.3 PW classification by subgroup. Only subgroups with full height specimens are considered.

Subgroup	Name	Description
1a	Commercial partially connected	Full-height specimens constructed using commercial practice and slip track connections
1b	Commercial fully connected	Full-height specimens constructed using commercial practice and full connections
2a	Institutional partially connected	Full-height specimens constructed using institutional practice and slip track connections
2b	Institutional fully connected	Full-height specimens constructed using institutional practice and full connections

Table 2.4 PW detailing.

Classification	Stud Thickness (in)	Number of Studs	Stud Spacing (in)
Commercial	0.0188	7	24
Institutional	0.0312	10	16

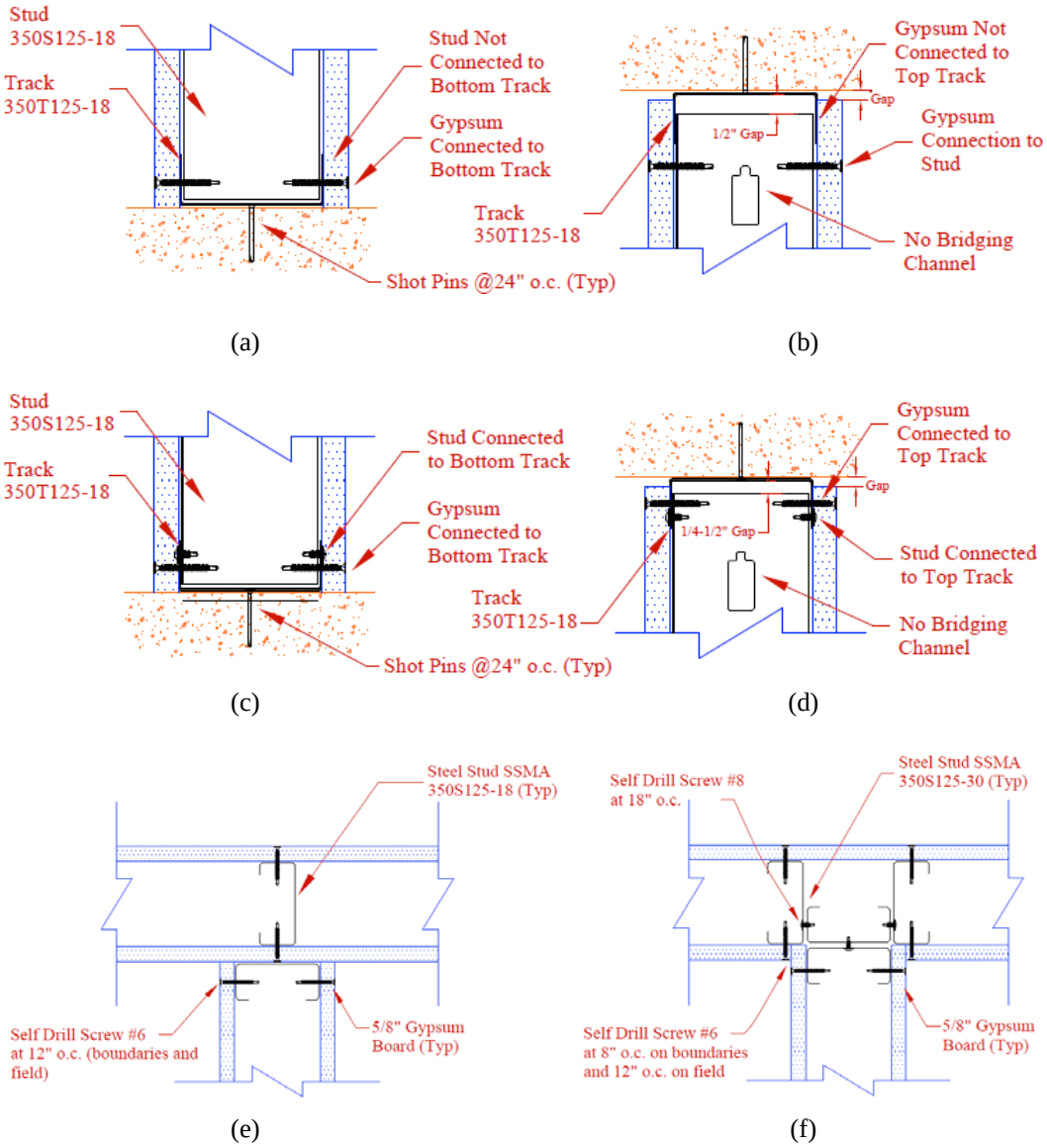

Figure 2.8 Sheathing and framing connectivity details: (a-b) bottom and top track connections for partially connected specimens (slip track), (c-d) bottom and top track connections for fully connected specimens, (e) wall intersection details for commercial construction practices and (f) wall intersection details for institutional construction practices.
(from Davies, 2009)

2.2.3 Comparison of most recent Experimental Data Available

In Table 2.5, a summary table outlines the comparison between the most recent experiments conducted on metal and wood stud PWs. Key findings and test limitations are highlighted providing background knowledge useful in the development of a PW model. It is notable that amongst prior experimental studies, most focused on in-plane behavior, only those conducted into the 2000s utilized cyclic loading, and a few included a database large enough by which experimental fragility curves could be derived.

Table 2.5 Comparison of experimental test setups.

Authors	Details	Specimen Variables	Type of Testing	Key Finding	Test Limitation
Serrette et al. (1997)	Shear resistance of steel stud walls with flat strap tension x-braces	• Type of fastener and installation method • Shear element (x-bracing or sheathing board)	Monotonic Pushover	1. Strength of wall governed by screw head penetration 2. Small scale tests found to scale to larger scale test	1. Monotonic loading
NAHB Research Center, Inc. (1997)	Use of oriented strand board and gypsum board on steel walls	• Window and door openings • Percent sheathing • Anchor bolt spacing	Monotonic Pushover	1. Initial loading was linear until screw pull-through occurrence 2. Damage concentrated in perimeter screw connections and tearing in top track	1. Monotonic loading
Arnold et al. (2003, 2005)	Woodframe partition walls with gypsum board	• Window and door openings • Boundary conditions simulating single or two story unit	Cyclic	1. Boundary conditions severely impacted wall strength	1. Tested on woodframe type walls
Restrepo and Bersofsky (2004)	Steel stud walls with gypsum board	• connector spacing • gypsum height • slip track consideration • gypsum thickness • stud thickness and spacing	Cyclic	1. Development of fragility curves using three damage states	1. Limited number of specimens
Lang and Restrepo (2007)	Steel stud walls with gypsum boards simulating an office room considering openings	• In- and out-of-plane response • Loading Protocol	Cyclic	1. Noted effect of loading protocol on specimen response. 2. In-plane wall response represented as a function of wall length.	1. Effect of different loading protocol noted 2. Limited number of specimens 3. Three-dimensional model
Lee et al. (2007)	Steel stud walls with gypsum board	• Quasi-static vs. dynamic • Effect of window cutout	Various	1. Dynamic loading effect on walls negligible 2. Drift values greater than 2% require repair cost equal to installation cost	1. Construction practice typical of Japan. Note vertical gap at the partition and return wall intersection
NEES Nonstructural (Davies, 2009)	Steel stud walls with gypsum board	• Various configurations typical of commercial and institutional usage • In- and out-of-plane response • Attached mass loading	Various	1. Experimental fragility curves 2. Large database of experimental data	1. Limited aspect ratio (H/L = 1) 2. Limited inspection points for damage state classification

2.2.4 Previous Numerical Modeling Efforts

Idealizing hysteretic behavior with rules to define loading and unloading characteristics is a straightforward strategy to facilitate models readily implementable in design-oriented analyses. In what follows, a number of related efforts adopting such a strategy are discussed. Walls of wood and steel studs are explored to provide a sense of the scope of techniques.

Dinehart et al. (2000) derived equations of motion governing the behavior of woodframe shear walls. In their approach, a discrete three degree-of-freedom model is developed capturing the dominant features including racking, rotation and translation. The model reasonably predicts the low to moderate displacement results, while some downsides include failure to predict the pinched hysteretic behavior at larger deformations and governing equations are cumbersome due to the nature of differential equations (Figure 2.9). Van de Lindt and Walz (2003) developed a hysteretic model for the dynamic analysis of wood shear walls using results from testing of ten shear wall specimens. The model was developed by applying the displacement at the top of the shear wall through a single degree-of-freedom oscillator, a piecewise approximation of the hysteresis, an idealized constant-valued pinching behavior, and the hysteretic response enveloped by the backbone curve.

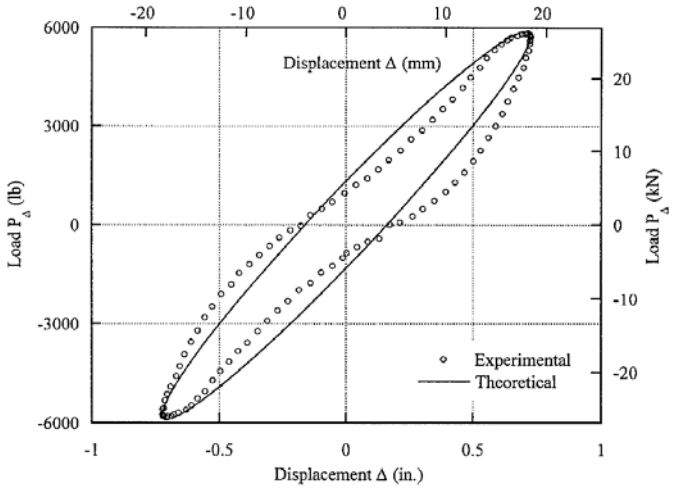

Figure 2.9 Single hysteretic loop comparison for experimental result against theoretical result demonstrating the pinching effect.
(from Dinehart et al., 2000)

Ibarra et al. (2004) postulated that lumped hysteretic models are capable of simulating the main characteristics of an experimental specimen. For example, an ideal model selected for capturing the hysteretic behavior of a plywood shear wall is a pinching model (Figure 2.10). The pinching model was described in two main parts. The reloading branch is directed towards a 'break point', which is defined as function of the maximum permanent deformation and maximum load experienced in the direction of loading. The critical break point, where the reloading stiffness increases, occurs when the reloading stiffness is directed towards the prior maximum deformation experienced for that direction of loading. For an example woodframe shear wall specimen, a pinching model was shown to match the global hysteretic behavior and hysteretic energy well (Figure 2.11).

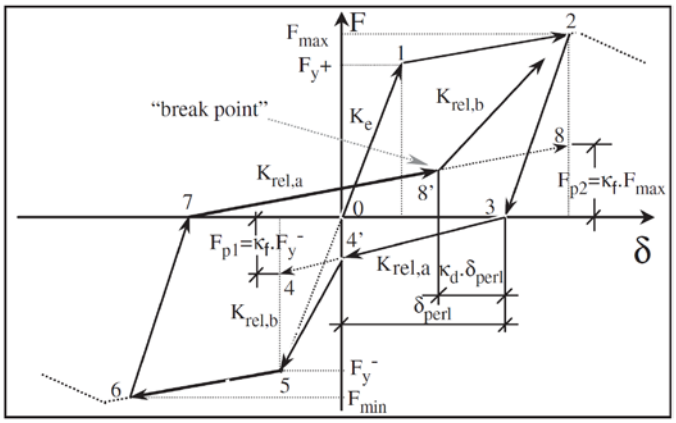

Figure 2.10 Pinching hysteretic model shown for basic model rules. (from Ibarra et al., 2004)

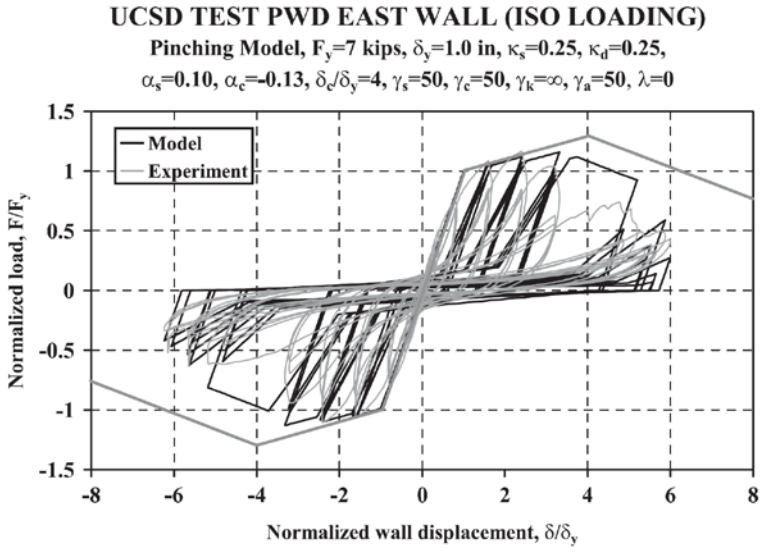

Figure 2.11 Model performance assessment for an example woodframe specimen considering a pinching model. (from Ibarra et al., 2004)

Folz and Filiatrault (2004a) developed a numerical model to predict the quasi-static and dynamic reversed cyclic response of woodframe buildings (Figure 2.12). Their approach targeted a shear spring element in an effort to reduce any computational demands associated within a large

finite-element model. In this sense, the model is well suited for design-level analysis efforts commonly adopted by a building designer (i.e. use of beam-column finite elements). The shear spring simplification lead to an element calibrated to represent the strength and stiffness degradation characteristics of the shear wall. Their study noted that the global deformation of the wood shear wall is dominated by the individual sheathing-to-framing connectors used in the construction of the wall. The cyclic analysis of shear walls (CASHEW) model utilized ten parameters to predict the behavior, a modified version of the Wayne-Stewart hysteresis model (Stewart 1987). Use of this model requires specification of wall geometry, shear stiffness of the sheathing panels, and hysteretic properties of the sheathing-to-framing connections to model reduced load capacity (strength degradation), failure of the wall at a prescribed maximum displacement, strength degradation based on the loading history, and the pinching effect (Folz and Filiatrault, 2004b).

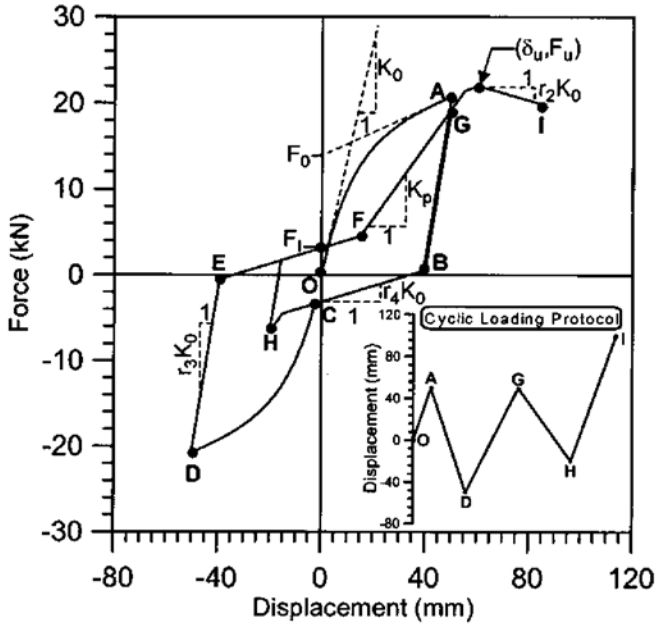

Figure 2.12 CASHEW model developed for woodframe shear walls. (from Folz and Filiatrault, 2004a)

Kanvinde and Deierlein (2006) proposed numerical models to determine the strength and stiffness of wood-framed gypsum PWs accounting for the effects of wall geometry, door or window openings, connector type and spacing, and boundary conditions. Their focus was limited to PWs constructed of gypsum board on wood framing, while recommending broader extension to PWs framed with light-gauge steel studs. Their study provided three relationships to determine the lateral strength and stiffness, the coefficients to describe the piecewise linear curve of the nonlinear response, and the coefficients for a peak-oriented hysteretic model to detail the nonlinear hysteretic behavior.

Pang et al. (2007) outlined an evolutionary parametric hysteretic model (EPHM) based on development of the CASHEW model (Folz and Filiatrault, 2001). The EPHM model retains the parameter estimation tools from the CASHEW model, while using exponential functions for the backbone, the loading path, and the unloading path (Figure 2.13). This model requires definition of 17 parameters, where seven of these parameters are required to characterize two exponential functions of the backbone curve. The loading and unloading curves are modeled using one exponential function each with evolutionary parameters and the remaining ten parameters are used in the degradation process by updating the evolutionary parameters. Types of degradation considered include backbone force, force-intercept (pinching effect), unloading stiffness and reloading stiffness values.

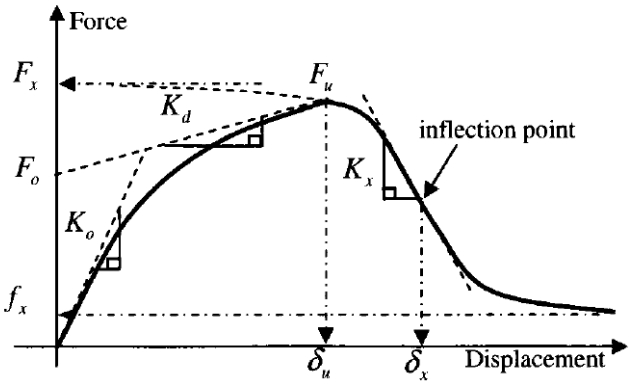

Figure 2.13 Shear wall backbone curve.
(from Pang et al., 2007)

Davies (2009) used regression analysis to analyze 35 PW specimens to develop representative hysteretic models of the in-plane PWs using a shear spring and the Wayne-Stewart model. Nine parameters were required to characterize this model: initial stiffness, post yield stiffness factor, post capping stiffness factor considering strength degradation, unloading stiffness factor, yield strength, capping strength, intercept strength, reloading or pinch power factor, and the beta or softening factor. Hysteretic behavior of the specimens followed a tri-linear relationship (Figure 2.14), where the ratcheting effect was not considered in the modeling technique. Two modeling sets were developed, one based on the mean values for each of the individual subgroups considered in the experimental program and a second set requiring only the mean initial stiffness and capping strength with the remaining seven parameters assigned via statistical ratios.

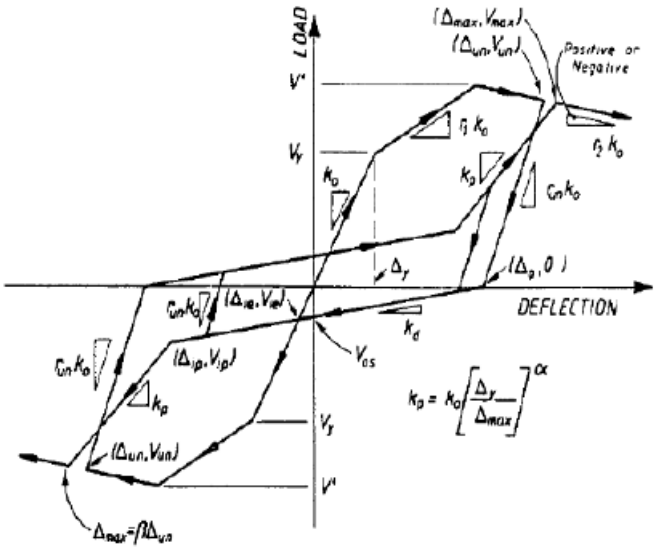

Figure 2.14 Wayne-Stewart hysteretic model with strength degradation. (from Carr, 2005)

Restrepo and Lang (2011) examined the influence of two reversed cyclic loading protocols on the response of cold-formed light-gauge PWs. The gypsum board partition response was characterized from these experiments and a previous test conducted by Restrepo and Bersofsky (2010) in a linear piecewise function, where the lateral force value of the wall was normalized by the wall length (Figure 2.15). These empirical formulae were developed by considering the individual components of the backbone responses in their test and a previous test conducted by Restrepo and Bersofsky (2010), where details on the setup of the experiments were presented in Section 2.2.1.

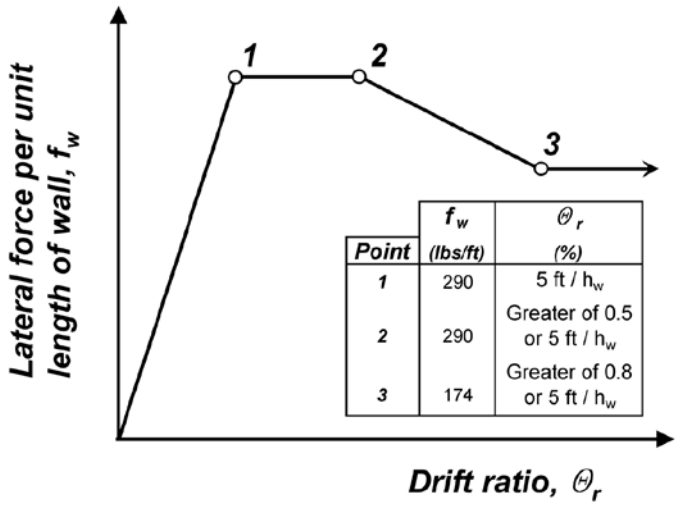

Figure 2.15 Proposed empirical backbone for gypsum board on light-gauge steel stud PWs. (from Restrepo and Lang, 2011)

The aforementioned studies have enriched the literature with a variety of modeling concepts and tools for capturing the hysteretic response, on a lumped level, of both wood and metal stud walls. However, to date, the experimental database available to calibrate and further develop similar tools within expanding simulation packages has been sparse. Recent data generated through the Network for Earthquake Engineering Simulation (NEES) experimental programs can fill the void with the much needed data sets.

2.3 Numerical Modeling Methodology

2.3.1 Platform

The platform selected to model the PWs is OpenSees, developed by the Pacific Earthquake Engineering Research (PEER) Center (Mazzoni et al., 2011). OpenSees is an open-source numerical platform based on finite element modeling that provides the capabilities to perform advanced nonlinear time history analysis of buildings, bridges and other structural

systems. However, to date it does not have tools available for modeling nonstructural components and systems.

To capture the nonlinear hysteretic behavior of the various PW models, a lumped material is created. The motivation for doing so is primarily simplification, as one may envision that partition subsystems are to be distributed throughout a building model and a finely discretized model of a PW would greatly increase the degrees-of-freedom. A finely discretized model would render the calculations of response computationally intense and potentially unstable if the PW model is implanted into a building model at various locations. Moreover, the use of lumped hysteresis is highly compatible with finite element models readily used by building analysts in design practice. To this end, the lumped material model is assigned to a zero-length one degree-of-freedom element. The lumped material behavior is created using the *pinching4* material, which is available within OpenSees. *Pinching4* is a uniaxial material model that allows for a “pinched” load-deformation response with an optional degradation contribution.

To best represent the experimental specimens, this *pinching4* material is used in a parallel configuration providing better control of the unload and reload parameters as a function of the displacement range. Sixteen parameters describe the force-displacement envelope or backbone of the model, while an additional eight parameters control the unloading and reloading behavior. Due to the parallel formulation, three additional unloading and reloading relationships are required, as compared to the original *pinching4* material model (Figure 2.16).

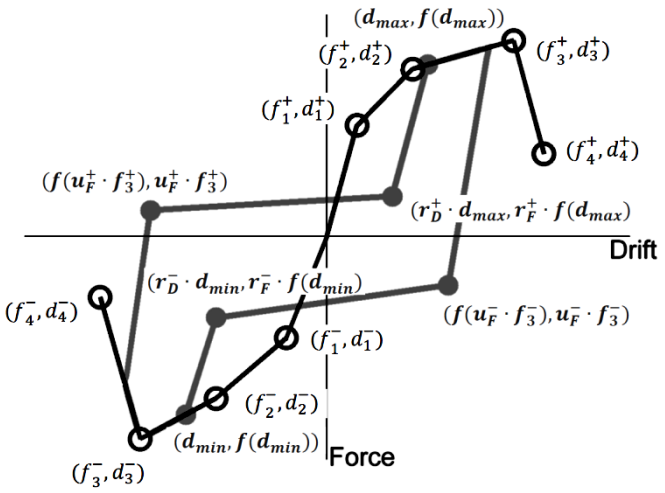

Figure 2.16 *Pinching4* material model.
(adapted from Mazzoni et al., 2011)

In the use of the material, the PW is characterized as a simple spring. This uniaxial spring is implemented only in the longitudinal direction; whereas, the out-of-plane behavior of the PW is not characterized numerically herein. The out-of-plane stiffness of the wall is approximately 10% of the in-plane PW stiffness and therefore provides a negligible contribution to the behavior of a building-partition wall system.

2.3.2 Model Verification

Ideally, each experimental specimen should have a detailed numerical model. However this would be impractical, alternatively, representative groups are identified based on their mechanical configuration, which drives their physical behavior. To test this methodology, the evaluation of the performance of an individual specimen is first conducted. Specimen 20, a specimen from group 2a of institutional style construction with a partially connected boundary condition is selected for this exercise.

2.3.3 PW Backbone Characterization

The initial step in the modeling approach is to determine the force-displacement backbone from the experimental data. This was done by taking the force associated with each maximum displacement excursion. The idealized force-displacement backbone is characterized by a total of eight points, four positive and four negative (denoted as "backbone points" in Figure 2.17). The selection of these points is based upon capturing the overall shape of the backbone curve, with some guidance provided by calculating the first derivative of the backbone (tangent stiffness).

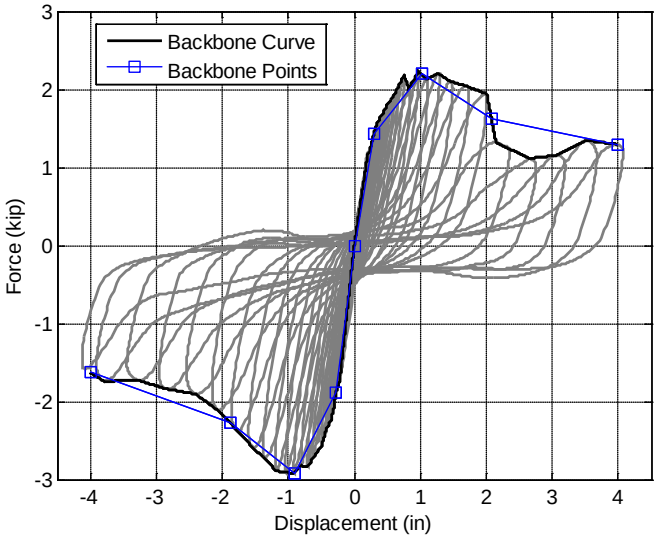

Figure 2.17 Force-Displacement backbone for specimen 20 and the selected backbone points.

2.3.4 PW Unloading and Reloading Behavior

After selection of the backbone points, a calibration procedure is executed to determine the unloading and reloading parameters. For simplicity in the unloading and reloading parameters, this behavior is assumed to be symmetrical; that is for each of the parallel materials, only one force and one displacement value is determined and it is the same in the positive and

negative regions. The remaining eight parameters (two for each individual material) are iterated such that the difference in the cumulative hysteretic area (between the model and experiment) is minimized. For specimen 20, the final hysteretic model overlay and hysteretic area (energy plots) are shown in Figure 2.18. The resultant hysteretic behavior and hysteretic area agree well. The comparison of cumulative hysteretic area provided in Figure 2.18b demonstrates that upon discrete calibration, the numerical model reasonably captures the experimental behavior across the range of damage states, through the end of testing. Appendix A presents the PW modeling script developed for OpenSees, for all models outlined in the next sections.

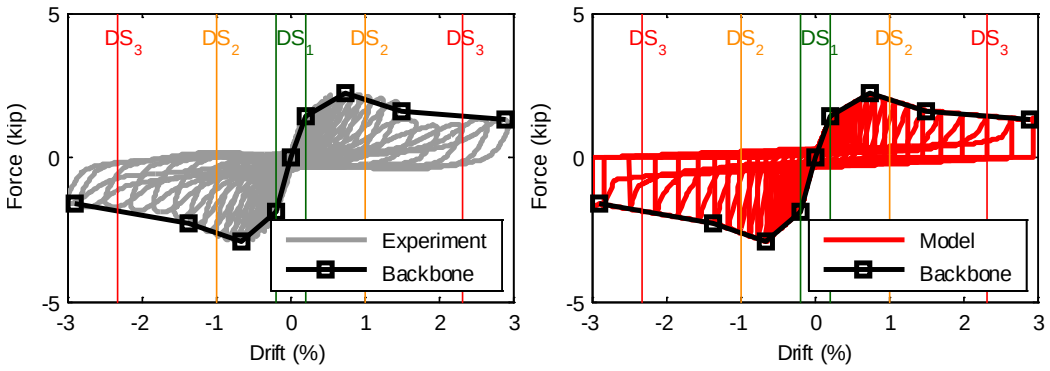

(a)

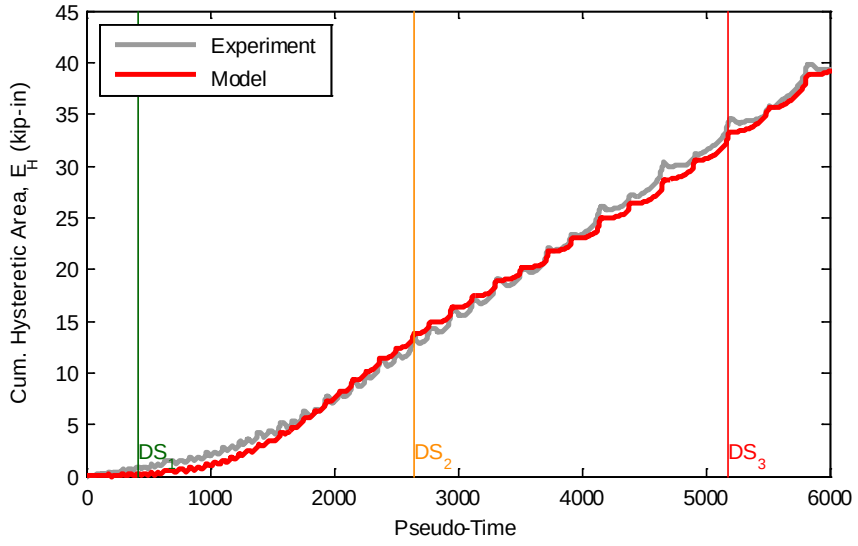

(b)

Figure 2.18 Experimental and numerical model comparison for specimen 20: (a) hysteretic behavior and (b) hysteretic area.

2.4 Developed PW Models

2.4.1 Subgroup Models

Although individual specimen results may be used to calibrate the numerical model parameters, as conducted in Figure 2.17, such an approach lacks extensibility. Therefore after analyzing the response of each wall within a subgroup, select walls are identified as outliers in the sense that their behavior is unexpected (in some cases premature, potentially attributed to

construction defects). For the remaining walls within a subgroup (Table 2.2), the model parameters are averaged and an arithmetic mean (average) model is developed. An illustration of subgroup outliers are shown in Figures 2.19 and 2.20 for subgroups 1a and 1b (commercial). These results show that three of the specimens exhibit hysteretic behaviors uncharacteristic of each other and the remaining specimens with like installation techniques. In comparing similar specimens 5, 6, and 10 without a return/boundary wall, specimen 10 is identified as an outlier because tearing of the top track occurred only in this specimen resulting in premature failure. In comparing similar specimens 7, 8, and 9 characterized as full connections, specimens 7 and 9 are identified as outliers due to the top and bottom track slipping after track tearing occurred around all nailed connections. Although Figure 2.20 may show a large number of outliers (three of seven tests), other subgroups observe more consistent specimen-specimen behavior (e.g. Figures 2.21 and 2.23). Repeating this analysis, four mean subgroup models are developed, namely: 1) 1a-commercial partial connection, 2) 1b-commercial full connection, 3) 2a-institutional partial connection and 4) 2b-institutional full connection. To develop each of the representative models, two details are required as previously discussed: (1) a piecewise force-displacement curve matching the subgroup response and (2) unload and reload parameters calibrated against the subgroup average energy.

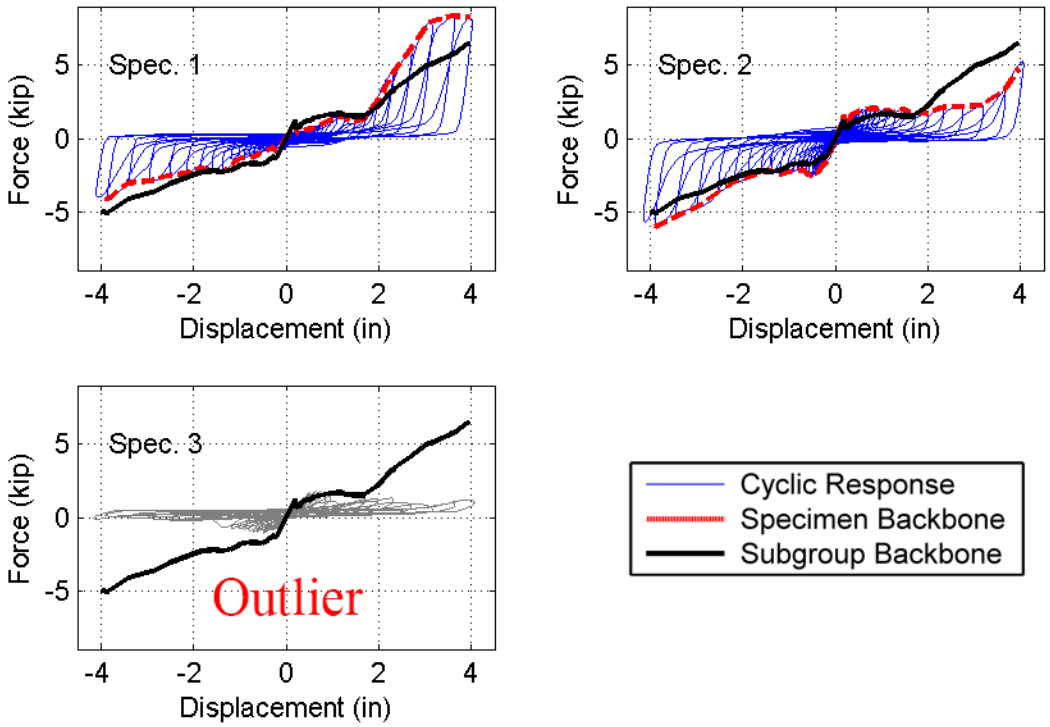

Figure 2.19 Subgroup 1a experimental hysteretic behavior showing identified backbone and average subgroup backbone.

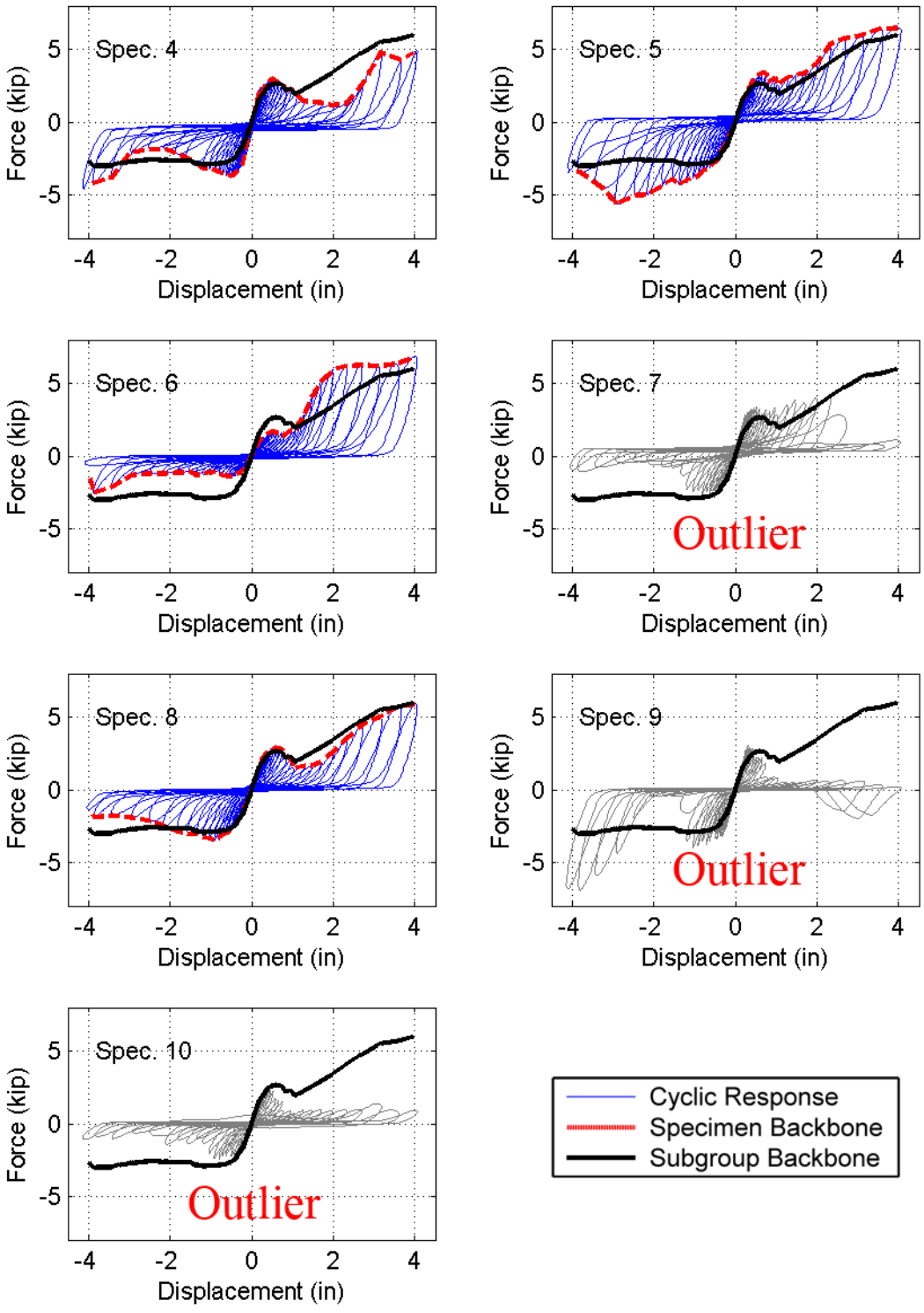

Figure 2.20 Subgroup 1b experimental hysteretic behavior showing identified backbone and average subgroup backbone.

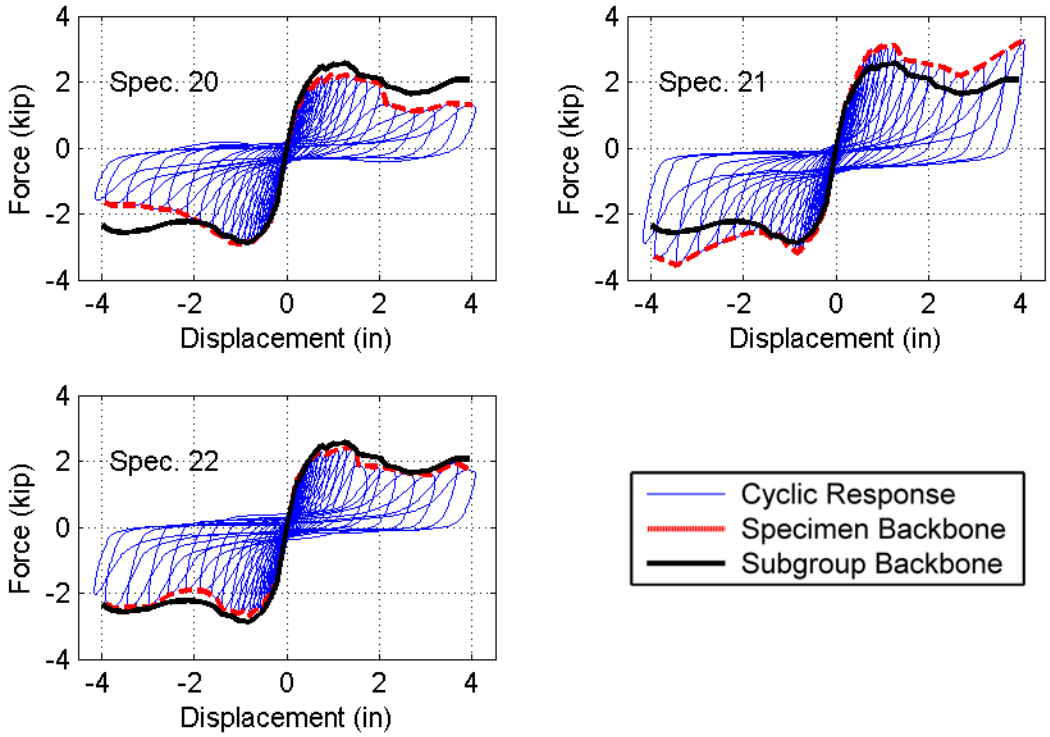

Figure 2.21 Subgroup 2a experimental hysteretic behavior showing identified backbone and average subgroup backbone.

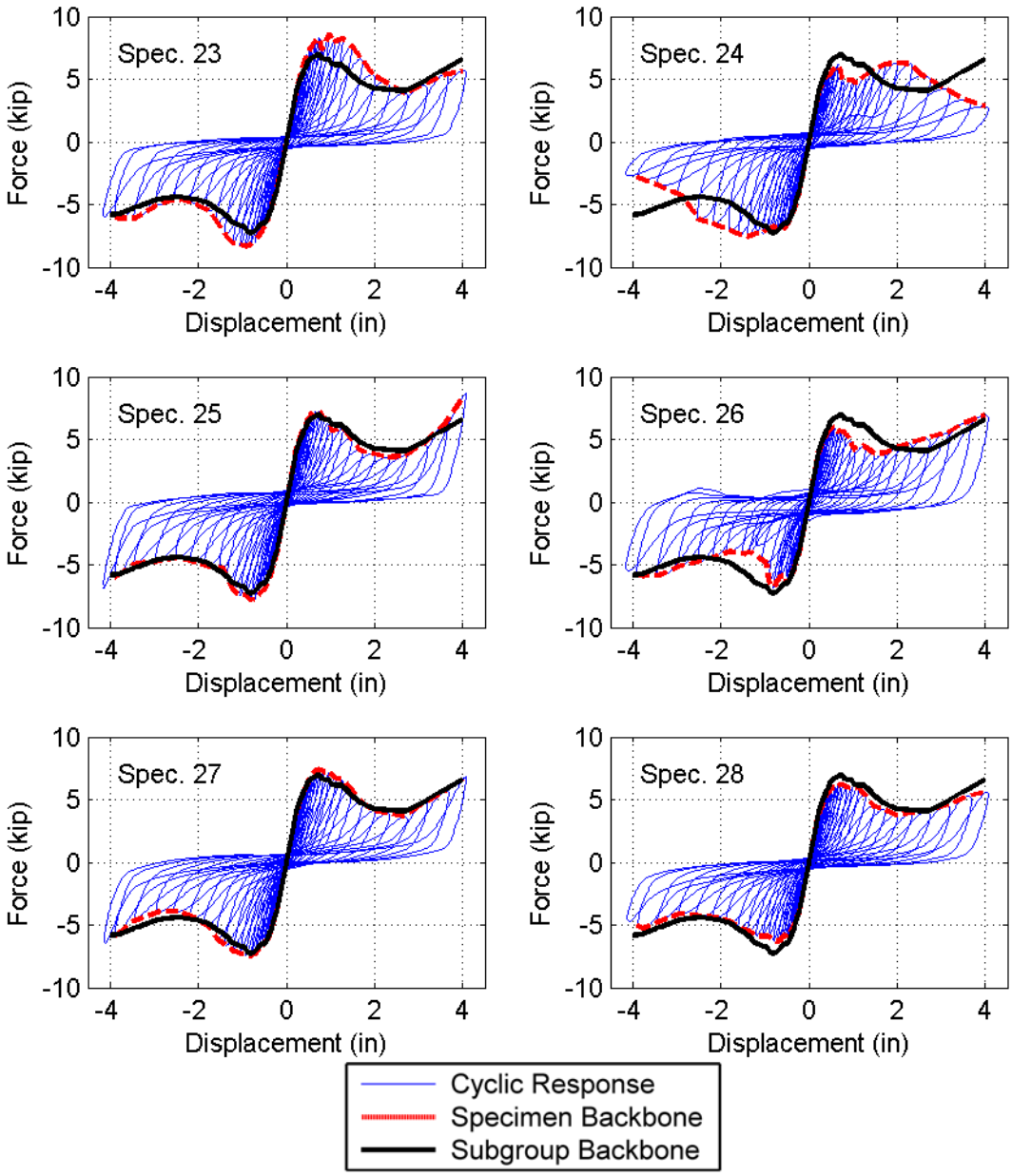

Figure 2.22 Subgroup 2b experimental hysteretic behavior showing identified backbone and average subgroup backbone.

2.4.2 Subgroup Model Discussion

Mean backbone curves are created for each subgroup (Figure 2.23 and Table 2.6). The overlay of each subgroup type indicates that subgroups 1a, 1b and 2a are somewhat similar in their backbone force-displacement characteristics. However, subgroup 2b stands out as the strongest and stiffest walls. One reason subgroup 2b is the strongest and stiffest wall is related to the institutional installation details and the thicker vertical studs. One may also note that subgroups 1a, 1b and 2b exhibit a post-peak hardening, for the former two (1a and 1b), this occurs at around 1% drift. This may be attributed to closure of a gap between the wall and the top track. This behavior is not significantly noted in the response of specimens within subgroup 2a, moreover it is less pronounced in the negative drift direction of subgroup 1b.

Table 2.6 Parameters for the subgroup models.

Model		Backbone Points				Unload/Reload	
		Disp (in)	Force (kip)	Disp (in)	Force (kip)	Force	Disp
1a	1	0.204	1.270	-0.214	-1.328	0.70	0.10
	2	1.196	1.680	-0.549	-1.770	0.10	0.70
	3	1.695	1.538	-1.572	-2.218	0.15	0.90
	4	4.000	6.650	-4.000	-5.060	0.08	0.93
1b	1	0.237	1.790	-0.216	-1.666	0.55	0.30
	2	0.599	2.645	-0.555	-2.810	0.06	0.92
	3	1.098	2.008	-1.451	-2.756	0.09	0.86
	4	4.000	6.620	-4.000	-3.080	0.08	0.90
2a	1	0.400	1.810	-0.356	-2.060	0.18	0.40
	2	1.100	2.550	-0.930	-2.900	0.18	0.85
	3	2.370	1.840	-1.984	-2.220	0.20	0.80
	4	4.000	2.100	-4.000	-2.510	0.20	0.99
2b	1	0.412	5.807	-0.336	-5.265	0.15	0.40
	2	0.694	6.912	-0.650	-6.900	0.01	0.90
	3	2.676	4.080	-2.433	-4.389	0.15	0.55
	4	4.000	6.650	-4.000	-5.850	0.01	0.99

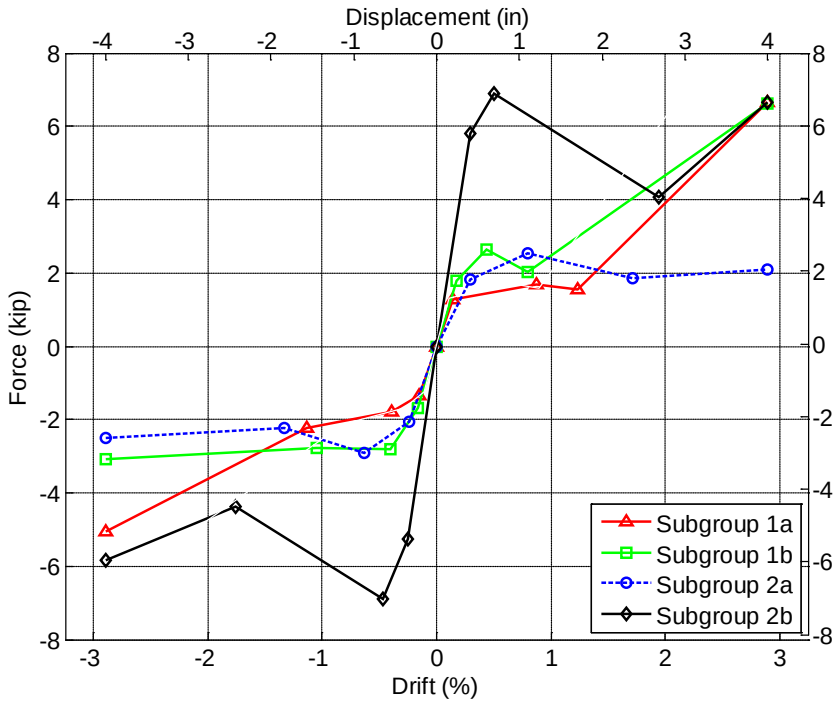

Figure 2.23 Overlay of each subgroup backbones shown demonstrating a large variability.

Backbone response for subgroups 1a, 1b, 2a and 2b are created using data from two, four, three and six specimens, respectively. With the number of specimens at most under six per subgroup, a variability assessment is difficult to justify due to the low specimen count. Therefore only the mean response is characterized. In the next section, a normalized approach is adopted with the goal of capturing the variability inherent in the PW response.

2.4.3 Normalized Models Introduction

To simplify the modeling approach and characterize the experimental variability, subgroups 1b and 2b are combined and used to develop normalized models. These subgroups involve only specimens with full connectivity. Subgroups 1a and 2a, partially connected specimens, are not considered for the normalized models due to different failure mechanisms developed during the testing. Namely, since the gypsum board was not connected to the top track

resulting in damage primarily in the return walls. By characterizing a normalized model, the analyst need only provide wall length and building occupancy (commercial or institutional). With knowledge of the building occupancy, the selected wall stud type and spacing will dictate the force response of the wall.

2.4.4 Force Normalization for Normalized Models

Using the plan details of each wall specimen, the sum of the thickness of the stud webs in the in-plane direction, denoted as Σt_{stud} is calculated. The actual value used for the thickness of the studs is the minimum required thickness as determined by the manufacturing standards. The commercial studs are SSMA 350S123-18 which corresponds to an 18 mil stud with a design thickness of 0.0188 inches. The institutional studs are SSMA 350S125-30, i.e. a 30 mil stud with a design thickness of 0.0312 inches (SSMA, 2010). Seven studs were used for the commercial configuration resulting in total thicknesses of 0.1316 inches, while ten studs were used in the institutional configuration for a total thickness of 0.3120. In Figure 2.24, the backbones are presented prior to normalization. In this figure, it is clearly visible that the institutional specimens are stiffer and stronger than those of the commercial specimens. By normalizing the force at each displacement by the sum of the stud thickness Σt_{stud}, the backbones collapse to a like range (Figure 2.25). After the normalization has been conducted on the backbone, variability is less significant within a range of less than 1% drift. One difference from the subgroup model is noted where specimen number 6 is excluded from this analysis due to the lower energy dissipation associated with this reused specimen. Using the nine specimens of subgroups 1b and 2b, 18 backbone curves (one positive and one negative per specimen) are then used to characterize the mean (μ) and standard deviation (σ) of the specimens (Figure 2.25).) to characterize the variability experienced in the experiments. It is noted that the experimental mean is synthesized

to a coarse linearly segmented behavior for simplifying the input parameters of the backbone to four .

In like fashion, the calculated hysteretic area should agree in a normalized fashion with that of the experimental model. In the same approach as the force-normalization, the hysteretic area (energy) is also normalized by the sum of the thickness of the studs in the lateral direction (Figures 2.26 and 2.27).

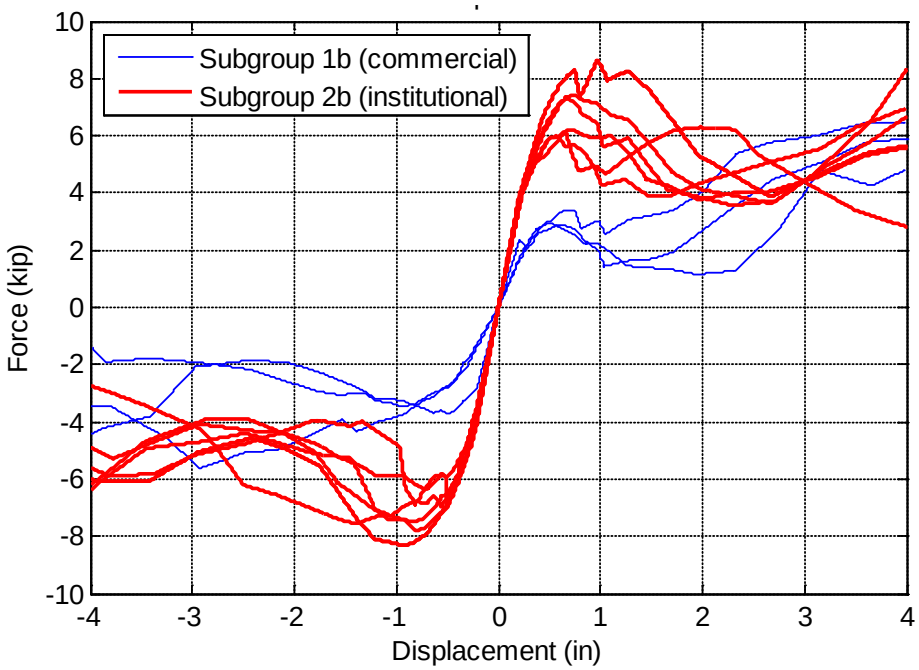

Figure 2.24 PW backbones (force-displacement relations) for subgroups 1b and 2b.

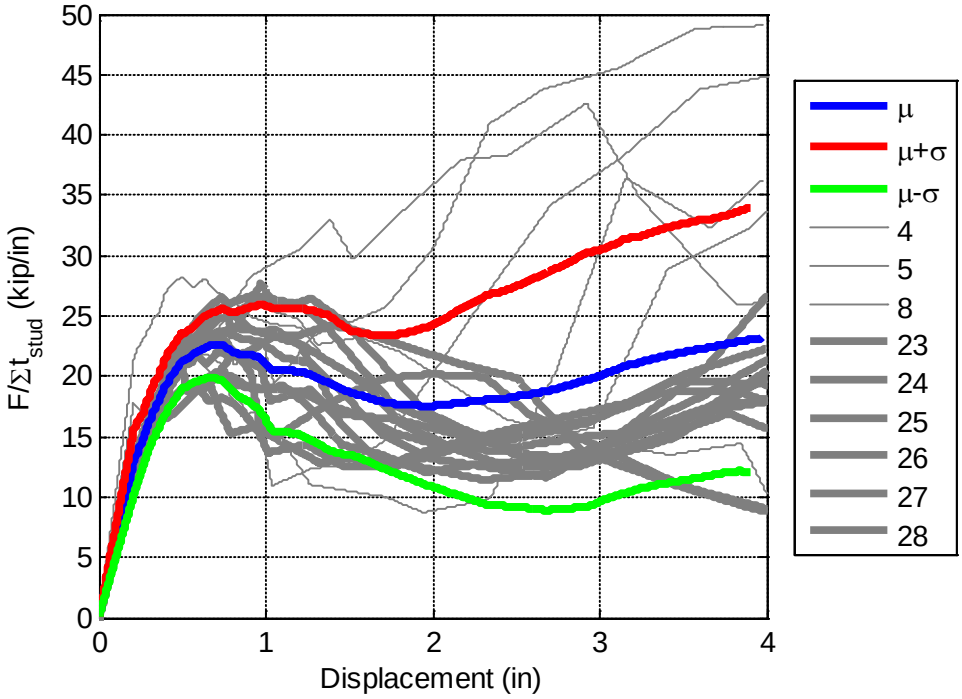

Figure 2.25 Absolute valued normalized backbones showing the mean, mean plus one standard deviation and mean minus one standard deviation.

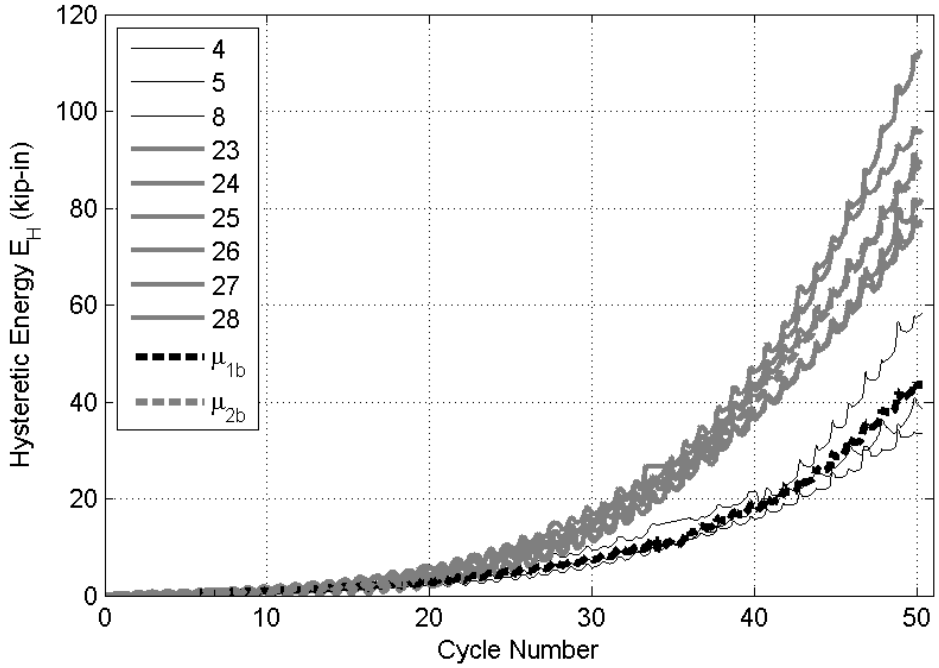

Figure 2.26 Hysteretic energy for subgroups 1b and 2b for each of the specimens considered along with their respective subgroup averages.

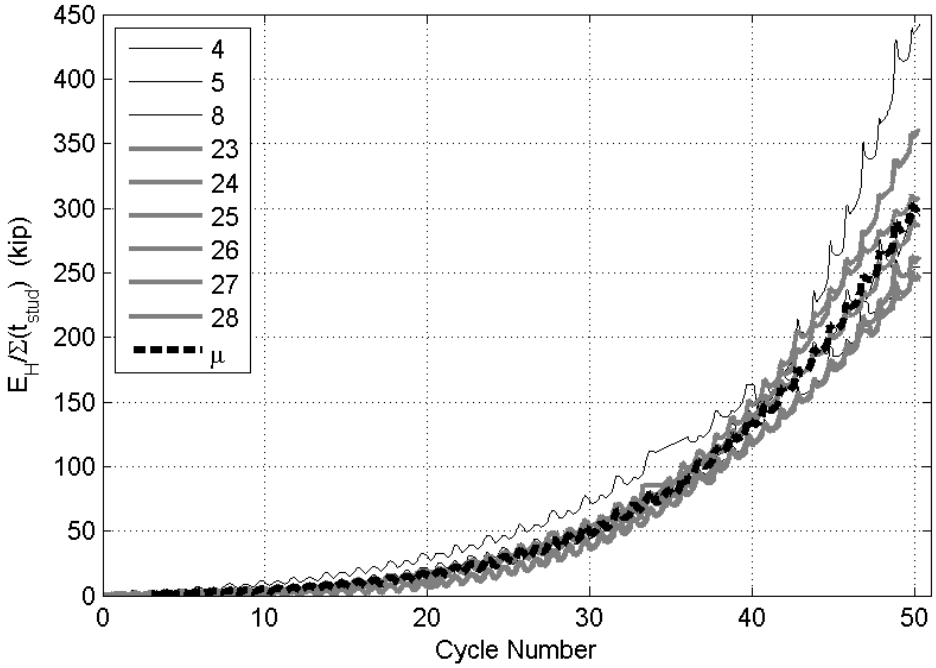

Figure 2.27 Normalized hysteretic energy for subgroups 1b and 2b.

2.4.5 Normalized Model Calibration

Similar to the subgroup model characterization, two key parameters involved in developing the representative models are the idealized backbone curve and the unload and reload parameters. Each of these is calibrated such that the hysteretic energy of the model matches that of the target experimental energy. In this approach three representative models are sought, namely: 1) mean response, 2) mean response plus one standard deviation and 3) mean response minus one standard deviation. The force-displacement backbone idealization is shown in Figure 2.28. The backbone points are selected based on significant backbone slope changes, which may be observed in tangent stiffness plots. Identifying the locations of significant slope change, the corresponding y-value pertaining to the normalized force quantity is iterated to minimize the difference between the target backbone and the idealized piecewise backbone curve. Consequently, for the (x-values) displacement, the selected normalized force quantity is the

closest match to the curve. For the selection of the unload and reload parameters, these are calibrated for each of the normalized models, the mean response is shown in Figure 2.29.

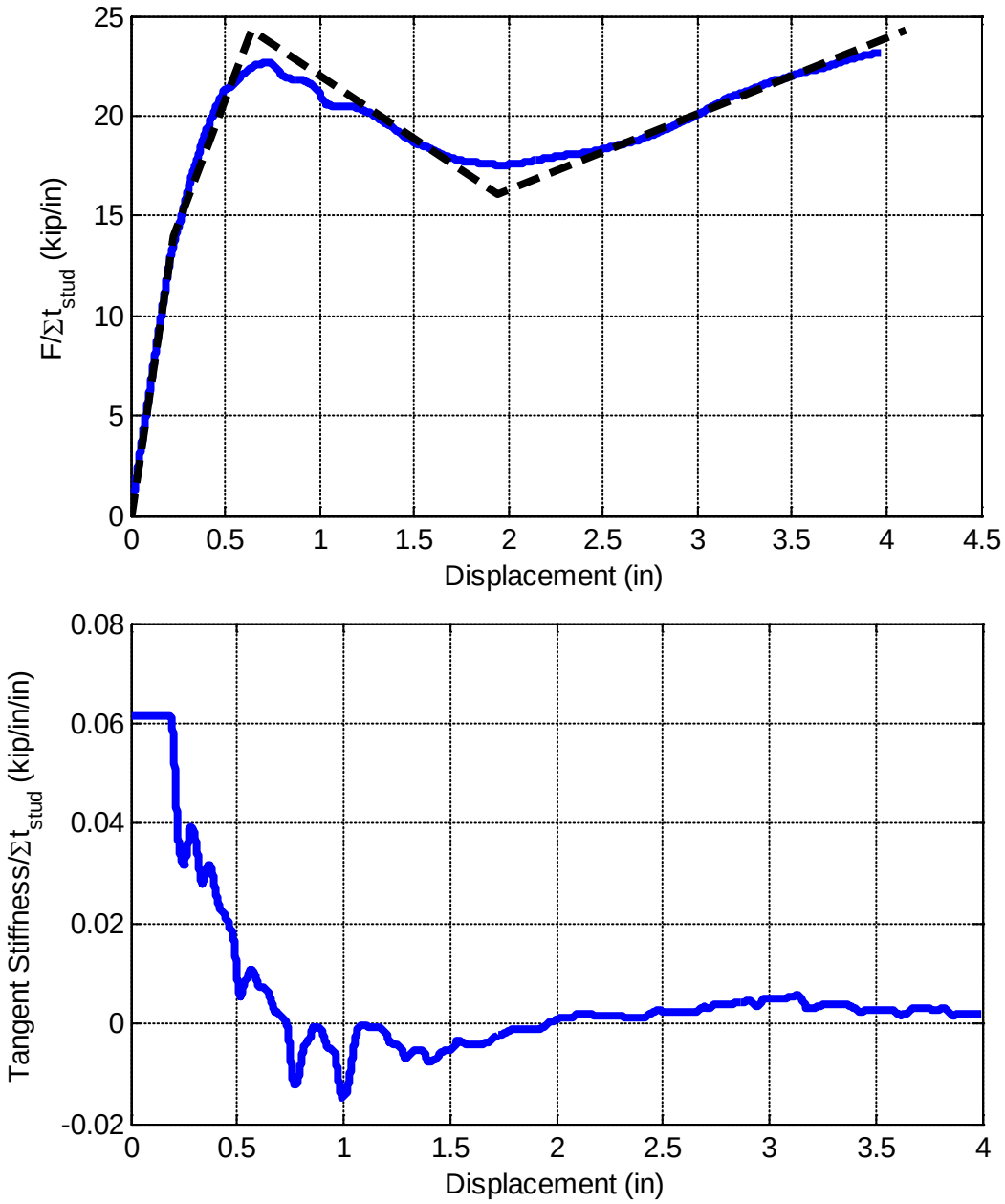

Figure 2.28 Selection of the mean response behavior of the PW model. Top shows normalized absolute valued hysteretic backbone while the bottom demonstrates the tangent stiffness of this backbone.

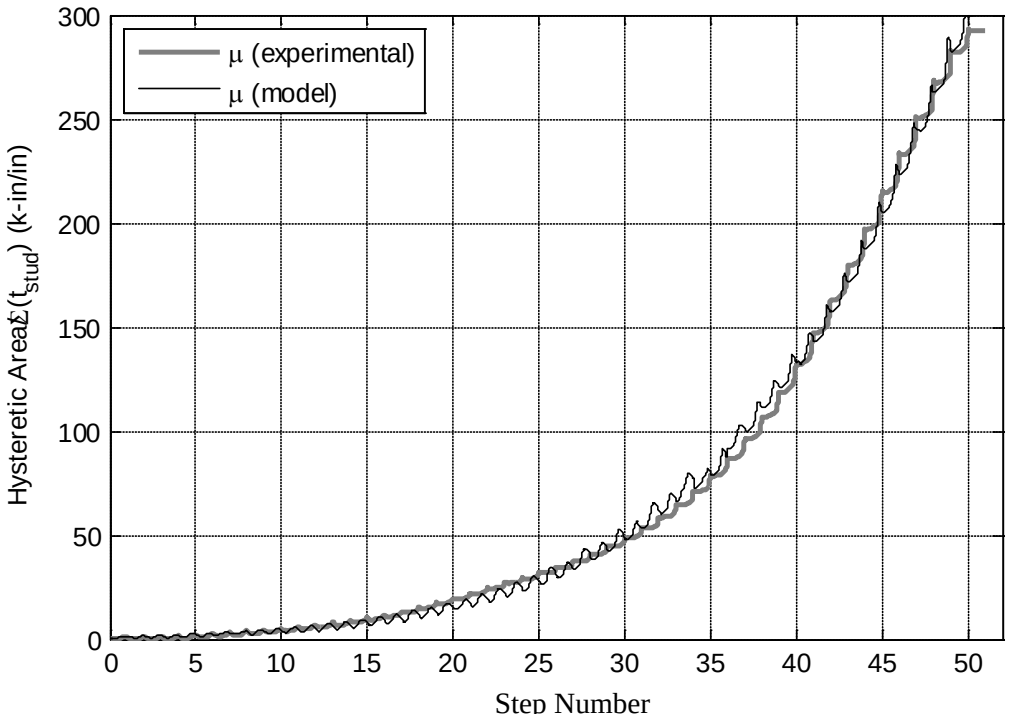

Figure 2.29 Hysteretic area of the mean model versus the target mean hysteretic area.

Normalized Model Verification

To assess the variability among the different statistical values of the normalized models, an individual comparison can be made to each specimen. In Figure 2.30, the model mean (μ) is compared against test results for specimen 4. Comparisons are provided for the hysteretic force-displacement response and the hysteretic energy (area) (

Figure 2.31). For this particular specimen, the backbone and hysteretic area is well characterized using the mean. Additional comparisons on a per specimen basis may be found in the original report (Wood and Hutchinson, 2012).

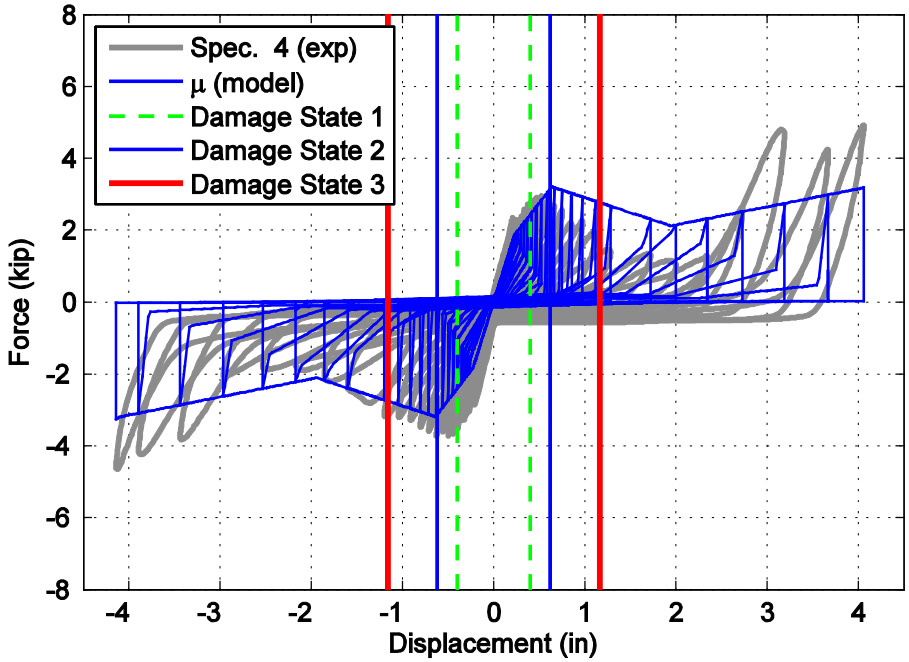

Figure 2.30 Hysteretic behavior of the mean response shown with specimen 4 as an example.

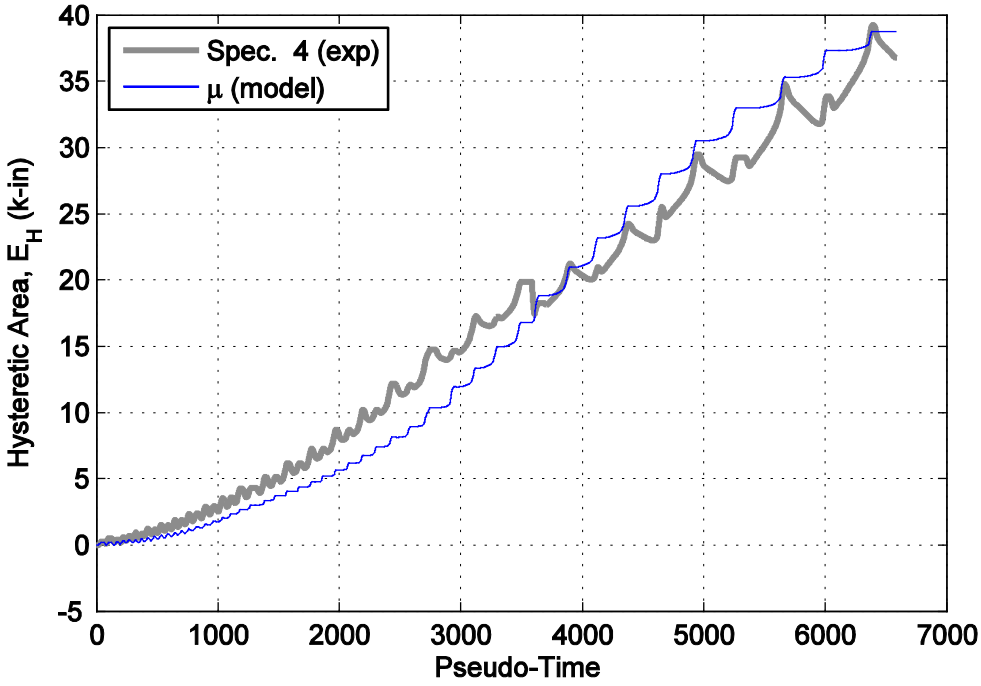

Figure 2.31 Hysteretic area of the mean model with specimen 4 as an example.

2.4.6 Normalized Model Discussion

In the development of the normalized models, a comparison is made between the various statistical levels. A comparison is made between the various backbones (Figure 2.32 and Table 2.7). In this figure, the mean and plus/minus standard deviations are somewhat similar in their initial stiffness, however their peak and post peak behavior do vary. The maximum force value also is not at a stable displacement value, indicating that specimens experience their maximum force over a range. The post-peak hardening is noted in all variations, however it is most pronounced in the mean plus a standard deviation model. However by visual inspection, it is not evident as to which model performs best overall. In order to determine which model most closely captures the experimental behavior a more rigorous error analysis is conducted in Chapter 3.

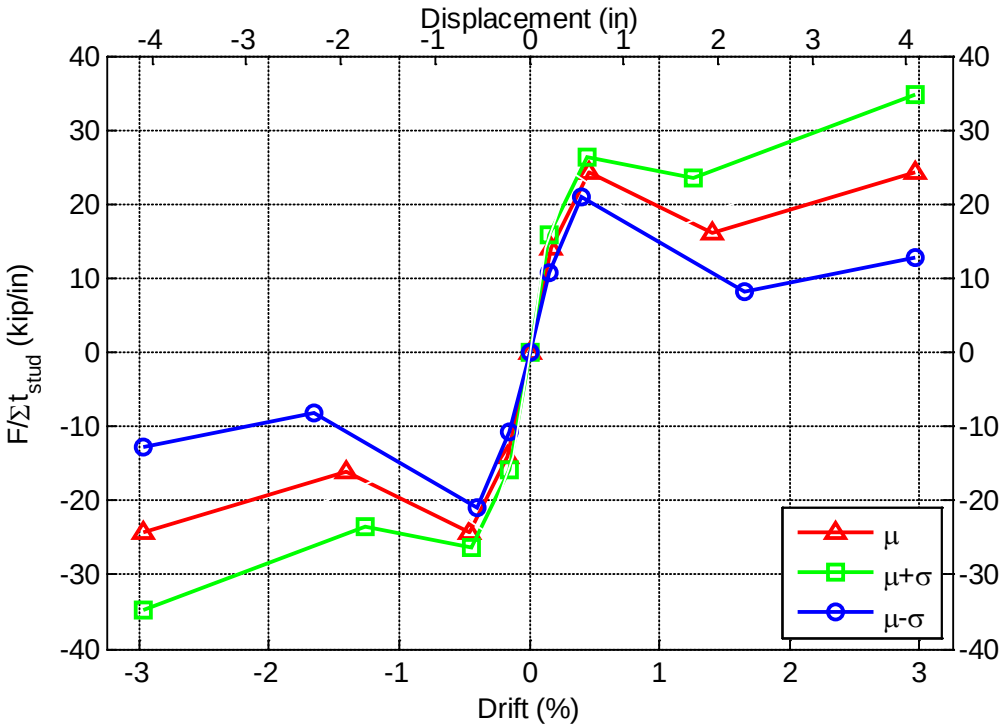

Figure 2.32 Overlay of each of the normalized model backbones.

Table 2.7 Parameters for the normalized PW model.

Model		Backbone Points		Unload/Reload	
		Disp (in)	Force/Σt_{stud} (kip/in)	Force	Disp
μ	1	0.225	13.95	0.15	0.4
	2	0.637	24.28	0.01	0.95
	3	1.945	16.04	0.13	0.62
	4	4.100	24.28	0.03	0.97
μ+σ	1	0.212	15.92	-0.03	1.1
	2	0.622	26.43	0.01	0.99
	3	1.734	23.61	0.55	0.6
	4	2.338	26.43	0	1
μ−σ	1	0.221	10.81	0.15	0.4
	2	0.545	21.07	0.03	0.91
	3	2.291	8.22	0.11	0.89
	4	7.258	21.07	0.07	0.93

2.5 Comparison of Developed PW Models

In this section, a comparison is made between the developed models herein and the model proposed by Restrepo and Lang (2011). While the model presented by Restrepo and Lang is based on length of wall, no prescription is made for walls where various stud spacing and thicknesses are used. For simplicity in comparison, the PW length is assumed to be 12 feet as tested in the NEES-GC project. Figure 2.33 illustrates the comparison for both the subgroup models and normalized models. Recall that the Restrepo and Lang model characterized the PW response for a commercial building with studs particularly thicker than those in the NEES-GC project. Consequently, the Restrepo and Lang model is most similar to the commercial installation types, while slight differences can be attributed to differences in installation practices and specimen variability.

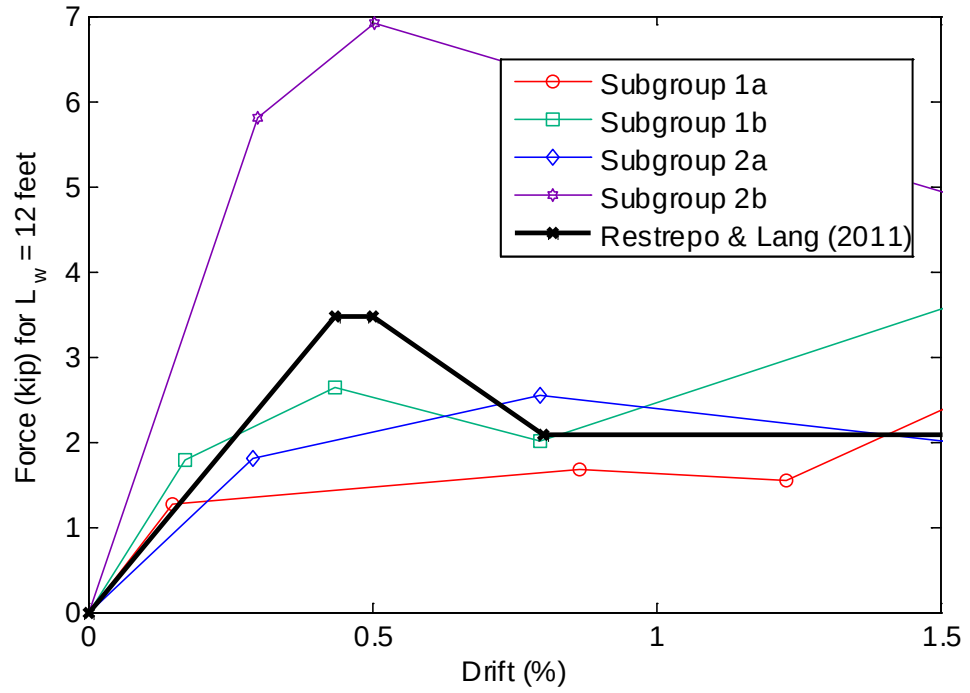

(a)

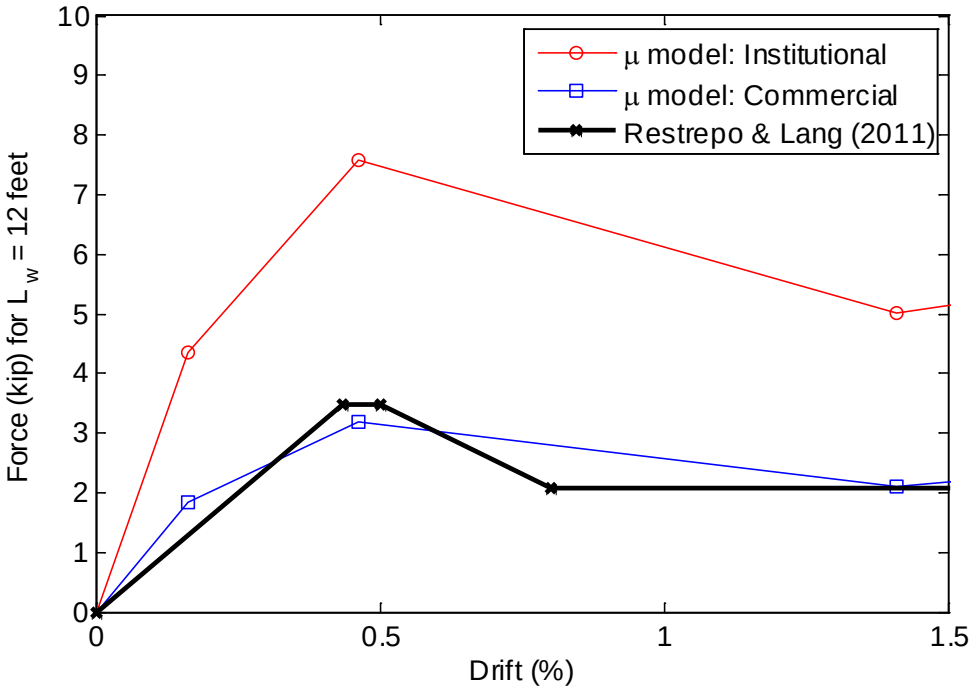

(b)

Figure 2.33 Comparison of developed models to the proposed model by Restrepo and Lang (2011): (a) subgroup models, and (b) normalized models, where the length of the partition walls were taken as 12 feet as tested in the NEES-GC project.

2.6 Summary Remarks

In this chapter, the PW in-plane behavior is realized using a lumped model which is discretized via a zero-length element coupled with the *pinching4* material, used in a parallel configuration. Robust performance of the model is sought across the drift levels associated with three commonly observed damage states of minor, moderate and major. In the use of the material, the PW is characterized as a simple uniaxial spring, implemented only in the in-plane direction whereas the out–of-plane behavior of the PW is not characterized numerically herein. Two different classes of models were developed: subgroup and normalized models. To simplify the modeling approach, subgroups 1b and 2b are combined into a normalized model and the variability in model response, as compared with the experiment, evaluated.

In this attempt of assessing the variability of the PW modeling, it is not evident as to which model performs best overall. Thus the analysis of model performance has largely been limited to visual inspection. In order to determine which model most closely captures the experimental behavior a more rigorous error analysis is needed. In the next chapter, two different error metrics are used to determine which model is most robust while closely capturing the experimental results.

2.7 Acknowledgement

Chapter 2 of this dissertation is based on the NEES-Nonstructural Report, *A Numerical Model for Capturing the In-Plane Seismic Response of Interior Metal Stud Partition Walls*, published at the State University of New York, University of Buffalo. The co-author of this report is Tara C. Hutchinson, while the dissertation author is the primary author and investigator.

Chapter 3 Error Metric and Assessment of Developed Partition Wall Models

3.1 Introduction

To characterize the model performance, error metrics and individual specimen level comparisons are conducted using all of the developed models. In the previous chapter, the development of four representative subgroup models (1a, 1b, 2a and 2b) and three normalized models for the fully connected walls are summarized. To justify the use of any of the developed models, particular attention regarding how successful the models are in the prediction of the experimental behavior must be assessed. In this section, two error metrics are adopted, namely the average error in maximum force and the error in the total half-cycle hysteretic energy. It should be mentioned that these models were implemented in displacement control; therefore, displacement error metrics are not meaningful.

3.2 Average Error in Maximum Force

The first error metric is the error associated with the maximum force. This error metric is a measure of how well the particular model backbone estimates the changing strength of the specimen. Identifying the maximum force attained throughout the displacement range is similar to comparing the "backbone points"; in this case, the maximum force attained is enveloped at all displacement levels, not just at load reversals. To illustrate this error metric, specimen 23 is shown as an example. In Figure 3.1, the maximum force envelope of subgroup 2b (institutional fully connected) model is shown along with specimen 23. In this figure, the damage states identified by the experimental team are also overlaid. While this maximum force overlay demonstrates a decent match, it is particularly hard to quantify visually. This figure highlights

how the maximum force obtained is particularly low in the model around specimen attainment of damage state 2 (DS_2) and damage state 3 (DS_3) and the estimation of the post-peak hardening behavior at large drifts (approaching 2%) is better in the negative direction in comparison with the positive direction.

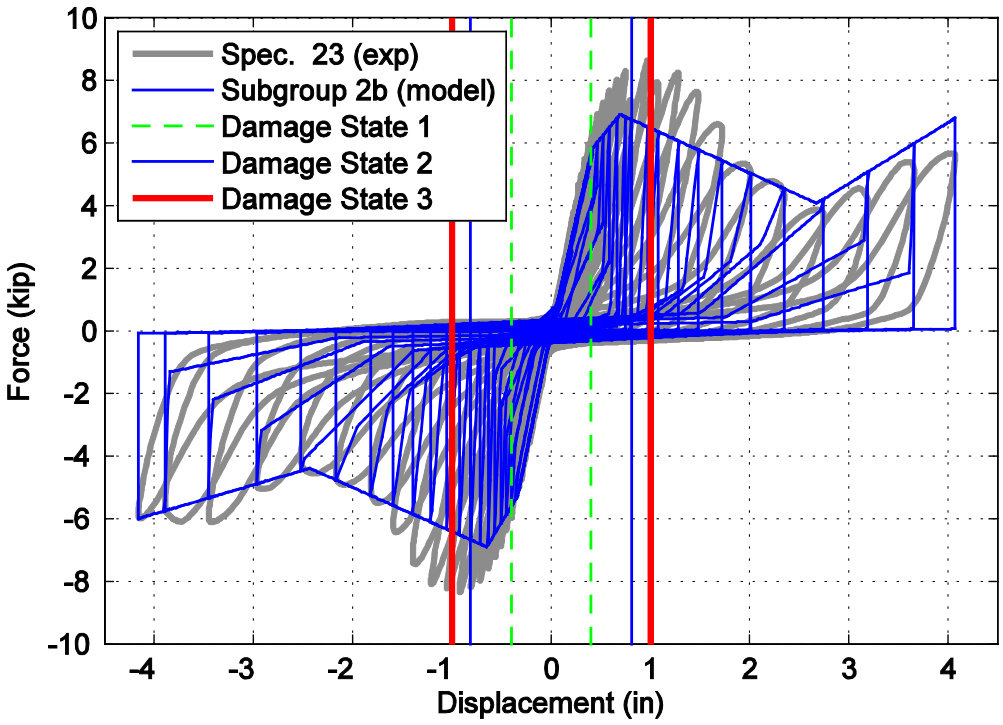

Figure 3.1 Hysteretic overlap comparison between specimen 23 and the 2b subgroup model.

Using the maximum force envelope (Figure 3.2), the residual force difference, denoted as EM_1, is calculated as shown in Equation 3-1 and shown in Figure 3.3.

$$EM_1 = F_{model} - F_{experiment} \tag{3-1}$$

Using the experimentally identified damage states to quantify the model's performance, an average force residual is calculated over each damage state range (i.e. beginning of test), namely: 1) $DS<DS_1$ (no damage), 2) $DS_1 \leq DS<DS_2$ (minor), 3) $DS_2 \leq DS<DS_3$ (moderate) and 4) $DS \geq DS_3$ (severe). When no damage was noted in the experiment, the average force residual is a mere 0.40

kip (or 5% of the maximum value of the specimen). Comparing the force residuals for the walls when damage occurred, for displacements greater than DS_1, but less than DS_2 (minor) the average force residual is 1.19 kip (or 15% of the maximum value of the specimen). For displacements greater than DS_2, but less than DS_3 (moderate), the average force residual is 1.53 kip (or 19% of the maximum value of the specimen). For drift levels where damage exceeded DS_3 (severe), the average force residual is 0.45 kip (or 6% of the maximum value of the specimen). Using this strategy, a modeling assessment is conducted considering all models and specimens.

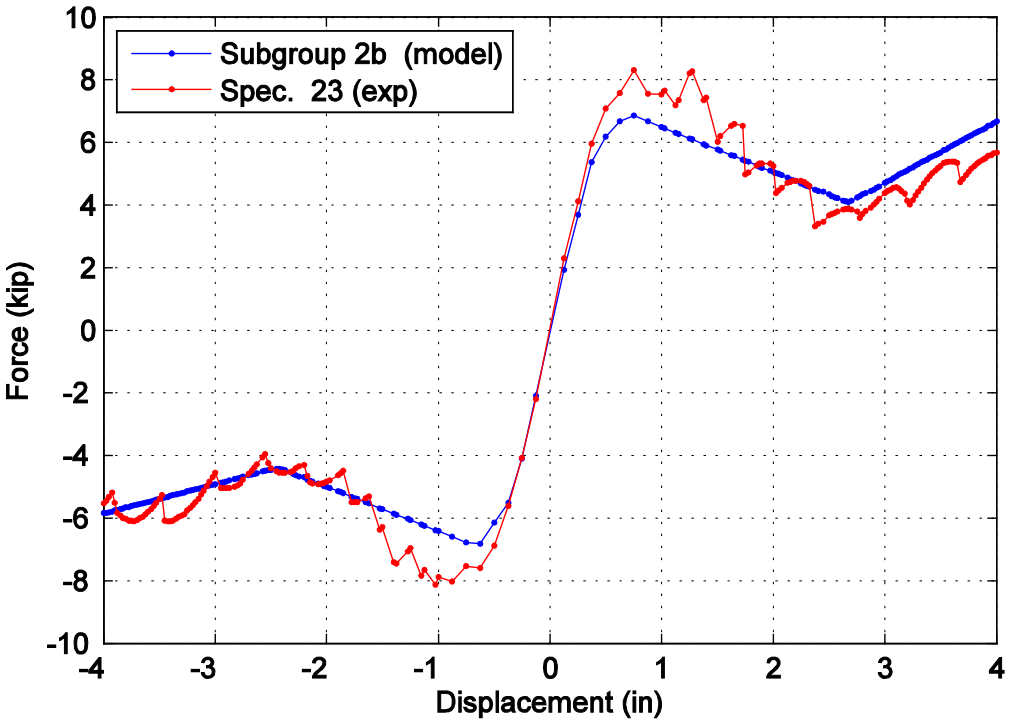

Figure 3.2 Captured maximum force envelope curve for specimen 23 and the 2b subgroup model.

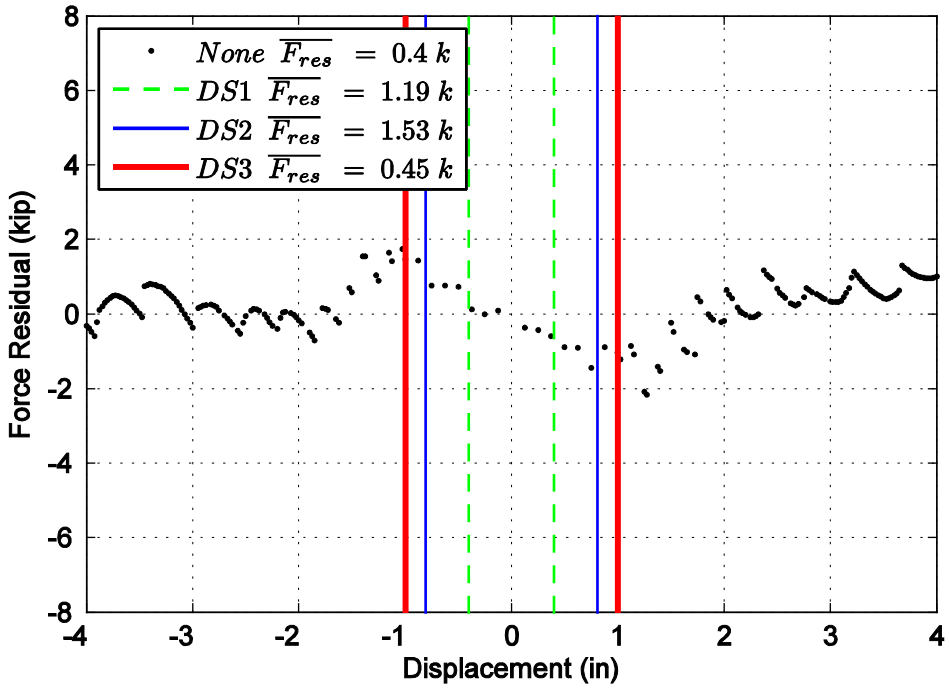

Figure 3.3 Difference in maximum attained force level when comparing specimen 23 and the 2b subgroup model.

3.3 Total Half-Cycle Hysteretic Energy

The second error metric is associated with the hysteretic energy (hysteretic area). In the model calibration, the cumulative hysteretic energy (Figure 3.4) was used to characterize the unloading parameters. However, the cumulative hysteretic energy does not explicitly demonstrate the model's performance for one individual displacement cycle or load reversal. By evaluating the hysteretic energy on a per half-cycle basis, some bias introduced with the use of one loading protocol can be reduced. To identify the half-cycle energy, the total hysteretic energy is calculated from a zero displacement location to an absolute extrema associated with the peak (target) displacement and then to the immediate next zero crossing.

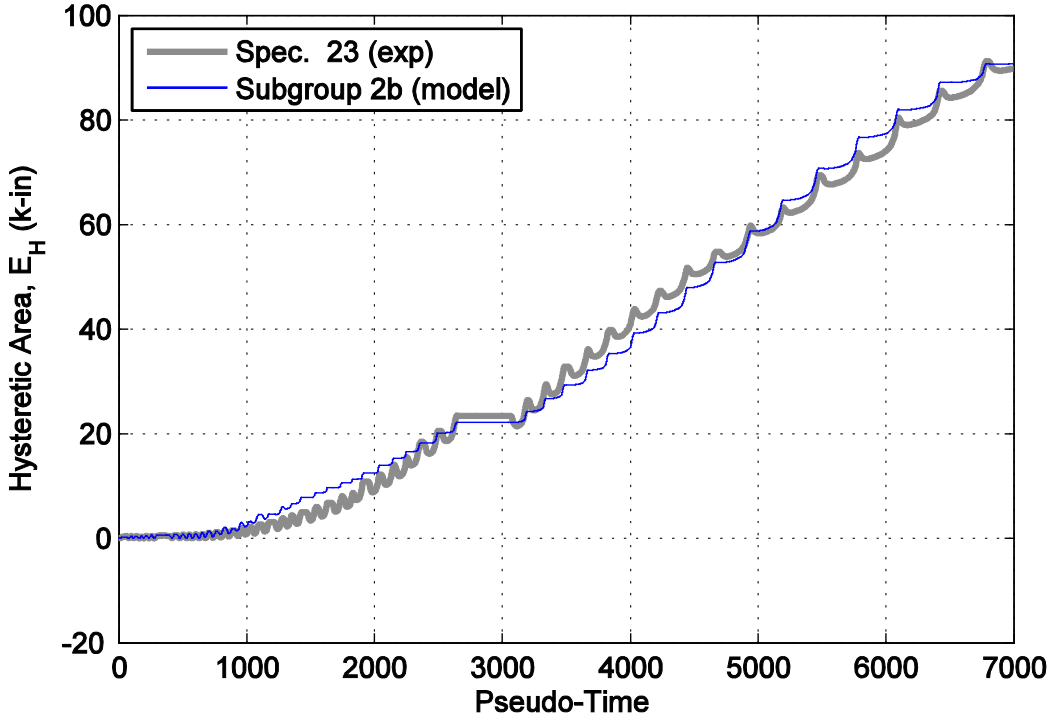

Figure 3.4 Hysteretic energy (area) comparison between specimen 23 and the 2b subgroup model.

The half-cycle hysteretic energy is then reported versus the target displacement, as demonstrated in Figure 3.5 for specimen 23. Using the experimentally identified damage states to quantify the model's performance, the total half-cycle energy residual (denoted as EM_2) is calculated over each damage state range, expressed in Equation 3-2:

$$EM_2 = \frac{\sum_{i=m}^{i=n} E_{H_{model}} - E_{H_{experiment}}}{E_{H_{experiment}}} == \frac{\sum_{i=m}^{i=n} E_{H_{diff}}}{E_{H_{experiment}}} \quad (3\text{-}2)$$

Where, $E_{H_{model}}$ is the hysteretic energy of the model, $E_{H_{experiment}}$ is the experimental hysteretic energy, $E_{H_{diff}}$ is the shorthand notation for the difference of the model and experimental hysteretic energies, where the summation is taken from point m to point n, where the damage state interval is from m up to and inclusive of point n. The residual is defined in this case as the total difference in half cycle energy at a target displacement between the experiment and model

(Figure 3.6). The sum is also calculated and reported in the legend, normalized by the cumulative experimental hysteretic energy for the same range, to evaluate the performance over the defined damage level intervals. When no damage was noted in the experiment, the normalized (cumulative) half-cycle hysteretic energy is 2.36, approximately 230% greater than what was observed in the physical specimen, due to normalization by a small number. When DS1 was achieved and before DS2 onset, the total (cumulative) normalized half-cycle hysteretic energy residual is 0.16. For damage levels between DS2 and DS3 and for damage levels greater than DS3, the normalized (cumulative) half-cycle hysteretic energy residual is 0.29 and 0.01, respectively. It is noted that for this test specimen, the maximum difference in target half cycle hysteretic energies is found before DS1 is achieved. As the specimen progresses, the ability of the model to capture the hysteretic model improves.

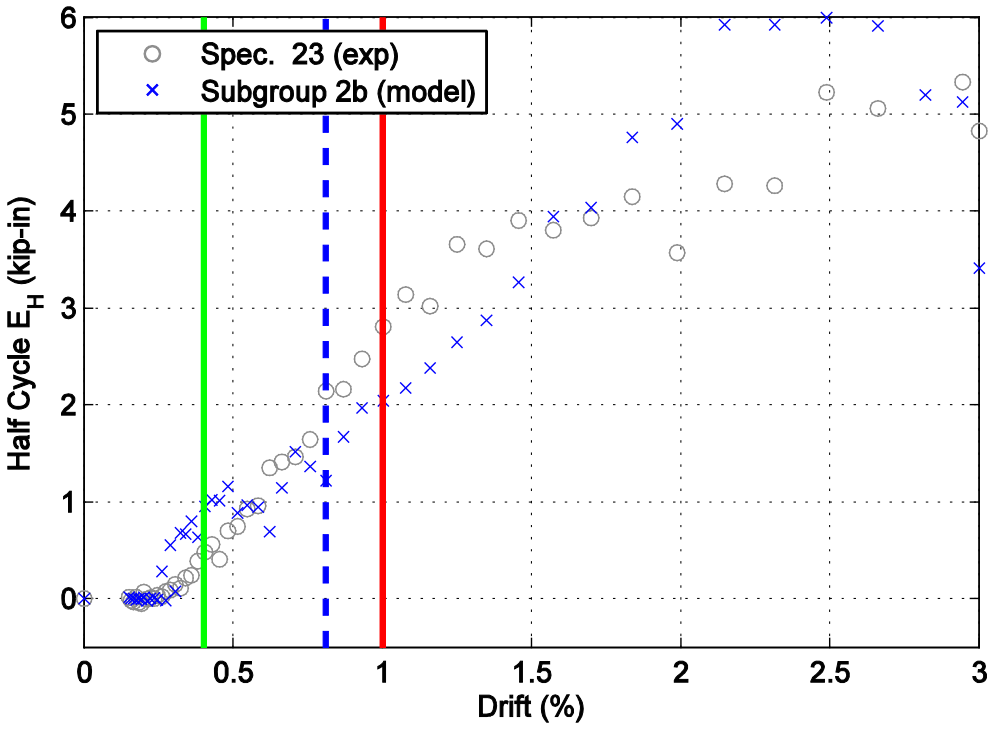

Figure 3.5 Hysteretic energy (area) per half cycle comparison between specimen 23 and the 2b subgroup model shown against maximum achieved drift level.

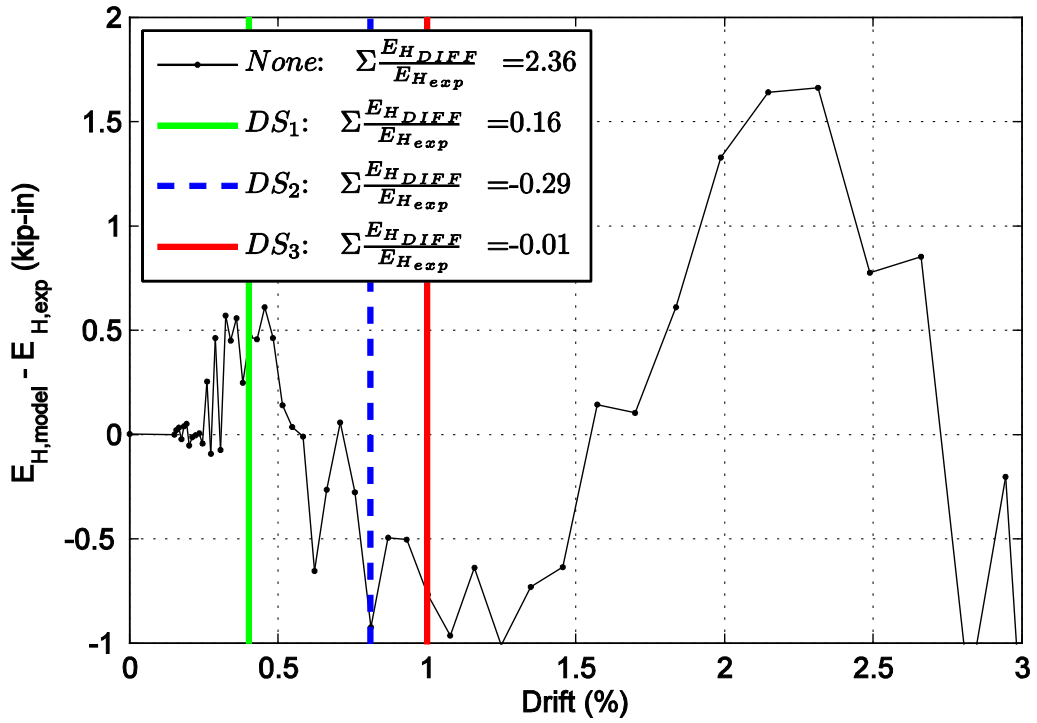

Figure 3.6 Difference in hysteretic energy (area) per half cycle comparison for specimen 23.

3.4 Use of Error Metrics to Assess all Models

Using the error metrics of residual force and half-cycle hysteretic area, an overall assessment of the model's performance for the various types of models developed is conducted. This assessment is broken into damage intervals, namely: 1) DS<DS_1, 2) DS_1≤DS<DS_2, 3) DS_2≤DS<DS_3 and 4) DS≥DS_3. Figures 3.7 and 3.8 demonstrate the average force residuals for the particular damage interval comparing the subgroup model and the mean response normalized models. When one compares the various formulations for the subgroup models and the normalized statistical models, it is noted that the mean statistical model (μ) performs just as well as the detailed subgroup models. When minor damage (<DS_2) has occurred to each of the specimens, the average normalized model performed better, as characterized by a smaller average force residual.

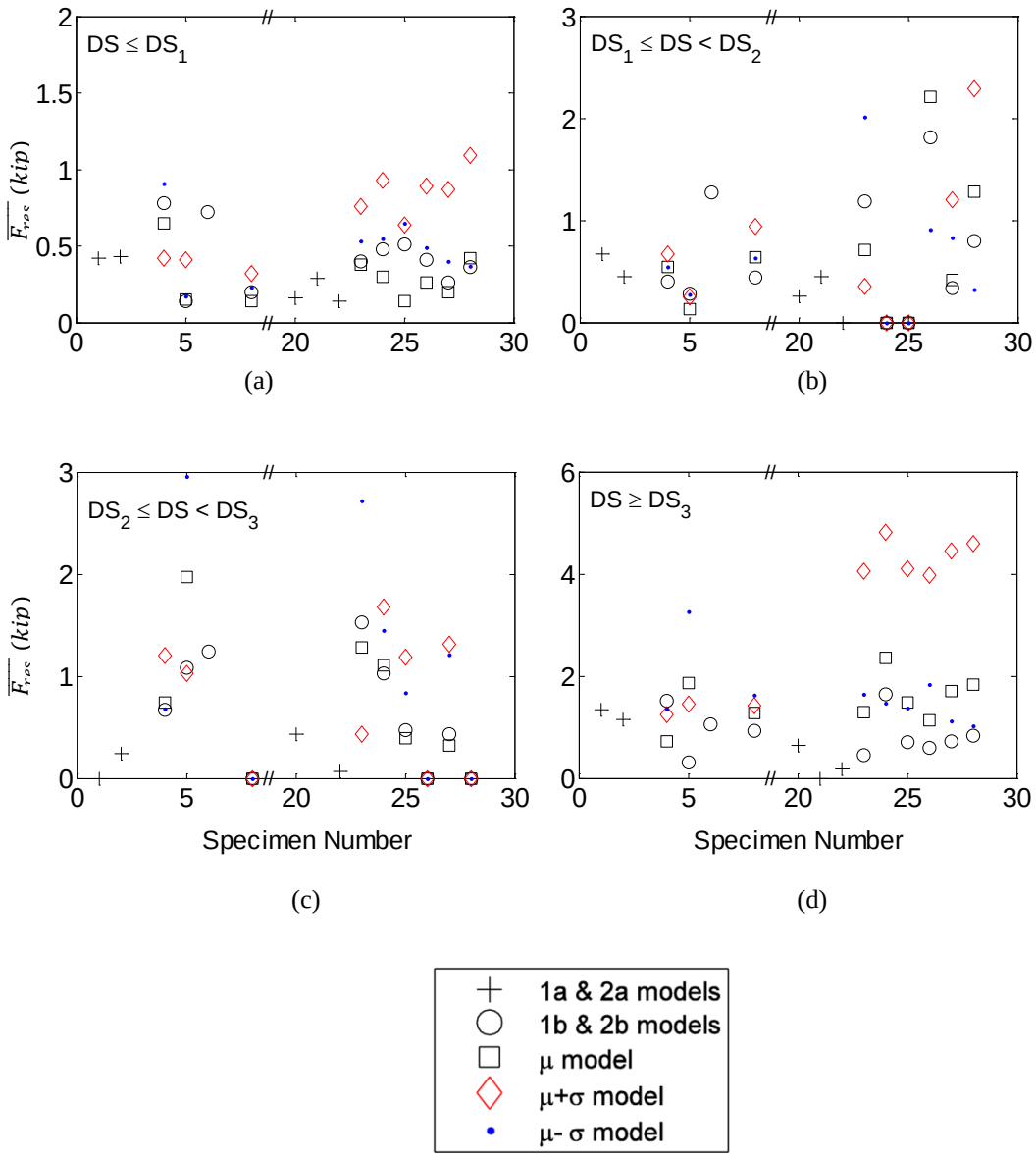

Figure 3.7 Average force residual comparing the experimental to the developed models by damage states: a) DS<DS_1, b) DS_1≤DS<DS_2, c) DS_2≤DS<DS_3 and d) DS≥DS_3.

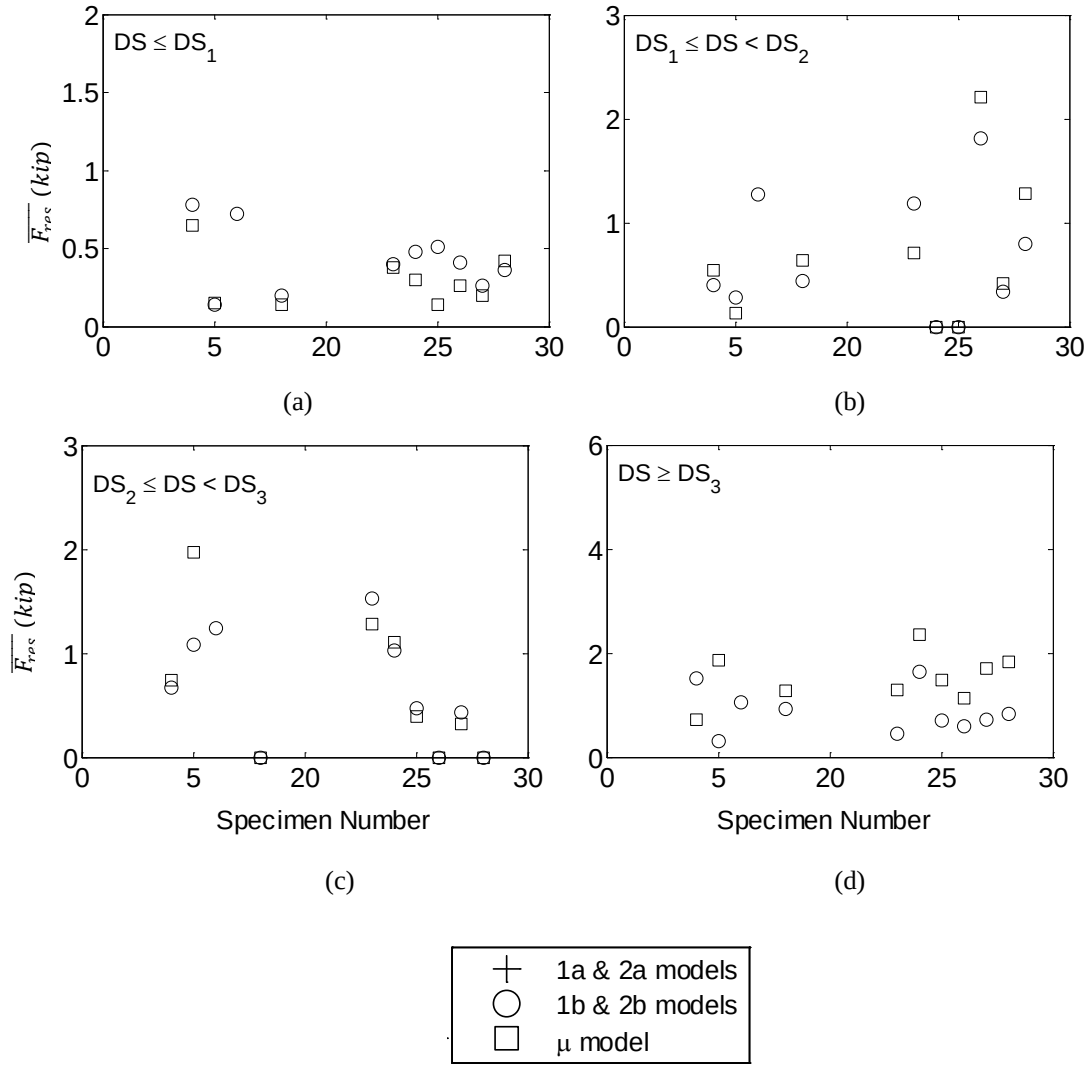

Figure 3.8 Average force residual comparing the experimental to the developed models by damage states: a) $DS<DS_1$, b) $DS_1 \leq DS<DS_2$, c) $DS_2 \leq DS<DS_3$ and d) $DS \geq DS_3$. Note only the subgroup model and mean models are presented.

In analyzing the second error metric, Figures 3.9 and 3.10 illustrate the difference in half-cycle hysteretic energy on a per damage interval. When one compares the various formulations for the subgroup models and the normalized statistical models, it is noted that the mean normalized model (μ) performs almost as well as the detailed subgroup models. When minor damage has occurred to each of the specimens ($DS_1 \leq DS<DS_2$), the mean normalized statistical model actually (μ) performs better for a few specimens. The mean normalized statistical model

(μ) overestimates the half-cycle hysteretic energy for displacement values greater than DS_3. Relating the error metrics to observed damage states, a justification can be made for use of either the subgroup or normalized statistical models when considering fully connected partition wall (PW) specimens.

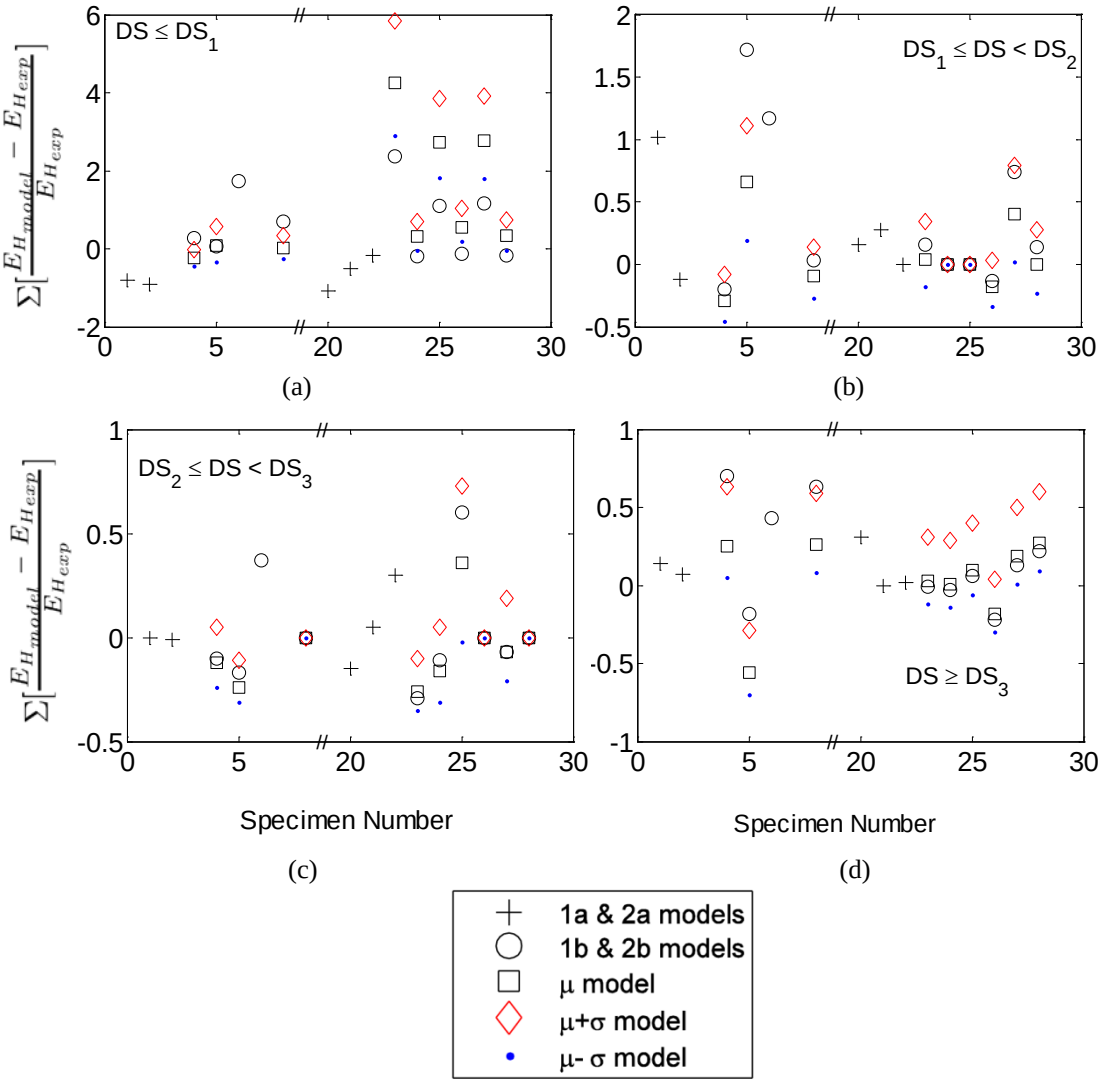

Figure 3.9 Overall residual in half-cycle hysteretic energy comparing the experimental to the developed models by damage states: (a) DS<DS_1, (b) DS_1≤DS<DS_2, (c) DS_2≤DS<DS_3 and (d) DS≥DS_3.

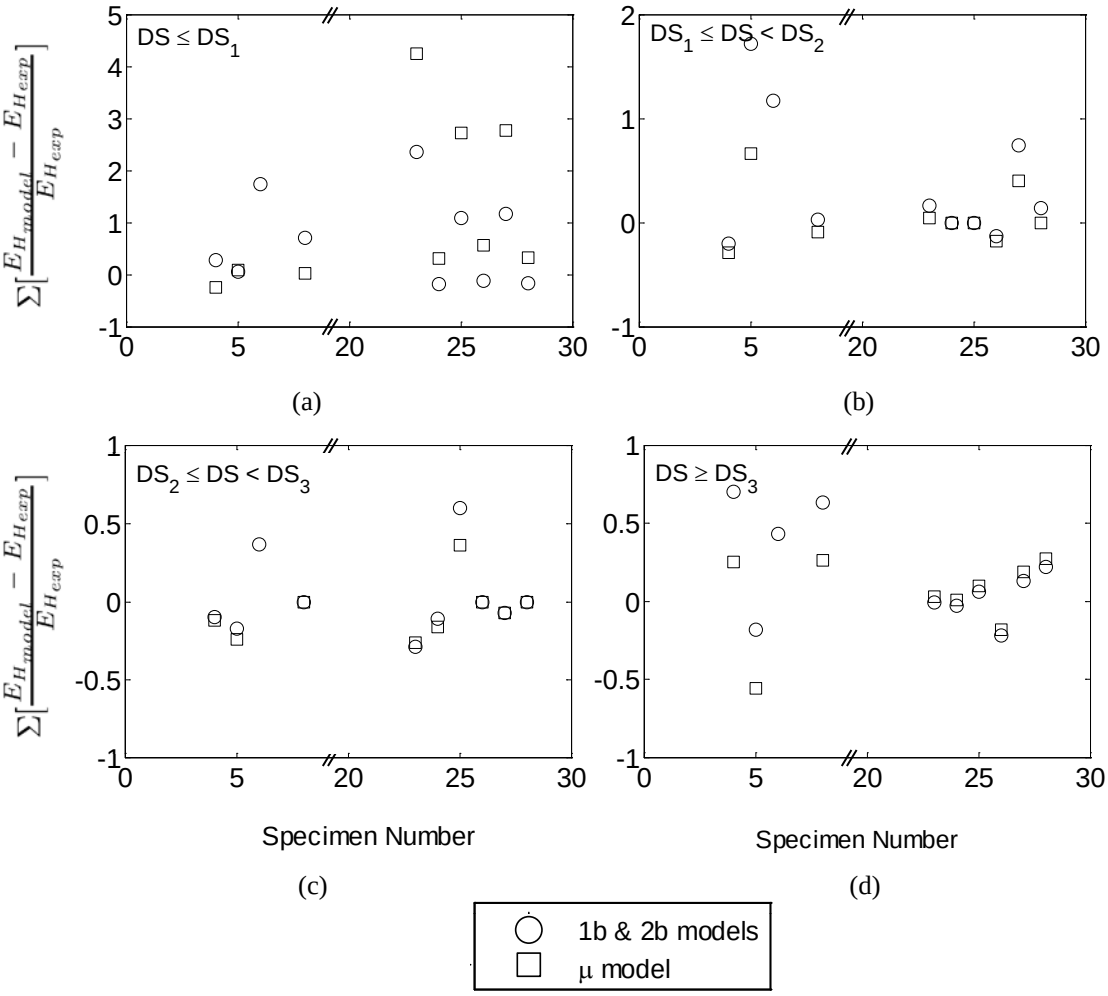

Figure 3.10 Overall residual in half-cycle hysteretic energy comparing the experimental to the developed models by damage states: (a) $DS<DS_1$, (b) $DS_1 \leq DS<DS_2$, (c) $DS_2 \leq DS<DS_3$ and (d) $DS \geq DS_3$.
Note just the subgroup model and mean models are presented.

3.5 Summary Remarks

A specimen level comparison for each model is conducted for all of the specimens considered in the modeling technique. Using two error metrics of average force residual and overall difference in half-cycle hysteretic energy, performance of each model is assessed. For complete details on the error metrics for each specimen, refer to Wood and Hutchinson (2012) and with an emphasis on Appendices A – D. Relating the error metrics to observed damage states,

a justification can be made for use of either the subgroup or normalized statistical models when considering fully connected PW specimens. In terms of the statistical models considering either plus/minus one standard deviation, the performance of the models degrade as expected, nonetheless the effect of the PWs can be later assessed through its implementation into building models.

For a fully connected specimen, use of the normalized mean model is shown to represent the PW subsystem well. For a known partially connected PW, the subgroup model 1b or 2b (commercial or institutional) would represent this PW subsystem. In the end either representation provides for fruitful assessment of the walls behavior, particularly within the drift ratios of interest, i.e. those linked with physical damage states of interest to qualify for repair or replacement of the wall. With justification of either PW model, the focus is now implementing this lumped model into realistic building models to assess its impact on the coupled system.

3.6 Acknowledgement

Chapter 3 of this dissertation is based on the NEES-Nonstructural Report, *A Numerical Model for Capturing the In-Plane Seismic Response of Interior Metal Stud Partition Walls*, published at the State University of New York, University at Buffalo. The co-author is Tara Hutchinson, where the dissertation author is the primary author and investigator.

Chapter 4 Coupled System: Building and Partition Wall Model

4.1 Introduction

This chapter presents building models and their discretization, implementation of the partition wall (PW) model into the buildings, and the selected analysis procedure. Nine building models, representative of typical design and construction, are used to demonstrate the effect of the inclusion of a PW model. Of these nine, five are reinforced concrete frame-braced buildings and four are steel frame-based buildings. For three of these building models, from the original nine, the effect of the coupled systems nonlinear time history response under realistic earthquakes is assessed. This chapter details an overview of the design of the developed building models, the calculation of representative lengths of PWs, and the analysis of the sensitivity to dynamic response of the inclusion of PWs. Building Models and Discretization

4.1.1 Overview

This section discusses the development of a numerical parametric space comprised of reinforced concrete and steel moment frame buildings. The suite of buildings is intended to represent typical building stock used in low to high-rise construction in the United States within regions of high seismicity.

Modern design codes are used in the design of these buildings. The building models are ultimately subjected to a coupled analysis where both the bare building frame and nonstructural component systems are considered, namely PWs. The remainder of this section presents an outline of the design and discretization of the developed building models.

4.1.2 Design of Concrete Buildings

Five perimeter concrete special moment resisting frame (SMRF) buildings of 2, 4, 8, 12 and 20 stories (Wood et al., 2010) were selected for this study. Herein they are denoted as RC-2, RC-4, RC-8, RC-12, and RC-20, respectively. The footprint of all concrete buildings is 150 feet by 120 feet with five bays in each direction. The building dimensions yield a longitudinal bay width of 30 feet, transverse bay width of 24 feet and story height of 12 feet. Building design did not include foundations as all buildings were assumed to have adequate support and to be fixed at their base. A plan and elevation view of the prototype building is shown in Figure 4.1.

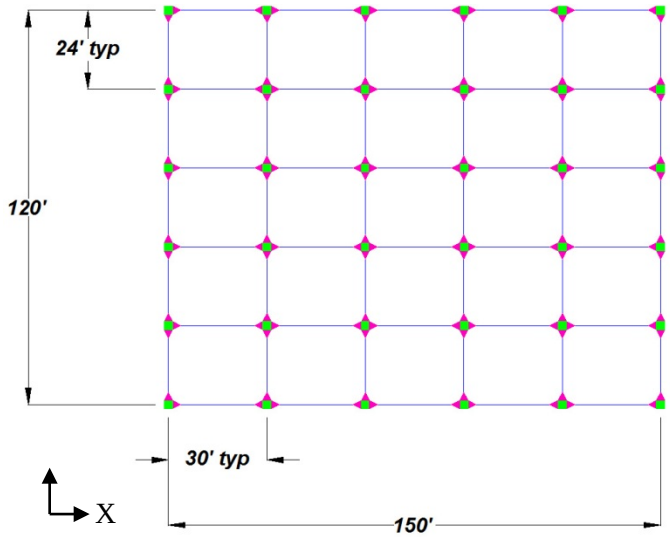

Figure 4.1 Prototype Building Plan View illustrated for concrete buildings.

Design and analysis were conducted for the longitudinal direction (x-direction) of the prototype building. Design was governed by IBC (ICC, 2006) and ACI 318-08 (ACI, 2008). The IBC 2006 design code provided estimates of the base shear, response modification factor (R factor), code-based period estimates and lateral force distribution, while ACI 318-08 was utilized for the general concrete design and detailing (Chapter 21). In the frame designs, strong-column weak-beam philosophy was adopted, i.e. the sum of the moment capacity at the columns was

designed to be at least 20% greater than the sum of the moment capacity at the beams. All of the SMRF buildings designed were governed by seismic loading except for the 2-story SMRF, which was governed by gravity loads. In the design of the SMRF buildings, the response modification factor was taken as 8. Deflection of the beams was checked to assure service load deflections did not exceed L/360 (where L is beam span).

In the detailing of the beams and columns, an ideal arrangement of the reinforcement was assumed. A typical beam is shown in Figure 4.2. The tension reinforcement, as specified in the design, was identical to the tension reinforcement for this symmetric section. The reinforcing steel was chosen to be in one layer for simplicity and double leg #4 stirrups were selected for shear reinforcement. The confinement spacing involved shear reinforcement as shown in the typical beam diagram and provided a minimum lateral pressure of 9% of the target f'_c (Englekirk, 2003) within the assumed plastic hinge zone. The reinforcement ratio for the column included all reinforcement in the cross section. The columns were detailed with a single longitudinal reinforcement layer on each face. The final SRMF building designs are presented in Figure 4.3, with detailing of the beams and columns summarized in Table 4.1. The longitudinal reinforcement ratio (ρ_l) was calculated for a tension area of reinforcement over the gross concrete area for the beams. The range of longitudinal reinforcing steel ratios, ρ_l, for the columns and beams was 1.1 – 2.7%. To obtain complete details on the development of these concrete building models and the represented seismic hazard, refer to the original study by Wood et al (2009).

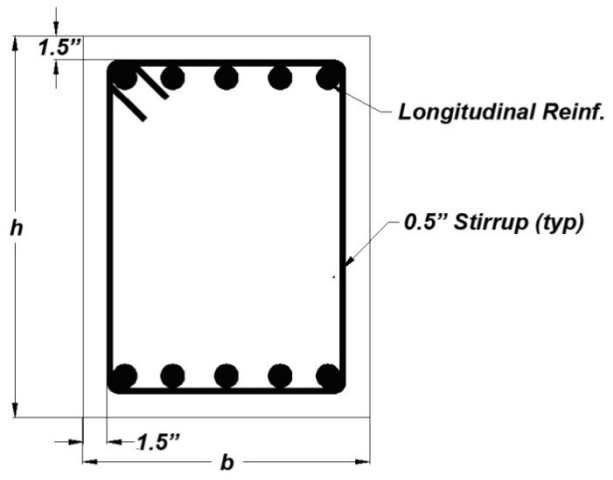

Figure 4.2 Typical beam - refer to Table 4.1 for specific details.

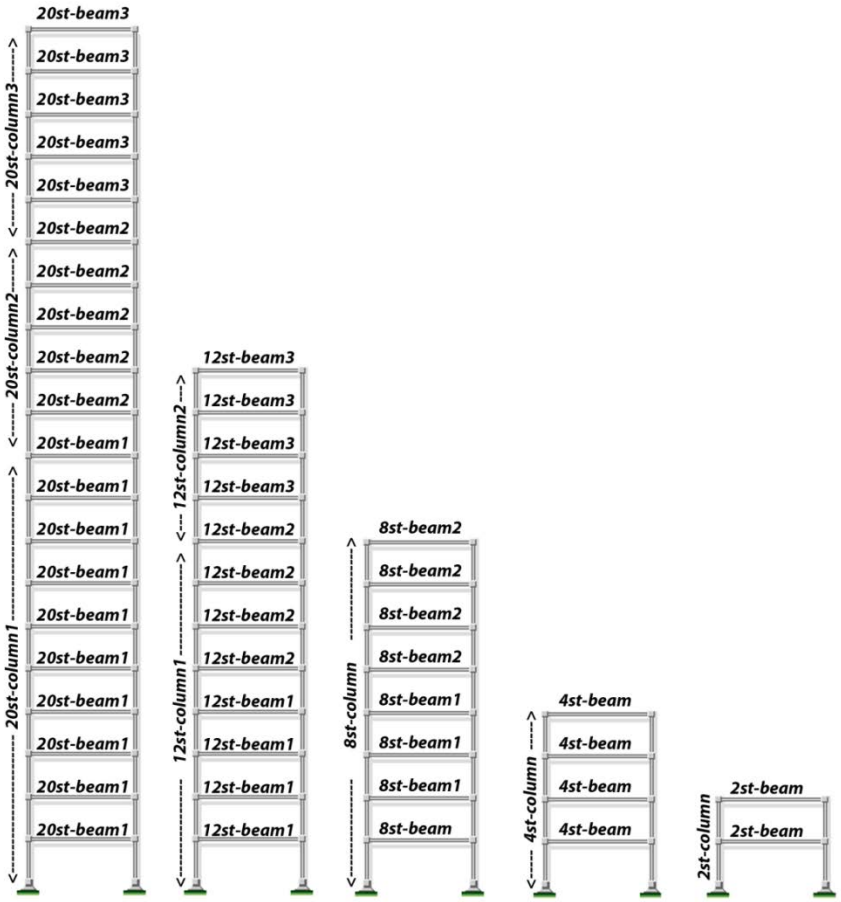

Figure 4.3 SMRF building designs for RC-20, RC-12, RC-8, RC-4 and RC-2. Note base of model fixed, and bottom of columns fixed.

Table 4.1 SMRF building design summary (refer to Figure 1.3)

Member	b (in)	h (in)	f'_c (ksi)	Longitudinal Reinforcing	ρ_l (%)	Confinement (c/c)
2st-beam	24	28	5	9 - #9	1.28	#5 @ 6.0"
2st-column	30	30	5	20 - #9	2.22	#5 @ 5.5"
4st-beam	26	30	5	10 - #9	1.28	#5 @ 6.0"
4st-column	30	30	5	24 - #9	2.67	#5 @ 5.5"
8st-beam1	30	30	5	12 - #9	1.34	#5 @ 5.5"
8st-beam2	26	30	5	10 - #9	1.28	#5 @ 6.0"
8st-column	32	32	6	20 - #10	2.67	#5 @ 4.0"
12st-beam1	30	30	5	12 - #9	1.34	#5 @ 5.5"
12st-beam2	28	30	5	11 - #9	1.10	#5 @ 5.5"
12st-beam3	24	28	5	9 - #9	1.28	#5 @ 6.0"
12st-column1	32	32	8	20 - #10	2.48	#5 @ 3.0"
12st-column2	32	32	8	16 - #10	1.98	#5 @ 3.0"
20st-beam1	32	32	5	13 - #9	1.27	#5 @ 5.0"
20st-beam2	30	30	5	12 - #9	1.34	#5 @ 5.5"
20st-beam3	24	28	5	9 - #9	1.28	#5 @ 6.0"
20st-column1	36	36	10	24 - #10	2.35	#5 @ 3.0"
20st-column2	34	34	10	20 - #10	2.20	#5 @ 3.0"
20st-column3	32	32	10	16 - #10	1.98	#5 @ 3.0"

4.1.3 Design of Steel Buildings

In the selection of representative steel buildings, those designed as part of the 1999 Steel SAC Project were selected as an ideal candidate (Gupta et al., 1999). From the SAC study, three buildings designed for the Los Angeles hazard were chosen. The selected steel buildings include three office buildings of 3, 9 and 20 stories, denoted as S-3, S-9 and S-20 respectively herein. An additional fourth steel building, a three story hospital, was considered as well. This hospital building helps to demonstrate the institutional style of construction for PWs. This hospital was a redesigned building from the SAC study modified for its critical functionality (Wieser 2011). The three story hospital building will be denoted as S-3H. Each of these steel buildings has a slightly different plan or elevation view as demonstrated in Figure 4.4 - Figure 4.7 for each structure. The differences noticed between these building models and the concrete buildings include a larger first story height to accommodate entryways and placement of a penthouse. Since these buildings

are modeled in two dimensions, any torsional effect induced by the placement of the penthouses would not be captured in buildings S-3, S-3H and S-9 due to stiffness eccentricity. Similarly, as assumed for the concrete buildings, adequate foundation support assumption was made and only floors above ground were considered. Subterranean levels were neglected for simplicity in this study as all models were assumed fixed at their base at the ground level.

Original design of the SAC buildings was governed by UBC 1994 (ICBO, 1994) where these office buildings were designed for an effective peak ground acceleration of 0.40 g and a site classification of s2, representing an intermediate soil characterization. UBC-94 subsequently became part of UBC-97 (ICBO, 1997). According to IBC 2006 (ICC, 2006), the redesigned hospital structure had a design acceleration of 1.51 g and 0.75 g in the short period (S_s) and one second period (S_1) accelerations and a site classification of D, characterized as “stiff soil”. Details on the structural members are listed in Table 4.2. For complete details on the building designs, refer to the original studies by Gupta et al (1999) and Wieser (2011).

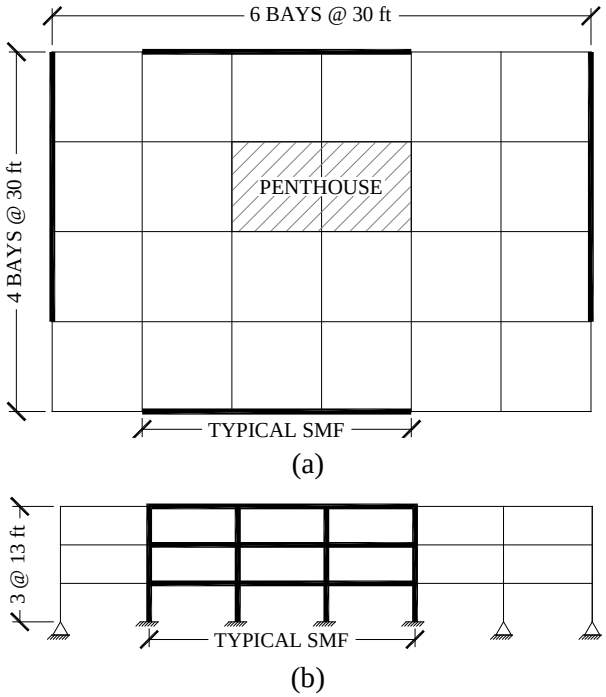

Figure 4.4 Plan (a) and elevation view (b) for the three story SAC building, denoted as S-3. Note base of model fixed, and bottom of columns fixed.

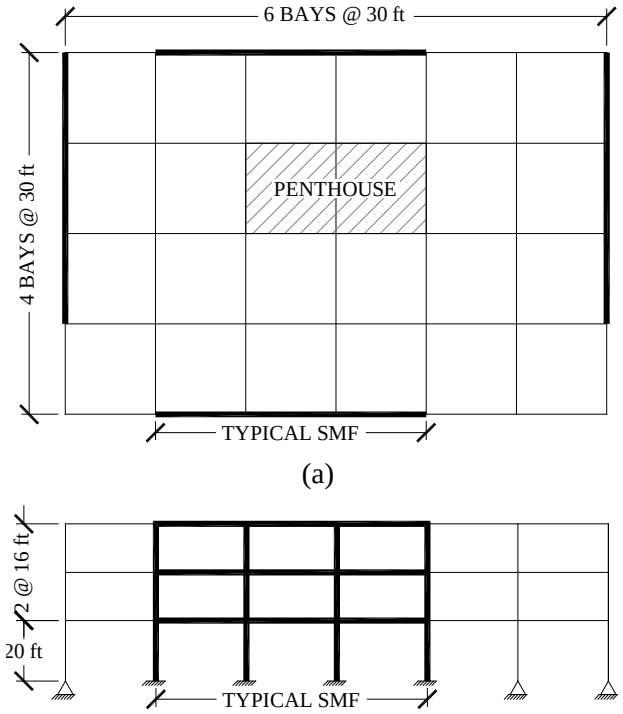

Figure 4.5 Plan (a) and elevation view (b) for the three story hospital building, denoted as S-3H.
Note base of model fixed, and bottom of columns fixed.

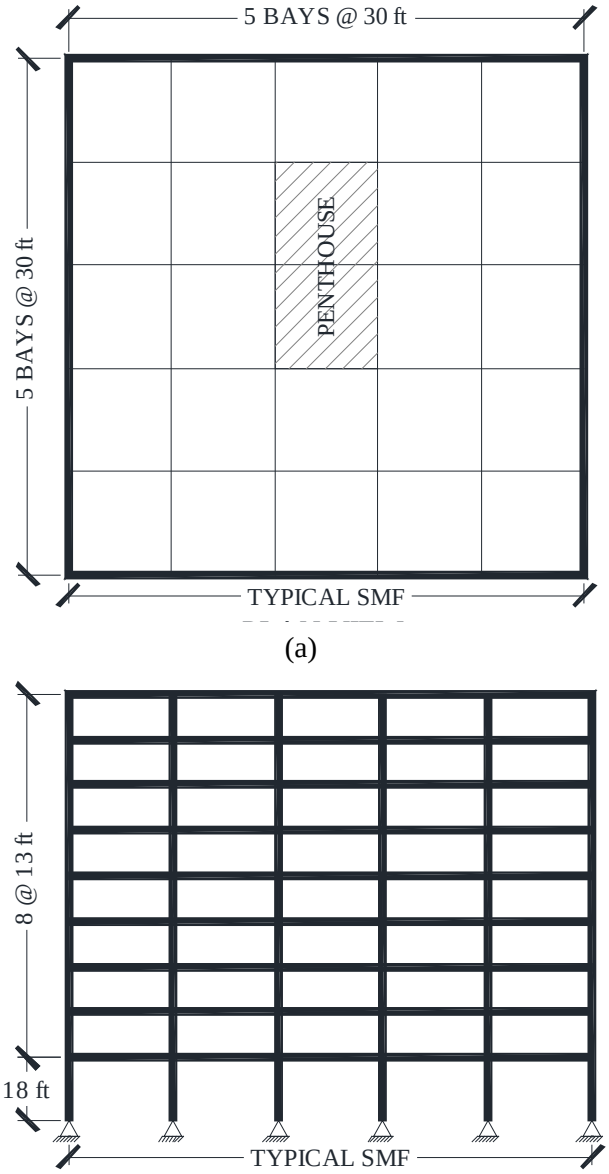

Figure 4.6 Plan (a) and elevation view (b) for the nine story SAC building, denoted as S-9. Note base of model fixed, and bottom of columns fixed.

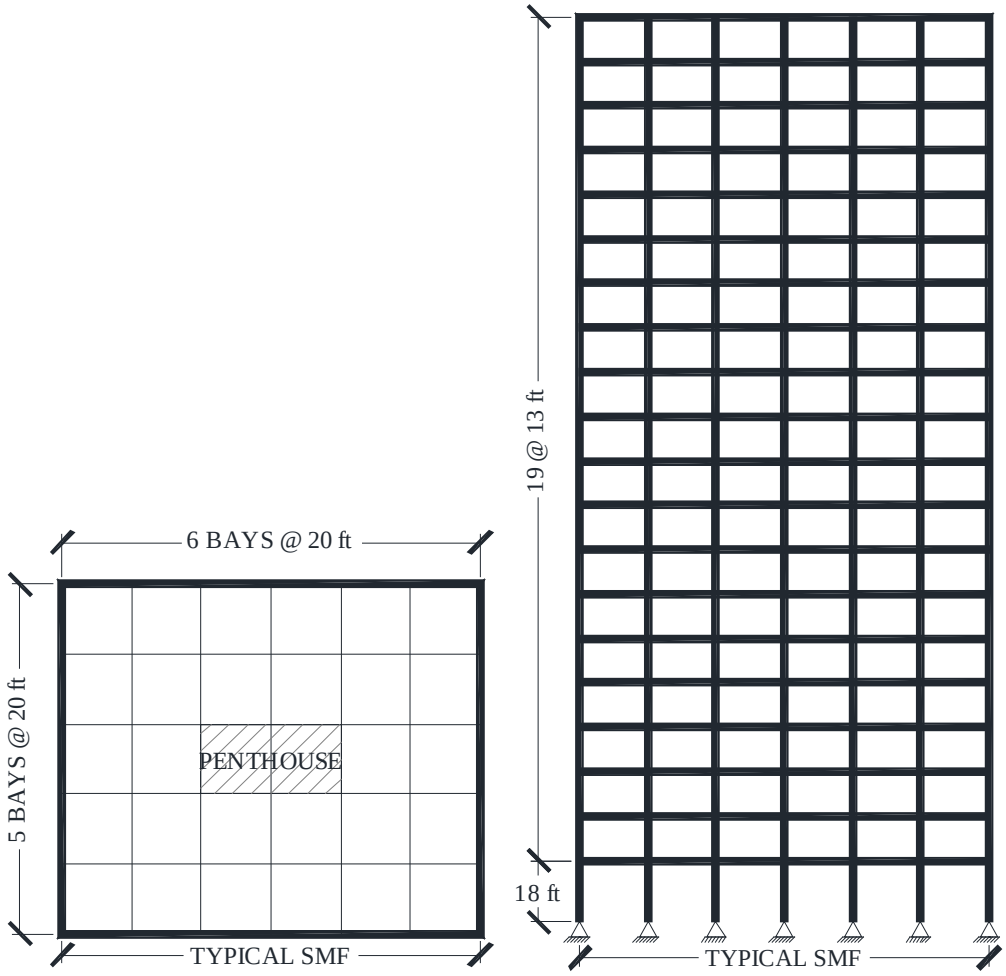

(a) (b)

Figure 4.7 Plan (a) and elevation view (b) for the twenty story SAC building, denoted as S-20.
Note base of model fixed, and bottom of columns fixed.

Table 4.2 Steel building design summary.

Building	Level	Column	Beam	Elevation (ft)
S-3	1	W14x311	W30x116	13
	2	W14x311	W30x116	26
	3	W14x311	W24x62	39
S-3H	1	W27x368	W33x152	20
	2	W27x368	W33x152	36
	3	W27x368	W33x152	52
S-9	1	W14x500	W36x150	18
	2	W14x500	W36x150	31
	3	W14x455	W33x141	44
	4	W14x455	W33x141	57
	5	W14x370	W33x141	70
	6	W14x370	W33x130	83
	7	W14x283	W27x102	96
	8	W14x283	W27x94	109
	9	W14x257	W24x62	122
S-20	1	W24x335	W30x99	18
	2	W24x335	W30x99	31
	3	W24x335	W30x99	44
	4	W24x335	W30x99	57
	5	W24x335	W30x108	70
	6	W24x279	W30x108	83
	7	W24x279	W30x108	96
	8	W24x279	W30x108	109
	9	W24x279	W30x108	122
	10	W24x279	W30x108	135
	11	W24x279	W30x99	148
	12	W24x229	W30x99	161
	13	W24x229	W30x99	174
	14	W24x229	W30x99	187
	15	W24x162	W30x99	200
	16	W24x162	W30x99	213
	17	W24x162	W27x84	226
	18	W24x117	W27x84	239
	19	W24x117	W24x62	252
	20	W24x94	W21x50	265

4.1.4 Model Discretization

Numerical modeling of all prototypical buildings was conducted in the OpenSees (Mazzoni et al., 2011) platform. It is noted that a single direction of the lateral resisting system was model for each building, resulting in two-dimensional model representations. Two different two-dimensional model discretizations were developed, one for the reinforced concrete buildings and one for the steel buildings. In both formulations, lumped masses and equivalent nodal loads were used. To account for large deformations, the corotational geometric transformation was used. Mass and stiffness proportional Rayleigh damping was specified in the first two modes at 5% of critical for the concrete buildings and 2% of critical for the steel buildings.

4.1.4.1 Reinforced Concrete Model Building Details

The reinforced concrete building models were discretized using only one type of element: namely the *BeamWithHinges* element (Figure 4.8), developed by Scott and Fenves (2006). This element was selected because it performs well for members anticipated to undergo reasonably localized nonlinear deformation as well as softening or degradation of the material (Scott and Fenves, 2006). The *BeamWithHinges* element also eliminates the nonobjective curvature response due to its sensitivity to the number of integration points (Coleman and Spacone, 2001). This element is developed as a force-based, lumped plasticity, zero-volume line element with two different sections: a fiber section at each end, which represents the plastic hinge over a discrete length l_p and an interior linear elastic section.

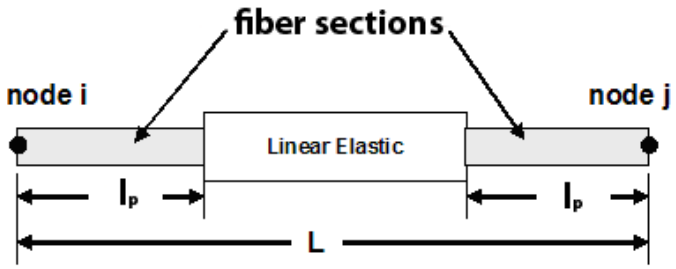

Figure 4.8 BeamWithHinges element diagram.
(from Mazzoni et al., 2011)

For concrete buildings, the length of the plastic hinge l_p was estimated using Paulay and Priestley's (1992) model:

$$l_p = 0.08L + 0.15 f_y d_b \; [kips, inches] \tag{4-1}$$

where L = length of the beam (inches), f_y = yield strength (ksi) of the longitudinal reinforcing steel of diameter d_b (inches). This plastic hinge estimate was determined experimentally accounting for the effects of strain softening, localization and penetration.

Since the middle of the element was defined as linear elastic, only the elastic gross sectional properties were of interest, namely, the Young's modulus of elasticity, cross-sectional area and the moment of inertia. In the development of the fiber section, two material models were selected from the library of materials available within OpenSees. Namely, the linear tension strength concrete model (concrete02; Figure 4.9) and the Reinforcing Steel model were used.

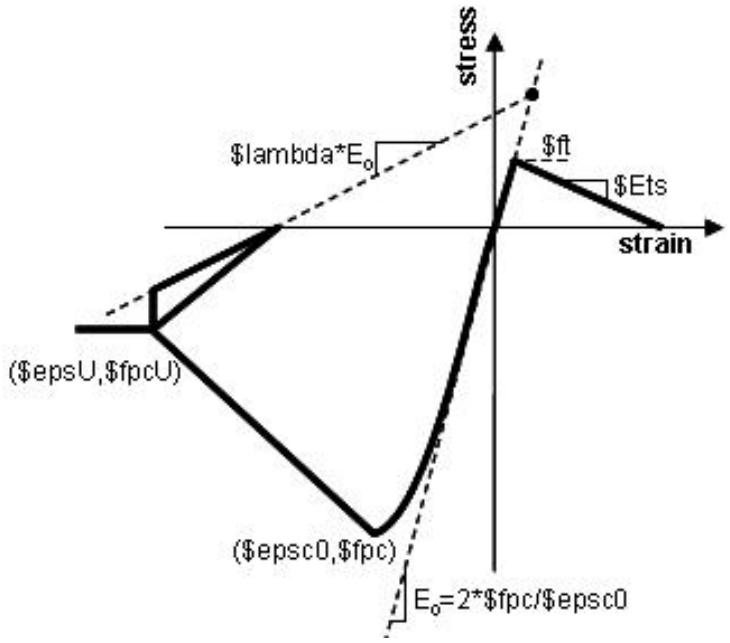

Figure 4.9 Linear tension strength concrete model.
(from Mazzoni et al., 2011)

The fiber sections were discretized into regions containing confined and unconfined concrete; core and cover, respectively. The unconfined concrete properties were based on the design f'_c, a strain at maximum concrete strength of $\varepsilon_{cu} = 0.003$, an ultimate stress set at 20% of the design f'_c, a strain at the ultimate stress defined at 0.01, and a tension strength of 14% of the design f'_c. The concrete elastic modulus E_c was set at $57000\sqrt{f'_c}$, where f'_c is in psi. The effects of confinement were accounted for using the model of Mander et al. (1988). The resulting increased strain ε_{cc}, ε_{ccu} and stress f'_{cc}, f'_{ccu} due to confinement for each section are summarized in Table 4.3. Additionally in the table, s = the spacing of the transverse reinforcement for confinement, f'_{cc} = the compression strength of confined concrete, ε_{cc} = strain at peak strength, ε_{ccu} = the ultimate compression strain, k_c = the effect of confinement ratio, and $f_{cc,u}$ = the stress at ultimate strain.

Table 4.3 Confined concrete properties for concrete buildings.

Element	f'_c (ksi)	ρ_l (%)	s (in)	f'_{cc} (ksi)	ε_{cc}	ε_{ccu}	k_c	$f_{cc,u}$ (ksi)
2st-Beam	5	1.28	6.0	6.34	0.0047	0.019	1.27	4.40
2st-Column	5	2.22	5.5	6.35	0.0047	0.018	1.27	4.54
4st-Beam	5	1.28	6.0	6.26	0.0045	0.018	1.25	4.33
4st-Column	5	2.67	5.5	6.35	0.0047	0.018	1.27	4.54
8st-Beam1	5	1.34	5.5	6.35	0.0047	0.018	1.27	4.55
8st-Beam2	5	1.28	6.0	6.26	0.0045	0.018	1.25	4.33
8st-Column	6	2.48	4.0	7.81	0.0050	0.022	1.30	5.12
12st-Beam1	5	1.34	5.5	6.35	0.0047	0.018	1.27	4.54
12st-Beam2	5	1.31	5.5	6.37	0.0047	0.019	1.27	4.53
12st-Beam3	5	1.28	6.0	6.34	0.0047	0.019	1.27	4.40
12st-Column1	8	2.48	3.0	10.49	0.0051	0.028	1.31	5.37
12st-Column2	8	1.98	3.0	10.49	0.0051	0.028	1.31	5.37
20st-Beam1	5	1.27	5.0	6.41	0.0048	0.018	1.28	4.64
20st-Beam2	5	1.34	5.5	6.35	0.0047	0.018	1.27	4.54
20st-Beam3	5	1.28	6.0	6.34	0.0047	0.019	1.27	4.40
20st-Column1	10	2.35	3.0	12.30	0.0043	0.025	1.23	3.90
20st-Column2	10	2.2	3.0	12.39	0.0044	0.027	1.24	4.07
20st-Column3	10	1.98	3.0	12.53	0.0045	0.028	1.25	4.26

The steel model selected to represent the reinforcing steel within the concrete members involves the following input parameters: yield strength f_y = 60 ksi, elastic modulus E_s = 29000 ksi, and strain hardening ratio = 0.01. Figure 4.10 presents the backbone curve of the model. Parameters selected for input include: the elastic modulus, E_s = 29000 ksi, the yield strength f_y = 60 ksi, post-yield modulus (transition to hardening region), E_{sh} = 1.85% of the elastic modulus, post yield strain (transition to hardening region), ε_{sh} = 0.003, strain at peak stress ε_{su} = 0.09, and peak stress f_{su} = 110% of the yield strength. The original development of these buildings did not use the *ReinforcingSteel* material model; however, may have also been appropriate to capture degradation effects (Mazzoni et. al, 2011).

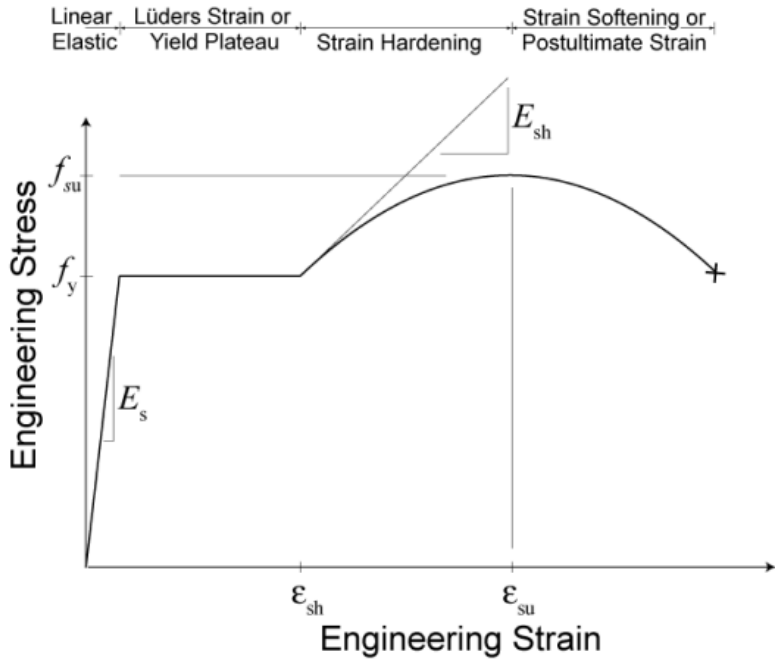

Figure 4.10 Steel model used for the reinforcing steel of the wall elements in the dual wall-frame building models.
(Mazzoni et al., 2011)

4.1.4.2 Steel Model Buildings Details

The steel building models were discretized using the *NonlinearBeamColumn* element. This element performs well for members anticipated to behave nonlinearly on the global response level (Spacone et. al, 1992). This element is developed as a force-based, lumped plasticity, zero-volume line element with fiber sections. Only one fiber section was defined at each of the six integration points along the beam and at the five integrations points for the column members. Each fiber section was idealized using a predefined W-section procedure. The beam-column connections were assumed to be simple moment connections, i.e. no panel-zone effects were considered.

For the steel moment frame buildings, the selected material model was Menegotto-Pinto (Filippou et. al, 1983). This model involves the following input parameters: yield strength f_y = 50

ksi, elastic modulus E_s = 29000 ksi, and strain hardening ratio = 0.02. In addition, specific to the Menegotto-Pinto steel model, select parameters were taken as recommended in the OpenSees manual. Namely, the parameter R_0, which controls the Bauschinger effect, was set at 10.0, cR_1 as 0.925, and cR_2 as 0.15. No isotropic strain hardening was considered, therefore a_1 and a_3 were set at 0 and a_2 and a_4 at 1.0. The values for a_2 and a_4 were not unique as long as they are non-zero. These material parameters match the parameters used by Wieser (2011).

4.1.5 Building Model Summary

In summary, nine building models were selected. The reinforced concrete buildings simulating office buildings varied from 2-20 stories where the fundamental period ranged from 0.24 seconds to 2.07 seconds (Table 4.4 and Figure 4.11). For the three steel buildings taken from the 1999 SAC project, office buildings were simulated again were the stories ranged from 3-20 with a corresponding period range of 0.34 seconds to 1.79 seconds. The redesigned hospital with a similar footprint as the three story SAC building had a fundamental period of 0.28 seconds. All nine buildings were designed according to modern building codes for areas of high seismicity. The reinforced concrete buildings have spectral accelerations at the short period 1.5-2 g and approximately 0.8 g at one second. Similarly, the SAC buildings were designed for high levels of acceleration for a seismic zone 4 with the corresponding effective design PGA of 0.4 g. The mass participation of the buildings is primarily above 80% for the fundamental mode, indicating a first-mode dominated response of the structure. However, a maximum value of 16% is observed for the second mode mass participation, indicating that higher modes are significant.

Table 4.4 Summary of building suite considered.

Model Name	Material	Design Code	Occupancy/Use	Number of Stories	Floor Plan[1]		Story Heights			Design Accelerations[2]		Site Classification (ASCE 7-05)	Period[3]
					NS	EW	First (ft)	Second (ft)	Upper (ft)	S_s (g)	S_1 (g)		T_1 (s)
RC-2	Concrete	IBC 2006, ACI 318-08	Office Bldg	2	5 @ 30ft	5 @ 30ft	12.0	12.0	12.0	2.00	0.77	C	0.20
RC-4	Concrete	IBC 2006, ACI 318-08	Office Bldg	4	5 @ 30ft	5 @ 30ft	12.0	12.0	12.0	2.00	0.77	C	0.42
RC-8	Concrete	IBC 2006, ACI 318-08	Office Bldg	8	5 @ 30ft	5 @ 30ft	12.0	12.0	12.0	2.00	0.77	C	0.84
RC-12	Concrete	IBC 2006, ACI 318-08	Office Bldg	12	5 @ 30ft	5 @ 30ft	12.0	12.0	12.0	2.00	0.77	C	1.19
RC-20	Concrete	IBC 2006, ACI 318-08	Office Bldg	20	5 @ 30ft	5 @ 30ft	12.0	12.0	12.0	2.00	0.77	C	2.07
S-3H	Steel	IBC 2006	Hospital	3	4 @ 30ft	6 @ 30ft	20.0	16.0	16.0	1.508	0.75	D	0.28
Model Name	Building	Design Code	Occupancy/Use	Number of Stories	Floor Plan		Story Heights			Seismic Design		Site Classification (UBC 1994)	
					NS	EW	First (ft)	Second (ft)	Upper (ft)	Zone	Effective PGA (g)		T_1 (s)
S-3	Steel	UBC 1994	Office Bldg	3	4 @ 30ft	6 @ 30ft	13.0	13.0	13.0	4	0.40	s2	0.34
S-9	Steel	UBC 1994	Office Bldg	9	5 @ 30ft	5 @ 30ft	12.0	18.0	13.0	4	0.40	s2	0.93
S-20	Steel	UBC 1994	Office Bldg	20	5 @ 20ft	6 @ 20ft	24.0	18.0	13.0	4	0.40	s2	1.40

1. Number of bays and span width between them.
2. S_s = short period spectral acceleration, S_1= 1 second spectral acceleration.
3. Fundamental period of the building model without the partition wall elements, as estimated with eigenvalue analyses.

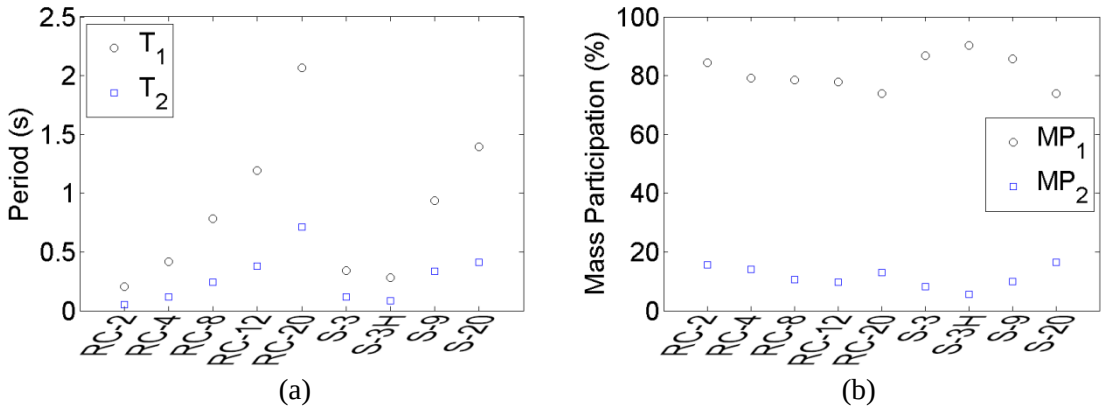

Figure 4.11 Summary statistics of the bare building (no PW): (a) first and second mode periods and (b) first and second mode mass participations.

4.2 Implementation of the PW into the Prototypical Building Models

This section details the implementation of the PW model into the building models. The PW is connected to the structural model, spanning the beam midpoints between adjacent floors using simulated rigid members, as illustrated in Figure 4.12. The simulated rigid members utilize the *equalDOF* command within OpenSees, slaving the two adjacent nodes in both displacement and rotation. As a result, the boundary conditions for the intersections at the beam midpoints for the fully connected PW models are modeled by restraining the two lateral displacement and one rotational degrees of freedom at both the top and bottom nodes (Figure 4.12) for a two dimensional model. This simplistic model allows for the PW to be lumped at the story mid-height and bay width, neglecting any torsional effect if placed in a three dimensional model. Note that the PW is assumed massless and its more critical in0plane behavior is considered. The monotonic force-displacement relations of the implemented walls are shown in Figure 4.13. In this selected study, only the normalized partition model is executed as it allows for the assessment of the PW variability.

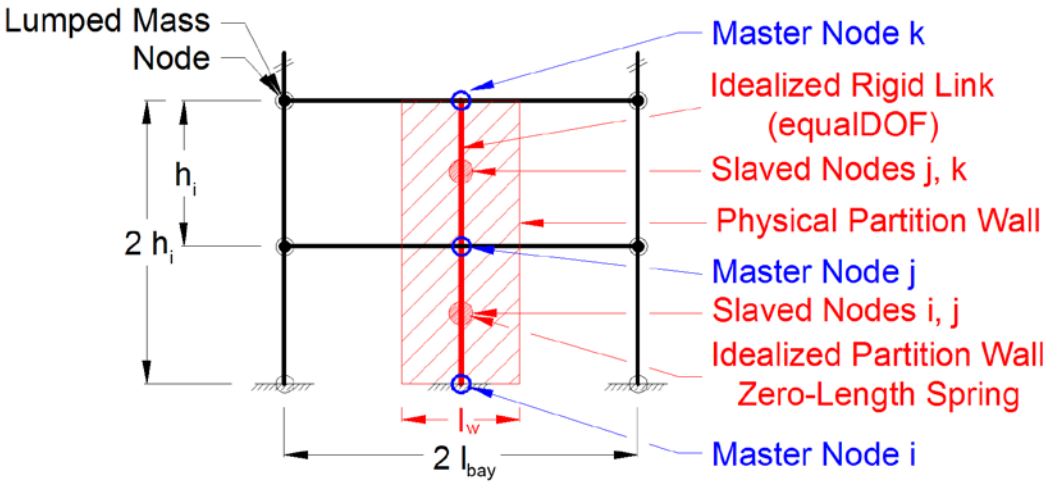

(a) Un-deformed shape

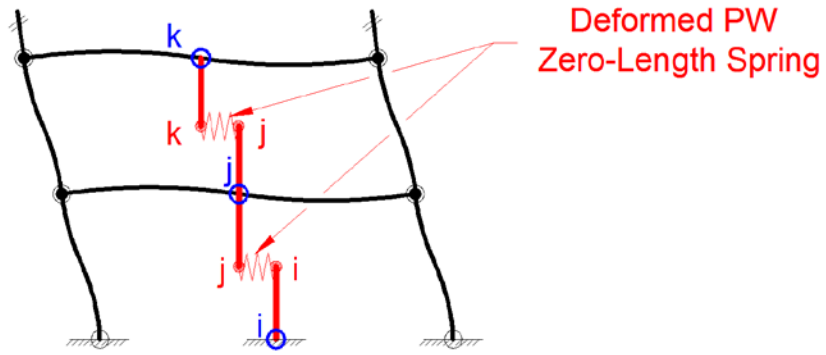

(b) Deformed shape

Figure 4.12 Partition wall implementation between two adjacent story levels. (Note L_w = length of partition wall, L_{bay} = width of bay, h_i = story height, blue nodes are "master" nodes, and red nodes are slaved nodes (connected by red idealized rigid links.)

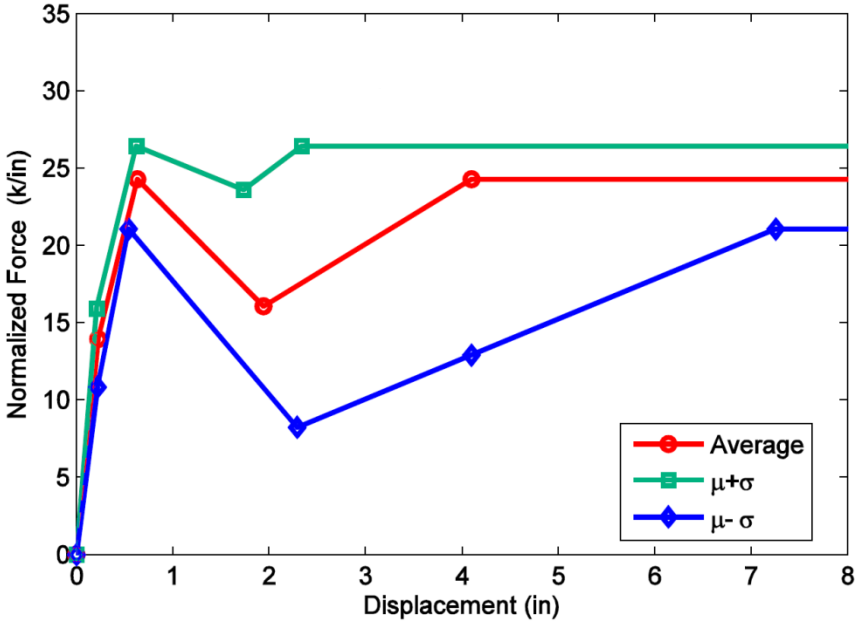

Figure 4.13 Normalized PW model (monotonic behavior) as implemented in OpenSees.

4.2.1 Scaling Rules and Recommended Wall Lengths

After the walls are placed between the building levels, the actual length of the PW must be determined. One method to determine representative wall lengths is based on partition indices (PI). The partition index is a takeoff quantity defined as the total lineal feet of PWs per floor divided by the floor area. French and Xu (2010) determined partition indices by analyzing three model building blueprints and compared their findings to ATC-58 values (ATC, 2011). To further explore the full range of PW lengths, the upper and lower bound values are utilized. Knowing the details of each of the building plans, the corresponding PW lengths are estimated assuming the walls are proportional to the building geometry and the tributary area of an interior frame, using the following equation (4-2):

$$L_{w_i} = \frac{n_i l_i}{n_x \mathrm{L_x} + n_y L_y} A_{TRIB} PI \tag{4-2}$$

where L_{wi} = calculated length of the PW in the i-direction (x or y),A_{TRIB} = area considered for partition area, n_i= number of bays in the i-direction, L_i = length of one bay in the i-direction and PI = partition index considered. Using the upper and lower bound partition indices, two PW length $L_{w,min}$ and $L_{w,max}$ are calculated for each of the representative buildings. To account for the varying lengths of PWs, the monotonic backbone force-displacement behaviors are linearly scaled, as shown in Figure 4.14. The scale amplitude for the multiplication is determined via the number of vertical studs, the example shown in Figure 4.14 assumes two walls with the same stud spacing, therefore if one wall is twice the length, the force amplitude at each displacement is amplitude scaled by 2.0. The number of studs will vary by construction practice; refer to the original report for complete details on the scaling of the PWs (Wood et al., 2012). Considering the example building suite, the corresponding maximum and minimum values for partition lengths are summarized in Table 4.5.

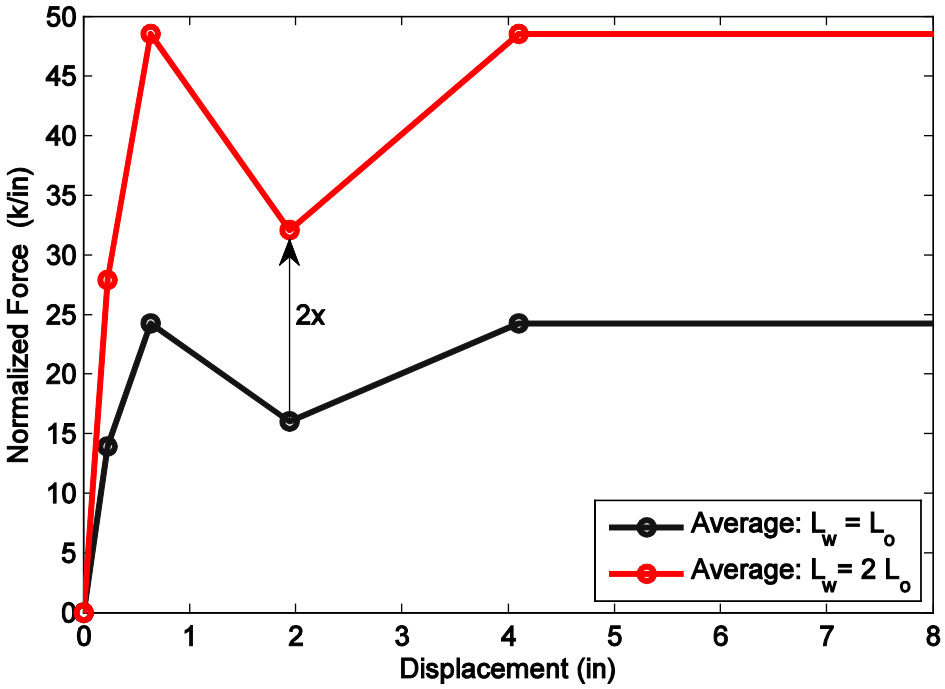

Figure 4.14 Example of PW scaling when the target wall is twice the length of the original wall with twice the number of vertical studs in the lateral direction.

Table 4.5 PW configuration combinations by building.

Building	**Occupancy**	**Partition Wall Characteristics**				
		Corresponding Experimental Subgroup	*Partition Index (1/ft)*		*Partition Wall Lengths*	
			Lower Bound	Upper Bound	$L_{w,min}$ (ft)	$L_{w,max}$ (ft)
RC-2	Office	1	0.07	0.13	56	104
RC-4	Office	1	0.07	0.13	56	104
RC-8	Office	1	0.07	0.13	56	104
RC-12	Office	1	0.07	0.13	56	104
RC-20	Office	1	0.07	0.13	56	104
S-3	Office	1	0.07	0.13	50	94
S-9	Office	1	0.07	0.13	63	117
S-20	Office	1	0.07	0.13	25	48
S-3H	Hospital	2	0.06	0.14	43	101

4.3 Effect of PW on Building Modal Properties

This section discusses an initial impression of the effect of the inclusion of the PW on the modal properties (periods, mode shapes, etc.) of the buildings. Prior to any time history analyses and selection of ground motions, comparisons in the modal properties of the uncoupled (bare structure) and coupled (building-partition wall) systems is made. Eigenvalue analyses and their corresponding mode shapes as well as nonlinear static pushover analyses are discussed in the following subsections for these comparative reasons.

4.3.1 Eigenvalue Analysis – Modal Periods and Mass Participation

The parameters collected and compared in the eigenvalue analyses are the modal frequencies (periods) and mass participation estimates for the first four periods, when the number of modes is equal or greater than four. Table 4.6 - Table 4.14 display the period and mass participation estimates for the first four modes by building type. In each table, the periods and mass participation estimates are shown for bare structure (no wall) and the minimum and maximum wall cases considering each of the normalized models: mean (μ), mean minus one standard deviation (μ−σ), and mean plus one standard deviation (μ+σ).

It is noted that the PW element, with equal wall lengths, is assumed at each floor, i.e. no vertical variability in wall length is assumed. These summary tables illustrate the initial impression that for all cases, inclusion of the PW reduces the period of the system, with the effect being most pronounced in the first mode. One may also note that doubling the length of PW (or more) produces a larger reduction in period (i.e. the maximum wall length cases consistently result in periods smaller than that of the minimum wall cases). To quantify the comparison, two normalized parameters are calculated:

$$T_i^* = \frac{T_i^n}{T_i^{bare}} \tag{4-3}$$

where T_i^* = normalized i^{th} period, T_i^n = the i^{th} period of the coupled building-partition wall model, T_i^{bare} = the i^{th} period of the bare building model. In addition the normalized mass participation, MP_i^*, is calculated as:

$$MP_i^* = \frac{MP_i^n}{MP_i^{bare}} \tag{4-4}$$

where MP_i^* = normalized mass participation in the i^{th} mode, MP_i^n = the mass participation in the i^{th} mode of the coupled building-partition wall model, MP_i^{bare} = the mass participation in the i^{th} mode of the bare building model. The illustration of these normalized parameters is shown in Figure 4.15 - Figure 4.23. These figures readily show that, when the wall length is increased the model stiffens and hence the period of the building decreases. Similarly, when one considers use of the average minus a standard deviation PW model, the increase in stiffness (to the bare building model) is less, therefore the effect on the model building-partition wall periods is reduced. The opposite occurs when considering the mean plus a standard deviation PW model, i.e. the "red bars" are consistently lower, representing a greater reduction in period when the stiffest, strongest PW model is consider. However, the degree to which this dynamic shift occurs is most influenced by the length of the wall rather than which of the normalized PW model parameters are used.

The largest change in the mass participation was noted in S-9, where the second mode mass participation was increased by approximately 40% when the longest wall and mean plus standard deviation PW model case considered. This, however, is not a significant change since the bare structure has a mass participation in the second mode of 0.4% and this increased to 0.6%. On average, the period reduction in the first two modes was 6% and 5%, respectively, where the maximum period shift was 14% the first mode and 10% in the second mode for S3-H considering the maximum wall length under the mean plus standard deviation PW model parameters. Recall that S-3H is a hospital building which considered use of institutional PWs (group 2). The average

change in mass participation is not as significant, where only less than 1% and 1.5% is noted for the first two modes. The maximum change in mass participations was found to be -7% in the second mode for S-3 considering the maximum wall length under the mean plus standard deviation PW model parameters. However, the change in mass participation from the bare structure of 8.1% to 7.5% is not significant. In examining all building cases, the mass participations did not shift uniformly as some increased while others decreased. The overall changes to the mass participations are not significant; however the changes are noted to be dependent on individual building designs.

Table 4.6 Modal periods and mass participation sensitivity for RC-2.
(Note μ = mean, μ+σ = mean plus on standard deviation, μ–σ = mean minus one standard deviation with reference to the PW model parameters)

	Mode	Bare (no wall)	μ		μ−σ		μ+σ	
			56 ft	104 ft	56 ft	104 ft	56 ft	104 ft
T_i (s)	1	0.203	0.196	0.192	0.198	0.194	0.195	0.190
	2	0.051	0.050	0.050	0.050	0.050	0.050	0.050
MP_i (%)	1	84.3	84.6	84.8	84.5	84.7	84.6	84.9
	2	15.7	15.4	15.2	15.5	15.3	15.4	15.1

Table 4.7 Modal periods and mass participation sensitivity for RC-4.
(Note μ = mean, μ+σ = mean plus on standard deviation, μ–σ = mean minus one standard deviation with reference to the PW model parameters)

	Mode	Bare (no wall)	μ		μ−σ		μ+σ	
			56 ft	104 ft	56 ft	104 ft	56 ft	104 ft
T_i (s)	1	0.419	0.400	0.387	0.403	0.393	0.396	0.381
	2	0.116	0.113	0.111	0.114	0.112	0.113	0.110
	3	0.056	0.056	0.055	0.056	0.055	0.055	0.055
	4	0.037	0.037	0.037	0.037	0.037	0.037	0.037
MP_i (%)	1	79.2	79.7	80	79.6	79.9	79.8	80.1
	2	14.0	13.7	13.5	13.7	13.6	13.6	13.4
	3	5.3	5.2	5.1	5.2	5.2	5.2	5.1
	4	1.5	1.5	1.4	1.5	1.4	1.4	1.4

Table 4.8 Modal periods and mass participation sensitivity for RC-8.
(Note μ = mean, μ+σ = mean plus on standard deviation, μ–σ = mean minus one standard deviation with reference to the PW model parameters)

	Mode	Bare (no wall)	μ		μ−σ		μ+σ	
			56 ft	104 ft	56 ft	104 ft	56 ft	104 ft
T_i (s)	1	0.784	0.748	0.724	0.755	0.735	0.742	0.714
	2	0.241	0.233	0.226	0.234	0.229	0.231	0.224
	3	0.126	0.122	0.120	0.123	0.121	0.122	0.119
	4	0.079	0.077	0.076	0.078	0.077	0.077	0.076
MP_i (%)	1	78.4	78.7	78.9	78.8	78.8	78.8	79.0
	2	10.6	10.5	10.5	10.6	10.5	10.5	10.5
	3	4.3	4.2	4.1	4.2	4.2	4.2	4.1
	4	2.7	2.6	2.6	2.6	2.6	2.6	2.6

Table 4.9 Modal periods and mass participation sensitivity for RC-12.
(Note μ = mean, μ+σ = mean plus on standard deviation, μ–σ = mean minus one standard deviation with reference to the PW model parameters)

	Mode	Bare (no wall)	μ		μ−σ		μ+σ	
			56 ft	104 ft	56 ft	104 ft	56 ft	104 ft
T_i (s)	1	1.190	1.137	1.101	1.147	1.117	1.127	1.086
	2	0.380	0.364	0.353	0.367	0.358	0.361	0.349
	3	0.207	0.199	0.194	0.201	0.196	0.198	0.191
	4	0.134	0.130	0.127	0.131	0.128	0.129	0.126
MP_i (%)	1	77.8	77.9	78.0	77.9	77.9	77.9	78.0
	2	9.7	9.8	9.9	9.8	9.8	9.8	9.8
	3	4.0	4.0	3.9	4.0	4.0	4.0	3.9
	4	2.4	2.3	2.3	2.3	2.3	2.3	2.3

Table 4.10 Modal periods and mass participation sensitivity for RC-20.
(Note μ = mean, μ+σ = mean plus on standard deviation, μ–σ = mean minus one standard deviation with reference to the PW model parameters)

	Mode	Bare (no wall)	μ		μ−σ		μ+σ	
			56 ft	104 ft	56 ft	104 ft	56 ft	104 ft
T_i (s)	1	2.067	1.984	1.929	1.999	1.953	1.969	1.907
	2	0.710	0.672	0.649	0.679	0.659	0.666	0.639
	3	0.394	0.372	0.358	0.376	0.364	0.368	0.353
	4	0.262	0.250	0.242	0.252	0.245	0.247	0.238
MP_i (%)	1	73.8	74.0	74.0	73.9	74.0	74.0	74.0
	2	13.1	13.2	13.3	13.2	13.3	13.2	13.4
	3	2.7	2.7	2.7	2.7	2.7	2.7	2.7
	4	3.0	2.9	2.9	2.9	2.9	2.9	2.9

Table 4.11 Modal periods and mass participation sensitivity for S-3.
(Note μ = mean, μ+σ = mean plus on standard deviation, μ–σ = mean minus one standard deviation with reference to the PW model parameters)

	Mode	Bare (no wall)	μ		μ−σ		μ+σ	
			50 ft	94 ft	50 ft	94 ft	50 ft	94 ft
T_i (s)	1	0.343	0.328	0.317	0.331	0.322	0.325	0.313
	2	0.119	0.114	0.111	0.115	0.112	0.113	0.109
	3	0.071	0.069	0.068	0.070	0.069	0.069	0.067
MP_i (%)	1	86.8	87.3	87.6	87.2	87.5	87.4	87.8
	2	8.1	7.7	7.5	7.8	7.6	7.7	7.5
	3	3.1	3.0	2.9	3.0	2.9	3.0	2.8

Table 4.12 Modal periods and mass participation sensitivity for S-3H.
(Note μ = mean, μ+σ = mean plus on standard deviation, μ–σ = mean minus one standard deviation with reference to the PW model parameters)

	Mode	Bare (no wall)	μ		μ−σ		μ+σ	
			43 ft	101 ft	43 ft	101 ft	43 ft	101 ft
T_i (s)	1	0.280	0.263	0.246	0.266	0.252	0.259	0.241
	2	0.082	0.079	0.075	0.079	0.076	0.078	0.074
	3	0.042	0.041	0.040	0.041	0.041	0.041	0.040
MP_i (%)	1	90.3	90.6	90.8	90.5	90.7	90.6	90.9
	2	5.6	5.4	5.3	5.5	5.3	5.4	5.3
	3	2.0	1.9	1.8	1.9	1.9	1.9	1.8

Table 4.13 Modal periods and mass participation sensitivity for S-9.
(Note μ = mean, μ+σ = mean plus on standard deviation, μ–σ = mean minus one standard deviation with reference to the PW model parameters)

	Mode	Bare (no wall)	μ		μ−σ		μ+σ	
			63 ft	117 ft	63 ft	117 ft	63 ft	117 ft
T_i (s)	1	0.934	0.897	0.869	0.904	0.882	0.890	0.855
	2	0.338	0.323	0.311	0.326	0.316	0.320	0.098
	3	0.197	0.189	0.183	0.190	0.185	0.187	0.028
	4	0.135	0.130	0.126	0.131	0.128	0.129	0.009
MP_i (%)	1	85.6	85.5	85.5	85.6	85.5	85.5	85.5
	2	9.9	9.8	9.8	9.8	9.8	9.8	9.8
	3	2.7	2.7	2.8	2.7	2.8	2.8	2.8
	4	0.8	0.9	0.9	0.9	0.9	0.9	0.9

Table 4.14 Modal periods and mass participation sensitivity for S-20.
(Note μ = mean, μ+σ = mean plus on standard deviation, μ–σ = mean minus one standard deviation with reference to the PW model parameters)

	Mode	Bare (no wall)	μ		μ−σ		μ+σ	
			25 ft	48 ft	25 ft	48 ft	25 ft	48 ft
T_i (s)	1	1.397	1.387	1.378	1.389	1.382	1.385	1.374
	2	0.413	0.408	0.404	0.409	0.406	0.407	0.402
	3	0.217	0.214	0.211	0.214	0.212	0.213	0.210
	4	0.151	0.149	0.147	0.149	0.147	0.148	0.146
MP_i (%)	1	73.8	73.7	73.6	73.7	73.6	73.7	73.5
	2	16.4	16.6	16.7	16.6	16.7	16.6	16.8
	3	4.2	4.2	4.3	4.2	4.3	4.2	4.3
	4	1.6	1.6	1.6	1.6	1.6	1.6	1.7

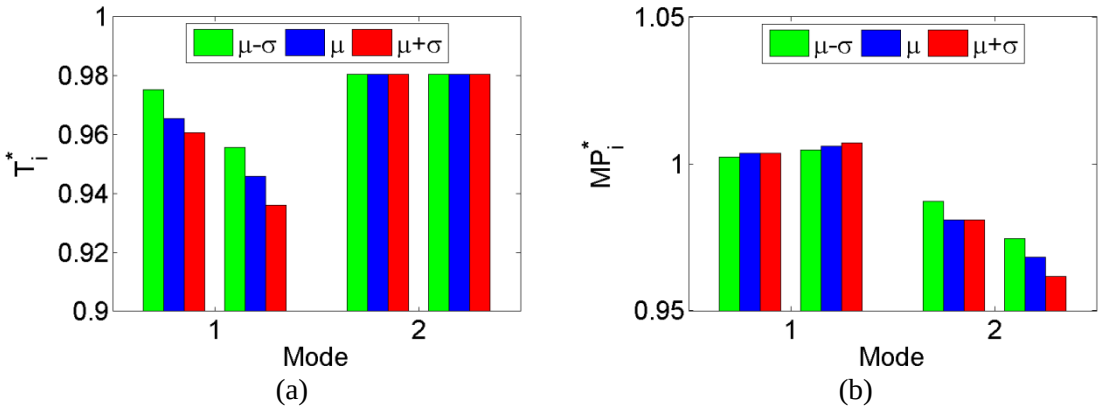

(a) (b)

Figure 4.15 Normalized plots demonstrating period and mass participations sensitivities for RC-2.
Note: in the period illustration, the right and left bars refer to the short and long wall lengths. Similarly for the mass participations, the immediate three bars to the right and left refer to the short and long wall lengths, for each statistical level.

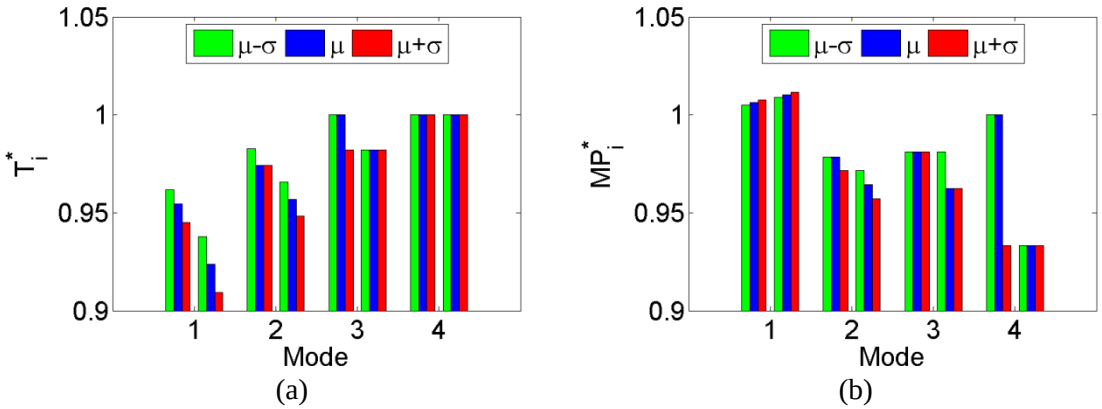

(a) (b)

Figure 4.16 Normalized plots demonstrating period and mass participations sensitivities for RC-4.
Note: in the period illustration, the right and left bars refer to the short and long wall lengths. Similarly for the mass participations, the immediate three bars to the right and left refer to the short and long wall lengths, for each statistical level.

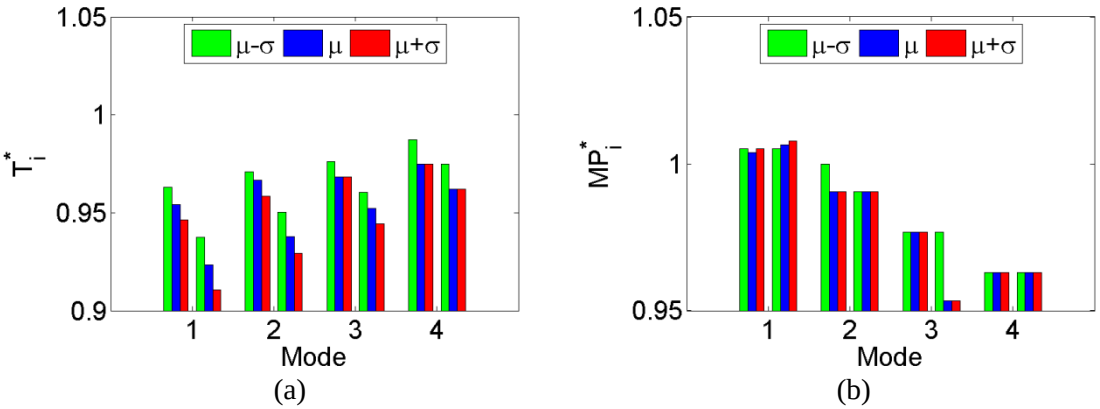

Figure 4.17 Normalized plots demonstrating period and mass participations sensitivities for RC-8.
Note: in the period illustration, the right and left bars refer to the short and long wall lengths. Similarly for the mass participations, the immediate three bars to the right and left refer to the short and long wall lengths, for each statistical level.

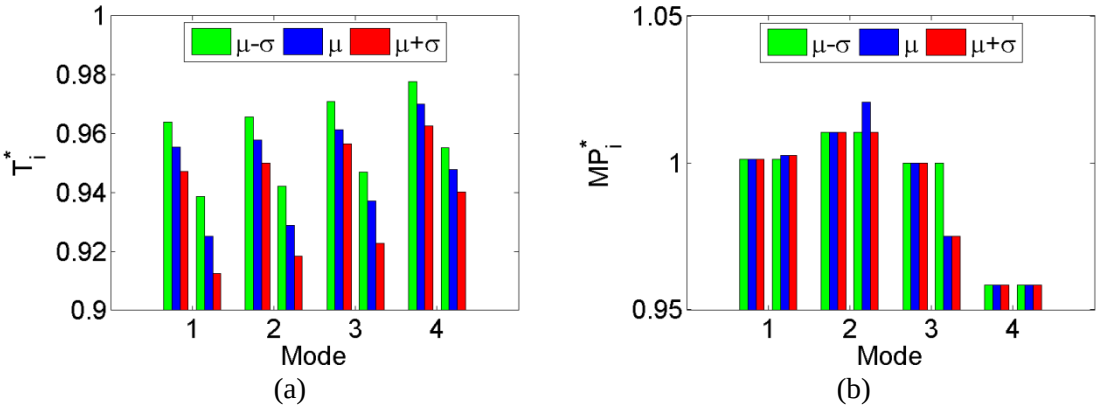

Figure 4.18 Normalized plots demonstrating period and mass participations sensitivities for RC-12.
Note: in the period illustration, the right and left bars refer to the short and long wall lengths. Similarly for the mass participations, the immediate three bars to the right and left refer to the short and long wall lengths, for each statistical level.

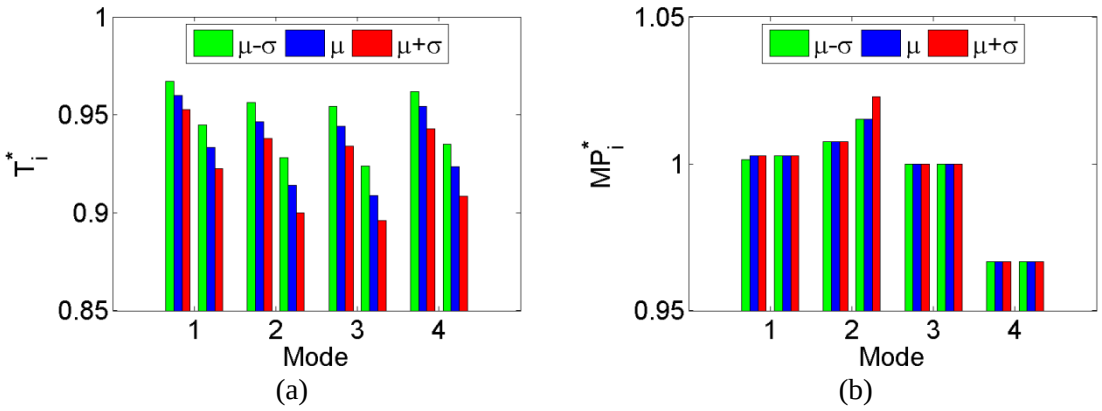

Figure 4.19 Normalized plots demonstrating period and mass participations sensitivities for RC-20.

Note: in the period illustration, the right and left bars refer to the short and long wall lengths. Similarly for the mass participations, the immediate three bars to the right and left refer to the short and long wall lengths, for each statistical level.

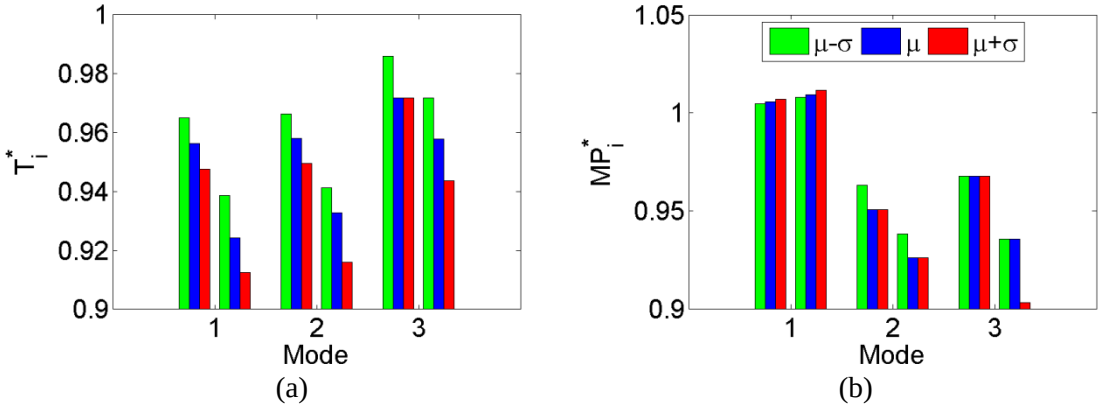

Figure 4.20 Normalized plots demonstrating period and mass participations sensitivities for S-3.

Note: in the period illustration, the right and left bars refer to the short and long wall lengths. Similarly for the mass participations, the immediate three bars to the right and left refer to the short and long wall lengths, for each statistical level. Legend removed from (a) to prevent overlapping of the bar chart, legend is the same for (a) and (b).

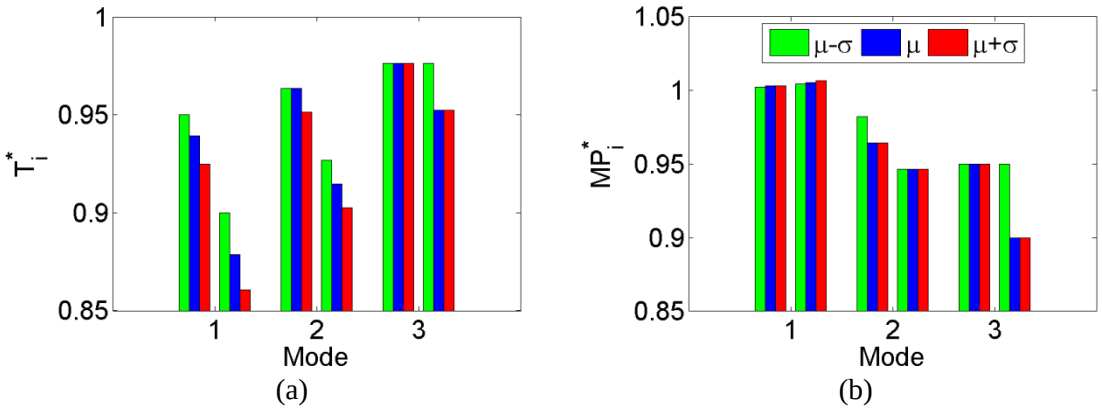

Figure 4.21 Normalized plots demonstrating period and mass participations sensitivities for S-3H.

Note: in the period illustration, the right and left bars refer to the short and long wall lengths. Similarly for the mass participations, the immediate three bars to the right and left refer to the short and long wall lengths, for each statistical level. Legend removed from (a) to prevent overlapping of the bar chart, legend is the same for (a) and (b).

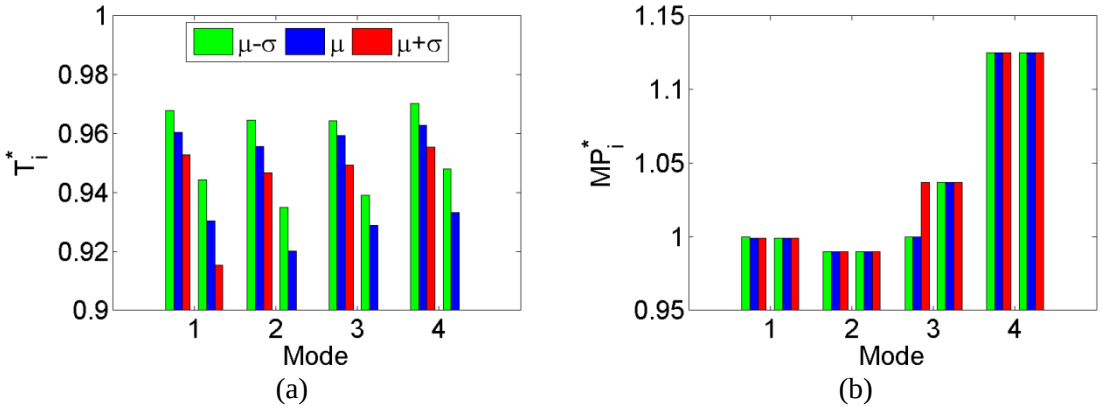

Figure 4.22 Normalized plots demonstrating period and mass participations sensitivities for S-9.

Note: in the period illustration, the right and left bars refer to the short and long wall lengths. Similarly for the mass participations, the immediate three bars to the right and left refer to the short and long wall lengths, for each statistical level. Legend removed from (b) to prevent overlapping of the bar chart, legend is the same for (a) and (b).

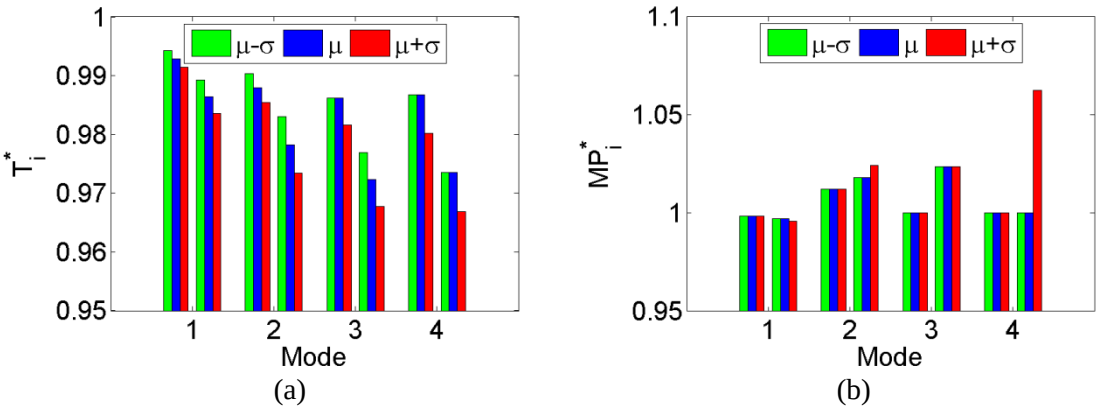

Figure 4.23 Normalized plots demonstrating period and mass participations sensitivities for S-20.
Note: in the period illustration, the right and left bars refer to the short and long wall lengths. Similarly for the mass participations, the immediate three bars to the right and left refer to the short and long wall lengths, for each statistical level.

4.3.2 Eigenvalue Analysis - Mode Shapes

The third parameter obtained from the eigenvalue analyses is the mode shapes, or eigenvectors. These mode shapes identify the fundamental shapes of vibrations experienced by the buildings, in this case which it responds elastically. The mode shapes were extracted for the bare building (no PW) and when the building contains both the minimum and maximum length of PWs, considering the mean PW model parameters. Figure 4.24 - Figure 4.32 illustrate the first four mode shapes, if the total number of modes is greater than four. For all of these analysis cases, little variation is apparent in the comparison of modes shapes, with the modal coordinates of the building with and without PWs being at most within 10%. The third mode of RC-20 demonstrates the largest variation where the maximum wall length case caused a variation in the modal coordinate for the 10^{th} of 27%. However, this variation is minimal because of the small value of the modal coordinate since it is near a node (zero-crossing).

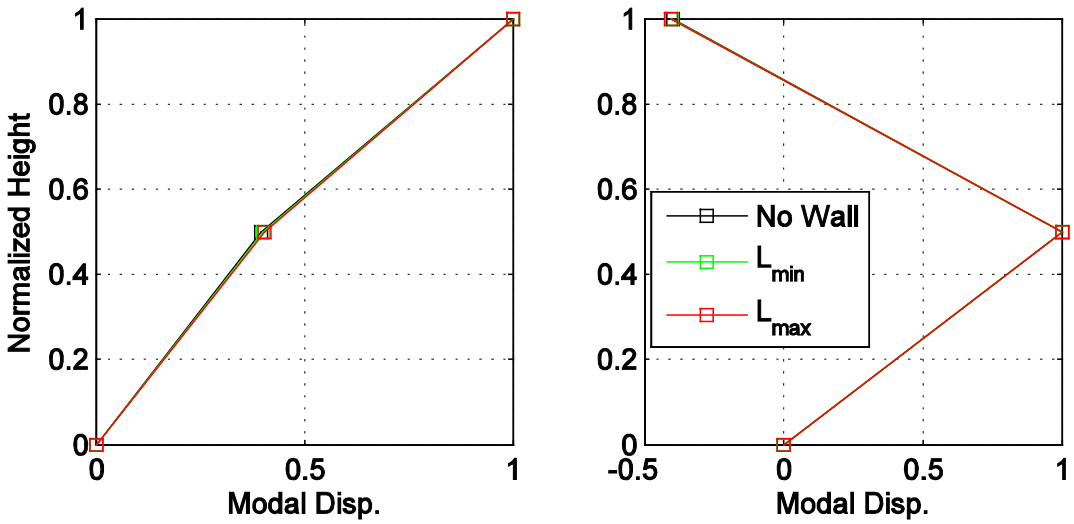

(a) mode 1 (b) mode 2

Figure 4.24 Mode shapes for the first two modes shown for building RC-2.

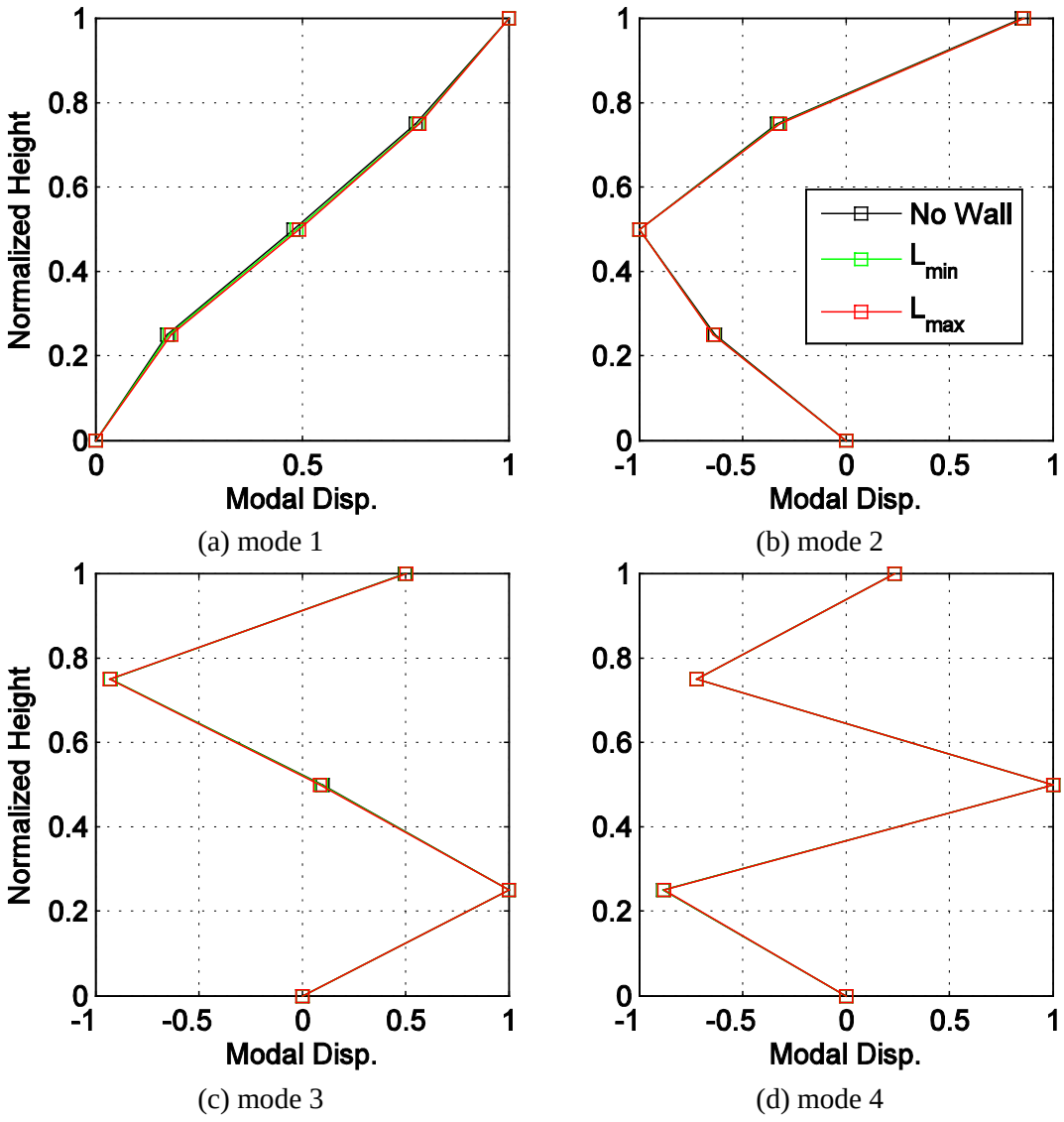

(a) mode 1 (b) mode 2

(c) mode 3 (d) mode 4

Figure 4.25 Mode shapes for the first four modes shown for building RC-4.

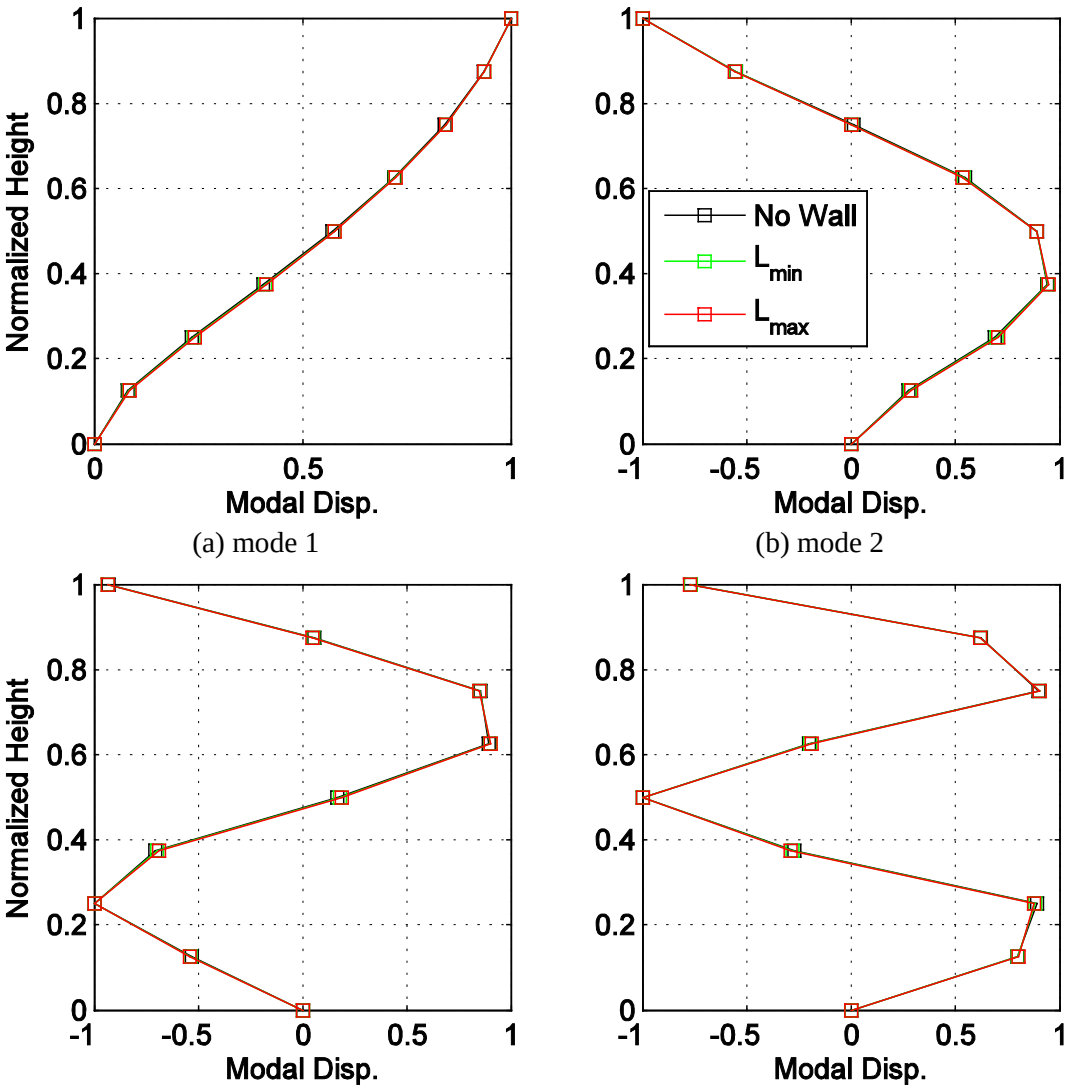

(a) mode 1

(b) mode 2

(c) mode 3

(d) mode 4

Figure 4.26 Mode shapes for the first four modes shown for building RC-8.

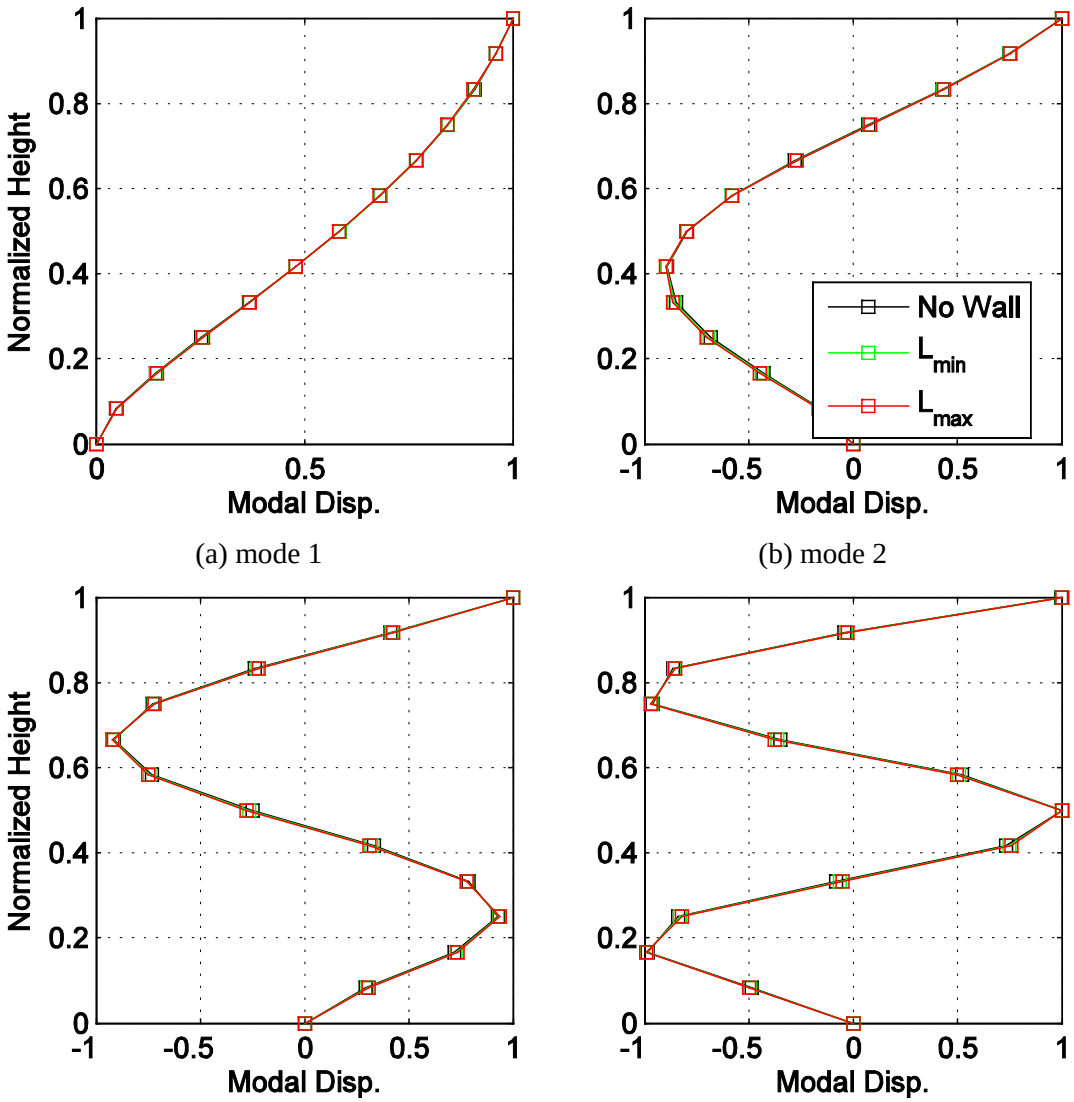

(a) mode 1

(b) mode 2

(c) mode 3

(d) mode 4

Figure 4.27 Mode shapes for the first four modes shown for building RC-12.

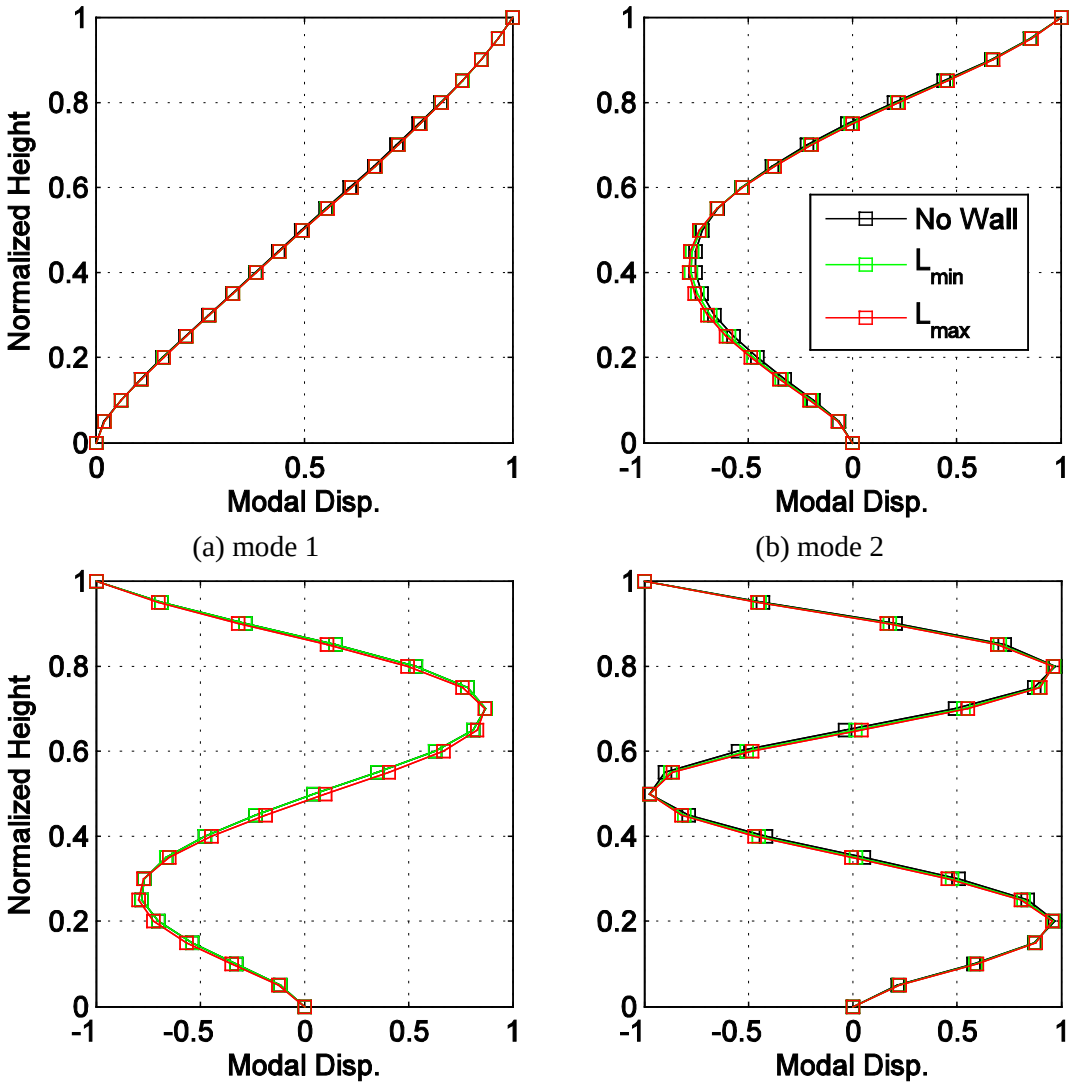

(a) mode 1 (b) mode 2

(c) mode 3 (d) mode 4

Figure 4.28 Mode shapes for the first four modes shown for building RC-20.

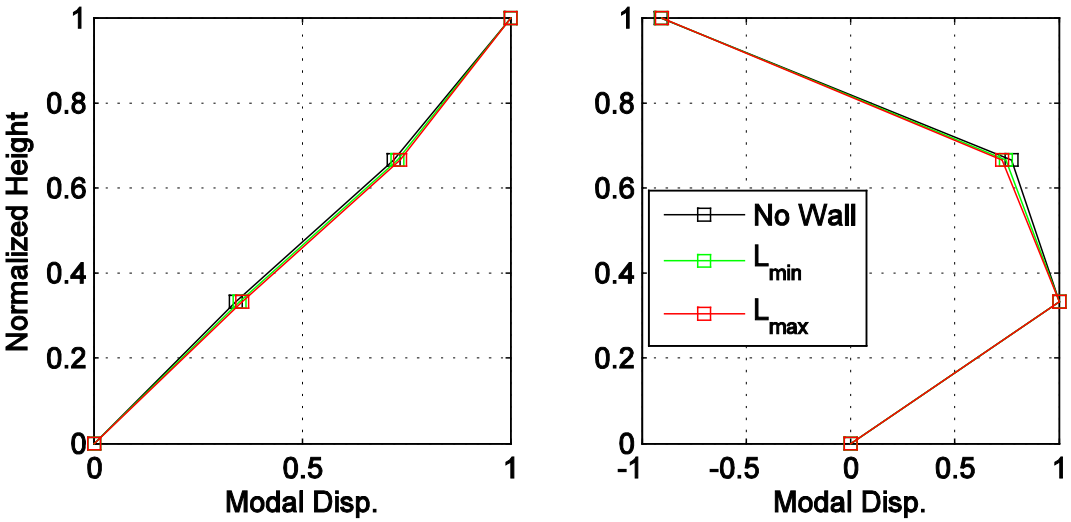

(a) mode 1

(b) mode 2

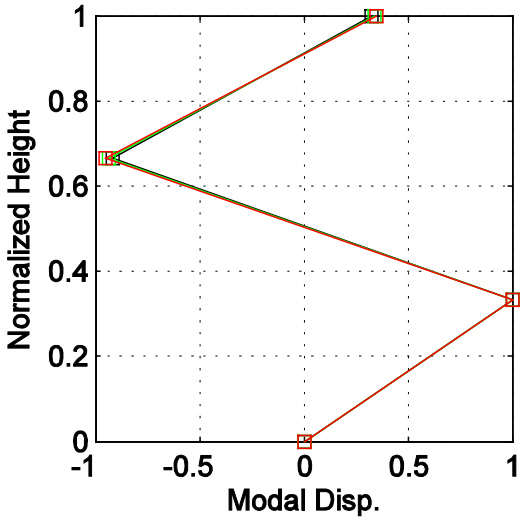

(c) mode 3

Figure 4.29 Mode shapes for the first three modes shown for building S-3.

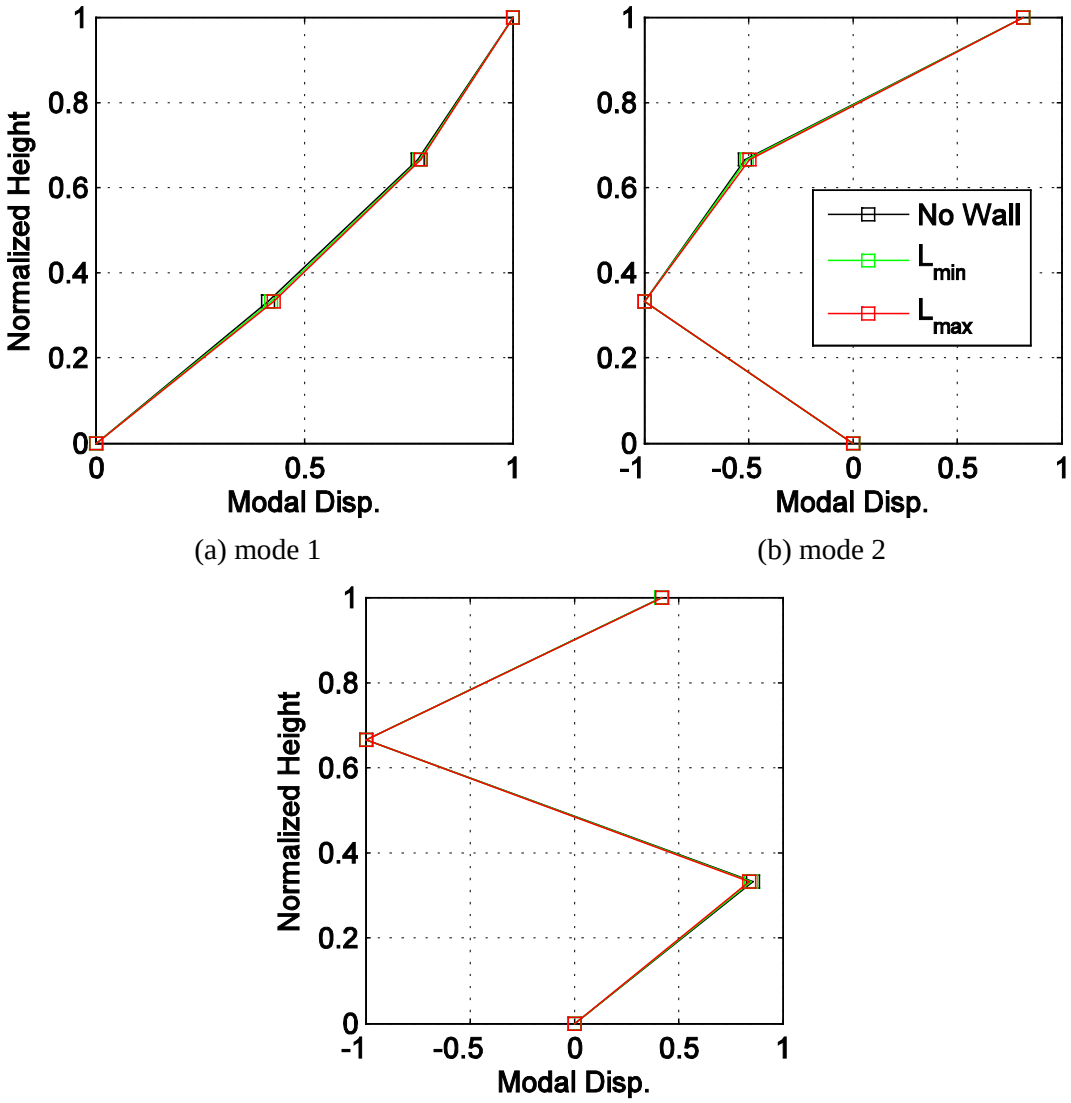

(a) mode 1

(b) mode 2

(c) mode 3

Figure 4.30 Mode shapes for the first three modes shown for building S-3H.

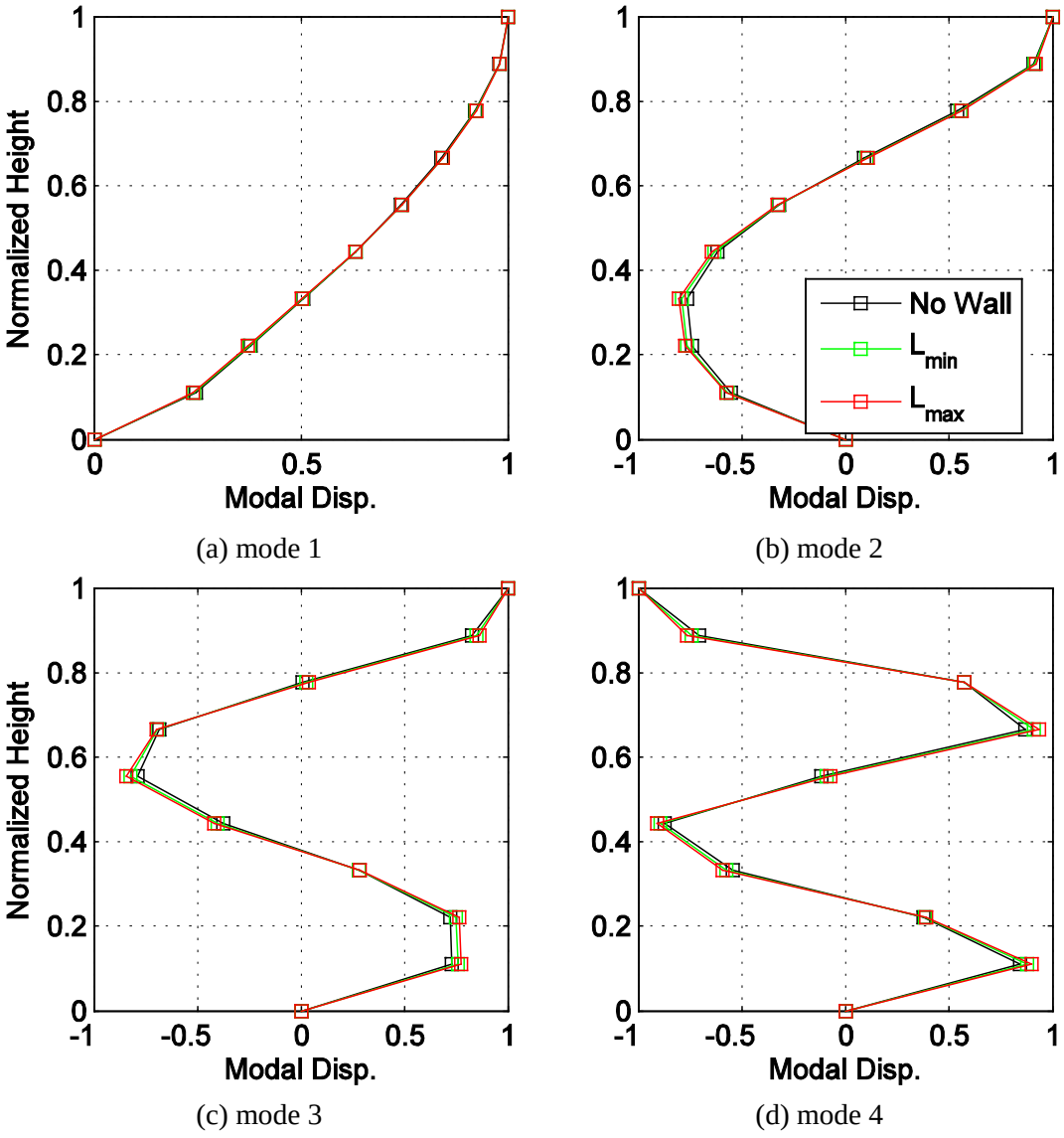

(a) mode 1

(b) mode 2

(c) mode 3

(d) mode 4

Figure 4.31 Mode shapes for the first four modes shown for building S-9.

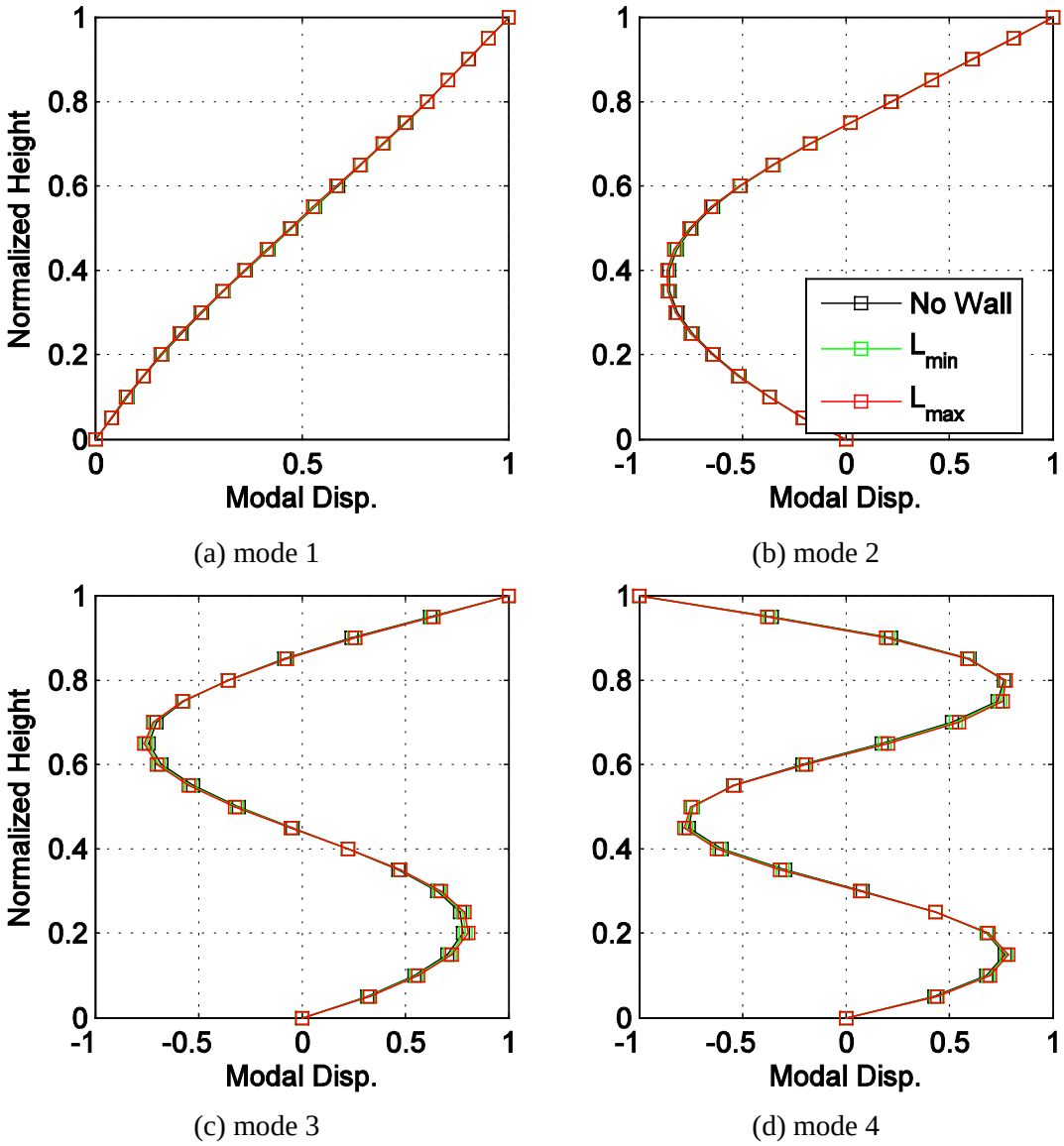

(a) mode 1 (b) mode 2

(c) mode 3 (d) mode 4

Figure 4.32 Mode shapes for the first four modes shown for building S-20.

4.3.3 Effect of PWs on Building Nonlinear Static "Pushover" Behavior

Nonlinear static pushover analyses were conducted on each of the building models to assess their global capacities. The assumed shape of the lateral force distribution used for the pushover analysis was a normalized curve accounting for 100% of the fundamental mode and 20% of the second mode. This lateral load distribution was implemented to account nominally for higher mode effects. The nonlinear static pushover analysis provided an estimation of the force-

deformation characteristics of the buildings in the linear and nonlinear range. In Figure 4.33 - Figure 4.41, the pushover curves are presented in terms of base shear versus the roof drift in part a. In part b of the figures, the pushover curves are normalized to show the significance of the inclusion of the PWs for the minimum and maximum wall lengths, considering the average response. The pushover curves are normalized such that the bare building frame is set to one at the maximum roof drift (3%).

To gather a sense of the effect of the PWs on the nonlinear static pushover behavior, the base shears corresponding to 1% and 3% roof drifts are summarized (Table 4.15). Using the values as summarized, the coupled building-partition wall systems are normalized by that of the bare building to quantify the additional force to push the buildings to the same corresponding roof drift (Table 4.16 and Figure 4.42). At 1% roof drift, the additional force required for the coupled systems range from 0.2% - 5%. All reinforced concrete buildings coupled systems with the maximum PW length considered required an additional 5% base shear, while the steel buildings required only at most 3%. At a roof drift of 3%, the additional required base shear to push the coupled building systems to target roof drift ranged from 0.7 to 15%. Again the concrete buildings typically required more additional force than the steel buildings, where the maximum additional force required was observed in RC-12 considering the maximum PW length. S-9, while not typical of the other steel buildings, required an additional force of 12% at a roof drift of 3%.

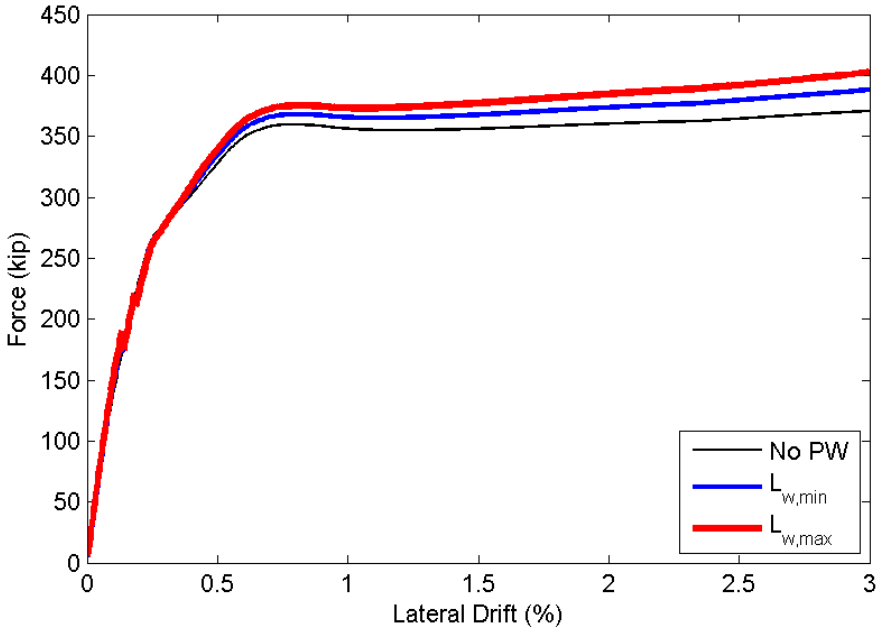

(a)

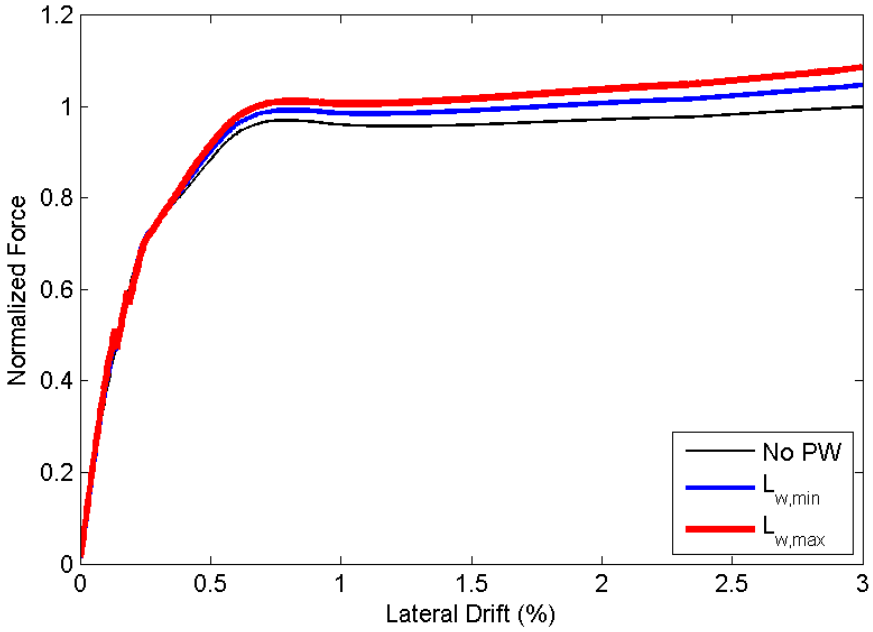

(b)

Figure 4.33 Normalized pushover response illustrated for RC-2 demonstrating effect of included PWs.

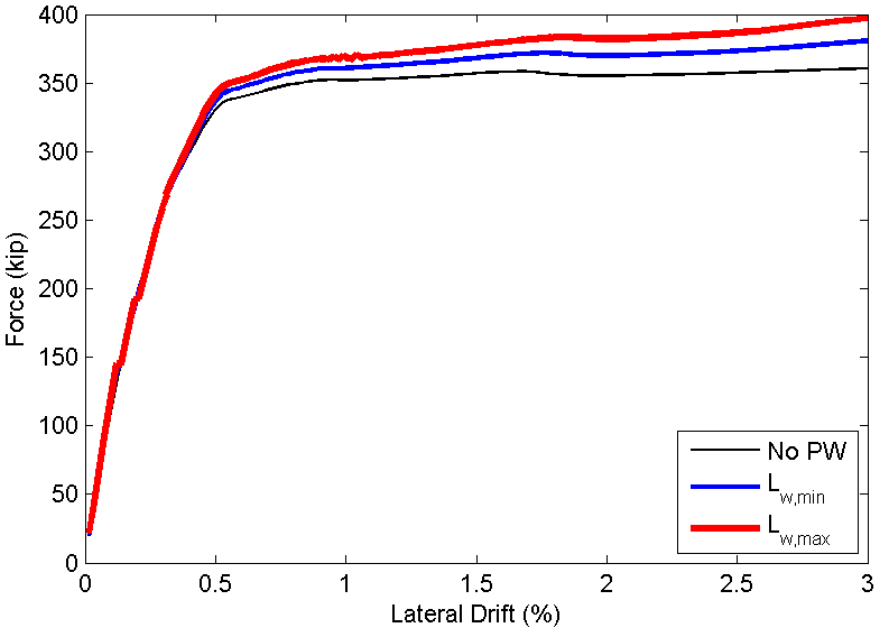

(a)

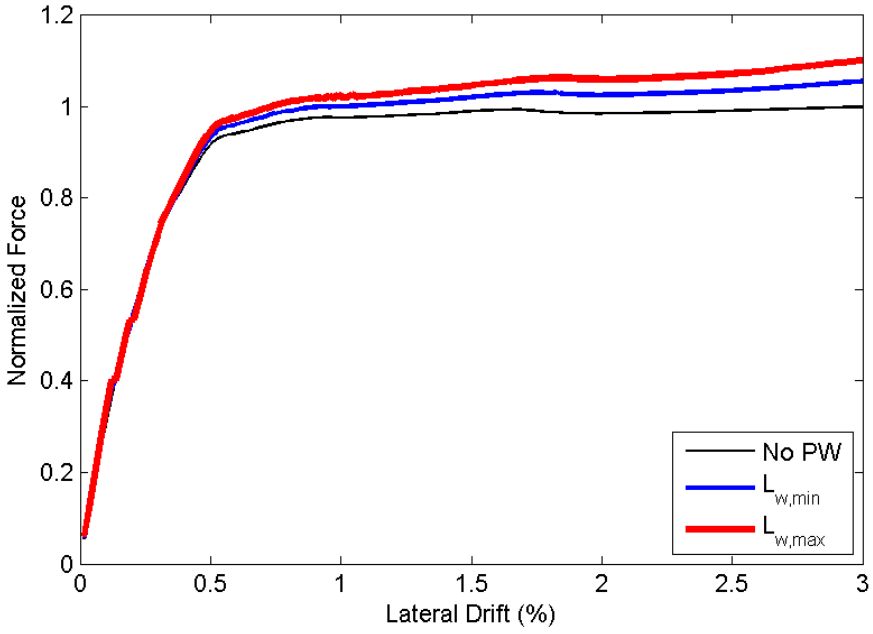

(b)

Figure 4.34 Normalized pushover response illustrated for RC-4 demonstrating effect of included PWs.

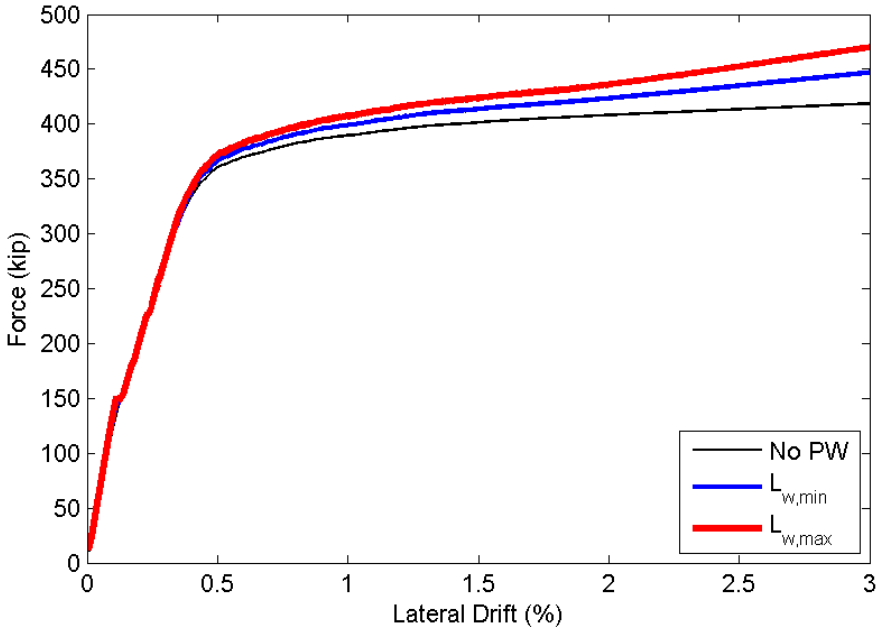

(a)

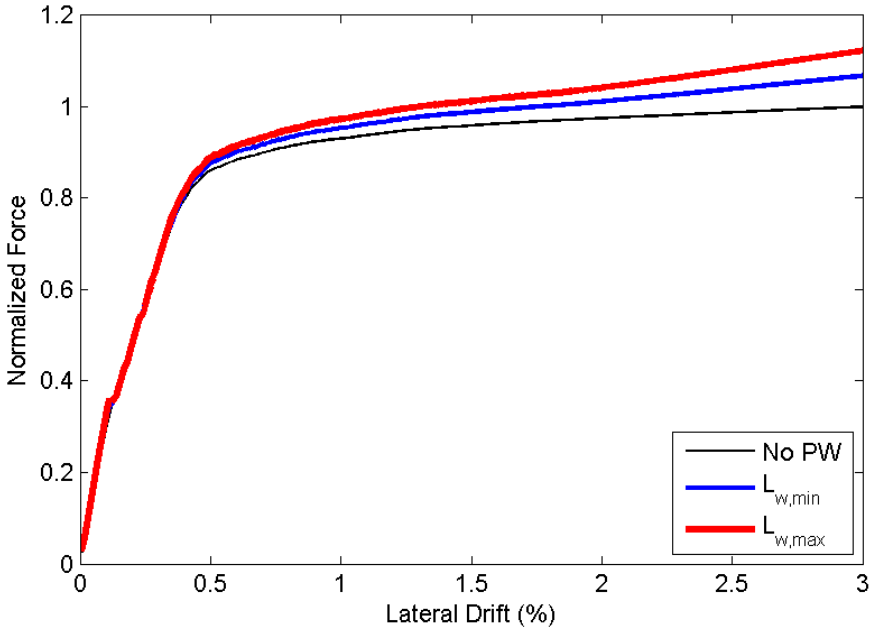

(b)

Figure 4.35 Normalized pushover response illustrated for RC-8 demonstrating effect of included PWs.

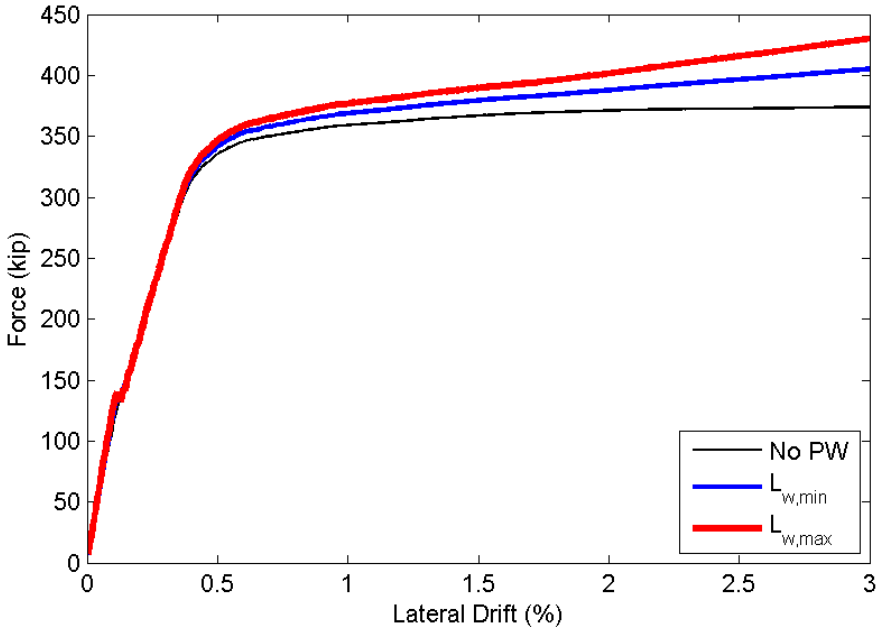

(a)

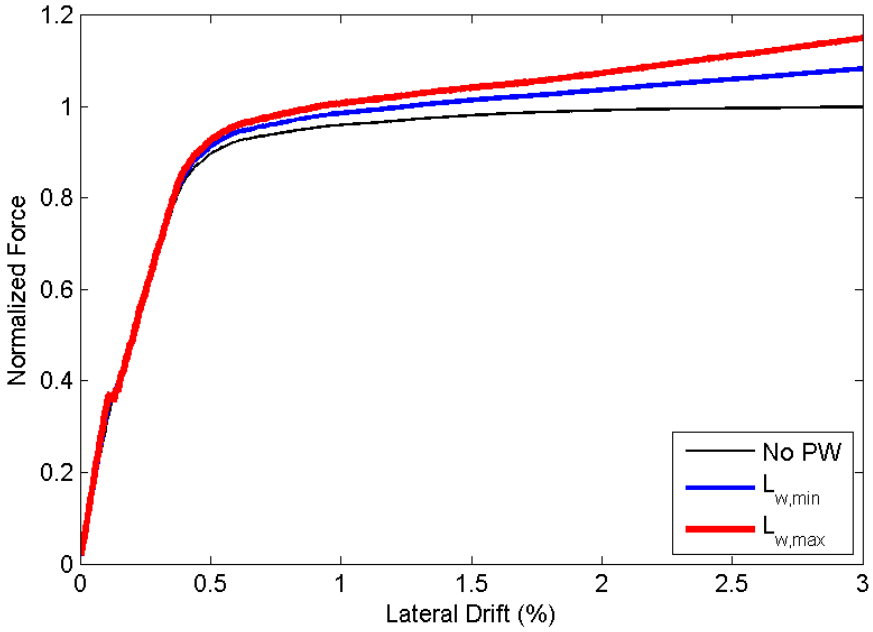

(b)

Figure 4.36 Normalized pushover response illustrated for RC-12 demonstrating effect of included PWs.

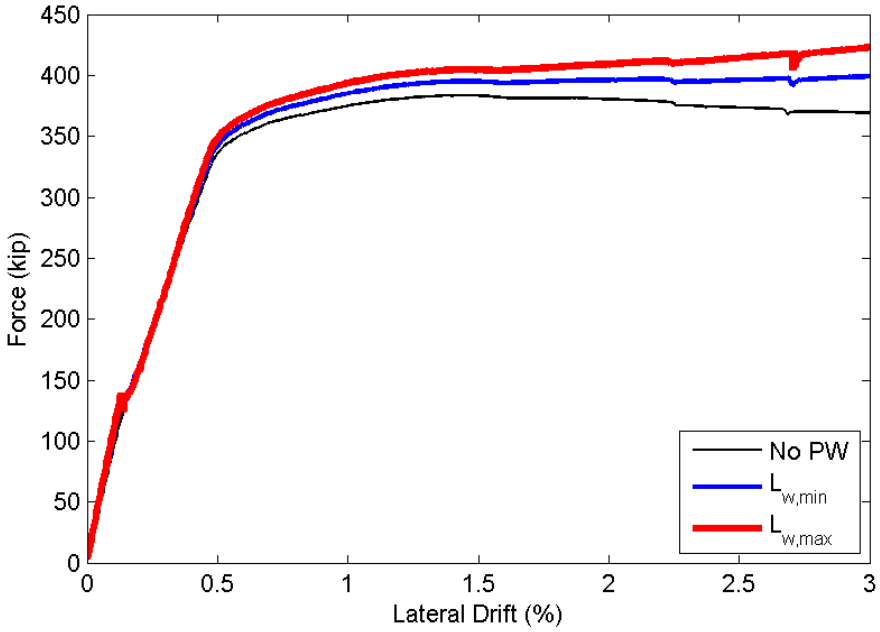

(a)

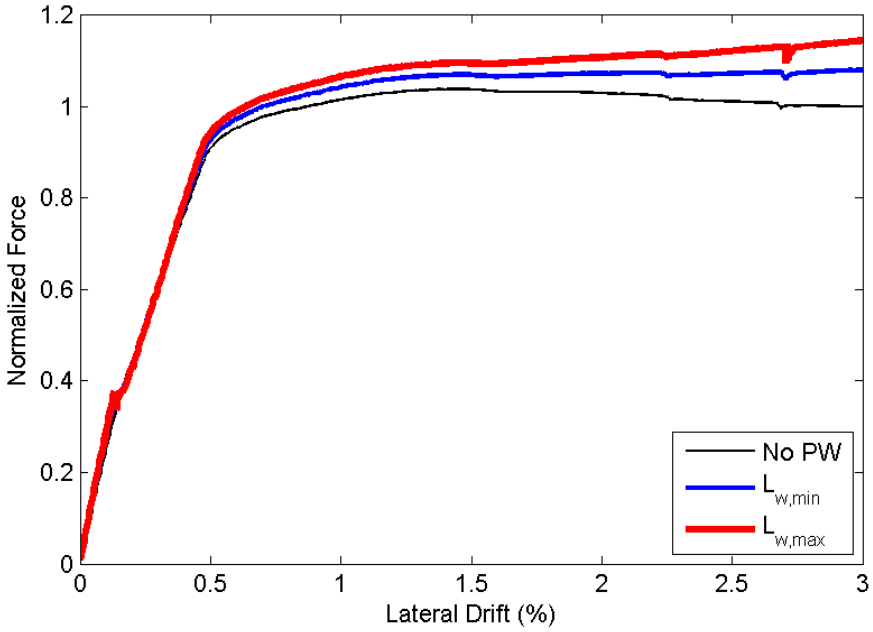

(b)

Figure 4.37 Normalized pushover response illustrated for RC-20 demonstrating effect of included PWs.

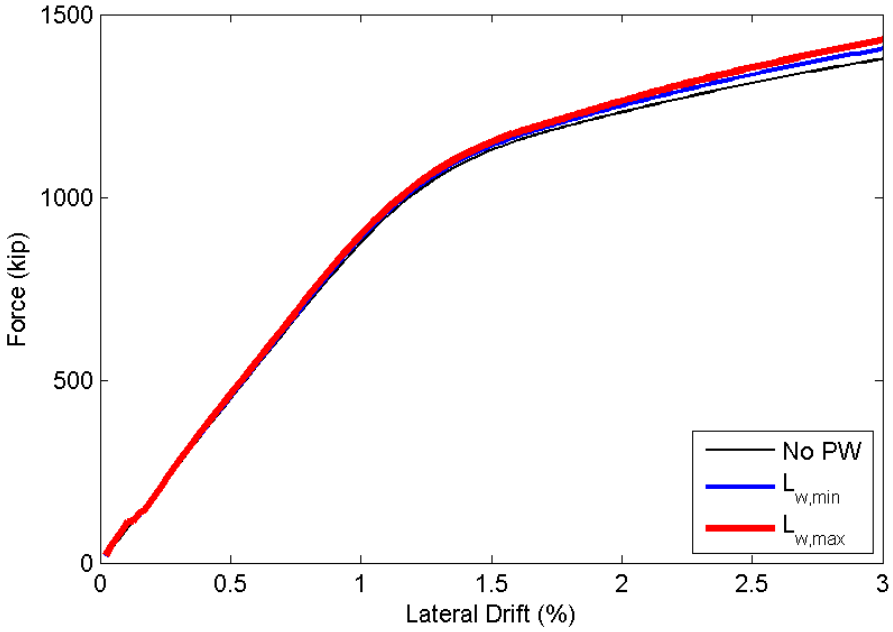

(a)

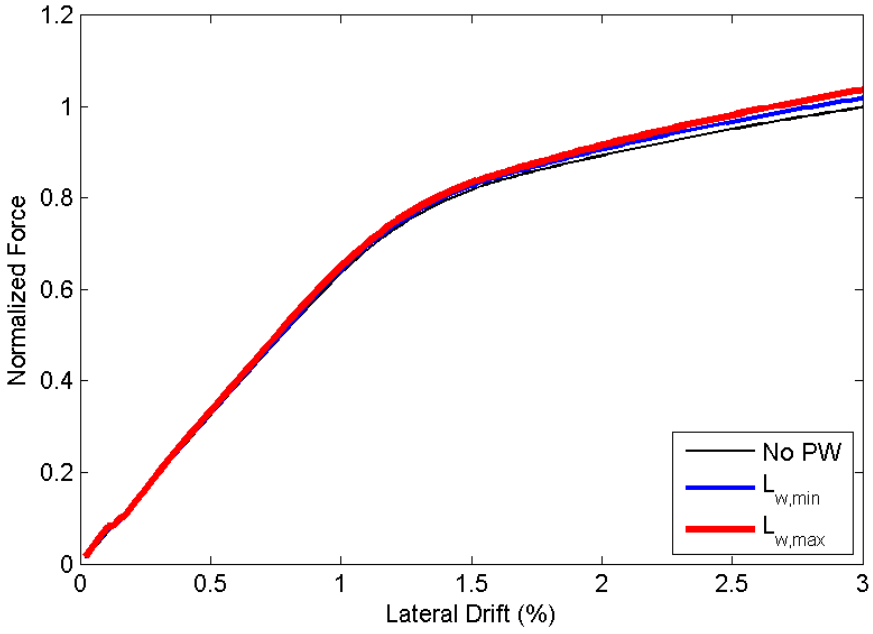

(b)

Figure 4.38 Normalized pushover response illustrated for S-3 demonstrating effect of included PWs.

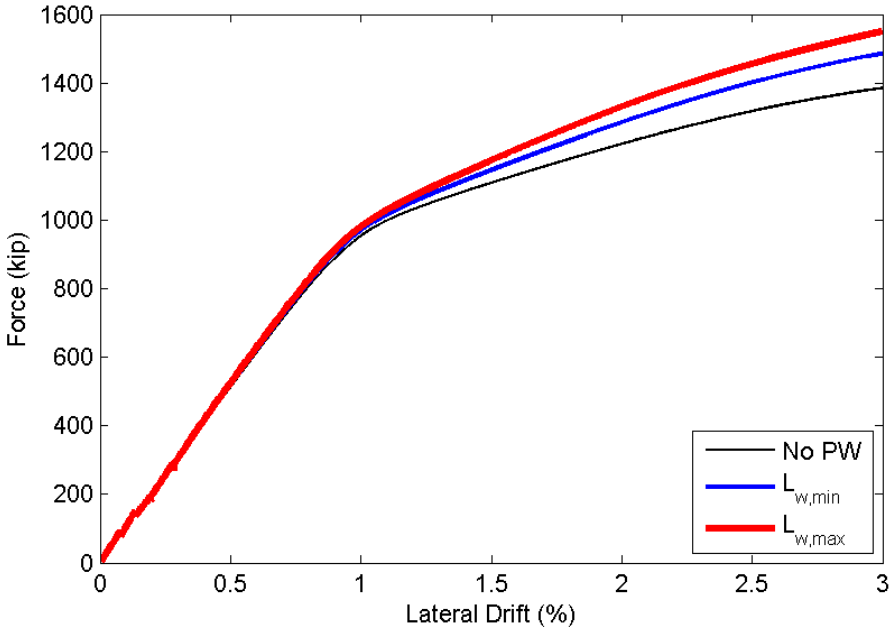

(a)

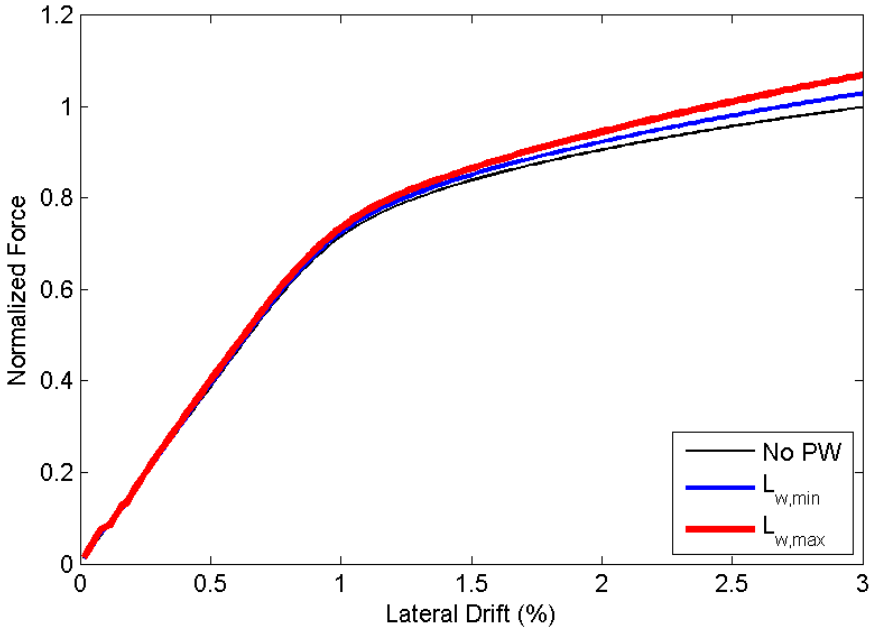

(b)

Figure 4.39 Normalized pushover response illustrated for S-3H demonstrating effect of included PWs.

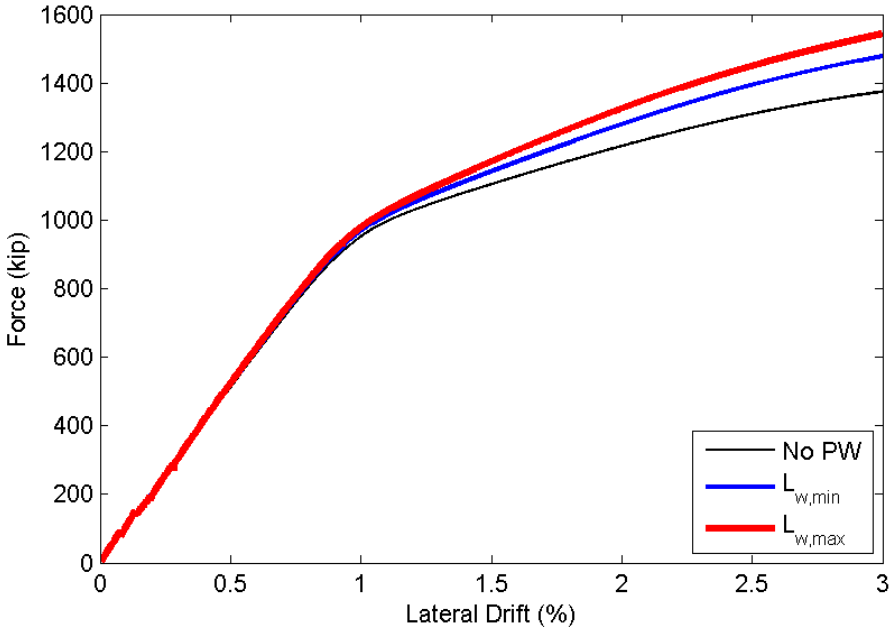

(a)

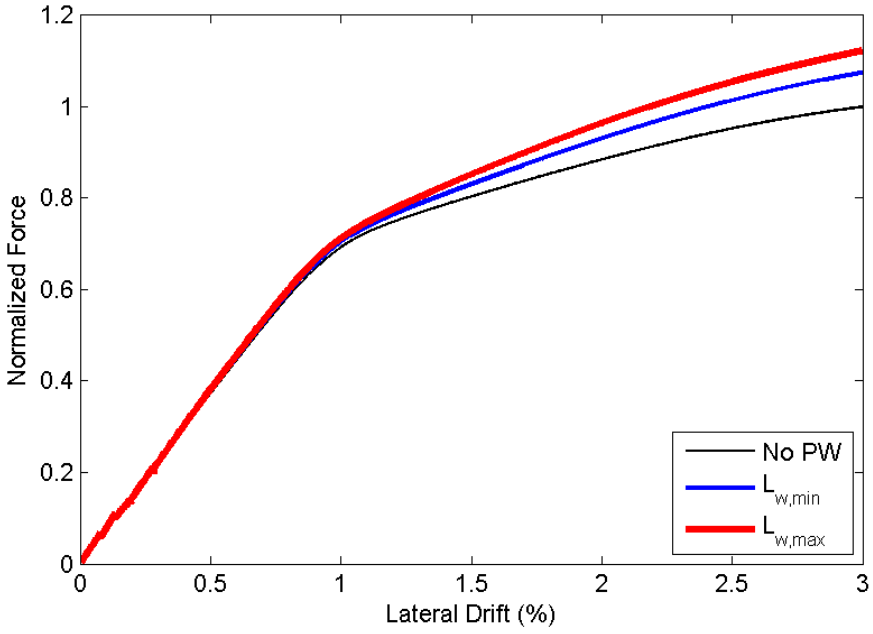

(b)

Figure 4.40 Normalized pushover response illustrated for S-9 demonstrating effect of included PWs.

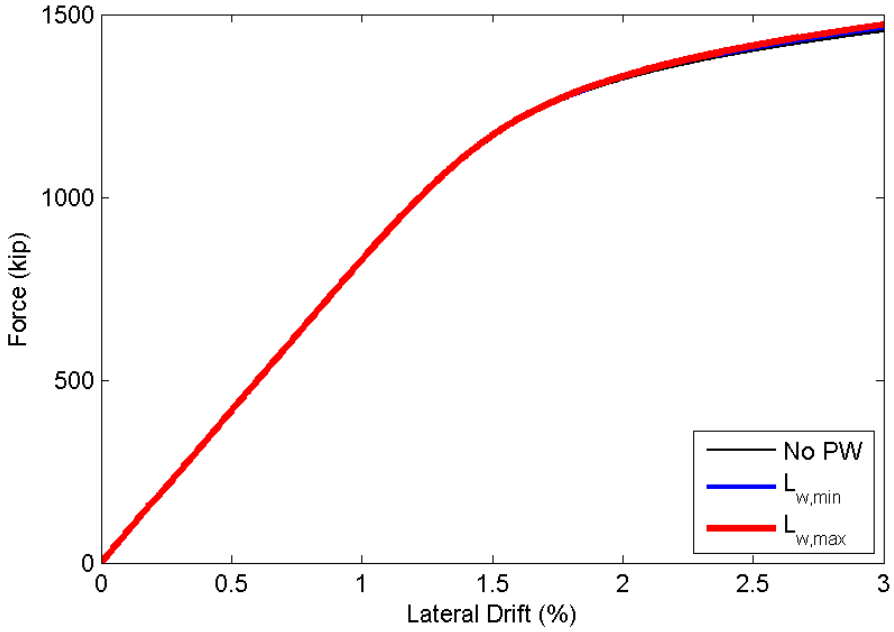

(a)

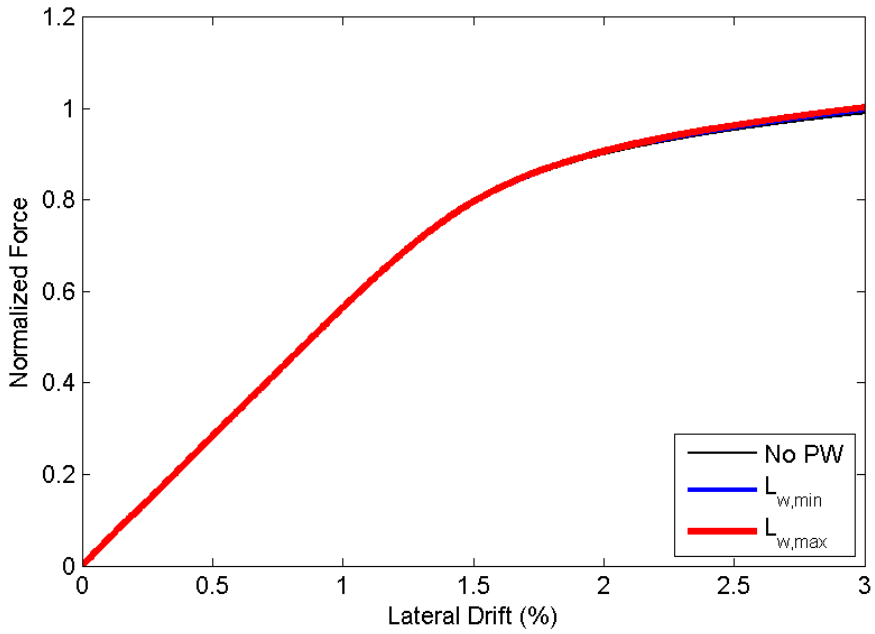

(b)

Figure 4.41 Normalized pushover response illustrated for S-20 demonstrating effect of included PWs.

Table 4.15 Summary of base shear values for roof drifts of 1 and 3%.

Building	V_b (kip) at Roof Drift = 1%			V_b (kip) at Roof Drift = 3%		
	Bare	$L_{w,min}$	$L_{w,max}$	Bare	$L_{w,min}$	$L_{w,max}$
RC-2	356.2	365.4	373.2	370.71	388.3	402.9
RC-4	352.0	360.8	367.8	360.6	380.6	397.4
RC-8	389.6	399.2	407.2	418.7	4467.0	470.0
RC-12	359.1	368.8	376.8	374.0	405.2	430.2
RC-20	374.7	385.0	393.4	369.3	399.1	422.8
S-3	879.0	890.8	900.7	1379.8	1408.2	1431.8
S-3H	1721.7	1743.0	1770.0	2439.6	2514.7	2609.3
S-9	950.2	965.2	976.4	1374.6	1478.6	1543.5
S-20	824.2	826.1	827.7	1467.3	1478.1	1486.5

Table 4.16 Summary of normalized base shear values for roof drifts of 1 and 3%. The coupled wall cases are normalized by the bare building (no wall) case.

Building	V_b^n/V_b^{bare} (%) at Roof Drift = 1%		V_b^n/V_b^{bare} (%) at Roof Drift = 3%	
	$L_{w,min}$	$L_{w,max}$	$L_{w,min}$	$L_{w,max}$
RC-2	102.6	104.8	104.7	108.7
RC-4	102.5	104.5	105.5	110.2
RC-8	102.5	104.5	106.8	112.3
RC-12	102.7	104.9	108.4	115.0
RC-20	102.7	105.0	108.1	114.5
S-3	101.3	102.5	102.1	103.8
S-3H	101.2	102.8	103.1	107.0
S-9	101.6	102.8	107.6	112.3
S-20	100.2	100.4	100.7	101.3

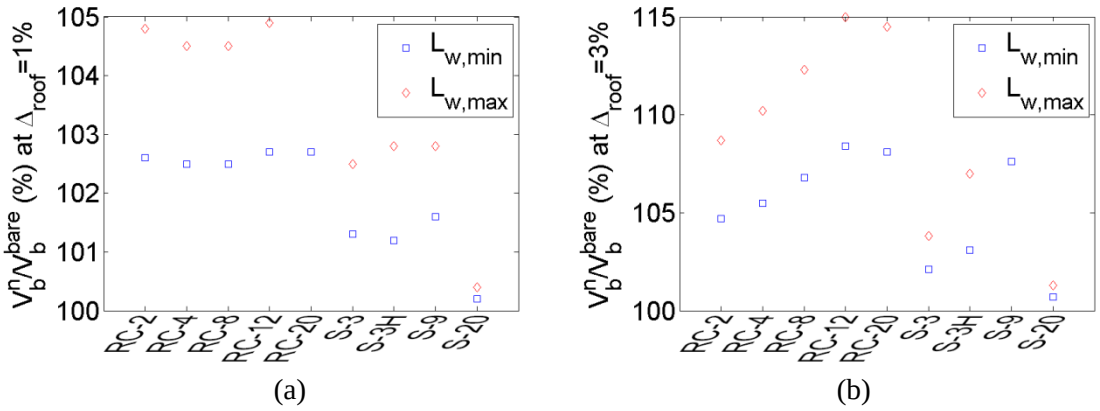

Figure 4.42 Summary of normalized base shear values for roof drifts of 1 and 3%, shown by building model.

4.4 Summary Remarks

In this chapter, an introduction to the building models, PW implementation, and the effect of considering the PW within a building model (i.e. coupled analyses) is considered in terms of the systems eigenvalue and nonlinear pushover response characteristics. The suite of buildings modeled is broad, considering both steel and reinforced concrete frame based structures with a wide fundamental period distribution of approximately 0.2 to 2.1 seconds. Eigenvalue analyses indicate period reductions of up to 14% occurred, however the amplitude of reduction is dependent upon the PW length. On average, the reduction in period was less than 10%. Results of the nonlinear static pushover analysis showed that in order to reach identical levels of drift, additional force of up to 20% are required with the inclusion of a PW. In the next chapter, an examination into the effect of scaling ground motions is explored. In chapter 6, the effect on the response of the nonlinear time history analysis is detailed.

4.5 Acknowledgement

Chapter 4 of this dissertation is based on a NEES-Nonstructural Report in preparation, *Fragility Function Development for Nonstructural Component System*, to be published at the State University of New York, University of Buffalo. The co-authors of this manuscript are Tara C. Hutchinson, Chang Hoon Lee, and Mircea Grigoriu; where the dissertation author is the lead author and investigator.

Chapter 5 Effects of Ground Motion Scaling on Building Response

5.1 Introduction

Given the broad nature of earthquake motions, coupled with limited resources to analyze a particular problem, a natural question that arises in design is: How should a suite of motions be scaled to reasonably represent the anticipated seismic hazard at the site where it will be constructed? In the assessment of the coupled building-partition wall system, scaling methods may influence the observed system behavior. To illustrate the diverse effects of ground motion scaling on the nonlinear response of buildings, this chapter details a scaling sensitivity study performed to evaluate linear scaling of ground records. The building models considered are a subset of those presented in Chapter 4, namely RC-8, RC-12 and RC-20. The suite of ground motions scaled in this chapter is for a target site in southern California selected through a probabilistic seismic hazard analysis and deaggregation.

5.2 Motion Scaling Strategies

Previous ground motion scaling methods have primarily focused on spectral acceleration amplitude scaling, based often at the fundamental period of the structure (T_1) (e.g. Shome and Cornell, 1998). Although appealing, this scaling method only focuses on the first-mode linear response of the structural building system. Buildings designed to respond nonlinearly, with anticipated soil-structure-interaction, or if there is concern with secondary system response (nonstructural components and systems), scaling at periods other than the fundamental mode are of interest. As a result, it may also be desirable to scale the motion across a period range in which the structure is anticipated to vibrate during seismic excitation rather than at a single period value.

ASCE 7-05 (2006) recognizes these issues by requiring that the average spectral acceleration of the suite of motions used for nonlinear time history analyses be greater than or equal to the target spectral acceleration over the range of $0.2T_1$ to $1.5T_1$ s. In design codes, the average spectral acceleration is required to match or exceed the target spectrum over the range of periods through which the structure is expected to respond nonlinearly and contain contributions from higher modes. The upper bound of this scaling range, $1.5T_1$, is suggested to account for period elongation due to anticipated nonlinear structural behavior. Eurocode 8 has a broader range to account for period elongation and requires an analyst to match or exceed the target spectrum over a range of $0.2T_1$ to $2.0T_1$ (European Committee for Standardization, 2003). At extensive levels of nonlinearity, such as performance levels of Life Safety and Collapse Prevention, the amount of period elongation is critical (Catalán et al., 2010). In a study by Katsanos et al. (2010), the required upper bound limit for spectrum matching ($2.0\ T_1$) is found to be excessive in most cases, due to the unlikely nature of the fundamental period of the structure doubling, unless subjected to extremely large seismic demands and structural damage. Katsanos et al. (2010) also proposes that a function of the higher mode contributions dictate the lower bound of the period range. Rather than the lower bound taken as $0.2T_1$, the authors suggest a lower bound of period, T_L associated with the highest mode of vibration satisfying the condition that the effective mass reaches 90%.

For single or limited range period sweep scaling approaches, the demands to systems with periods less than the fundamental mode or accounted higher modes can be misrepresented. Most nonstructural components and systems (NCS) for example have primary modes of vibration with periods much smaller than the building itself (less than 0.2 seconds). For example, in a survey and modal testing program of building mechanical and electrical (ME) systems, Watkins et al. (2009) found that more than half of the ME service equipment in typical buildings would likely be characterized as rigid ($T_1 < 0.06$s). For these NCSs, the higher mode responses of the buildings are important. Within the period range of approximately 0.05 – 0.20 sec, a reasonable

transfer of the vibration energy is needed to reliably predict the performance of the NCS. Scaling procedures based on the fundamental mode of a tall building can misrepresent this vibration energy associated with the NCSs, due to its lack of constraints upon the demand in the short periods. However as of yet, a consensus on the scaling for higher modes does not exist. One appealing method to account for higher mode effects and their impacts on secondary systems may be to adopt mean scaling across a period sweep, such as proposed by Somerville et al. (1997) and adopted by Huang et al. (2009). In this approach, termed the *Geometric Mean Method*, a motion scale factor is selected to minimize the sum of the squared errors between the design (target) spectral acceleration and spectral acceleration ordinate of the selected record over a specified period range.

In this chapter, an investigation is conducted to evaluate the sensitivity of a building's nonlinear response considering four different motion scaling approaches. The scaling methods involve applying a scale factor over three different period ranges, namely: (*i*) zero to four seconds (denoted *sweep*), (*ii*) $0.2T_1$ to $1.5T_1$ (denoted *code*) and (*iii*) over the first two fundamental building periods (denoted *range*). The fourth method (*iv*) for comparison invokes scaling only at the fundamental period (T_1) of the structure (denoted *fundamental*). It is noted that the *code* (ii) and *range* (iii) methods studied herein are similar to that proposed by Hancock et al. (2008), whereby a scaling range of $0.5T_1$ to $2.0T_1$ is suggested. Although these and prior studies have revealed limitations in the aforementioned scaling approaches (with particular concern toward code-based scaling), the validity of these approaches is herein evaluated via comparison with spectral matching of the suite of ground motions. For reasons discussed in Section 5.5, the spectrally matched motions are identified as the method for '*baseline'* comparison to other methods. Using a suite of ground motions selected to capture magnitude and distance pairs from a probabilistic seismic hazard analysis (PSHA), each record is scaled according to the various methods. Nonlinear time history analyses are cross-compared with each other and the *baseline*.

5.3 Building Design and Modeling

Three reinforced concrete special moment resisting frame (SMRF) buildings intended to represent mid and high-rise buildings are used in the study, namely the eight, 12 and 20 story reinforced concrete buildings denoted as RC-8, RC-12, and RC-20, respectively. Chapter 4 describes these buildings and their design in detail. One difference exists where the material model utilized in this chapter is the Menegotto-Pinto model (steel02) for the reinforcing steel. This material model is not considered in other sections of this thesis since it lacks strength degradation, a key parameter to include in the incremental dynamic analysis. The lack of strength degradation is acceptable for the nonlinear time history analysis at the anticipated demand level of the ground motion scaling study (design level event) since the level of nonlinearity and building damage is minor to moderate.

5.4 Dynamic Characteristics of the Considered Buildings

To determine the building dynamic characteristics, an eigenvalue analysis is carried out for all buildings models, where these values vary from those presented in Chapter 4. Results from these analyses, in terms of the modal periods of vibration and modal mass participation estimates are shown in Table 5.1. The range of fundamental building periods is 0.89 seconds for the eight story SMRF to 2.07 seconds for the 20 story SMRF, with greater than 85% of the mass participating in the first two modes of vibration for all buildings.

Table 5.1 Building eigenvalue analysis.

Building	Period (sec)			
	1st	2nd	3rd	4th
8 story	0.89	0.29	0.15	0.1
12 story	1.33	0.45	0.24	0.16
20 story	2.07	0.71	0.39	0.26
Building	**Mass Participation (%)**			
	1st	2nd	3rd	4th
8 story	76.8	12.2	4.1	2.7
12 story	75.3	11.4	4.6	2.3
20 story	72.8	12.1	4.1	2.5

5.5 Site Location and Hazard

The site selected for this study is located within a densely populated region of Southern California, in the city of Charter Oaks (longitude 117.856 W and latitude 34.102 N). The site is selected due to its high rate of seismic activity and proximity to a number of known fault zones. The site class was selected as C (dense soil), as defined by ASCE 7-05 (2006). Using the most recently available data at the time, the National Seismic Hazard Maps (USGS, 2008a), the spectral acceleration at short periods (S_s) and at a period of one second (S_1) are conservatively estimated as 2.01 g and 0.61 g, respectively, in the vicinity of the site. Using procedures of ASCE 7-05 (2006), a target design acceleration response spectrum was generated. This target design spectrum is representative of a design based event.

A PSHA of the site estimated the magnitude and source-to-site distance (M, R) bins associated with a seismic hazard with a probability of exceedance of 10% in 50 years, closely corresponding to the design level scenario. The hazard analysis was conducted using the online USGS PSHA tools, with the most recent update available at the time, namely the 2002 edition of the National Seismic Hazards Mapping Project models (USGS, 2008b; Figure 5.1 and Table 5.2).

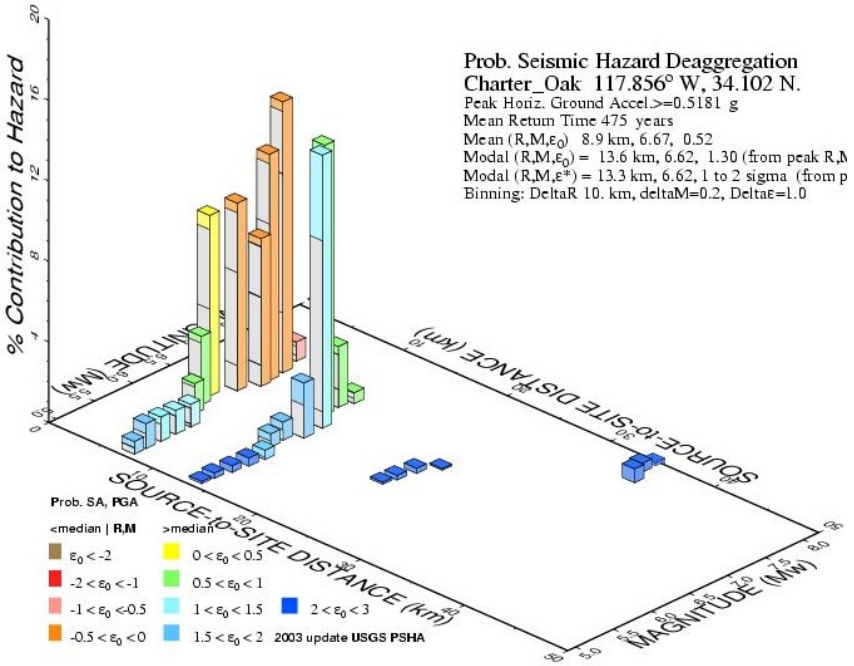

Figure 5.1 Probabilistic Seismic Hazard Deaggregation generated using the 2002 USGS interactive deaggregation tools.
(Note: 1 km = 0.621 miles)

Table 5.2 Deaggregation bin details (% hazard).

M_w	Source-to-Site Distance (miles) [km]				
	0-6 [0-10]	6-12 [10-20]	12-19 [20-30]	19-25 [30-40]	**SUM**
5.0 - 5.25	1.9	0.4			**2.3**
5.25 - 5.50	1.2	0.3			**1.5**
5.50 - 5.75	1.2	0.4			**1.6**
5.75 - 6.00	2.6	1.1			**3.7**
6.0 - 6.25	3.4	0.9	0.1		**4.4**
6.25 - 6.50	9.0	2.7	0.2		**11.9**
6.50 - 6.75	9.3	13.6	0.3		**23.2**
6.75 - 7.00	18.6	16.4			**35.0**
7.0 - 7.25	13.5	0.5			**14.0**
7.25 - 7.50	1.0				**1.0**
7.5 - 7.75					
7.75 - 8.00				0.7	**0.7**
8.0 - 8.25				0.6	**0.6**
SUM	**61.5**	**36.4**	**0.7**	**1.3**	**99.9**

The probabilistic seismic hazard analysis was conducted with respect to the peak ground acceleration due to the range of building dynamic characteristics adopted in this study (Wood et al., 2009). While this negates the need for building specific record selection and may be construed as inconsistent with the motion scaling, it is noted that in practice such an approach is not uncommon due to uncertainty in actual building characteristics at a site. In this study, it is more important to include a broader set of building model types. Comparison with deaggregated hazard at spectral periods near those of the taller building models indicates that this method underestimates hazard in the large magnitude far field. However, individual records within these bins are selected, scaled, and nonlinear time history analyses conducted. These results indicate that the response results are generally within the significant statistical bounds of the PGA-based PSHA, namely that 98% of the hazard is associated with sources within 12 miles (20 km) or less, and approximately 60% of the hazard is associated with sources within 6 miles (10 km) of the site. The deaggregation also indicates that 75% of the hazard is associated with magnitudes larger than 6.50, with 58% of the hazard associated with the magnitude range of 6.5-7.0. With the 2008 deaggregation tools updated after the motions were selected, comparison between the 2002 and 2008 editions (USGS, 2009) is conducted for the site of interest. This comparison indicated overall greater contributions in (M,R) (6.75-7.0, 0-6 miles (0-10km)), (6.75-7.0, 6-12 miles (10-20km)) and (7.0-7.25,0-6 miles (0-10km)) bins. A lower number of motions were selected in these bins as a result of the deaggregation tools available at the time of the initial study. The hazard deaggregation guides the selection of ground motion records (Table 5.3). The selection and scaling of ground motions is a broad and currently debated topic; however, based on the recommendations of ASCE 7-05, those of Bommer and Acevedo (2004), and similarly Haselton's Group I (2009), it was decided that the selected ground motion records should conform to the following criteria:

- Strong motion records should be compatible with the tectonic regime anticipated at the site and of similar anticipated source mechanisms (i.e. strike-slip, reverse, or normal fault),
- Magnitude-distance (M, R) pairs of the selected records should be compatible with results of the deaggregation analysis from the probabilistic seismic hazard for the site of interest. With regard to record selection, records were relaxed to magnitudes within 0.2 units of the target magnitude and 2 km of their target distance, as the dependency on seismological characteristics in site-specific record selection is not as critical when undertaking nonlinear analysis (Iervolino and Cornell, 2005),
- The selected ground motion records should be compatible with the soil characteristics of the site of interest (namely site class C, with a shear wave velocity in the upper 100 feet (30 m) ranging from 1200 ft/s to 2500 ft/s (365 to 760 m/s)). Records at soft soil sites should be excluded,
- Ground motion records should be obtained from strong motion instruments installed in the free field.

Table 5.3 Selected ground motions (seed records) details (PEER-NGA, 2009).

	Event	*Date*	*Location*	*Focal Mechanism*	*Site Class (IBC 2006)*	*Magnitude (Mw)*
1	**Baja California**	Jul 2, 1987	Mexicali, Mexico	Strike-Slip	C	5.50
2	**Cape Mendocino**	Apr 25, 1992	Cape Mendocino, CA, USA	Reverse	C/D	7.01
3	**Cape Mendocino**	Apr 25, 1992	Cape Mendocino, CA, USA	Reverse	C	7.01
4	**Chi Chi**	Sep 25, 1999	Taichung City, Taiwan	Reverse	C	6.30
5	**Friuli**	Nov 12, 1999	Fruili, Italy	Reverse	C	6.50
6	**Gazli**	May 17, 1976	Gazli, USSR	Reverse	C	6.80
7	**Irpina**	Nov 23, 1980	Irpina, Italy	Normal	C	6.90
8	**Kobe**	Jan 16, 1995	Kobe, Japan	Strike-Slip	C	6.90
9	**Kobe**	Jan 16, 1995	Nishi-Akashi, Japan	Strike-Slip	C	6.90
10	**Landers**	Jun 28, 1992	Lucerne, CA, USA	Strike-Slip	C	7.28
11	**Loma Prieta**	Oct 18, 1989	San Jose, CA, USA	Reverse-Oblique	C	6.93
12	**Loma Prieta**	Oct 18, 1989	Saratoga, CA, USA	Reverse-Oblique	C	6.93
13	**Morgan Hill**	Apr 24, 1984	Morgan Hill, CA, USA	Strike-Slip	C	6.19
14	**Nahanni**	Dec 23, 1985	Nahanni, Canada	Reverse	C	6.76
15	**Northridge**	Jan 17, 1994	Castaic, CA, USA	Reverse	C	6.69
16	**Northridge**	Jan 17, 1994	Los Angeles, CA, USA	Reverse	C	6.69
18	**San Fernando**	Feb 9, 1971	Castaic, CA, USA	Reverse	C	6.61
17	**San Salvador**	Oct 10, 1986	San Salvador, El Salvador	Strike-Slip	C	5.80
19	**Superstition**	Nov 24, 1987	Superstition Mtn, CA, USA	Strike-Slip	C	6.54
20	**Tabas**	Jun 28, 1991	Tabas, Iran	Reverse	C	7.35
21	**Victoria**	Jun 9, 1980	Mexicali, Mexico	Strike-Slip	C	6.33

To obtain meaningful statistical results, a reasonable number of ground motion records are needed. Hancock et al. (2008) suggest that 17 motions are sufficient to capture peak drift response, whereas 22 records are more suitable for capturing base rotation. Herein, a suite of 21 one directional strong motion records with the aforementioned characteristics were selected from the PEER-NGA strong motion database (PEER, 2009). Of the selected motions, 11 were from the United States and Canada, two were from Italy and Japan, and one each were from Taiwan, USSR (Uzbekistan), Iran, Mexico and El Salvador. The magnitudes and distance pairs of the selected ground motions represent 94% of the deaggregated contributions with ground motions of PGA > 0.51g. The details on the ground motions are summarized in Table 5.3 along with the spectral acceleration plots for the unscaled records in Figure 5.2a.

5.6 Ground Motion Scaling Methods

5.6.1 Linear Scaling

The motions are linearly scaled using four different methods. The first three methods involve scaling over a range of periods utilizing a variation of the Geometric Mean Method proposed by Huang et al. (2009), which was first developed by Somerville et al. (1997). In this approach, the scale factor is selected to minimize the sum of the squared errors between the design (target) spectral acceleration and spectral acceleration ordinate of the selected record over a specified period range. The scale factor, a, for an individual record is determined as:

$$a = \frac{\sum_{i=1}^{n} y_i \cdot y_i^t}{\sum_{i=1}^{n} y_i^2} \tag{5-1}$$

where, y_i = the spectral acceleration at period i and y^t_i = target design spectral acceleration at period i. The geometric mean scaling approach is applied in three ways: (*i*) with a period range from zero to four seconds, denoted "*sweep*" where no relevant account is made for the building dynamic characteristics; (*ii*) with a period range from $0.2T_1$ to $1.5T_1$ where T_1 represents the fundamental building period based-this approach is defined in ASCE 7-05 (2006) and "*code*"; and, (*iii*) with a period range corresponding to the first two fundamental building modes, denoted "*range*". These methods proceed from largest period range to shortest period range considered. While the *range* method may appear similar to the Im_IE&2E method evaluated by Luco and Cornell (2007), it is slightly different. The Im_IE&2E method assesses the contribution of higher modes using modal combination rules (SRSS in this case), whereas the *range* method considered herein adopts linear scaling by calculating the equally weighted scale factor, which minimizes the error over the period range of T_1 to T_2. In the application of the *code* scaling approach (*ii*), an additional step is performed by increasing the scale factors by the same percentage such that the

average spectra is greater or equal to the design acceleration spectrum over the specified period range of $0.2T_1$ to $1.5T_1$ to assess current code requirements. While increasing the scale factors to meet this code requirement limits the comparison to the baseline ground motion as discussed in future sections, it is performed to demonstrate the severe penalty it creates. A scaling approach considering a period range of $0.2T_1$ to 1.5 is not addressed herein, but it is anticipated that its effect would be similar to the range method while accounting for potential period elongation. The *range* method (*iii*) is used to minimize the residuals over an approximate 85% mass participation range (first two fundamental modes), a similar period range suggested by Katsanos et al. (2010). The (*iv*) fourth scaling method involves scaling only at the fundamental period. Denoted "*fundamental*" this strategy is reminiscent of the earliest (and still adapted) traditional approach to motion scaling. Table 5.4 and Figure 5.2 summarize the resulting scale factors per motion considering each of the aforementioned methods and show the spectral acceleration responses of the scaled motions, respectively.

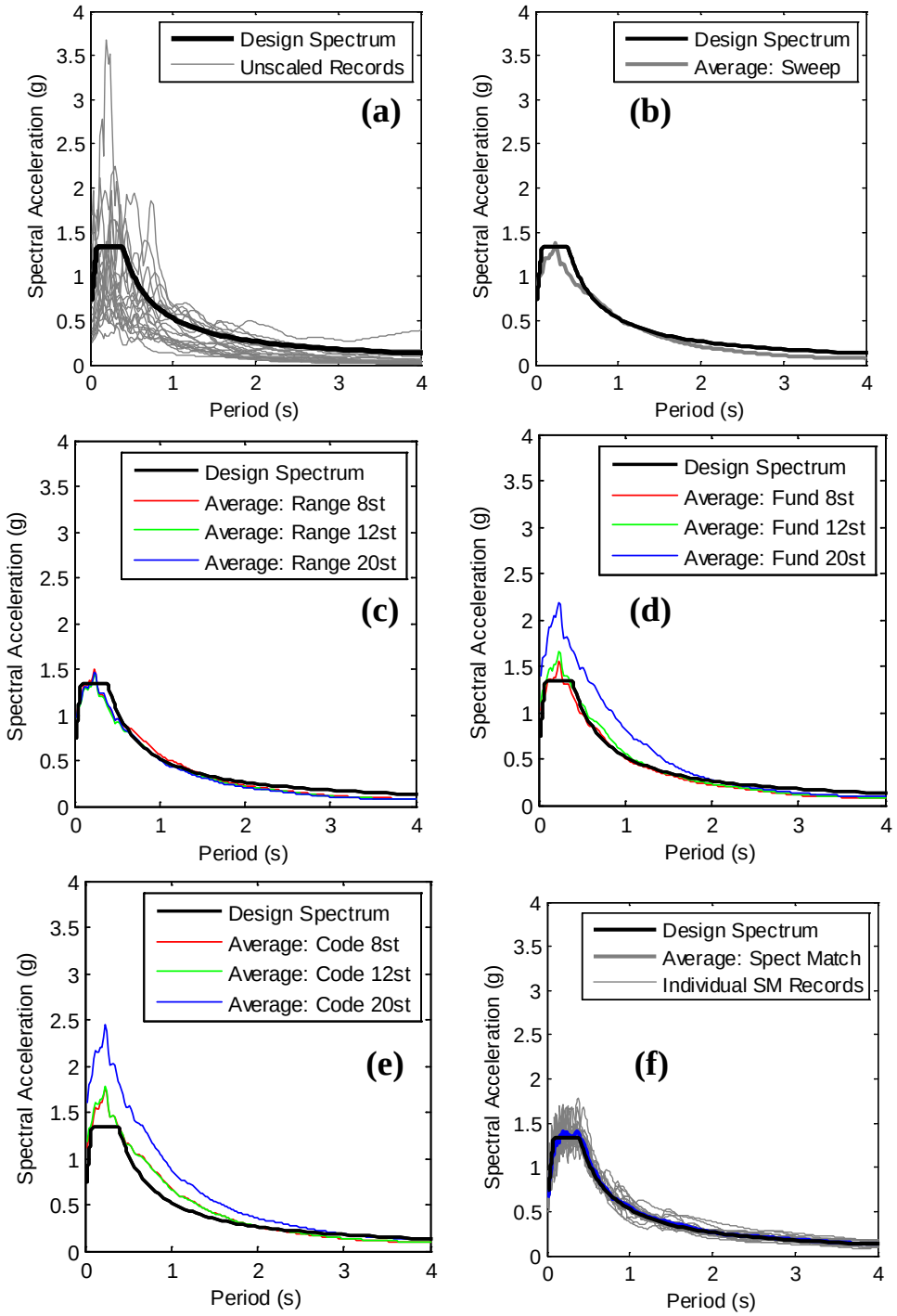

Figure 5.2 Elastic 5% damped spectral acceleration curves showing for all buildings (a) the target design spectrum and unscaled motions, (b) *sweep*, (c) *range*, (d) *fundamental*, (e) *code* scaling approaches, and (f) the average baseline (SM= spectrally matched) response and the individual spectrally matched records responses.

Table 5.4 Scale factors for each ground motion record and summary statistics.

Record No.	Sweep	Code			Range			Fundamental		
	All	*20*	*12*	*8*	*20*	*12*	*8*	*20*	*12*	*8*
1	0.79	1.29	0.97	1.02	0.75	0.73	0.77	1.60	0.69	0.87
2	1.36	2.00	1.53	1.61	1.09	1.12	1.31	2.01	0.94	1.19
3	1.46	2.96	2.39	2.48	1.58	2.11	2.27	1.11	1.57	1.84
4	1.89	3.04	2.22	2.27	1.57	1.67	1.94	3.20	1.62	1.27
5	1.82	3.32	2.12	2.17	2.25	1.89	1.74	4.39	2.36	2.26
6	1.03	1.85	1.28	1.36	1.05	1.35	1.07	0.97	1.14	1.47
7	2.68	3.82	3.03	3.35	1.88	2.19	2.63	2.74	2.31	1.52
8	1.17	1.70	1.32	1.37	1.17	0.97	1.00	1.44	2.09	1.45
9	0.91	2.39	1.13	1.14	1.73	1.41	0.89	1.38	2.01	2.08
10	1.82	3.90	3.13	3.15	2.22	2.33	2.65	2.09	2.51	1.99
11	2.06	3.68	2.78	2.62	2.39	2.09	2.17	5.10	2.33	2.05
12	1.23	1.71	1.37	1.55	0.83	0.99	1.43	1.15	0.75	0.89
13	1.38	2.08	1.60	1.63	1.00	1.15	1.51	2.86	1.01	0.90
14	2.37	4.59	2.99	3.08	3.99	2.82	2.28	3.75	4.10	4.59
15	0.97	1.59	1.12	1.16	0.85	0.93	0.92	1.21	0.98	0.77
16	1.57	3.26	2.44	2.11	1.92	2.09	2.15	1.35	1.67	2.18
17	1.16	1.60	1.30	1.47	0.80	0.95	1.20	0.79	0.83	0.67
18	2.27	3.79	2.79	2.82	2.22	2.11	2.20	4.74	2.88	1.95
19	0.87	1.69	1.25	1.17	1.09	0.93	1.01	2.81	1.63	0.86
20	0.55	0.99	0.74	0.67	0.57	0.56	0.59	0.56	0.86	0.59
21	1.19	1.82	1.41	1.46	1.01	1.02	1.23	2.76	0.97	0.97
Average	1.45	2.53	1.85	1.89	1.52	1.50	1.57	2.29	1.68	1.54
Standard Deviation	0.57	1.04	0.77	0.78	0.80	0.64	0.64	1.35	0.87	0.89
Maximum	2.68	4.59	3.13	3.35	3.99	2.82	2.65	5.10	4.10	4.59
Minimum	0.55	0.99	0.74	0.67	0.57	0.56	0.59	0.56	0.69	0.59

The high spectral acceleration curves when compared with the design target are apparent for the *fundamental* and *code* scaling approaches. This is due to the longer period of RC-20, T_1 = 2.07 seconds, and for the *code* scaling approach the prescription requiring the average spectral acceleration response be equal to or greater than the design spectrum – this severely penalizes the scaled motions. This results in a large difference in average spectral accelerations, particularly within the short period range apparent in Figure 5.2b-d. Comparing the *sweep* scaling approach, when swept through a broader range of 0 to 4 seconds, baseline comparison with the design spectrum is more reasonable. In contrast the *fundamental* and *code* based scaling is highly conservative (Figure 5.2e).

Table 5.4 indicates that on average the scale factors range from about 1.5 to 2.5, with less than 10% requiring scaling greater than 3.0. In the amplitude scaling of ground motions, the use of minimal scale factors are desired to minimize the bias introduced in the median nonlinear structural response, which increases with the degree of scaling to the first mode spectral

acceleration (Luco and Bazzurro, 2007). This issue is evaluated initially when minimizing the error over the period *sweep* range (method *i*), however this limit was relaxed to allow for the various scaling methods to be investigated. A maximum scale factor of 5.10 is obtained in the *fundamental* scaling approach for the 20 story SMRF building.

5.6.2 Frequency Scaling and Defining Baseline Ground Motions

For comparison with the linear scaling, a baseline is desirable. Within the context of this study, spectral matching the motion suite to develop *baseline* time histories for each event is adopted for reference comparison. To spectrally match each motion, RSPMatch (Abrahamson, 1992) was used in a multiple pass approach (Al Atik and Abrahamson, 2010). Each ground motion was spectrally matched using the spectral acceleration response for 5% damped of critical using four passes with increasing frequency ranges of 1-50 Hz, 0.5-50 Hz, 0.3 to 50 Hz, and 0.2-50 Hz. It is noted that spectrally matching records to the design spectrum produces non-physical ground motions because this spectrum represents many potential seismic events. However, this procedure is adopted for anticipated design code demands, at the expense of nonrealistic motions lacking the troughs and valleys of the spectral acceleration. The individual spectral acceleration matched motions and the resulting average are shown in Figure 5.2f. Compared with the target design spectrum, the average of the spectral matched motions is favorable. Further analysis of the use of the spectrally matched motions as a baseline will be assessed in Section 5.7, by studying the dispersion in the nonlinear time history response parameters.

5.7 Nonlinear Time History Response Results

Nonlinear time history analyses were conducted in OpenSees (Mazzoni et al., 2011). Nonlinear time history was performed for the uniform excitation after gravity loads were applied using Newmark’s method where gamma and beta defined as 0.5 and 0.25, respectively. In the transient analysis, Newton Line Search algorithm was used with a radius of 0.8 where the

displacement tolerance set as 10^{-8} for each time step increment. Nonlinear time history results relevant to NCSs include floor acceleration and interstory drift responses. To gather a sense of the experienced plasticity in the building, curvature ductilities are extracted throughout the building members to determine the locations of plasticity.

5.7.1 Maximum Floor Acceleration Distribution

The maximum floor accelerations are extracted from each nonlinear time history and presented in the form of distributions for each building model (Figure 5.3). The maximum acceleration distribution is calculated as the average of the maximum of the absolute value acceleration at each floor obtained from each record. Plots are shown as a function of normalized height ($h^*=h_i/H$; where h_i = height of floor i and H = overall building height) for ease in cross comparison between the different building models. At $h^*=0$ the maximum acceleration is the average peak ground acceleration. Note that the distribution of maximum acceleration does not follow a linear trend, but rather is linear at the lower floors (shear-like mode) and parabolic (bending-like mode) at the upper floors. Such a distribution indicates higher mode effects influence the nonlinear time history response.

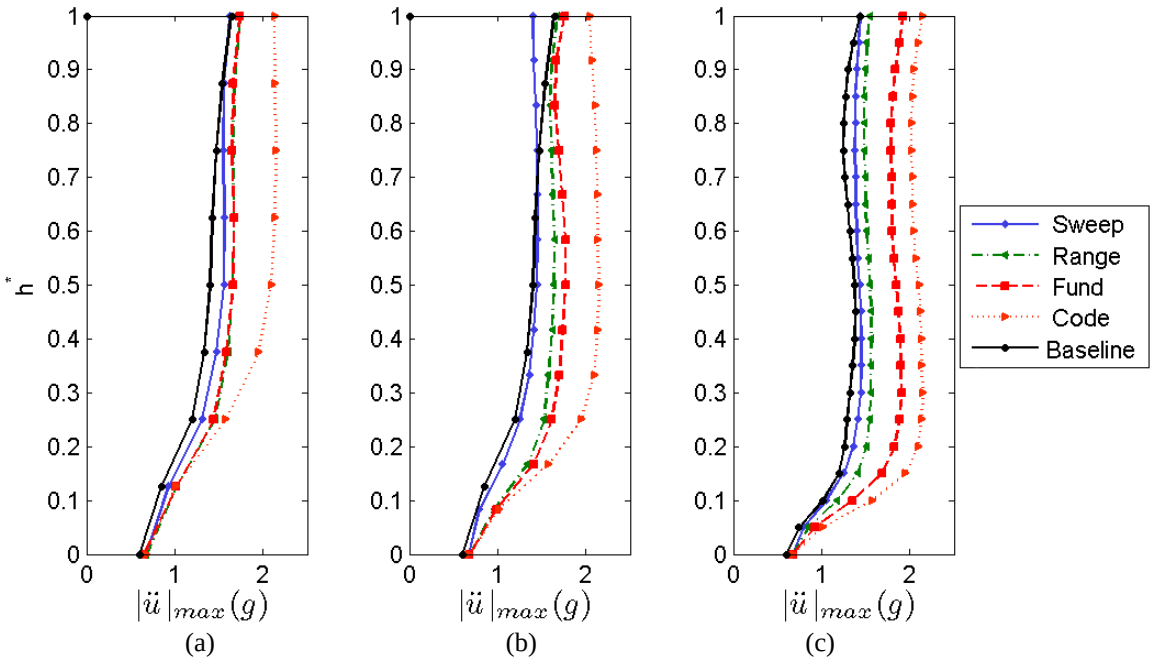

Figure 5.3 Average maximum absolute floor acceleration by building type for (a) RC-8, (b) RC-12, and (c) RC-20 buildings. (y-axis unitless).

Considering the five different motion scaling methods, the amplitude of average maximum acceleration varied most notably in the 20 story building. For all three buildings, the *code* scaling approach provides the largest maximum acceleration distribution. The maximum acceleration experienced by all of the buildings is approximately 2 g, demonstrating the strong seismic design of the buildings, as result of the code prescription requiring high scaling factors so the average acceleration spectrum is above the design spectrum. In comparing the three scaling methods of: *sweep*, *range* and *fundamental*; the dispersion between the methods increases with building height, indicating that higher mode response is influenced most significantly by the motion scaling method. Note that as the buildings increase in height, the first mode participation factor decreases, increasing the influence of scaling on higher mode response. The spectrally matched (*baseline*, referred to as *BL* in subsequent discussions) method produced the lowest acceleration values, which are closest to the *sweep* method. Comparison between the four linearly scaling methods to the *BL* is discussed in more detail later.

5.7.2 Acceleration Amplification Ratio Distribution

In the context of design of force-sensitive components placed within a building, it is instructive to evaluate the relation between maximum input acceleration and maximum floor acceleration. When uncorrelated, one may calculate an uncorrelated acceleration amplification ratio i.e.:

$$\Omega_i = \frac{\max\left(\left|\ddot{u}_i\right|\right)}{PGA} \tag{5-2}$$

Where $\ddot{u}_i$ = the acceleration response of floor i and PGA = the peak ground acceleration. This relationship is uncorrelated in the sense that the maximum floor acceleration may not necessarily occur simultaneously with the peak ground acceleration. The average uncorrelated acceleration amplification ratio distributions are shown in Figure 5.4, considering the average of the suite of motions. The linear code-based suggestion varying from 1 to 3 IBC (ICC, 2006) is shown for comparison.

As in the average maximum floor acceleration plot (Figure 5.3); these plots demonstrate the significant influence of higher modes. As a result of higher mode effects, the prescribed code values underestimate the acceleration amplification ratio in the lower most floors for taller buildings, while conservatively overestimate amplifications in the upper most floors. This amplification trend of underestimation in the lower floors and overestimating in the upper floors holds valid for the spectrally matched motions as well. The design code most severely underestimates the acceleration amplification demand when the *code* scaling approach is applied for all buildings. In addition, for the 20 story building, the *fundamental* scaling is severely underestimated, nearly to the same extent of the *code* scaling approach. The scaling method adopted affects the magnitude of the response, however, it does not affect the overall shape. For the *code* scaling approach, the amplification ratio for the 8 and 12 story buildings tend to plateau

at mid-height of the buildings. The *code* scaling approach provides the largest acceleration amplification. The most consistent comparison of average uncorrelated acceleration amplification ratios with the *baseline (BL)* is observed with the *sweep* and *range* methods.

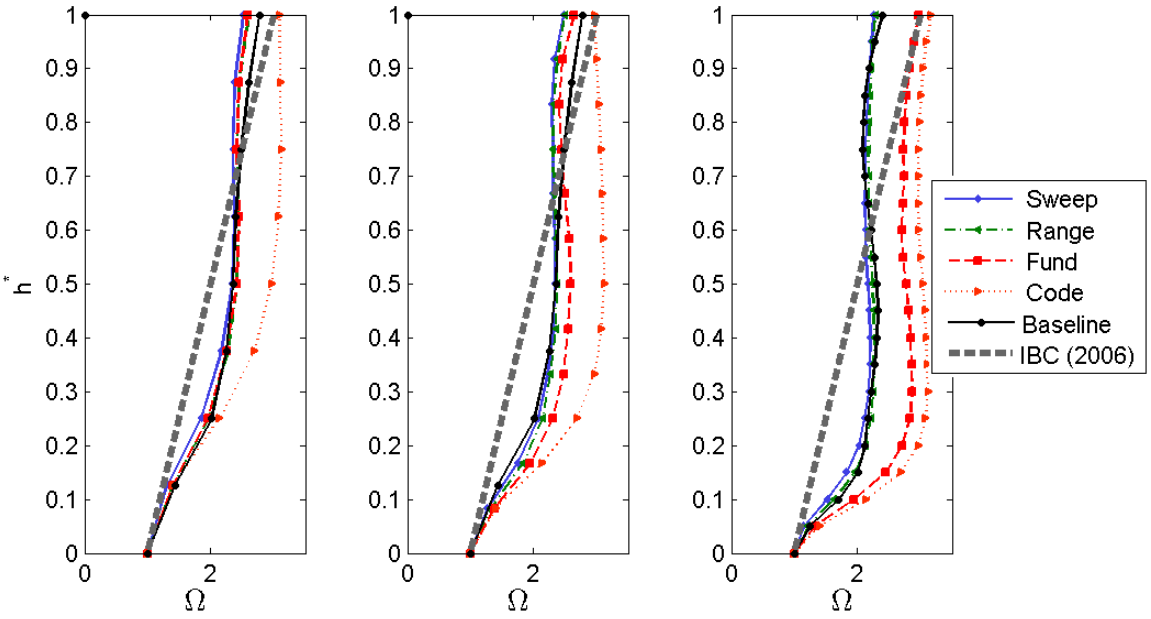

(a) (b) (c)

Figure 5.4 Average uncorrelated acceleration amplification ratio Ω by building type for (a) RC-8, (b) RC-12, and (c) RC-20 buildings. (x- and y-axes unitless).

5.7.3 Baseline Normalized Acceleration Distribution

To compare the response of the buildings using the four scaling methods, the *baseline (BL)* response, normalized acceleration is presented. In this case, the maximum floor acceleration for each linear scaling method is normalized by the corresponding spectrally matched (BL) response at each floor on a record-to-record basis. The average (for the suite of motions) of the maximum normalized values are presented in Figure 5.5. With the spectrally normalized acceleration values, values less than one indicate an average response less than the BL, while, average response values gran than one indicate values greater than the BL. These results demonstrate that the *sweep* scaling method most closely matches the *baseline*, while sometimes slightly underestimating it. As may be expected, the *code* scaling method severely overestimates

the maximum floor acceleration response, in excess of 166% that of the *baseline* in the twenty story building.

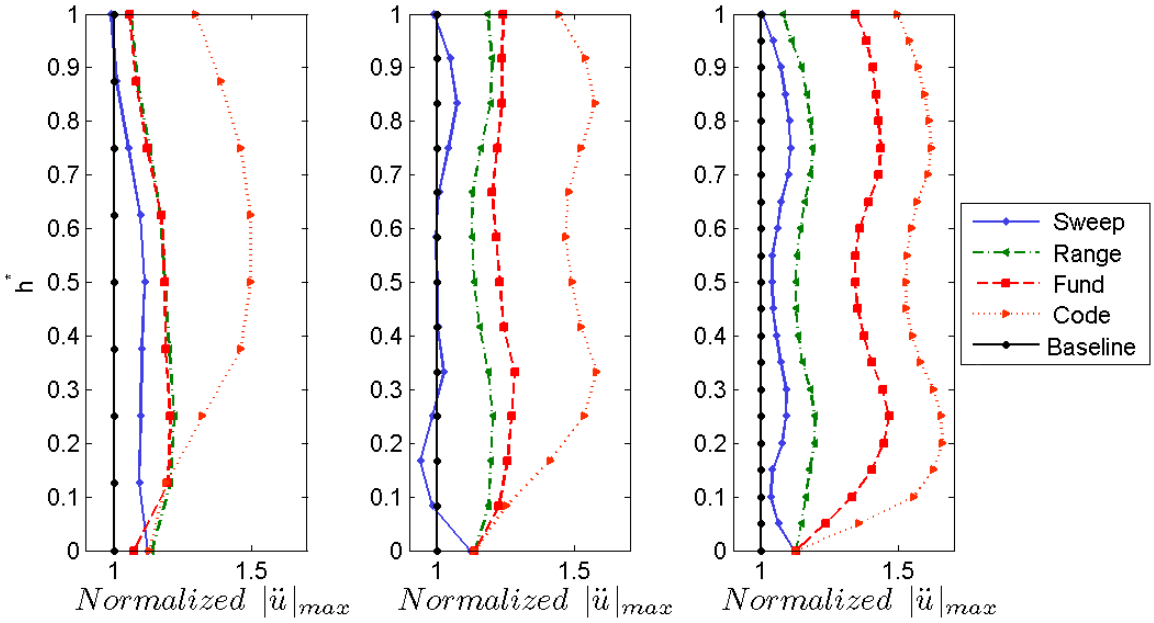

(a) (b) (c)

Figure 5.5 Average maximum acceleration distribution normalized by the baseline response by building type for (a) RC-8, (b) RC-12, and (c) RC-20 buildings. (x- and y-axes unitless).

5.7.4 Baseline Normalized Interstory Drift Distribution

To assess the distribution of deformation demands, the displacement demands between floors is evaluated as:

$$\gamma_{is} = \frac{\Delta_i - \Delta_{i-1}}{h_i - h_{i-1}} \tag{5-3}$$

where γ_{is} = interstory drift at floor i, Δ_i =displacement at floor i and h_i = height of floor i. Then to compare the effect of scaling approaches, the maximum interstory drift ratio per record is normalized by the *baseline (BL)* response. The interstory drift is evaluated as Similarly, the average (of the suite of motions) of the maximum interstory drift values is presented in Figures 5.6, while the normalized interstory drift in Figure 5.7. As previously observed, in the maximum acceleration distributions, the interstory distribution demonstrates higher mode effects, as the

shape is parabolic in nature, and the dispersion in the results increases with increasing building height, except when comparing the *code* scaling approach. When analyzing the normalized interstory drift distribution, the *sweep* and *range* scaling methods closely match the *baseline*. However, these methods predict values only 37% of that of the BL for the lower floors for the taller, 20 story building. Consistent with the acceleration response comparisons, the *code* scaling method severely overestimates the building interstory drift responses.

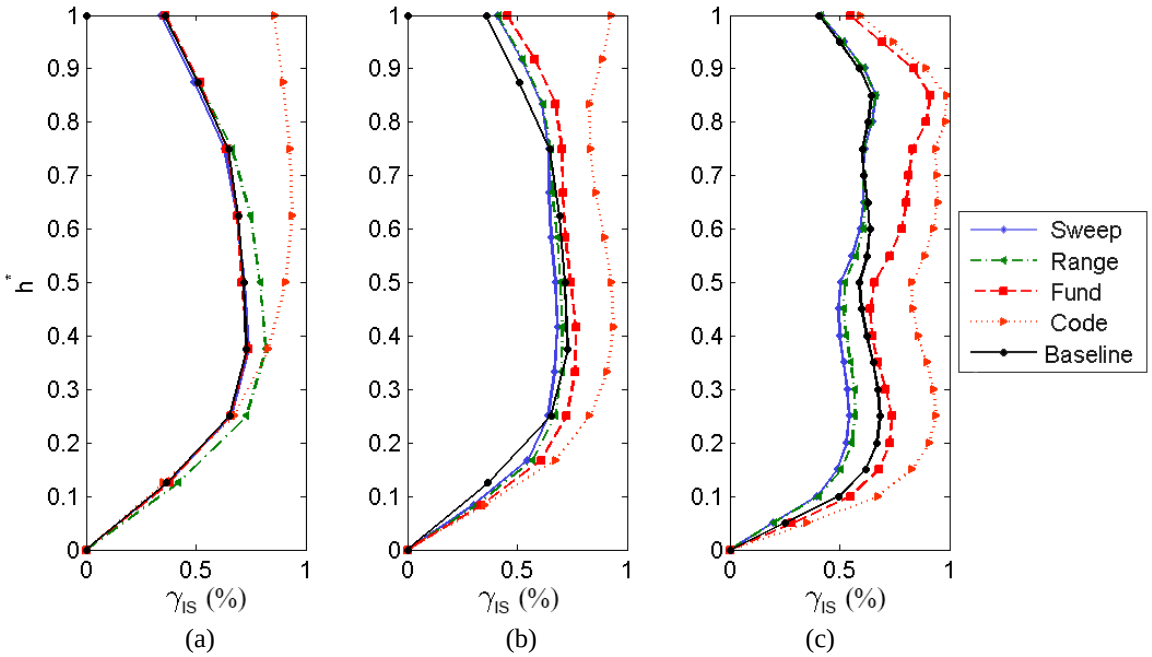

(a) (b) (c)

Figure 5.6 Average maximum average interstory drift (γ_{is}) distributions response by building type for (a) RC-8, (b) RC-12, and (c) RC-20 buildings. (x- and y-axes unitless).

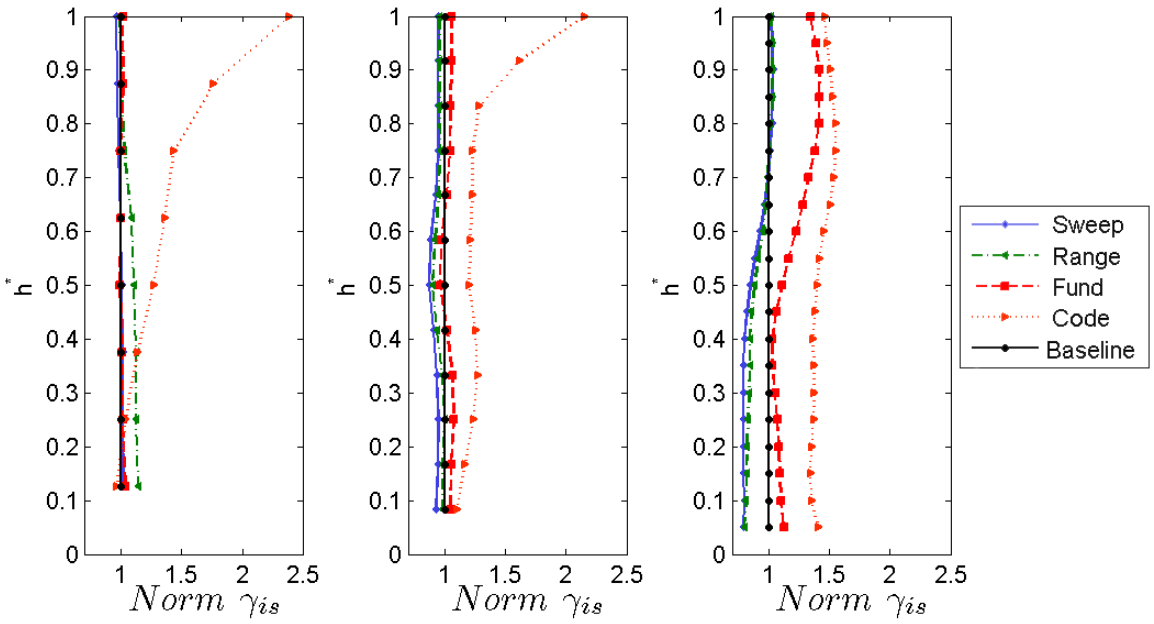

(a) (b) (c)

Figure 5.7 Average maximum average interstory drift (γ_{is}) distributions normalized by *baseline* response by building type for (a) RC-8, (b) RC-12, and (c) RC-20 buildings. (x- and y-axes unitless).

5.7.5 Curvature Ductility Distributions

Curvature time histories provide an indication of the extent of plasticity the buildings experience during earthquake excitation. The extent of plasticity controls the mechanism of load transfer throughout the building; therefore, it is an important indicator of seismic demand distribution. To render these results graphically, curvature ductility distribution diagrams are developed (Figure 5.8), whereby the average maximum curvature ductility values are presented (Table 5.5), considering the suite of ground motions. In the determination of the yield curvature, a sectional analysis was conducted to assess the moment-curvature behavior (Wood et al., 2009). The curvature ductility (μ_u) is defined:

$$\mu_\phi = \frac{\phi_{max}}{\phi_y} \tag{5-4}$$

where ϕ_{max} is the maximum curvature observed during the simulation and ϕ_y is the yield curvature. These curvature distribution diagrams show at the locations where plasticity occurred via bubbles, which are scaled to represent a range of demands (refer to legends). These data are reported as the average maximum of all ground motions, i.e. the maximum from a motion history is taken, and the average of all maximum presented. For the 8 story building, only minimal differences exist when comparing the linear scaling approaches with the *baseline (BL)*, the most significant difference being development of plastic hinging at the column base of the building. However, for the 12 and 20 story buildings, the differences in response become more pronounced. A concentration in upper floor plastic demands is most evident for the 20 story building, when subjected to the *sweep* and *range* scaled motions. In contrast, the *code* scaling method results in plastic demands that are well distributed with elevation, indicating a greater fundamental mode influence on the response.

The amount of plasticity experienced by these buildings was moderate, with average maximum curvature ductility values ranging from about 1.3 to 2.3 (Table 5.5). The *code* scaling approach resulted in the largest average maximum curvature ductility of 2.32 for the 8 story building, while the *range* scaling approach resulted in the minimum value of 1.25 for the 20 story building. When comparing the average maximum curvature ductility demands to the *baseline (BL)* response results, variations are observed per building. For comparison, normalizing the maximum curvature ductility by the maximum curvature ductility corresponding to the *baseline* yields a ratio of μ_ϕ^i/μ_ϕ^{BL}. For the eight story building, both the *fundamental* and the *sweep* method resulted in average maximum curvature ductility demands within 3% that of the *baseline*. For the 12 story building, the fundamental scaling approach resulted in average maximum curvature ductility demands within 1%, with the *range* and *sweep* methods within 10% and 12% respectively of the *baseline*. In the 20 story building analysis, the *sweep* method provided the most robust comparison with average maximum curvature ductility demands of within 12% of the

baseline, followed closely by the *range* method, which was within 14% of the *baseline*. The *range* method also best represents the occurrences of plasticity throughout the height of the building. For the 20 story building, the *fundamental* scaling approach resulted in a poor representation of the spectrally matched plasticity demands. Consistent for all buildings, the *code* scaling approach resulted in more than 50% overestimation in maximum curvature ductility demands, on average.

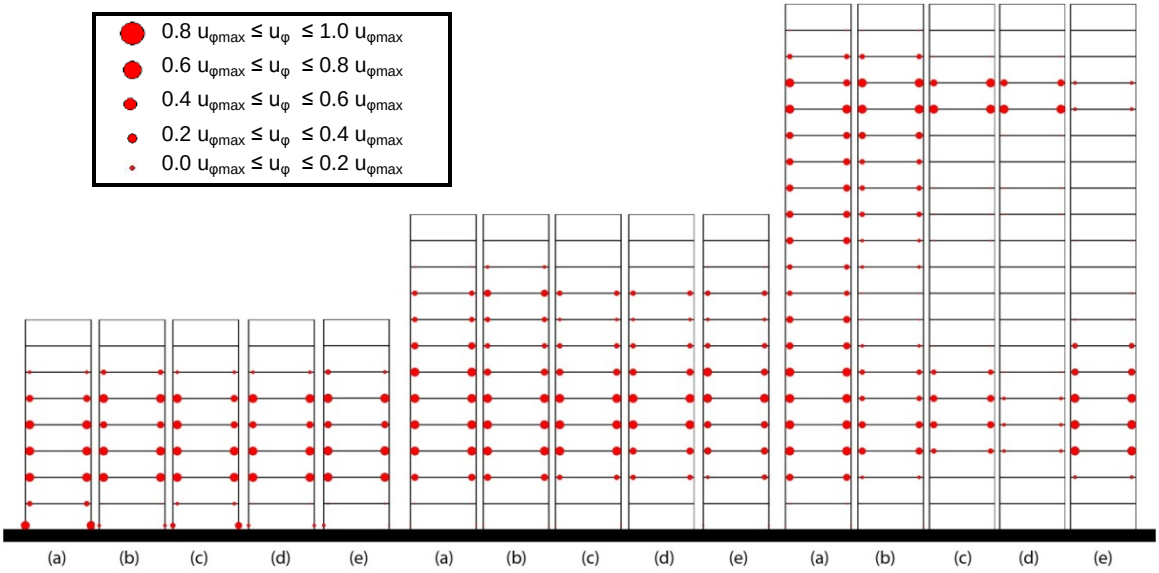

Figure 5.8 Average maximum plastic curvature induced from time history analyses. From left to right: eight, twelve and twenty story buildings scaled according to the follow methods: (a) *code*, (b) *fundamental*, (c) *range*, (d) *sweep* and (e) *baseline (BL)*.

Table 5.5 Average and normalized maximum curvature ductility (μ_ϕ) demands. Note μ_ϕ^i = average maximum curvature ductility for each scaling method, i.e. μ_ϕ^{BL} = average maximum curvature ductility for the baseline scaling method).

Building	*Scaling Method*	μ_ϕ	μ_ϕ^i/μ_ϕ^{BL}
8-story	Code	2.32	1.48
	Fundamental	1.55	0.99
	Range	1.84	1.17
	Sweep	1.62	1.03
	Baseline	1.57	1.00
12-story	Code	2.00	1.22
	Fundamental	1.62	0.99
	Range	1.48	0.90
	Sweep	1.44	0.88
	Baseline	1.64	1.00
20-story	Code	2.24	1.54
	Fundamental	1.99	1.37
	Range	1.25	0.86
	Sweep	1.27	0.88
	Baseline	1.45	1.00

5.7.6 Evaluating Robustness of Spectrally Matched Motions as a Baseline

To assess the validity of the use of the spectrally matched ground motions as a baseline (assuming that they are unbiased records) for comparison, the dispersion between scaling methods is analyzed. Figure 5.9 - Figure 5.11 illustrate dispersion as a function of the building height for the maximum acceleration, maximum uncorrelated acceleration amplification and interstory drift by plotting the mean number with error bars representing the plus and minus one standard deviation for each of the three buildings. Assuming a normal distribution, this represents a 68% confidence interval, where evaluating this assumption:

- For acceleration values (first row of plots, Figures 5.9 - 5.11): 77% of the individual floor values fell within the range mean +/- standard deviation.
- For amplification values (second row of plots, Figures 5.9 - 5.11): 83% of the individual floor values fell within the range mean +/- standard deviation.

- For interstory drift values (third row of plots, Figures 5.9 - 5.11): only 65% of the individual floor values fall within the range mean +/- standard deviation.
    - To further evaluate for interstory drift values: 42%, 79%, and 88% of values fit within the 50%, 80% (1.28σ) and 90% (1.64σ) confidence intervals.

To compare the dispersion of the standard deviation of the nonlinear response parameters (maximum floor acceleration and interstory drift) for each scaling method, it is noted that the dispersion under the spectrally matched case is the smallest (Figure 5.12). The spectrally matched case has the smallest average standard deviation per floor comparison and the smallest range of standard deviations. This finding supports its consideration as a baseline for comparison, since record to record variability of the building response is greatly reduced. One may also note that the dispersion in the sweep method is lowest when compared to the other scaling methods. These results were consistent with distribution and maximum, though only maximum values are shown.

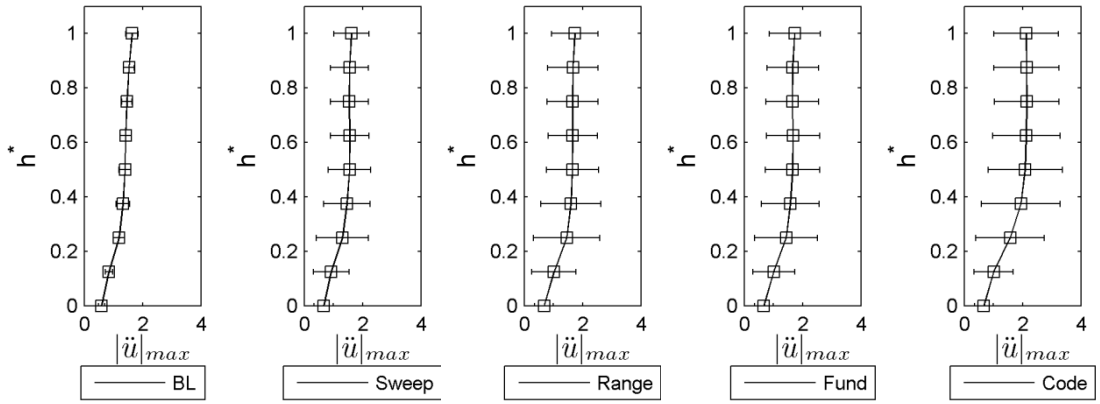

(a)

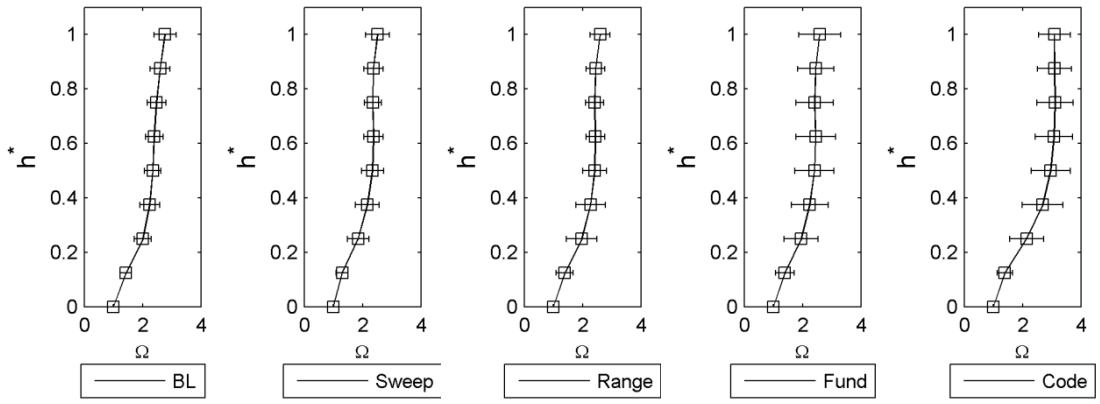

(b)

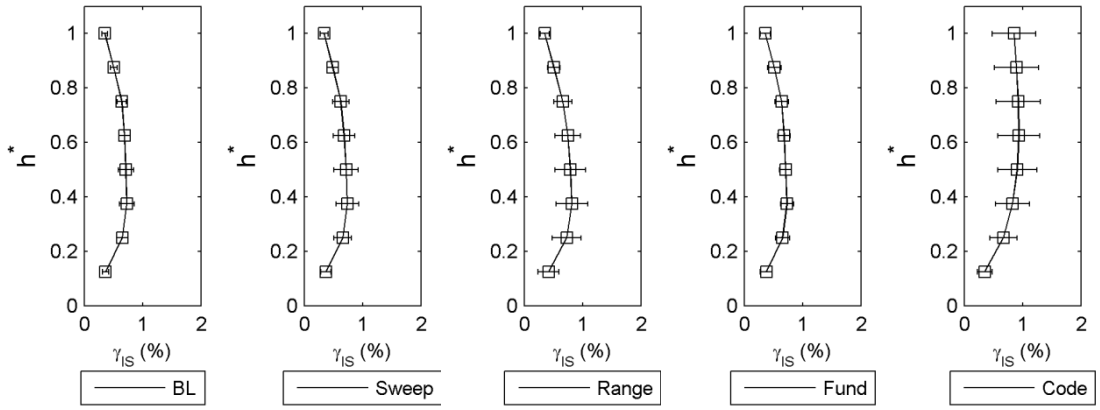

(c)

Figure 5.9 68% confidence interval plots identifying: (a) acceleration, (b) <u>uncorrelated</u> acceleration amplification, and (c) interstory drift dispersion along the height of the building for RC-8. (BL = baseline or spectrally matched case).

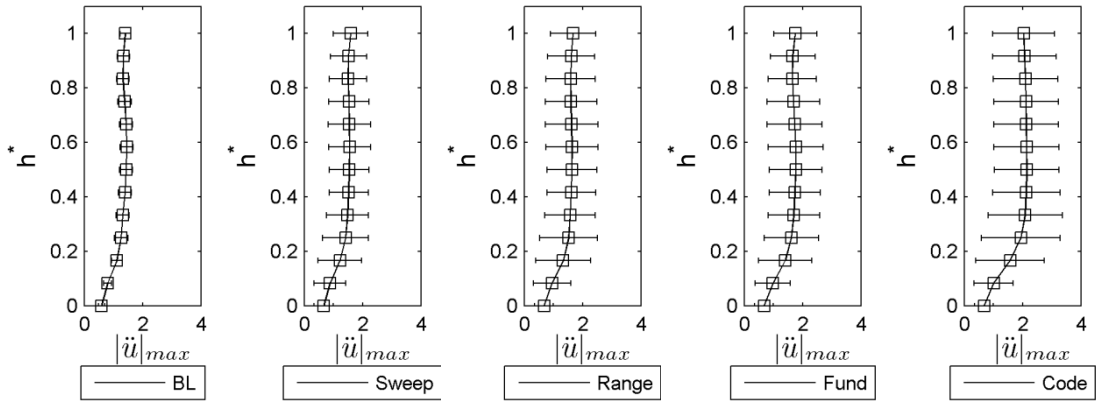

(a)

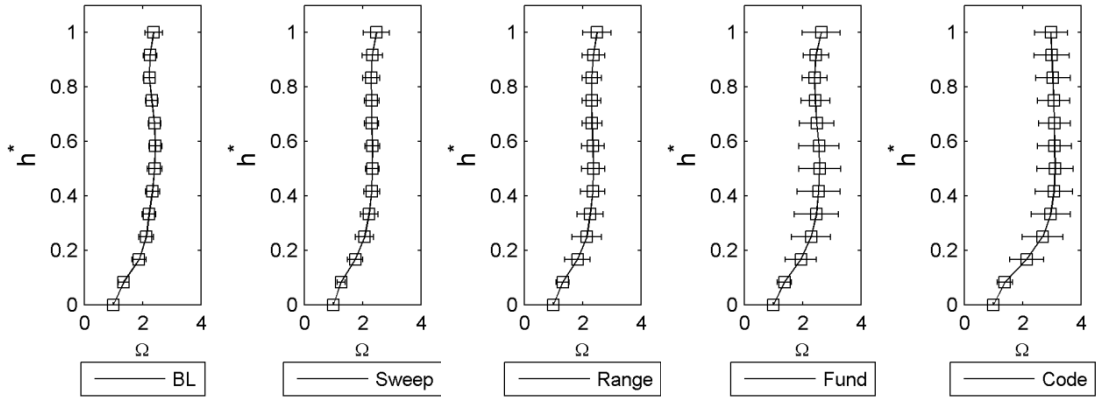

(b)

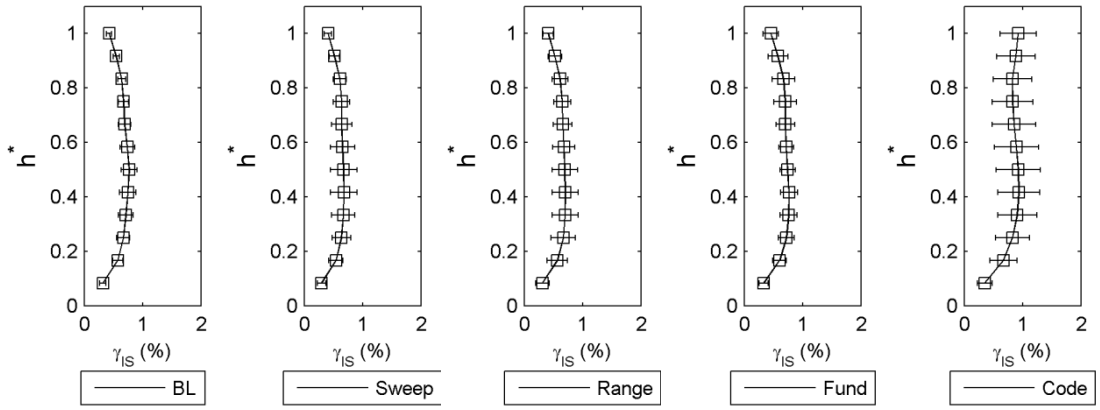

(c)

Figure 5.10 68% confidence interval plots identifying: (a) acceleration, (b) <u>uncorrelated</u> acceleration amplification, and (c) interstory drift dispersion along the height of the building for RC-12. (BL = baseline or spectrally matched case).

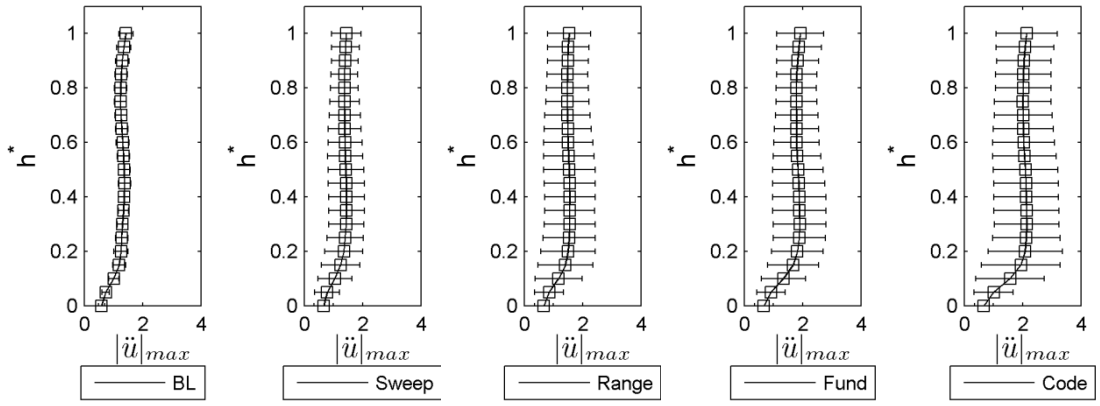

(a)

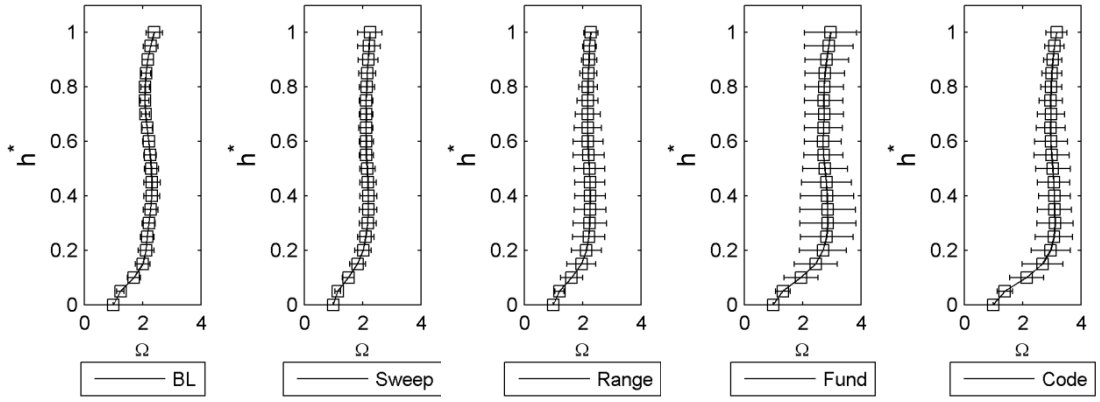

(b)

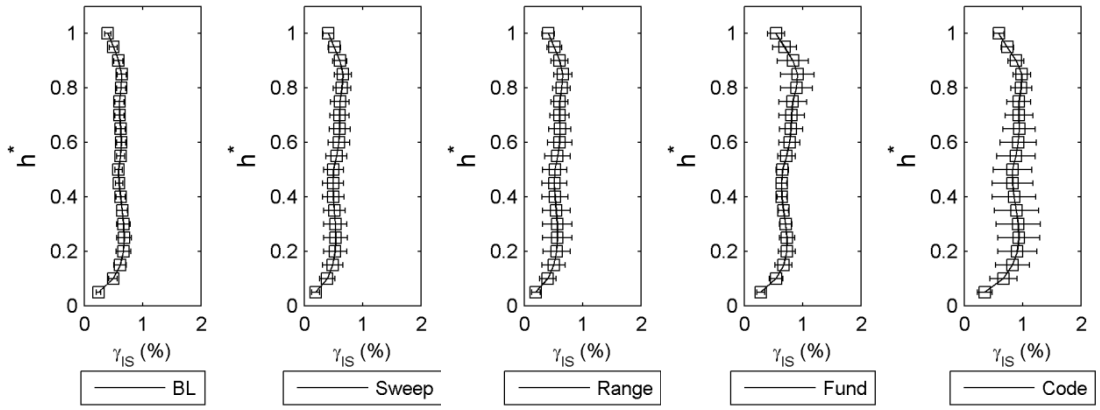

(c)

Figure 5.11 68% confidence interval plots identifying: (a) acceleration, (b) <u>uncorrelated</u> acceleration amplification, and (c) interstory drift dispersion along the height of the building for RC-20. (BL = baseline or spectrally matched case).

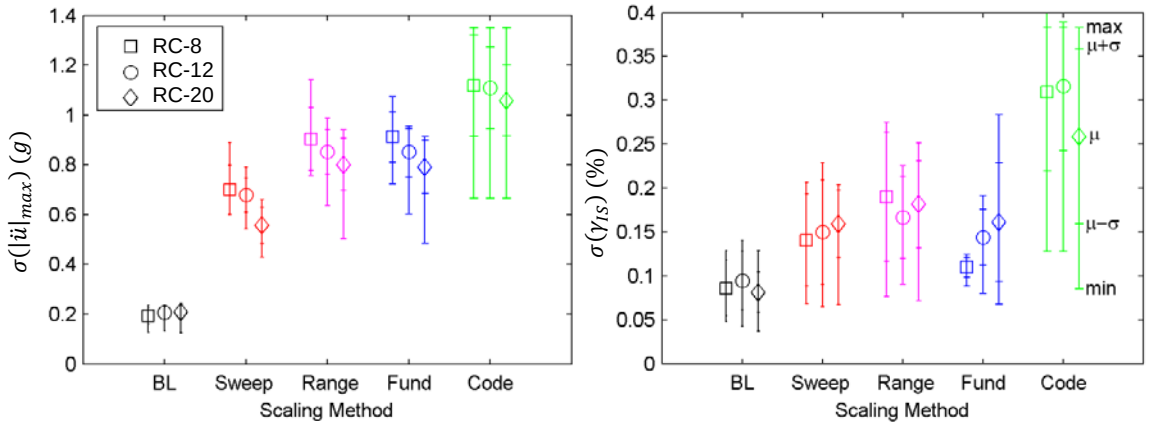

(a) (b)

Figure 5.12 Dispersion comparison of the building response (left to right: RC-8, RC-12, and RC-20) by scaling method: (a) standard deviation of the maximum acceleration and (b) standard deviation of the maximum interstory drift values.
The middle marker (annotated as μ) identifies the average standard deviation (of all floors) for that particular scaling method, the inner set of error bars indicates average plus or minus one standard deviation of the standard deviations per floor (annotated as μ±σ), and the outer set of error bars indicates the upper and lower bound of the standard deviations (annotated as min or max, i.e. envelope) for a given scaling method.

5.8 Summary Remarks

Four ground motion scaling methods are considered and nonlinear time history analyses of mid- and high-rise planar frame-idealized buildings are conducted systematically using the same suite of earthquake motions. This was done in an effort to shed light on the most reasonable scaling approach for use when predicting nonlinear building response. A suite of spectrally matched ground motions are adopted and denoted as the *baseline (BL)*, with the assumption that they are unbiased. The results of the analyses use these *BL* motions to compare the four scaling methods. The baseline motions experienced the least variability of the scaling methods, providing a reduced record-to-record variable comparison to the anticipated design code requirements. One limitation is that these baseline motions are non-physical due to limited trough and valley characteristics of the spectral acceleration.

Nonlinear response of the planar frame-idealized buildings is evaluated in terms of maximum floor acceleration, maximum uncorrelated acceleration amplification ratio, maximum interstory drift, and curvature distributions. It is consistently observed that scaling the input motions across a sweep of periods results in a more reasonable comparison to the *baseline*, particularly when higher modes influence the building's nonlinear demands. These results reveal a weakness in the traditional scaling approaches in that higher mode effects cause divergent acceleration and interstory drift distributions. In contrast, broad period range scaling is shown to capture the higher mode response well, when compared to the spectrally compatible motions.

In the end, the most simplistic approach of scaling across a period sweep (0 to 4 seconds as was adopted herein) or range of periods (T_1 to T_2) results in a very reasonable comparison of nonlinear building demands when compared with the *baseline* response results. Of these two, the period *sweep* scaling suggests the most consistent results for the building types considered in this study. Nonetheless, the *range* scaling method adopted herein, which resulted in a period range which captured 85-90% of the mass participation resulted in reasonably robust comparison, thus supporting recent suggestions that period bounds for scaling be selected based on percentage of mass participation (e.g. Katsanos et al. 2010). However, from a simplicity point of view, invoking a building period-independent scaling procedure is also appealing and provided a very reasonable estimation of nonlinear building demands, including buildings that were influenced by higher modes.

As to provide insight into the effect of including a partition wall (PW) on these models, this study helps to provide insight on the diverse effects of ground motion scaling, particularly on the higher mode response of buildings. While the PWs are implemented into the building model with a constant length throughout the height, the additional stiffness effects are constant per floor and may affect several of the dynamic modes of the structure. Through use of an incremental

dynamic analysis, the effects of ground motion scaling are reduced as no target period range is sought. Consequently, using incremental dynamic analysis will assist in reducing bias into the effect of the PWs on the dynamic response by reducing the dependency on a single record for each intensity level. Given the computational demands imposed by running incremental dynamic analysis, use of the sweep or range scaling approaches are recommended for coupled system analyses.

5.9 Acknowledgement

Chapter 5 of this dissertation is based on an accepted manuscript in *Earthquakes and Structures*, "Ground Motion Effects on Nonlinear Higher Mode Building Response". The co-author of this manuscript is Tara C. Hutchinson, where the dissertation author is the primary author and investigator.

Chapter 6 Coupled Building-Partition Wall System: Nonlinear Time History Analyses

6.1 Introduction

This chapter presents the nonlinear time history analysis of the coupled building-partition wall systems described in Chapter 4. These dynamic analyses of the coupled system are necessary to assess the effect of the partition wall (PW) on the buildings' response to earthquake motions. The nonlinear analyses were conducted with an incremental dynamic analysis (IDA) procedure in order to reduce the dependence on individual ground motions. To explore the effect of the PW on the building model, the effects of wall length, wall strength, and post-peak hardening are studied in this chapter. These characteristics are investigated by examining the maximum interstory drift, maximum floor acceleration, and the extent of period elongation of the coupled system and the effect of the PW on the fragility curve of the system. In what follows, the selection of ground motions, the incremental dynamic analysis procedure, and the engineering demand parameters are presented. Subsequently, sample response histories are presented, followed by synthesis of the results.

6.2 Selected Ground Motions

The ground motions proposed within ATC-63/FEMA p695 project are adopted (ATC, 2009). The ATC-63 project focused on quantifying the seismic performance factors of various types of buildings (concrete, steel, masonry infill), with an emphasis on collapse evaluation. In this project the selection of the ground motions was conducted with the following criteria:

- Magnitude greater than 6.5
- Focal mechanism is either strike-slip or reverse

- Local site condition is either C or D
- No more than two records selected from a single event
- Record set selected with highest peak ground velocity if other previous criteria are satisfied
- Location of seismograph either free-field or ground floor of a small building

The set of motions is considered to be reasonably robust for the purposes of the current study. Moreover, it has been vetted through the engineering community for use in simulation studies. Using this criteria, the far-field (FF) record set is proposed (Table 6.1). The FF motions are those occurring at distances greater than 6.2 miles (10 km) from the epicenter. The set of FF records contain 22 motions. Some of the record characteristics of these motions include minimum peak ground acceleration of 0.2 g, maximum peak ground acceleration of 0.56 g, minimum peak ground velocity of 0.14 feet/sec (15 cm/sec) and valid frequency content for at least four seconds. Figure 6.1 and Figure 6.2 present the spectral acceleration and displacement curves for the suite of unscaled motions. The selected ground motions are input to the base of the building models. The methodology applied to the scaling of each motion is described in the next subsection

Table 6.1 Selected ground motions from the ATC-63 Far-Field Record Set. Note: "Record Seq. No." corresponds to the event number from the PEER-NGA database (PEER, 2009).

Record No.	Magnitude	Event	Year	Station Location	Record Seq. No.
1	6.7	Northridge	1994	Beverly Hills - Mulhol	953
2	6.7	Northridge	1994	Canyon Country-WLC	960
3	7.1	Duzce, Turkey	1999	Bolu	1602
4	7.1	Hector Mine	1999	Hector	1787
5	6.5	Imperial Valley	1979	Delta	169
6	6.5	Imperial Valley	1979	El Centro Array #11	174
7	6.9	Kobe, Japan	1995	Nishi-Akashi	1111
8	6.9	Kobe, Japan	1995	Shin-Osaka	1116
9	7.5	Kocaeli, Turkey	1999	Duzce	1158
10	7.5	Kocaeli, Turkey	1999	Arcelik	1148
11	7.3	Landers	1992	Yermo Fire Station	900
12	7.3	Landers	1992	Coolwater	848
13	6.9	Loma Prieta	1989	Capitola	752
14	6.9	Loma Prieta	1989	Gilroy Array #3	767
15	7.4	Manjil, Iran	1990	Abbar	1633
16	6.5	Superstition Hills	1987	El Centro Imp. Co.	721
17	6.5	Superstition Hills	1987	Poe Road (temp)	725
18	7	Cape Menocino	1992	Rio Dell Overpass	829
19	7.6	Chi-Chi, Taiwan	1999	CHY101	1244
20	7.6	Chi-Chi, Taiwan	1999	TCU045	1485
21	6.6	San Fernando	1971	LA Hollywood Storage	68
22	6.5	Friuli, Italy	1976	Tolmezzo	125

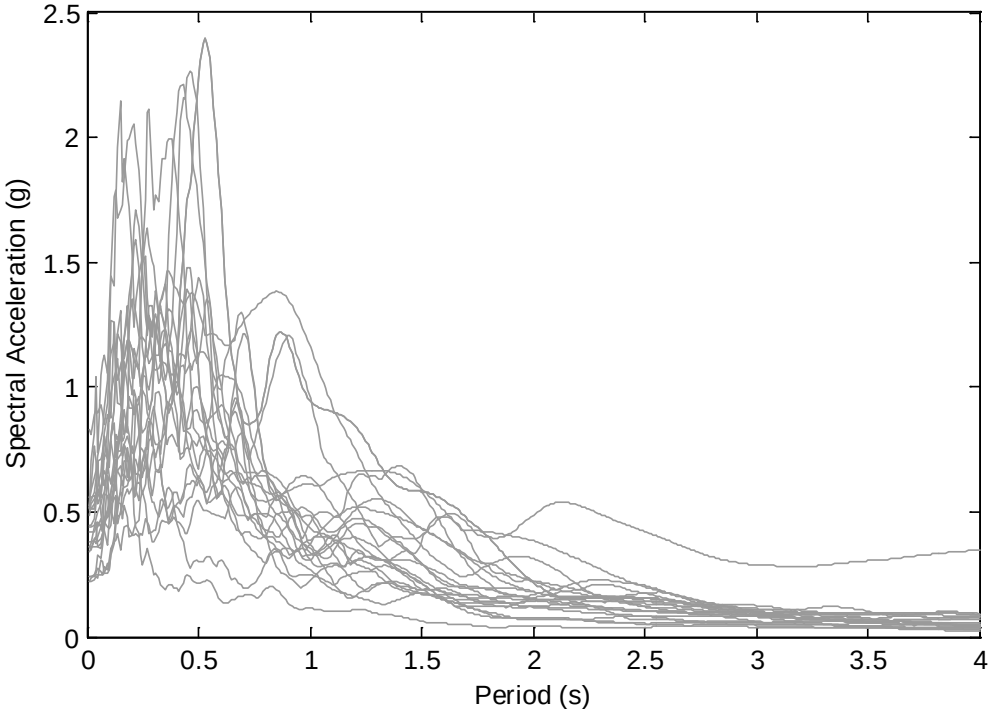

Figure 6.1 Elastic 5% Damped Spectral acceleration curves for entire ground motion suite (unscaled) for the ATC-63 Far-Field Record Set.

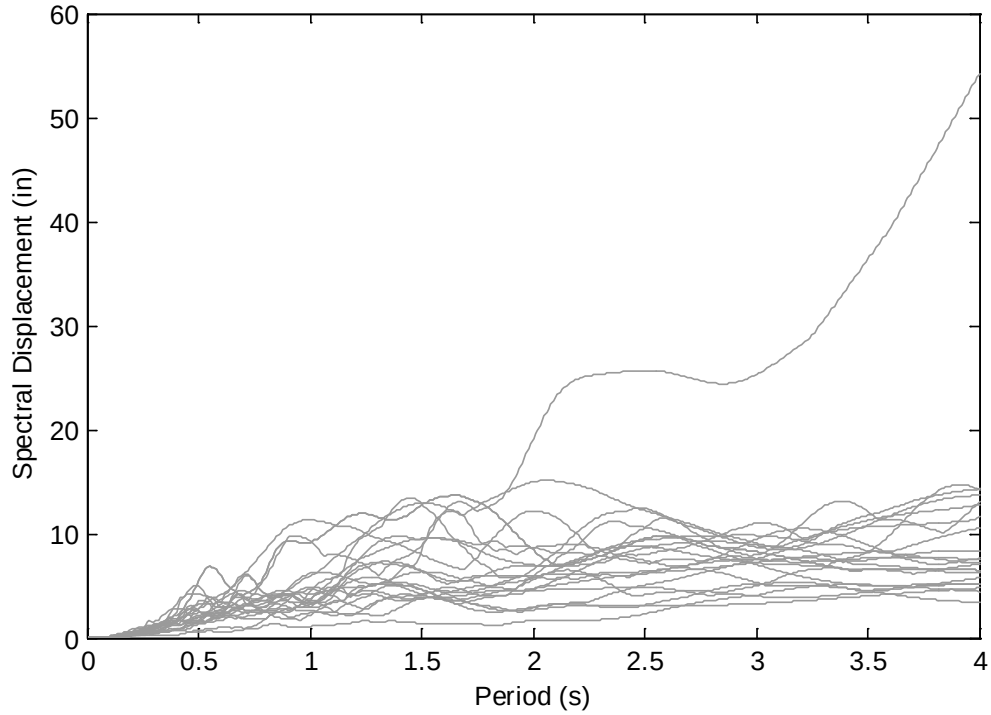

Figure 6.2 Elastic 5% Damped Spectral displacement curves for entire ground motion suite (unscaled) for the ATC-63 Far-Field Record Set.

6.3 Analysis Procedure

To provide sufficient data for comparison purposes, the records proposed by ATC-63 are applied using the concept of incremental dynamic analysis (IDA) (Vamvatsikos and Cornell, 2002). Incremental dynamic analysis applies multiple scale factors to each ground motion for a particular building in order to develop multiple intensity levels. This procedure allows for a direct assessment of the relationship between an intensity measure (i.e.: PGA, $Sa(T_1)$) to a damage measure of interest, such as interstory drift. The use of IDA allows the structural behavior of a building model to be examined at the various intensity levels, while reducing the dependency on a single record for each intensity level. Since the scaling of the motions is performed multiple times, this procedure can become computationally intensive. Analyses using IDA were conducted with a coupled (building + partition walls) or uncoupled (bare frame building only) model. It is noted that the coupled time history analysis is much more computationally demanding. The IDA analysis procedure is repeated for each PW configuration case.

6.3.1 Numerical Strategy

Individual nonlinear time history analyses representing each case of the incremental dynamic analysis (IDA) were conducted in OpenSees using Newmark's method. Prior to the uniform excitation pattern representing the earthquake motion, an eigenvalue analysis was conducted to characterize the buildings' dynamic properties. Constant average acceleration was considered per iteration step by defining gamma and beta as 0.5 and 0.25, respectively, to solve the nonlinear equilibrium equation. In the transient analysis, the Newton Line Search algorithm was utilized with a radius of 0.5. The normalized displacement increment tolerance was set as 10^{-6} for each step. After completion of the nonlinear time histories, a second eigenvalue analysis was conducted to characterize the post-event buildings' dynamic properties. This second eigenvalue analysis case quantified the final periods of the building.

6.3.2 Time History Response

To illustrate the behavior of the coupled system, building RC-8 with PWs of the minimum length (mean model) is selected. First, interstory drift behavior of the building is presented. From the simulation results, relative displacement time history response at each floor may be obtained. To determine the displacement demands between floors, the interstory drift is evaluated as described in Equation 5-3. Using this equation, the interstory drift time histories are examined at all floors considering record #1 (Northridge) scaled to a PGA = 0.40g (Figure 6.3). This figure illustrates larger deformation demands at the lower floor levels of the building, with the largest demands at floor 3. Using the absolute value of the maximum values from the individual floor time histories, the interstory drift envelope is constructed (Figure 6.4). The parabolic distribution indicates higher mode effects are present and, for this case, a peak interstory drift of 0.86% is obtained on floor 3.

Figure 6.4 illustrates the interstory drift envelope for record #1 (Northridge) scaled to a PGA of 0.40 g for RC-8 where no wall was considered, minimum length wall, and maximum length walls considering the mean PW model. The increase in peak interstory drift values for the coupled building-partition wall system , which may seem counterintuitive, is attributed to the systems period shift, while the difference between the minimum and maximum wall length is due to the extra stiffness when the maximum wall length is considered. To inspect the effect attributed to the period shift, the elastic 5% damped of critical spectral displacement is assessed for record #1 after scaling it to a PGA = 0.40 g (Figure 6.5). In this figure, the fundamental periods are overlaid with vertical lines and are within a region where local extrema exist. The period elongation experienced only in the coupled building-partition wall model is shown through the arrows between the initial fundamental building period ($T_1^{initial}$) to final fundamental building period (T_1^{final}). By close inspection of this region in Figure 6.6, the maximum and minimum

values over the range of period elongation experienced during the time history (for all coupled systems) is identified to be 4.1 and 7.2 inches. By evaluating the percent difference (normalized by the maximum value), a 43% difference occurs in this region. In evaluating the percent difference from the interstory drift envelopes in Figure 6.4, an increase is noted in the maximum interstory drift at floor 3 where the percent difference between the no wall case (0.56%) to the minimum wall length case (0.86%) is 35%. The percent difference between the spectral displacements is similar; however a slight overestimation of the drift demands occurred. This is noted because the maximum spectral displacement is not attainable because the building deteriorated into discrete periods which are not excited equally throughout the nonlinear response (Figure 6.6). The subtle changes in periods result in a significant effect on the interstory drift demands. These differences in interstory drifts can drastically influence the damage states of the PWs, especially at low DS. For this case, considering a coupled building-PW model DS_2 (moderate damage) is obtained, while in a uncoupled bare building analysis, only DS_1 (minor damage) is obtained.

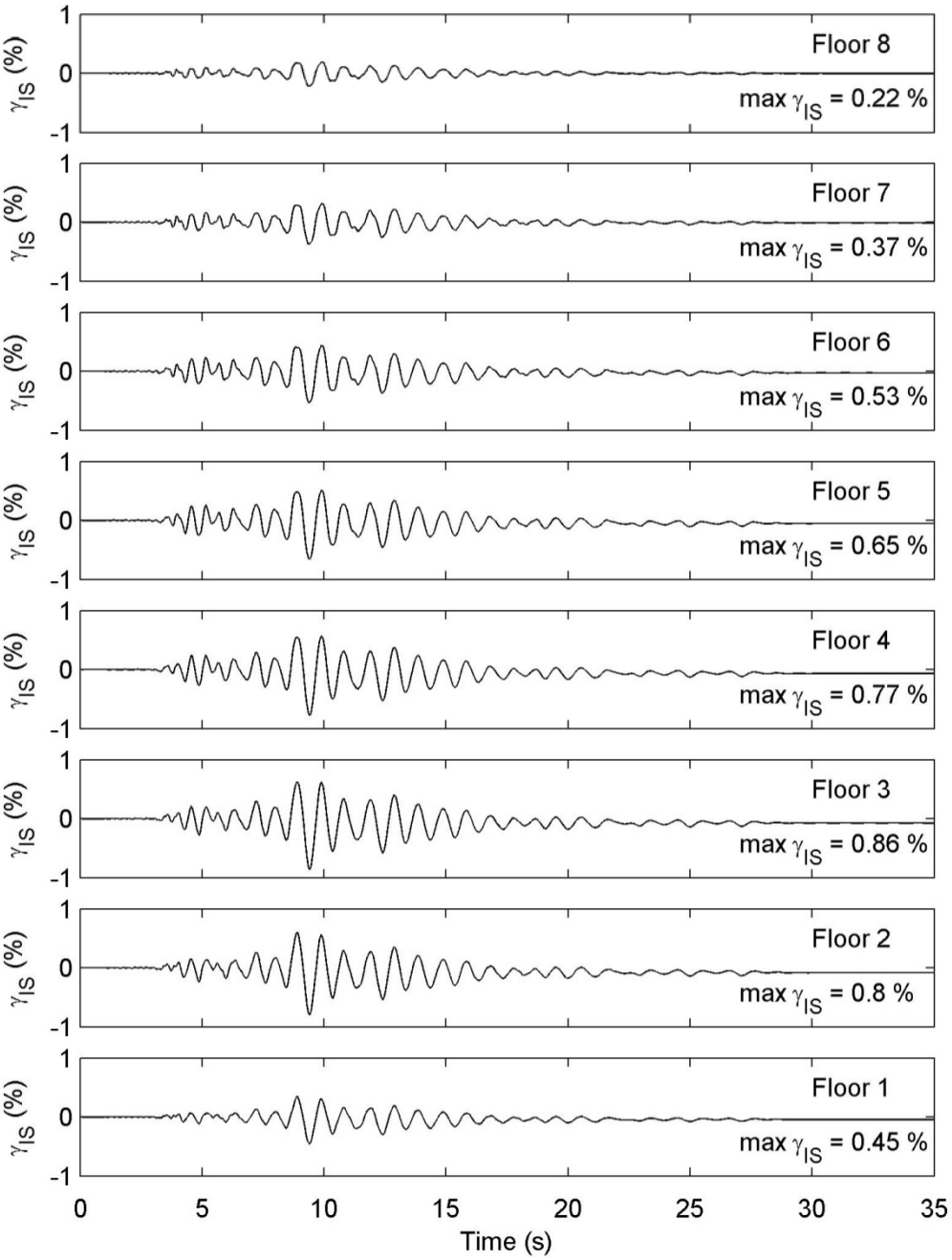

Figure 6.3 Interstory drift time history example illustrated by floor: RC-8 with PW assuming the minimum wall case ($L_{w,min}$) and the mean PW model under record #1 (Northridge) scaled to a PGA of 0.40 g.

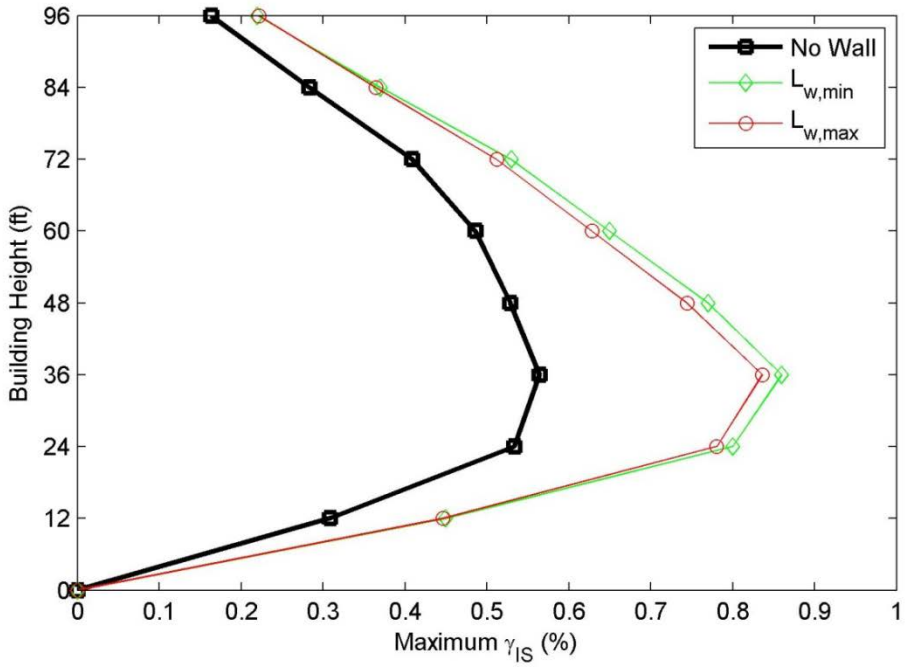

Figure 6.4 Maximum interstory drift envelope curve for RC-8 for no wall, $L_{w,min}$, and $L_{w,max}$ consider the mean PW model under record #1 scaled to a PGA of 0.40 g.

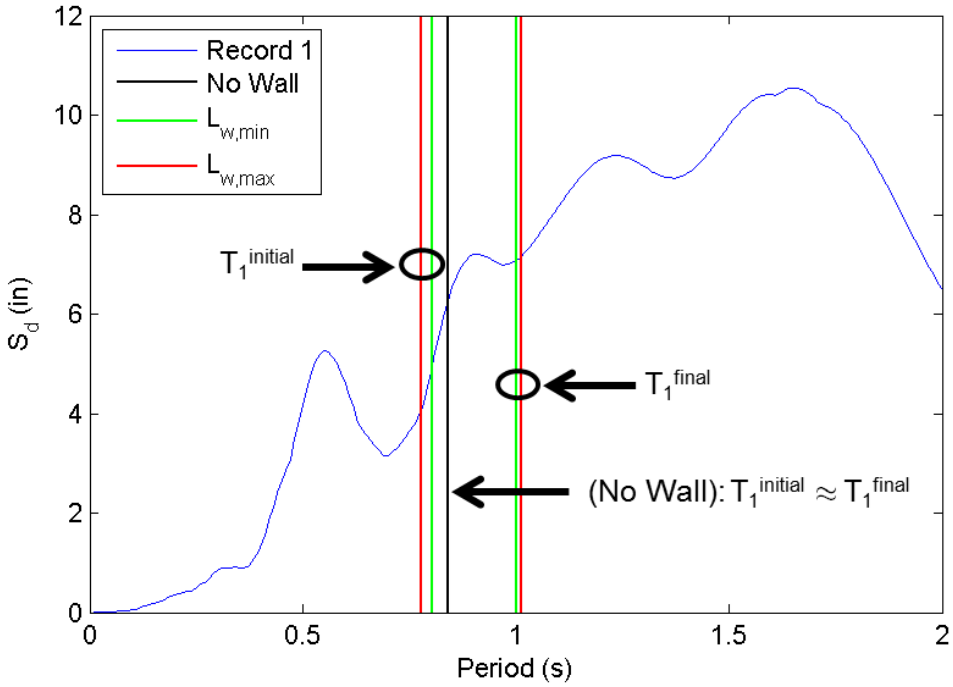

Figure 6.5 Elastic 5% damped spectral displacement for a scaled record #1 (Northridge, PGA=0.4 g) where the vertical lines identify the fundamental periods (initial and final) of the uncoupled and coupled cases.

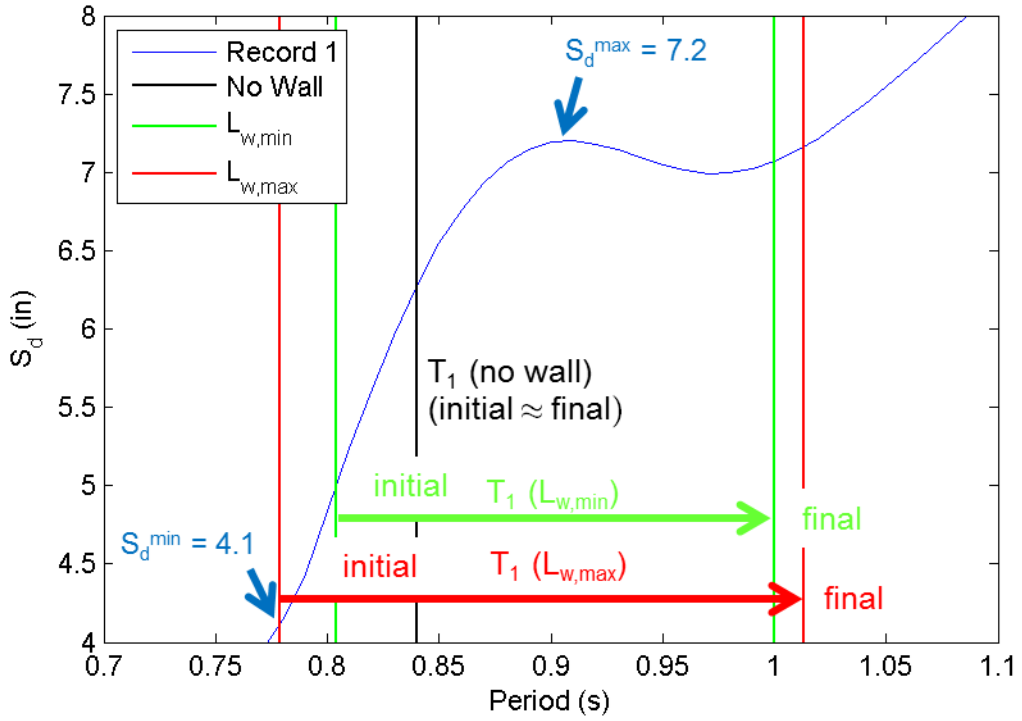

Figure 6.6 Annotated elastic 5% damped spectral displacement curve for a scaled record #1 (Northridge, PGA=0.4 g) where the vertical lines identify the fundamental periods (initial and final) of the uncoupled and coupled cases.
Note: S_d^{min} and S_d^{max} values are identified for the period range of $T_1^{initial}$ to T_1^{final} for $L_{w,max}$ (shown with arrows).

The second example demonstrating the building's behavior with and without the PW is to study acceleration time histories. Examining the floor acceleration histories provides insight into how the building filters and amplifies the input ground motion on each floor. From the simulation results, absolute acceleration response at each floor may be obtained. The floor acceleration histories are illustrated for the same case of RC-8 with the minimum wall length (mean PW model) excited by record #1 (Northridge) scaled to PGA = 0.40g (Figure 6.7). In this figure, the accelerations generally increase in height, identifying a dominative first mode response. Acceleration time history responses are used to extract maximum response envelopes for each model case (Figure 6.8). The acceleration envelope was developed by determining the maximum

of the absolute value acceleration at each floor. For this example, floor 8 experiences the maximum acceleration of 1.00 g with a general increasing trend as the height of the building increases. The nonlinear nature of the curve indicates the influence of higher modes on the nonlinear time history response. Note that the distribution of maximum acceleration follows a trend suggestive in a linear fashion at the lower floors (shear-like mode), while parabolic (bending-like mode) at the upper floors.

Figure 6.8 illustrates the maximum floor acceleration envelope for record #1 scaled to a PGA of 0.40 g for RC-8 where no wall was considered, minimum length wall, and maximum length walls considering the mean PW model. The increase in floor maximum floor acceleration values of the coupled building-partition wall system as compared to the bare building model demonstrates effects of period shift and associated stiffening of the building when the PWs are considered. To inspect the effect attributed to the period shift, the elastic 5% damped of critical spectral acceleration is assessed for record #1 (Northridge) after scaling it to a PGA = 0.40 g (Figure 6.9). In this figure, the fundamental periods are overlaid with vertical lines and are within in a region where local extrema exist. The period elongation experienced only in the coupled building-partition wall model is shown through the arrows between the initial fundamental building period ($T_1^{initial}$) to final fundamental building period (T_1^{final}). By close inspection of this region in Figure 6.10, the maximum and minimum values over the range of period elongation experienced during the time history (for all coupled systems) is identified to be 0.70 g and 0.94g. By evaluating the percent difference (normalized by the maximum value), a 26% difference occurs in this region. In evaluating the percent difference from the maximum floor acceleration envelopes in Figure 6.8, an increase is noted in the maximum accelerations at the roof level where the percent difference between the no wall case (0.77 g) to the maximum wall length case (1.00 g) is 23%. Similar to the case for the spectral displacement, the percent difference between the spectral acceleration is similar; however a slight overestimation of the acceleration demands

occurred. This is noted because the maximum spectral acceleration is not attainable because the building deteriorated into discrete periods which are not excited equally throughout the nonlinear response. The subtle changes in periods result in a significant effect on the floor acceleration demands, affecting other NCSs components within a building.

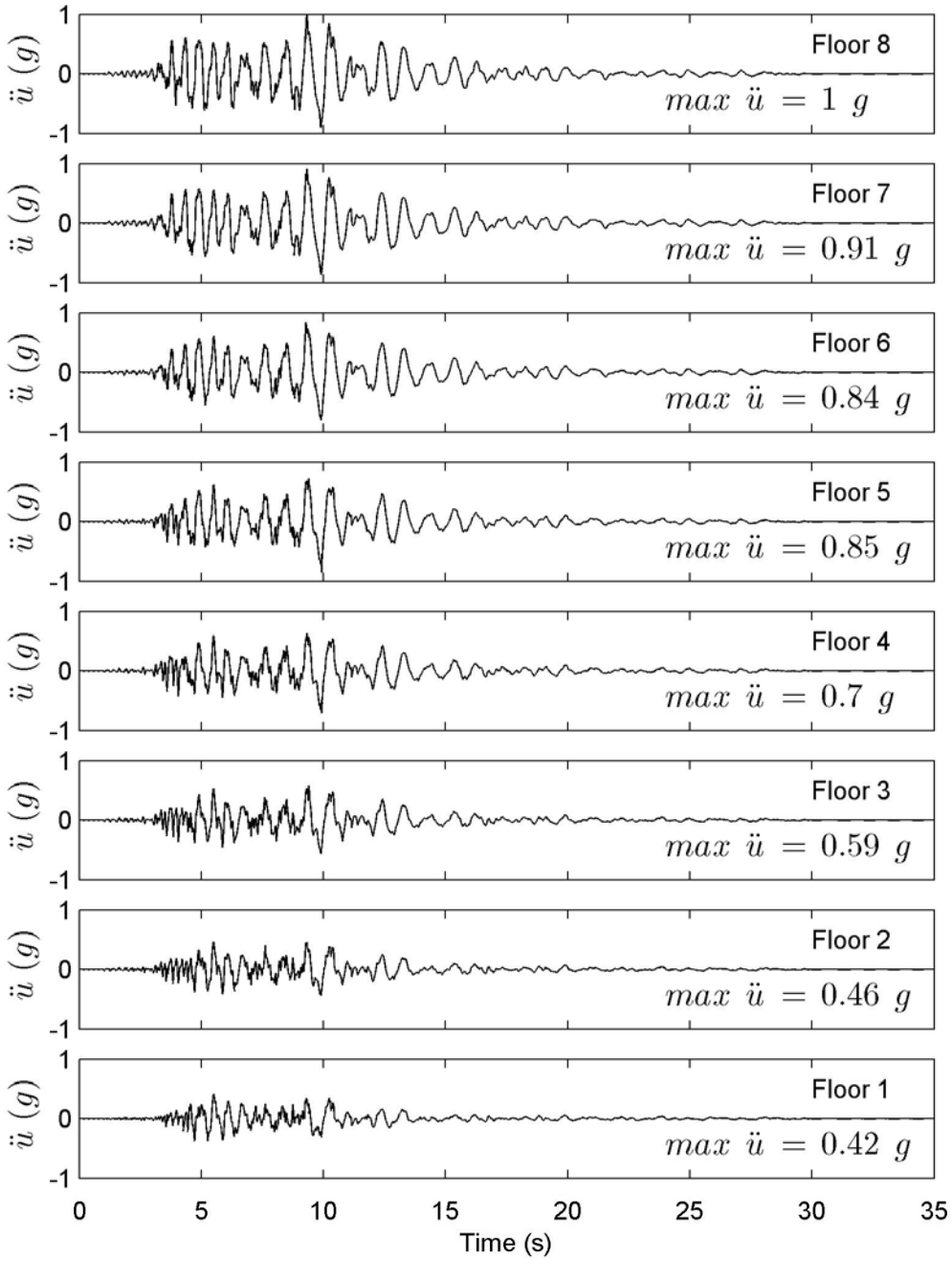

Figure 6.7 Acceleration time history example illustrated by floor RC-8 with PW assuming the minimum wall case ($L_{w,min}$) and the mean PW model under record #1 (Northridge) scaled to a PGA of 0.40 g.

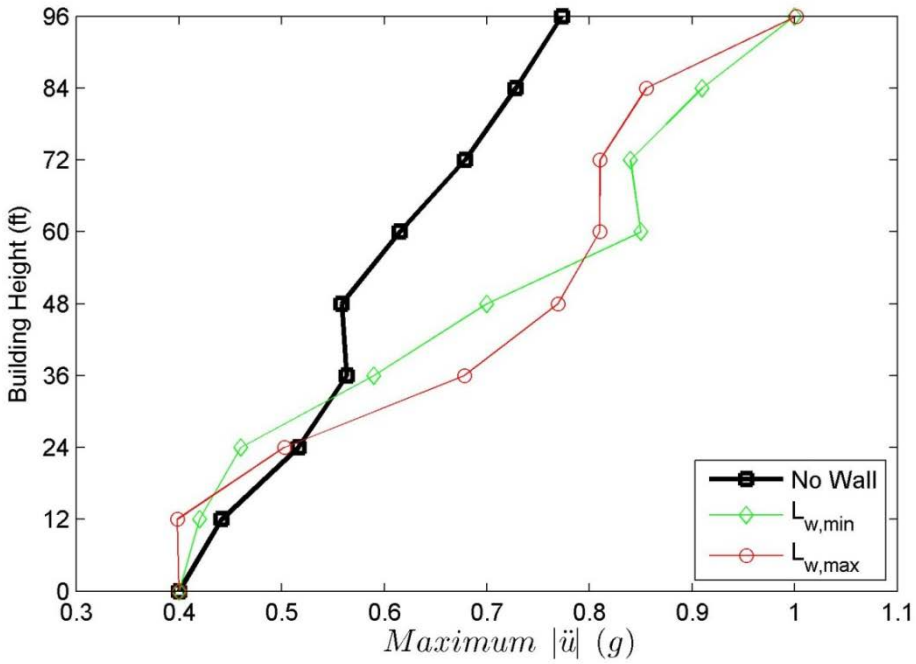

Figure 6.8 Maximum floor acceleration envelope curve for RC-8 for no wall, $L_{w,min}$, and $L_{w,max}$ consider the mean PW model under record #1 (Northridge) scaled to a PGA of 0.40 g.

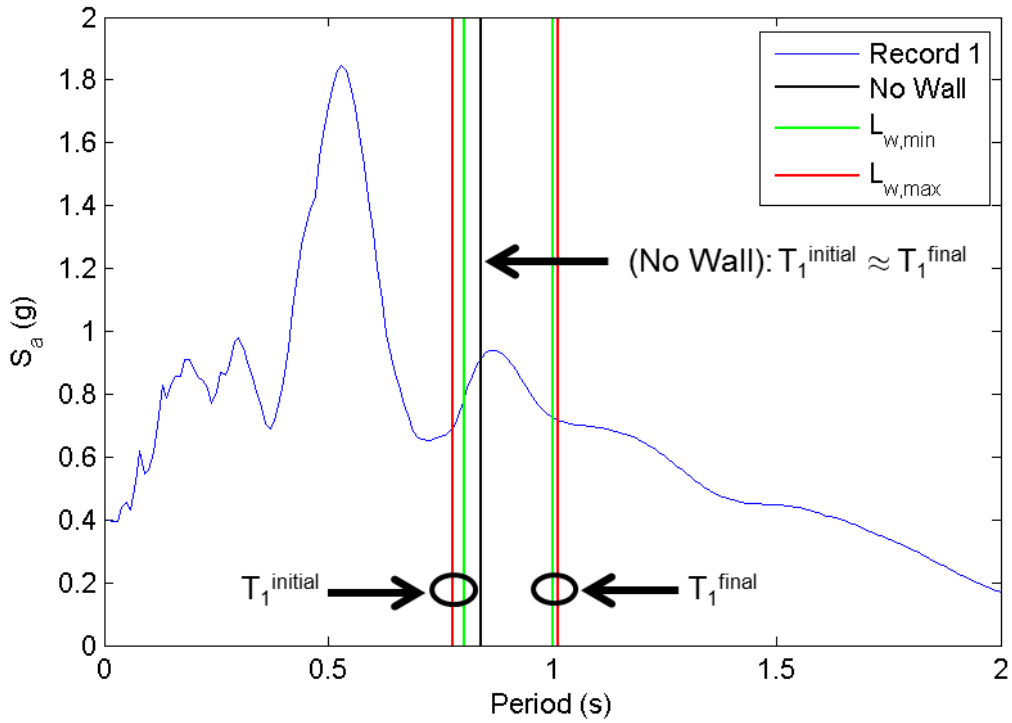

Figure 6.9 Elastic 5% damped spectral acceleration for a scaled record #1 (Northridge, PGA=0.4 g) where the vertical lines identify the fundamental periods (initial and final) of the uncoupled and coupled cases.

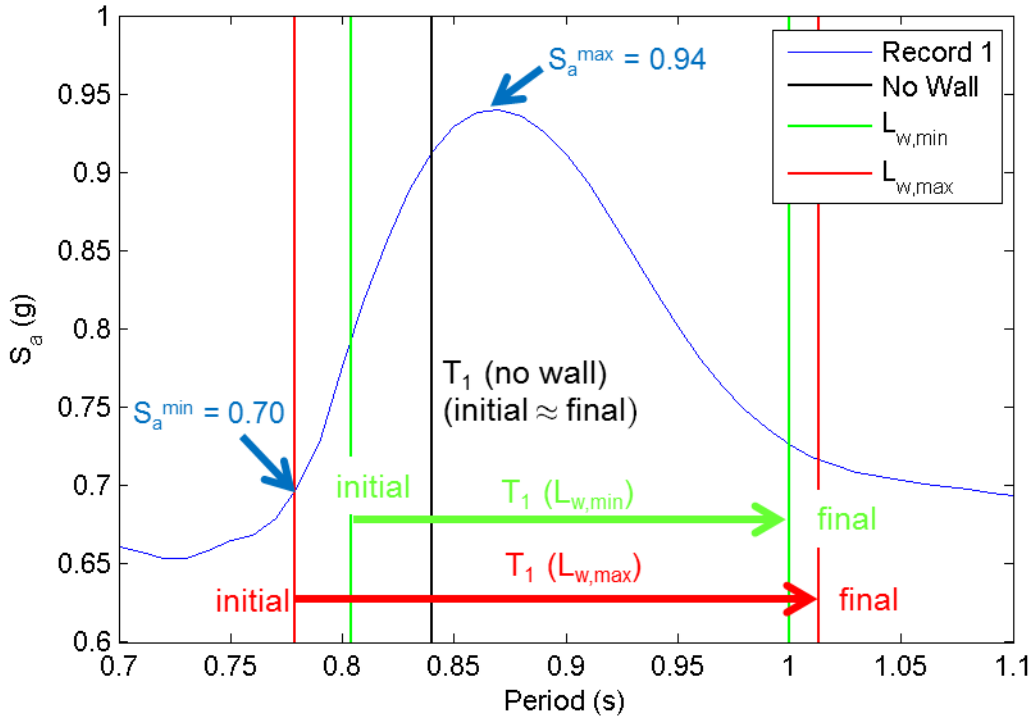

Figure 6.10 Annotated elastic 5% damped spectral acceleration curve for a scaled record #1 (Northridge, PGA=0.4 g) where the vertical lines identify the fundamental periods (initial and final) of the uncoupled and coupled cases.
Note: S_a^{min} and S_a^{max} values are identified for the period range of $T_1^{initial}$ to T_1^{final} for $L_{w,max}$ (shown with arrows).

6.3.3 Example IDA Results

Using the nonlinear time history approach outlined previously, one example is presented. Using the eight story reinforced concrete building (RC-8), a PW representing commercial construction practices is placed between adjacent floors. The minimum anticipated PW is assumed, which corresponds to a partition index of 0.07 1/feet, of a length of PW of 56 feet. In this example, the considering the PW with mean parameters is assumed. This wall length requires a scaling factor of approximately 5, applied to the strength of the wall, when compared to the base parameters, which were determined using the NEES-GC PW database. PWs were placed at each floor within the 2D OpenSees model, considering the same lengths.

Results from the incremental dynamic analysis are presented in Figure 6.11. In this figure, the peak ground acceleration is shown against the interstory drift demands experienced on all floors of the structure. While shown against peak ground acceleration (PGA), this intensity measure is not ideal. While PGA is an easy intensity parameter used by some engineers, its relationship to structural performance and particularly the interstory drift response is poorly correlated. Consequently, PGA is mapped on a record-to-record variation to spectral acceleration and spectral displacement at the fundamental period of the coupled building system (T_1). The remapped data is shown in Figure 6.12 and Figure 6.13. Interstory drift demands are observed to be parabolic in nature and vary as a function of the building height. This is observed in Figure 6.12 and Figure 6.13 as with increasing intensity the average response contains less dispersion and a distinct linear trend can be noted.

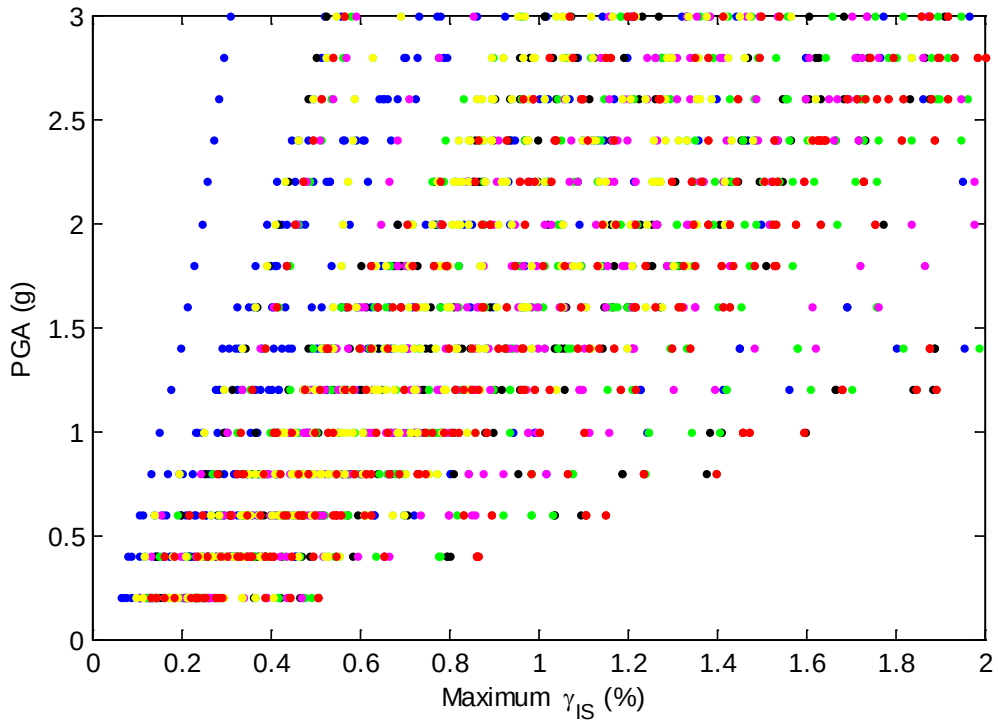

Figure 6.11 IDA results for RC-8 with PW assuming the minimum wall case ($L_{w,min}$) and the mean PW model: maximum interstory drift demands at each floor versus peak ground acceleration (PGA).
(Colors represent different ground motions).

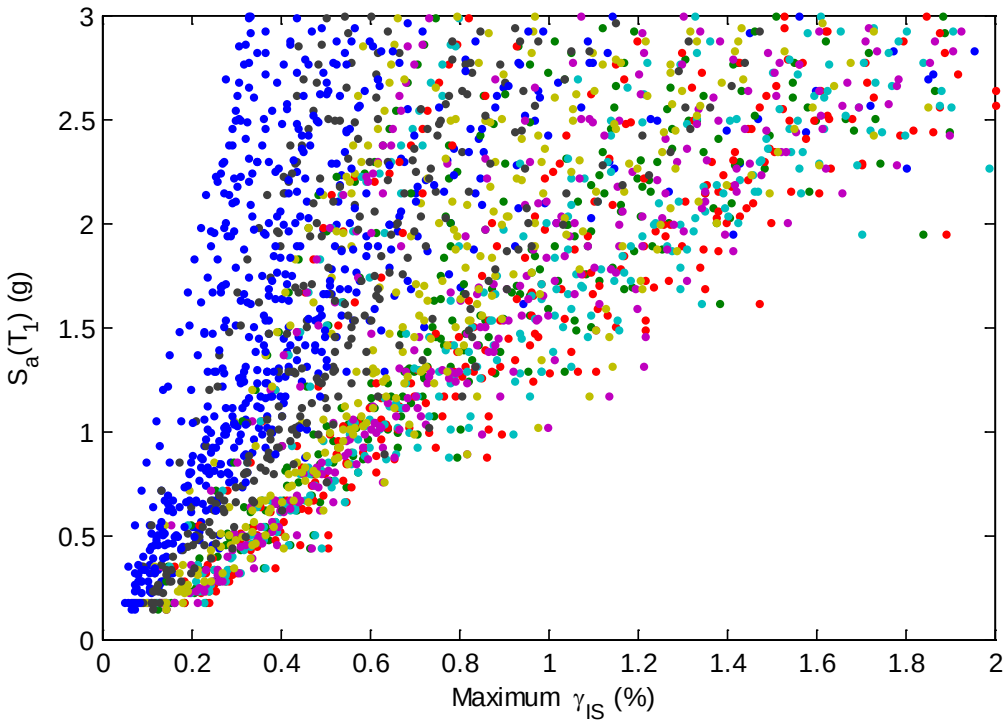

Figure 6.12 IDA results for RC-8 with PW assuming the minimum wall case ($L_{w,min}$) and the mean PW model: maximum interstory drift demands at each floor versus elastic 5% damped spectral acceleration at the fundamental period (T_1). (Colors represent different ground motions).

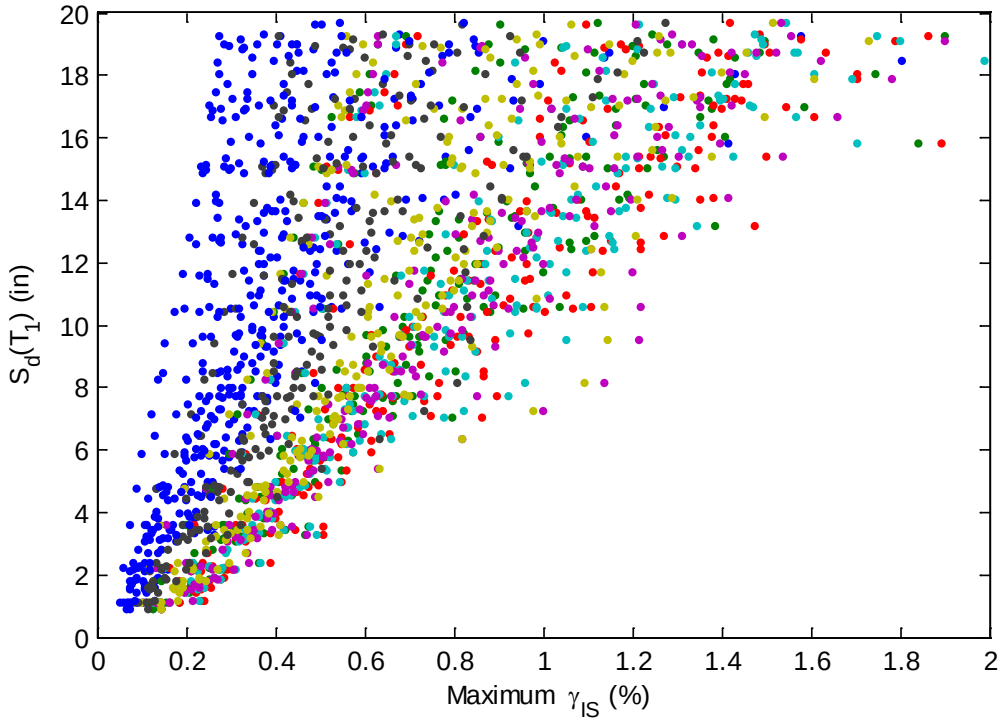

Figure 6.13 IDA results for RC-8 with PW assuming the minimum wall case ($L_{w,min}$) and the mean PW model: maximum interstory drift demands at each floor versus elastic 5% damped spectral displacement at the fundamental period (T_1). (Various colors represent various ground motions).

6.3.4 Analysis Cases

To define the analysis cases to determine the effect of the coupled building-partition wall system, two sets of cases are developed. For coupled building-partition wall systems incremental dynamic analyses are characterized by the following:

- Scale each record in increments of 0.2g in terms of peak ground acceleration (PGA)
- Incremental dynamic analysis is conducted until the first occurrence of:
    - 2% interstory building drift (PW transitions into DS_3 – severe damage)
    - Localized failure due to bar buckling or excessive strength degradation

- Sufficiently high PGA not associated with realistic records, defined in this case to be 3 g

For bare building (no wall) incremental dynamic analyses:

- Scale each record in increments of 0.05 g in terms of peak ground acceleration (PGA)
- Incremental dynamic analysis is conducted until the first occurrence of:
  - 3% interstory building drift (higher interstory drift value when compared to the coupled case due to a possible underestimation of interstory drifts when no PW is considered)
  - Localized failure due to bar buckling or excessive strength degradation
  - Sufficiently high PGA not associated with realistic records, defined in this case to be, 3 g

Due to the high computational demands imposed by the coupled (building-partition wall analysis), a subset of buildings were chosen to demonstrate the difference between coupled and uncoupled analyses. The ten coupled analyses selected include:

- RC-8 considering:
  - Mean response model parameters:
    - Maximum wall length ($L_{w,max}$)
    - Minimum wall length ($L_{w,min}$)
  - Mean plus one standard deviation model parameters:
    - Minimum wall length ($L_{w,min}$)
  - Mean minus one standard deviation model parameters:
    - Minimum wall length ($L_{w,min}$)
  - Mean response model parameters with minimum wall length ($L_{w,min}$):
    - No wall at first floor

    - No wall at top level
- S-3H considering the mean model parameters:
    - Maximum wall length ($L_{w,max}$)
    - Minimum wall length ($L_{w,min}$)
- S-9 considering mean model parameters:
    - Minimum wall length ($L_{w,min}$)
- RC-20 considering mean model parameters:
    - Minimum wall length ($L_{w,min}$)

This subset of buildings was selected because S-3H had the largest dynamic shifts introduced by inclusions of the PWs, the only building considering an institutional construction for PWs, and the largest mass participation in the fundamental mode. RC-8 was selected for most of the coupled cases because it had average period characteristics, pushover characteristics, and represented a typical midrise building. Likewise, S-9 was chosen because of the significant shifts in mass participation, required a larger additional force in the pushover characteristics, and a typical midrise building with a yield drift of twice that of RC-8 (approximately 1% versus 0.5%). RC-20 was selected to demonstrate the effect of the coupled system on a taller building.

6.3.5 Synthesis of IDA results

Expanding on the interstory drift and acceleration envelopes outlined in 6.3.2, the remaining runs of the IDA were processed in the same fashion. IDA summary plots are then created considering a range of PGA values. Figure 6.14 and Figure 6.15 illustrate the IDA curves for interstory drift and floor acceleration against PGA on a per floor response. Since the maximum interstory drifts vary parabolically and the floor accelerations vary generally linearly throughout the building height, it is instructive to evaluate and compare on a per floor basis. Typically, it is of interest to represent the response in a statistical format (i.e. average response);

however, PGA is a poorly constrained parameter when predicting building response. PGA neglects the dynamic response of the building and internal building-specific ground motion filtering. Consequently, to investigate the effect of the PW, PGA values are converted to other spectral quantities as outlined in the following subsection.

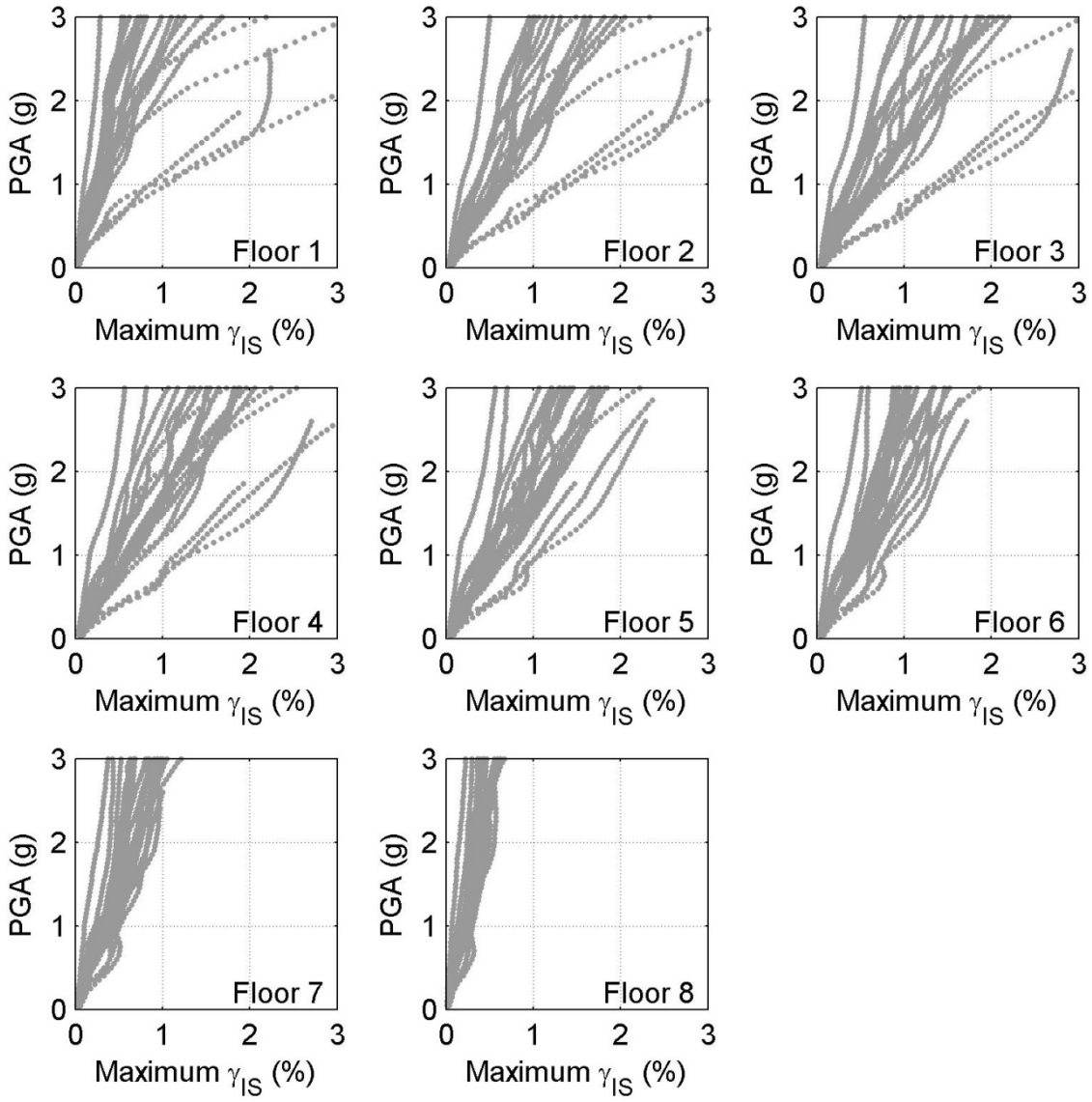

Figure 6.14 IDA results for RC-8 bare building (no wall case): peak ground acceleration (PGA) against maximum interstory drift.

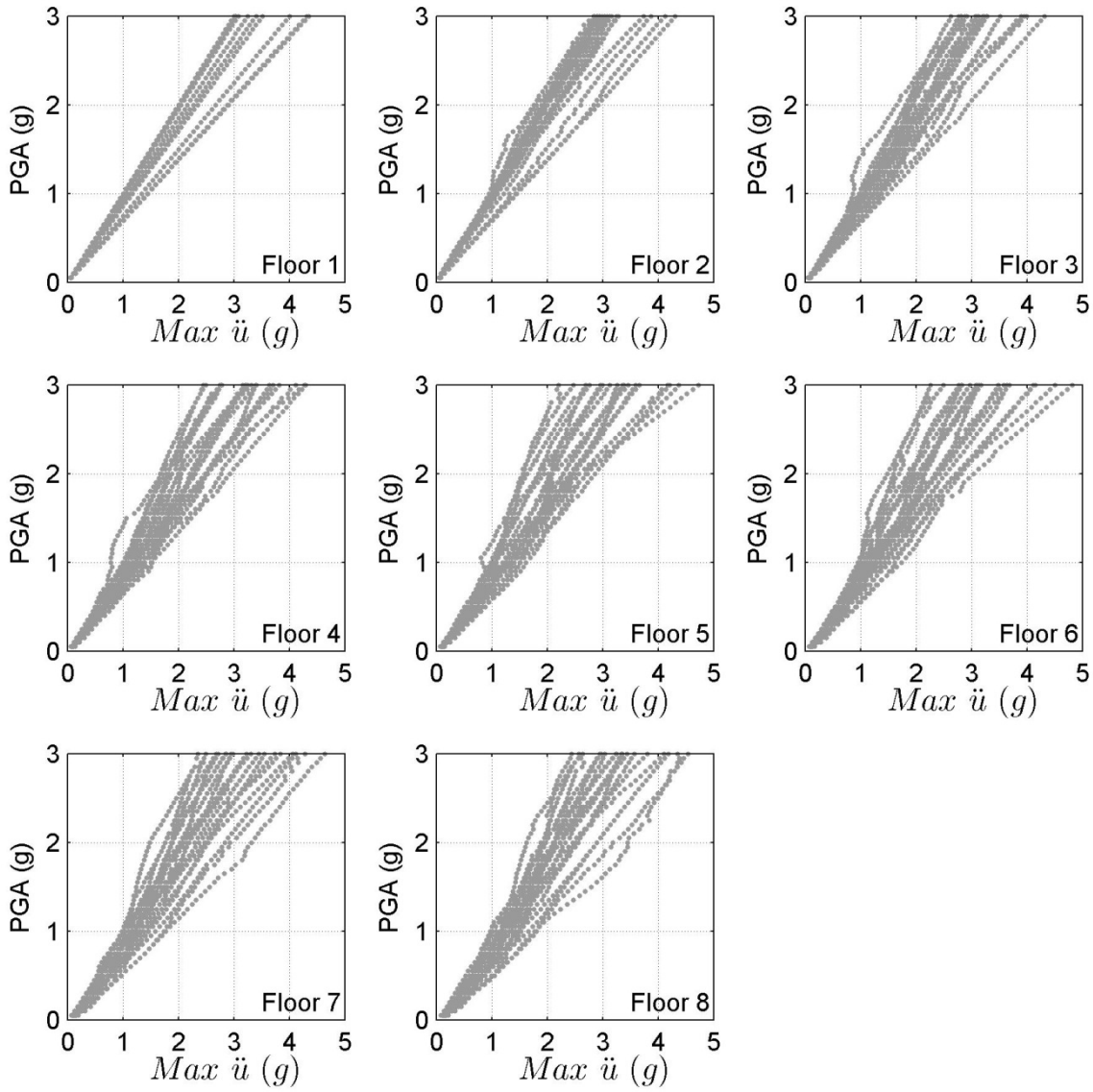

Figure 6.15 IDA results for RC-8 bare building (no wall case): peak ground acceleration (PGA) against maximum floor acceleration.

6.3.6 Converting to Spectral Quantities

As outlined in the previous subsection, for a more meaningful representation of the analysis of the coupled system, the conversion to other spectral quantities is necessary. Traditionally, spectral quantities are considered at the fundamental mode of the building, namely spectral acceleration at T_1 or spectral displacement at T_1. The conversion of the IDA curves to $S_a(T_1)$ and $S_d(T_1)$ was performed for the bare RC-8 building (no wall) case in Figure 6.22 and Figure 6.23, considering the elastic period of the building. While typically these metrics perform better than PGA, they do not directly assess either higher mode effects or period elongation associated with accumulated inelastic response of the building. While the influence of higher modes was noted in previous sections, characterization of the contribution of different modes to the nonlinear time history response is a non-trivial task. To this end, the focus is to characterize the spectral quantity associated with the period elongation. To achieve a spectral quantity of either acceleration or displacement associated with a range of periods:

$$\Delta T_1 = \langle T_1^{initial}, T_1^{final} \rangle \tag{6-1}$$

where: ΔT_1 represents the span from $T_1^{initial}$ (elastic or uncracked value fundamental period) to T_1^{final} (fundamental period following the earthquake motion) associated with the period elongation. The value of T_1^{final} is obtained after completion of the nonlinear time history simulation, by conduction of a post time history eigenvalue analysis. Using the elastic spectral quantities over the period range of ΔT_1 the median, mean, and maximum statistic values are compiled (Figure 6.16 and 6.17). The mean spectral quantity represents the average spectral quantity (acceleration or displacement) achieved over the period range ΔT_1. Likewise, median or maximum spectral values represent the corresponding spectral quantities over the period range ΔT_1. Figures 6.16 and 6.17 illustrate the calculation of the various spectral acceleration (or displacement values), for record 1 (Northridge). Notice that the difference is minimal for the

mean or median, however a slight difference is noted. These values are only hypothetical because the period elongation due to inelastic response may occur prior to all period values throughout the range being realized. The mean and the median response have little difference between the two and justifications could be made to use either. To this end, the median spectral quantity is chosen because it represents the 50^{th} percentile, an unbiased physical middle, and commonly adopted in ground motion relationships (Abrahamson and Silva, 2008). To demonstrate the mean response spectra, Figures 6.18 – 6.21 show the mean acceleration and displacement spectra for all records scaled to a peak ground acceleration of 0.4 g with an overlay of ΔT_1. Figures 6.19 and 6.21 illustrate the mean spectra for the period range ΔT_1, where the minimum $T_1^{initial}$ and maximum T_1^{final} are considered for each building. These figures illustrate the range of acceleration and displacement values over each period range associated with the period elongation throughout the time history.

In Figure 6.22 – Figure 6.31, individual simulation points are plotted along with a moving average. A moving average is used to best represent the IDA response because the engineering demand parameter (EDP) is not evenly spaced. Horizontal lines on Figures 6.22 – 6.31 denote the design earthquake (DE) and maximum considered earthquake (MCE) for the bare building case at $T_1^{initial}$, which is typically assumed during the building design. Due to the lower dispersion noted in the spectral displacements versus spectral acceleration quantities, spectral displacement is identified as a more representative EDP. These figures show the spectral conversions for sample floors where interstory drift demand is typically greater, floors 1, 3 and 5. Additional details for all floors can be found in Appendix B. These plots demonstrate the spectral quantities at $T_1^{initial}$ and mean, median, or maximum spectral quantities over ΔT_1, where in the end the median spectral quantity is chosen for further comparisons.

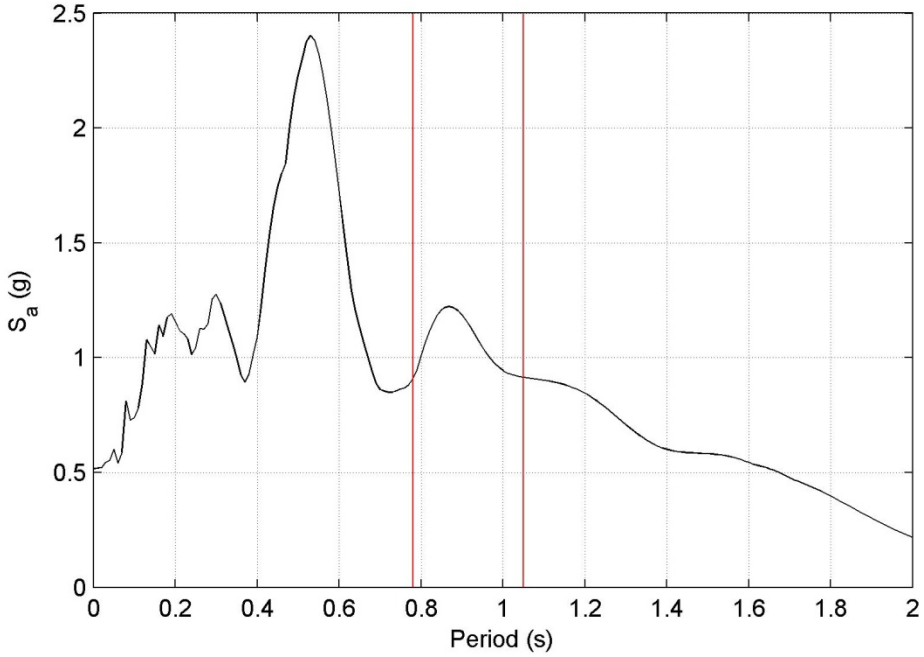

(a)

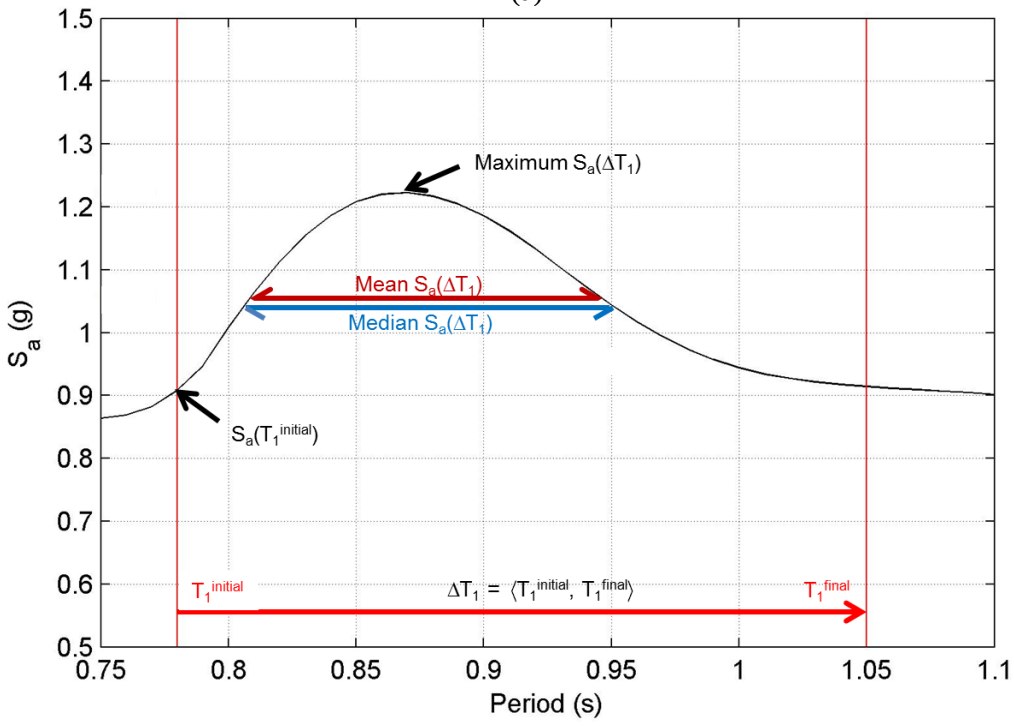

(b)

Figure 6.16 Elastic 5% damped spectral acceleration for record 1 (Northridge) with example ΔT_1 overlaid: a) overall view and b) zoomed in view with $S_a(T_1^{initial})$ and median, mean and maximum spectral acceleration over ΔT_1 ($Sa(\Delta T_1)$) values.

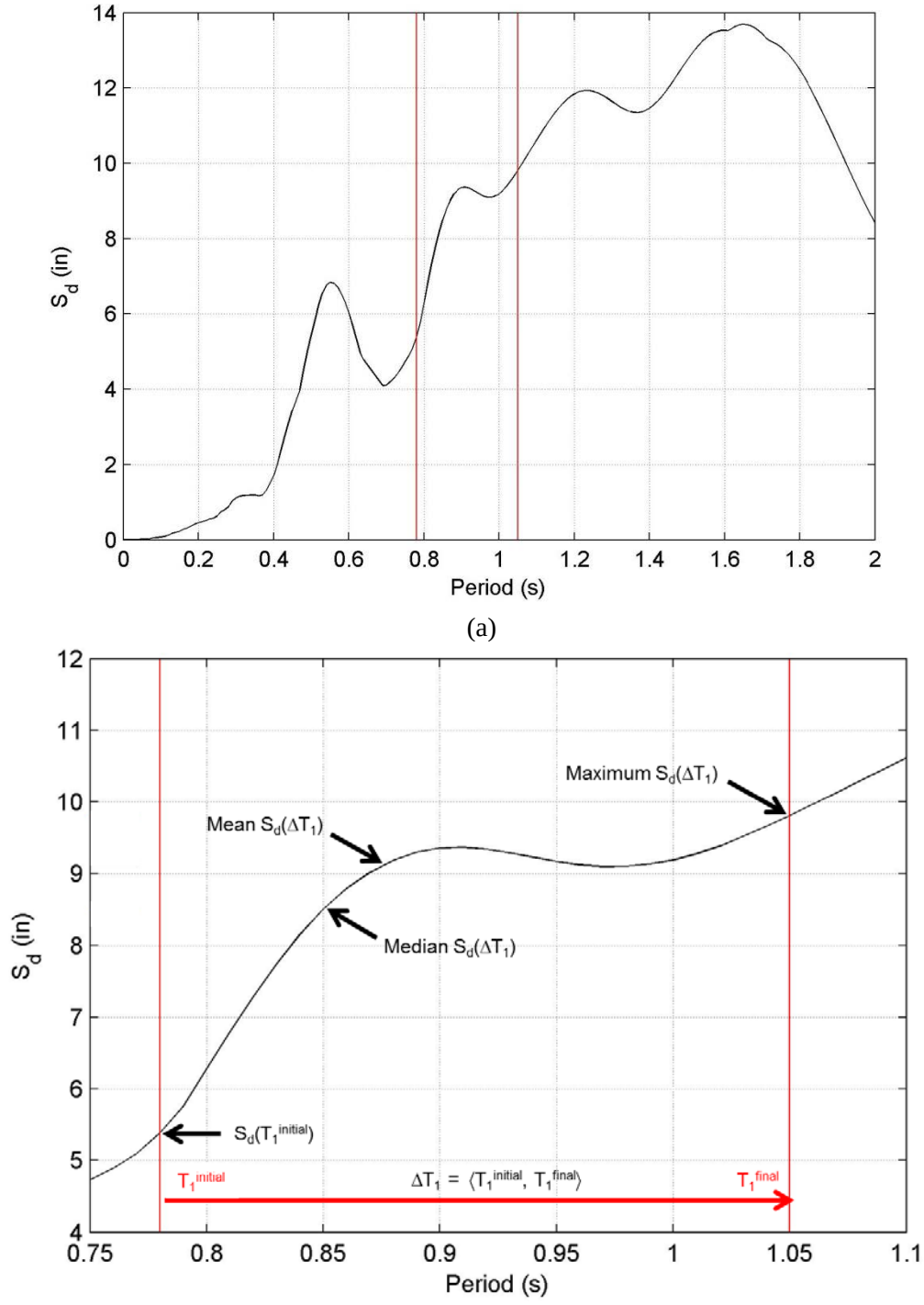

Figure 6.17 Elastic 5% damped spectral displacement for record 1 (Northridge) with example ΔT_1 overlaid: a) overall view and b) zoomed in view with $S_a(T_1^{initial})$ and median, mean and maximum spectral displacement over ΔT_1 ($Sa(\Delta T_1)$) values.

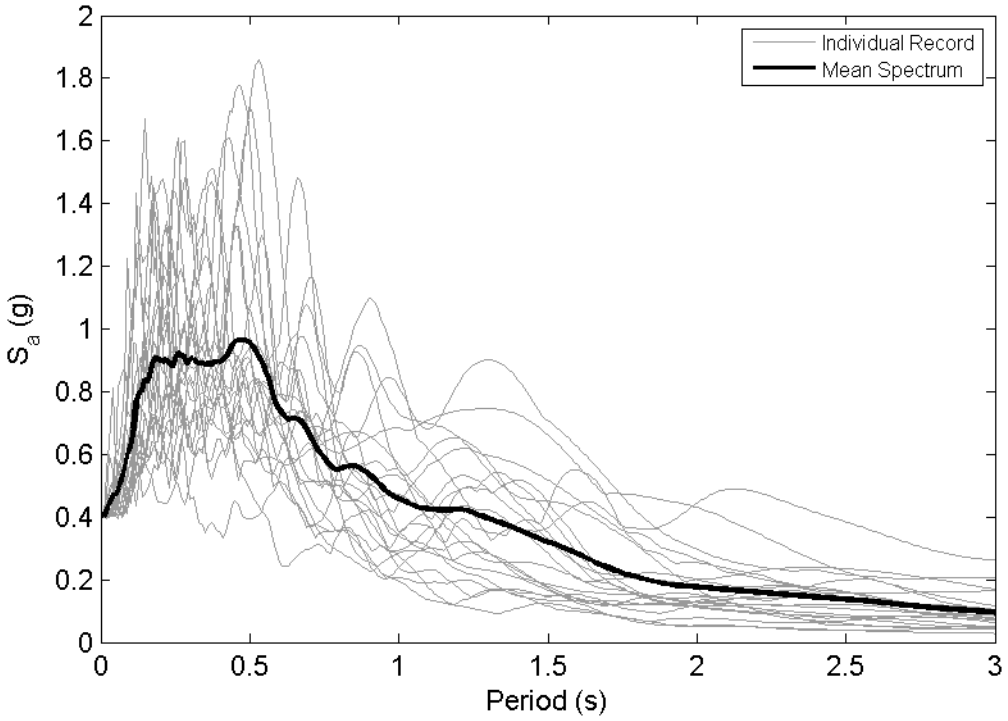

Figure 6.18 Elastic 5% damped spectral acceleration for all records scaled to a PGA = 0.4 g with overall mean shown.

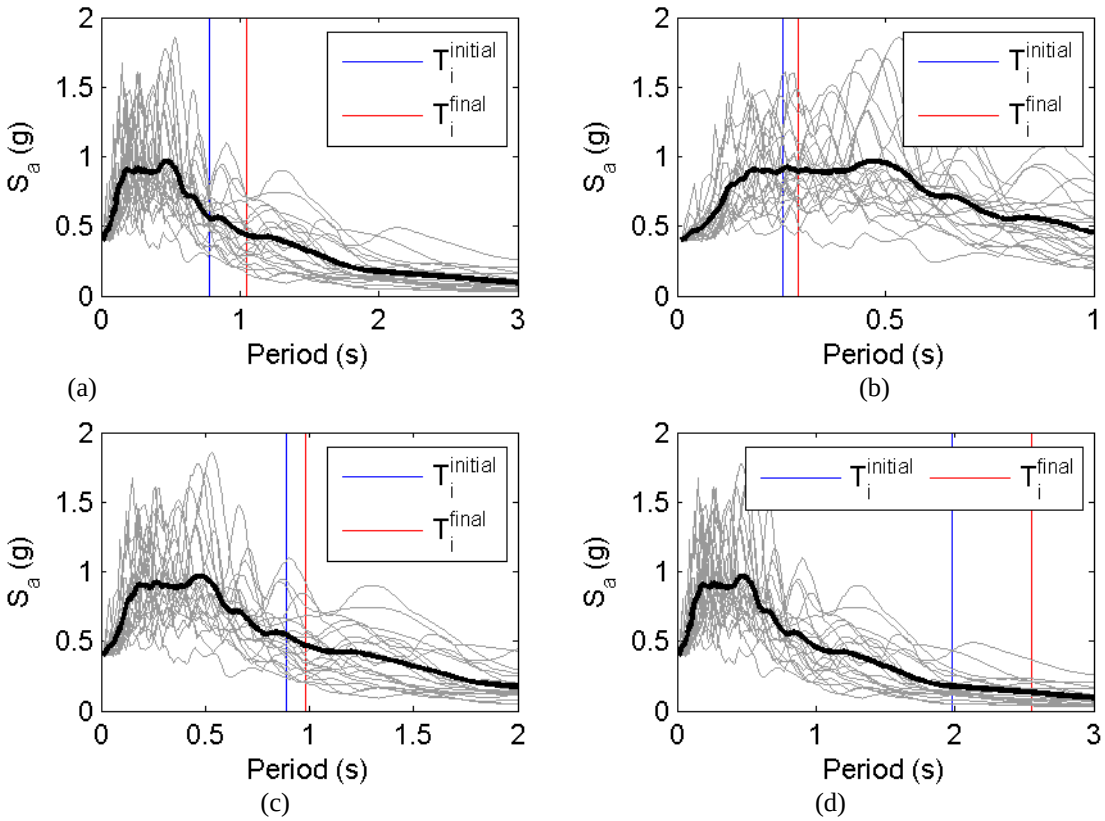

Figure 6.19 Elastic 5% damped spectral acceleration for all records scaled to a PGA = 0.4 g with overall mean shown with overlaid period ranges: (a) RC-8, (b) S-3H, (c) S-9, and (d) RC-20.

Note: extreme period ranges are shown, that is the smallest $T_1^{initial}$ to the largest T_1^{final} for all coupled cases.

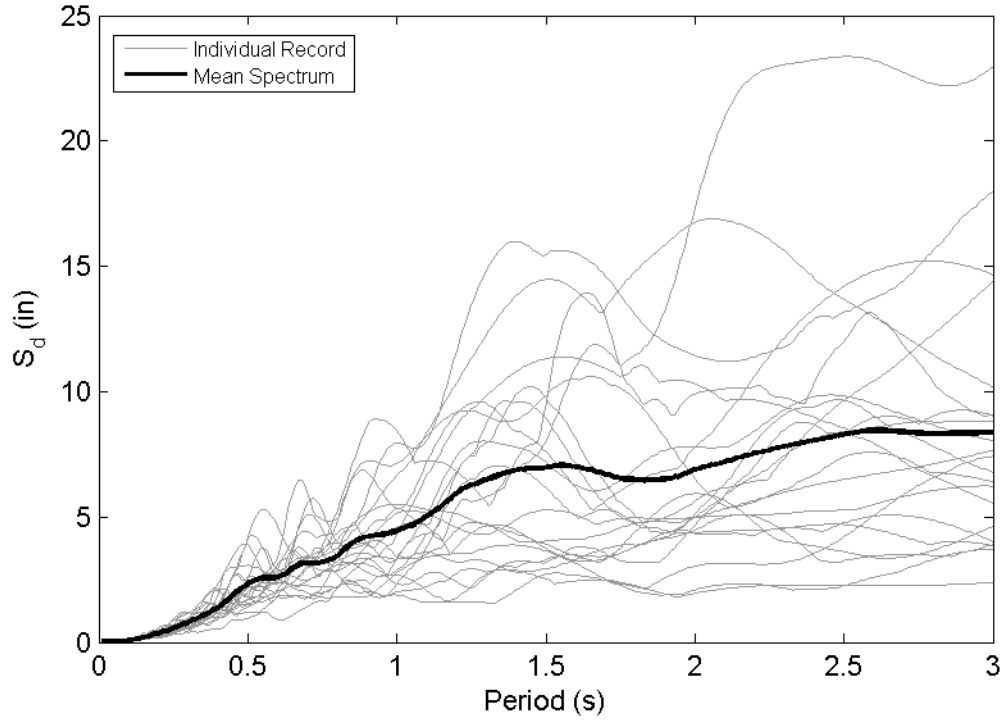

Figure 6.20 Elastic 5% damped spectral displacement for all records scaled to a PGA = 0.4 g with overall mean shown.

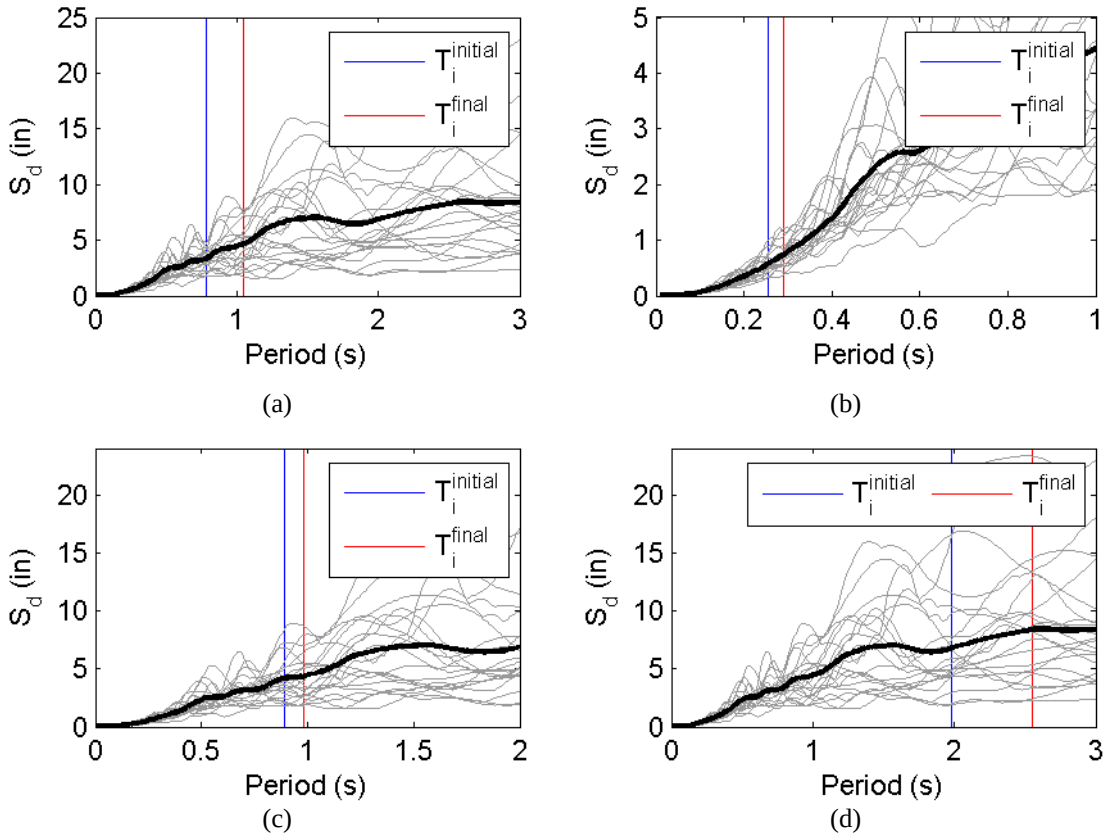

Figure 6.21 Elastic 5% damped spectral displacement for all records scaled to a PGA = 0.4 g with overall mean shown with overlaid period ranges: (a) RC-8, (b) S-3H, (c) S-9, and (d) RC-20.

Note: extreme period ranges are shown, that is the smallest $T_1^{initial}$ to the largest T_1^{final} for all coupled cases.

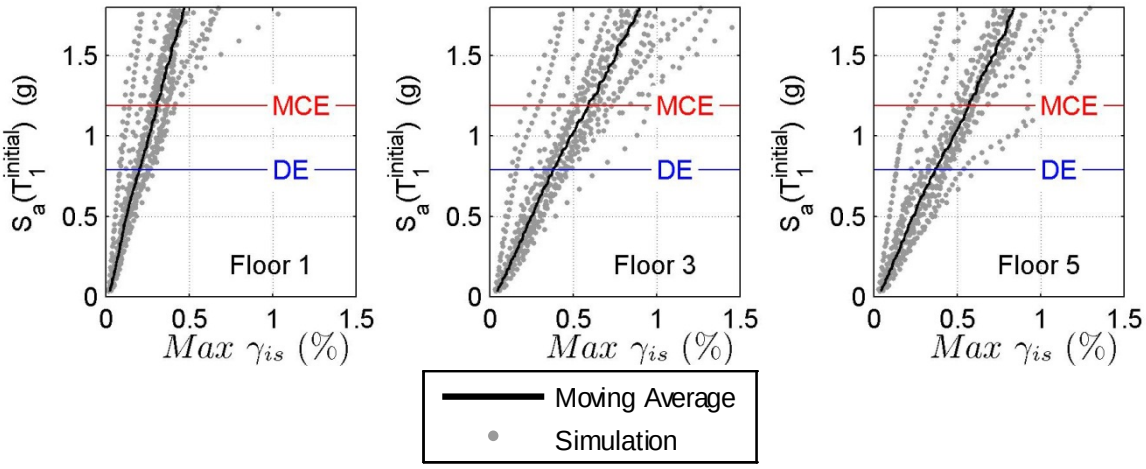

Figure 6.22 IDA results for RC-8 (no wall): maximum interstory drift against spectral acceleration at $T_1^{initial}$.
Note: DE and MCE represent design spectral acceleartions of the building (at $T_1^{initial}$) for the design and maximum considered earthquakes.

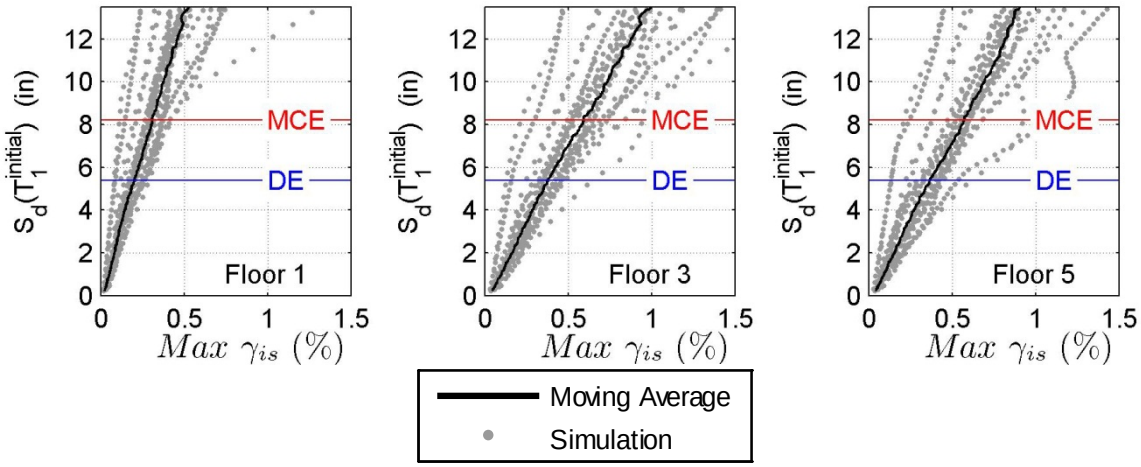

Figure 6.23 IDA results for RC-8 (no wall): maximum interstory drift against spectral displacement at $T_1^{initial}$.
Note: DE and MCE represent design spectral displacements of the building (at $T_1^{initial}$) for the design and maximum considered earthquakes.

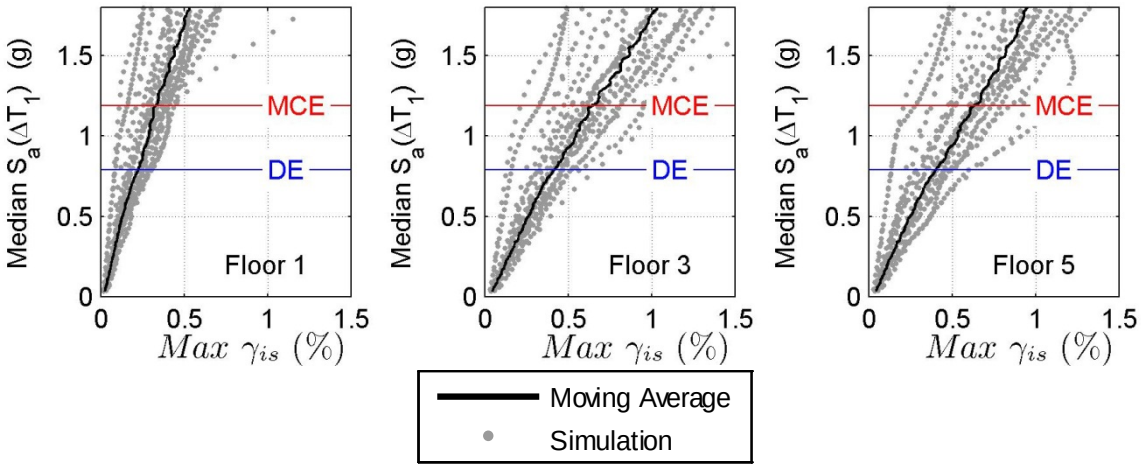

Figure 6.24 IDA results for RC-8 (no wall): maximum interstory drift against median spectral acceleration over ΔT_1.
Note: where $\Delta T_1 = \langle T_1^{initial}, T_1^{final} \rangle$ and DE and MCE represent design spectral acceleartions of the building (at $T_1^{initial}$) for the design and maximum considered earthquakes.

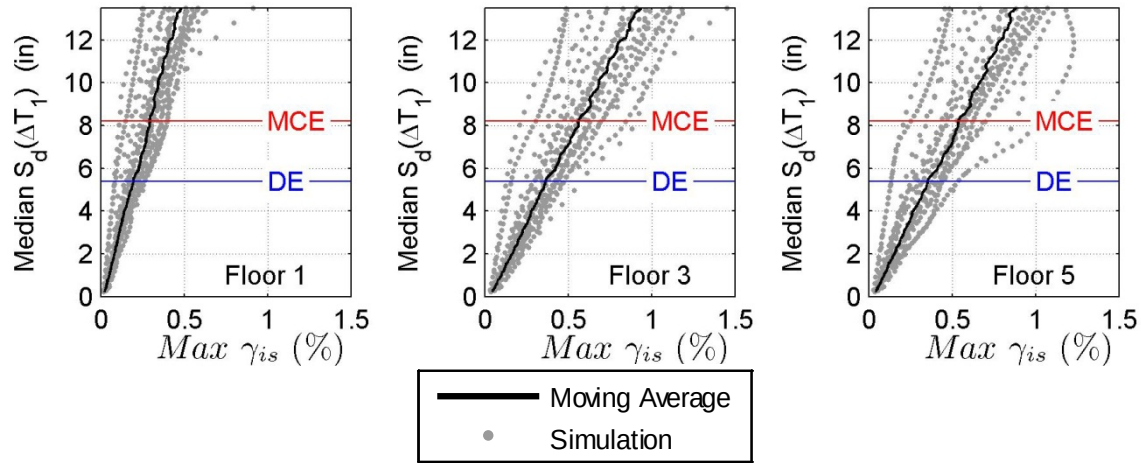

Figure 6.25 IDA results for RC-8 (no wall): maximum interstory drift against median spectral displacement over ΔT_1.
Note: where $\Delta T_1 = \langle T_1^{initial}, T_1^{final} \rangle$ and DE and MCE represent design spectral acceleartions of the building (at $T_1^{initial}$) for the design and maximum considered earthquakes.

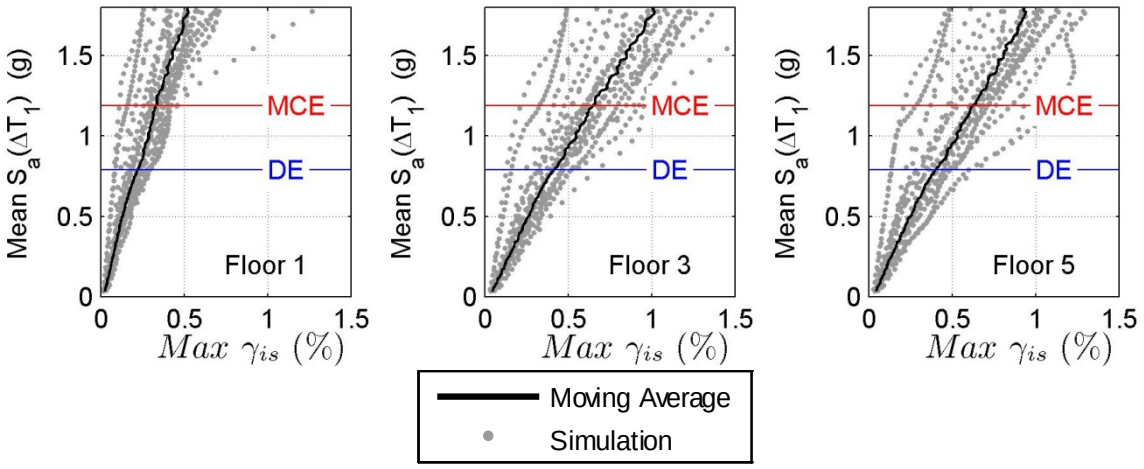

Figure 6.26 IDA results for RC-8 (no wall): maximum interstory drift against mean spectral acceleration over ΔT_1.
Note: where $\Delta T_1 = \langle T_1^{initial}, T_1^{final} \rangle$ and DE and MCE represent design spectral acceleartions of the building (at $T_1^{initial}$) for the design and maximum considered earthquakes.

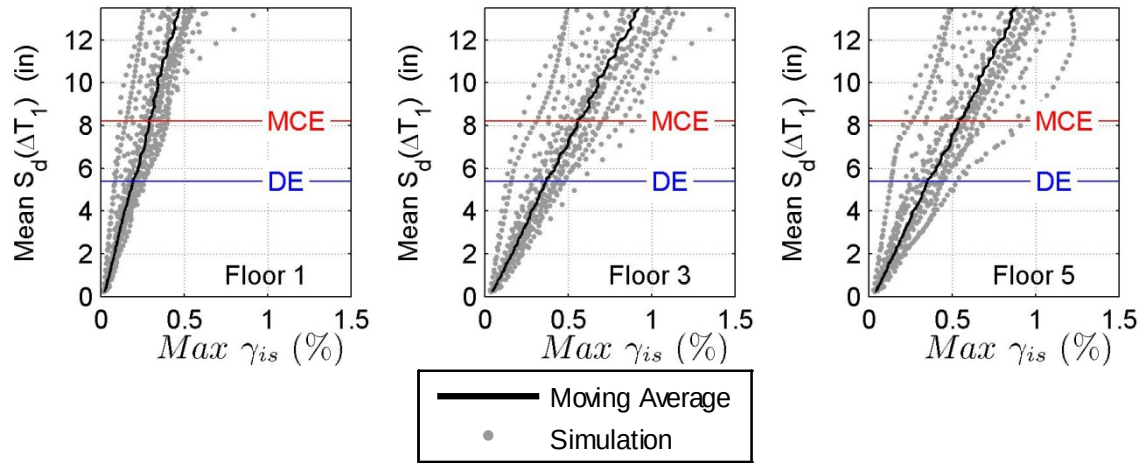

Figure 6.27 IDA results for RC-8 (no wall): maximum interstory drift against mean spectral displacement over ΔT_1.
Note: where $\Delta T_1 = \langle T_1^{initial}, T_1^{final} \rangle$ and DE and MCE represent design spectral acceleartions of the building (at $T_1^{initial}$) for the design and maximum considered earthquakes.

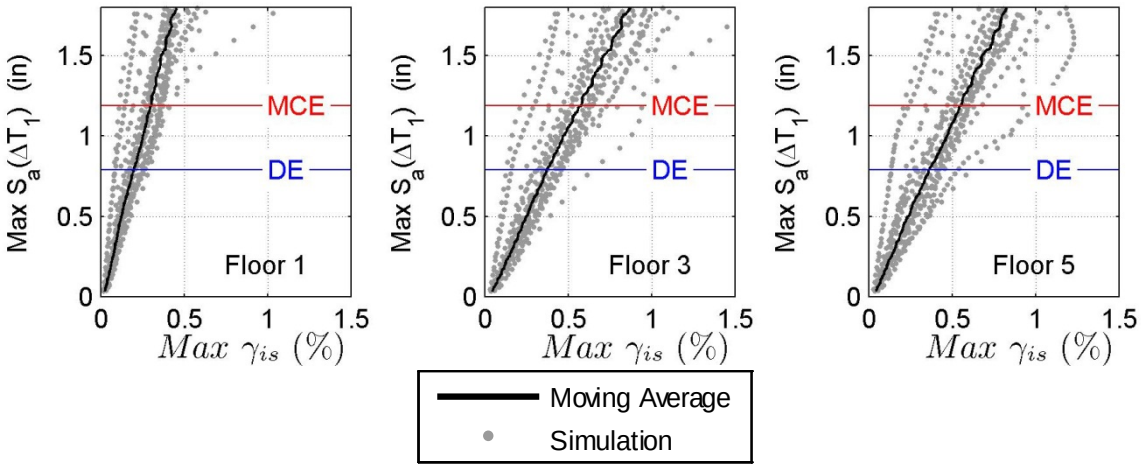

Figure 6.28 IDA results for RC-8 (no wall): maximum interstory drift against maximum spectral acceleration over ΔT_1.

Note: where $\Delta T_1 = \langle T_1^{initial}, T_1^{final} \rangle$ and DE and MCE represent design spectral acceleartions of the building (at $T_1^{initial}$) for the design and maximum considered earthquakes.

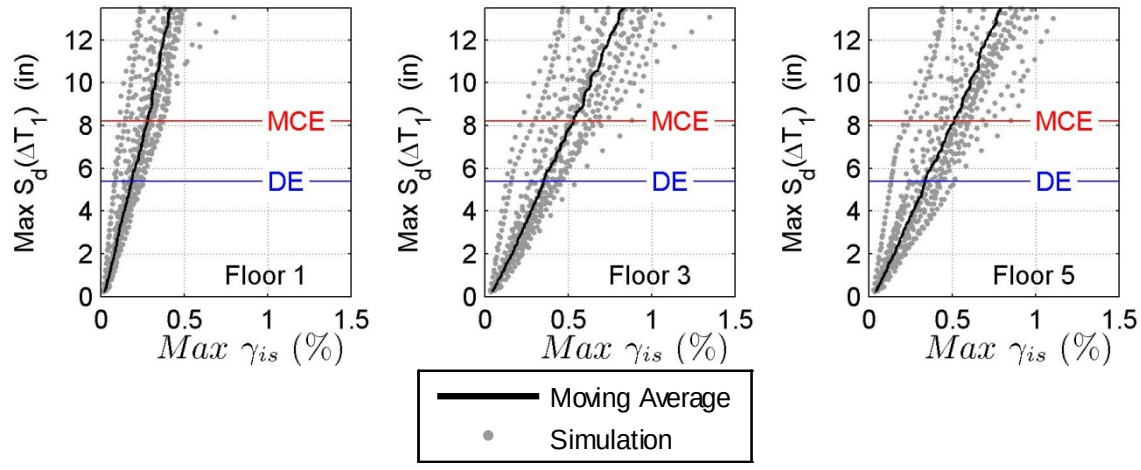

Figure 6.29 IDA results for RC-8 (no wall): maximum interstory drift against maximum spectral displacement over ΔT_1.

Note: where $\Delta T_1 = \langle T_1^{initial}, T_1^{final} \rangle$ and DE and MCE represent design spectral acceleartions of the building (at $T_1^{initial}$) for the design and maximum considered earthquakes.

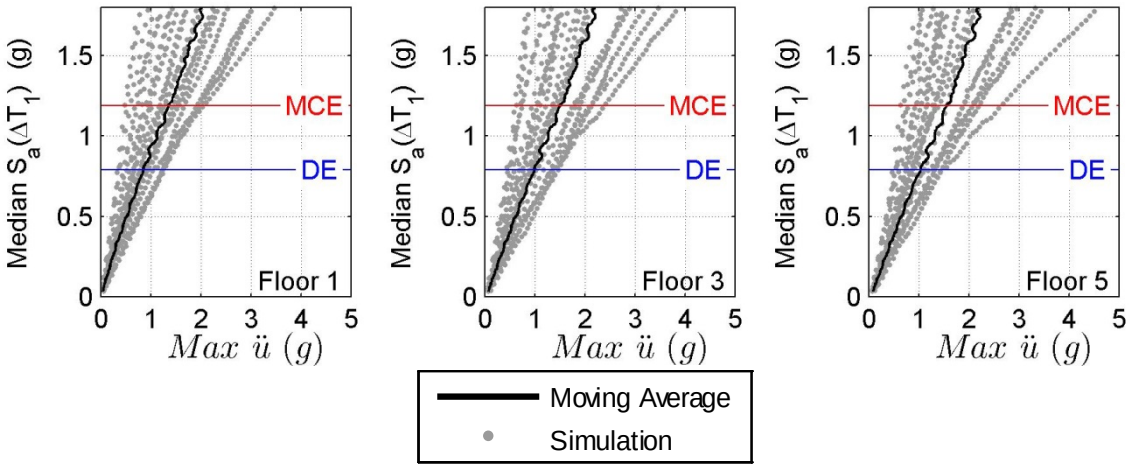

Figure 6.30 IDA results for RC-8 (no wall): maximum floor acceleration against median spectral acceleration over ΔT_1.
Note: DE and MCE represent design spectral acceleartions of the building (at $T_1^{initial}$) for the design and maximum considered earthquakes.

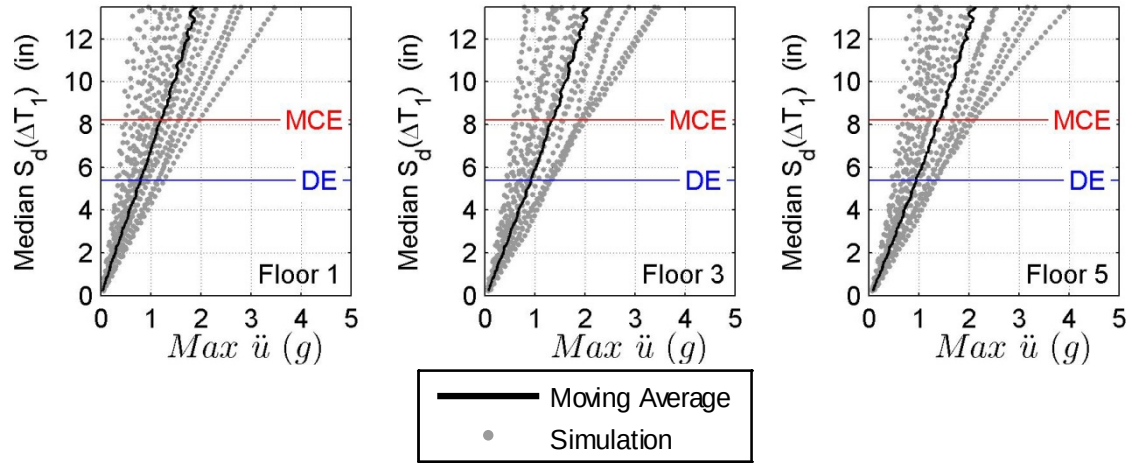

Figure 6.31 IDA results for RC-8 (no wall): maximum floor acceleration drift against median spectral displacement over ΔT_1.
Note: where $\Delta T_1 = \langle T_1^{initial}, T_1^{final} \rangle$ and DE and MCE represent design spectral acceleartions of the building (at $T_1^{initial}$) for the design and maximum considered earthquakes.

6.4 Effect of PW Inclusion on IDA results

Using the moving average curves associated with the median spectral quantities over the period range, an assessment of the effect of the PW on the building system is considered. Appendix A provides detailed construction of the moving average curves for the median spectral quantities associated with both interstory drift and floor acceleration used in the following subsections. Section 6.4.1 examines the effect of the consideration of wall length within RC-8 considering the median spectral quantities. As an example to illustrate the effect of considering the mean and maximum spectral quantities over the period range and the elastic fundamental period of the building (T_1), Appendix C outlines the same comparison for all the representative spectral quantities for the period range for the effect of wall length on RC-8. It is noted that the moving average representations of the coupled building-partition wall system are very similar no matter which statistical spectral quantity is chosen (median spectral acceleration over ΔT_1, mean spectral displacement over ΔT_1, etc.). However the median spectral quantities over ΔT_1 will be considered since, as outlined previously, it represents the 50^{th} percentile and is commonly adopted in ground motion relationships (Abrahamson and Silva, 2008).

6.4.1 RC-8 Model: Effect of Wall Length

In comparing the effect of the wall length on RC-8 using the minimum and maximum wall length (mean model), the interstory drift and floor response are examined. First, the maximum interstory drift moving averages are compared on a per floor basis in Figure 6.32 and Figure 6.33. Examining the influence of the PW is difficult to assess using the moving averages, therefore the response of the coupled system (minimum and maximum wall length) cases are normalized by the response of the bare building (no wall) in Figure 6.34 and Figure 6.35. In both figures, it is noted that interstory drift is initially severely underestimated when only considering the bare building case (no wall). Approximately 50% of the interstory drift is underestimated by

neglecting the PW for small spectral acceleration and spectral displacement values, with only a slight difference noted due to wall lengths. When the wall length is longer, the initial underestimation of the interstory drift is reduced but after the longer wall degrades, the effect of the wall length is less apparent. When the spectral acceleration and displacement demands approach that of the design earthquake level (denoted DE on the figures), the effect of the PW on interstory drift is greatly reduced to within 25% that of the no wall case. For RC-8, the building experiences yielding around 0.5% roof drift which translates to a displacement of 5.8. At the DE level demands, the PWs experience approximately 0.50% interstory drift and the corresponding stiffness is reduced and consequently the effect on the coupled system is diminished. For spectral demands greater than the DE case, an increase of 25% is noted up to the spectral demands associated with the maximum credible earthquake (denoted MCE). For spectral values greater than the MCE, the effect of the partition wall is diminished to around 10-20% for interstory drift values, and correspondingly would influence the collapse potential of the coupled building-partition wall system.

In like fashion, the maximum floor acceleration moving averages are illustrated on a per floor basis in Figure 6.36 and Figure 6.37. Normalizing the coupled moving average curves by the bare building demonstrates the effect of the PW as well as the impact of wall length on the maximum floor acceleration (Figure 6.38 and Figure 6.39). An approximate underestimation of up to 80% is observed if the PW is neglected, with minor differences noted between walls of different lengths (within 10-20%). This high effect occurs when spectral demands or accelerations are low, representing a service level earthquake. For spectral demands up to the design earthquake (DE) level, on average the floor accelerations were underestimated by 30% if the PW was neglected. At spectral demands around the MCE level, floor accelerations were underestimated up to approximately 20%, where the floor and the wall length influenced the response. The effect of the PW on the lower floor accelerations is observed to be reduced up to

30% when compared to the higher floors. This is noted because the effect of the PW is not noticeable when the columns sizes and floor level stiffness increase. The effect of the PW is most observed on the roof level, where typically the columns are the lightest and the story stiffness the smallest. However, recall that the roof level typically experiences the highest floor accelerations, highlighting the importance to consider the coupled building-partition wall system.

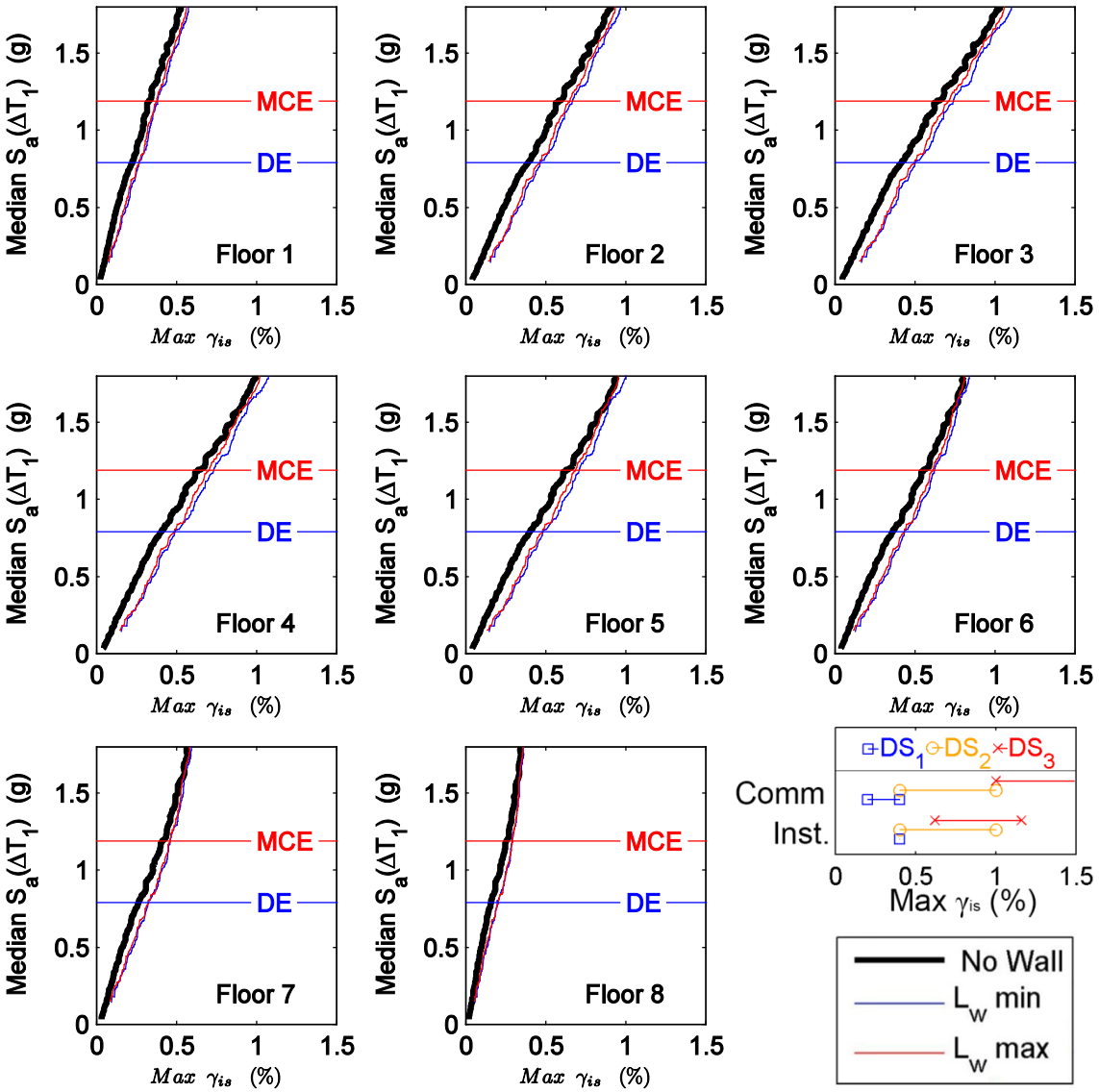

Figure 6.32 Maximum interstory drift moving average curves for RC-8 with cases of no wall, minimum wall length, and maximum wall length considering mean model parameters against median spectral acceleration over ΔT_1.

Note: where $\Delta T_1 = \langle T_1^{initial}, T_1^{final} \rangle$ and DE and MCE represent design spectral acceleartions of the building (at $T_1^{initial}$) for the design and maximum considered earthquakes. Comm and Inst denote commerical and institional wall types, respectively.

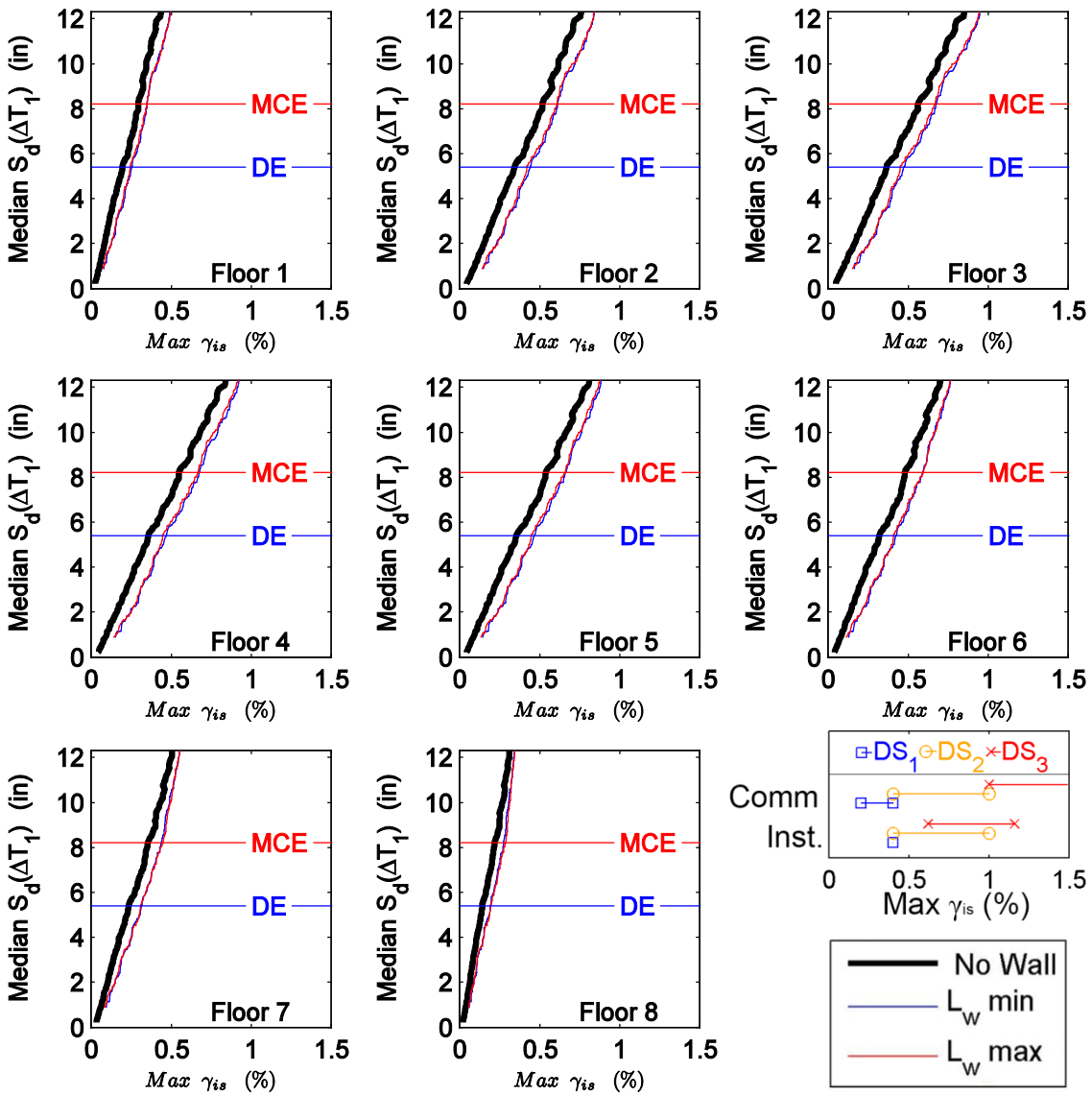

Figure 6.33 Maximum interstory drift moving average curves for RC-8 with cases of no wall, minimum wall length, and maximum wall length considering mean model parameters against median spectral displacement over ΔT_1.

Note: where $\Delta T_1 = \langle T_1^{initial}, T_1^{final} \rangle$ and DE and MCE represent design spectral acceleartions of the building (at $T_1^{initial}$) for the design and maximum considered earthquakes. Comm and Inst denote commerical and institional wall types, respectively.

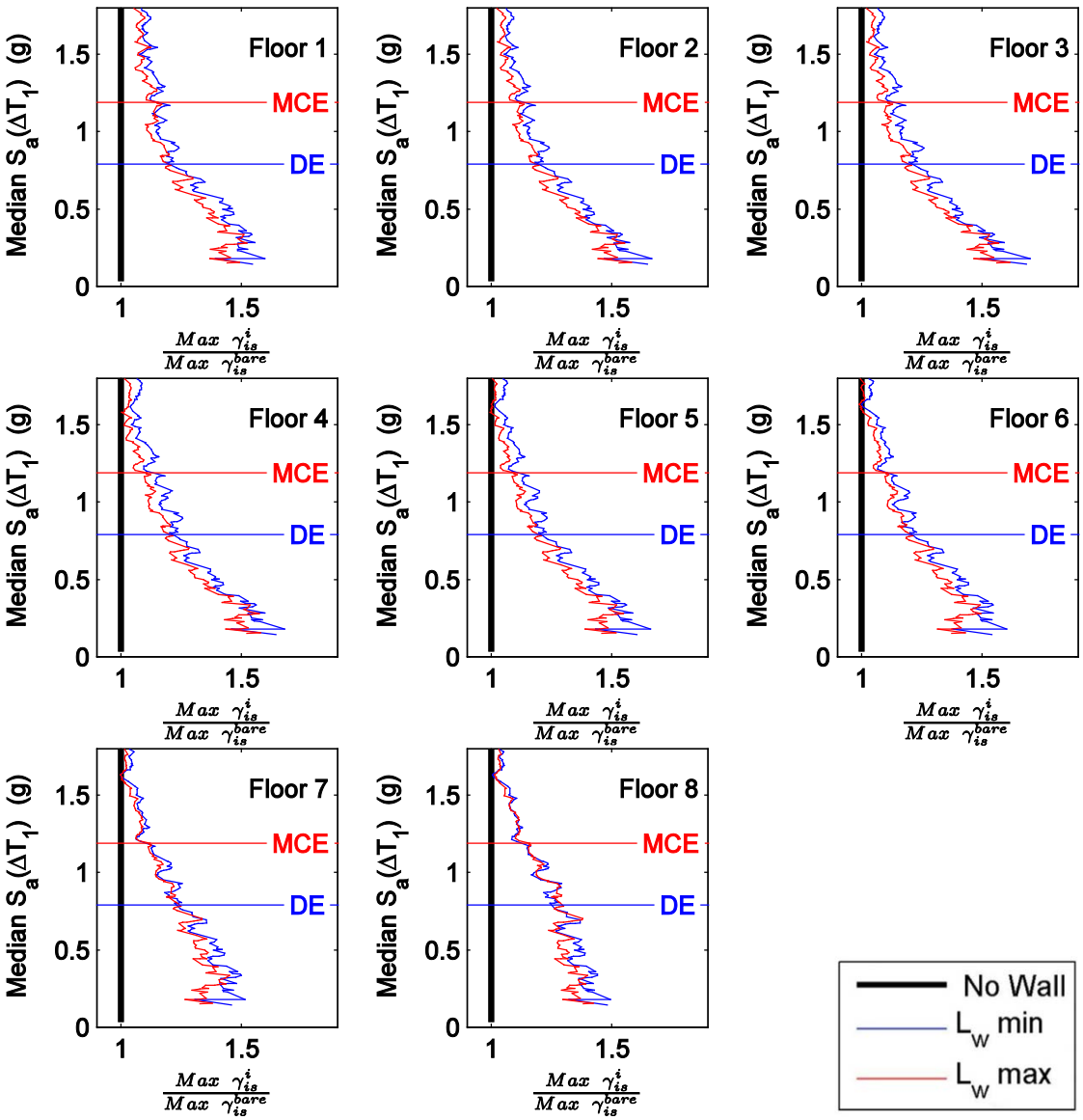

Figure 6.34 Normalized maximum interstory drift moving average curves for RC-8 with cases of no wall, minimum wall length, and maximum wall length considering mean model parameters against median spectral acceleration over ΔT_1.

Note: where $\Delta T_1 = \langle T_1^{initial}, T_1^{final} \rangle$ and DE and MCE represent design spectral acceleartions of the building (at $T_1^{initial}$) for the design and maximum considered earthquakes.

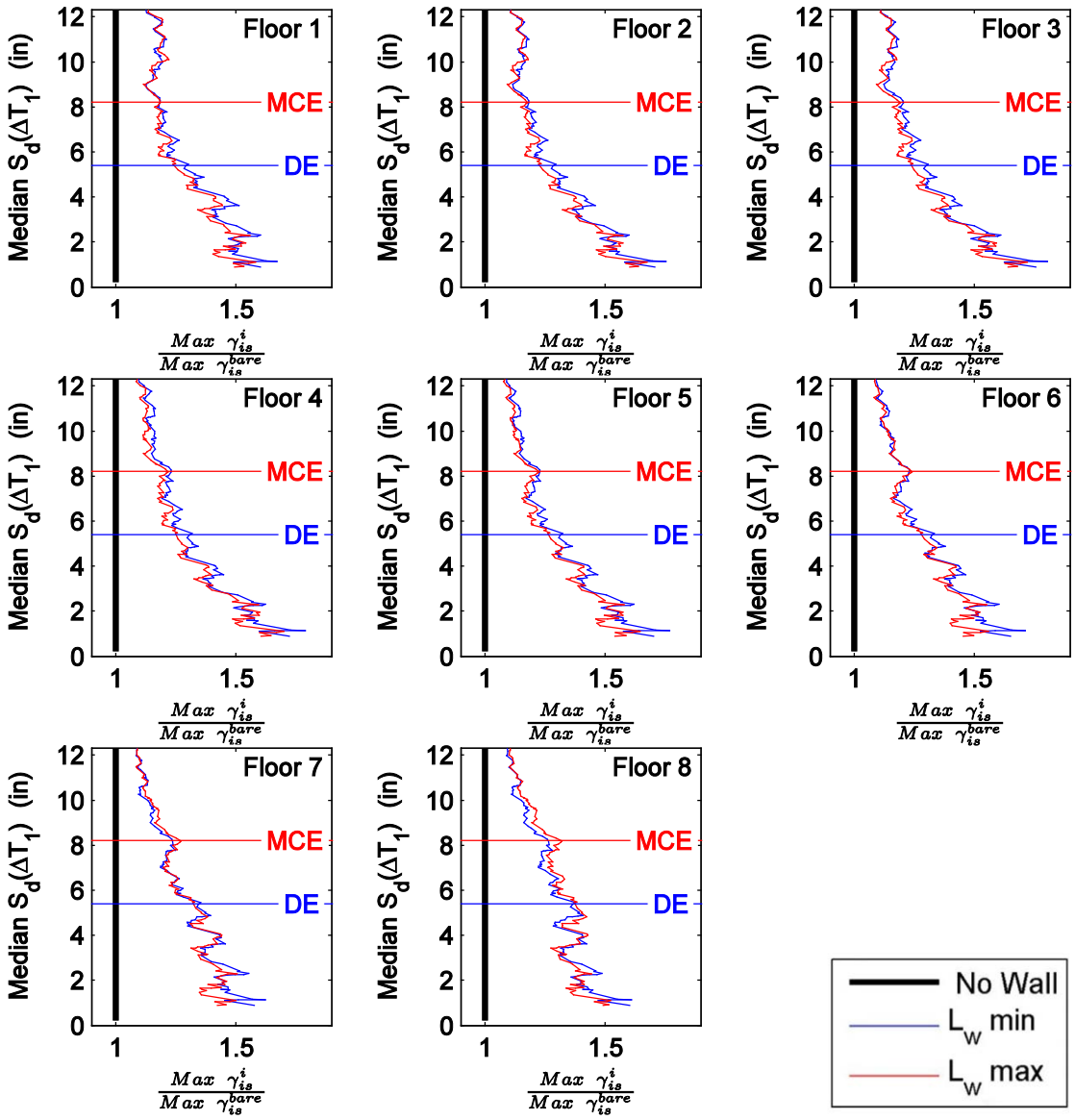

Figure 6.35 Normalized maximum interstory drift moving average curves for RC-8 with cases of no wall, minimum wall length, and maximum wall length considering mean model parameters against median spectral displacement over ΔT_1.

Note: where $\Delta T_1 = \langle T_1^{initial}, T_1^{final} \rangle$ and DE and MCE represent design spectral acceleartions of the building (at $T_1^{initial}$) for the design and maximum considered earthquakes.

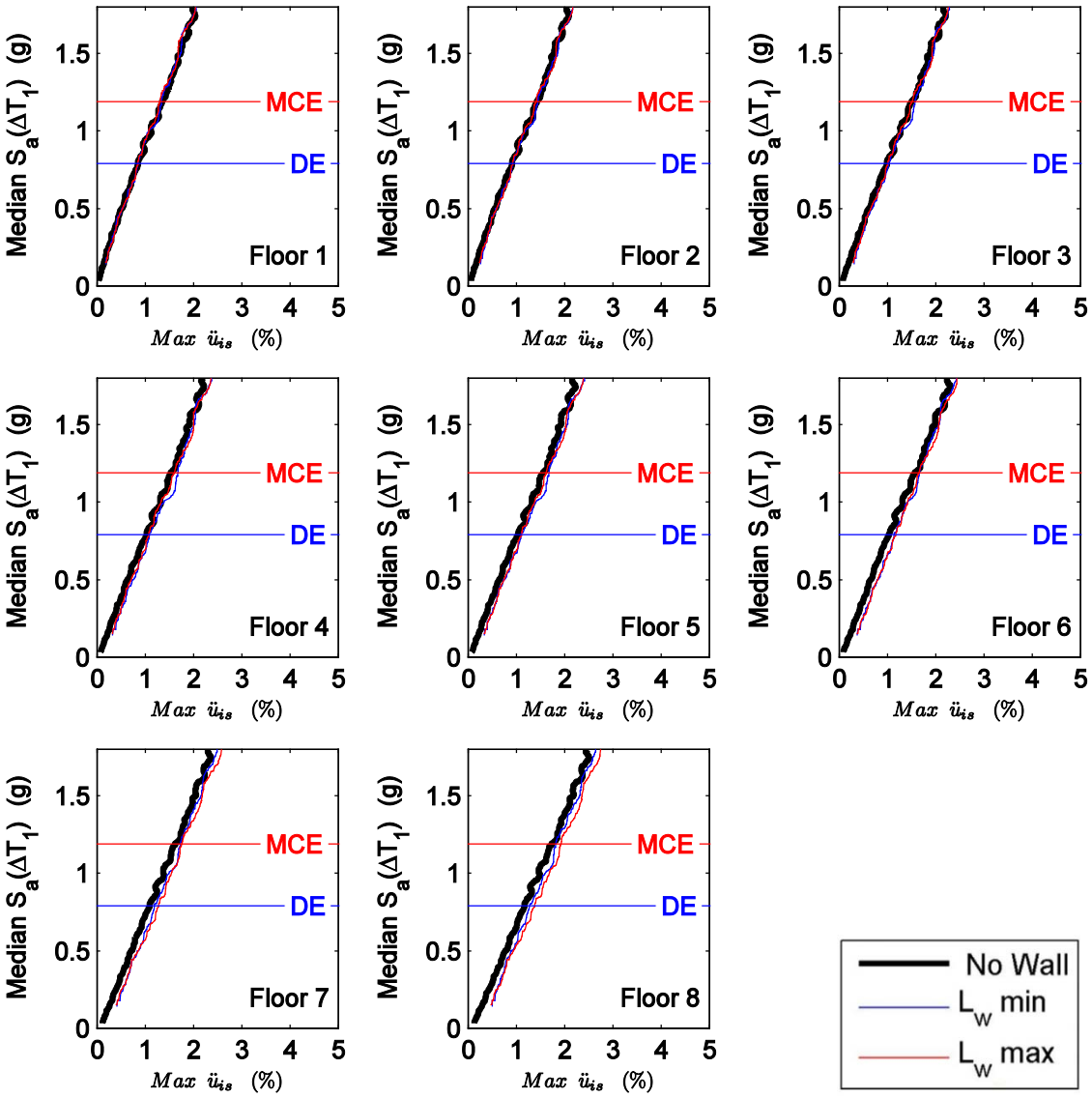

Figure 6.36 Maximum floor acceleration moving average curves for RC-8 with cases of no wall, minimum wall length, and maximum wall length considering mean model parameters against median spectral acceleration over ΔT_1.

Note: where $\Delta T_1 = \langle T_1^{initial}, T_1^{final} \rangle$ and DE and MCE represent design spectral acceleartions of the building (at $T_1^{initial}$) for the design and maximum considered earthquakes.

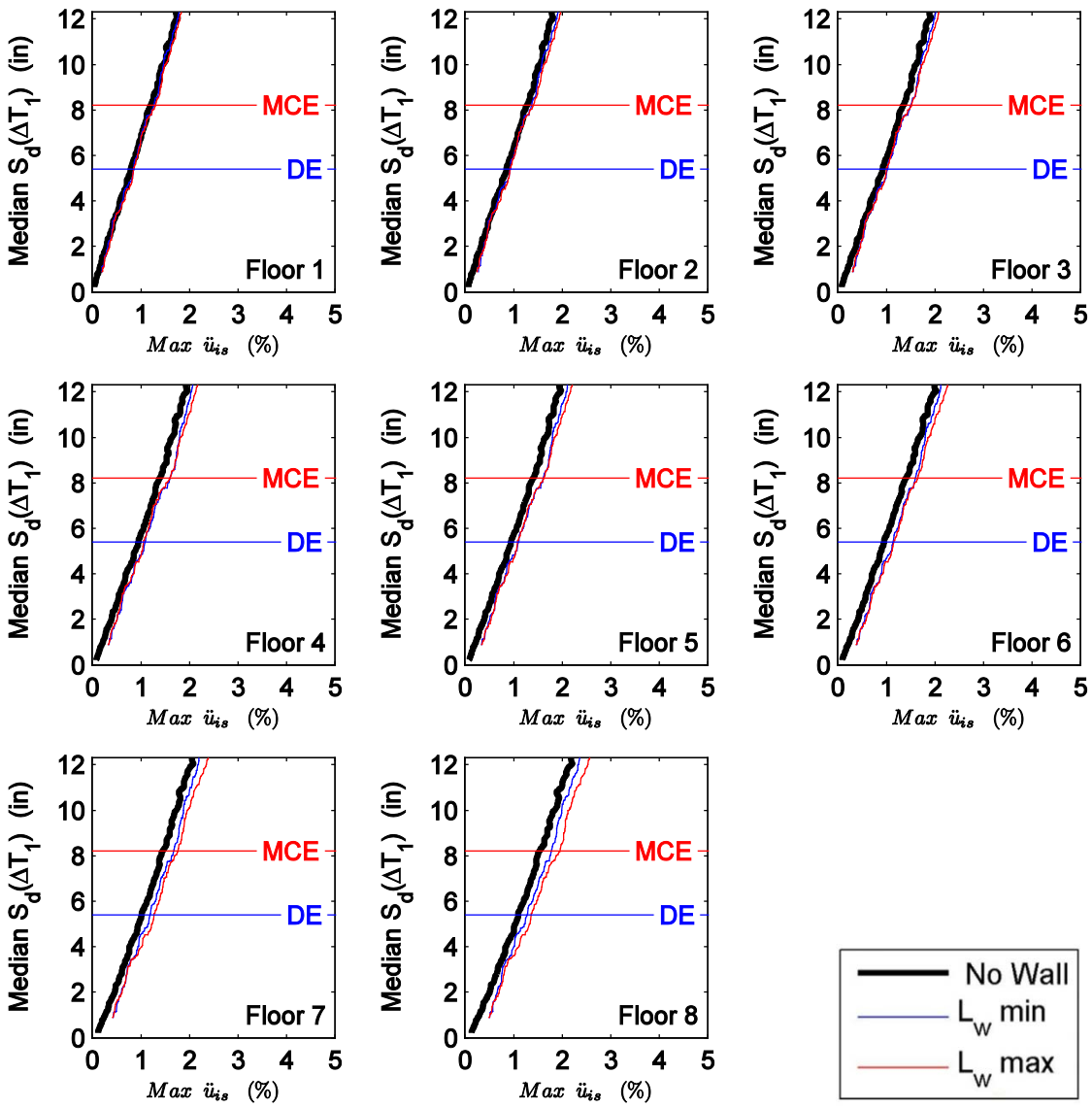

Figure 6.37 Maximum floor acceleration moving average curves for RC-8 with cases of no wall, minimum wall length, and maximum wall length considering mean model parameters against median spectral displacement over ΔT_1.

Note: where $\Delta T_1 = \langle T_1^{initial}, T_1^{final} \rangle$ and DE and MCE represent design spectral acceleartions of the building (at $T_1^{initial}$) for the design and maximum considered earthquakes.

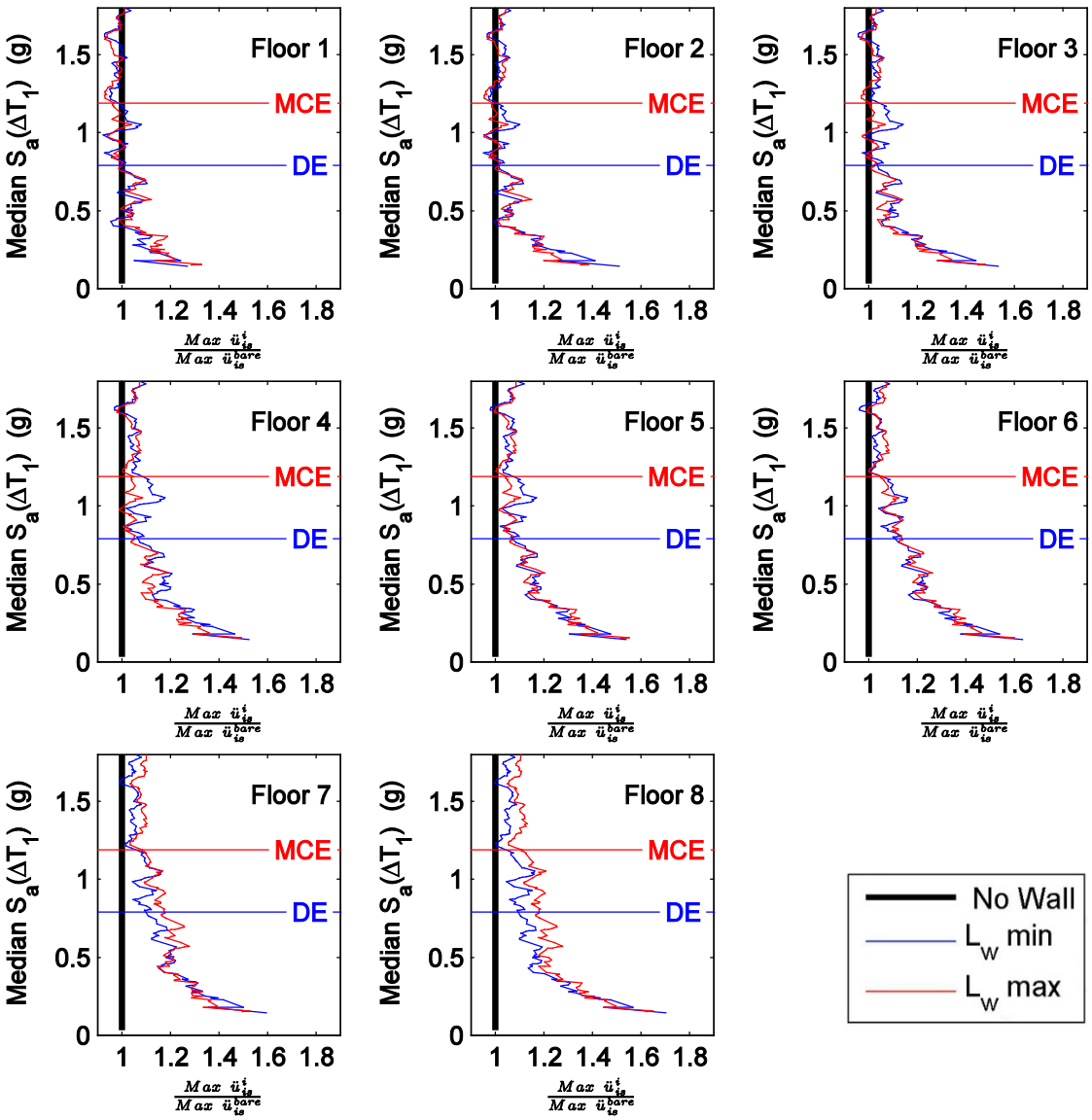

Figure 6.38 Normalized maximum floor acceleration moving average curves for RC-8 with cases of no wall, minimum wall length, and maximum wall length considering mean model parameters against median spectral acceleration over ΔT_1.

Note: where $\Delta T_1 = \langle T_1^{initial}, T_1^{final} \rangle$ and DE and MCE represent design spectral acceleartions of the building (at $T_1^{initial}$) for the design and maximum considered earthquakes.

.

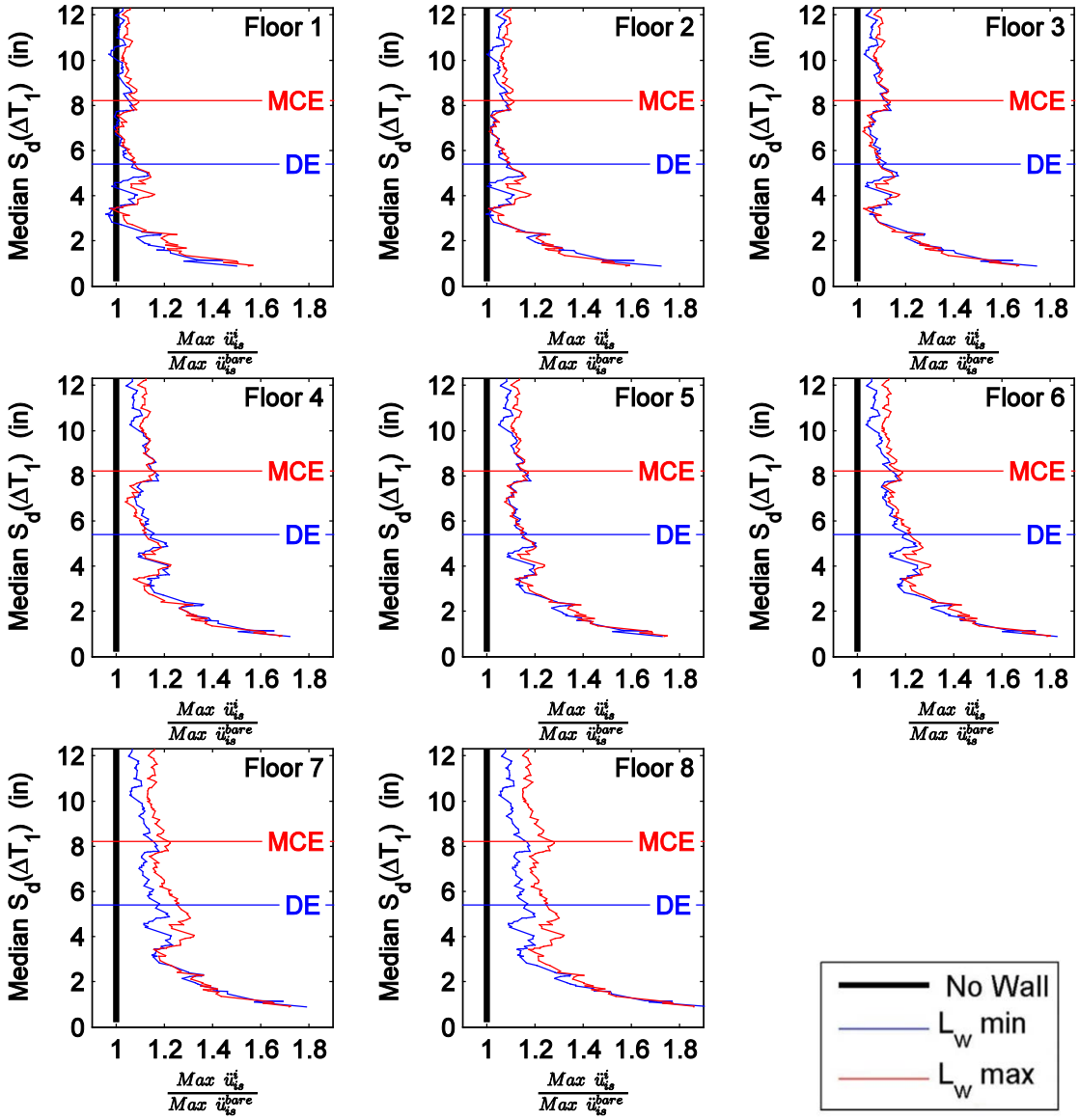

Figure 6.39 Normalized maximum floor acceleration moving average curves for RC-8 with cases of no wall, minimum wall length, and maximum wall length considering mean model parameters against median spectral displacement over ΔT_1.

Note: where $\Delta T_1 = \langle T_1^{initial}, T_1^{final} \rangle$ and DE and MCE represent design spectral acceleartions of the building (at $T_1^{initial}$) for the design and maximum considered earthquakes.

6.4.2 RC-8 Model: Effect of PW Strength

In comparing the effect of the PW strength on the response of RC-8, the mean, mean plus standard deviation, and mean minus standard deviation PW models are considered using the minimum wall length. To assess the effect of the PW strength, the interstory drift and floor responses are examined. The detailed moving averages are found in Appendix C. Herein the focus is on the normalized maximum interstory drift moving averages as compared on a per floor basis in Figure 6.40 and Figure 6.41. In both figures, it is noted that interstory drift is initially underestimated for all cases where a significant difference is noted for the mean plus standard deviation PW model on the upper floors. This is associated with the greater relative stiffness of the PW in comparison in the floor level stiffness. The effect of the mean model to the mean minus standard deviation is not as pronounced. Reasons for the greater effect of the mean plus a standard deviation include greater stiffness, greater force values, limited post-yield degradation, and an earlier occurrence of post-peak hardening (Figure 2.32). The effect of the post peak hardening versus degradation is characterized in the next section. When the spectral demands are below that of an anticipated design earthquake (DE), the difference in wall strength can cause up to a 30% additional underestimation between the mean plus standard deviation PW model when compared that to the mean minus standard deviation. When the spectral demands exceed those associated with the maximum credible earthquake event (MCE), the mean plus standard deviation PW model parameters still result in 40% of interstory drift underestimation when compared to that of the no wall case. However as noted earlier, the effect of the PW on the response of the coupled system is most evident on the higher floor levels and the influence of PW regardless of strength is least noted on the lower floors.

In like fashion, the normalized maximum floor acceleration moving averages are shown on a per floor basis (Figure 6.42 and Figure 6.43). Significant differences are noted in the mean

plus standard deviation model in the lower values of the spectral quantities. In general for low spectral values, values less than the design earthquake level (median $S_A(\Delta T_1) < 1g$), underestimation of the of the maximum acceleration response is observed . However through the spectral demands, even values greater than the maximum credible earthquake (MCE), the mean plus standard deviation PW model had interstory drift values greater than 10% when compared to the mean and mean minus one standard deviation PW model parameters.

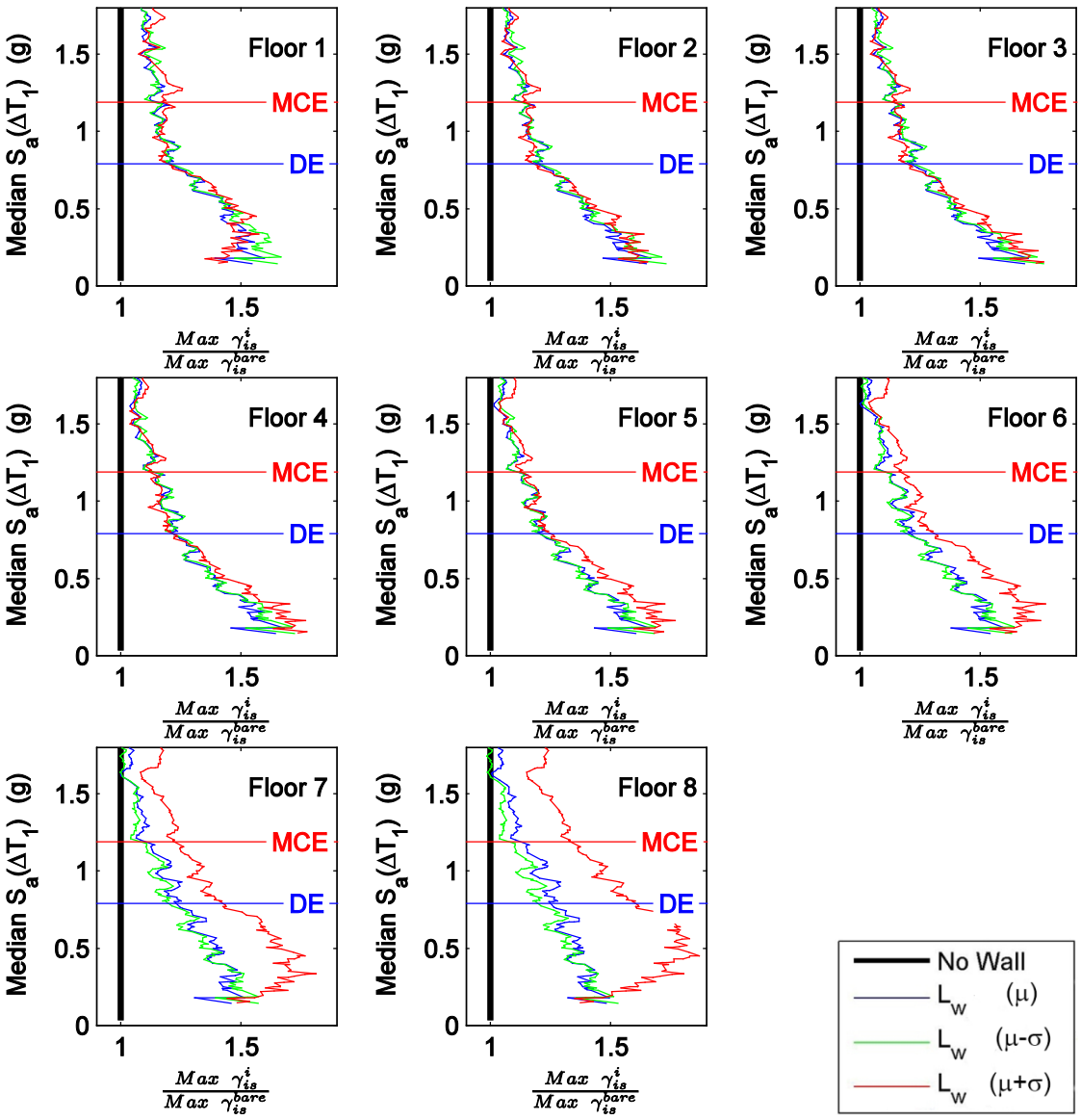

Figure 6.40 Normalized maximum interstory drift moving average curves for RC-8 with cases of no wall and the minimum wall length considering mean (μ), mean minus standard deviation (μ–σ), and mean plus standard deviation (μ+σ) model parameters against median spectral acceleration over ΔT_1.

Note: where $\Delta T_1 = \langle T_1^{initial}, T_1^{final} \rangle$ and DE and MCE represent design spectral acceleartions of the building (at $T_1^{initial}$) for the design and maximum considered earthquakes.

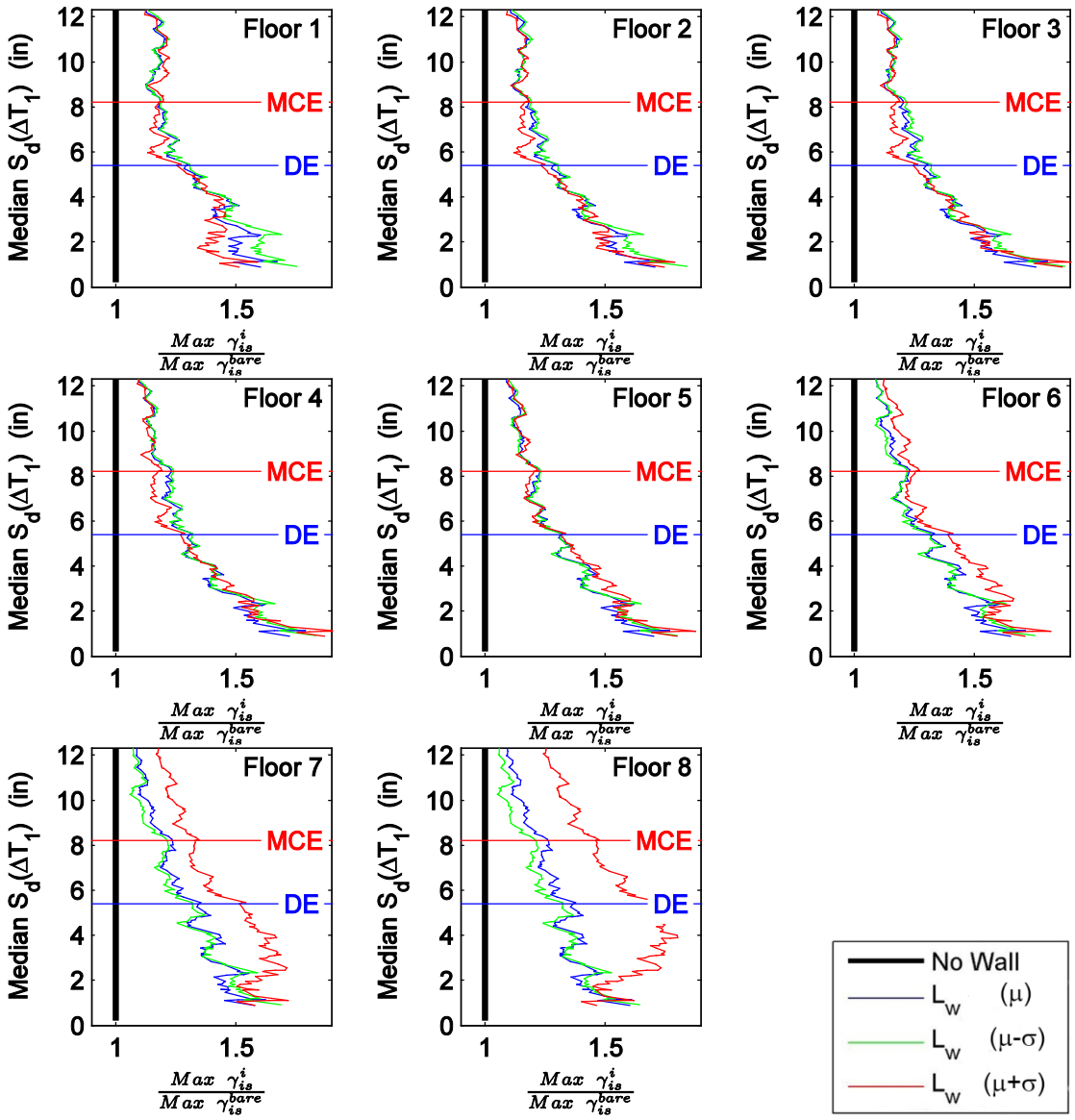

Figure 6.41 Normalized maximum interstory drift moving average curves for RC-8 with cases of no wall and the minimum wall length considering mean (μ), mean minus standard deviation (μ−σ), and mean plus standard deviation (μ+σ) model parameters against median spectral displacement over ΔT_1.

Note: where $\Delta T_1 = \langle T_1^{initial}, T_1^{final} \rangle$ and DE and MCE represent design spectral acceleartions of the building (at $T_1^{initial}$) for the design and maximum considered earthquakes.

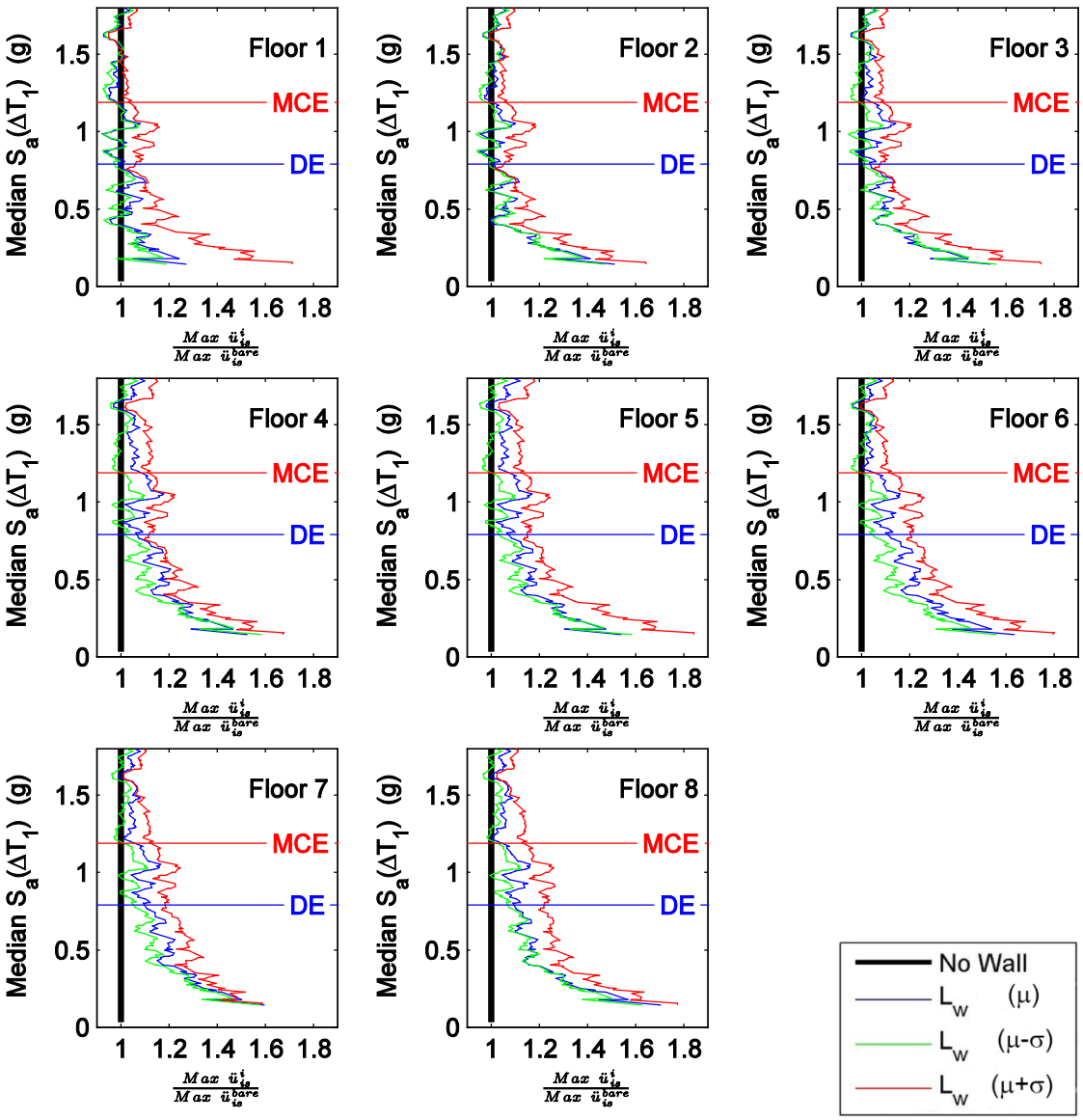

Figure 6.42 Normalized maximum floor acceleration moving average curves for RC-8 with cases of no wall and the minimum wall length considering mean (μ), mean minus standard deviation (μ−σ), and mean plus standard deviation (μ+σ) model parameters against median spectral acceleration over ΔT_1.

Note: where $\Delta T_1 = \langle T_1^{initial}, T_1^{final} \rangle$ and DE and MCE represent design spectral acceleartions of the building (at $T_1^{initial}$) for the design and maximum considered earthquakes.

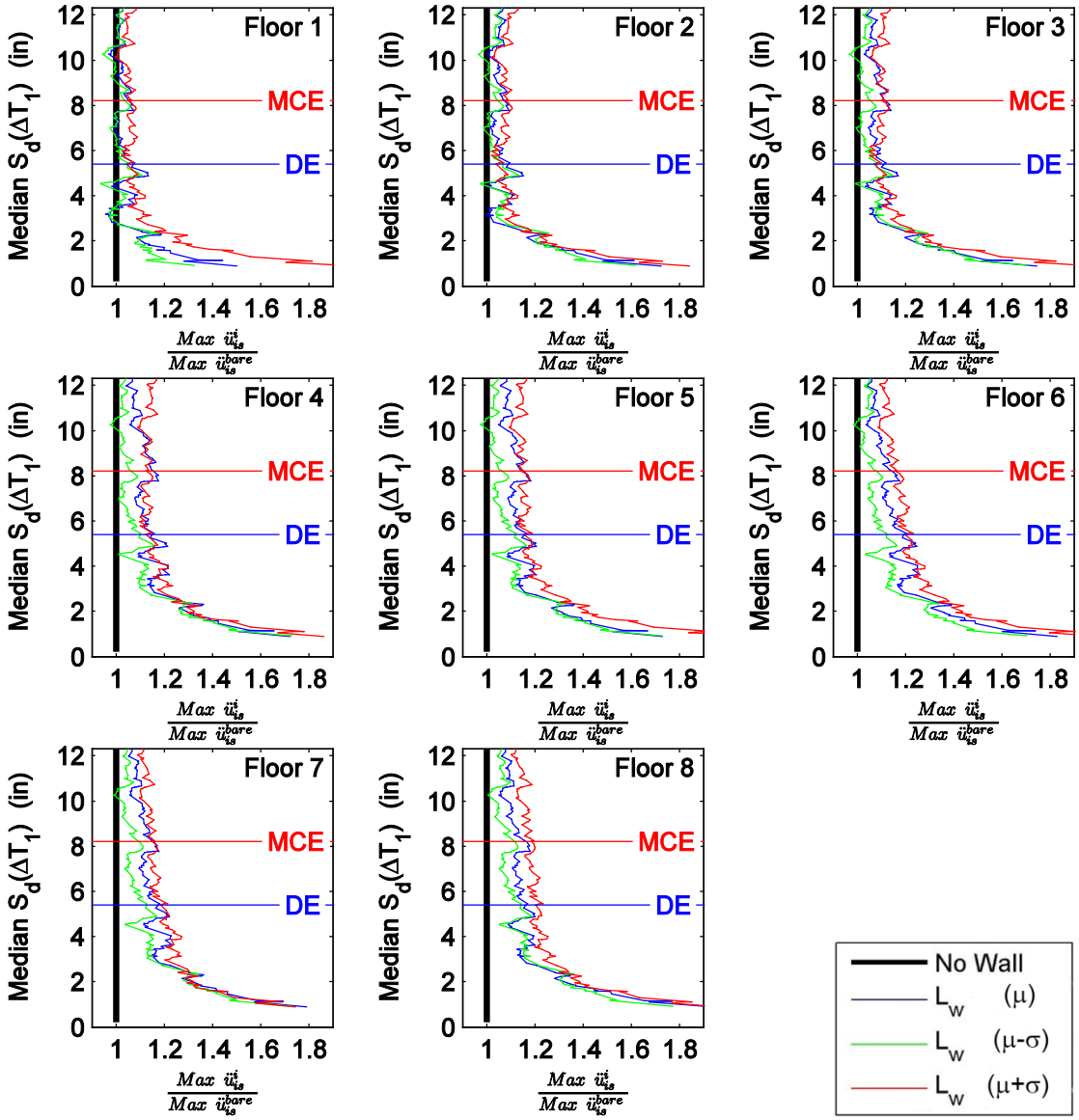

Figure 6.43 Normalized maximum floor acceleration drift moving average curves for RC-8 with cases of no wall and the minimum wall length considering mean (μ), mean minus standard deviation (μ–σ), and mean plus standard deviation (μ+σ) model parameters against median spectral displacement over ΔT_1.

Note: where $\Delta T_1 = \langle T_1^{initial}, T_1^{final} \rangle$ and DE and MCE represent design spectral acceleartions of the building (at $T_1^{initial}$) for the design and maximum considered earthquakes.

6.4.3 RC-8 Model: Effect of Post-Yield Degradation

In order to assess the effect of post-peak hardening versus a degrading model on the effect of PW on the building model, the PW model required a modification. To remove the post-peak hardening (and force plateau) from the backbone, it is assumed that after the PW backbone begins to degrade it continues to zero (Figure 6.44, noted as "degrading"). Recall that this post peak hardening may be attributed to closure of a gap between the wall and the top track. The degrading partition wall model is envisioned to continue its degrading behavior until a zero force level, without any considerations of post-peak hardening associated with gap closure and/or experimental setup.

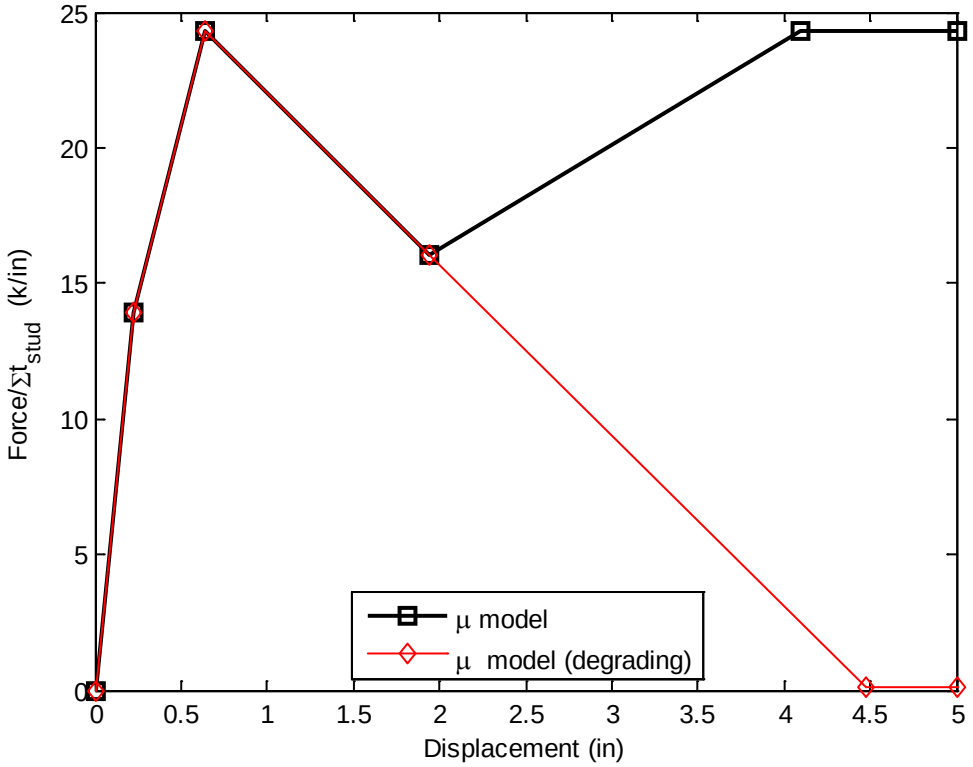

Figure 6.44 PW model backbones: μ (mean) model and μ model with degrading branch.

In comparing the effect of PW degradation, the interstory drift and floor acceleration response are examined considering RC-8 with minimum and maximum wall lengths considering the mean response (with and without degradation). The normalized maximum interstory drift moving averages are compared on a per floor basis are in Figure 6.45 - Figure 6.48. On all floors, the interstory drift is initially underestimated with the general trend of lower interstory drift estimates if the PW model degrades. For most floors, the difference between the effect of degradation is minimal; however, the degrading PW model effects in the case of the maximum partition wall length is most noted in the upper stories, where spectral demands vary from moderate levels below the design earthquake (DE) to values exceeding the maximum considered earthquake (MCE). For the top floor between spectral demands associated with DE and MCE levels, the degrading model estimated drifts close to that of the bare building, while the PW model without degradation produced greater interstory drift values by 30%.

In like fashion, the normalized maximum floor acceleration moving averages are illustrated on a per level basis (Figure 6.49- Figure 6.52). The effect of the post-peak hardening is most minimal, with differences between the non-degrading and degrading model around 10%. Due to the low interstory drifts observed in the simulation (<2%), the difference between the degrading and non-degrading model is not fully characterized as it is anticipated it would have a more pronounced effect when the interstory drift exceeds 2%.

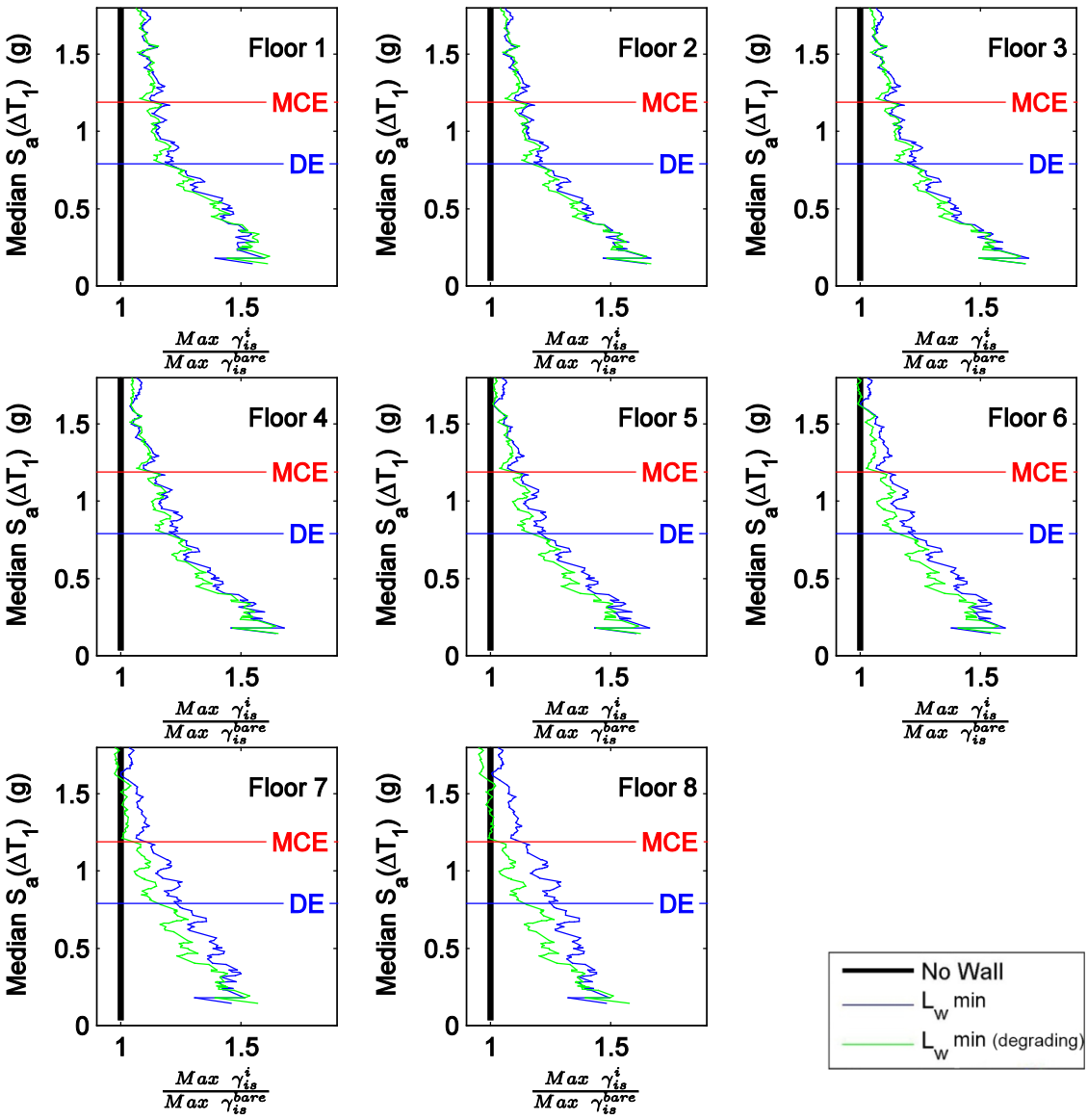

Figure 6.45 Normalized maximum interstory drift moving average curves for RC-8 with cases of no wall and the minimum wall length considering post-peak hardening and a degrading model against median spectral accelerations over ΔT_1.

Note: where $\Delta T_1 = \langle T_1^{initial}, T_1^{final} \rangle$ and DE and MCE represent design spectral acceleartions of the building (at $T_1^{initial}$) for the design and maximum considered earthquakes.

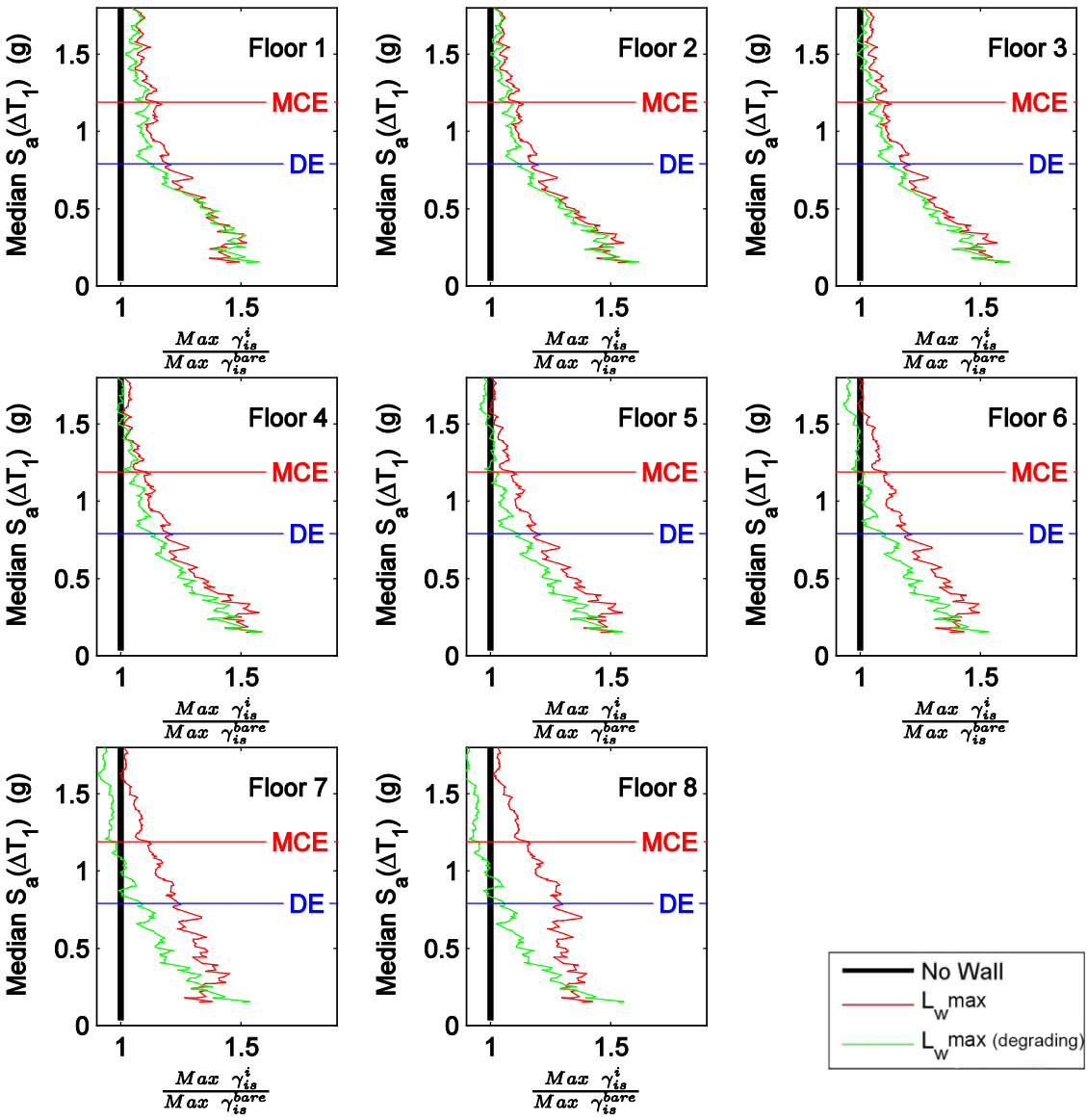

Figure 6.46 Normalized maximum interstory drift moving average curves for RC-8 with cases of no wall and the maximum wall length considering post-peak hardening and a degrading model against median spectral accelerations over ΔT_1.

Note: where $\Delta T_1 = \langle T_1^{initial}, T_1^{final} \rangle$ and DE and MCE represent design spectral acceleartions of the building (at $T_1^{initial}$) for the design and maximum considered earthquakes.

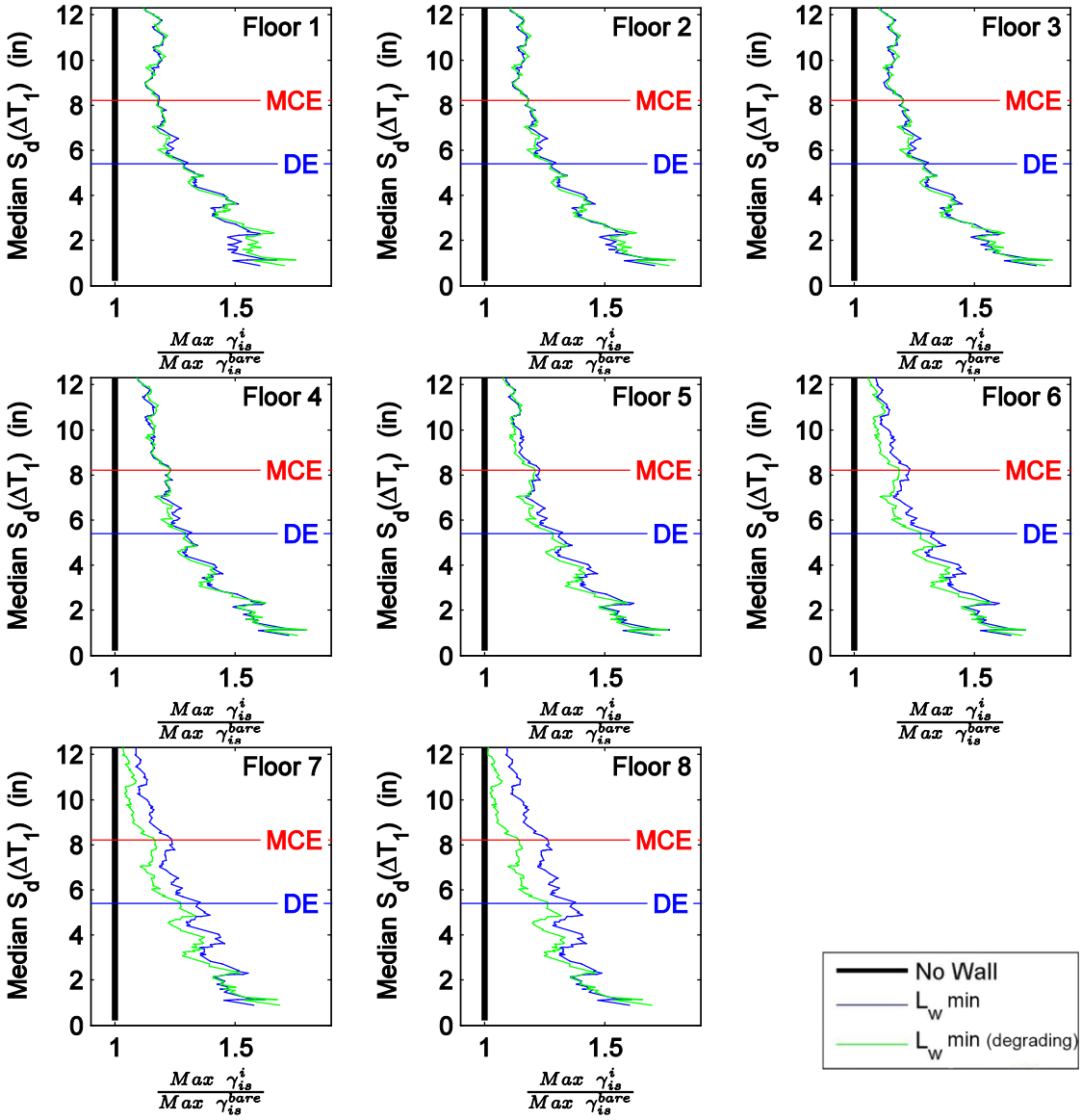

Figure 6.47 Normalized maximum interstory drift moving average curves for RC-8 with cases of no wall and the minimum wall length considering post-peak hardening and a degrading model against median spectral displacement over ΔT_1.

Note: where $\Delta T_1 = \langle T_1^{initial}, T_1^{final} \rangle$ and DE and MCE represent design spectral acceleartions of the building (at $T_1^{initial}$) for the design and maximum considered earthquakes.

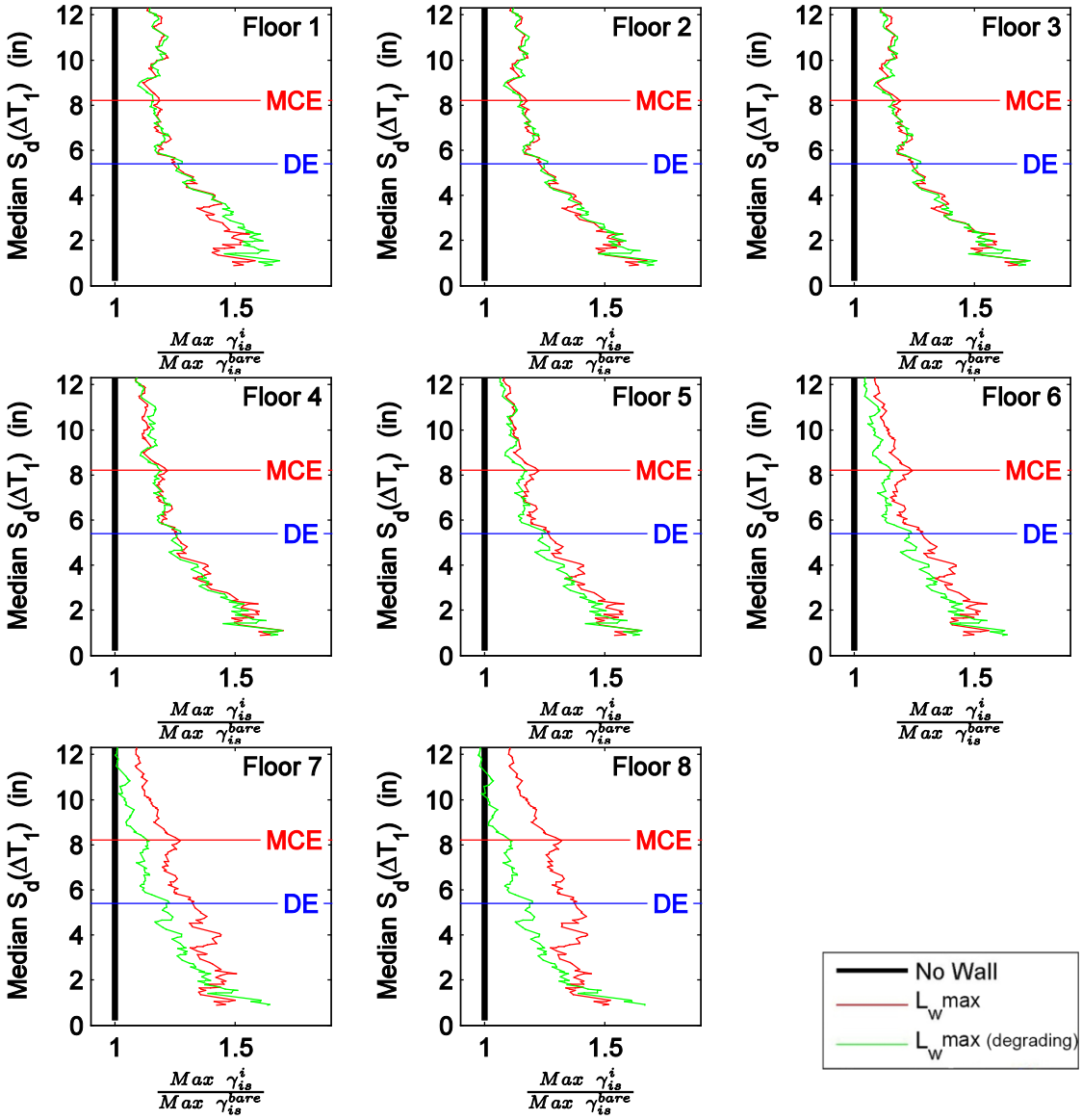

Figure 6.48 Normalized maximum interstory drift moving average curves for RC-8 with cases of no wall and the maximum wall length considering post-peak hardening and a degrading model against median spectral displacement over ΔT_1.

Note: where $\Delta T_1 = \langle T_1^{initial}, T_1^{final} \rangle$ and DE and MCE represent design spectral acceleartions of the building (at $T_1^{initial}$) for the design and maximum considered earthquakes.

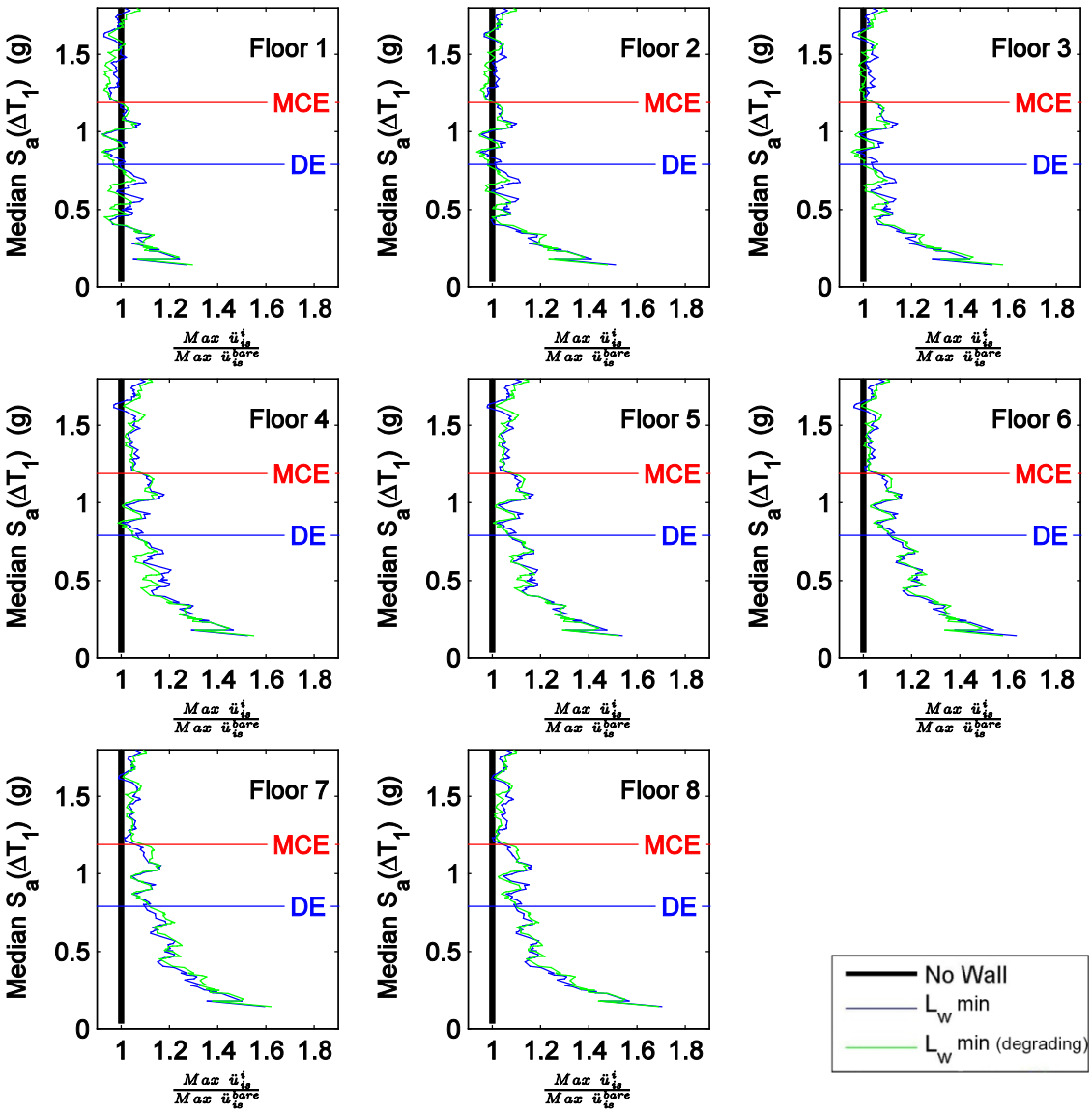

Figure 6.49 Normalized maximum floor acceleration moving average curves for RC-8 with cases of no wall and the minimum wall length considering post-peak hardening and a degrading model against median spectral acceleration over ΔT_1.

Note: where $\Delta T_1 = \langle T_1^{initial}, T_1^{final} \rangle$ and DE and MCE represent design spectral acceleartions of the building (at $T_1^{initial}$) for the design and maximum considered earthquakes.

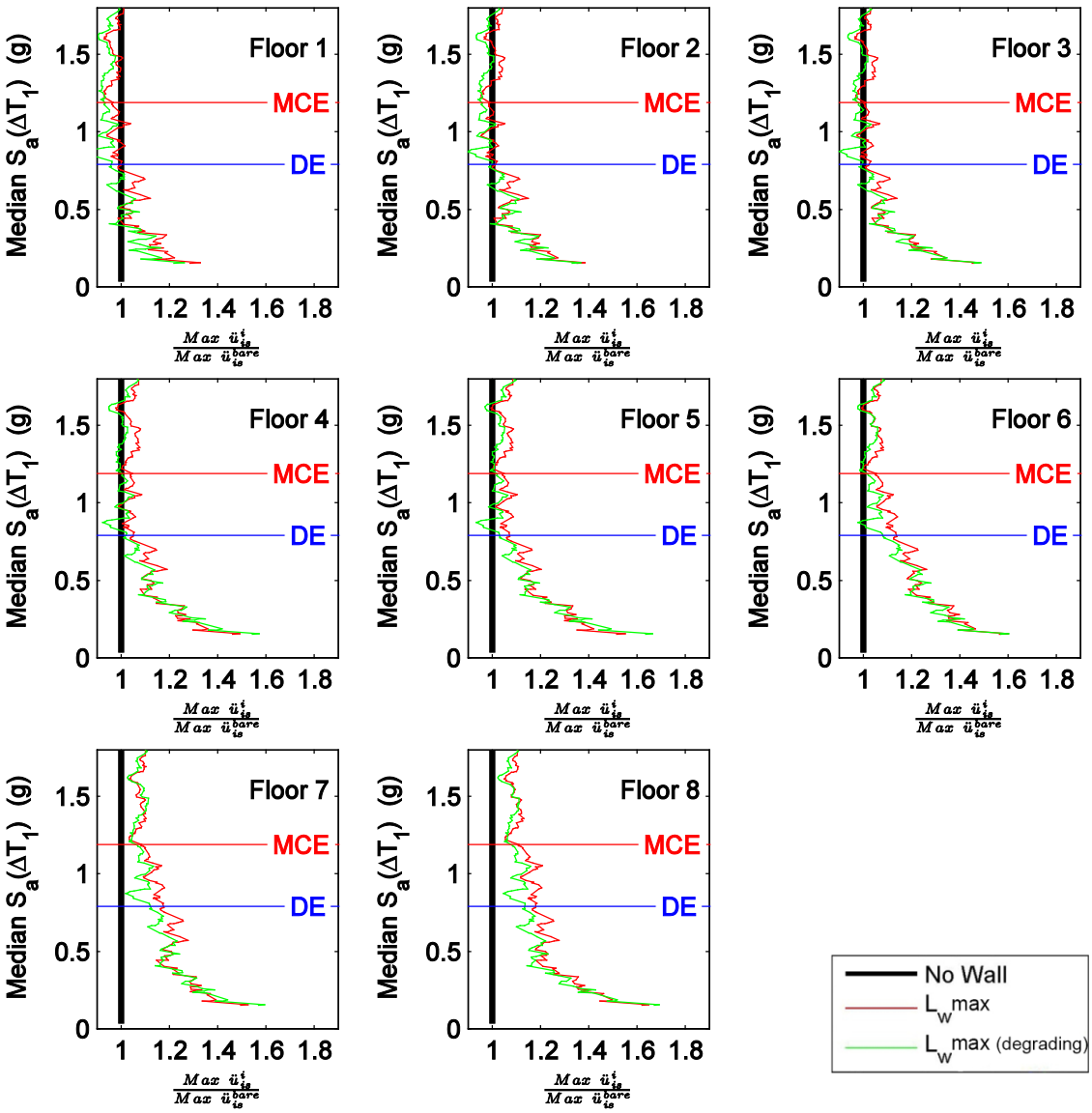

Figure 6.50 Normalized maximum floor acceleration moving average curves for RC-8 with cases of no wall and the maximum wall length considering post-peak hardening and a degrading model against median spectral acceleration over ΔT_1.

Note: where $\Delta T_1 = \langle T_1^{initial}, T_1^{final} \rangle$ and DE and MCE represent design spectral acceleartions of the building (at $T_1^{initial}$) for the design and maximum considered earthquakes.

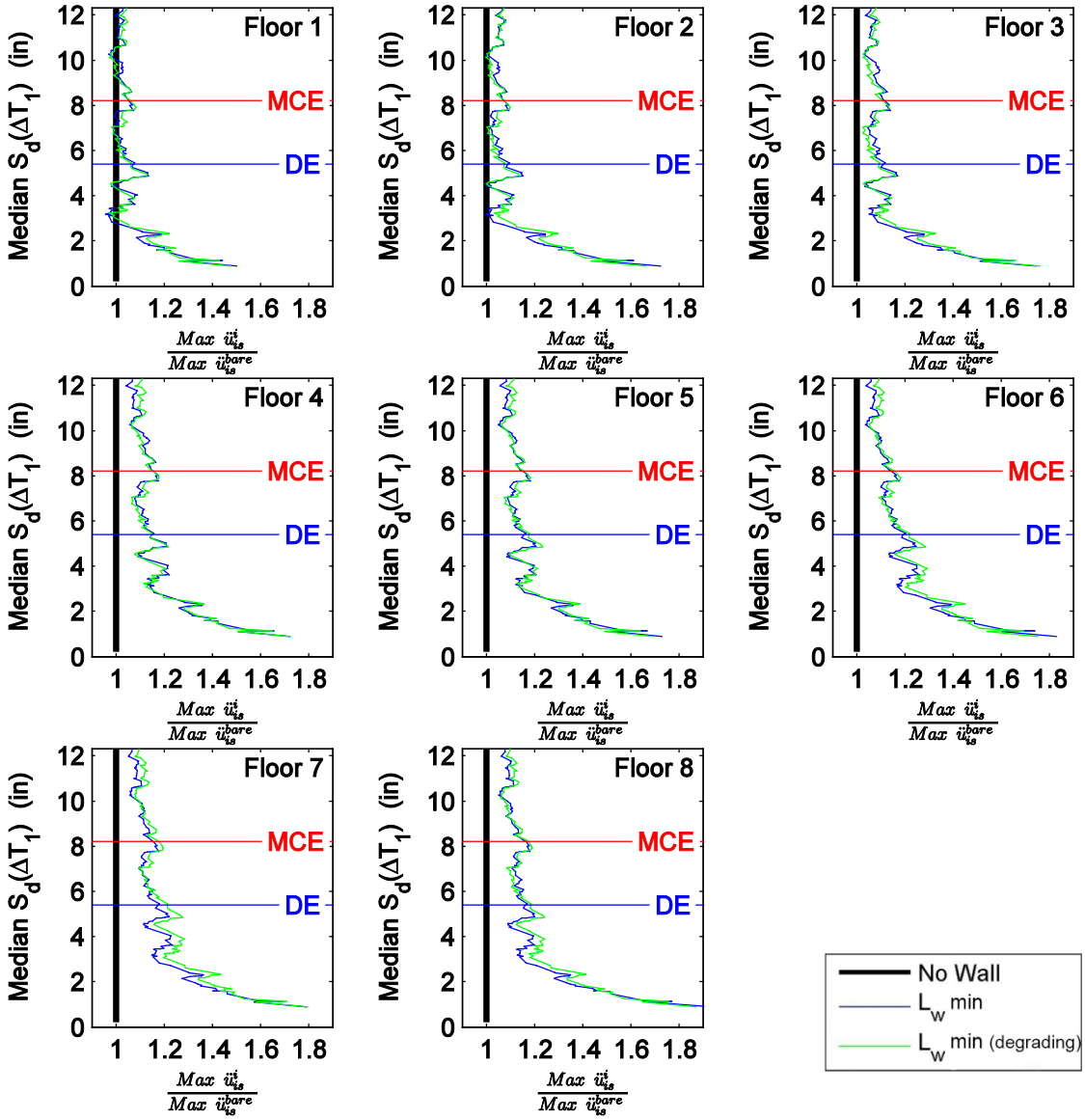

Figure 6.51 Normalized maximum floor acceleration moving average curves for RC-8 with cases of no wall and the minimum wall length considering post-peak hardening and a degrading model against median spectral displacement over ΔT_1.

Note: where $\Delta T_1 = \langle T_1^{initial}, T_1^{final} \rangle$ and DE and MCE represent design spectral acceleartions of the building (at $T_1^{initial}$) for the design and maximum considered earthquakes.

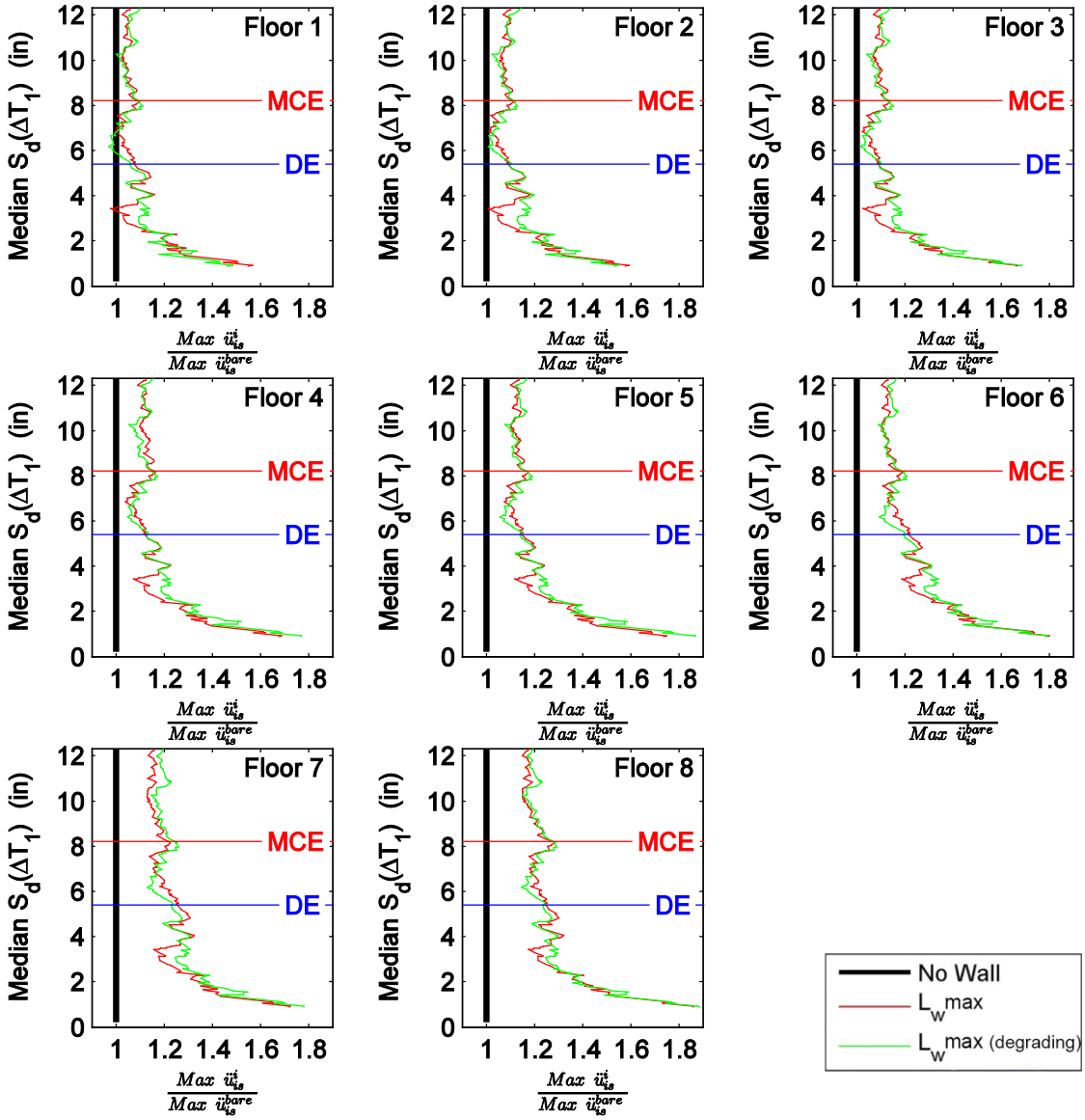

Figure 6.52 Normalized maximum floor acceleration moving average curves for RC-8 with cases of no wall and the maximum wall length considering post-peak hardening and a degrading model against median spectral displacements over ΔT_1.

Note: where $\Delta T_1 = \langle T_1^{initial}, T_1^{final} \rangle$ and DE and MCE represent design spectral acceleartions of the building (at $T_1^{initial}$) for the design and maximum considered earthquakes.

6.4.4 RC-8 Model: Effect of Wall Placement

In previous sections, the PW was placed on all floors throughout the building model; however, this section compares the effect of variable placement within RC-8 using the minimum wall length (mean model parameters). For comparative reasons, three coupled cases are considered to assess the effect of wall placement: PWs are placed on every floor level (denoted all floors), the PW is removed from the bottom floor (denoted no wall first floor (FF)), and the PW is removed from the top level (denoted no wall top level (TL)). The wall was removed from the first floor to examine its effect if a lobby or entry way is considered, and similarly no wall on the top floor if an open space or utility room is present. Using these cases, the maximum interstory drift and maximum floor acceleration responses are examined. The detailed moving averages for this case are found in Appendix C. Figure 6.53 and Figure 6.54 illustrate the normalized maximum interstory drift moving averages per floor. In both figures, it is noted that varying the wall placement has a minimal effect on the difference for maximum interstory drift (within 5%) up to the design earthquake (DE) spectral demands. Noticeable differences are found at the first and top stories due to the absence of a wall on the first story or the absence of a wall on the top level, respectively; however, little effect is observed throughout the building.

In like fashion, the normalized maximum floor acceleration moving averages are illustrated on a per level basis (Figure 6.55 and Figure 6.56). The effect of wall placements on the floor accelerations are observed again to be minimal (within 3-5%) throughout the range of spectral demands. Minimal influence on the floor acceleration responses for all floors is observed for both the absence of the first floor wall or the top floor wall. This is in contrast with the interstory drift floor responses where the effects were noticeable on the floors with no wall.

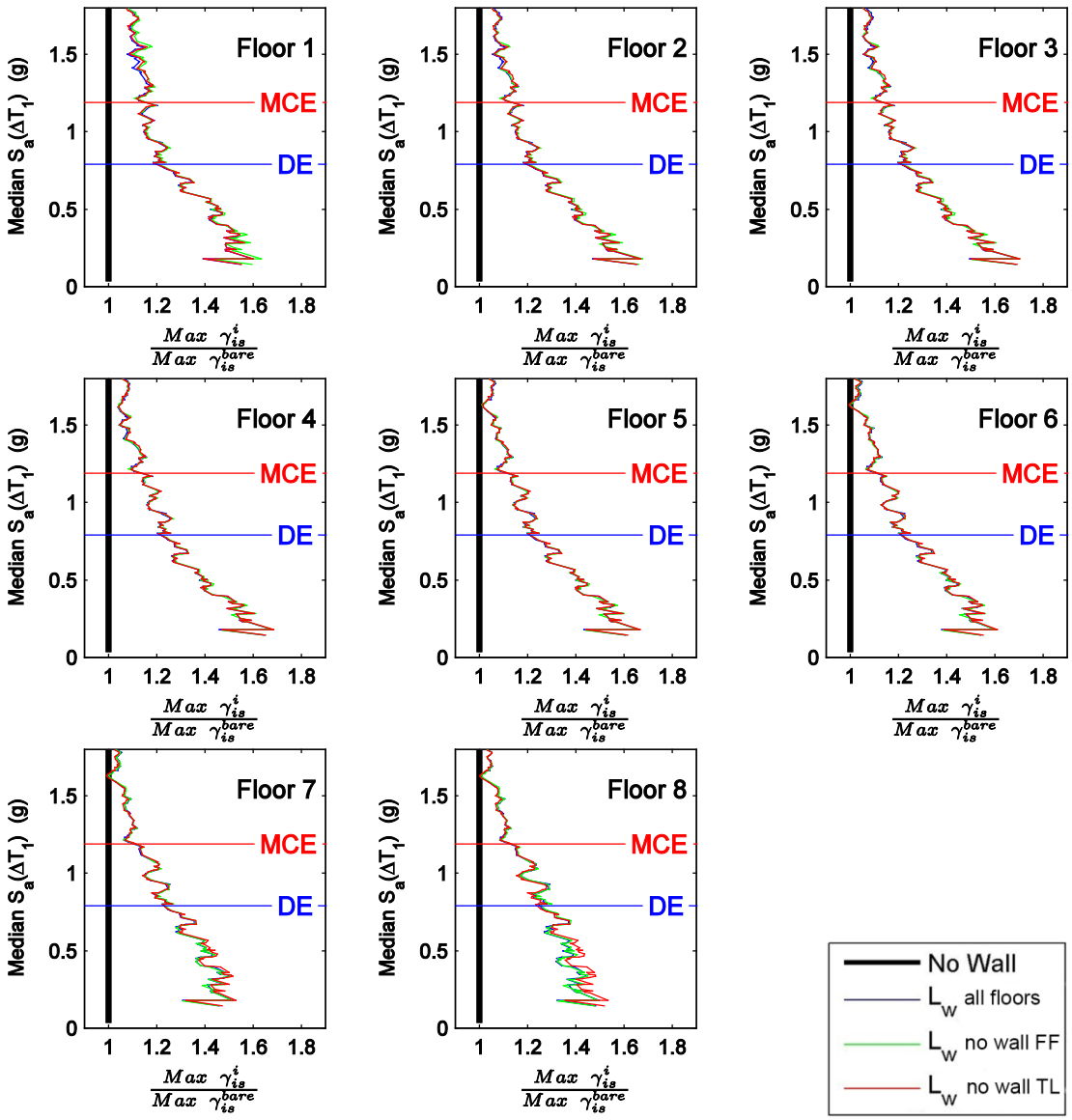

Figure 6.53 Normalized maximum interstory drift moving average curves for RC-8 considering the cases of wall placement: no wall, minimum wall length (all floors), no wall first floor, and no wall on top level against median spectral acceleration over ΔT_1.

Note: where $\Delta T_1 = \langle T_1^{initial}, T_1^{final} \rangle$ and DE and MCE represent design spectral acceleartions of the building (at $T_1^{initial}$) for the design and maximum considered earthquakes.

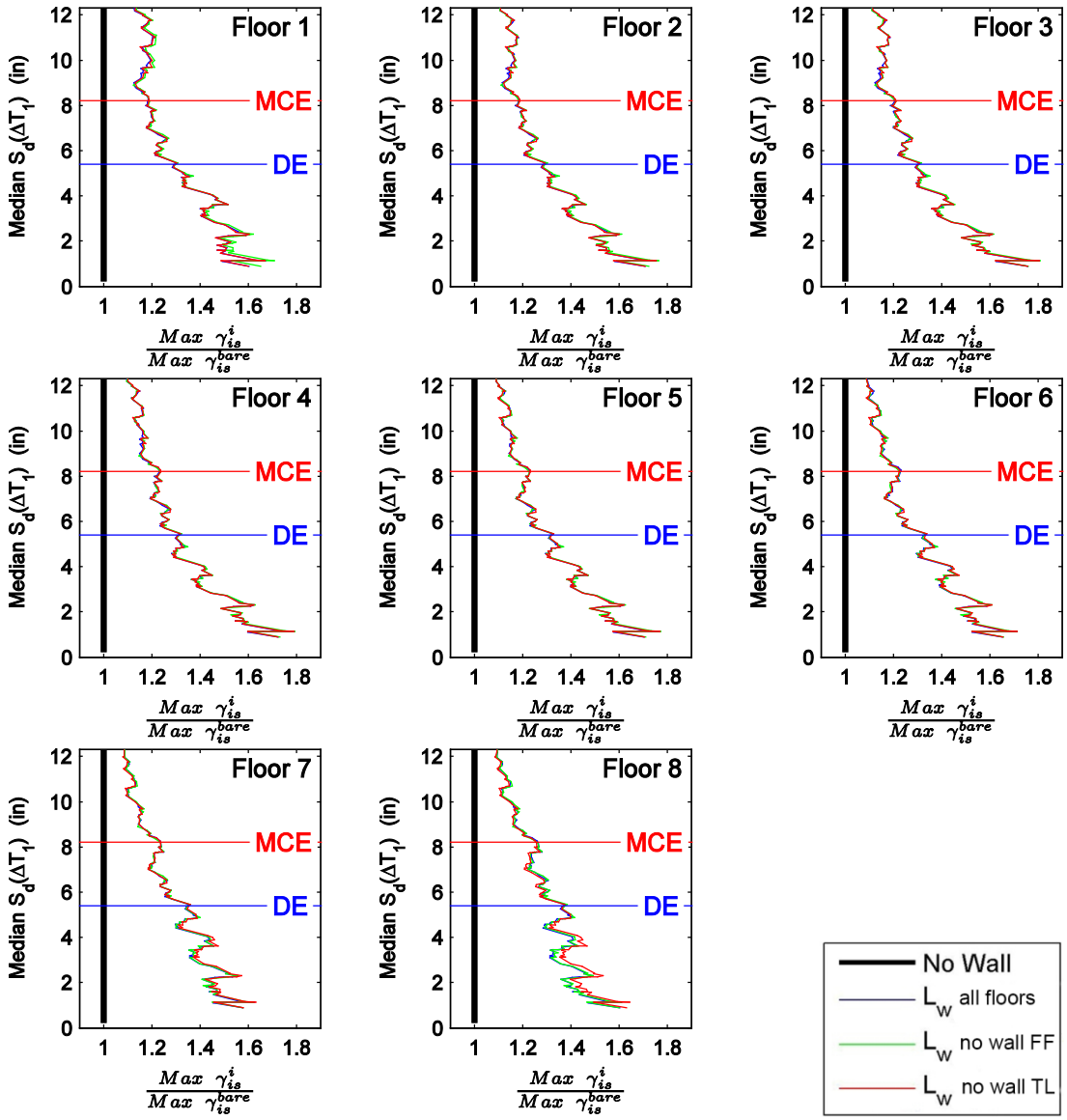

Figure 6.54 Normalized maximum interstory drift moving average curves for RC-8 considering the cases of wall placement: no wall, minimum wall length (all floors), no wall first floor, and no wall on top level against median spectral displacement over ΔT_1. Note: where $\Delta T_1 = \langle T_1^{initial}, T_1^{final} \rangle$ and DE and MCE represent design spectral acceleartions of the building (at $T_1^{initial}$) for the design and maximum considered earthquakes.

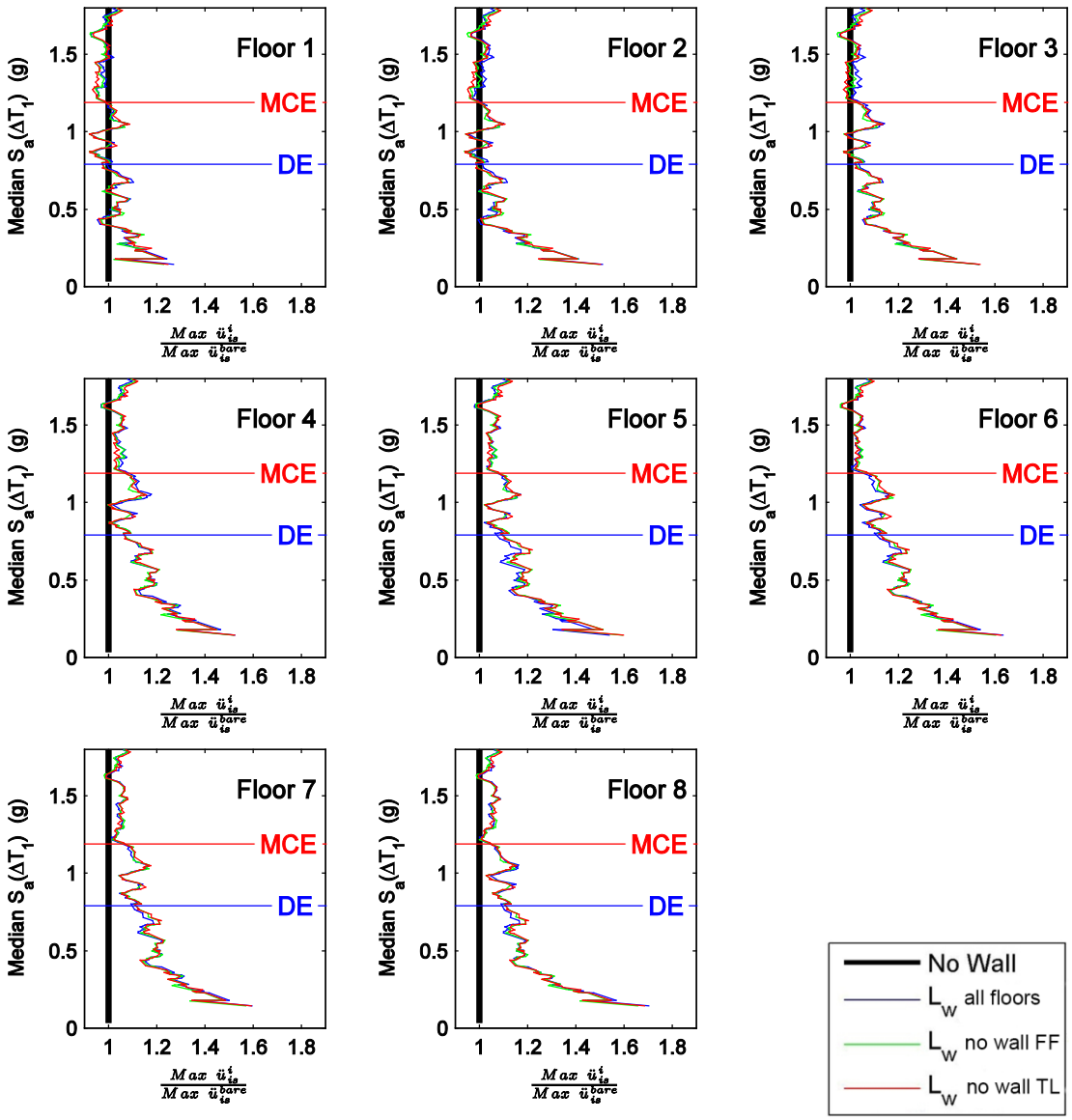

Figure 6.55 Normalized maximum floor acceleration moving average curves for RC-8 considering the cases of wall placement: no wall, minimum wall length (all floors), no wall first floor, and no wall on top level against median spectral acceleration over ΔT_1.

Note: where $\Delta T_1 = \langle T_1^{initial}, T_1^{final} \rangle$ and DE and MCE represent design spectral acceleartions of the building (at $T_1^{initial}$) for the design and maximum considered earthquakes.

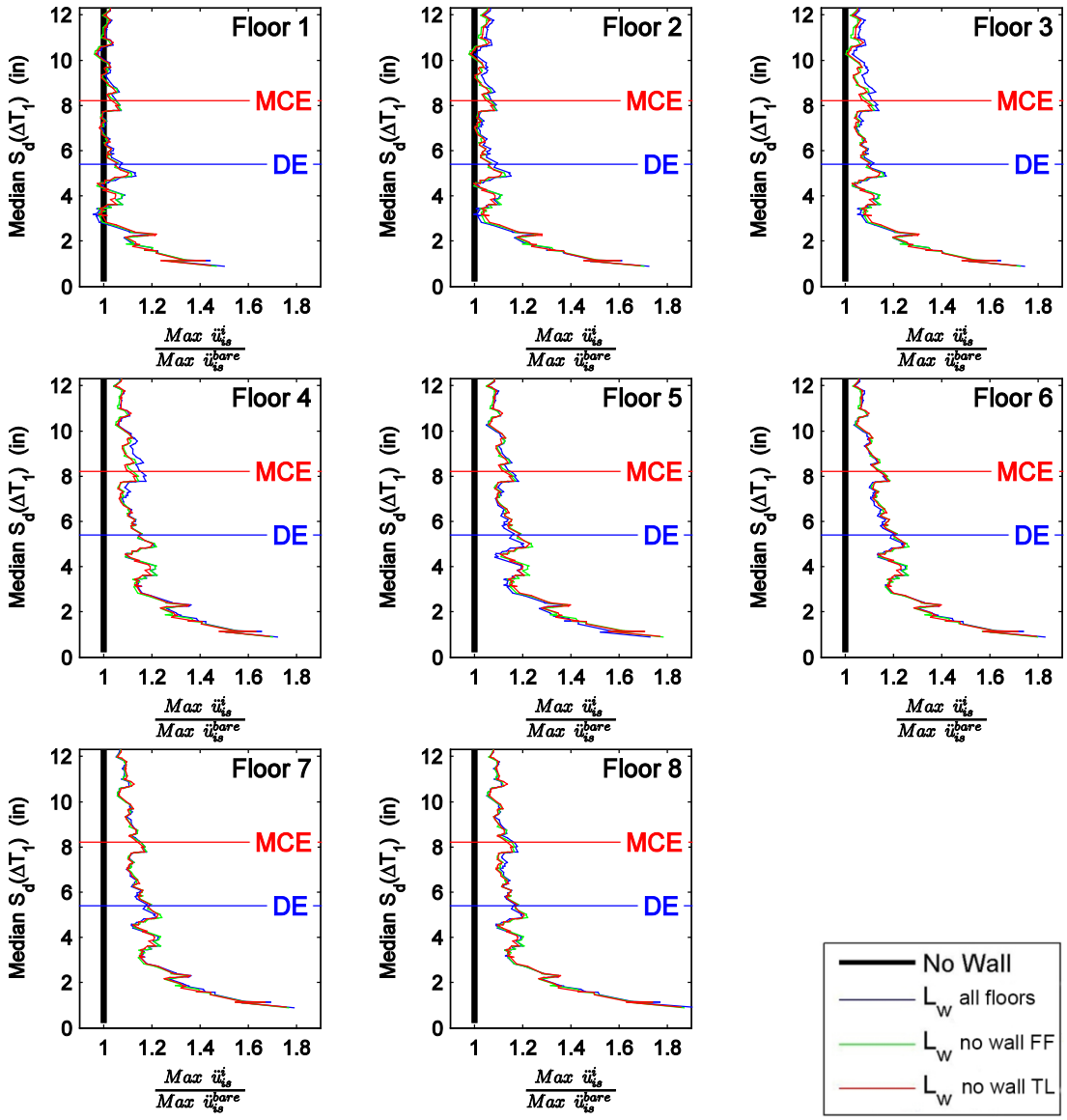

Figure 6.56 Normalized maximum floor acceleration moving average curves for RC-8 considering the cases of wall placement: no wall, minimum wall length (all floors), no wall first floor, and no wall on top level against median spectral displacement over ΔT_1.

Note: where $\Delta T_1 = \langle T_1^{initial}, T_1^{final} \rangle$ and DE and MCE represent design spectral acceleartions of the building (at $T_1^{initial}$) for the design and maximum considered earthquakes.

6.4.5 RC-20 Model: Effect of PW

In comparing the effect of placing PWs within a building, RC-20, using the minimum wall length (mean model parameters), the maximum interstory drift and maximum floor acceleration response are examined. The detailed moving averages for this case are found in Appendix C. Figure 6.57 and Figure 6.58 illustrate the normalized maximum interstory drift moving averages per floor. In both figures, it is noted that for this case interstory drift is initially severely underestimated (two-fold for some floor levels) at low spectral demands associated with a service level earthquake when compared to that of the bare building (no wall) case. The effect of the PW reduces significantly (20-30%) at spectral demands associated with the design earthquake (DE) and maximum considered earthquake (MCE).

In like fashion, the normalized maximum floor acceleration moving averages are illustrated on a per level basis (Figure 6.59 and Figure 6.60). Initially interstory drifts of the coupled building-partition wall system are over 200% greater than the bare building (no wall) at spectral demands associated with a service level earthquake. After the PW significantly degrades, the floor accelerations are generally within 20-30% of the bare building case near the DE and MCE spectral demands. Around the DE and MCE spectral demands, the floor acceleration response is both under and overestimated on a floor to floor basis.

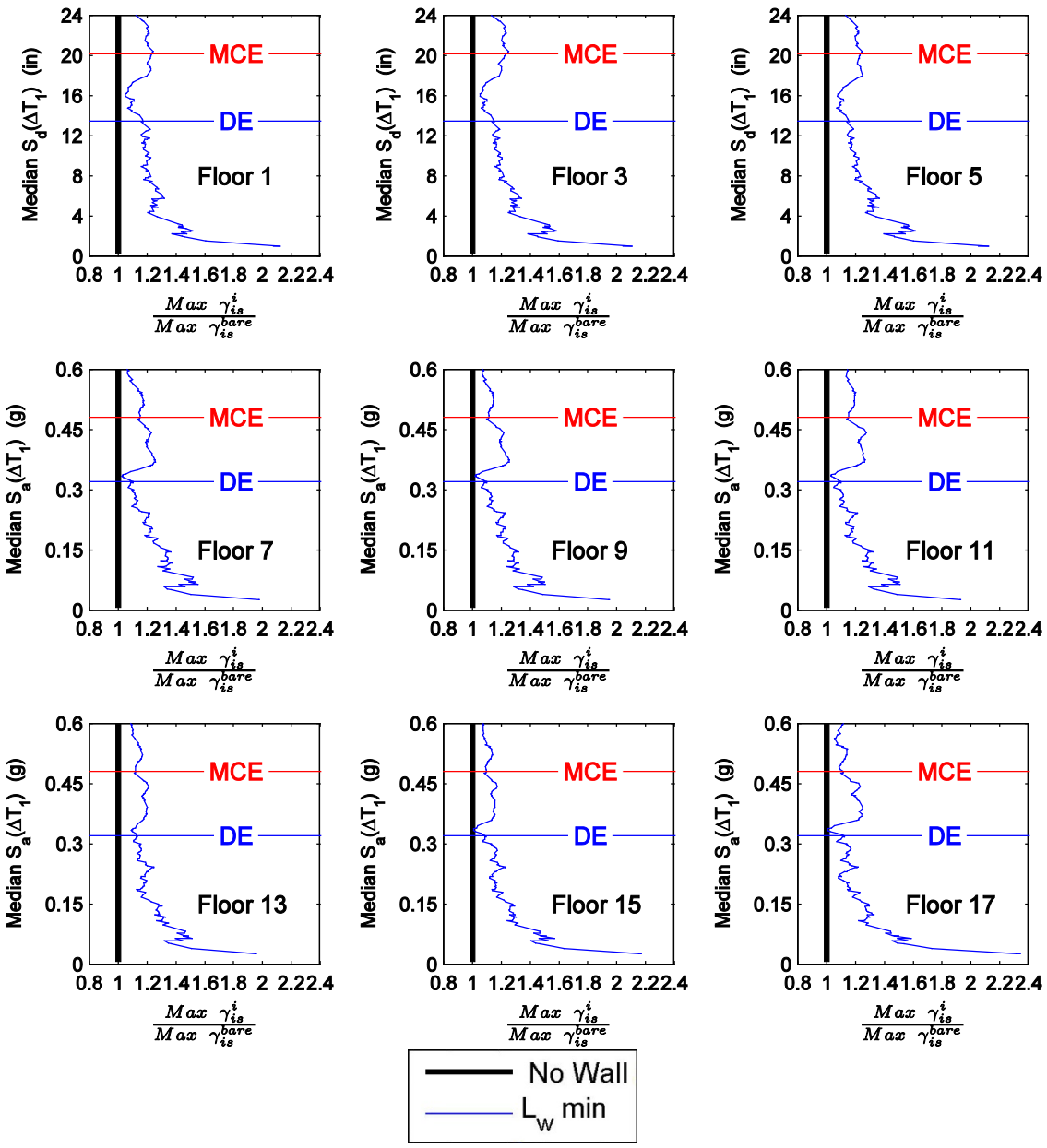

Figure 6.57 Normalized maximum interstory drift moving average curves for RC-20 with cases of no wall and minimum wall length considering mean model parameters against median spectral acceleration over ΔT_1.

Note: select floor levels are shown, reference appendix C for all floors, $\Delta T_1 = \langle T_1^{initial}, T_1^{final} \rangle$ and DE and MCE represent design spectral acceleartions of the building (at $T_1^{initial}$) for the design and maximum considered earthquakes.

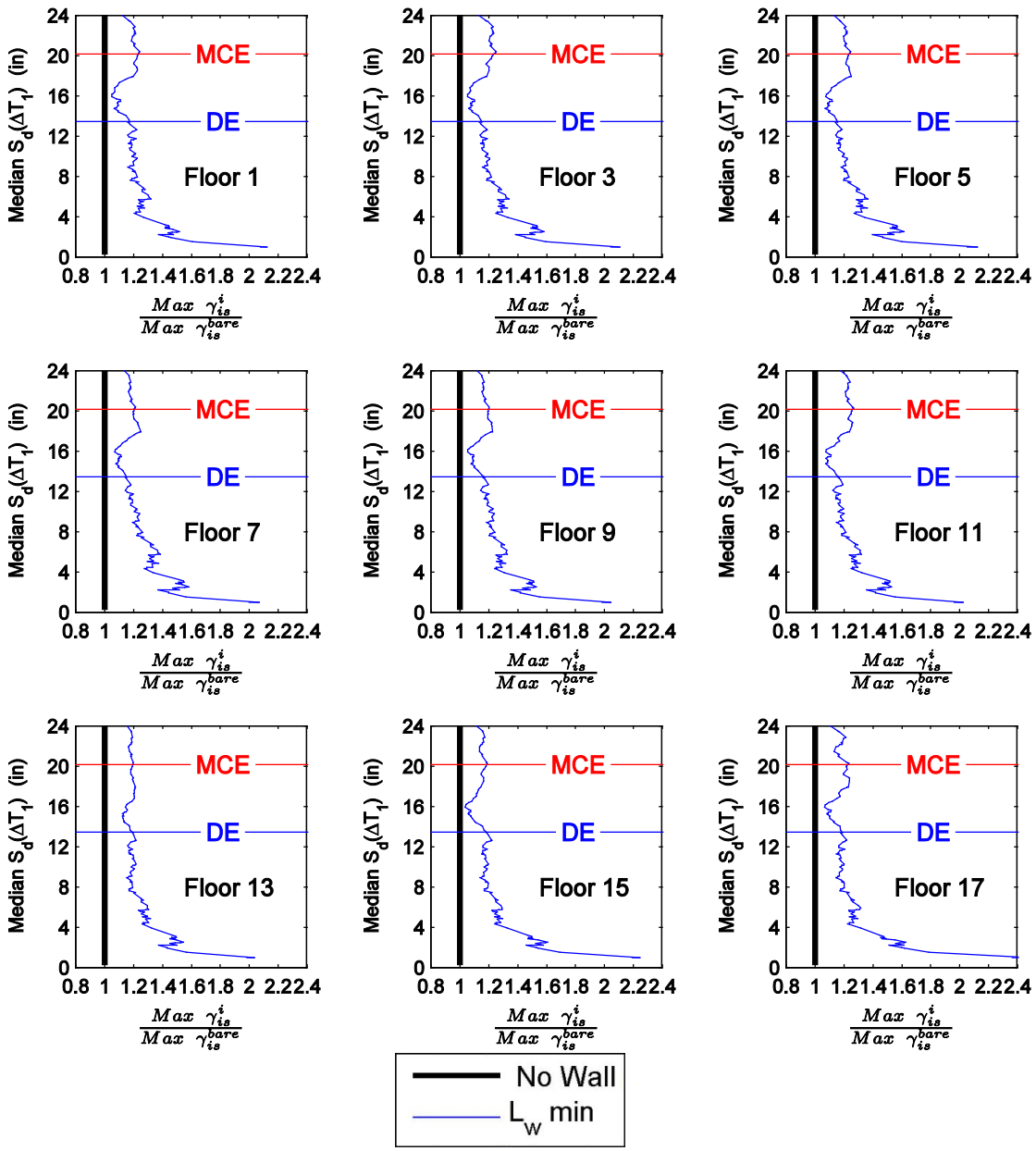

Figure 6.58 Normalized maximum interstory drift moving average curves for RC-20 with cases of no wall and minimum wall length considering mean model parameters against median spectral displacement over ΔT_1.

Note: select floor levels are shown, reference appendix C for all floors, $\Delta T_1 = \langle T_1^{initial}, T_1^{final} \rangle$ and DE and MCE represent design spectral acceleartions of the building (at $T_1^{initial}$) for the design and maximum considered earthquakes.

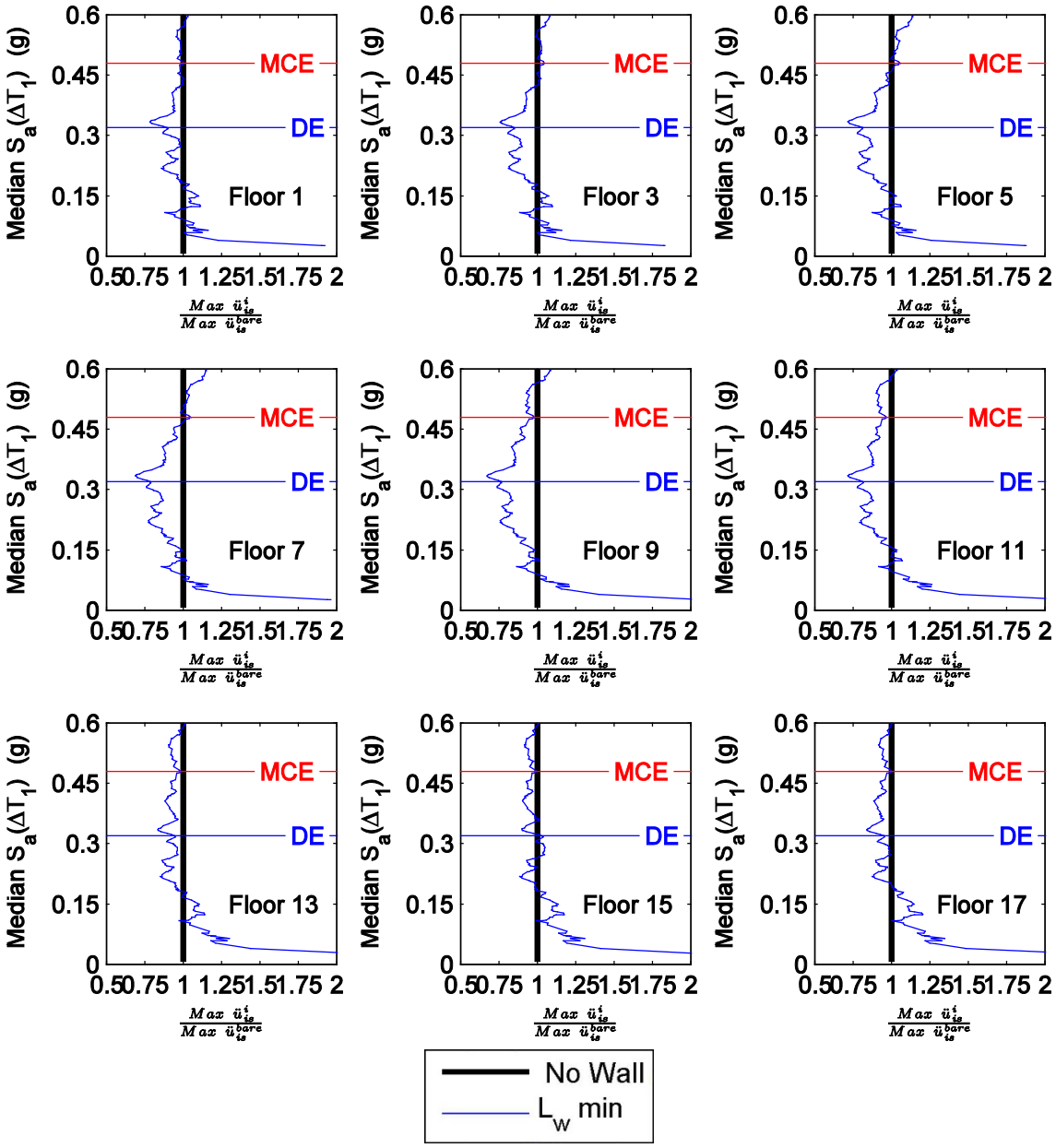

Figure 6.59 Normalized maximum floor acceleration moving average curves for RC-20 with cases of no wall and minimum wall length considering mean model parameters against median spectral acceleration over ΔT_1.

Note: select floor levels are shown, reference appendix C for all floors, $\Delta T_1 = \langle T_1^{initial}, T_1^{final} \rangle$ and DE and MCE represent design spectral acceleartions of the building (at $T_1^{initial}$) for the design and maximum considered earthquakes.

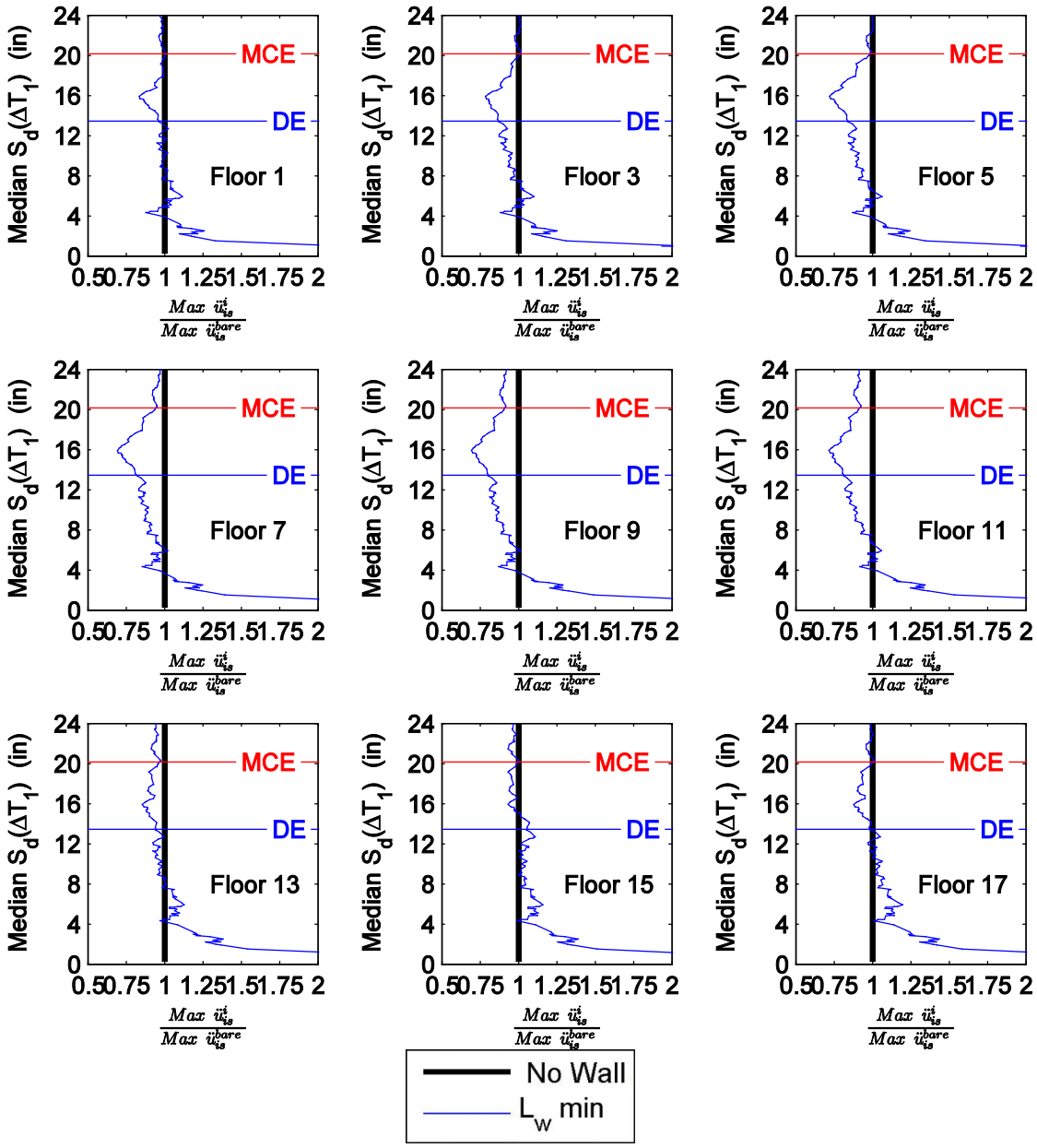

Figure 6.60 Normalized maximum floor acceleration moving average curves for RC-20 with cases of no wall and minimum wall length considering mean model parameters against median spectral displacement over ΔT_1.

Note: select floor levels are shown, reference appendix C for all floors, $\Delta T_1 = \langle T_1^{initial}, T_1^{final} \rangle$ and DE and MCE represent design spectral acceleartions of the building (at $T_1^{initial}$) for the design and maximum considered earthquakes.

6.4.6 S-3H Model: Effect of Wall Length

In comparing the effect of the PW on a different building mode, S3-H is selected with the minimum and maximum wall lengths considering the mean model parameters. S3-H is a redesigned hospital building, where the PW installation is typical of experimental group 2 indicated by thicker vertical studs and smaller stud spacing. To examine the effect of the PW on this building, the interstory drift and floor acceleration response are examined. Figure 6.61 and Figure 6.62 illustrate the normalized maximum interstory drift moving averages per floor. In both figures, it is noted that interstory drift is underestimated for both cases. When the spectral demands are below that of the design earthquake (DE), the interstory drift values from 80% greater when the minimum wall length case to values between 30-40% at the design earthquake level. At the maximum considered earthquake level (MCE) and greater, the coupled building-partition wall model experienced interstory drift values 20% greater than that of the no wall case.

In like fashion, the normalized maximum floor acceleration moving averages are illustrated on a per floor basis (Figure 6.63 and Figure 6.64). Initial underestimation of the floor acceleration is noted up to 60%, and then after the wall significant degrades, the floor accelerations are both underestimated and overestimated depending on case. In comparing the spectral acceleration to spectral displacement, minimal differences (within 10%) are noted in the trends between each spectral quantity. Typically for values greater than the design earthquake (DE) the floor accelerations are within 10-20% of that of the bare building (no wall) case.

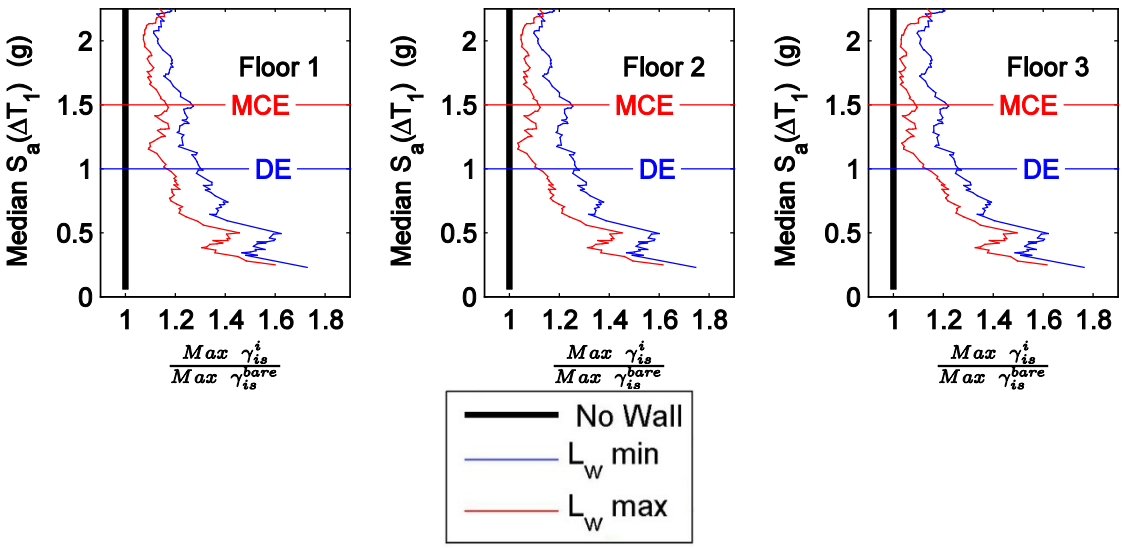

Figure 6.61 Normalized maximum interstory drift moving average curves for S-3H with cases of no wall, minimum wall length, and maximum wall length considering mean model parameters against median spectral acceleration over ΔT_1.

Note: where $\Delta T_1 = \langle T_1^{initial}, T_1^{final} \rangle$ and DE and MCE represent design spectral acceleartions of the building (at $T_1^{initial}$) for the design and maximum considered earthquakes.

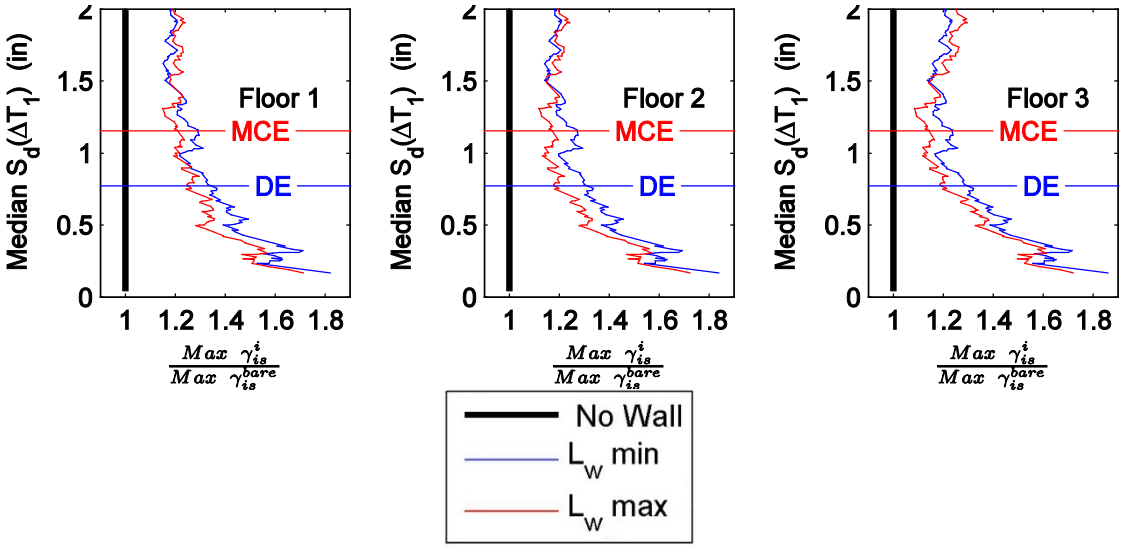

Figure 6.62 Normalized maximum interstory drift moving average curves for S-3H with cases of no wall, minimum wall length, and maximum wall length considering mean model parameters against median spectral displacement over ΔT_1.

Note: where $\Delta T_1 = \langle T_1^{initial}, T_1^{final} \rangle$ and DE and MCE represent design spectral acceleartions of the building (at $T_1^{initial}$) for the design and maximum considered earthquakes.

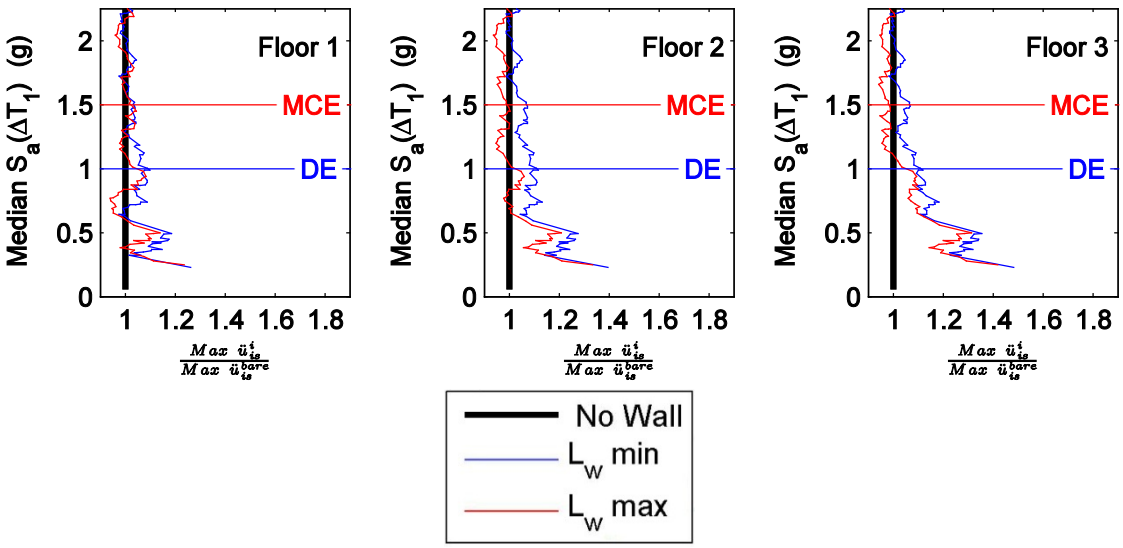

Figure 6.63 Normalized maximum floor acceleration drift moving average curves for S-3H with cases of no wall, minimum wall length, and maximum wall length considering mean model parameters against median spectral acceleration over ΔT_1.

Note: where $\Delta T_1 = \langle T_1^{initial}, T_1^{final} \rangle$ and DE and MCE represent design spectral acceleartions of the building (at $T_1^{initial}$) for the design and maximum considered earthquakes.

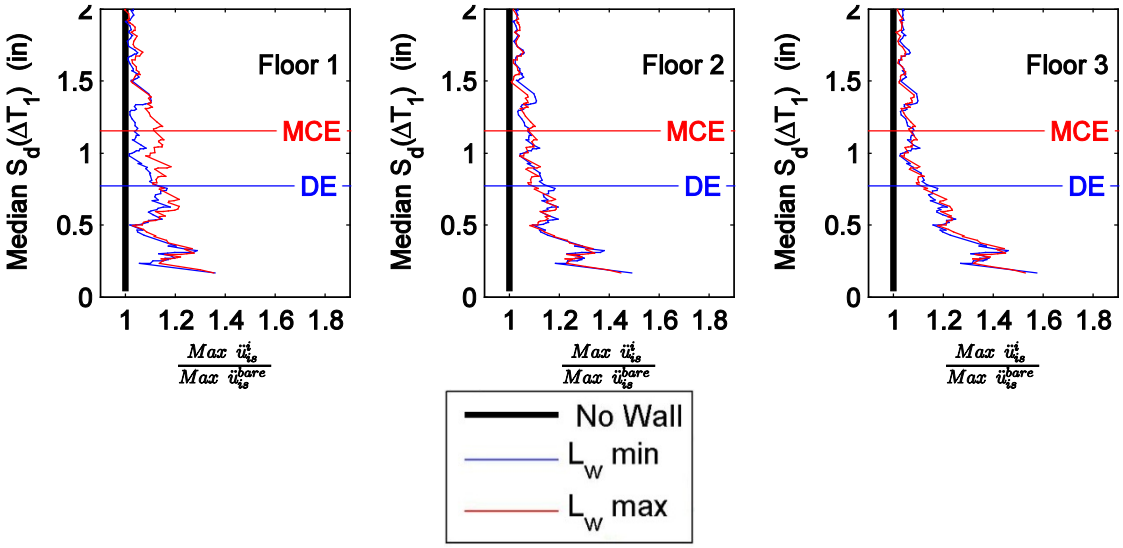

Figure 6.64 Normalized maximum floor acceleration drift moving average curves for S-3H with cases of no wall, minimum wall length, and maximum wall length considering mean model parameters against median spectral acceleration over ΔT_1.

Note: where $\Delta T_1 = \langle T_1^{initial}, T_1^{final} \rangle$ and DE and MCE represent design spectral acceleartions of the building (at $T_1^{initial}$) for the design and maximum considered earthquakes.

6.4.7 S-9 Model: Effect of PW

In comparing the effect of placing PWs within a building, S-9, using the minimum wall length (mean model parameters), the maximum interstory drift and maximum floor acceleration response are examined. The detailed moving averages for this case are found in Appendix C. Figure 6.65 and Figure 6.66 illustrate the normalized maximum interstory drift moving averages per floor. In both figures, it is noted that even for this case interstory drift is initially severely underestimated (up to 50%). The effect of the PW reduces significantly where at spectral demands at the design earthquake level (DE) around 10-20% and reduced even more to 10-20% at the maximum considered earthquake (MCE).

In like fashion, the normalized maximum floor acceleration moving averages are illustrated on a per level basis (Figure 6.67 and Figure 6.68). Initially interstory drifts of the coupled building-partition wall system are up to 80% greater than the bare building (no wall), and then after the wall significant degrades, the floor accelerations are within 10-20% around the DE and MCE spectral demands. Due to the design of S-9, no significant effect of the PW is noted on the upper floors as shown previously in RC-8. This indicates that while the general trends of PWs on the coupled system response are dependent on the design of the building.

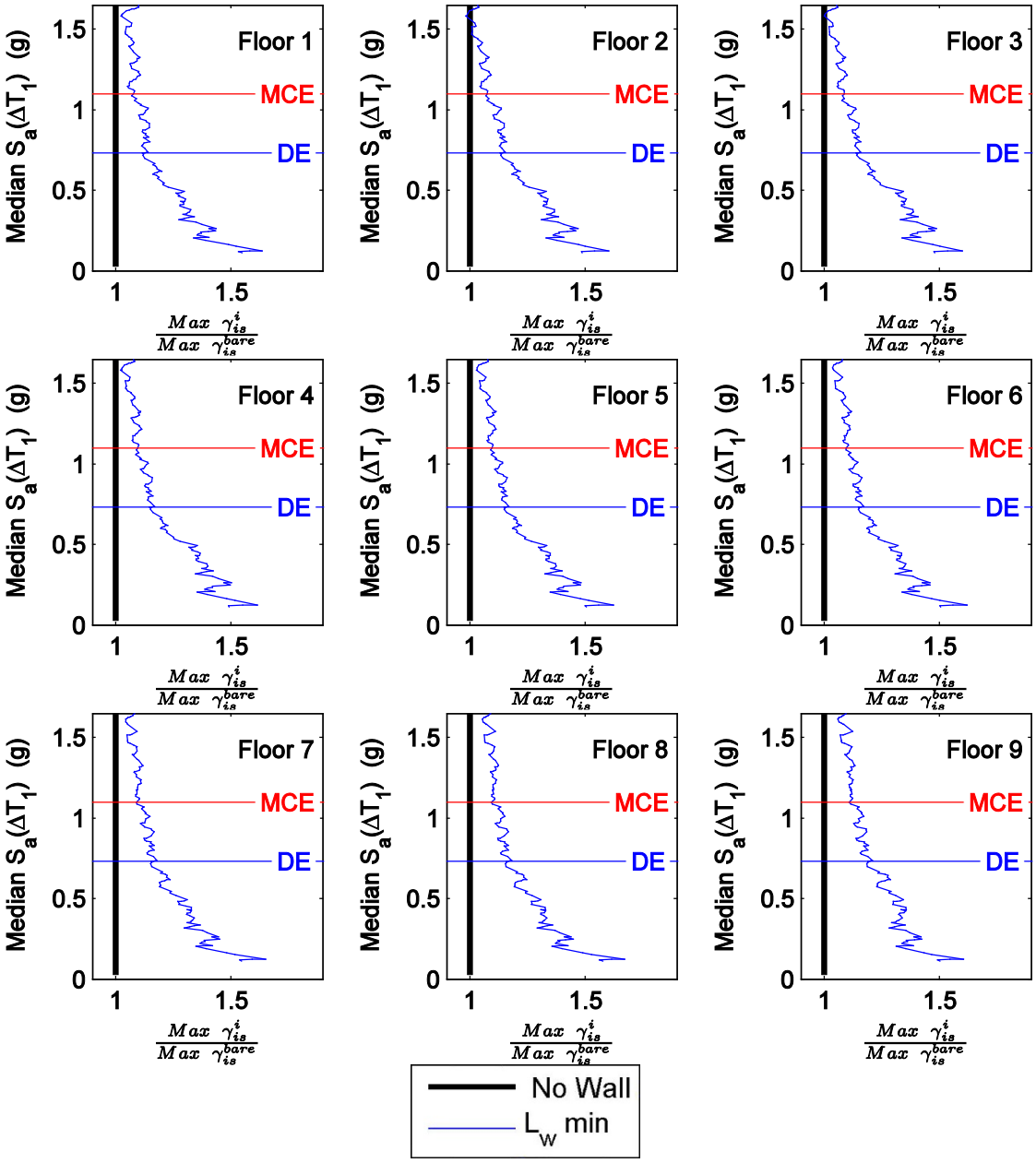

Figure 6.65 Normalized maximum interstory drift moving average curves for S-9 with cases of no wall and minimum wall length considering mean model parameters against median spectral acceleration over ΔT_1.

Note: where $\Delta T_1 = \langle T_1^{initial}, T_1^{final} \rangle$ and DE and MCE represent design spectral acceleartions of the building (at $T_1^{initial}$) for the design and maximum considered earthquakes.

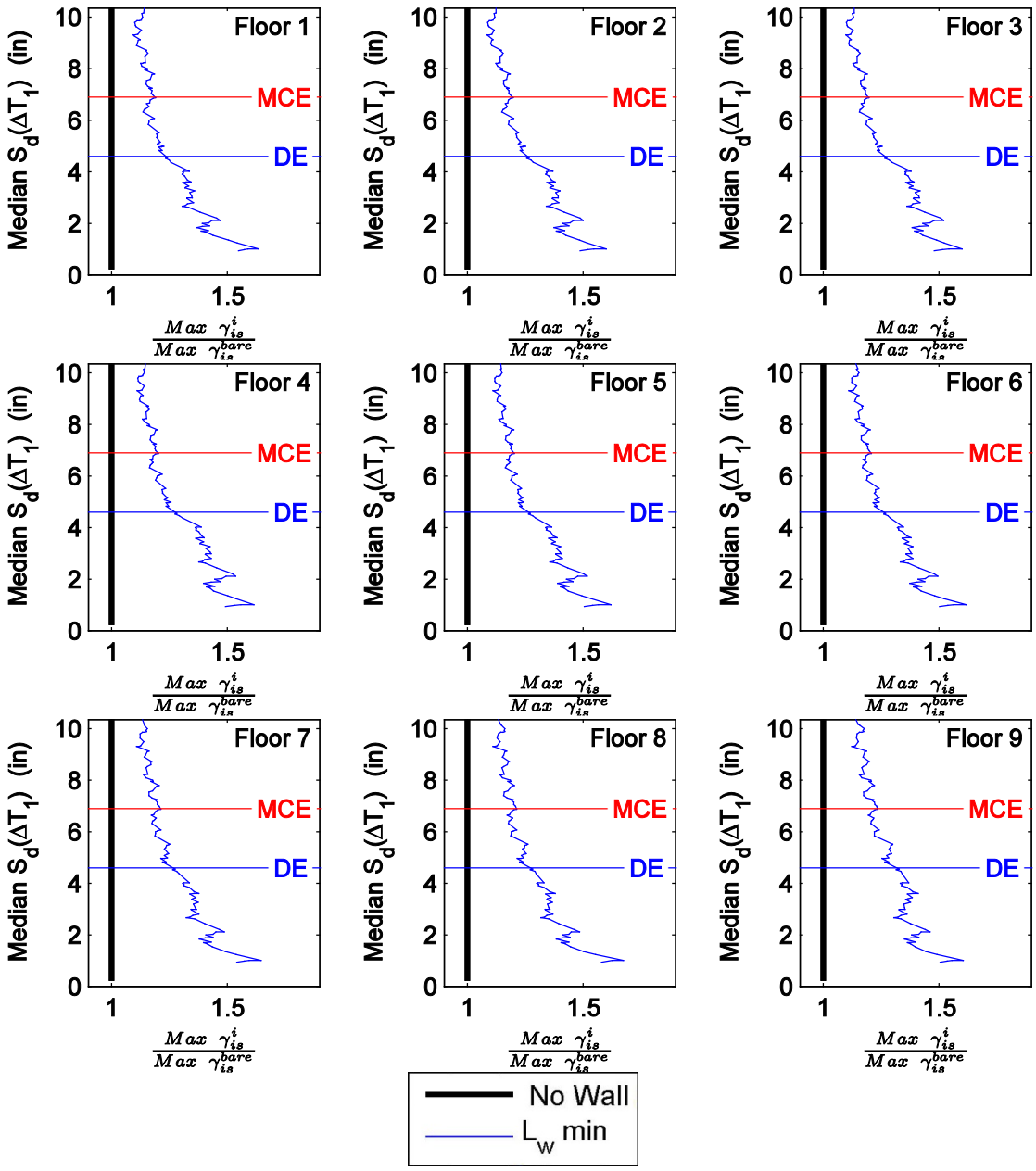

Figure 6.66 Normalized maximum interstory drift moving average curves for S-9 with cases of no wall and minimum wall length considering mean model parameters against median spectral displacement over ΔT_1.

Note: where $\Delta T_1 = \langle T_1^{initial}, T_1^{final} \rangle$ and DE and MCE represent design spectral acceleartions of the building (at $T_1^{initial}$) for the design and maximum considered earthquakes.

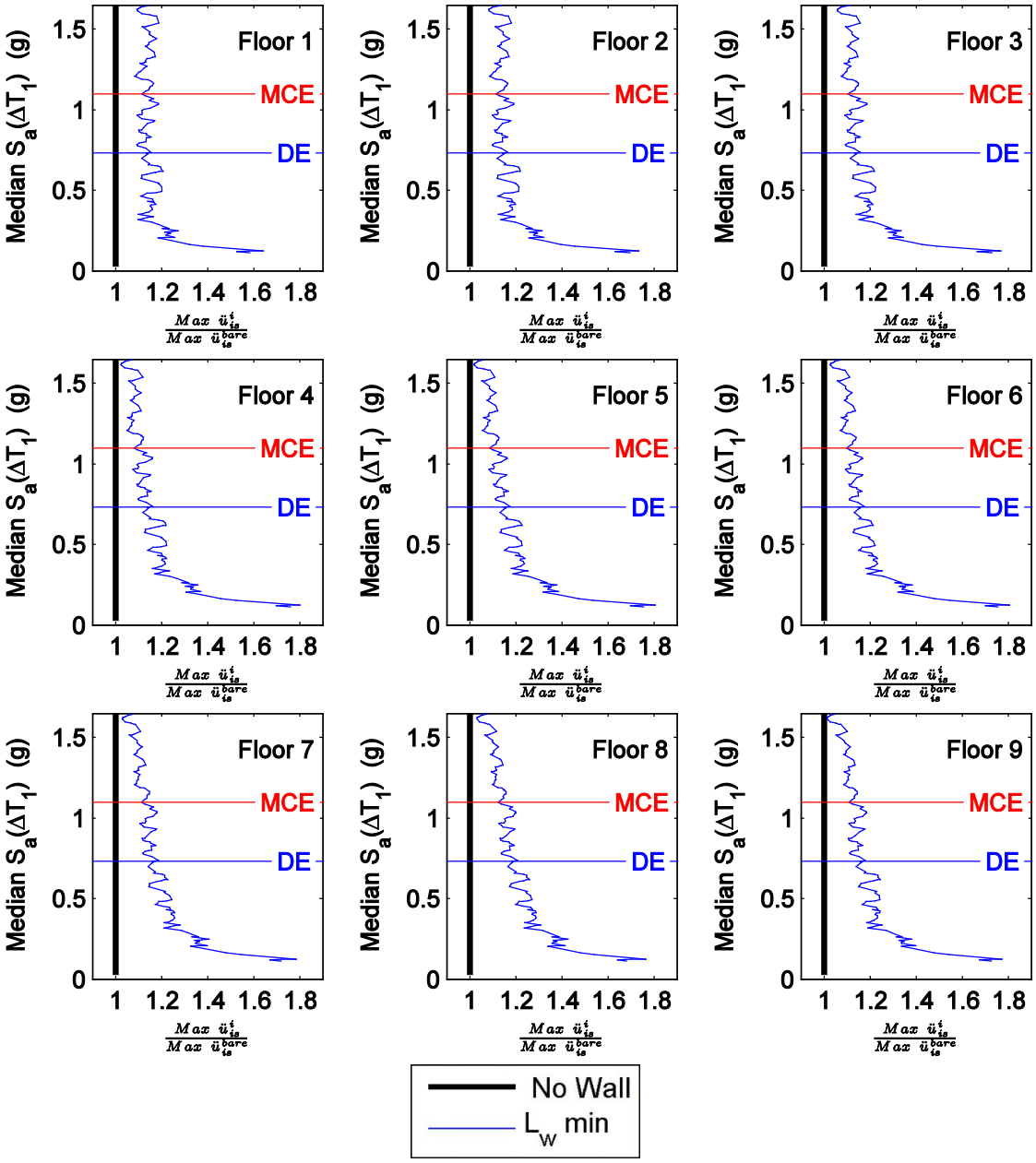

Figure 6.67 Normalized maximum floor acceleration moving average curves for S-9 with cases of no wall and minimum wall length considering mean model parameters against median spectral acceleration over ΔT_1.

Note: where $\Delta T_1 = \langle T_1^{initial}, T_1^{final} \rangle$ and DE and MCE represent design spectral acceleartions of the building (at $T_1^{initial}$) for the design and maximum considered earthquakes.

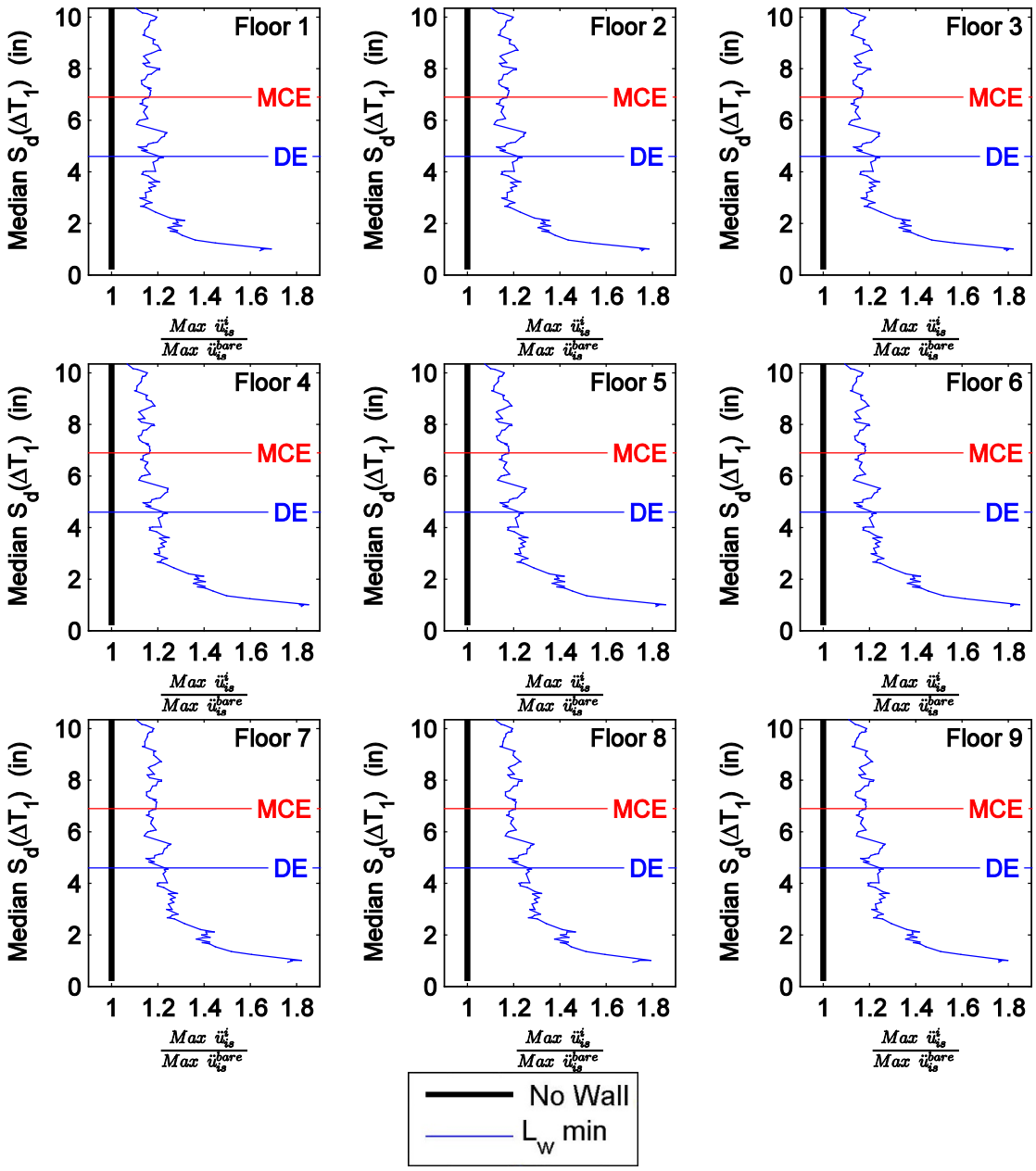

Figure 6.68 Normalized maximum floor acceleration moving average curves for S-9 with cases of no wall and minimum wall length considering mean model parameters against median spectral displacement over ΔT_1.

Note: where $\Delta T_1 = \langle T_1^{initial}, T_1^{final} \rangle$ and DE and MCE represent design spectral acceleartions of the building (at $T_1^{initial}$) for the design and maximum considered earthquakes.

6.5 Period Elongation of the Building-PW System

6.5.1 Introduction

When a reinforced concrete building undergoes nonlinear seismic response, damage is accumulated in terms of spalling and cracking. These damage mechanisms affect the stiffness of the building and ultimately elongate its fundamental period. This study selects period elongation as an indicator of the level of damage indicator. For example, period elongation of 20% clearly experienced more damage than a case that elongated 10%.

In the assessment of period elongation, in this study, it is defined as the ratio between the final fundamental period of the building system after the response to an earthquake motion (T_1^{final}) divided by the initial elastic fundamental period of the building system($T_1^{initial}$). The final fundamental period of the building is determined from a second eigenvalue analysis after the nonlinear time history simulation is complete. If the building system is elastic and the elements remain uncracked that is, no nonlinearity was experienced in the primary or structural system (members encompassing the moment frame), the maximum period elongation is 1. An assessment of the period elongation provides insight regarding the softening of the PWs within the building system. Before analyzing the period elongation, average representative curves are required to provide a baseline for comparison. Figure 6.69 illustrates the period elongation moving average for RC-8 considering the minimum wall length (mean model parameters) against median spectral acceleration and spectral displacement over ΔT_1. Appendix B demonstrates the calculation of the period elongation moving averages for all the considered cases in this section. Herein the focus is on the period elongation moving average comparisons against median spectral displacement, since using median spectral displacement over the range of T_1 performs well as an EDP.

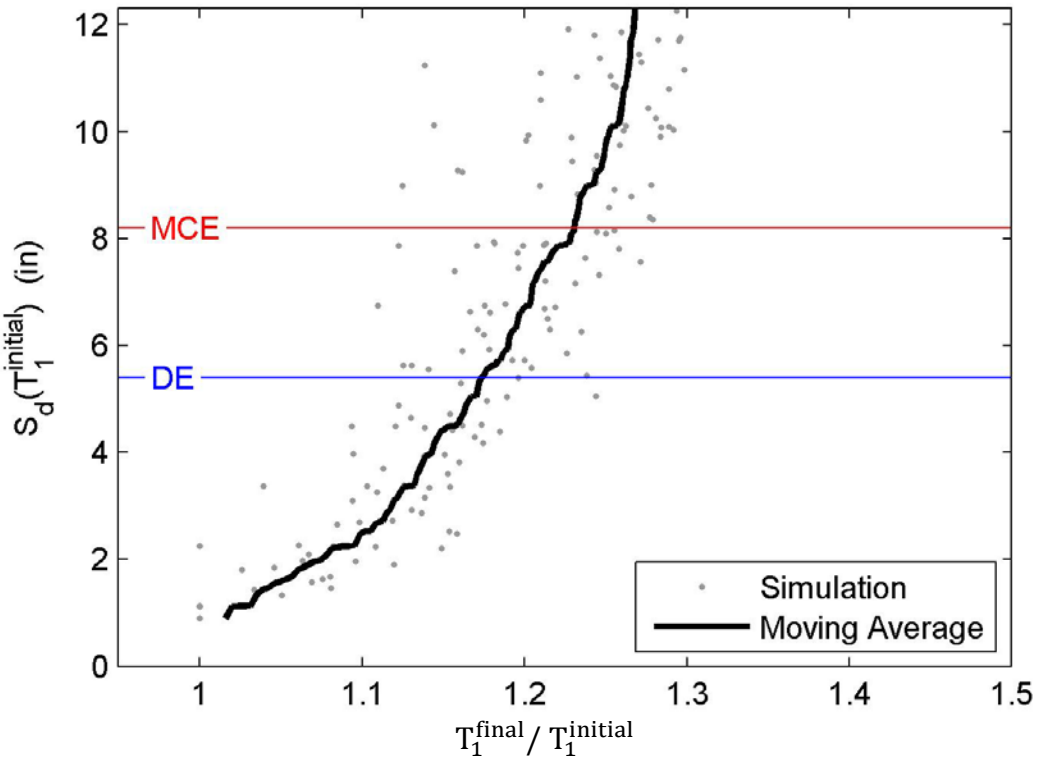

Figure 6.69 IDA results for RC-8 with the minimum length wall considering the mean model parameters: period elongation against spectral displacement over ΔT_1.

6.5.2 RC-8 Model: Effect of Wall Length

In the first comparison of period elongation, the effect of wall lengths (mean model parameters) within RC-8 is illustrated in Figure 6.70. For a median spectral displacement of approximately 1 inch, only 2-3% period elongation is noted for the coupled building-partition wall system. Before the initiation of period elongation in the bare building (no wall), the period elongation of both coupled analysis cases with a wall approaches 10%. As anticipated, this percentage is noted to be approximately the same value of the initial period shift by placing the PWs within the building models, refer to Chapter 4. As the intensity increases, the period elongation of all systems increase in the same general shape and as illustrated the maximum period elongation of the bare building is 20%. When RC-8 is considered with the minimum wall length and maximum wall lengths, an additional 5-7% and 8-11% of period elongation is

experienced, respectively. While this figure provides insight to the performance of the building, a key concept is clearly illustrated. Due to the early onset of period elongation in buildings with a PW, it reinforces the vulnerability of the PW system to lower spectral demands than that of the primary or structural system, which is more pronounced for longer walls.

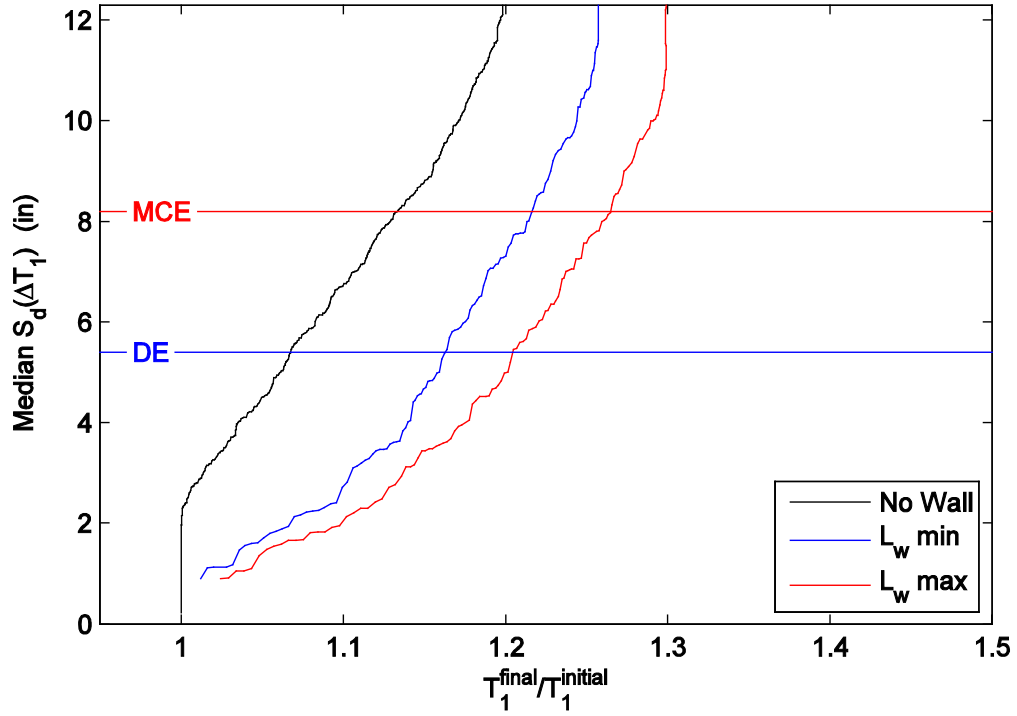

Figure 6.70 Period elongation moving average curves for RC-8 with cases of no wall, minimum wall length, and maximum wall length considering mean model parameters against median spectral displacement over ΔT_1.
Note: where $\Delta T_1 = \langle T_1^{initial}, T_1^{final} \rangle$ and DE and MCE represent design spectral acceleartions of the building (at $T_1^{initial}$) for the design and maximum considered earthquakes.

6.5.3 RC-8 Model: Effect of PW Strength

In assessing the period elongation considering the effect of wall strength, the period elongation moving averages are compared for RC-8 considering the minimum wall length with the mean, mean minus standard deviation and mean plus standard deviation PW model

parameters (Figure 6.71). Once again the vulnerability of the PW system to lower intensities is demonstrated since no period elongation is noted in the bare building (no wall) until nearly a median spectral displacement of 3 inches. Initial period elongation was noted in the PW elements only, with a similar result for both the mean and mean minus standard deviation PW model parameters within 1-3% each other. Initially most PW systems experienced a period elongation of 8-10%, just prior to period elongation of the primary structural system. However, the period elongation for the mean plus standard deviation PW model resulted in an initial period elongation of 15%, with a peak period elongation just prior to period elongation of the primary system of 20%. The pronounced effect of mean plus one standard deviation model does reduce throughout the illustrated values of median spectral displacement. Reasons for a much greater difference in the mean plus standard deviation model relate to a smaller degrading branch, earlier onset of post-peak hardening, and an overall greater force and stiffness consideration in comparison to the other PW models.

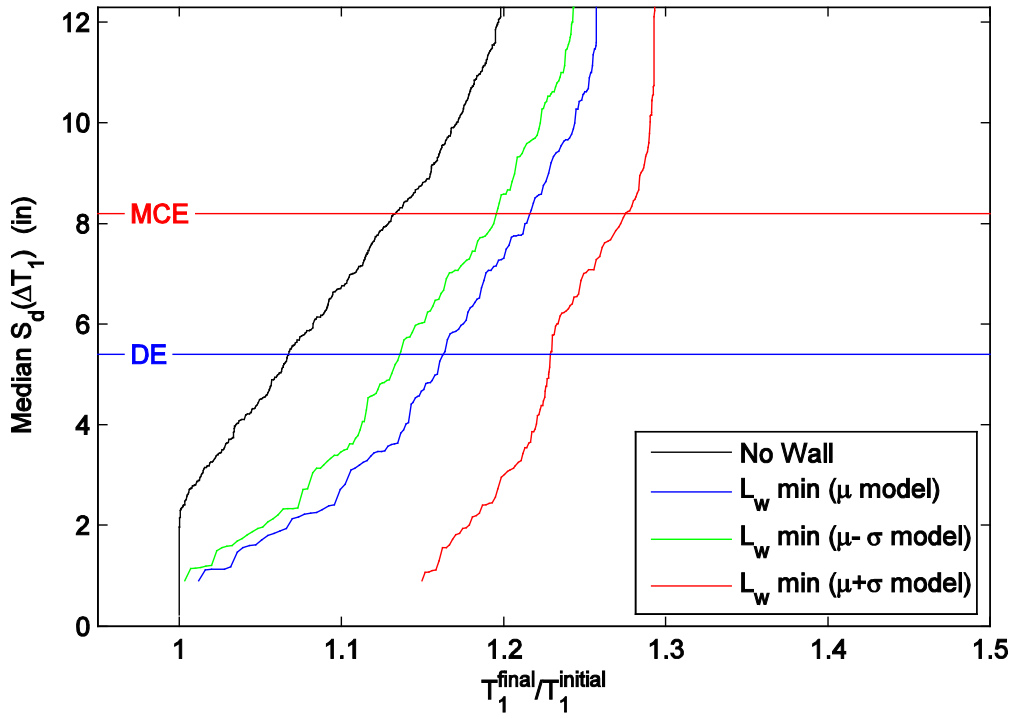

Figure 6.71 Period elongation moving average curves for RC-8 with cases of no wall and the minimum wall length considering mean (μ), mean minus standard deviation (μ–σ), and mean plus standard deviation (μ+σ) model parameters against median spectral displacement over ΔT_1.

Note: where $\Delta T_1 = \langle T_1^{initial}, T_1^{final} \rangle$ and DE and MCE represent design spectral acceleartions of the building (at $T_1^{initial}$) for the design and maximum considered earthquakes.

6.5.4 RC-8 Model: Effect of Post-Yield Degradation

In assessing the period elongation considering the effect of post-peak hardening versus post-yield strength degrading model, the period elongation moving averages are compared for RC-8 considering the minimum and maximum wall length for the mean PW model parameters with and without the strength degradation in Figure 6.44 (Figure 6.72 and Figure 6.73). The effect of the period elongation of the coupled building systems for either PW model are within 5% of each other demonstrating a minimal difference in the nonlinear time history responses as an effect of the post-peak hardening consideration as previously noted.

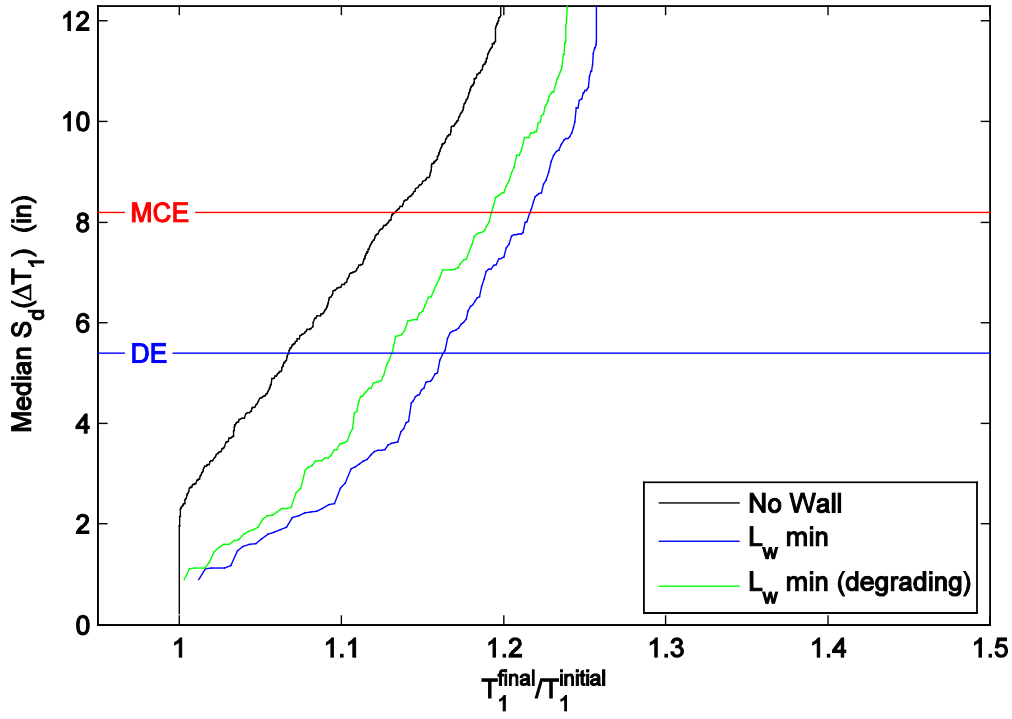

Figure 6.72 Period elongation moving average curves for RC-8 with cases of no wall and the minimum wall length considering post-peak hardening and a degrading model against median spectral displacement over ΔT_1.

Note: where $\Delta T_1 = \langle T_1^{initial}, T_1^{final} \rangle$ and DE and MCE represent design spectral acceleartions of the building (at $T_1^{initial}$) for the design and maximum considered earthquakes.

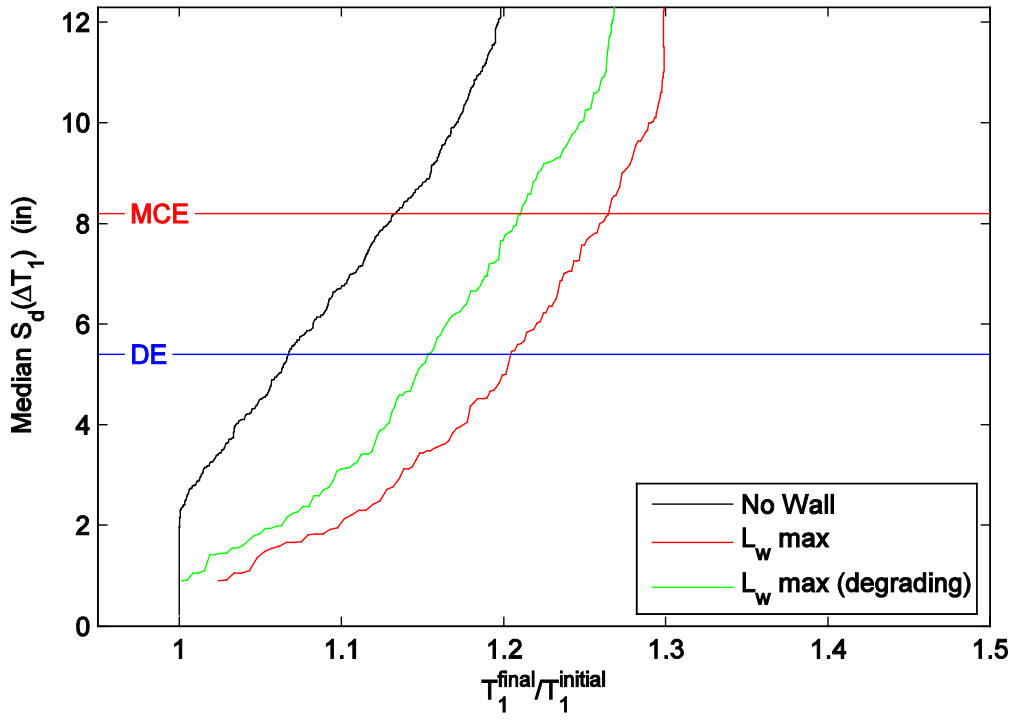

Figure 6.73 Period elongation moving average curves for RC-8 with cases of no wall and the maximum wall length considering post-peak hardening and a degrading model against median spectral displacement over ΔT_1.

Note: where $\Delta T_1 = \langle T_1^{initial}, T_1^{final} \rangle$ and DE and MCE represent design spectral acceleartions of the building (at $T_1^{initial}$) for the design and maximum considered earthquakes.

6.5.5 RC-8 Model: Effect of Wall Placement

In assessing the period elongation considering the effect of wall placement, the period elongation moving averages are compared for RC-8 considering the minimum wall lengths for a no wall case, walls at all floors, no wall at the first floor, and no wall at the top level (Figure 6.74). In comparing the various wall placement cases, only an minimal effect it noted between the cases.

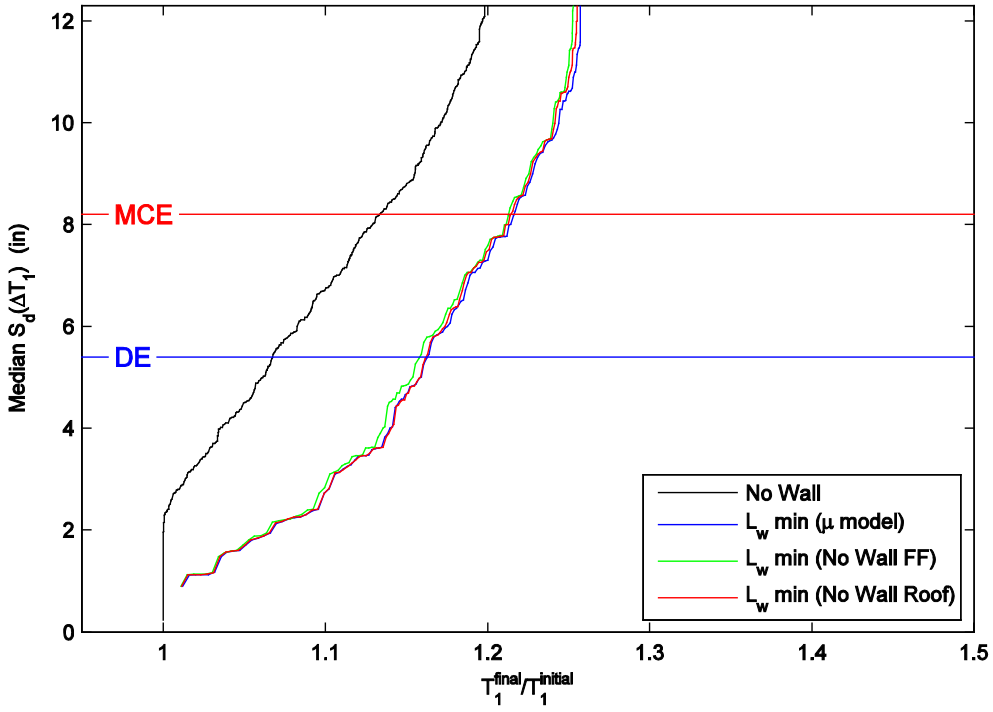

Figure 6.74 Period elongation moving average curves for RC-8 considering the cases of wall placement: no wall, minimum wall length (all floors), no wall first floor, and no wall on top level against median spectral displacement over the range of T_1.

Note: where $\Delta T_1 = \langle T_1^{initial}, T_1^{final} \rangle$ and DE and MCE represent design spectral acceleartions of the building (at $T_1^{initial}$) for the design and maximum considered earthquakes.

6.5.6 RC-20 Model: Effect of PW

In assessing the period elongation considering the effect of PW, the period elongation moving averages are compared for RC-20 considering the minimum wall length for the mean PW model parameters (Figure 6.75). As in the case of RC-8, at low spectral demands only period elongation is observed in the coupled building-PW system. This confirms that the PW is the most vulnerable system in the coupled system. Just prior to period elongation in the bare building, a 7% period elongation is noted in the coupled system.

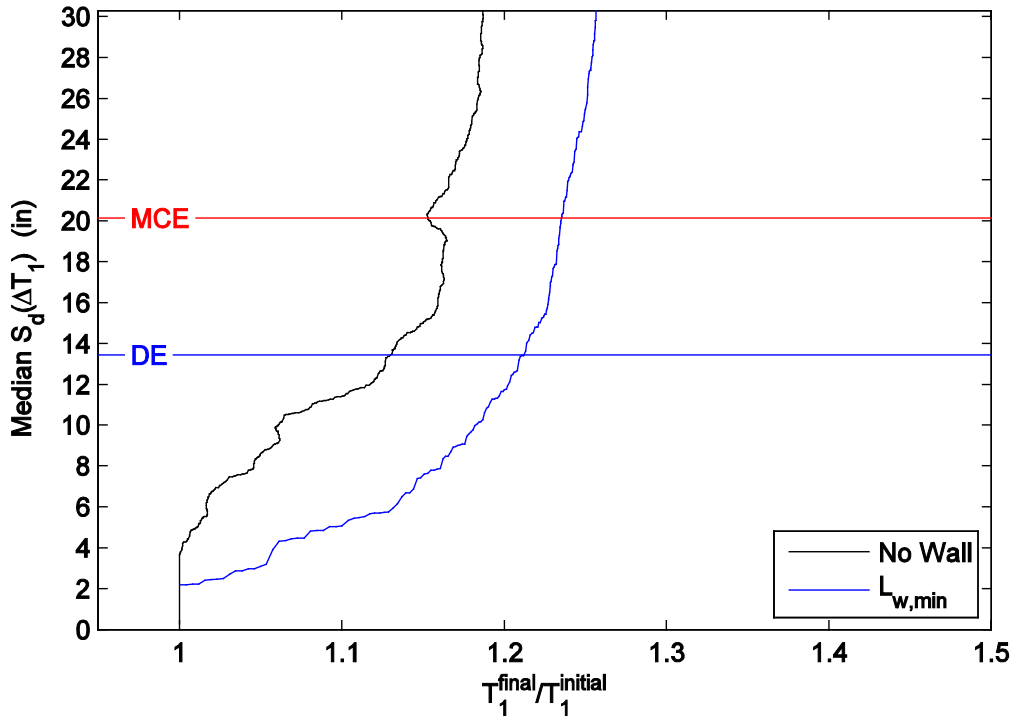

Figure 6.75 Period elongation moving average curves for RC-20 considering the cases of no wall and minimum wall length against median spectral displacement over the range of T_1. Note: where $\Delta T_1 = \langle T_1^{initial}, T_1^{final} \rangle$ and DE and MCE represent design spectral acceleartions of the building (at $T_1^{initial}$) for the design and maximum considered earthquakes.

6.5.7 S-3H Model: Effect of Wall Length

Steel buildings do not experience significant degradation, and in this work, the material selected for the discretization of the building, *steel02*, also does not degrade. However, clearly the PW will degrade and therefore its effect can be assessed. Figure 6.76 illustrates the period elongation for S-3H with both minimum and maximum wall length models (mean model parameters). The variance in period elongation is nearly uniform (within 5% over the spectral demands) with its source only of period elongation being isolated in PW model.

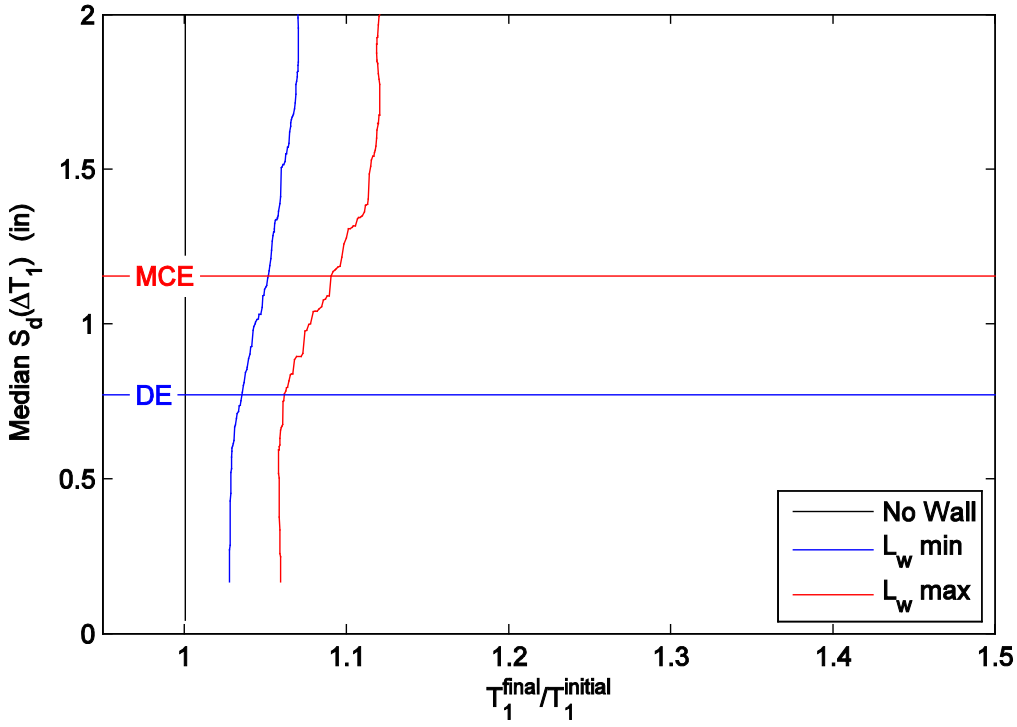

Figure 6.76 Period elongation moving average curves for S-3H with cases of no wall, minimum wall length, and maximum wall length considering mean model parameters against median spectral displacement over ΔT_1.
Note: where $\boldsymbol{\Delta T_1 = \langle T_1^{initial}, T_1^{final} \rangle}$ and DE and MCE represent design spectral acceleartions of the building (at $T_1^{initial}$) for the design and maximum considered earthquakes.

6.5.8 S-9 Model: Effect of PW

Despite S-9 being a steel building, the period elongation is assessed to illustrate the PW softening. Figure 6.77 illustrates the period elongation moving average curves for S-9 with the minimum length PW (mean model parameters). Once again, the variance in period elongation is nearly uniform with the source of period elongation only related to the PWs. The period elongation within the PWs of S-9 was very minimal throughout the spectral demands (5%).

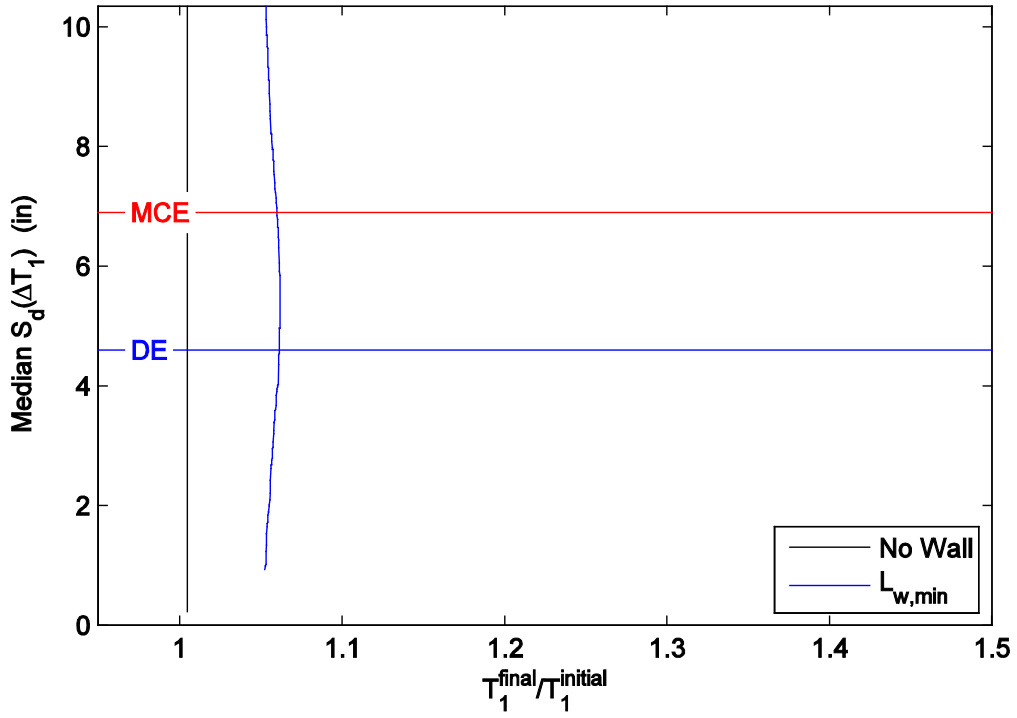

Figure 6.77 Period elongation moving average curves for S-9 with cases of no wall and minimum wall length considering mean model parameters against median spectral displacement over ΔT_1.
Note: where $\Delta T_1 = \langle T_1^{initial}, T_1^{final} \rangle$ and DE and MCE represent design spectral acceleartions of the building (at $T_1^{initial}$) for the design and maximum considered earthquakes.

6.6 Effect on Fragility Curves

In this section, the aim is to demonstrate the possible effect of including PWs in building model fragilities. Initially the first subsection introduces fragility analysis. Subsequently, the simplification and downfalls of typical fragility construction are discussed. Due to these limitations, the focus shifts to a Bayesian framework accounting for the variability of the component (i.e. PW) explicitly. Example fragility curves demonstrate the effect of PW variability.

6.6.1 Introduction to the Concept of Seismic Fragility Curves

Fragility curves identify the likelihood that a component or system reaches or exceeds a particular damage state (DS) as a function of an engineering demand parameter (EDP). Fragility curves provide a graphical representation of this relationship, facilitating a probabilistic assessment of a component or system performance, as traditionally done in performance based earthquake engineering and/or loss estimation in risk assessment (e.g. Moehle et al., 2004; Porter et al., 2007). Damage states are highly dependent on characteristics of the physical specimen and the imposed intensity of the EDP. For the PWs, fragility curves are generally constructed with respect to interstory drift as the EDP. EDPs for other components or systems may include peak acceleration, displacement, or rotation. Typically, a lognormal function relates a DS to an EDP (e.g. ATC-58, 2011). Lognormal fragility functions require definition of the median demand θ at which the i^{th} damage state, DS_i, initiates and a lognormal standard deviation denoted as $\sigma_{lnq}(\beta)$. The fragility function is generally calibrated using experimental data from incrementally increasing applied loads or deformations on the component or system.

6.6.2 Typical Fragility Approach

ATC-58 (ATC, 2011) outlines guidelines for constructing typical fragility curves representing the mean and dispersion values under five different data conditions, denoted as methods A-E. Method B is applied herein and can be summarized as: “Bounding Demand Data” when test or earthquake reconnaissance data is available from M number of specimens, however the damage state of interest did not occur in all specimens. For these specimens it is assumed, testing terminated or the earthquake demands did not produce damage. The value of the maximum demand, D_i, corresponding to each specimen is known, however this demand did not initiate the damage state. Other methods, not described herein, are detailed in ATC-58 (ATC, 2011).

Typical fragility functions defined by a median value θ and standard deviation β assume an idealized normalized lognormal distribution and presented as such in ATC-58 (Porter et al., 2007; ATC, 2011), i.e.:

$$F_i(DS_i) = \Phi\left(\frac{\ln\left(\frac{DS_i}{\theta}\right)}{\beta}\right) \tag{6-2}$$

where F_i represents the fragility curve for the i^{th} damage state, DS_i, Φ denotes the standard normal (Gaussian) cumulative distribution, θ denotes the median value and β denotes the logarithmic standard deviation. The logarithmic standard deviation indicates the amount of dispersion present in the data (Equation 6-3).

$$\beta = \sqrt{\beta_r^2 + \beta_u^2} \tag{6-3}$$

The parameter β_r represents the random variability that is observed in the test data, while β_u represents the uncertainty that the experimental tests demonstrate in realistic conditions or the uncertainty in an inadequate sample size (assigned 0.25 or 0.10 based on the data used).

These definitions combine to form a simplified fragility function with verification by a goodness-of-fit test. ATC-58 recommends Pierce's Criterion to eliminate a potential outlier not reflective of the true demands on the system. However, Porter et al. (2007) suggest the Lilliefors test, which is a special case of the Kolmogorov-Smirnov test. This test is applicable when the parameters of the distribution are estimated from the same data set. An example of typical ATC-58 fragility curves is illustrated in Figure 6.78, considering fragility method B. This figure identifies three damage states from the experimental program conducted at SUNY-Buffalo (Chapter 2) considering all in-plane pseudo-statically tested specimens.

In using the ATC-58 fragility approach, a simplistic fit is assumed which may or may not be a reasonable representation of the laboratory test data, earthquake reconnaissance information, and/or expert opinion. This inherent simplification assumes that fragilities always follow a lognormal distribution, which may not be applicable while additional complications arise when damage states obtained in the experimental program overlap and the need to integrate simulation data (Grigoriu et al., 2010). These limitations lead to the development of fragility curves within a Bayesian framework.

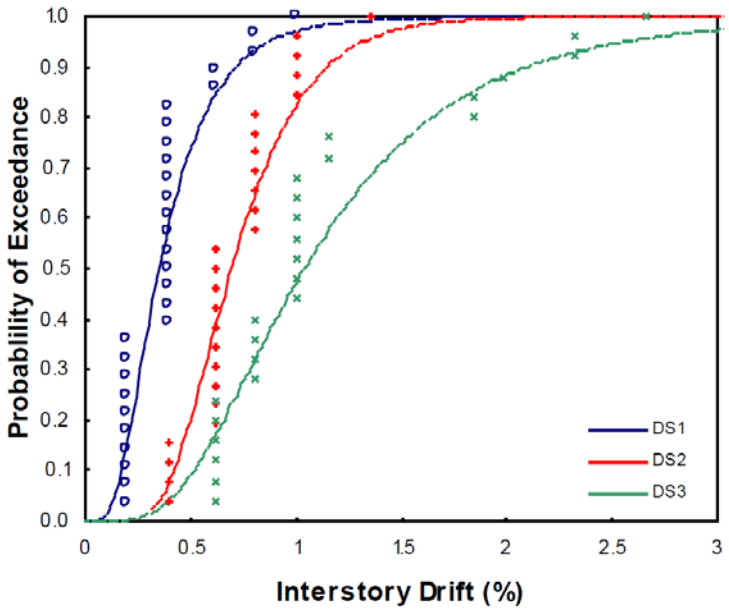

Figure 6.78 Example ATC-58 fragility curves for all in-plane PWs from the NEES-Nonstructural Project.
(from Davies, 2009)

6.6.3 Bayesian Fragilities

Although simplicity and adoption in the engineering community exists in the ATC-58 fragility approach, a Bayesian framework creates an ideal method to explicitly account for the variability of measurements in a fragility calculation. By accounting for this variability explicitly, the vulnerability of a given PW or other system can be more accurately represented. A brief summary of Bayesian fragility follows.

The methodology for constructing fragilities for PW systems within the NEES-Nonstructural project is based on in-plane experimental data obtained by the University at Buffalo, probabilistic models for damage states, prior densities on the uncertain parameters of their models, and two limit states (Lee and Grigoriu, 2012). The developed fragility methodology in the report defines the probability of a PW system for four damage states (DS). Damage state 0 is defined as the undamaged case; while damage states 1, 2, and 3 correspond to previously

defined states of the PWs considering minor, moderate and severe damage (refer to Chapter 2). Using this definition, two limit states are considered (Lee and Grigoriu, 2012):

1) Uncorrelated: the critical damage states $(DS_{1,k}, DS_{2,k}, DS_{3,k}), k = 1, \cdots, n,$ are independent copies of (DS_1, DS_2, DS_3). Under this assumption, the system of PWs enters damage state 0, 1, 2, and 3 with probabilities:

$$\text{Damage state 0: } p_{0,i}(\xi) = \prod_{k=1}^{n} P(d_{i,k}(\xi) < DS_{1,k}) \tag{6-4}$$

$$\text{Damage state 1: } p_{1,i}(\xi) = 1 - \prod_{k=1}^{n} P(d_{i,k}(\xi) < DS_{1,k}) \tag{6-5}$$

$$\text{Damage state 2: } p_{2,i}(\xi) = 1 - \prod_{k=1}^{n} P(d_{i,k}(\xi) < DS_{2,k}) \tag{6-6}$$

$$\text{Damage state 3: } p_{3,i}(\xi) = 1 - \prod_{k=1}^{n} P\left(d_{i,k}(\xi) < DS_{3,k}\right) \tag{6-7}$$

2) Perfectly correlated: the critical damage states $(DS_{1,k}, DS_{2,k}, DS_{3,k})$ are perfectly correlated. Under this assumption, the system of PWs enters damage state 0, 1, 2, and 3 with probabilities:

$$\text{Damage state 0: } p_{0,i}(\xi) = P(\max_{1 \le k \le n} d_{i,k}(\xi) < DS_1) \tag{6-8}$$

$$\text{Damage state 1: } p_{1,i}(\xi) = P(\max_{1 \le k \le n} d_{i,k}(\xi) \ge DS_1) \tag{6-9}$$

$$\text{Damage state 2: } p_{2,i}(\xi) = P(\max_{1 \le k \le n} d_{i,k}(\xi) \ge DS_2) \tag{6-10}$$

$$\text{Damage state 3: } p_{3,i}(\xi) = P(\max_{1 \le k \le n} d_{i,k}(\xi) \ge DS_3) \tag{6-11}$$

Assuming that any of the ground motions are equally likely to occur, system level fragilities can be obtained from the probabilities in equation 6-12.

$$p_r(\xi) = \frac{1}{m} \sum_{i=1}^{m} p_{r,i}(\xi), r = 0,1,2,3 \tag{6-12}$$

In the generation of the Bayesian fragilities, it is noted that the fragilities based on state-dependent density functions result in slightly higher values than those of state-independent functions at a given PGA value for damage states 1, 2, and 3. In comparing the two limt states considered, the fragilities defined by state-independence are therefore more conservative than the perfectly-correlated fragilities. However, a disclaimer is noted that these results could be specific to this set of data (Wood et al., 2012).

6.6.4 Example Bayesian Fragility of PWs within Building Models

In this section, fragility curves as considered within a performance based earthquake engineering approach or loss assessment within a risk analysis demonstrate the effect of including the PW within the numerical building model. Herein, the assessment focuses on the normalized mean and mean plus or minus standard deviation PW models. The fragilities are developed with the assumption that all models have PWs within the structure; however, for the case of the bare building (no wall), the modeling efforts neglected the PW implementation into the building model (Figure 6.79). The fragilities for the coupled simulation data of RC-8 are higher than that for the bare building case (no wall). By not implementing the PW model in the bare building, up to a difference of 40% is noted between the bare building and the coupled system considering the mean plus standard deviation PW model for the no-damage state. A smaller difference is noted for damage states 1-4, with a maximum difference of approximately 20%. The differences between the bare building and the coupled building system illustrate the importance of considering PWs in modeling efforts, particularly for undamaged to moderate damage states. Due to the effect of the PW on the response of the coupled building-partition wall system, specific details on the partition wall lengths and building design are critical to fully assess the impact on fragility curves.

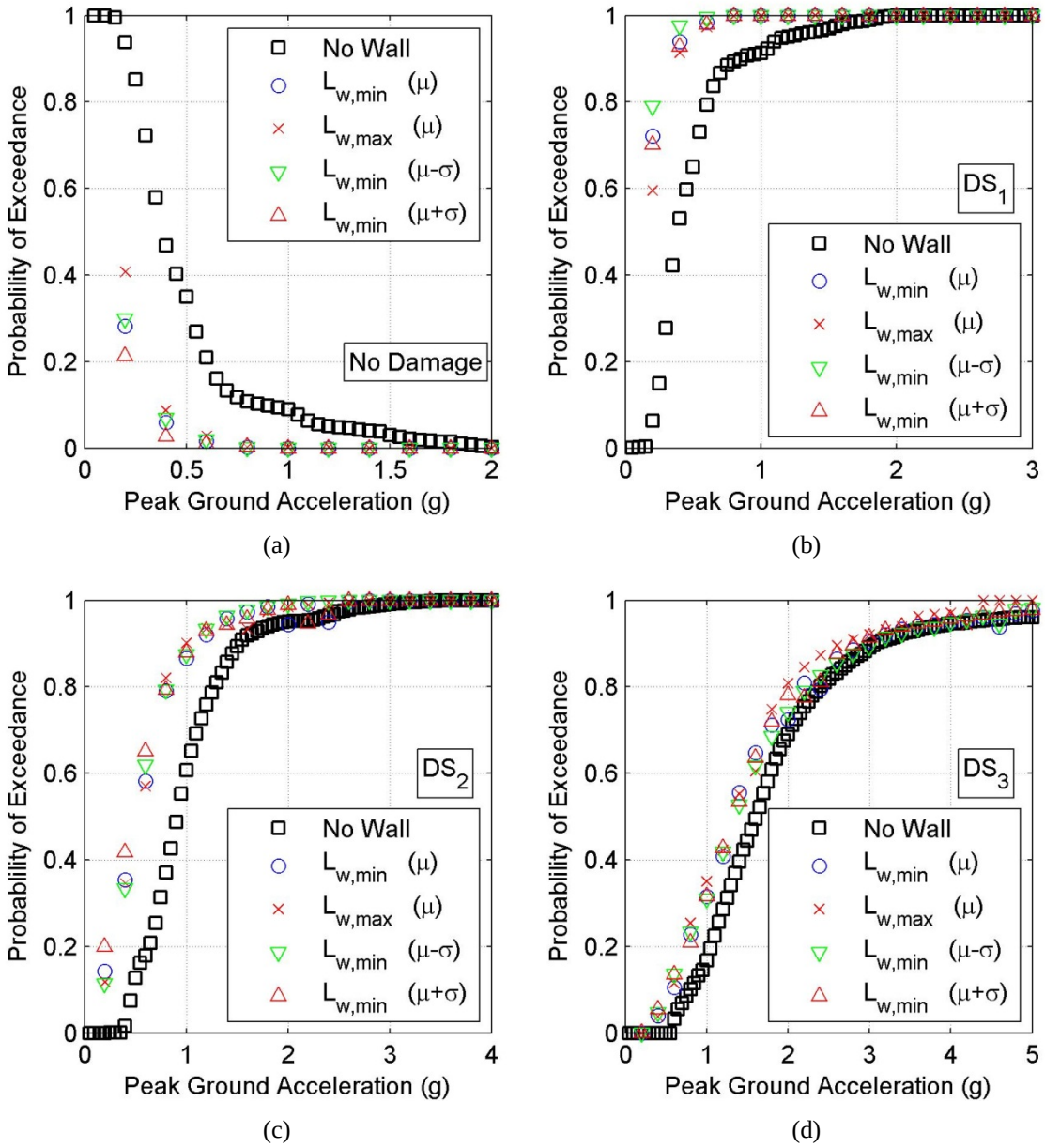

Figure 6.79 Comparison of fragilities for simulation data in RC-8 group for state-independent shape parameters, where: (a) DS_0 (no damage), (b) DS_1, (c) DS_2 and (d) DS_3. Note: the range of x-axis varies for each subplot.

6.7 Concluding Remarks

In this chapter, the effect of the coupled building-partition wall system is characterized using nonlinear time history analysis and fragility analysis. Incremental dynamic analysis is

utilized by scaling peak ground acceleration of each motion. To develop meaningful comparisons against a representative EDP, the IDA cases were converted to median spectral acceleration and spectral displacement over the period range of T_1 from the initial uncracked state to the final state. The key findings on the effect of the coupled building-partition wall system include:

- Initially for low intensity median spectral quantities, maximum interstory drift and maximum floor acceleration values are severely underestimated (approximately 50%) compared to those estimated for the bare building, as anticipated for service level earthquakes. After the PWs degrade, the effect is diminished, but still exists (10-20%) for some floors as the results depend highly on building design.
- Although up to 50% underestimation of the maximum interstory drift is observed within approximately service level earthquake intensities, the actual maximum interstory drifts under this intensity range are generally less than 0.20% therefore a 50% underestimation implies the maximum values would approach 0.30% or so. This underestimation is observed to be minor, yet it may result in a change from no damage (DS_0) to minor damage (DS_1).
- The effect of considered PW lengths influences the coupled building-partition wall system behavior to a moderate effect. Maximum interstory drift and floor accelerations vary by 20% depending on wall length.
- The chosen PW model parameters, which reflect the wall variability (i.e. mean model versus mean plus standard deviation) influences the coupled system behavior by underestimating nearly two-fold the maximum interstory drift and maximum floor accelerations when compared to either the mean or mean minus standard deviation PW models.
- The effect of a post-peak hardening or degrading behavior in terms of characterizing the PW model minimally influences the coupled system behavior. However, the

maximum interstory demands on the PWs were at 2.0%. This effect may substantially influence the system when interstory drift demands exceed 2.0%.

- The effect of PWs on different coupled building-partition wall systems, namely RC-20 and S-3H, resulted in a few cases were both underestimation and overestimation of maximum floor acceleration responses.
- The period elongation of the building is affected if the PW system is included in the model, because the PW degrades prior to the onset of structural damage. Just prior to the elongation of the primary structural system, the period elongation associated with the PWs are similar to that observed in the eigenvalue study performed in Chapter 4 (5-15%).
- Differences greater than 50% are observed in the median probability of exceedance given DS_0, when comparing the fragility of a bare building to that of a building-PW system. The difference in peak ground acceleration associated with a probability of exceedance of 50% is more pronounced for low to moderate damage (i.e. DS_0, DS_1, or DS_2) than that of DS_3 (major damage).

6.8 Acknowledgement

Section 6.6 of this dissertation is based on a NEES-Nonstructural Report in preparation, *Fragility Function Development for Nonstructural Component System*, to be published at the State University of New York, University of Buffalo. The co-authors of this manuscript are Tara C. Hutchinson, Chang Hoon Lee, and Mircea Grigoriu; where the dissertation author is the lead author and investigator.

Chapter 7 Conclusions and Recommendations

7.1 Motivation and Scope

In recent earthquakes, the damage to nonstructural components and systems (NCSs) has well exceeded the cost of structural damage in buildings (e.g. Filiatrault et al., 2002; EERI, 2010a; EERI, 2010b). One such important NCS, common to nearly all buildings, is the interior partition wall (PW) subsystem. PWs are a complex system with multiple attachments at floors, structural walls, and ceilings or upper floor levels. While typically not anticipated to participate in the dynamic response of the building, the PW subsystem is subject to the dynamic environment of the building and, since they are typically distributed on all floors, they will be subject to motion which has been filtered by the building itself. Therefore it is important to understand what impact the PW may have on the building, and vise-versa.

This dissertation presents modeling and quantification of the seismic response of the building-partition wall system. First, a design-oriented PW model is developed using a lumped representation to characterize the PW hysteretic behavior. The motivation for using a lumped model is primarily simplification, whereby a single zero-length one degree-of-freedom element is adopted. In this fashion, the overall degrees-of-freedom of the building as a system are not greatly increased. The methodology for the model development is outlined; namely, using experimental data to characterize the force-displacement relationship and the dissipated energy. A large database of recent experimental data generated by the University at Buffalo is utilized to calibrate model parameters and refine the model parameter selection protocol. Error metrics associated with average residual force and half-cycle hysteretic energy are used to assess the model's robustness and justify its use with particular focus on how successful the models are in the prediction of experimental behavior.

Using the design orientated PW model, the effect of placing it within a suite of building models and later subjecting them to realistic earthquake motions is evaluated. Eigenvalue and nonlinear pushover analyses were conducted on the suite of nine building-partition wall models with a broad fundamental period distribution of approximately 0.2 to 2.1 seconds. Of the nine buildings, a subset of the buildings were chosen to demonstrate the effect of PWs on the nonlinear time response of the coupled building-partition wall system under a range of motions.

7.2 Key Results

The goal of characterizing the effect of the coupled building-partition wall system is realized through eigenvalue analysis, nonlinear pushover analysis, nonlinear time history analyses, and development of fragility curves. The most significant results from these investigations are the following:

- The addition of the PW into the building model is observed to stiffen the model consistently, resulting in an average period reduction of 7%, and a maximum period reduction of 15%. The impact on the fundamental elastic period is highly dependent on the partition wall length and building.
- Results of the nonlinear static pushover analysis showed that in order to reach a roof drift of 3%, an additional force of up to 15% can be required with the inclusion of a PW, i.e. the PW provides an additional strength to the building, even at large total drift ratios.
- The effect of adding the PW to form a coupled analysis model is most pronounced at lower spectral intensities. Initially, maximum interstory drift and maximum floor acceleration values are observed to be severely underestimated (approximately 50-80%) compared to those estimated for the bare building. After the PWs degrade, this effect is diminished, however a pronounced effect (approximately 30%) is still

observed for larger spectral intensities associated with a design or maximum considered earthquakes, when the story stiffnesses are reduced as typically found in higher floors.

- From the nonlinear time history responses, it is evident that the selection of PW lengths in this study and model variability type can moderately influence the behavior. Maximum interstory drift and maximum floor accelerations varied by about 20%, depending on wall length and can vary two-fold when considering a mean plus standard deviation model compared to a mean minus standard deviation model.
- The period elongation of the building is affected if the PW system is included in the model, because the PW degrades prior to the onset of structural damage. Just prior to the elongation of the primary structural system, the period elongation associated with the PWs are similar to that observed in the eigenvalue study performed in Chapter 4 (5-15%).
- Differences greater than 50% are observed in the median probability of exceedance given DS_0, when comparing the fragility of a bare building to that of a building-PW system. The difference in peak ground acceleration associated with a probability of exceedance of 50% is more pronounced for low to moderate damage (i.e. DS_0, DS_1, or DS_2) than that of DS_3 (major damage).

7.3 Impacts on Analysis Techniques

Using the proposed design oriented PW model, a more accurate prediction of the seismic response of buildings and nonstructural elements can be achieved. These analyses studies verified that addition of simple lumped models to represent the hysteretic behavior of the PW in a building model can be readily realized should a designer choose to do so. It is noted that the level of sophistication utilized herein need not be adopted, in fact simplistic trilinear hysteretic models

might be adopted to capture the prominent force-displacement backbone features of the PW behavior. Absent the ability to integrate a lumped or other hysteretic model into a larger building model, a designer may choose to reduce the elastic fundamental period of a bare building by 10-15% in consideration of the plausible stiffening the PW may have on the building. In like fashion, from a designer's point of view it may be assumed that the PW will amplify the maximum interstory drift and maximum floor accelerations within the service levels of design by 30-50%. This conservative amplification could be adopted as a worst case scenario in lieu of developing a coupled building-partition wall numerical model.

7.4 Recommendations for Future Work

Recommendations for future work in this area include:

1. Validation of the PW model using full scale system level tests would be useful to demonstrate the effects of the PW subsystem on the building system.
2. In this study, the PW lengths remained constant up the height of the building. In practice this may not be the case. Therefore, exploration of the effects of varying the PW length at individual floors is warranted.
3. PW of partial heights should be explored. Particularly for very flexible building framing systems. Although the effect on the building may be less than that of a full height PW, due to the increased flexibility of the PW, flexible beams may be impacted by the potentially concentration rotations expected along the beams.
4. Invariably, the PW will interact with not only the building, but other NCSs, e.g. ceilings, stairs, elevators, contents (especially furnishings), etc. This interaction may dramatically change the PW response. Future studies should attempt to mimic practical situations whereby the PW interaction with neighboring NCSs may be envisioned-particularly considering the potential for pounding between the various subsystems.

References

Abrahamson, N. and Silva, W. (2008). "Summary of the Abrahamson & Silva NGA Ground-Motion Relations" *Earthq. Spectra*, **24**(1): 67-97.

Abrahamson, N.A. (1992). "Non-stationary spectral matching", *Seismol. Res. Lett.*, **31**(1): 30-30.

Al Atik, L., and Abrahamson, N. (2010). "An Improved Method for Nonstationary Spectral Matching", *Earthq. Spectra*, **26**(3): 601-617.

American Concrete Institute (2008). "*Building code requirements for structural concrete"ACI 318-08*, Farmington Hills, Michigan.

Applied Technology Council. (2009). *FEMA P695 / Quantification of Building Seismic Performance Factors.* Redwood City, CA, June.

Applied Technology Council. (2011). *ATC-58-1 75% Draft. Seismic Performance Assessment of Buildings. Volume 1 - Methodology.* Redwood City, CA.

Arnold, A.E., Uang, C.M., Filiatrault, A. (2003). *Cyclic Behavior and Repair of Stucco and Gypsum Sheathed Woodframe Walls: Phase I.* Report No. SSRP 2002/07, Department of Structural Engineering, University of California, San Diego, La Jolla, CA.

ASCE 7-05. (2006). *Minimum Design Loads for Buildings and Other Structures*. American Society of Civil Engineers, Reston, VA.

Bersofsky, A. (2004). *A Seismic Performance Evaluation of Gypsum Wallboard Partitions.* MS Thesis, Department of Structural Engineering, University of California, San Diego, La Jolla, CA.

Bommer, J. J., and Acevedo, A. B. (2004). "The Use of Real Earthquake Accelerograms as Input to Dynamic Analysis", *J. Earthquake Eng.*, **8**(1): 43-91.

Building Seismic Safety Council (BSSC). (2000). *Standard and Commentary for the Seismic Rehabilitation of Buildings, FEMA-356*, Federal Emergency Management Agency, Washington, D.C

Carr, A.J. (2005). *Computer Program RUAUMOKO*. Department of Civil Engineering, University of Canterbury, Christchurch, New Zealand.

Catalán, A., Benavent-Climent, A., and Cahis, X. (2010). "Selection and scaling of earthquake records in assessment of structures in low-to-moderate seismicity zones", *Soil Dyn. Earthq. Eng.*, **30**(1-2): 40-49.

Coleman, J., and Spacone, E. (2001). "Localization Issues in Force-Based Frame Elements", *J. Struct. Eng.*, ASCE, **127**(11): 1257-1265.

Davies, R. D. (2009). *Seismic Evaluation, Parameterization, and Effect of Light-Frame Steel Studded Gypsum Partition Walls.* MS Thesis, Department of Civil, Structural and Environmental Engineering, University at Buffalo, State University of New York (SUNY).

Dinehart, D.W. and Shenton, H.W. (2000). "Model for Dynamic Analysis of Wood Frame Shear Walls." *J. Eng. Mech., ASCE*, **126**(9): 899-908.

Earthquake Engineering Research Institute (EERI). (2010a). *The El Mayor Cucapah, Baja California Earthquake April 4, 2010. An EERI Reconnaissance Report 2010-02*. Meneses, J. (ed), Oakland, California.

Earthquake Engineering Research Institute (EERI). (2010b). *Learning from Earthquakes: The M_w 8.8 Chile Earthquake of February 27, 2010. EERI Special Earthquake Report – June 2010.* Oakland, California.

Englekirk, R. E. (2003). *Seismic Design of Reinforced and Precast Concrete Buildings.* Wiley, NJ.

Eureka Earthquake Clearinghouse . (2010). "Images and Captions Captured from the Web by CSSC Staff". EERI Earthquake Clearinghouse. Accessed August 12, 2012. <http://www.eqclearinghouse.org/20100110-eureka/uncategorized/images-captions-captured-from-the-web-by-cssc-staff>.

European Committee for Standardization (CEN) (2003). *Eurocode Designing of structures for earthquake resistance-Part 1: General rules, seismic actions,* prEN 1998-1, Final Draft.

Filiatrault, A., Christopoulos, C., and Stearns, C. (2002). *Guidelines, Specifications, and Seismic Performance Characterization of Nonstructural Building Components and Equipment.* PEER Report 2002/05. Pacific Earthquake Engineering Research Center, College of Engineering, UC Berkeley.

Filippou, F. C., Popov, E. P., Bertero, V. V. (1983). *Effects of Bond Deterioration on Hysteretic Behavior of Reinforced Concrete Joints.* Earthquake Engineering Research Center Report 83-19, University of California, Berkeley.

Folz, B and Filiatrault, A. (2001). "Cyclic Analysis of Wood Shear Walls." *J. Struct. Eng.*, ASCE, **127**(4): 433-441.

Folz, B and Filiatrault, A. (2004a). "Seismic Analysis of Woodframe Structures. I: Model Formulation." *J. Struct. Eng.*, ASCE, **130**(9): 1353-1360.

Folz, B and Filiatrault, A. (2004b). "Seismic Analysis of Woodframe Structures. I: Model Implementation and Verification." *J. Struct. Eng.*, ASCE, **130**(9): 1361-1370.

French, S. and Xu, J. (2010). Internal project correspondent. Not published.

Grigoriu, M., Gupta, A., Hutchinson, T., Reinhorn, A., and Wood, R. (2010). "A Methodology for Constructing Seismic Fragilities Based on Experimental and Mechanical Models" *9th U.S. National and 10th Canadian Conference on Earthquake Engineering Proceedings*, Toronto, ON. July.

Gupta, A. and Krawinkler, H. (1999). *Seismic Demands for Performance Evaluation of Steel Moment Resisting Frame Structures (SAC Task 5.4.3). Report No. 132,* Department of Civil and Environmental Engineering, Stanford University.

Hancock, J., Bommer, J. J., and Stafford, P. J. (2008). "*Numbers of scaled and matched accelerograms required for inelastic dynamic analyses*", Earthq. Eng. & Struct. Dyn., **37**(14): 1585-1607.

Haselton, C.B. (Ed.) (2009). *Evaluation of Ground Motion Selection and Modification Methods: Predicting Median Interstory Drift Response of Buildings*. PEER Technical Report 2009/01.

Huang, Y.-N., A. S. Whittaker, N. Luco, and R. O. Hamburger (2009). “Selection and scaling of earthquake ground motions in support of performance-based design”, *J. Struct. Eng.*, ASCE, In Press.

Ibarra, L.F., Medina, R.A., and Krawinkler, H. (2004). “Hysteretic Models that Incorporate Strength and Stiffness Deterioration.” Earthq. Eng. & Struct. Dyn., **34**(12): 1489-1511.

Iervolino, I., and Cornell, C.A. (2005). "Record Selection for Nonlinear Seismic Analysis of Structures", *Earthq. Spectra*, **21**(3): 685-713.

International Code Council, ICC. (2006). *International building code 2006*. International Code Council, Falls Church, Va.

International Conference of Building Officials. (1994). *Uniform Building Code 1994*. Whittier, CA.

International Conference of Building Officials. (1997). *Uniform Building Code 1997*. Whittier, CA.

Kanvinde, A.M. and Deierlein, G.G. (2006). “Analytical Models for the Seismic Performance of Gypsum Drywall Partitions.” *Earthq. Spectra*, **22**(2): 391-411

Katsanos, E.I., Sextos, A.G., and Manolis, G.D. (2010). “Selection of earthquake ground motion records: A state-of-the-art review from a structural engineering perspective”, *Soil Dyn. Earthq. Eng.*, **30**(4): 157-169.

Krawinkler, H., Parisi, F., Ibarra, L. Ayoub, A. and Medina, R. (2000). *Development of a testing protocol for wood frame structures*, Report No. W-02, CUREE, Richmond, California.

Lang, A.F. and Restrepo, J.I. (2007). *Seismic Performance Evaluation of Gypsum Wallbaord Partitions. Structural Systems Research Program Report* SSRP 2007/07, University of California, San Diego, La Jolla, CA.

Lee, C. and Grigoriu, M. (2012) Bayesian Fragility for Nonstructural Systems. NEES-Nonstructural Technical Report Series, MCEER-12-0006, University at Buffalo, State University of New York (SUNY).

Lee, T.H., Kato, M., Tomohiro, M., Suita, K., and Nakashima, M. (2007). "Seismic performance evaluation of non-structural components: Drywall partitions." *Earthq. Eng. Struct. Dyn.*, **36**(3): 367-382.

Luco, N., and Bazzurro, P. (2007). “Does *amplitude* scaling of ground motion records result in biased nonlinear structural drift responses?”, *Earthq. Eng. Struct. Dyn.*, **36**(13): 1813-1835.

Luco, N., and Cornell, C. A. (2007). "Structure-Specific Scalar Intensity Measures for Near-Source and Ordinary Earthquake Ground Motions." *Earthq. Spectra*, **23**(2): 357-392.

Magenes, G., Bracchi, S., Graziotti, F., Mandirola, M., Manzini, C.F., Morandi, P., Palmieri, M., Penna, A., Rosti, A., Rota, M., and Tondelli, M. (2012). *Rapporto Preliminare sul Rilievo dei Danni alle Strutture in Muratura dopo I Terremoti Dell’Emilia Del Maggio 2012 (Translated: Preliminary report on the damage survey to masonry structures after the May 2012 Emilia earthquakes).* Centro Europea di Formazione e Ricerca in Ingegneria Sismica (EUCENTRE). V. 1. (in Italian) <http://www.eqclearinghouse.org/2012-05-20-italy/>.

Mander, J.B., Priestley, M. J. N., and Park, R. (1988). "Theoretical Stress-Strain Model for Confined Concrete", J. *Struct. Eng.,* ASCE, **114**(8): 1804-1826.

Mazzoni, S., McKenna, F., Scott, M. H., and Fenves, G. L., (2011). *Open System for Engineering Simulation User-Command-Language Manual*, version 2.0, Pacific Earthquake Engineering Research Center, University of California, Berkeley. <http://opensees.berkeley.edu/>.

Moehle, J. and Deierlein, G. (2004). "A framework methodology for performance-based earthquake engineering." *Proceedings of the 13th World Conference on Earthquake Engineering.* Vancouver, Canada.

Mosqueda, G., Retamales, R., Filiatrault, A., and Reinhorn, A.M. (2009). "Testing Facility for Experimental Evaluation of Nonstructural Components under Full-scale Floor Motions," *Struct. Desn. Tall Buil.*, **18**(4): 387-404.

NAHB Research Center, Inc. (1997*). Monotonic Tests of Cold-Formed Steel Shear Walls with Openings*. The American Iron and Steel Institute Washington, DC.

National Institute for Land and Infrastructure Management (NILIM) and Building Research Institute (BRI). (2011). *Summary of the Field Survey and Research on "The 2011 off the Pacific coast of Tohoku Earthquake" (the Great East Japan Earthquake).* Technical Note of NILIM No. 647, BRI Research Paper No. 150. Japan.

NEES Nonstructural Project (2012). *Simulation of the Seismic Performance of Nonstructural Systems.* Accessed May 1, 2012. http://www.nees-nonstructural.org/.

Pang, W.C., Rosowsky, D.V., Pei, S., and van de Lindt, J.W. (2007). "Evolutionary Parameter Hysteretic Model for Shear Walls." *J. Struct. Eng.*, ASCE, **133**(8): 1118-1129.

Paulay, T. and Priestley, M. J. N. (1992). *Seismic design of reinforced concrete and masonry buildings*. John Wiley, and Sons Inc.

PEER-NGA (2009), Pacific Earthquake Engineering Research Center: NGA Database. http://peer.berkeley.edu/nga/

Porter, K., Kennedy, R., Bachman, R. (2007). "Creating Fragility Functions for Performance-Based Earthquake Engineering," *Earthq. Spectra*, **23**(2): 471-489.

Restrepo, J.I. and Bersofsky, A.M. (2010). "Performance Characteristics of Light Gage Steel Stud Partition Walls" *Thin Wall. Struct.*, **49**(2): 317-324.

Restrepo, J.I. and Lang, A.F. (2011). "Study of Loading Protocols in Light Gage Stud Partition Walls" *Earthq. Spectra, **27**(4): 1169-1185.*

Retamales, R., Mosqueda, G., Filiatrault, A., and Reinhorn, A. (2011). "Testing Protocol for Experimental Seismic Quantification of Distributed Nonstructural Systems" *Earthq. Spectra*, **27**(3): 835-856.

Scott, M. H., and Fenves, G.L. (2006). "Plastic Hinge Integration Methods for Force-Based Beam-Column Elements", *J. Struct. Eng.*, ASCE, **132**(2): 244-252

Serrette, R., Encalada, J., Juadines, M., and Nguyen H. (1997). "Static Racking Behavior of Plywood, OSB, Gypsum, and FiberBond Walls with Metal Framing," *J. Struct. Eng.*, ASCE, **123**(8): 1079-1086.

Shome, N., and Cornell, C. A., (1998). Normalization and scaling accelerograms for nonlinear structural analysis, in *Proceedings of the Sixth U. S. Notional Conference on Earthquake Engineering*, CD-ROM, Seattle, WA

Somerville, P., Smith, N., Punyamurthula, S., and Sun, J. (1997). "Development of ground motion time histories for phase 2 of the FEMA/SAC steel project." *Report SAC/BC-97/04*, SAC Joint Venture, Sacramento, CA.

Spacone, E., Ciampi, V., Filippou, F.C. (1992*). A Beam Element for Seismic Damage Analysis. Report No.* UCB/EERC-92/07. Earthquake Engineering Research Center, University of California, Berkeley.

SSMA. Steel Stud Manufactures Association. (2010). *Product Technical Information. SSMA PTIC rev 12/2010*. Accessed November 2010. http://www.ssma.com/documents/ ssmatechcatalog.pdf>

Stewart, W.G. (1987). *The Seismic Design of Plywood Sheathed Shear-Walls*. PhD Thesis, University of Canterbury, Christchurch, New Zealand.

Taghavi, S. and Miranda, E. (2003). *Response Assessment of Nonstructural Building Elements*. PEER Report 2003/05. Pacific Earthquake Engineering Research Center, College of Engineering, UC Berkeley.

United States Geological Survey (USGS). (2008a). Custom Mapping and Analysis Tools. USGS, Reston, Virginia. http://earthquake.usgs.gov/research/hazmaps/interactive.

United States Geological Survey (USGS). (2008b). 2002 Interactive Deaggregations. USGS, Reston, Virginia. http://eqint.cr.usgs.gov/deaggint/2002/.

United States Geological Survey (USGS). (2009). 2008 Interactive Deaggregations (Beta). USGS, Reston, Virginia. http://eqint.cr.usgs.gov/deaggint/2008/.

Vamvatsikos, D. and Cornell, C.A. (2002). "Incremental Dynamic Analysis" *Earthq. Eng. Struct. Dyn.,* **31**(3): 491-514.

Van de Lindt, J.W. and Walz, M.A. (2003). "Development and Application of Wood Shear Wall Reliability Model." *J. Struct. Eng.*, ASCE, **129**(3): 405-413.

Villaverde, R. (2009). *Fundamental Concepts of Earthquake Engineering.* CRC Press, Boca Raton, FL.

Watkins, D., Chui, L., Hutchinson, T.C., and Hoehler, M.S. (2009). *Survey and characterization of floor and wall mounted mechanical and electrical equipment in buildings.* Structural Systems Research Project Report Series. SSRP 09/11. Department of Structural Engineering, University of California, San Diego. La Jolla, CA.

Wieser, J. (2011). *Assessment of Floor Accelerations in Yielding Buildings.* MS Thesis, Department of Civil and Environmental Engineering, University of Nevada, Reno.

Wood, R.L. and Hutchinson, T.C. (2012). *A Numerical Model for Capturing the In-Plane Seismic Response of Interior Metal Stud Partition Walls*, NEES-Nonstructural Technical Report Series, MCEER-12-0007, University at Buffalo, State University of New York (SUNY).

Wood, R.L., Hutchinson, T.C., and Hoehler, M.S. (2009). *Cyclic Load and Crack Protocols for Anchored Nonstructural Components and Systems*. Structural Systems Research Project Report Series. SSRP 09/12. Department of Structural Engineering, University of California, San Diego. La Jolla, CA.

Appendix A Partition Wall Model

Pwall.tcl Procedure File

The file below provides the brief user manual and a description of the model parameters.

```
#-------------------------------------------------------------------------------------------------------------
#-------------------------------------------------------------------------------------------------------------
proc pwall { eleTag iNode jNode IDPW PWType lenwall recorderFlag dir} {
# ###########################################################################
# Partition wall implementation scheme and procedure designed for use into OpenSees
# Reference http://opensees.berkeley.edu
# Units are prescribed as kips and inches exclusively throughout this procedure
#
# Developed by: Richard L. Wood, University of California, San Diego
# Latest revision:  July 19, 2011
#
# First script pwall.tcl is the initial procedure file for the beginning of the partition wall
# implementation
# Second script RUNpwall.tcl is file containing all the calibrated parameters which should
# not be changed
#
# Explanation of General Procedure Parameters:
# eleTag - unique element object tag for created partition wall element
# Note: created internal partitions node will take the form as "eleTag+1" or "eleTag+2"
# (i.e. eleTag=1000 creates nodes 10001 and 10002 where 1 is lower-story and 2 upper-story)
# iNode - created upper-story node of partition wall
# jNode - created lower-story node of partition wall
# recorderFlag - toggle for partition wall element-by-element output (1 = on)
# dir - string input referring to created directory folder for recorder output
#
# Explanation of Partition Wall Specific Parameters:
# IDPW – partition wall identifier signifying statistical value represented
# IDPW = -1 refers to average minus standard deviation force-displacement response
```

```
# IDPW = 0 refers to average force-displacement response
# IDPW = 1 refers to average plus standard deviation force-displacement response
# PWType – partition wall type construction grade
# PWType = 0 is classified as commercial grade construction (18 gauge placed 24 inches on center)
# PWType = 1 is classified as institutional grade construction (30 gauge placed 16 inches on center)
# lenwall – partition wall length (feet)
#
# Advanced User Input:
# PWType– partition wall type identifying subgroup models.  Note that the wall scaling for the
#  subgroup models is completely based on linear length where the original length of
#  the wall (experimentally tested) is 11.5 feet excluding return walls
# PWType = 11 is classified as subgroup 1a (commercial, partially connected)
# PWType = 12 is classified as subgroup 1b (commercial, fully connected)
#  PWType = 13 is classified as subgroup 2a (institutional, partially connected)
# PWType = 14 is classified as subgroup 2b (institutional, fully connected)

# Example Input:
# The average response of a 43.0 ft long institutional PW spanning between nodes 2 and 5
# set dir FolderName
# pwall 1000 5 2 0 1 43.0 1 $dir;
################################################################################
# End User Document ------------------------------------------------------------------------------

source proc/RUNpwall.tcl
}
# End PWall Procedure
#--------------------------------------------------------------------------------------------------
#--------------------------------------------------------------------------------------------------
```

RUNwall.tcl File

The file below is the model script, reference the file pwall.tcl for details and explanations.

```
#-----------------------------------------------------------------------------------------------------------
#-----------------------------------------------------------------------------------------------------------
##############################################################################
# Developed by: Richard L. Wood, University of California, San Diego
# Latest revision:  July 19 2011
# Use in conjunction with pwall.tcl
# Reference pwall.tcl for details and explanations
#
##############################################################################
# Calibrated partition wall parameters are identified here. Warning changing of parameters is not recommended.


# Create Internal Partition Wall Nodes
set Xpw [nodeCoord $iNode 1]; # location of the created partition wall node in x
set Ypw [expr [expr [nodeCoord $iNode 2] + [nodeCoord $jNode 2]] * 0.5]; # location of the created partition wall node in y
set NodeB [expr $eleTag*10 + 1]; # created partition wall node for the bottom floor
set NodeT [expr $eleTag*10 + 2]; # created partition wall node for the top floor
node $NodeB $Xpw $Ypw; # lower-story node (NodeB)
node $NodeT $Xpw $Ypw; # upper-story node (NodeT)

################### Determination of scaling factors: ##################################
# Commercial grade (18 guage/0.0188 in), 24" o.c. (2.0 ft)
if {$PWType == 0} { set corr_wl [expr [expr [expr ceil([expr $lenwall/2]) + 1] * 0.0188]]
puts "total thickness of partition wall studs is:"
}
# Institutional grade (30 guage/0.0312 in), 16" o.c. (1.3333 ft)
if {$PWType == 1} {set corr_wl [expr [expr [expr ceil([expr $lenwall/1.3333]) + 1] *0.0312]]
puts "total thickness of partition wall studs is:"
}
# Use of subgroup models, only considering length of wall
```

```
if {$PWType == 10} {
set originalwall 11.5;  # wall length in lateral direction(ft)
set corr_wl [expr ($lenwall/$originalwall)];
puts "correction factor for wall length is:"
}
puts $corr_wl
###################### Normalized Models: ######################################
# Typical variable explanation
# pForce - positive force values for each respective model (in kips)
# nForce - negative force values for each respective model (in kips)
# pDisp  - positive displacement values for each respective model (in kips)
# nDisp  - negative displacement values for each respective model (in kips)
# rD     - displacement unloading and reloading parameters for each of the elements used in the parallel formulation
# rF     - force unloading and reloading parameters for each of the elements used in the parallel formulation
# IDPW   - statistical variation flag for modeling type where [-1,0,1] refer to minus one, zero and plus one standard deviations when the default value here is 0
if {$IDPW == -1} {
set pForce [list [expr $corr_wl*10.82] [expr $corr_wl*21.07] [expr $corr_wl*8.22] [expr $corr_wl*21.07] [expr $corr_wl*21.07]];
set nForce [list [expr $corr_wl*-10.82] [expr $corr_wl*-21.07] [expr $corr_wl*-8.22] [expr $corr_wl*-21.07] [expr $corr_wl*-21.07]];
set pDisp [list 0.221 0.545 2.291 7.258 200.0];
set nDisp [list -0.221 -0.545 -2.291 -7.258 -200.0];
set rD [list 1.10 0.99 0.60 1.00 1.0];
set rF [list -0.03 0.01 0.55 0.00 0.00];
}
if {$IDPW == 0} {
set pForce [list [expr $corr_wl*13.95] [expr $corr_wl*24.28] [expr $corr_wl*16.04] [expr $corr_wl*24.28] [expr $corr_wl*24.28]];
set nForce [list [expr $corr_wl*-13.95] [expr $corr_wl*-24.28] [expr $corr_wl*-16.04] [expr $corr_wl*-24.28] [expr $corr_wl*-24.28]];
set pDisp [list 0.225 0.637 1.945 4.1 200.0];
set nDisp [list -0.225 -0.637 -1.945 -4.1 -200.0];
set rD [list 0.40 0.95 0.62 0.97 0.97];
```

```
set rF [list 0.15 0.01 0.13 0.03 0.03];

}

if {$IDPW == 1} {

set pForce [list [expr $corr_wl*15.92] [expr $corr_wl*26.43] [expr $corr_wl*23.61] [expr $corr_wl*26.43] [expr $corr_wl*26.43]];

set nForce [list [expr $corr_wl*-15.92] [expr $corr_wl*-26.43] [expr $corr_wl*-23.61] [expr $corr_wl*-26.43] [expr $corr_wl*-26.43]];

set pDisp [list 0.212 0.622 1.734 2.338 200.0];

set nDisp [list -0.212 -0.622 -1.734 -2.338 -200.0];

set rD [list 0.40 0.91 0.89 0.93 0.93];

set rF [list 0.15 0.03 0.11 0.07 0.07];

}

##################### Subgroup Models (Advanced Input Options: ######################

# Use of these models is qualified when interest directs the assessment of a particular type of wall and connection

#  PWType – partition wall type identifying subgroup models.  Note that the wall scaling for the

#  subgroup models is completely based on linear length with the original length of

#  the wall (experimentally tested) is 11.5 feet excluding return walls

#  PWType = 11 is classified as subgroup 1a (commercial, partially connected)

#  PWType = 12 is classified as subgroup 1b (commercial, fully connected)

#  PWType = 13 is classified as subgroup 2a (institutional, partially connected)

#  PWType = 14 is classified as subgroup 2b (institutional, fully connected)

if {$IDPW == 11} {

set pForce [list [expr $corr_wl*1.27] [expr $corr_wl*1.68] [expr $corr_wl*1.538] [expr $corr_wl*6.65] [expr $corr_wl*6.65]];

set pDisp [list 0.204 1.196 1.695  4.0 200.0];

set nForce [list [expr $corr_wl*-1.328] [expr $corr_wl*-1.777] [expr $corr_wl*-2.218] [expr $corr_wl*-5.06] [expr $corr_wl*-5.06]];

set nDisp [list -0.214 -0.549 -1.572 -4.0 -200.0];

set rD [list 0.1 0.7 0.9 0.93 0.93];

set rF [list 0.7 0.1 0.15 0.08 0.08];

}

if {$IDPW == 12} {

set pForce [list [expr $corr_wl*1.79] [expr $corr_wl*2.645] [expr $corr_wl*2.008]  [expr $corr_wl*6.62] [expr $corr_wl*6.62]];

set pDisp [list 0.237 0.599 1.098  4.0 200.0];
```

```
set nForce [list [expr $corr_wl*-1.666] [expr $corr_wl*-2.81] [expr $corr_wl*-2.756] [expr $corr_wl*-3.08] [expr $corr_wl*-3.08]];

set nDisp [list -0.216 -0.555 -1.451  -4.0 -200];

set rD [list 0.30 0.92 0.86 0.90 0.90];

set rF [list 0.55 0.06 0.09 0.08 0.08];

}

if {$IDPW == 13} {

set pForce [list [expr $corr_wl*1.81] [expr $corr_wl* 2.55] [expr $corr_wl*1.84]  [expr $corr_wl*2.55] [expr $corr_wl*2.55]];

set pDisp [list 0.40 1.10 2.37 6.821 200.0];

set nForce [list [expr $corr_wl*-2.06] [expr $corr_wl*-2.90] [expr $corr_wl*-2.22] [expr $corr_wl*-2.90] [expr $corr_wl*-2.90]];

set nDisp [list -0.3559 -0.93 -1.984 -6.711 -200.0];

set rD [list 0.40 0.85 0.80 0.99 0.99];

set rF [list 0.18 0.18 0.20 0.20 0.20];

}

if {$IDPW == 14} {

set pForce [list [expr $corr_wl*5.807] [expr $corr_wl*6.912] [expr $corr_wl*4.080] [expr $corr_wl*6.6912] [expr $corr_wl*6.6912]];

set pDisp [list 0.412 0.694 2.676 6.912 200.0];

set nForce [list [expr $corr_wl*-5.265] [expr $corr_wl*-6.900] [expr $corr_wl*-4.389] [expr $corr_wl*-6.900] [expr $corr_wl*-6.900]];

set nDisp [list -0.336 -0.65 -2.433 -5.126 -200.0];

set rD [list 0.40 0.90 0.55 0.99 0.99];

set rF [list 0.15 0.01 0.15 0.01 0.01];

}

########################## General Terms #######################################

# Now setting up the Sub-materials for a 5 piece material combination:

# eps and neps essentially zero terms used in the parallel formulation and combination

# uForce, gammaD, gammaF, gammaE, damage - additional unloading and reloading behavior term not varied through parallel combination (reference pinchig4 documentation)

# gammaK - unloading stiffness set to be stiff based on the initial formulation

set eps 0.00000001;

set neps -0.00000001;

set uForce [list -0.01 -0.01]

set gammaD [list 0.0 0.0 0.0 0.0 0.0]
```

```
set gammaF [list 0.0 0.0 0.0 0.0 0.0]

set gammaE 100.0;

set gammaK [list -10000.0 -10000.0 -10000.0 -10000.0 -100000.0 ]

set damage "cycle";

######################### SubMaterial 1 ########################################

# Creating each of the submaterials to be used in the parallel formulation

# refernce pinching4 script for complete details on its use

set matID1 [expr $eleTag*100 + 1];

set pEnvelopeStress [list [expr [lindex $pForce 0]] $eps $eps $eps $eps]

set nEnvelopeStress [list [expr [lindex $nForce 0]] $neps $neps $neps $neps]

set rDisp [list [expr [lindex $rD 0]] [expr [lindex $rD 0]]]

set rForce [list [expr [lindex $rF 0]] [expr [lindex $rF 0]]]

uniaxialMaterial Pinching4 $matID1 [lindex $pEnvelopeStress 0] [lindex $pDisp 0] [lindex $pEnvelopeStress 1] [lindex $pDisp 1] [lindex $pEnvelopeStress 2] [lindex $pDisp 2] [lindex $pEnvelopeStress 3] [lindex $pDisp 3] [lindex $nEnvelopeStress 0] [lindex $nDisp 0] [lindex $nEnvelopeStress 1] [lindex $nDisp 1] [lindex $nEnvelopeStress 2] [lindex $nDisp 2] [lindex $nEnvelopeStress 3] [lindex $nDisp 3] [lindex $rDisp 0] [lindex $rForce 0] [lindex $uForce 0] [lindex $rDisp 1] [lindex $rForce 1] [lindex $uForce 1] [lindex $gammaK 0] [lindex $gammaK 1] [lindex $gammaK 2] [lindex $gammaK 3] [lindex $gammaK 4] [lindex $gammaD 0] [lindex $gammaD 1] [lindex $gammaD 2] [lindex $gammaD 3] [lindex $gammaD 4] [lindex $gammaF 0] [lindex $gammaF 1] [lindex $gammaF 2] [lindex $gammaF 3] [lindex $gammaF 4] $gammaE $damage

######################### SubMaterial 2 ########################################

set matID2 [expr $eleTag*100 + 2];

set pEnvelopeStress [list $eps [expr [lindex $pForce 1]] $eps $eps $eps]

set nEnvelopeStress [list $neps [expr [lindex $nForce 1]] $neps $neps $neps]

set rDisp [list [expr [lindex $rD 1]] [expr [lindex $rD 1]]]

set rForce [list [expr [lindex $rF 1]] [expr [lindex $rF 1]]]

uniaxialMaterial Pinching4 $matID2 [lindex $pEnvelopeStress 0] [lindex $pDisp 0] [lindex $pEnvelopeStress 1] [lindex $pDisp 1] [lindex $pEnvelopeStress 2] [lindex $pDisp 2] [lindex $pEnvelopeStress 3] [lindex $pDisp 3] [lindex $nEnvelopeStress 0] [lindex $nDisp 0] [lindex $nEnvelopeStress 1] [lindex $nDisp 1] [lindex $nEnvelopeStress 2] [lindex $nDisp 2] [lindex $nEnvelopeStress 3] [lindex $nDisp 3] [lindex $rDisp 0] [lindex $rForce 0] [lindex $uForce 0] [lindex $rDisp 1] [lindex $rForce 1] [lindex $uForce 1] [lindex $gammaK 0] [lindex $gammaK 1] [lindex $gammaK 2] [lindex $gammaK 3] [lindex $gammaK 4] [lindex $gammaD 0] [lindex $gammaD 1] [lindex $gammaD 2] [lindex $gammaD 3] [lindex $gammaD 4] [lindex $gammaF 0] [lindex $gammaF 1] [lindex $gammaF 2] [lindex $gammaF 3] [lindex $gammaF 4] $gammaE $damage
```

```
######################### SubMaterial 3 ########################################

set matID3 [expr $eleTag*100 + 3];

set pEnvelopeStress [list $eps $eps [expr [lindex $pForce 2]] $eps $eps]

set nEnvelopeStress [list $neps $neps [expr [lindex $nForce 2]] $neps $neps]

set rDisp [list [expr [lindex $rD 2]] [expr [lindex $rD 2]]]

set rForce [list [expr [lindex $rF 2]] [expr [lindex $rF 2]]]

uniaxialMaterial Pinching4 $matID3 [lindex $pEnvelopeStress 0] [lindex $pDisp 0] [lindex $pEnvelopeStress 1] [lindex $pDisp 1] [lindex $pEnvelopeStress 2] [lindex $pDisp 2] [lindex $pEnvelopeStress 3] [lindex $pDisp 3] [lindex $nEnvelopeStress 0] [lindex $nDisp 0] [lindex $nEnvelopeStress 1] [lindex $nDisp 1] [lindex $nEnvelopeStress 2] [lindex $nDisp 2] [lindex $nEnvelopeStress 3] [lindex $nDisp 3] [lindex $rDisp 0] [lindex $rForce 0] [lindex $uForce 0] [lindex $rDisp 1] [lindex $rForce 1] [lindex $uForce 1] [lindex $gammaK 0] [lindex $gammaK 1] [lindex $gammaK 2] [lindex $gammaK 3] [lindex $gammaK 4] [lindex $gammaD 0] [lindex $gammaD 1] [lindex $gammaD 2] [lindex $gammaD 3] [lindex $gammaD 4] [lindex $gammaF 0] [lindex $gammaF 1] [lindex $gammaF 2] [lindex $gammaF 3] [lindex $gammaF 4] $gammaE $damage

######################### SubMaterial 4 ########################################

set matID4 [expr $eleTag*100 + 4];

set pEnvelopeStress [list $eps $eps $eps [expr [lindex $pForce 3]] $eps]

set nEnvelopeStress [list $neps $neps $neps [expr [lindex $nForce 3]] $neps]

set rDisp [list [expr [lindex $rD 3]] [expr [lindex $rD 3]]]

set rForce [list [expr [lindex $rF 3]] [expr [lindex $rF 3]]]

uniaxialMaterial Pinching4 $matID4 [lindex $pEnvelopeStress 0] [lindex $pDisp 0] [lindex $pEnvelopeStress 1] [lindex $pDisp 1] [lindex $pEnvelopeStress 2] [lindex $pDisp 2] [lindex $pEnvelopeStress 3] [lindex $pDisp 3] [lindex $nEnvelopeStress 0] [lindex $nDisp 0] [lindex $nEnvelopeStress 1] [lindex $nDisp 1] [lindex $nEnvelopeStress 2] [lindex $nDisp 2] [lindex $nEnvelopeStress 3] [lindex $nDisp 3] [lindex $rDisp 0] [lindex $rForce 0] [lindex $uForce 0] [lindex $rDisp 1] [lindex $rForce 1] [lindex $uForce 1] [lindex $gammaK 0] [lindex $gammaK 1] [lindex $gammaK 2] [lindex $gammaK 3] [lindex $gammaK 4] [lindex $gammaD 0] [lindex $gammaD 1] [lindex $gammaD 2] [lindex $gammaD 3] [lindex $gammaD 4] [lindex $gammaF 0] [lindex $gammaF 1] [lindex $gammaF 2] [lindex $gammaF 3] [lindex $gammaF 4] $gammaE $damage

######################### SubMaterial 5 ########################################

set matID5 [expr $eleTag*100 + 5];

set pEnvelopeStress [list $eps $eps $eps $eps [expr [lindex $pForce 4]]]

set nEnvelopeStress [list $neps $neps $neps $neps [expr [lindex $nForce 4]] ]

set rDisp [list [expr [lindex $rD 4]] [expr [lindex $rD 4]]]

set rForce [list [expr [lindex $rF 4]] [expr [lindex $rF 4]]]

uniaxialMaterial Pinching4 $matID5 [lindex $pEnvelopeStress 0] [lindex $pDisp 0] [lindex $pEnvelopeStress 1] [lindex $pDisp 1] [lindex $pEnvelopeStress 2] [lindex $pDisp 2] [lindex
```

```
$pEnvelopeStress 3] [lindex $pDisp 3] [lindex $nEnvelopeStress 0] [lindex $nDisp 0] [lindex $nEnvelopeStress 1] [lindex $nDisp 1] [lindex $nEnvelopeStress 2] [lindex $nDisp 2] [lindex $nEnvelopeStress 3] [lindex $nDisp 3] [lindex $rDisp 0] [lindex $rForce 0] [lindex $uForce 0] [lindex $rDisp 1] [lindex $rForce 1] [lindex $uForce 1] [lindex $gammaK 0] [lindex $gammaK 1] [lindex $gammaK 2] [lindex $gammaK 3] [lindex $gammaK 4] [lindex $gammaD 0] [lindex $gammaD 1] [lindex $gammaD 2] [lindex $gammaD 3] [lindex $gammaD 4] [lindex $gammaF 0] [lindex $gammaF 1] [lindex $gammaF 2] [lindex $gammaF 3] [lindex $gammaF 4] $gammaE $damage


############################ Lumped Material ###################################

# creation of the target partition wall material using the uniaxial parallel command

set matID [expr $eleTag*100 + 11];; # material identification assigned to the developed partition wall material, used internally herein

uniaxialMaterial Parallel $matID $matID1 $matID2 $matID3 $matID4 $matID5


###################### Partition Wall Implementation ###################################

# establishment of the slaved partition wall nodes and placement of the partition wall material as a zerolength element in the x-direction

equalDOF $iNode $NodeT 1 2 3;   # slaving the top beam node to the top internal partition wall node

equalDOF $jNode $NodeB 1 2 3;    # slaving the bottom beam node to the bottom internal partition wall node

element zeroLength $eleTag $NodeB $NodeT -mat $matID -dir 1 ;  # placement of the partition wall element in the x-direction (direction 1)


###################### Recorder Output ########################################

# if the recorderFLag is 1, seperate folders named by partition wall element number are created to output the acceleartion, displacement and force resposne

if {$recorderFlag == 1} {

file mkdir $dir/$eleTag

recorder Node -file $dir/$eleTag/pw_acc.txt -time -node $NodeB $NodeT -dof 1 accel; # record acceleration values in the x-direction (lateral) (in/s^2)

recorder Node -file $dir/$eleTag/pw_disp.txt -time -node $NodeB $NodeT -dof 1 disp; # record displacement values in the x-direction (inches)

recorder Element -file $dir/$eleTag/partion_forces.txt -time -ele $eleTag force; # record internal partition wall developed (kip)

}

#-----------------------------------------------------------------------------------------------------------------
#-----------------------------------------------------------------------------------------------------------------
```

RC-8 with Partition Wall

Example building model (RC-8) with an implemented PW at every floor level.

```
#-----------------------------------------------------------------------------------------------------------------
#-----------------------------------------------------------------------------------------------------------------
# script by Richard Wood
# units are prescribed as: kip, inch, second

# SET UP ----------------------------------------------------------------------------------------------------------
wipe analysis;
wipe;                                   # clearing OpenSees model
model basic -ndm 2 -ndf 3;              # 2 dimensions, 3 dof per node

# Input PARAMETERS ------------------------------------------------------------------------------------------------
set dir record22_2_iter_8 ;
set scale 1.7873 ;
set eq_record record22_2.txt ;
set Npoints 3000 ;
set dt 0.01 ;

#-----------------------------------------------------------------------------------------------------------------
file mkdir $dir;                        # create data directory
puts $dir
puts "8 Storey File Loaded - working..."
set damping 0.05;
set g 386.4;

# define GEOMETRY -------------------------------------------------------------------------------------------------
#node   $node#  $x      $y
node    1       0.00    0.00    ;
node    2       180.00  0.00    ;
node    3       360.00  0.00    ;
node    4       0.00    144.00  ;
node    5       180.00  144.00  ;
node    6       360.00  144.00  ;
node    7       0.00    288.00  ;
node    8       180.00  288.00  ;
node    9       360.00  288.00  ;
node    10      0.00    432.00  ;
node    11      180.00  432.00  ;
node    12      360.00  432.00  ;
node    13      0.00    576.00  ;
node    14      180.00  576.00  ;
node    15      360.00  576.00  ;
node    16      0.00    720.00  ;
node    17      180.00  720.00  ;
```

```
node    18      360.00  720.00  ;
node    19      0.00    864.00  ;
node    20      180.00  864.00  ;
node    21      360.00  864.00  ;
node    22      0.00    1008.00;
node    23      180.00  1008.00;
node    24      360.00  1008.00;
node    25      0.00    1152.00;
node    26      180.00  1152.00;
node    27      360.00  1152.00;

node    101     180.00  72.00   ;
node    102     180.00  72.00   ;
node    201     180.00  216.00  ;
node    202     180.00  216.00  ;
node    301     180.00  360.00  ;
node    302     180.00  360.00  ;
node    401     180.00  504.00  ;
node    402     180.00  504.00  ;
node    501     180.00  648.00  ;
node    502     180.00  648.00  ;
node    601     180.00  792.00  ;
node    602     180.00  792.00  ;
node    701     180.00  936.00  ;
node    702     180.00  936.00  ;
node    801     180.00  1080.00;
node    802     180.00  1080.00;

# Single point constraints -- Boundary Conditions
fix 1 1 1 1;                    # node DX DY RZ (node 1)
fix 2 1 1 1;                    # fixing node 2 and 3 as well
fix 3 1 1 1;

# nodal masses:
#mass   $node# $massX$massY$massZ
mass    4       0.073   1.00E-12        1.00E-12        ;
mass    5       0.145   1.00E-12        1.00E-12        ;
mass    6       0.073   1.00E-12        1.00E-12        ;
mass    7       0.073   1.00E-12        1.00E-12        ;
mass    8       0.145   1.00E-12        1.00E-12        ;
mass    9       0.073   1.00E-12        1.00E-12        ;
mass    10      0.073   1.00E-12        1.00E-12        ;
mass    11      0.145   1.00E-12        1.00E-12        ;
mass    12      0.073   1.00E-12        1.00E-12        ;
mass    13      0.073   1.00E-12        1.00E-12        ;
mass    14      0.145   1.00E-12        1.00E-12        ;
mass    15      0.073   1.00E-12        1.00E-12        ;
mass    16      0.073   1.00E-12        1.00E-12        ;
mass    17      0.145   1.00E-12        1.00E-12        ;
```

```
mass    18      0.073   1.00E-12        1.00E-12        ;
mass    19      0.073   1.00E-12        1.00E-12        ;
mass    20      0.145   1.00E-12        1.00E-12        ;
mass    21      0.073   1.00E-12        1.00E-12        ;
mass    22      0.073   1.00E-12        1.00E-12        ;
mass    23      0.145   1.00E-12        1.00E-12        ;
mass    24      0.073   1.00E-12        1.00E-12        ;
mass    25      0.073   1.00E-12        1.00E-12        ;
#mass   26      0.145   1.00E-12        1.00E-12        ;
mass    27      0.073   1.00E-12        1.00E-12        ;

# Define ELEMENTS -------------------------------------------------------------------------------------
geomTransf Corotational 1;

#### Defining Concrete Materials (Linear Tensile Strength) ----------------------------------------
# confined concrete 1
set IDconcC1 2;                 # material ID tag -- unconfined cover
set fc1C1       [expr -6.3];    # CONFINED concrete, maximum stress
set eps1C1      [expr -0.0047]; # strain at maximum stress
set fc2C1       [expr -4.5];    # ultimate stress
set eps2C1      [expr -0.018];  # strain at ultimate stress
set ftC1 [expr -0.14*$fc1C1];   # tensile strength (confined)
set EtsC1 [expr -0.14*5/0.002]; # tension softening stiffness

# confined concrete 2
set IDconcC2 3;                 # material ID tag -- unconfined cover
set fc1C2       [expr -6.3];    # CONFINED concrete, maximum stress
set eps1C2      [expr -0.0045]; # strain at.8 maximum stress
set fc2C2       [expr -4.3];    # ultimate stress
set eps2C2      [expr -0.018];  # strain at ultimate stress
set ftC2 [expr -0.14*$fc1C2];   # tensile strength (confined)
set EtsC2 [expr -0.14*5/0.002]; # tension softening stiffness

# confined concrete 3
set IDconcC3 4;                 # material ID tag -- unconfined cover
set fc1C3       [expr -7.8];    # CONFINED concrete, maximum stress
set eps1C3      [expr -0.0050]; # strain at maximum stress
set fc2C3       [expr -5.1];    # ultimate stress
set eps2C3      [expr -0.022];  # strain at ultimate stress
set ftC3 [expr -0.14*$fc1C3];   # tensile strength (confined)
set EtsC3 [expr -0.14*6/0.002]; # tension softening stiffness

# unconfined concrete 1
set IDconcU1 991;               # material ID tag -- unconfined cover
set fc    [expr -5.0];          # CONCRETE Compressive Strength, ksi
set fc1U1               $fc;    # UNCONFINED concrete, maximum stress
set eps1U1      -0.003;         # strain at max strength
set fc2U1 [expr 0.2*$fc1U1];    # ultimate stress
set eps2U1      -0.01;          # strain at ultimate stress
```

```
set lambda 0.1;                 # ratio unloading/initial slope
set ftU1 [expr -0.14*$fc1U1];   # tensile strength
set EtsU1 [expr $ftU1/0.002];   # tension softening stiffness

# unconfined concrete 2
set IDconcU2 992;               # material ID tag -- unconfined cover
set fc1U2  [expr -6.0];         # UNCONFINED concrete, maximum stress
set eps1U2       -0.003;        # strain at maximum strength
set fc2U2  [expr 0.2*$fc1U2];   # ultimate stress
set eps2U2       -0.01;         # strain at ultimate stress
set lambda 0.1;                 # ratio unloading/initial slope set ftU2 [expr -0.14*$fc1U2];
                                # tensile strength +tension
set EtsU2 [expr $ftU2/0.002];   # tension softening stiffness

uniaxialMaterial Concrete02 $IDconcU1 $fc1U2 $eps1U1 $fc2U1 $eps2U1 $lambda $ftU1
$EtsU1;                         # build cover concrete (unconfined)

uniaxialMaterial Concrete02 $IDconcU2 $fc1U2 $eps1U2 $fc2U2 $eps2U2 $lambda $ftU2
$EtsU2;                         # build cover concrete (unconfined)

uniaxialMaterial Concrete02 $IDconcC1 $fc1C1 $eps1C1 $fc2C1 $eps2C1 $lambda $ftC1
$EtsC1;                         # build core concrete (confined)

uniaxialMaterial Concrete02 $IDconcC2 $fc1C2 $eps1C2 $fc2C2 $eps2C2 $lambda $ftC2
$EtsC2;                         # build core concrete (confined)

uniaxialMaterial Concrete02 $IDconcC3 $fc1C3 $eps1C3 $fc2C3 $eps2C3 $lambda $ftC3
$EtsC3;                         # build core concrete (confined)

# Defining Reinforcing Steel (Menegotto-Pinto Model) ------------------------------------------------
#reinforcing steel model (with degradation):
set fy 60;                      # yield strength of reinforcing steel
set Et 29000;                   # initial young's modulus
set IDreinf 100;                # material tag for reinforcing steel
set Esh [expr 0.0185*$Et];
set esh 0.003;
set eult 0.2;
set lsr 6.0;
set beta 1.0;
set r 0.4;
set gama 0.5;
set fu [expr 1.1*$fy];

set Cf 0.260;
set alpha 0.506;
set Cd 0.389;

uniaxialMaterial ReinforcingSteel $IDreinf $fy $fu $Et $Esh $esh $eult -CMFatigue $Cf $alpha
$Cd ;
```

```
# Defining Section Tags ----------------------------------------------------------------------------
# section GEOMETRY Interior Beam 1 -----------------------------------------------------------------
set HSec 30.0;              # Column Depth
set BSec 30.0;              # Column Width
set coverSec 2.0;           # Column cover to reinforcing steel NA.
set numBarsSec 12;          # number of longitudinal-reinforcement bars
                            # in steel layer. (symmetric top & bot)
set barAreaSec  1;          # area of longitudinal-reinforcement bars
set SecTag 1;               # set tag for symmetric section

source RCbeam.tcl
RCbeam $SecTag $IDconcU1 $IDreinf $BSec $HSec $coverSec $numBarsSec $barAreaSec

#########################################################################
# Defining Section Tags Beam Exteriors (PH Region 1) -----------------------------------------------
set HSec 30.0;              # Column Depth
set BSec 30.0;              # Column Width
set coverSec 2.0;           # Column cover to reinforcing steel NA.
set numBarsSec 12;          # number of longitudinal-reinforcement
                            # bars in steel layer. (symmetric top & bot)
set barAreaSec 1;           # area of longitudinal-reinforcement bars
set SecTag 301;             # set tag for symmetric section

source RCbeamConf.tcl

RCbeamConf $SecTag $IDconcC1 $IDconcU1 $IDreinf $BSec $HSec $coverSec $numBarsSec
$barAreaSec

#########################################################################

# section GEOMETRY Interior Beam 2 -----------------------------------------------------------------
set HSec 26.0;              # Column Depth
set BSec 30.0;              # Column Width
set coverSec 2.0;           # Column cover to reinforcing steel NA.
set numBarsSec 10;          # number of longitudinal
                            # reinforcement bars in steel layer.
                            # (symmetric top & bot)
set barAreaSec  1;          # area of longitudinal-reinforcement bars
set SecTag 2;               # set tag for symmetric section

source RCbeam.tcl
RCbeam $SecTag $IDconcU1 $IDreinf $BSec $HSec $coverSec $numBarsSec $barAreaSec

#########################################################################
Tags Beam Exteriors (PH Region 2) ----------------------------------------------------------------------
set HSec 26.0;              # Column Depth
set BSec 30.0;              # Column Width
set coverSec 2.0;           # Column cover to reinforcing steel NA.
```

```
set numBarsSec 10;      # number of longitudinal-reinforcement
                        # bars in steel layer. (symmetric top & bot)
set barAreaSec 1;       # area of longitudinal-reinforcement bars
set SecTag 302;         # set tag for symmetric section

source RCbeamConf.tcl

RCbeamConf $SecTag $IDconcC2 $IDconcU1 $IDreinf $BSec $HSec $coverSec $numBarsSec
$barAreaSec

#########################################################################

# section GEOMETRY (Columns) -------------------------------------------------------------------
set HSec 32.0;          # Column Depth
set BSec 32.0;          # Column Width
set cover 2.5;          # Column cover to reinforcing steel NA,
                        # parallel to H
set numBarsSec 20;      # Number of bars in the whole section, "equal # sides"
set barAreaSec 1.27;    # area of longitudinal-reinforcement bars
set SecTag 201;         # set tag for symmetric section

source RCcolumn.tcl

RCcolumn $SecTag $IDconcC3 $IDconcU2 $IDreinf $BSec $HSec $cover $numBarsSec
$barAreaSec

# Defining Elements ----------------------------------------------------------------------------------
# element beamWithHinges $eleTag $iNode $jNode $secTagI $Lpi
# secTagJ $Lpj $E $A $Iz $transfTag

element beamWithHinges 1 4 5  301 28.81 301 0 4031 900 90949 1;
element beamWithHinges 2 5 6  301 0 301 28.81 4031 900 90949 1;
element beamWithHinges 3 7 8  301 28.81 301 0 4031 900 90949 1;
element beamWithHinges 4 8 9  301 0 301 28.81 4031 900 90949 1;


element beamWithHinges 5 10 11 301 28.81 301 0 4031 900 90949 1;
element beamWithHinges 6 11 12 301 0 301 28.81 4031 900 90949 1;
element beamWithHinges 7 13 14 301 28.81 301 0 4031 900 90949 1;
element beamWithHinges 8 14 15 301 0 301 28.81 4031 900 90949 1;


element beamWithHinges 9 16 17 302 28.81 302 0 4031 780 78041 1;
element beamWithHinges 10 17 18 302 0 302 28.81 4031 780 78041 1;
element beamWithHinges 11 19 20 302 28.81 302 0 4031 780 78041 1;
element beamWithHinges 12 20 21 302 0 302 28.81 4031 780 78041 1;


element beamWithHinges 13 22 23 302 28.81 302 0 4031 780 78041 1;
```

```
element beamWithHinges 14 23 24 302 0 302 28.81 4031 780 78041 1;
element beamWithHinges 15 25 26 302 28.81 302 0 4031 780 78041 1;
element beamWithHinges 16 26 27 302 0 302 28.81 4031 780 78041 1;

element beamWithHinges 17 1 4 201 11.53 201 11.53 4415 1024 81016 1;
element beamWithHinges 18 3 6 201 11.53 201 11.53 4415 1024 81016 1;
element beamWithHinges 19 4 7 201 11.53 201 11.53 4415 1024 81016 1;
element beamWithHinges 20 6 9 201 11.53 201 11.53 4415 1024 81016 1;

element beamWithHinges 21 7 10 201 11.53 201 11.53 4415 1024 81016 1;
element beamWithHinges 22 9 12 201 11.53 201 11.53 4415 1024 81016 1;
element beamWithHinges 23 10 13 201 11.53 201 11.53 4415 1024 81016 1;
element beamWithHinges 24 12 15 201 11.53 201 11.53 4415 1024 81016 1;

element beamWithHinges 25 13 16 201 11.53 201 11.53 4415 1024 81016 1;
element beamWithHinges 26 15 18 201 11.53 201 11.53 4415 1024 81016 1;
element beamWithHinges 27 16 19 201 11.53 201 11.53 4415 1024 81016 1;
element beamWithHinges 28 18 21 201 11.53 201 11.53 4415 1024 81016 1;

element beamWithHinges 29 19 22 201 11.53 201 11.53 4415 1024 81016 1;
element beamWithHinges 30 21 24 201 11.53 201 11.53 4415 1024 81016 1;
element beamWithHinges 31 22 25 201 11.53 201 11.53 4415 1024 81016 1;
element beamWithHinges 32 24 27 201 11.53 201 11.53 4415 1024 81016 1;

# Define Partition Wall Elements ------------------------------------------------------------------------
set PWType 0;
set IDPW 1;
set lenwall 56.0;
puts $lenwall;
set matID 1000;
source pwall.tcl

# Placing Partition Walls:-------------------------------------------------------------------------------
equalDOF 2 101 1 2 3;
equalDOF 5 102 1 2 3;
equalDOF 5 201 1 2 3;
equalDOF 8 202 1 2 3;
equalDOF 8 301 1 2 3;
equalDOF 11 302 1 2 3;
equalDOF 11 401 1 2 3;
equalDOF 14 402 1 2 3;
equalDOF 14 501 1 2 3;
equalDOF 17 502 1 2 3;
equalDOF 17 601 1 2 3;
equalDOF 20 602 1 2 3;
equalDOF 20 701 1 2 3;
equalDOF 23 702 1 2 3;
equalDOF 23 801 1 2 3;
equalDOF 26 802 1 2 3;
```

```
element zeroLength 1001 101 102 -mat $matID -dir 1 ;
element zeroLength 1002 201 202 -mat $matID -dir 1 ;
element zeroLength 1003 301 302 -mat $matID -dir 1 ;
element zeroLength 1004 401 402 -mat $matID -dir 1 ;
element zeroLength 1005 501 502 -mat $matID -dir 1 ;
element zeroLength 1006 601 602 -mat $matID -dir 1 ;
element zeroLength 1007 701 702 -mat $matID -dir 1 ;
element zeroLength 1008 801 802 -mat $matID -dir 1 ;
#-----------------------------------------------------------------------------------------------------------

# Define RECORDERS ----------------------------------------------------------------------------------------
recorder Node -file $dir/reacts.txt -node 1 2 3 -dof 1 2 3 reaction;
recorder Node -file $dir/reacts.txt -node 4 5 6 -dof 1 2 3 reaction;

recorder Node -file $dir/floor_acc.txt -time -dT 0.01 -node 4 5 6 7 8 9 10 11 12 13 14 15 16 17 18
19 20 21 22 23 24 25 26 27 -dof 1 accel;
recorder Node -file $dir/floor_disp.txt -time -dT 0.01 -node 4 5 6 7 8 9 10 11 12 13 14 15 16 17
18 19 20 21 22 23 24 25 26 27 -dof 1 disp;
recorder Node -file $dir/floor_rot.txt -time -dT 0.01 -node 4 5 6 7 8 9 10 11 12 13 14 15 16 17 18
19 20 21 22 23 24 25 26 27 -dof 3 disp;

recorder Node -file $dir/pw_acc.txt -time -dT 0.01 -node 101 102 201 202 301 302 401 402 501
502 601 602 701 702 801 802 -dof 1 accel;
recorder Node -file $dir/pw_disp.txt -time -dT 0.01 -node 101 102 201 202 301 302 401 402 501
502 601 602 701 702 801 802 -dof 1 disp;
recorder Node -file $dir/pw_rot.txt -time -dT 0.01 -node 101 102 201 202 301 302 401 402 501
502 601 602 701 702 801 802 -dof 3 disp;

recorder Element -file $dir/partion_forces.txt -time -dT 0.01 -ele 1001 1002 1003 1004 1005
1006 1007 1008 force;
logFile $dir/log.txt

# determing Eigenvalues -----------------------------------------------------------------------------------
set outfile [open $dir/eigenvalues.txt w]
set eigenvalues [eigen 8]
puts $outfile $eigenvalues
close $outfile
# determing EigenVectors ----------------------------------------------------------------------------------
recorder Node -file $dir/eigen1.txt -node 1 3 5 -dof 1 "eigen 1"
recorder Node -file $dir/eigen2.txt -node 1 3 5 -dof 1 "eigen 2"
recorder Node -file $dir/eigen3.txt -node 1 3 5 -dof 1 "eigen 3"
recorder Node -file $dir/eigen4.txt -node 1 3 5 -dof 1 "eigen 4"
recorder Node -file $dir/eigen5.txt -node 1 3 5 -dof 1 "eigen 5"
recorder Node -file $dir/eigen6.txt -node 1 3 5 -dof 1 "eigen 6"
recorder Node -file $dir/eigen7.txt -node 1 3 5 -dof 1 "eigen 7"
recorder Node -file $dir/eigen8.txt -node 1 3 5 -dof 1 "eigen 8"
```

```
## define GRAVITY -------------------------------------------------------------------------------------------
pattern Plain 1 Linear {
#       $node   $Fx     $Fy     $Mz     ;
load    4       1.00E-12        -56.06  -3363.75;
load    6       1.00E-12        -56.06  3363.75;
load    7       1.00E-12        -56.06  -3363.75;
load    9       1.00E-12        -56.06  3363.75;
load    10      1.00E-12        -56.06  -3363.75;
load    12      1.00E-12        -56.06  3363.75;
load    13      1.00E-12        -56.06  -3363.75;
load    15      1.00E-12        -56.06  3363.75;


load    16      1.00E-12        -56.06  -3363.75;
load    18      1.00E-12        -56.06  3363.75;
load    19      1.00E-12        -56.06  -3363.75;
load    21      1.00E-12        -56.06  3363.75;
load    22      1.00E-12        -56.06  -3363.75;
load    24      1.00E-12        -56.06  3363.75;
load    25      1.00E-12        -56.06  -3363.75;
load    27      1.00E-12        -56.06  3363.75;
};

constraints Transformation;
numberer Plain;
system BandGeneral;
test NormDispIncr 1.0 20;
algorithm Newton;
integrator LoadControl 0.1;
analysis Static
analyze 10;
loadConst -time 0.0;

puts "File loading, ready to run analysis now"

source analysis.tcl

# determing Post-event Eigenvalues ----------------------------------------------------------------------
set outfile [open $dir/eigenvalues2.txt w]
set eigenvalues2 [eigen 8]
puts $outfile $eigenvalues2
close $outfile

# END SCRIPT ----------------------------------------------------------------------------------------------

#-------------------------------------------------------------------------------------------------------------
#-------------------------------------------------------------------------------------------------------------
```

Appendix B Nonlinear Time History Analysis Summary

LIST OF FIGURES

Figure B.1. IDA results for RC-8 bare building (no wall case): peak ground acceleration (PGA) against maximum interstory drift. 300

Figure B.2. IDA results for RC-8 bare building (no wall case): peak ground acceleration (PGA) against maximum floor level acceleration. 301

Figure B.3 IDA results for RC-8 (no wall): maximum interstory drift against spectral acceleration at $T_1^{initial}$. 302

Figure B.4 IDA results for RC-8 (no wall): maximum interstory drift against spectral displacement at $T_1^{initial}$. 303

Figure B.5 IDA results for RC-8 (no wall): maximum interstory drift against median spectral acceleration over ΔT_1. 304

Figure B.6 IDA results for RC-8 (no wall): maximum interstory drift against median spectral displacement over ΔT_1. 305

Figure B.7 IDA results for RC-8 (no wall): maximum interstory drift against mean spectral acceleration over ΔT_1. 306

Figure B.8 IDA results for RC-8 (no wall): maximum interstory drift against mean spectral displacement over ΔT_1. 307

Figure B.9 IDA results for RC-8 (no wall): maximum interstory drift against maximum spectral acceleration over ΔT_1. 308

Figure B.10 IDA results for RC-8 (no wall): maximum interstory drift against maximum spectral displacement over ΔT_1 309

Figure B.11 IDA results for RC-8 (no wall): maximum floor level acceleration against spectral acceleration at $T_1^{initial}$. 310

Figure B.12 IDA results for RC-8 (no wall): maximum floor level acceleration drift against spectral displacement at $T_1^{initial}$. 311

Figure B.13 IDA results for RC-8 (no wall): maximum floor level acceleration against median spectral acceleration over ΔT_1. 312

Figure B.14 IDA results for RC-8 (no wall): maximum floor level acceleration drift against median spectral displacement over ΔT_1. 313

Figure B.15 IDA results for RC-8 (no wall): maximum floor level acceleration against mean spectral acceleration over ΔT_1. 314

Figure B.16 IDA results for RC-8 (no wall): maximum floor level acceleration drift against mean spectral displacement over ΔT_1. 315

Figure B.17 IDA results for RC-8 (no wall): maximum floor level acceleration against maximum spectral acceleration over ΔT_1. 316

Figure B.18 IDA results for RC-8 (no wall): maximum floor level acceleration drift against maximum spectral displacement over ΔT_1. 317

Figure B.19 IDA results for RC-8: period elongation against median spectral acceleration over the range of T_1 318

Figure B.20 IDA results for RC-8: period elongation against median spectral displacement over the range of T_1 319

Figure B.21 IDA results for RC-8 ($L_{w,min}$ (μ)): maximum interstory drift against median spectral acceleration over the range of T_1. 320

Figure B.22 IDA results for RC-8 ($L_{w,min}$ (μ)): maximum interstory drift against median spectral displacement over the range of T_1. 321

Figure B.23 IDA results for RC-8 ($L_{w,min}$ (μ)): maximum floor level acceleration against median spectral acceleration over the range of T_1. 322

Figure B.24 IDA results for RC-8 ($L_{w,min}$ (μ)): maximum floor level acceleration against median spectral displacement over the range of T_1. 323

Figure B.25 IDA results for RC-8 ($L_{w,min}$ (μ)): period elongation against median spectral acceleration over the range of T_1. 324

Figure B.26 IDA results for RC-8 ($L_{w,min}$ (μ)): period elongation against median spectral displacement over the range of T_1. 325

Figure B.27 IDA results for RC-8 ($L_{w,max}$ (μ)): maximum interstory drift against median spectral acceleration over the range of T_1. 326

Figure B.28 IDA results for RC-8 ($L_{w,max}$ (μ)): maximum interstory drift against median spectral displacement over the range of T_1. 327

Figure B.29 IDA results for RC-8 ($L_{w,max}$ (μ)): maximum floor level acceleration against median spectral acceleration over the range of T_1. 328

Figure B.30 IDA results for RC-8 ($L_{w,max}$ (μ)): maximum floor level acceleration against median spectral displacement over the range of T_1. 329

Figure B.31 IDA results for RC-8 ($L_{w,max}$ (μ)): period elongation against median spectral acceleration over the range of T_1. 330

Figure B.32 IDA results for RC-8 ($L_{w,max}$ (μ)): period elongation against median spectral displacement over the range of T_1. 331

Figure B.33 IDA results for RC-8 ($L_{w,min}$ ($\mu-\sigma$)): maximum interstory drift against median spectral acceleration over the range of T_1. 332

Figure B.34 IDA results for RC-8 ($L_{w,min}$ ($\mu-\sigma$)): maximum interstory drift against median spectral displacement over the range of T_1. 333

Figure B.35 IDA results for RC-8 ($L_{w,min}$ ($\mu-\sigma$)): maximum floor level acceleration against median spectral acceleration over the range of T_1. 334

Figure B.36 IDA results for RC-8 ($L_{w,min}$ ($\mu-\sigma$)): maximum floor level acceleration against median spectral displacement over the range of T_1. 335

Figure B.37 IDA results for RC-8 ($L_{w,min}$ ($\mu-\sigma$)): period elongation against median spectral acceleration over the range of T_1. 336

Figure B.38 IDA results for RC-8 ($L_{w,min}$ ($\mu-\sigma$)): period elongation against median spectral displacement over the range of T_1. 337

Figure B.39 IDA results for RC-8 ($L_{w,min}$ ($\mu+\sigma$)): maximum interstory drift against median spectral acceleration over the range of T_1. 338

Figure B.40 IDA results for RC-8 ($L_{w,min}$ ($\mu+\sigma$)): maximum interstory drift against median spectral displacement over the range of T_1. 339

Figure B.41 IDA results for RC-8 ($L_{w,min}$ ($\mu+\sigma$)): maximum floor level acceleration against median spectral acceleration over the range of T_1. 340

Figure B.42 IDA results for RC-8 ($L_{w,min}$ ($\mu+\sigma$)): maximum floor level acceleration against median spectral displacement over the range of T_1. 341

Figure B.43 IDA results for RC-8 ($L_{w,min}$ ($\mu+\sigma$)): period elongation against median spectral acceleration over the range of T_1. 342

Figure B.44 IDA results for RC-8 ($L_{w,min}$ ($\mu+\sigma$)): period elongation against median spectral displacement over the range of T_1. 343

Figure B.45 IDA results for RC-8 ($L_{w,min}$ no post peak hardhening): maximum interstory drift against median spectral acceleration over the range of T_1. 344

Figure B.46 IDA results for RC-8 ($L_{w,min}$ no post peak hardhening): maximum interstory drift against median spectral displacement over the range of T_1. 345

Figure B.47 IDA results for RC-8 ($L_{w,min}$ no post peak hardhening): maximum floor level acceleration against median spectral acceleration over the range of T_1. 346

Figure B.48 IDA results for RC-8 ($L_{w,min}$ no post peak hardhening): maximum floor level acceleration against median spectral displacement over the range of T_1. 347

Figure B.49 IDA results for RC-8 ($L_{w,min}$ no post peak hardhening): period elongation against median spectral acceleration over the range of T_1. 348

Figure B.50 IDA results for RC-8 ($L_{w,min}$ no post peak hardhening): period elongation against median spectral displacement over the range of T_1. 349

Figure B.51 IDA results for RC-8 ($L_{w,max}$ no post peak hardhening): maximum interstory drift against median spectral acceleration over the range of T_1. 350

Figure B.52 IDA results for RC-8 ($L_{w,max}$ no post peak hardhening): maximum interstory drift against median spectral displacement over the range of T_1. 351

Figure B.53 IDA results for RC-8 ($L_{w,max}$ no post peak hardhening): maximum floor level acceleration against median spectral acceleration over the range of T_1. 352

Figure B.54 IDA results for RC-8 ($L_{w,max}$ no post peak hardhening): maximum floor level acceleration against median spectral displacement over the range of T_1. 353

Figure B.55 IDA results for RC-8 ($L_{w,max}$ no post peak hardhening): period elongation against median spectral acceleration over the range of T_1. 354

Figure B.56 IDA results for RC-8 ($L_{w,max}$ no post peak hardhening): period elongation against median spectral displacement over the range of T_1. 355

Figure B.57 IDA results for RC-8 ($L_{w,min}$ (μ) – no wall first floor): maximum interstory drift against median spectral acceleration over the range of T_1. 356

Figure B.58 IDA results for RC-8 ($L_{w,min}$ (μ)– no wall first floor): maximum interstory drift against median spectral displacement over the range of T_1. 357

Figure B.59 IDA results for RC-8 ($L_{w,min}$ (μ) – no wall first floor): maximum floor level acceleration against median spectral acceleration over the range of T_1..... 358

Figure B.60 IDA results for RC-8 ($L_{w,min}$ (μ)– no wall first floor): maximum floor level acceleration against median spectral displacement over the range of T_1. 359

Figure B.61 IDA results for RC-8 ($L_{w,min}$ (μ)– no wall first floor): period elongation against median spectral acceleration over the range of T_1. 360

Figure B.62 IDA results for RC-8 ($L_{w,min}$ (μ) – no wall first floor): period elongation against median spectral displacement over the range of T_1. 361

Figure B.63 IDA results for RC-8 ($L_{w,min}$ (μ) – no wall top level): maximum interstory drift against median spectral acceleration over the range of T_1. 362

Figure B.64 IDA results for RC-8 ($L_{w,min}$ (μ) – no wall top level): maximum interstory drift against median spectral displacement over the range of T_1. 363

Figure B.65 IDA results for RC-8 ($L_{w,min}$ (μ) – no wall top level): maximum floor level acceleration against median spectral acceleration over the range of T_1..... 364

Figure B.66 IDA results for RC-8 ($L_{w,min}$ (μ) – no wall top level): maximum floor level acceleration against median spectral displacement over the range of T_1. 365

Figure B.67 IDA results for RC-8 ($L_{w,min}$ (μ) – no wall top level): period elongation against median spectral acceleration over the range of T_1. 366

Figure B.68 IDA results for RC-8 ($L_{w,min}$ (μ) – no wall top level): period elongation against median spectral displacement over the range of T_1. 367

Figure B.69 IDA results for S-3H (no wall): maximum interstory drift against median spectral acceleration over the range of T_1. 368

Figure B.70 IDA results for S-3H (no wall): maximum interstory drift against median spectral displacement over the range of T_1. 368

Figure B.71 IDA results for S-3H (no wall): maximum floor level acceleration against median spectral acceleration over the range of T_1. 369

Figure B.72 IDA results for S-3H (no wall): maximum floor level acceleration against median spectral displacement over the range of T_1. 369

Figure B.73 IDA results for S-3H (no wall): period elongation against median spectral acceleration over the range of T_1. 370

Figure B.74 IDA results for S-3H (no wall): period elongation against median spectral displacement over the range of T_1. 371

Figure B.75 IDA results for S-3H ($L_{w,min}$): maximum interstory drift against median spectral acceleration over the range of T_1. 372

Figure B.76 IDA results for S-3H ($L_{w,min}$): maximum interstory drift against median spectral displacement over the range of T_1. 372

Figure B.77 IDA results for S-3H ($L_{w,min}$): maximum floor level acceleration against median spectral acceleration over the range of T_1. 373

Figure B.78 IDA results for S-3H ($L_{w,min}$): maximum floor level acceleration against median spectral displacement over the range of T_1. 373

Figure B.79 IDA results for S-3H ($L_{w,min}$): period elongation against median spectral acceleration over the range of T_1. 374

Figure B.80 IDA results for S-3H ($L_{w,min}$): period elongation against median spectral displacement over the range of T_1. 375

Figure B.81 IDA results for S-3H ($L_{w,max}$): maximum interstory drift against median spectral acceleration over the range of T_1. 376

Figure B.82 IDA results for S-3H ($L_{w,max}$): maximum interstory drift against median spectral displacement over the range of T_1. 376

Figure B.83 IDA results for S-3H ($L_{w,max}$): maximum floor level acceleration against median spectral acceleration over the range of T_1. 377

Figure B.84 IDA results for S-3H ($L_{w,max}$): maximum floor level acceleration against median spectral displacement over the range of T_1. 377

Figure B.85 IDA results for S-3H ($L_{w,max}$): period elongation against median spectral acceleration over the range of T_1. 378

Figure B.86 IDA results for S-3H ($L_{w,max}$): period elongation against median spectral displacement over the range of T_1. 379

Figure B.87 IDA results for S-9 (no wall): maximum interstory drift against median spectral acceleration over the range of T_1. 380

Figure B.88 IDA results for S-9 (no wall): maximum interstory drift against median spectral displacement over the range of T_1. 381

Figure B.89 IDA results for S-9 (no wall): maximum floor level acceleration against median spectral acceleration over the range of T_1. 382

Figure B.90 IDA results for S-9 (no wall): maximum floor level acceleration against median spectral displacement over the range of T_1. 383

Figure B.91 IDA results for S-9 (no wall): period elongation against median spectral acceleration over the range of T_1. 384

Figure B.92 IDA results for S-9 (no wall): period elongation against median spectral displacement over the range of T_1. 385

Figure B.93 IDA results for S-9 ($L_{w,min}$): maximum interstory drift against median spectral acceleration over the range of T_1. 386

Figure B.94 IDA results for S-9 ($L_{w,min}$): maximum interstory drift against median spectral displacement over the range of T_1. 387

Figure B.95 IDA results for S-9 ($L_{w,min}$): maximum floor level acceleration against median spectral acceleration over the range of T_1. 388

Figure B.96 IDA results for S-9 ($L_{w,min}$): maximum floor level acceleration against median spectral displacement over the range of T_1. 389

Figure B.97 IDA results for S-9 ($L_{w,min}$): period elongation against median spectral acceleration over the range of T_1. 390

Figure B.98 IDA results for S-9 ($L_{w,min}$): period elongation against median spectral displacement over the range of T_1. 391

Figure B.99 IDA results for RC-20 (no wall): maximum interstory drift against median spectral acceleration over the range of T_1 for floors 1-9. 392

Figure B.100 IDA results for RC-20 (no wall): maximum interstory drift against median spectral acceleration over the range of T_1 for floors 10-18. 393

Figure B.101 IDA results for RC-20 (no wall): maximum interstory drift against median spectral acceleration over the range of T_1 for floors 19-20. 394

Figure B.102 IDA results for RC-20 (no wall): maximum interstory drift against median spectral displacement over the range of T_1 for floors 1-9..... 395

Figure B.103 IDA results for RC-20 (no wall): maximum interstory drift against median spectral displacement over the range of T_1 for floors 10-18..... 396

Figure B.104 IDA results for RC-20 (no wall): maximum interstory drift against median spectral displacement over the range of T_1 for floors 19-20..... 397

Figure B.105 IDA results for RC-20 (no wall): maximum floor level acceleration against median spectral acceleration over the range of T_1 for floors 1-9. 398

Figure B.106 IDA results for RC-20 (no wall): maximum floor level acceleration against median spectral acceleration over the range of T_1 for floors 10-18. 399

Figure B.107 IDA results for RC-20 (no wall): maximum floor level acceleration against median spectral acceleration over the range of T_1 for floors 19-20 400

Figure B.108 IDA results for RC-20 (no wall): maximum floor level acceleration against median spectral displacement over the range of T_1 for floors 1-9. 401

Figure B.109 IDA results for RC-20 (no wall): maximum floor level acceleration against median spectral displacement over the range of T_1 for floors 10-18. 402

Figure B.110 IDA results for RC-20 (no wall): maximum floor level acceleration against median spectral displacement over the range of T_1 for floors 19-20. 403

Figure B.111 IDA results for RC-20 (no wall): period elongation against median spectral acceleration over the range of T_1. 403

Figure B.112 IDA results for RC-20 (no wall): period elongation against median spectral displacement over the range of T_1. 404

Figure B.113 IDA results for RC-20 ($L_{w,min}$): maximum interstory drift against median spectral acceleration over the range of T_1 for floors 1-9. 405

Figure B.114 IDA results for RC-20 ($L_{w,min}$): maximum interstory drift against median spectral acceleration over the range of T_1 for floors 10-18. 406

Figure B.115 IDA results for RC-20 ($L_{w,min}$): maximum interstory drift against median spectral acceleration over the range of T_1 for floors 19-20. 407

Figure B.116 IDA results for RC-20 ($L_{w,min}$): maximum interstory drift against median spectral displacement over the range of T_1 for floors 1-9..... 408

Figure B.117 IDA results for RC-20 ($L_{w,min}$): maximum interstory drift against median spectral displacement over the range of T_1 for floors 10-18..... 409

Figure B.118 IDA results for RC-20 ($L_{w,min}$): maximum interstory drift against median spectral displacement over the range of T_1 for floors 19-20. 410

Figure B.119 IDA results for RC-20 ($L_{w,min}$): maximum floor level acceleration against median spectral acceleration over the range of T_1 for floors 1-9. 411

Figure B.120 IDA results for RC-20 ($L_{w,min}$): maximum floor level acceleration against median spectral acceleration over the range of T_1 for floors 10-18. 412

Figure B.121 IDA results for RC-20 ($L_{w,min}$): maximum floor level acceleration against median spectral acceleration over the range of T_1 for floors 19-20. 413

Figure B.122 IDA results for RC-20 ($L_{w,min}$): maximum floor level acceleration against median spectral displacement over the range of T_1 for floors 1-9. 414

Figure B.123 IDA results for RC-20 ($L_{w,min}$): maximum floor level acceleration against median spectral displacement over the range of T_1 for floors 10-18. 415

Figure B.124 IDA results for RC-20 ($L_{w,min}$): maximum floor level acceleration against median spectral displacement over the range of T_1 for floors 19-20. 416

Figure B.125 IDA results for RC-20 ($L_{w,min}$): period elongation against median spectral acceleration over the range of T_1. 416

Figure B.126 IDA results for RC-20 ($L_{w,min}$): period elongation against median spectral displacement over the range of T_1. 417

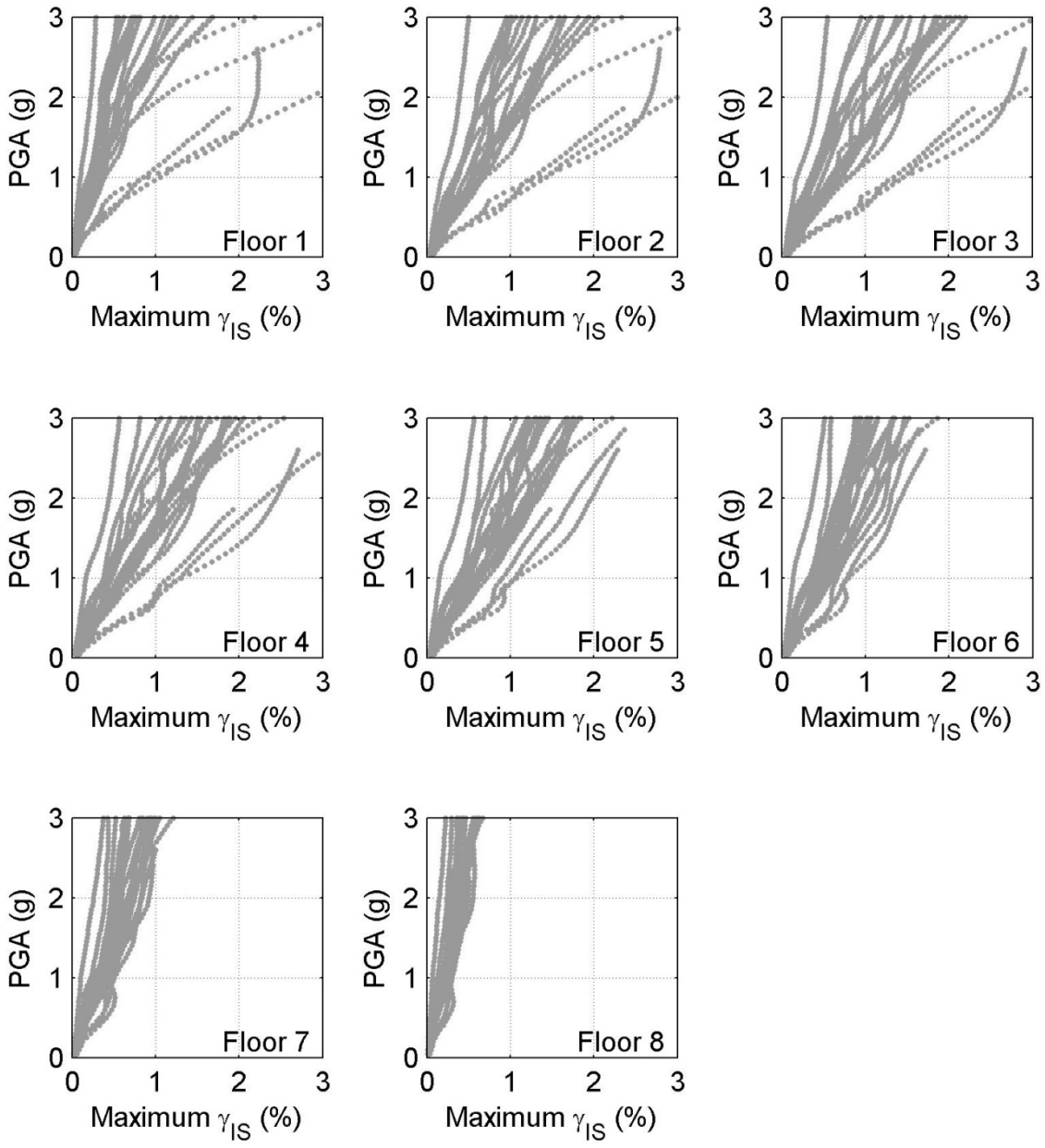

Figure B.1. IDA results for RC-8 bare building (no wall case): peak ground acceleration (PGA) against maximum interstory drift.

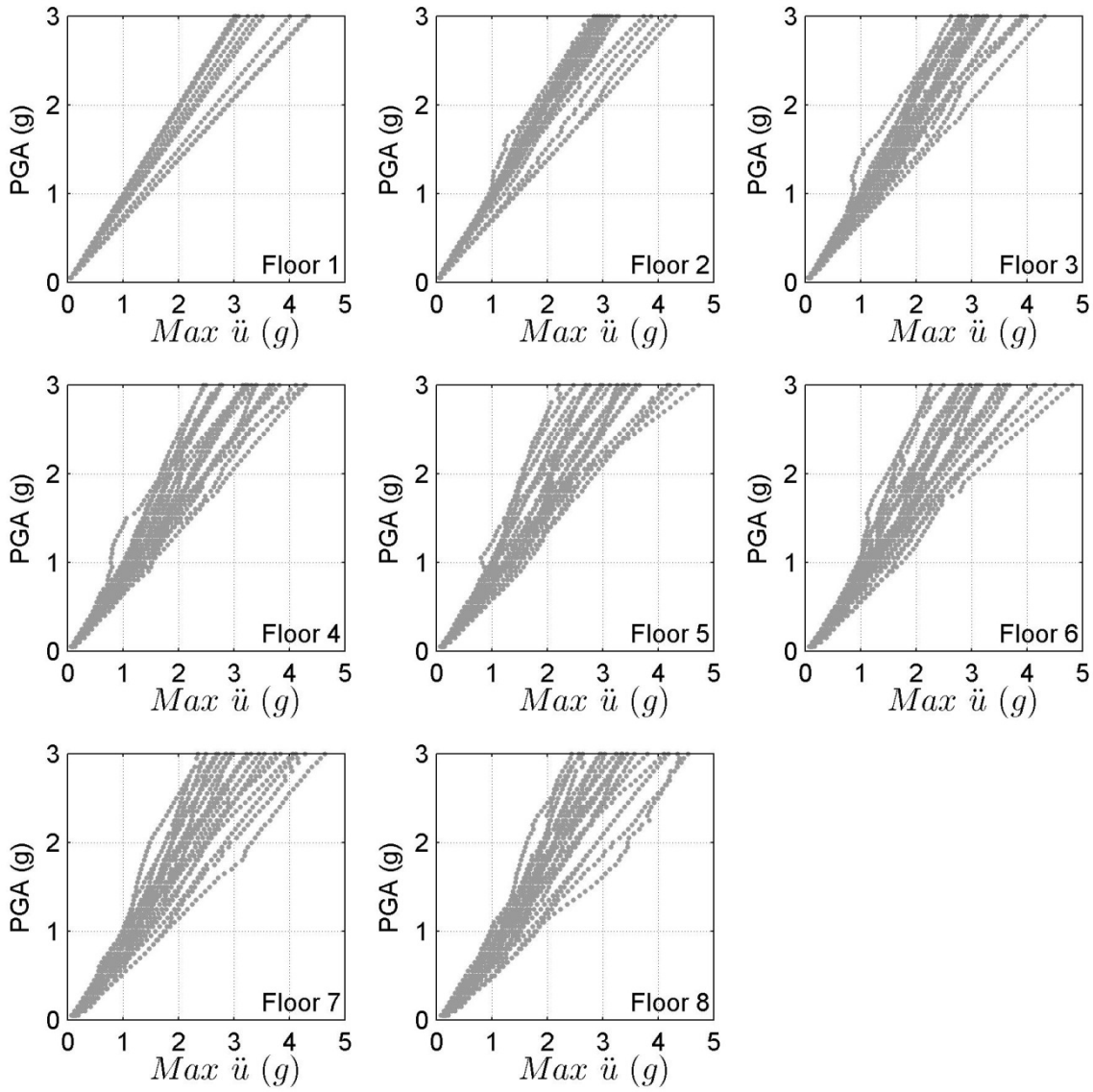

Figure B.2. IDA results for RC-8 bare building (no wall case): peak ground acceleration (PGA) against maximum floor level acceleration.

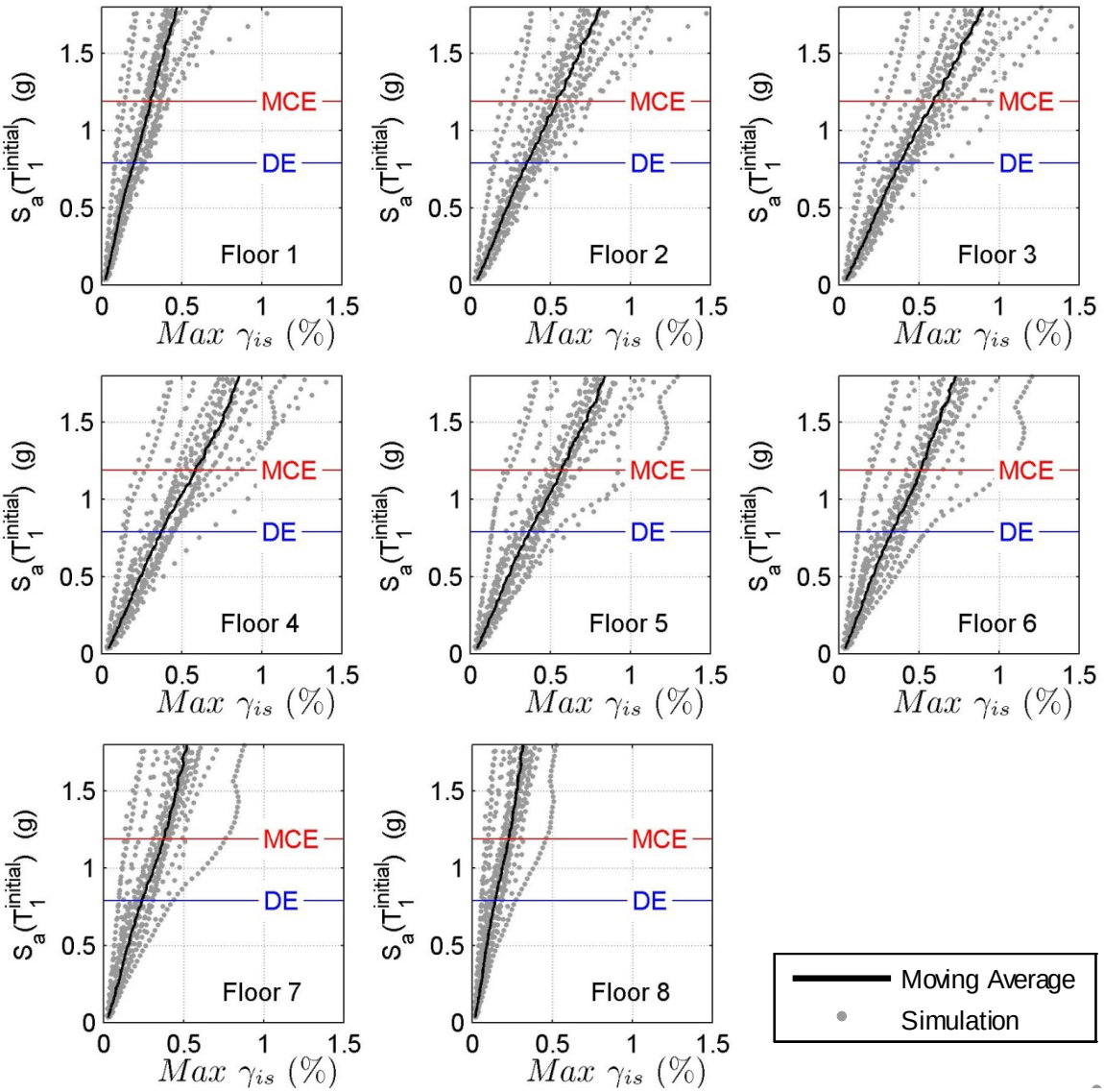

Figure B.3 IDA results for RC-8 (no wall): maximum interstory drift against spectral acceleration at $T_1^{initial}$.

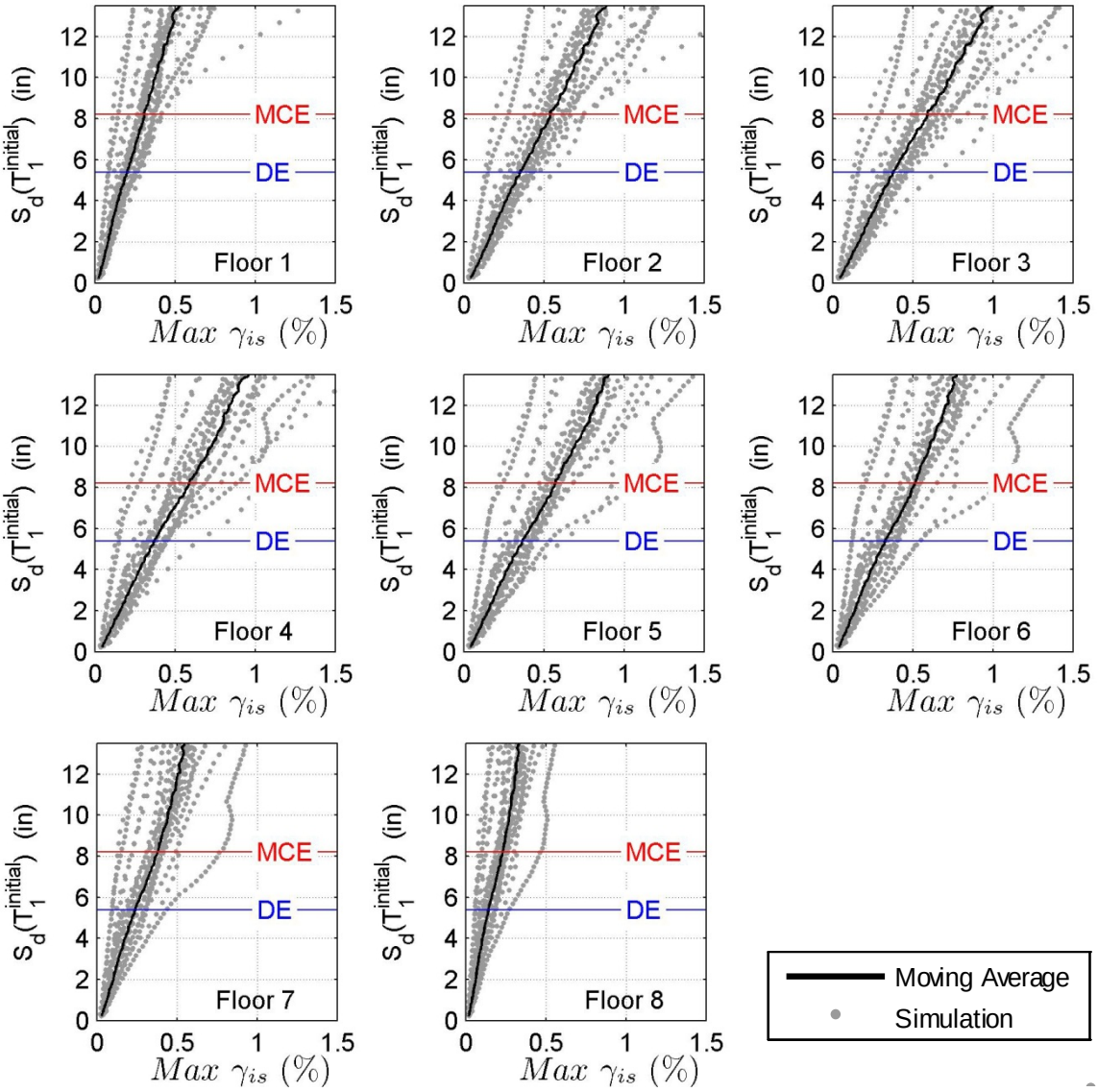

Figure B.4 IDA results for RC-8 (no wall): maximum interstory drift against spectral displacement at $T_1^{initial}$.

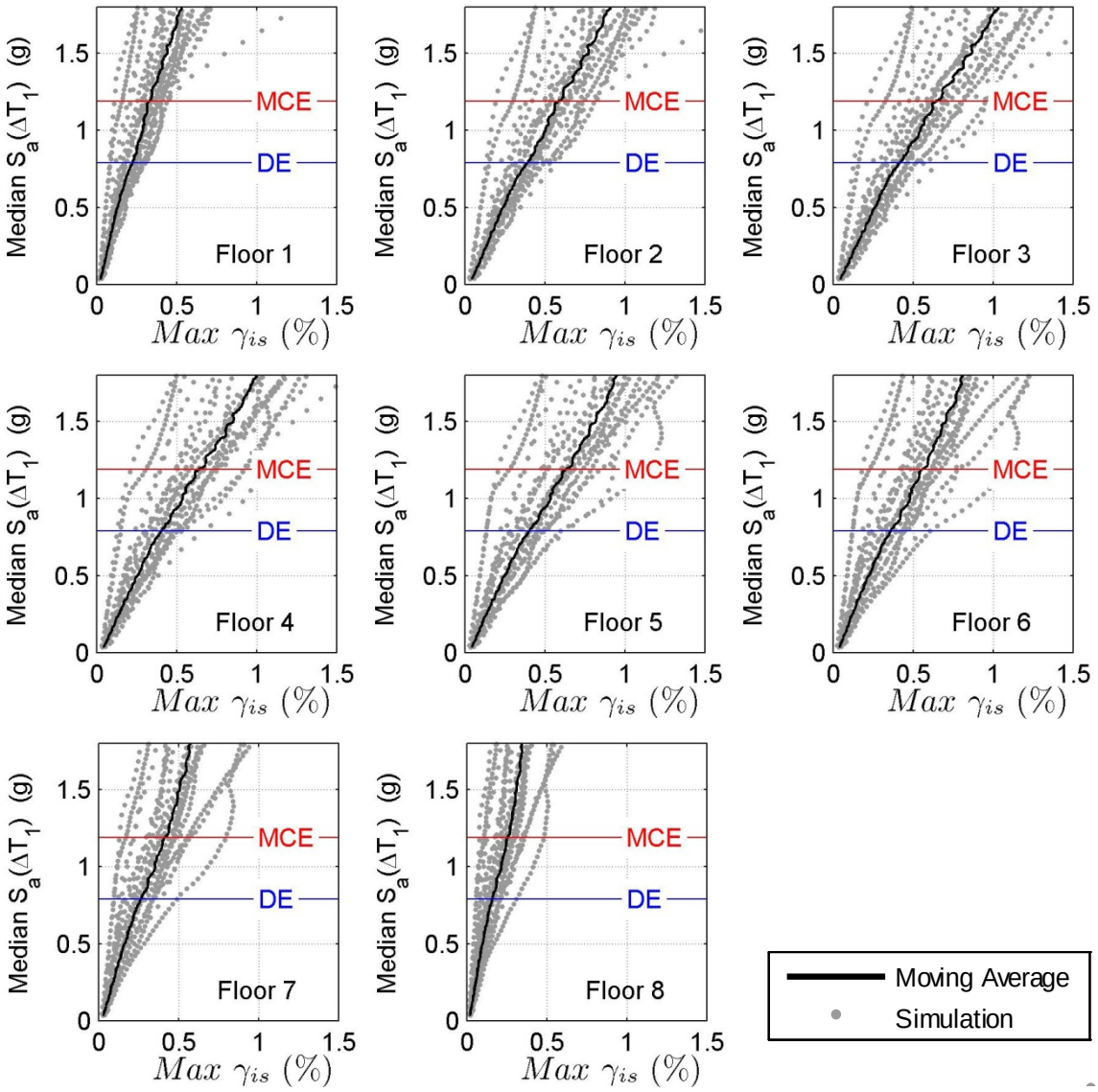

Figure B.5 IDA results for RC-8 (no wall): maximum interstory drift against median spectral acceleration over ΔT_1.

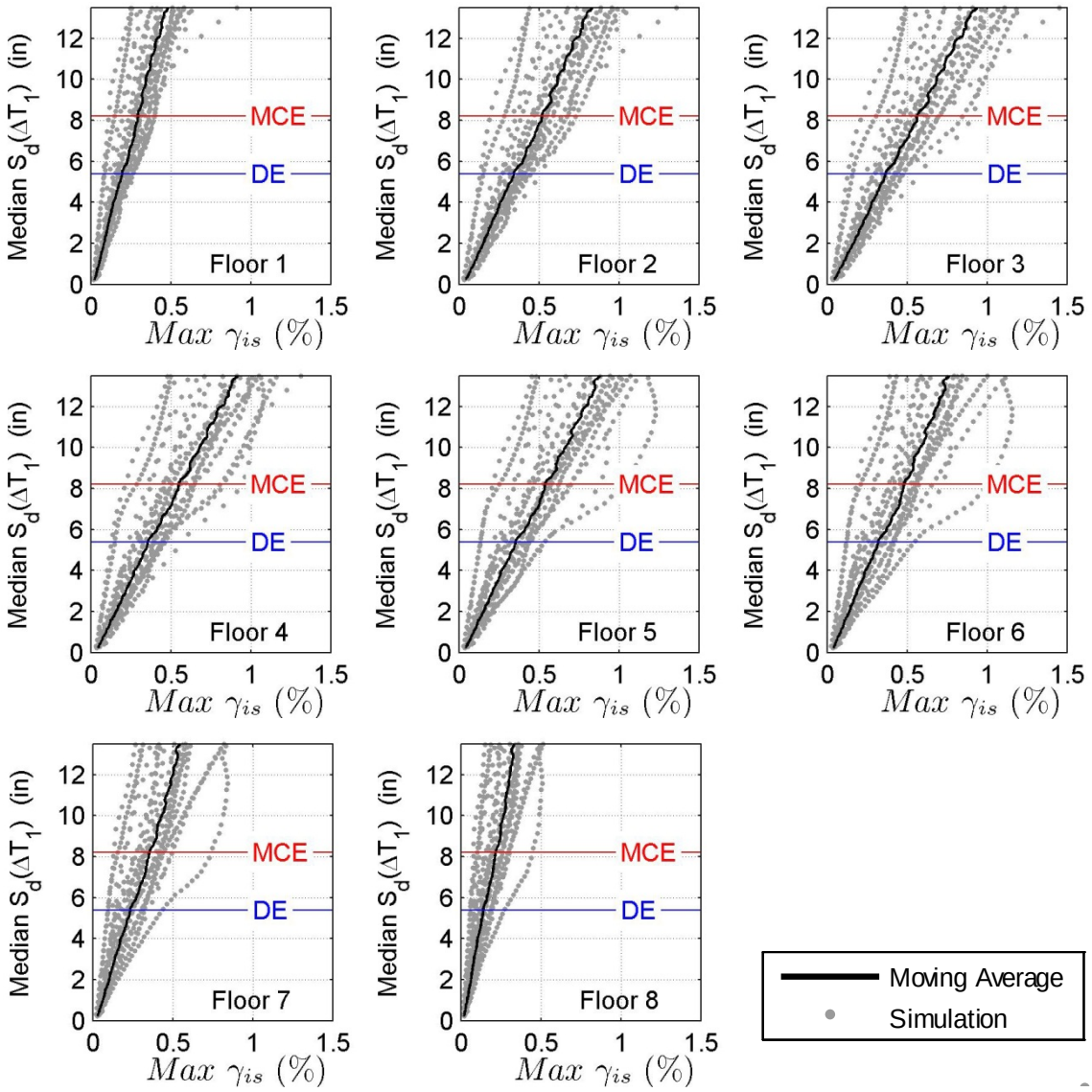

Figure B.6 IDA results for RC-8 (no wall): maximum interstory drift against median spectral displacement over ΔT_1.

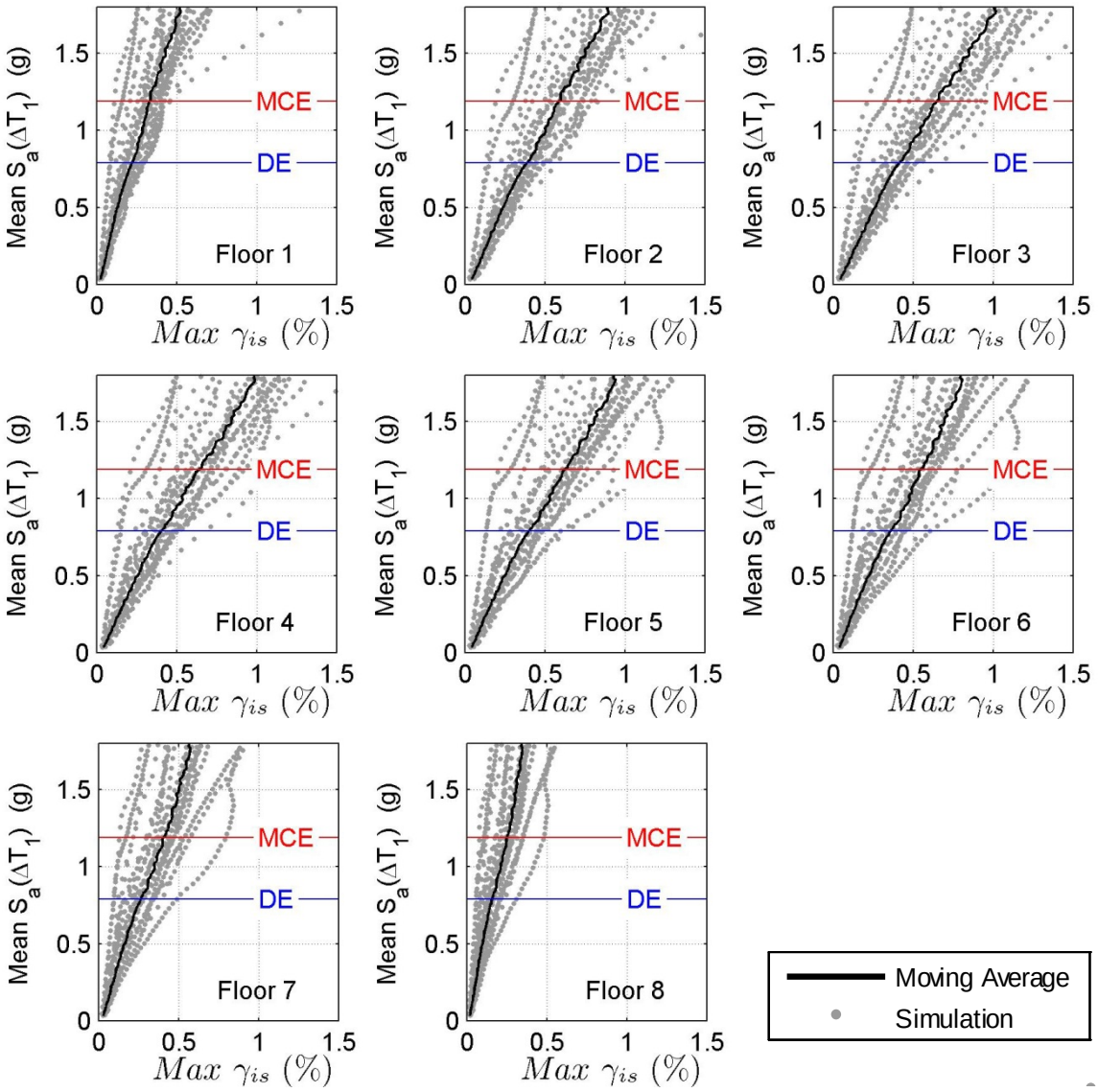

Figure B.7 IDA results for RC-8 (no wall): maximum interstory drift against mean spectral acceleration over ΔT_1.

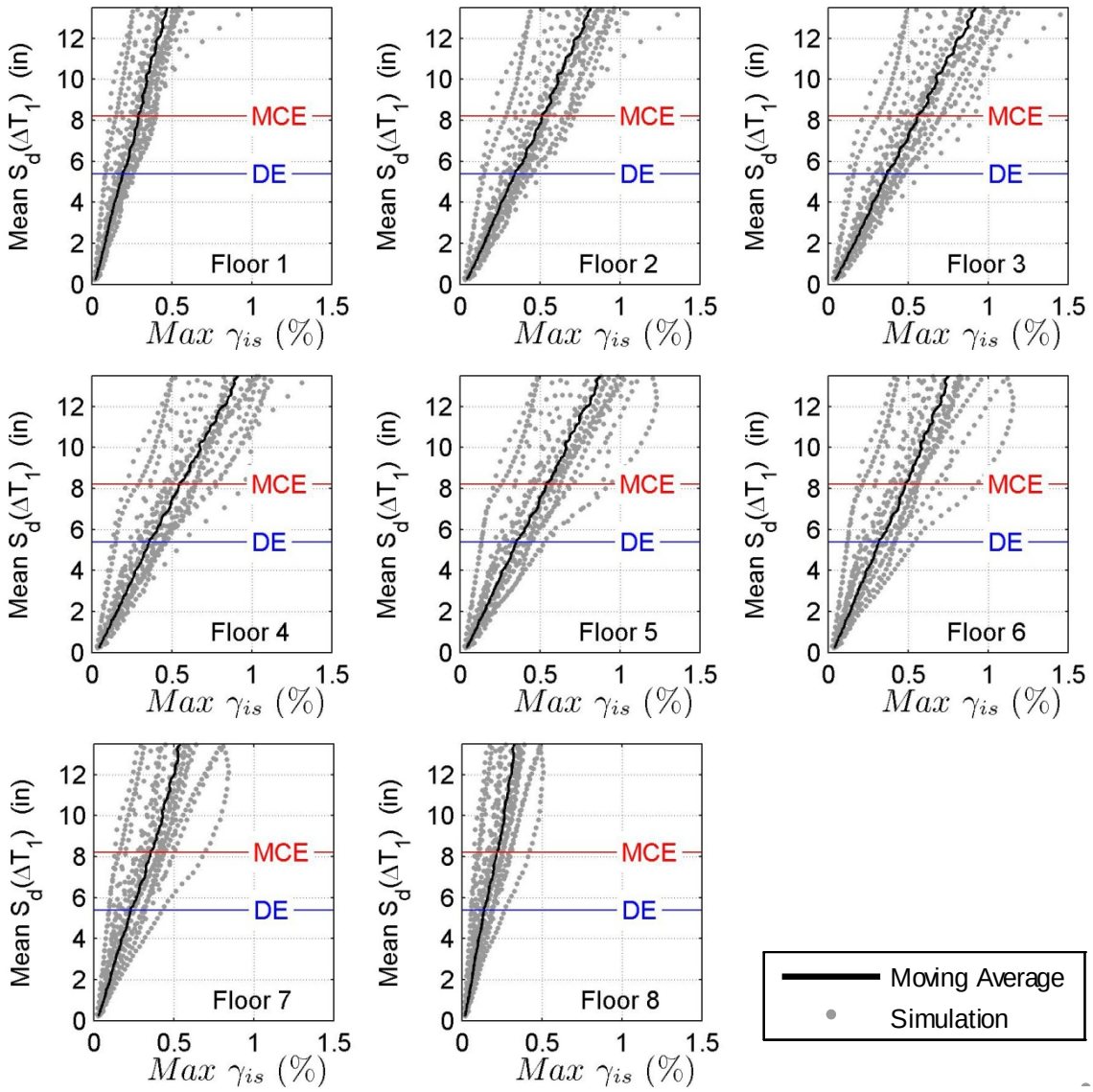

Figure B.8 IDA results for RC-8 (no wall): maximum interstory drift against mean spectral displacement over ΔT_1.

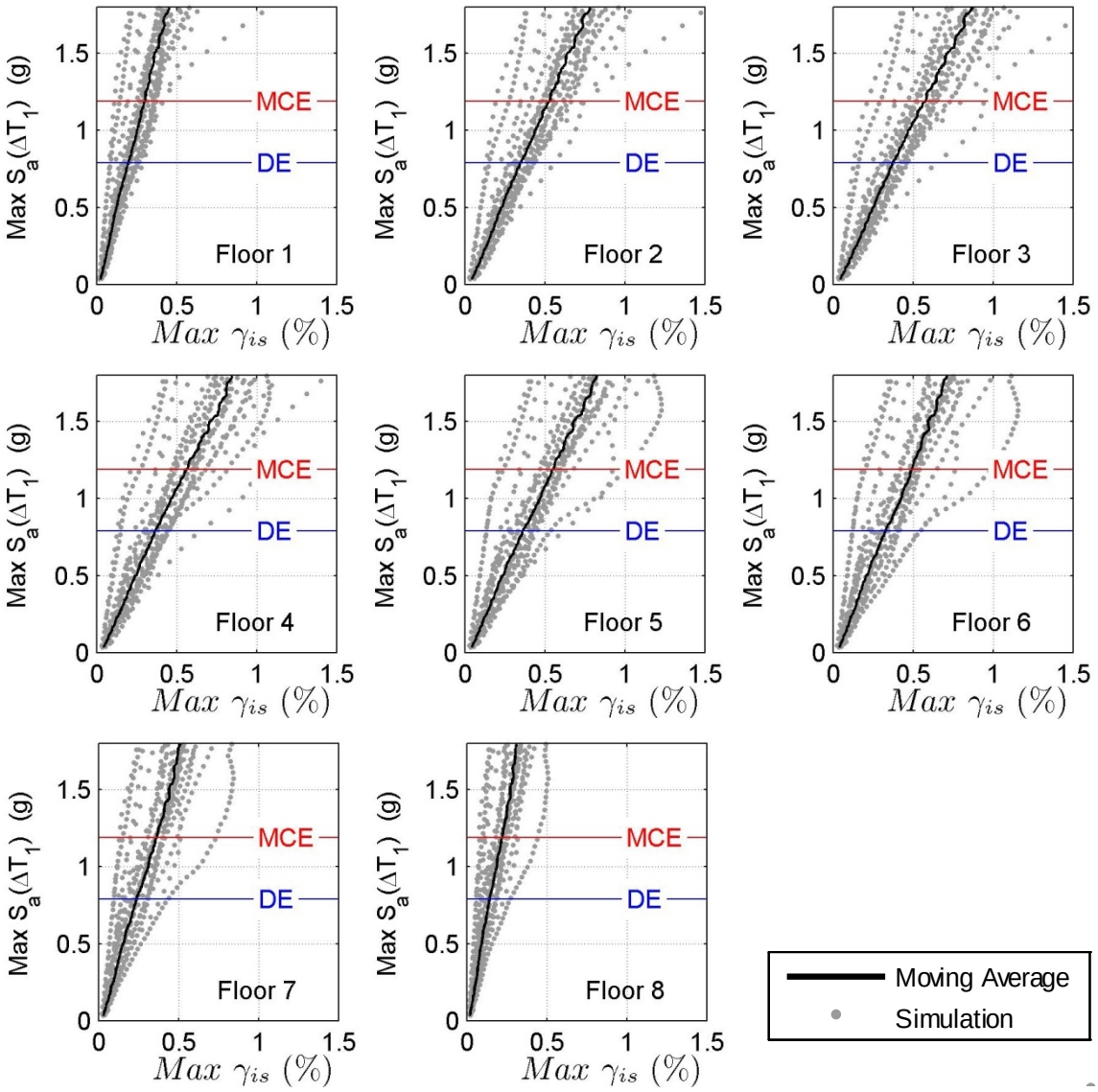

Figure B.9 IDA results for RC-8 (no wall): maximum interstory drift against maximum spectral acceleration over ΔT_1.

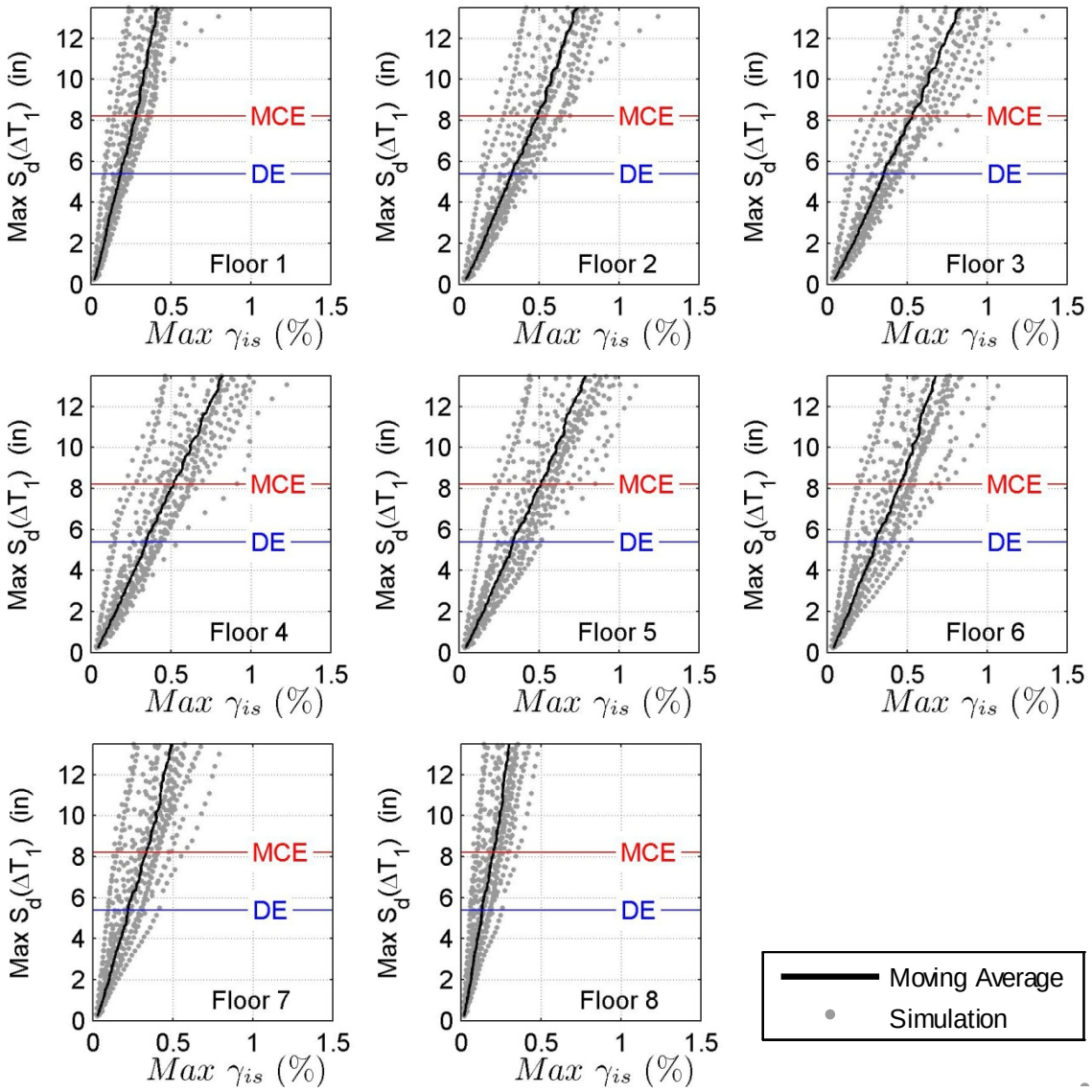

Figure B.10 IDA results for RC-8 (no wall): maximum interstory drift against maximum spectral displacement over ΔT_1.

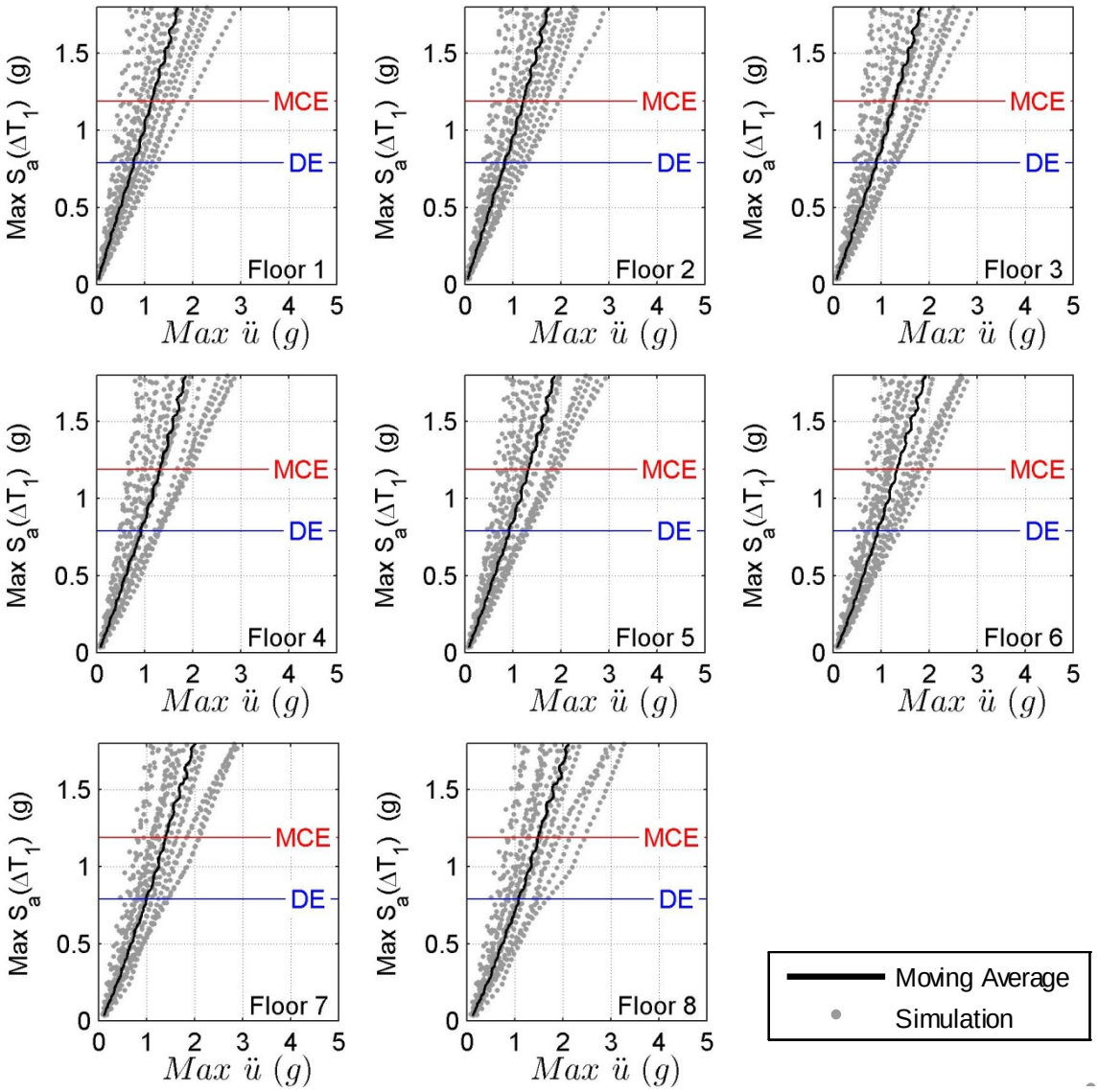

Figure B.11 IDA results for RC-8 (no wall): maximum floor level acceleration against spectral acceleration at $T_1^{initial}$.

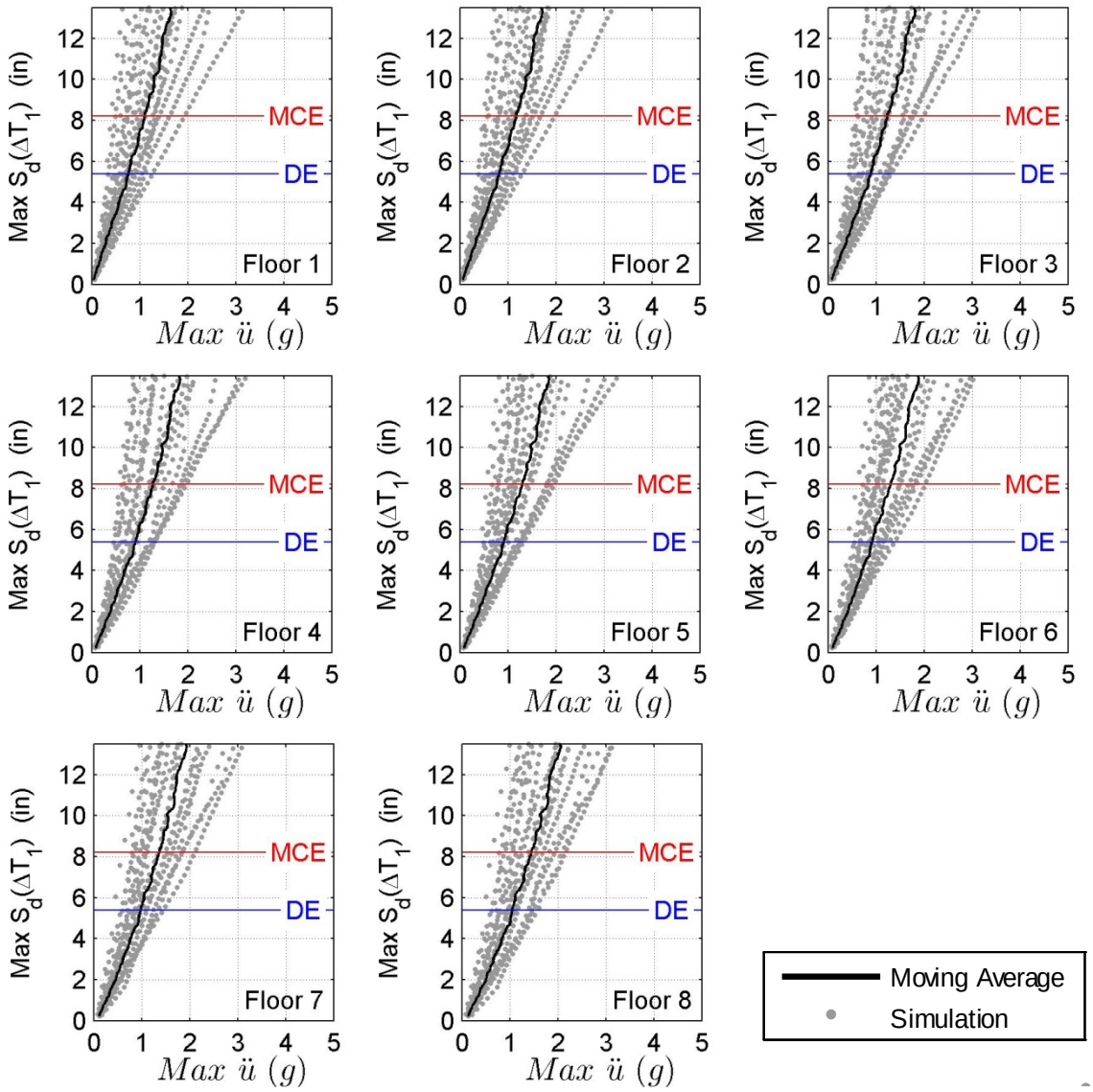

Figure B.12 IDA results for RC-8 (no wall): maximum floor level acceleration drift against spectral displacement at $T_1^{initial}$.

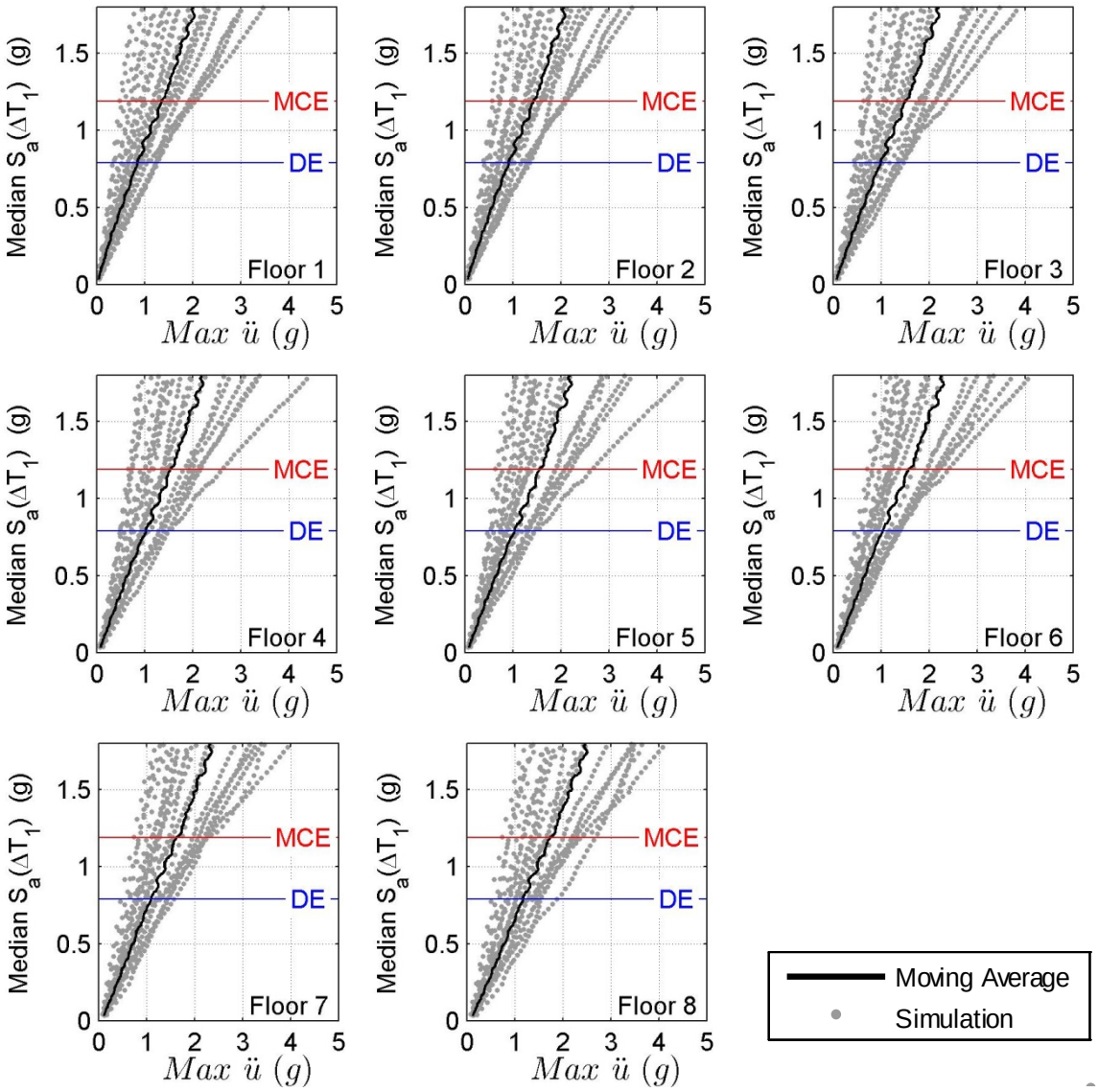

Figure B.13 IDA results for RC-8 (no wall): maximum floor level acceleration against median spectral acceleration over ΔT_1.

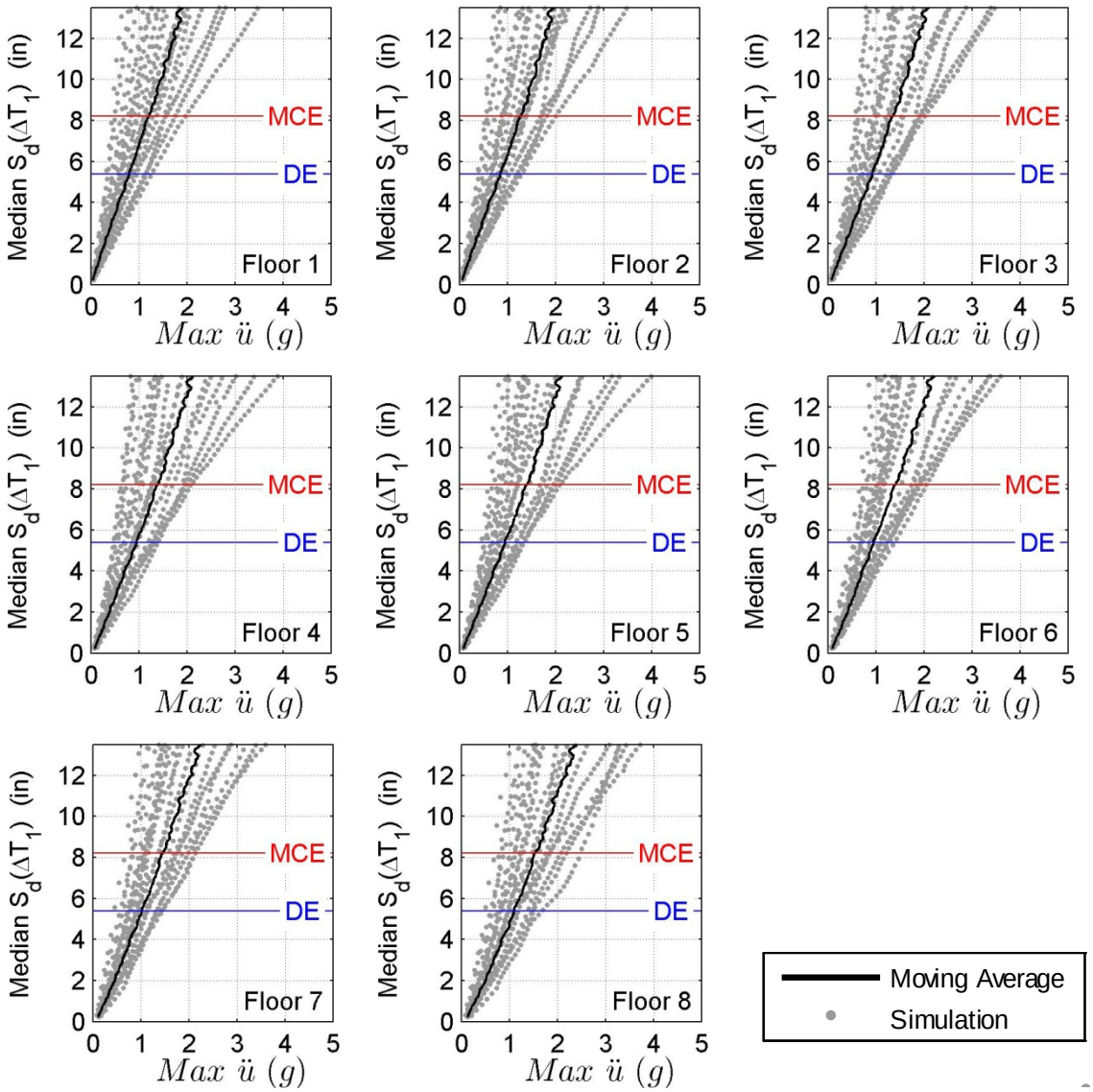

Figure B.14 IDA results for RC-8 (no wall): maximum floor level acceleration drift against median spectral displacement over ΔT_1.

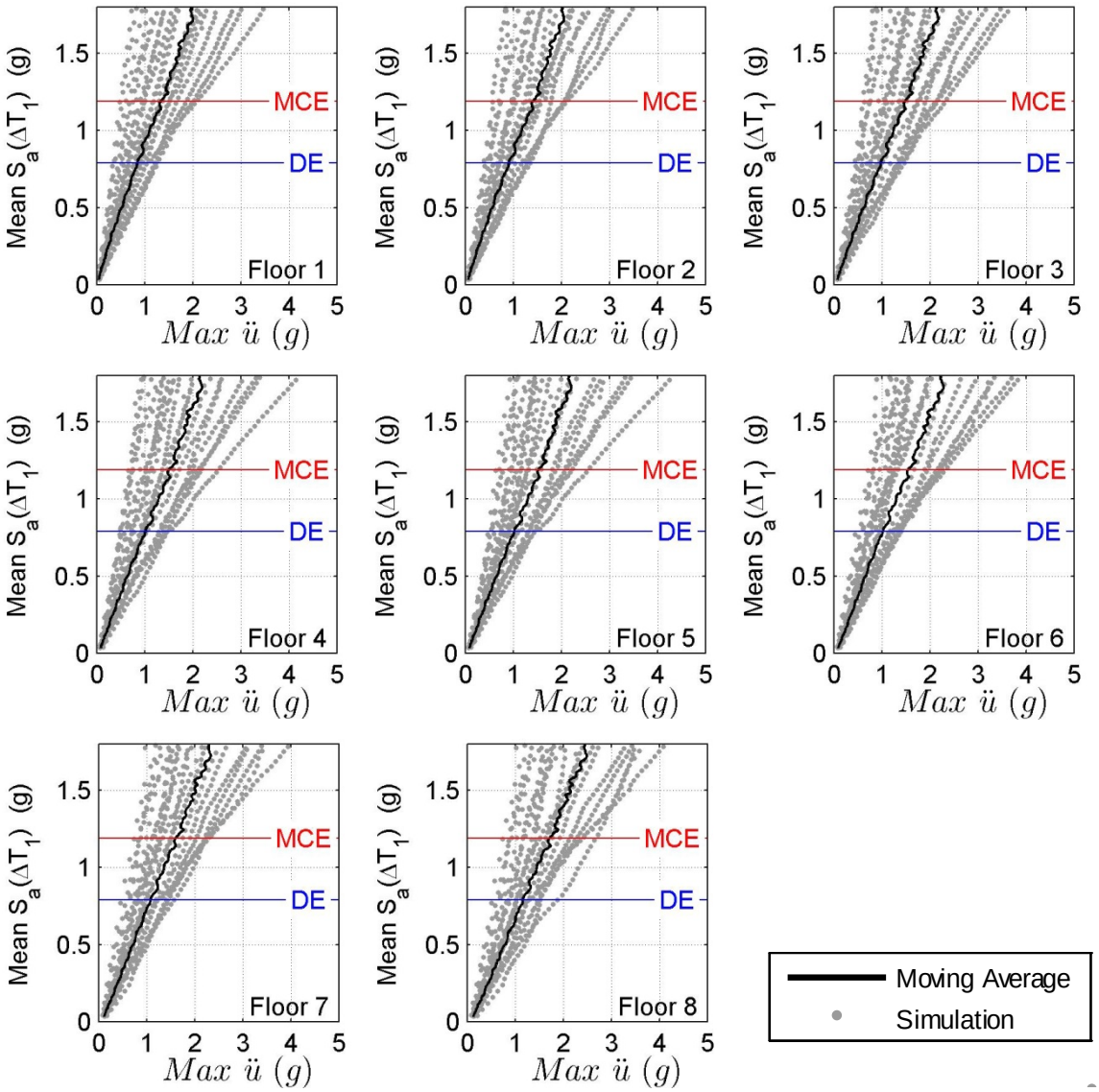

Figure B.15 IDA results for RC-8 (no wall): maximum floor level acceleration against mean spectral acceleration over ΔT_1.

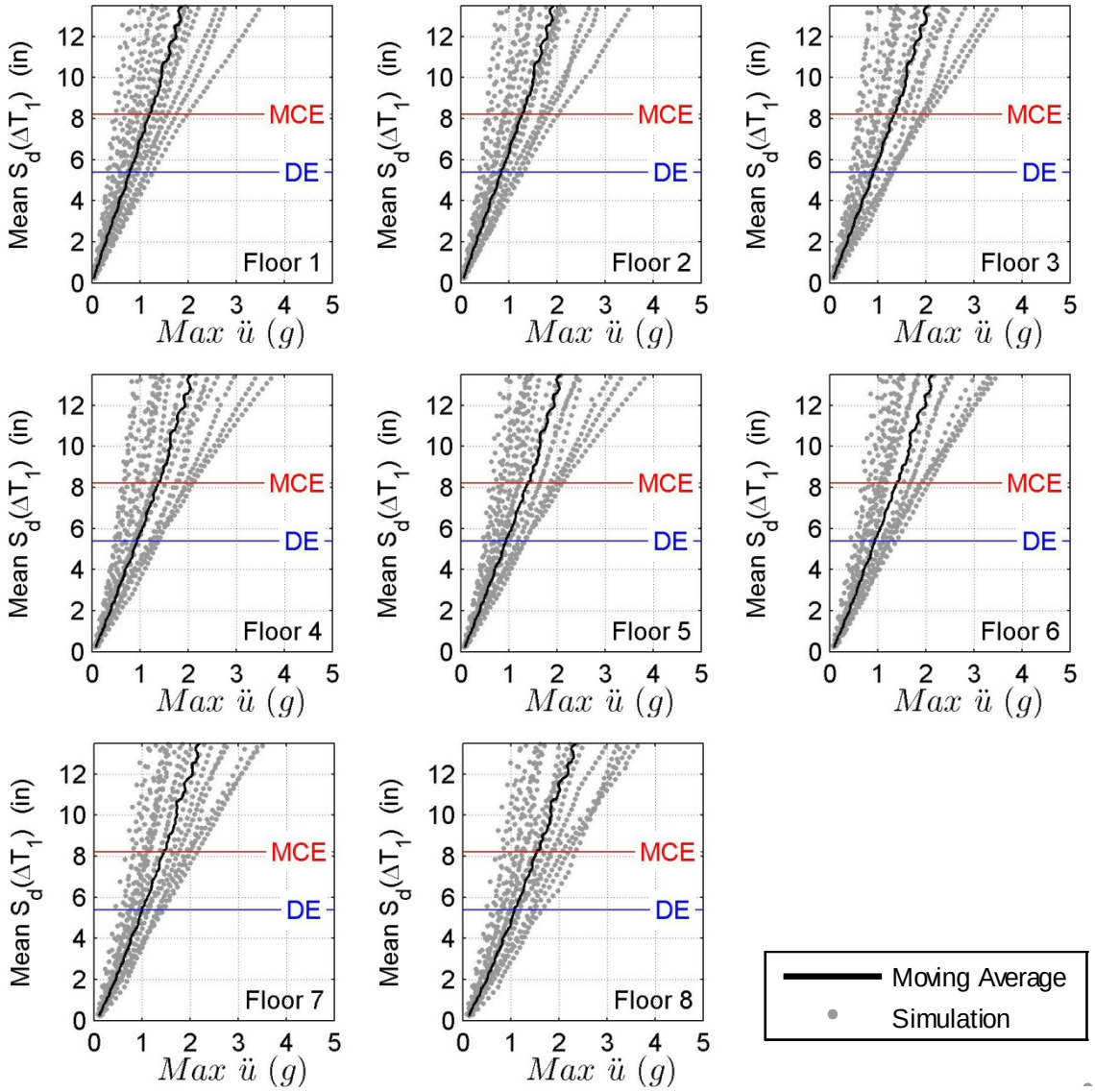

Figure B.16 IDA results for RC-8 (no wall): maximum floor level acceleration drift against mean spectral displacement over ΔT_1.

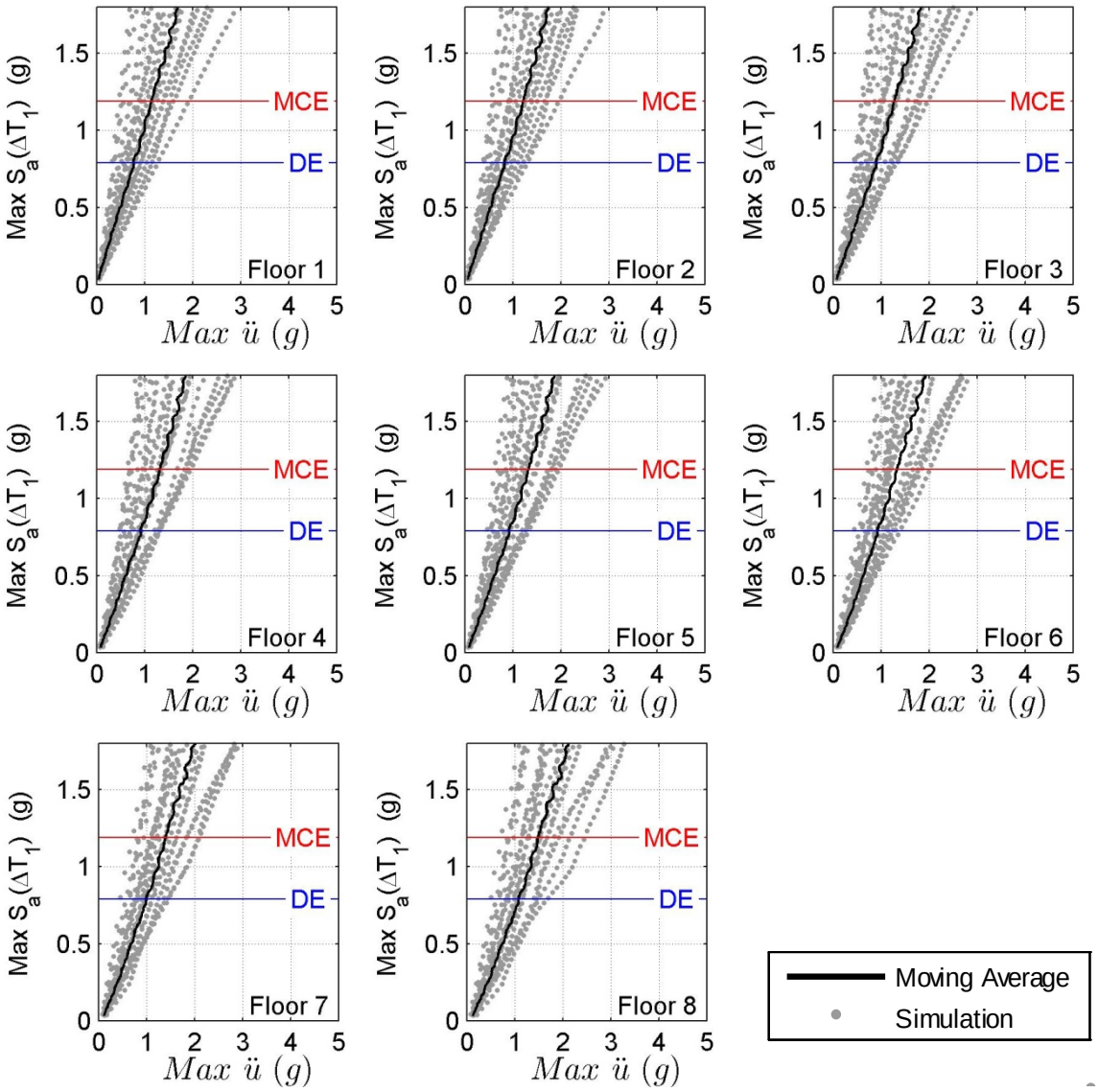

Figure B.17 IDA results for RC-8 (no wall): maximum floor level acceleration against maximum spectral acceleration over ΔT_1.

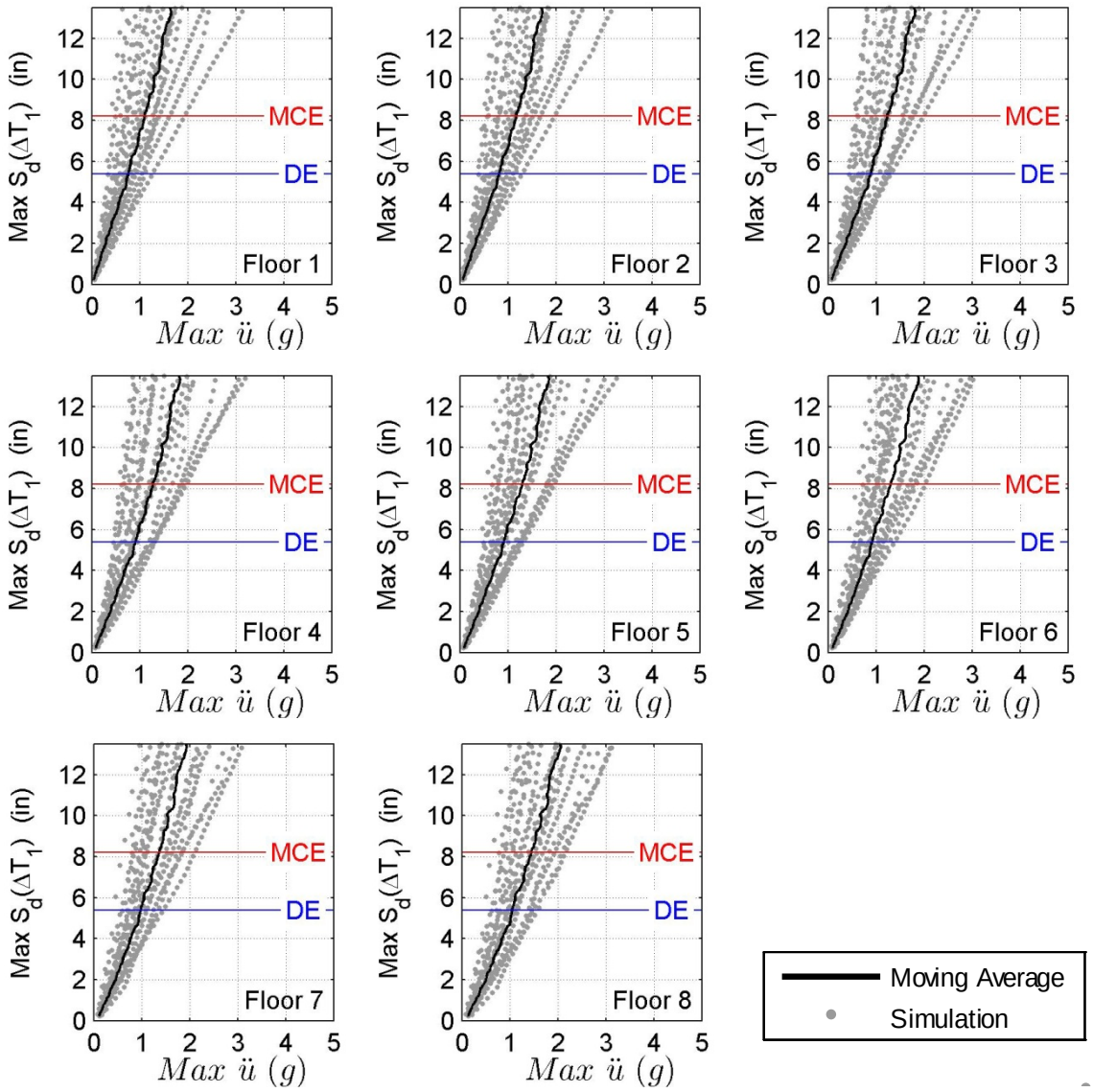

Figure B.18 IDA results for RC-8 (no wall): maximum floor level acceleration drift against maximum spectral displacement over ΔT_1.

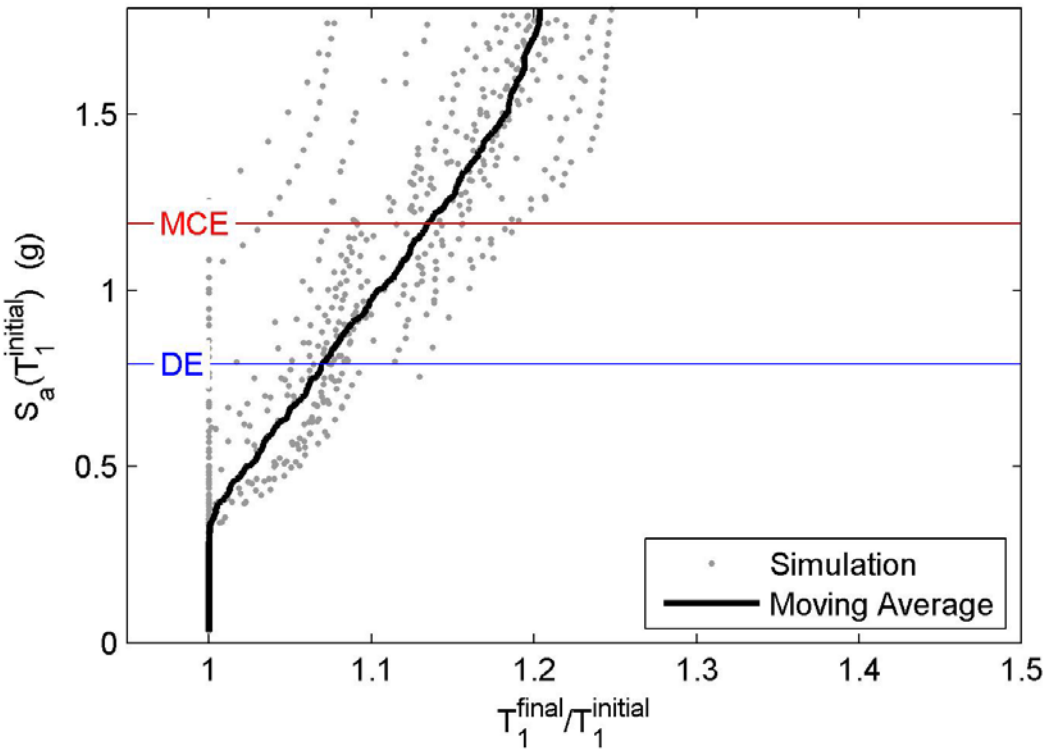

Figure B.19 IDA results for RC-8: period elongation against median spectral acceleration over the range of T_1.

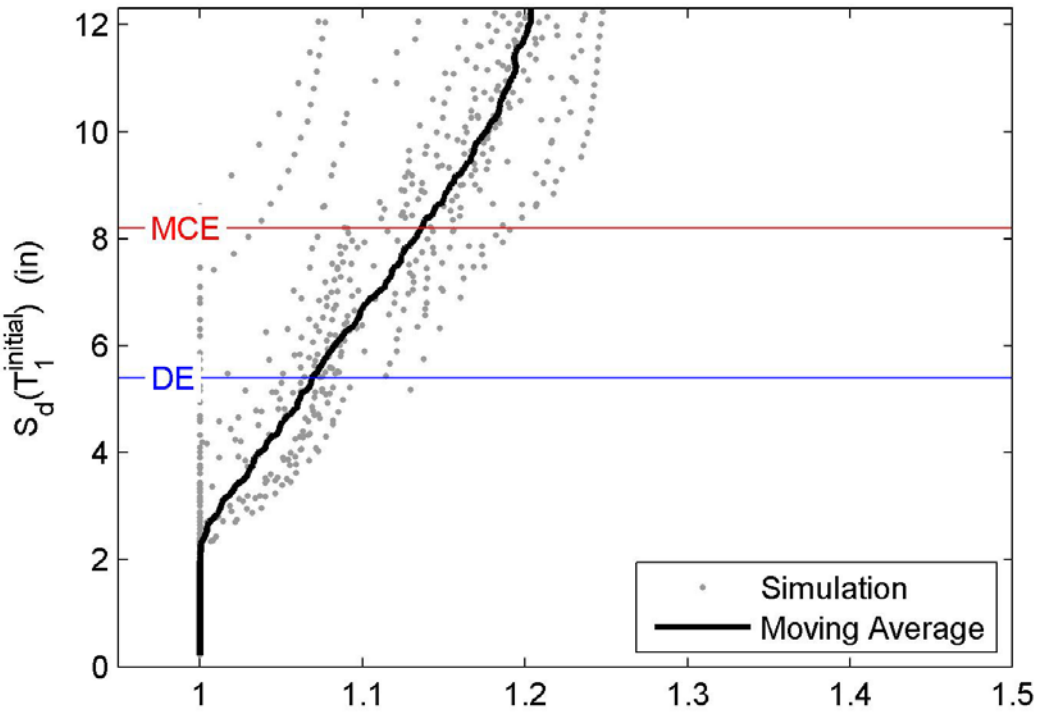

Figure B.20 IDA results for RC-8: period elongation against median spectral displacement over the range of T_1.

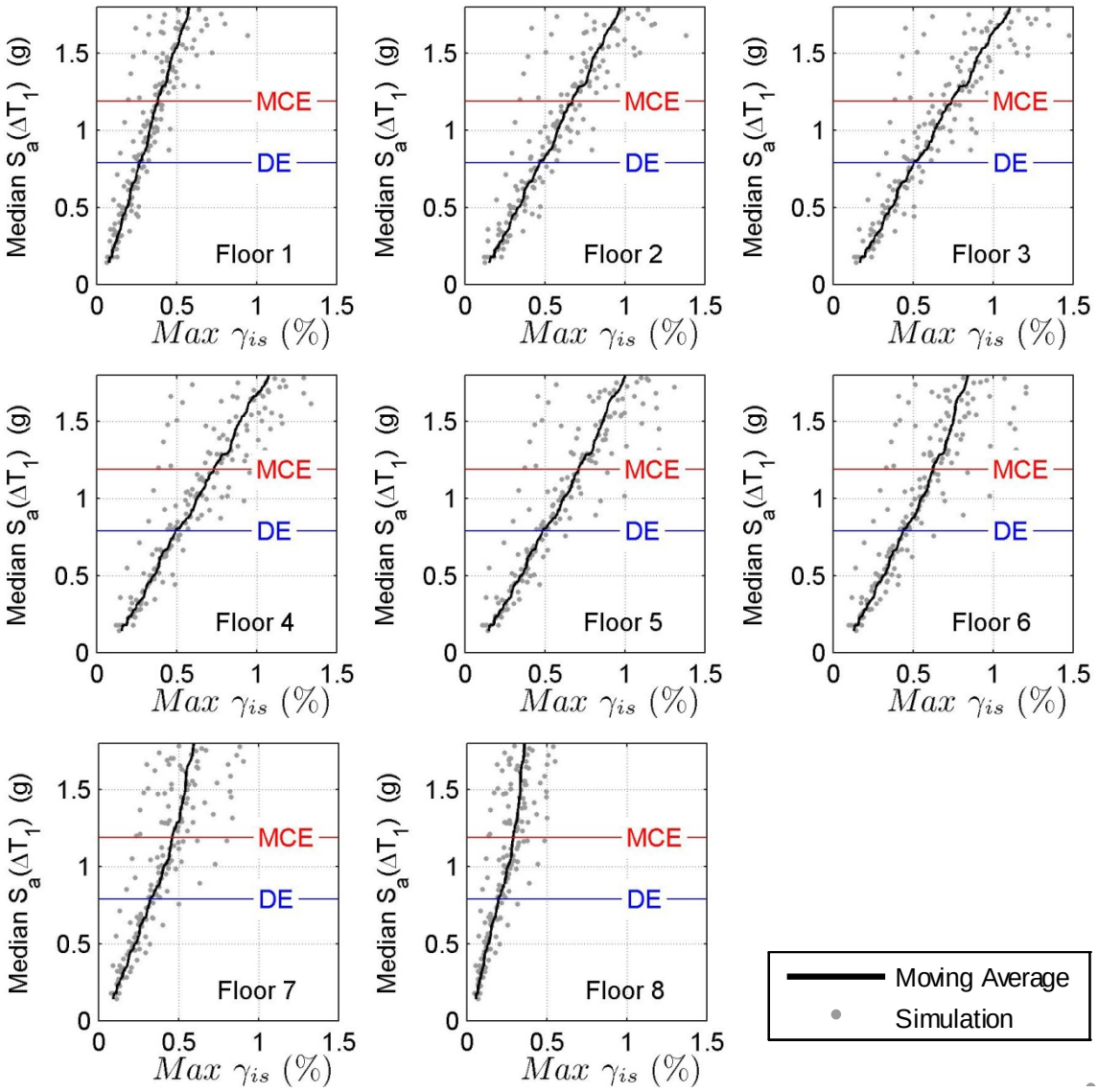

Figure B.21 IDA results for RC-8 ($L_{w,min}$ (μ)): maximum interstory drift against median spectral acceleration over the range of T_1.

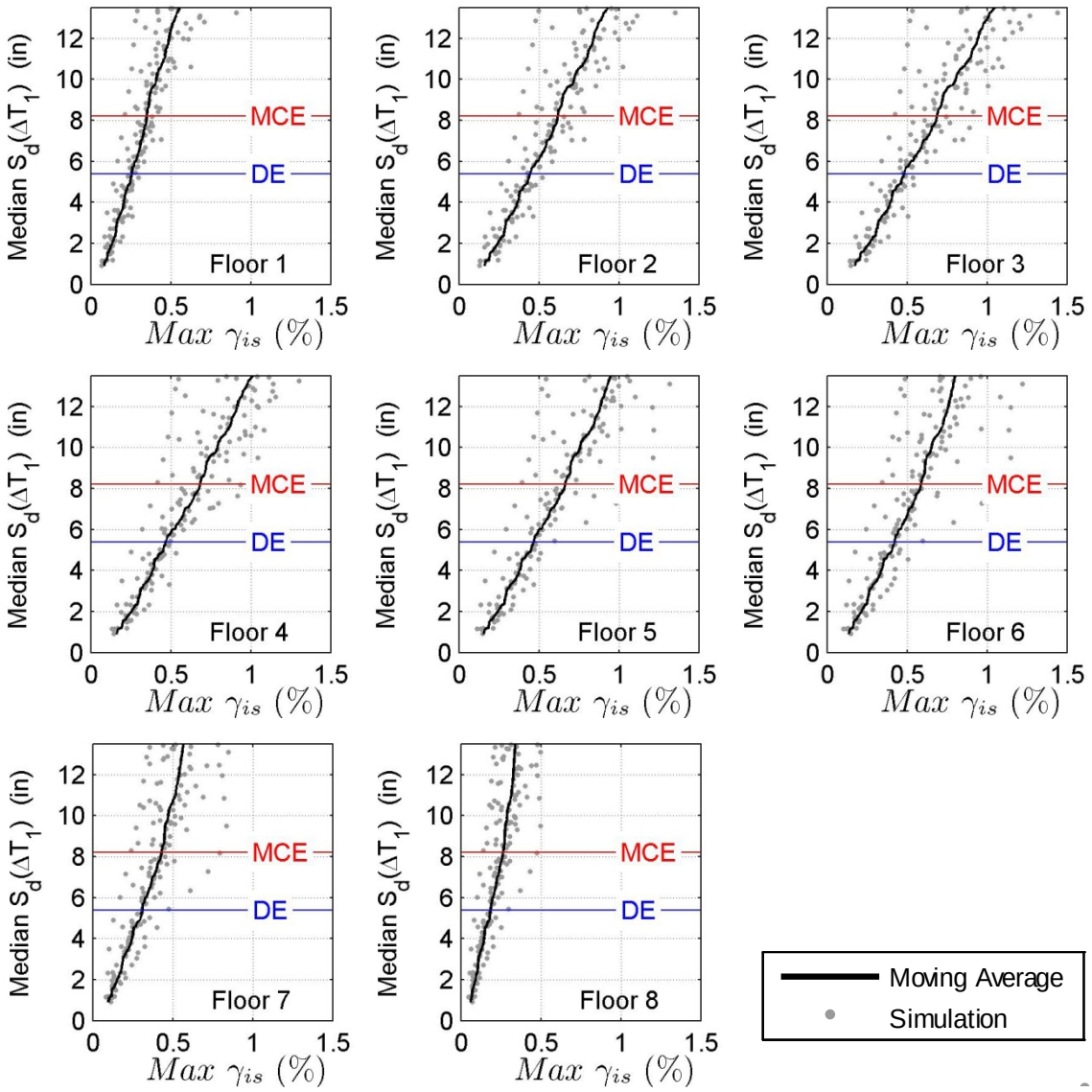

Figure B.22 IDA results for RC-8 ($L_{w,min}$ (μ)): maximum interstory drift against median spectral displacement over the range of T_1.

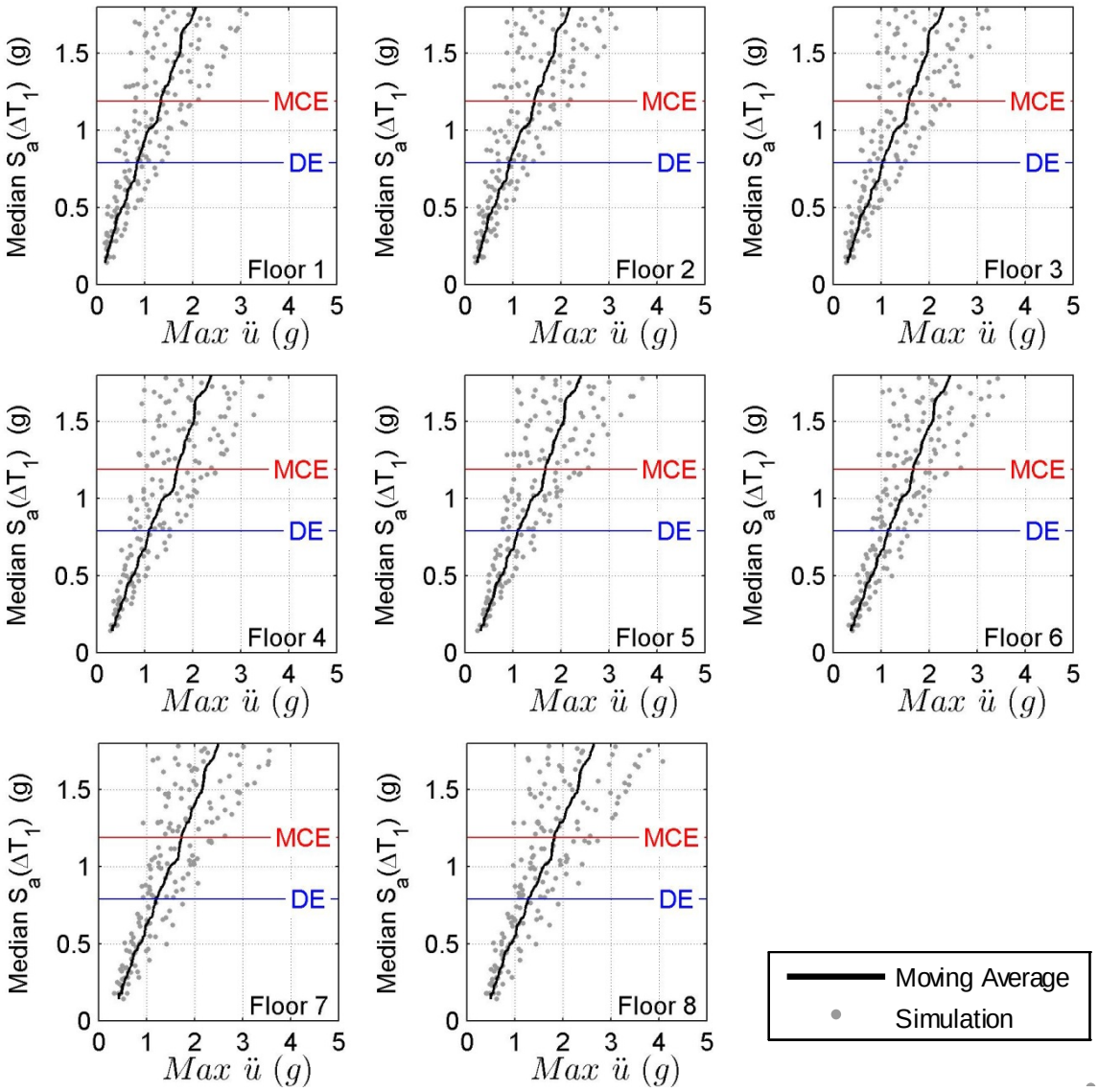

Figure B.23 IDA results for RC-8 ($L_{w,min}$ (μ)): maximum floor level acceleration against median spectral acceleration over the range of T_1.

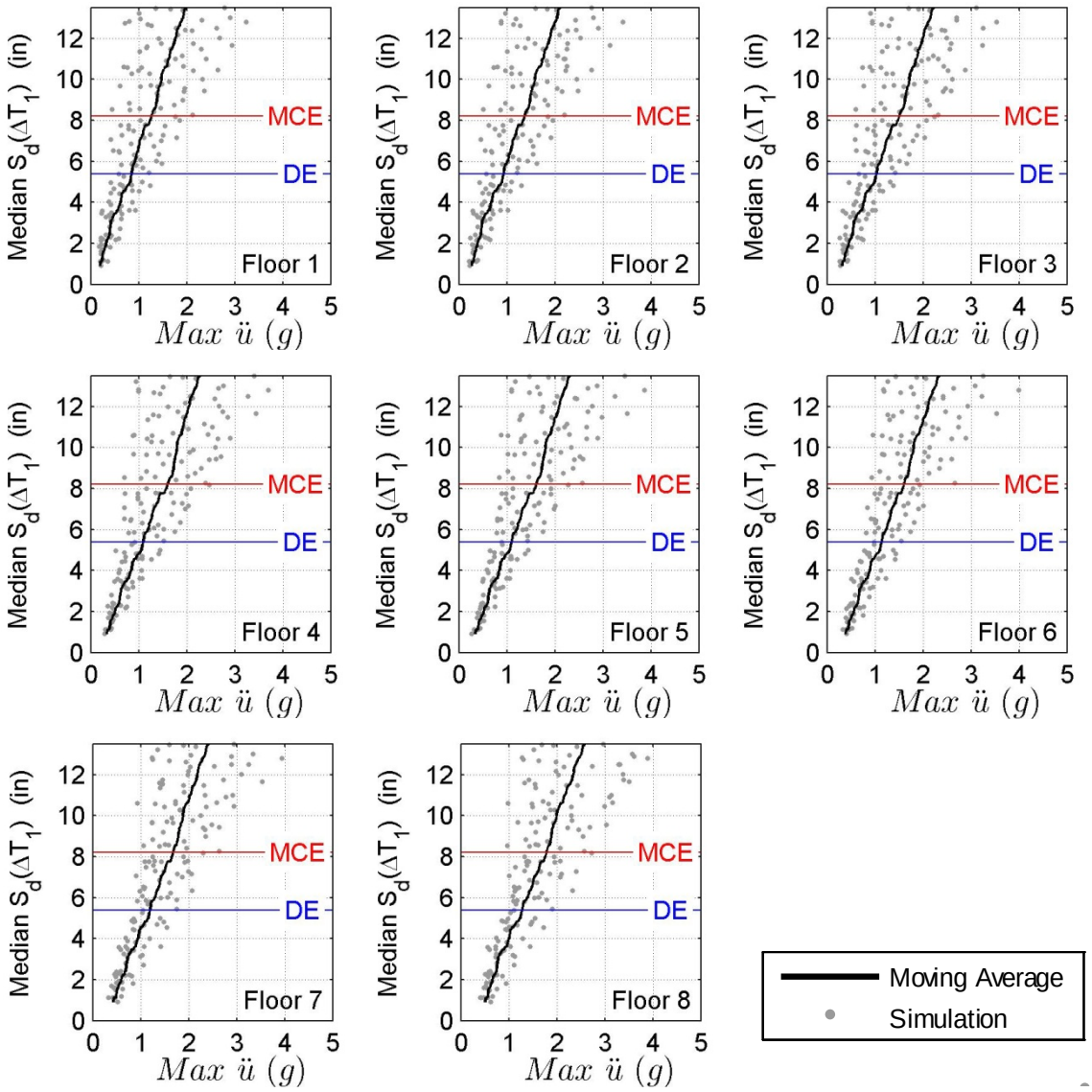

Figure B.24 IDA results for RC-8 ($L_{w,min}$ (μ)): maximum floor level acceleration against median spectral displacement over the range of T_1.

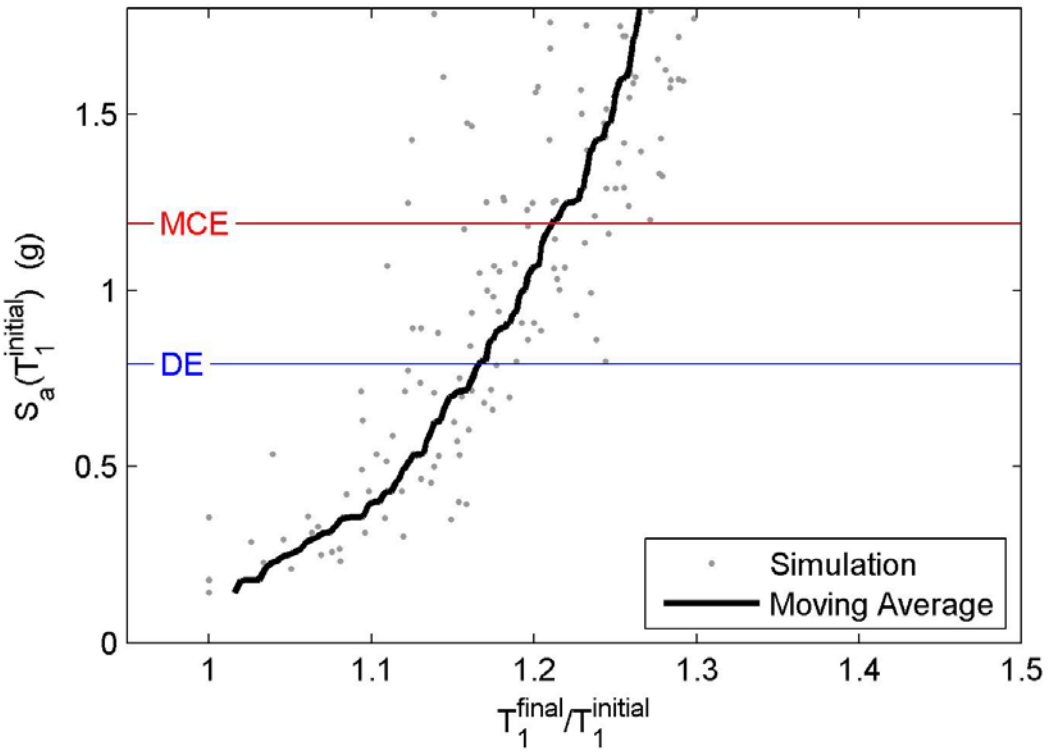

Figure B.25 IDA results for RC-8 ($L_{w,min}$ (μ)): period elongation against median spectral acceleration over the range of T_1.

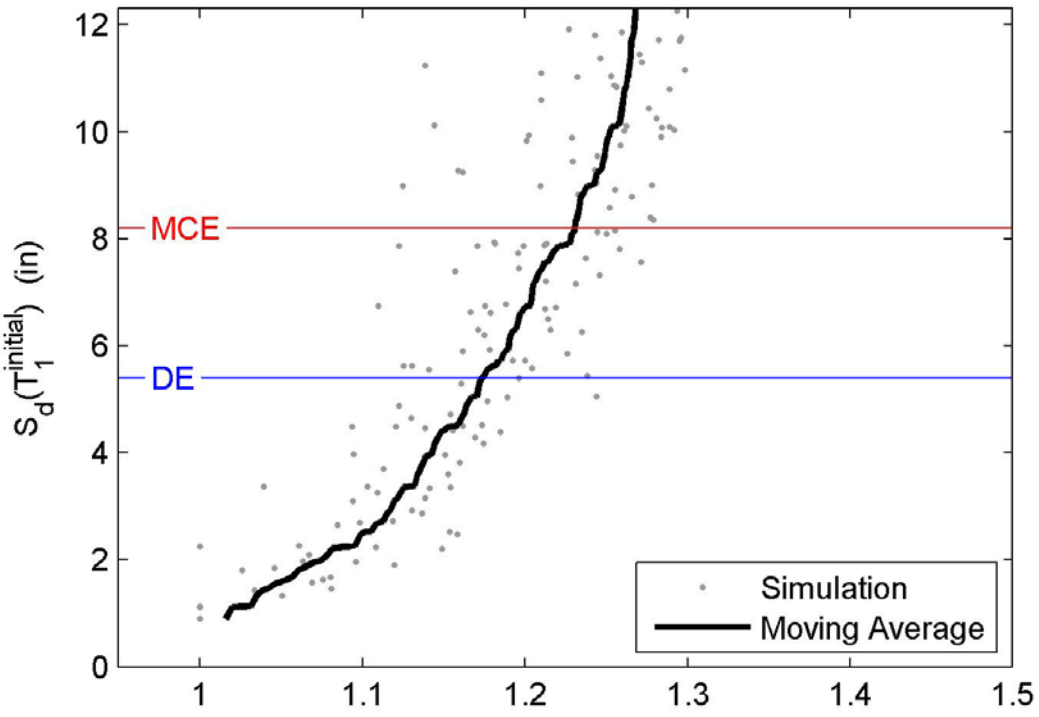

Figure B.26 IDA results for RC-8 ($L_{w,min}$ (μ)): period elongation against median spectral displacement over the range of T_1.

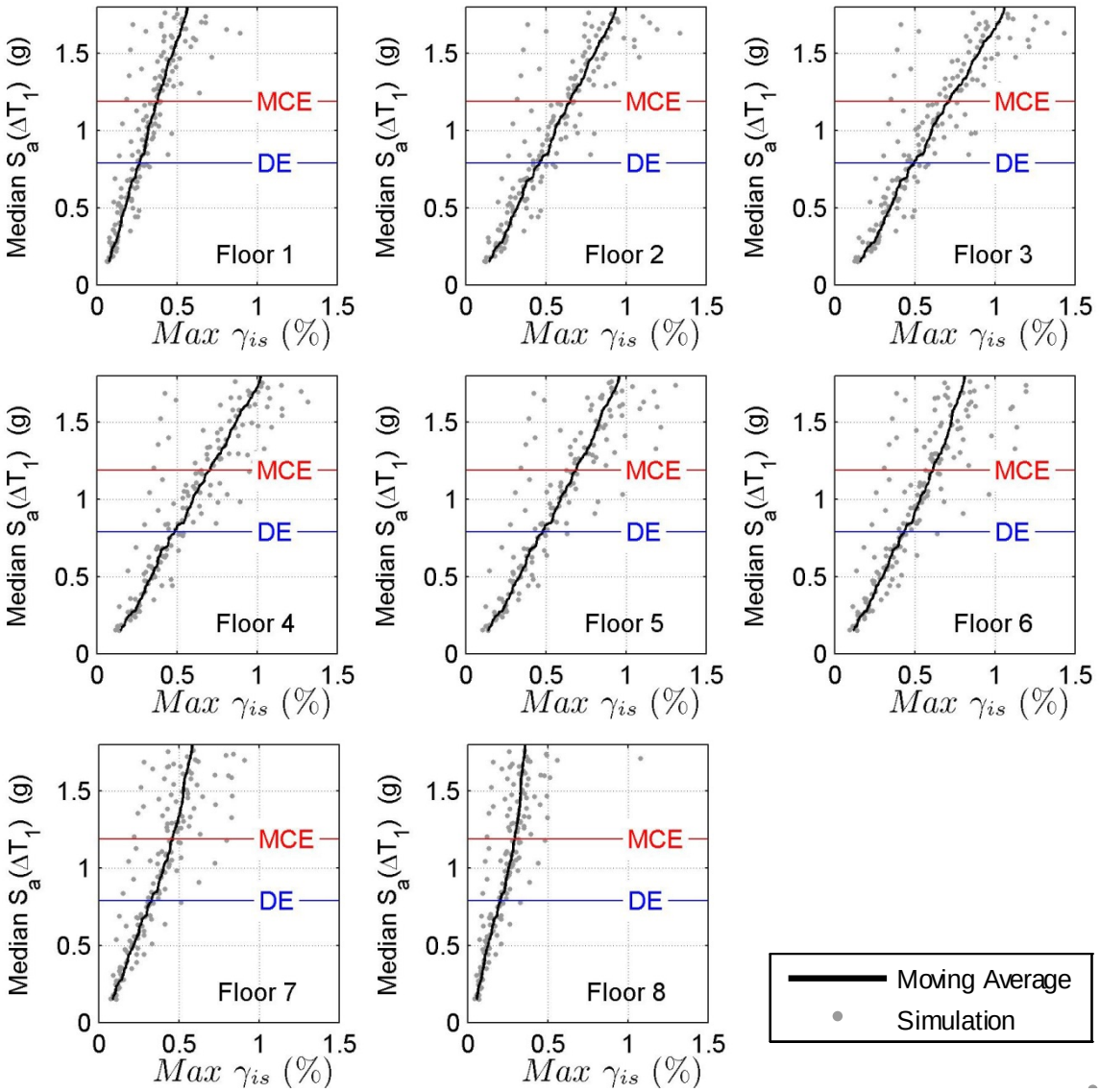

Figure B.27 IDA results for RC-8 ($L_{w,max}$ (μ)): maximum interstory drift against median spectral acceleration over the range of T_1.

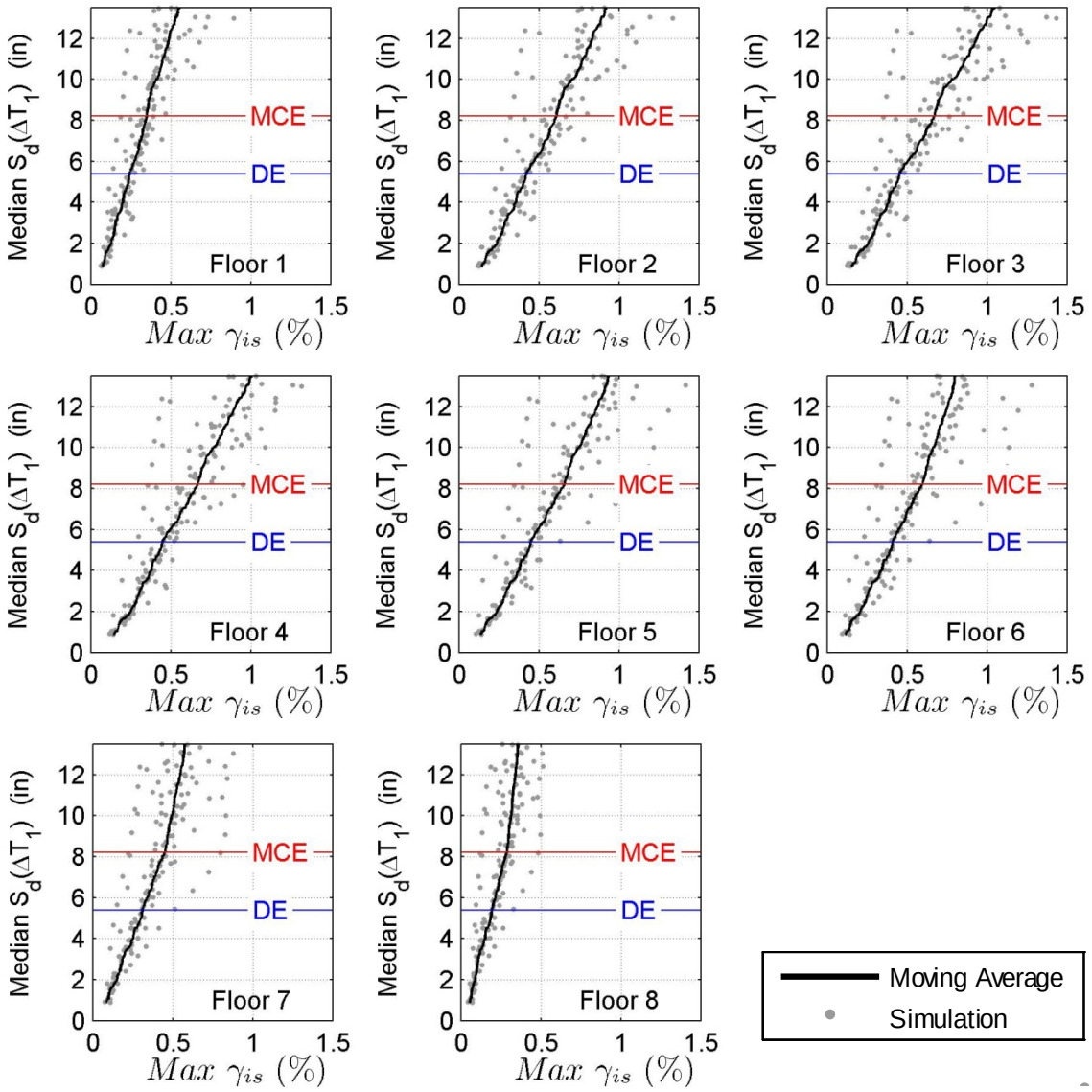

Figure B.28 IDA results for RC-8 ($L_{w,max}$ (μ)): maximum interstory drift against median spectral displacement over the range of T_1.

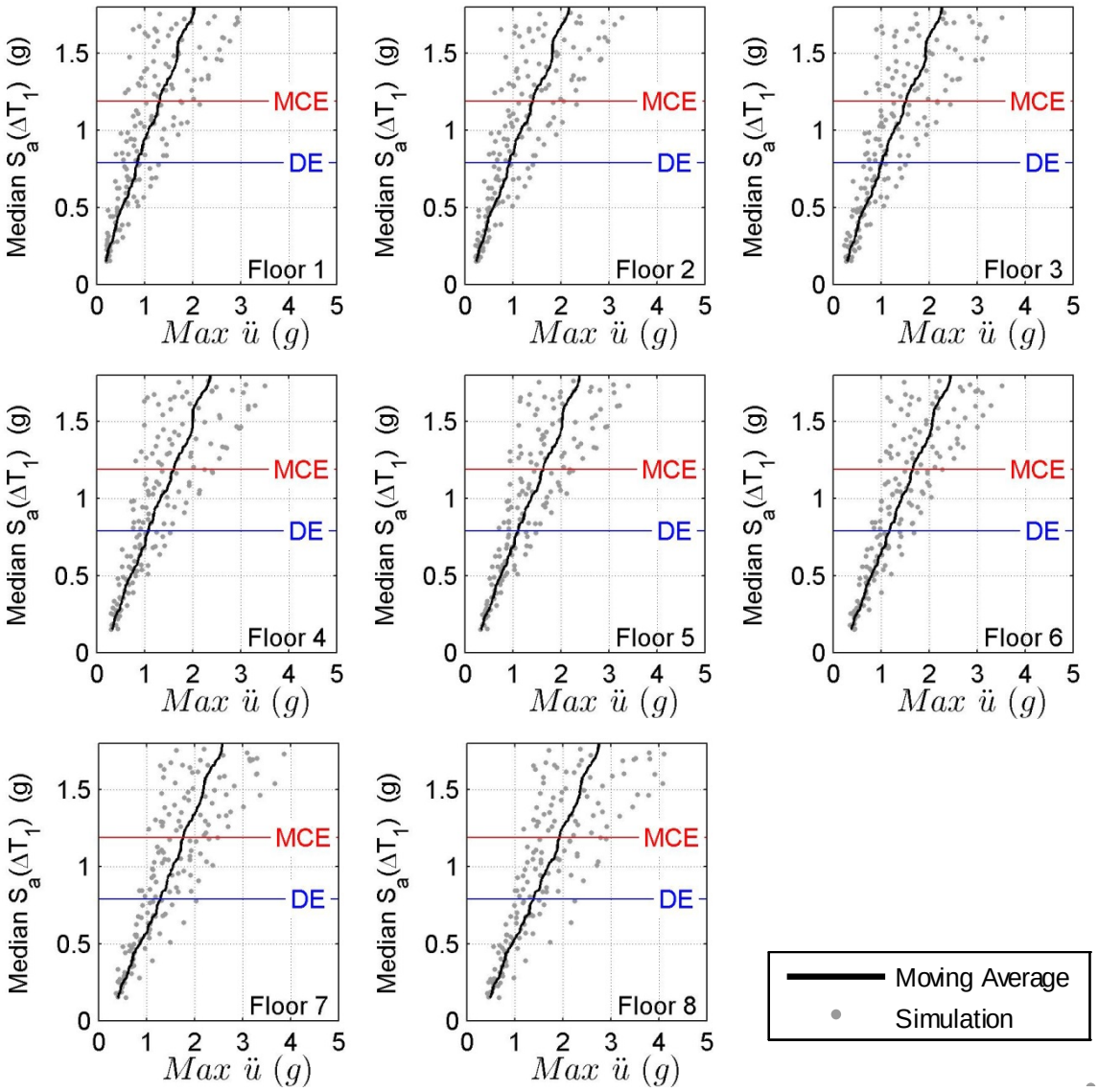

Figure B.29 IDA results for RC-8 ($L_{w,max}$ (μ)): maximum floor level acceleration against median spectral acceleration over the range of T_1.

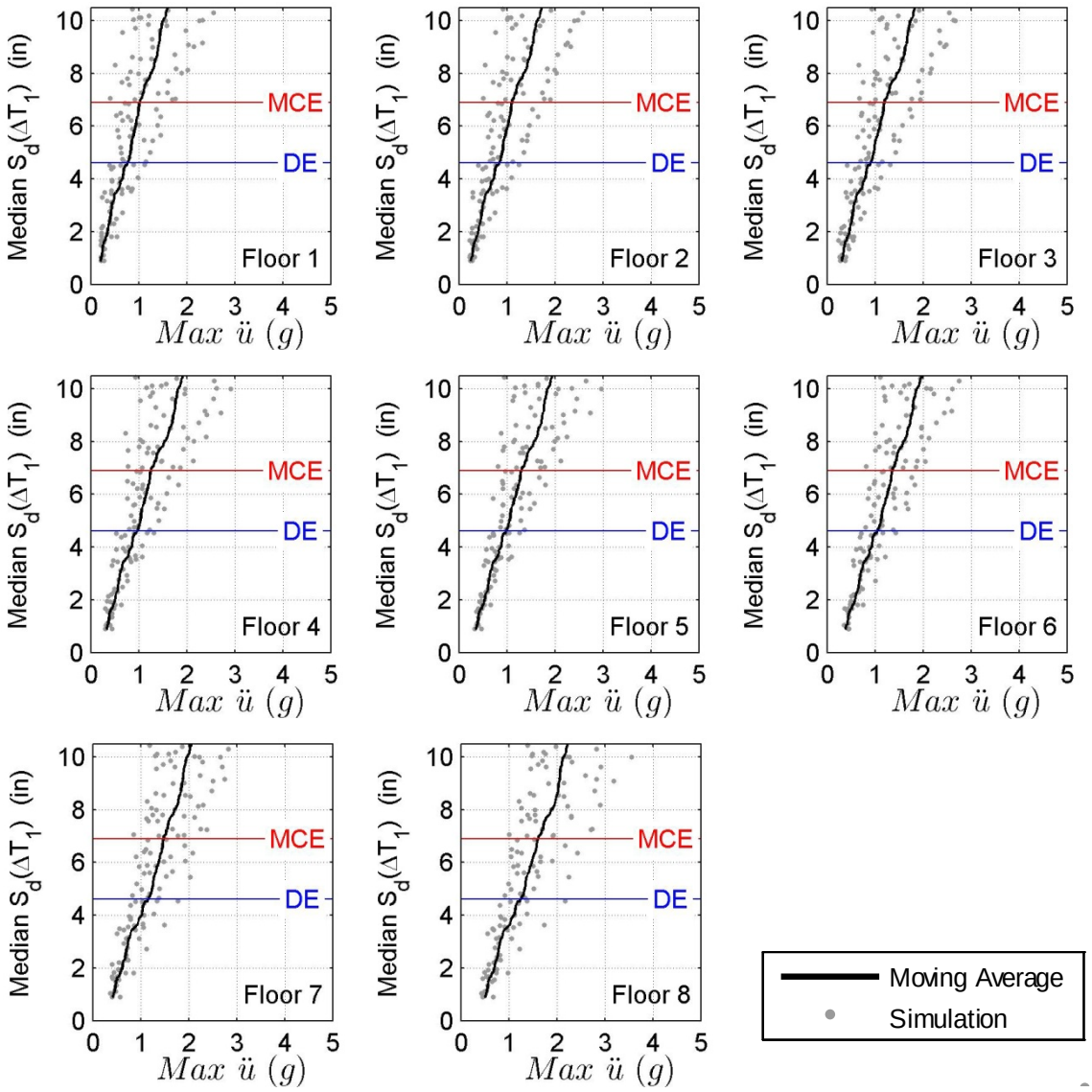

Figure B.30 IDA results for RC-8 ($L_{w,max}$ (μ)): maximum floor level acceleration against median spectral displacement over the range of T_1.

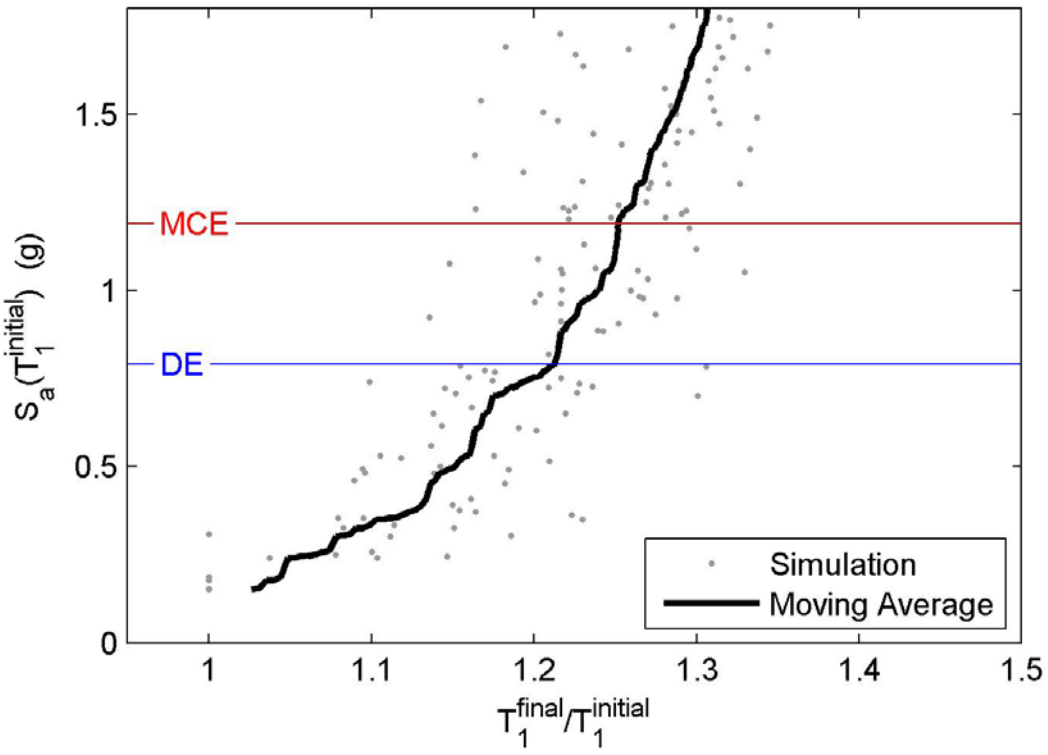

Figure B.31 IDA results for RC-8 ($L_{w,max}$ (μ)): period elongation against median spectral acceleration over the range of T_1.

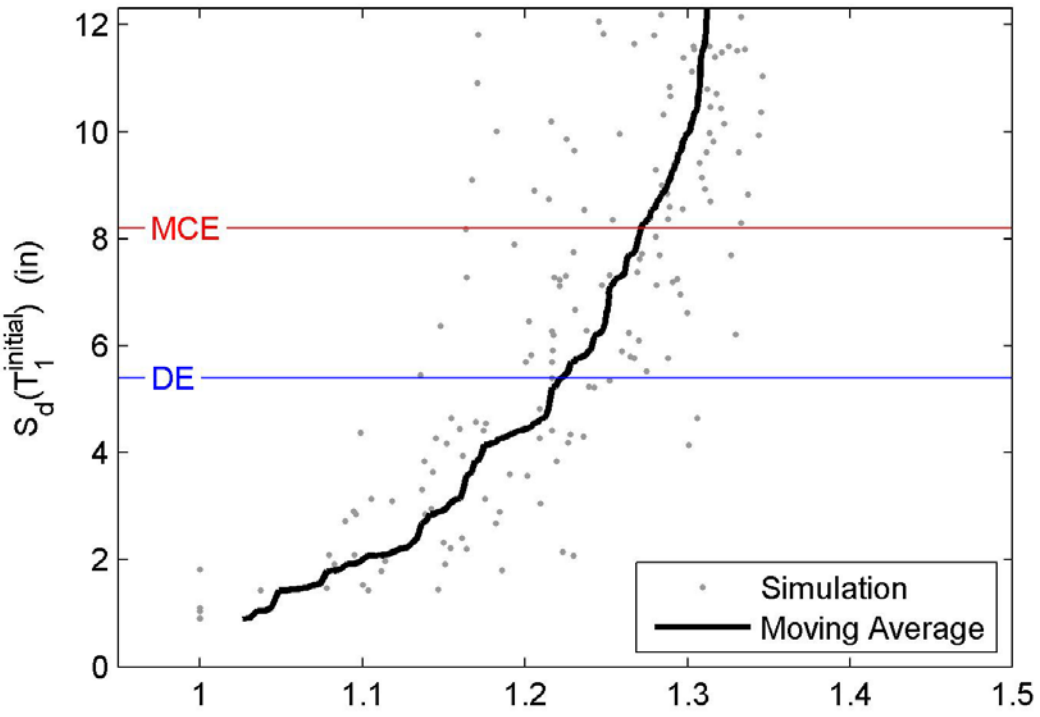

Figure B.32 IDA results for RC-8 ($L_{w,max}$ (μ)): period elongation against median spectral displacement over the range of T_1.

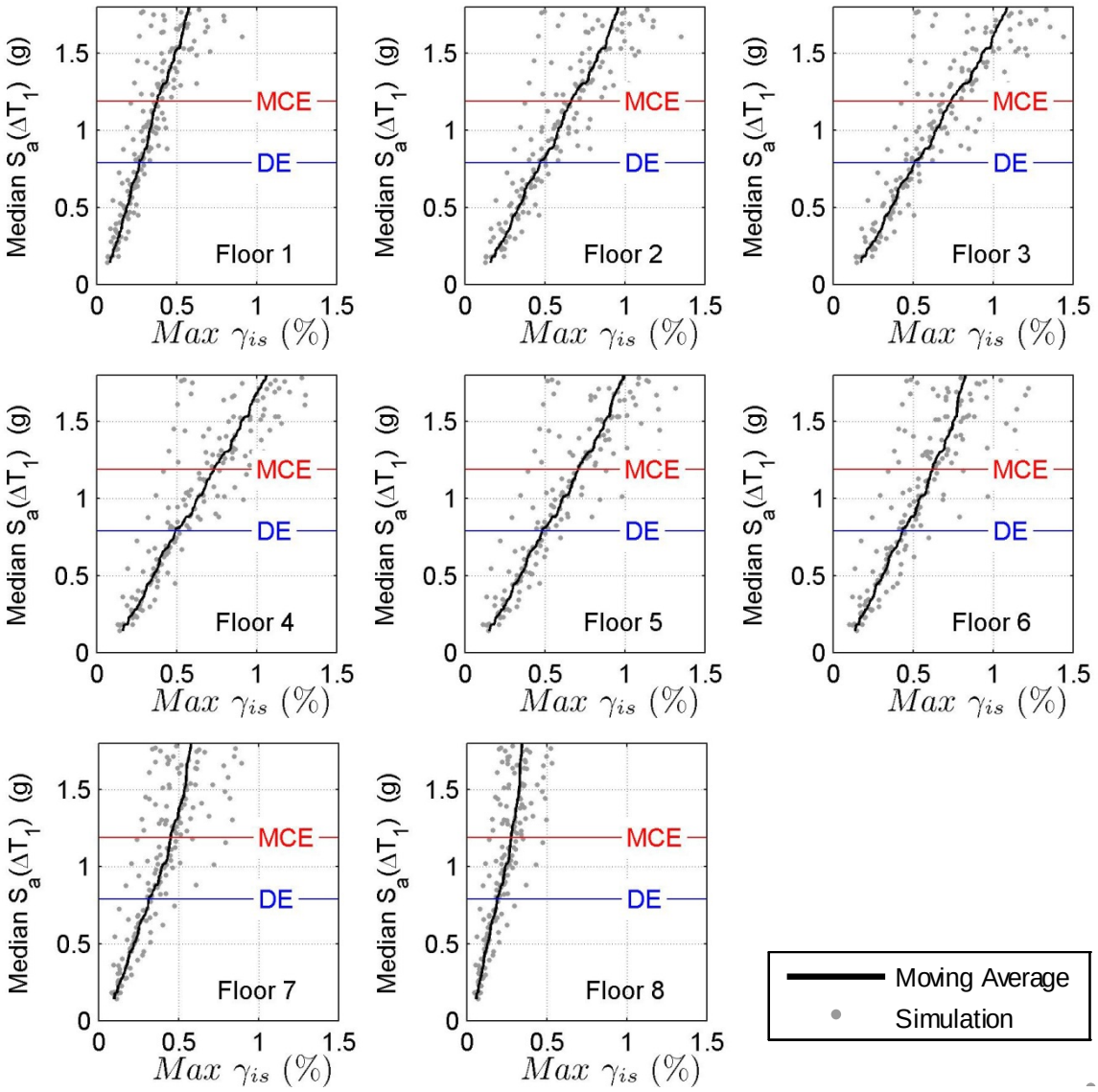

Figure B.33 IDA results for RC-8 ($L_{w,min}$ (μ–σ)): maximum interstory drift against median spectral acceleration over the range of T_1.

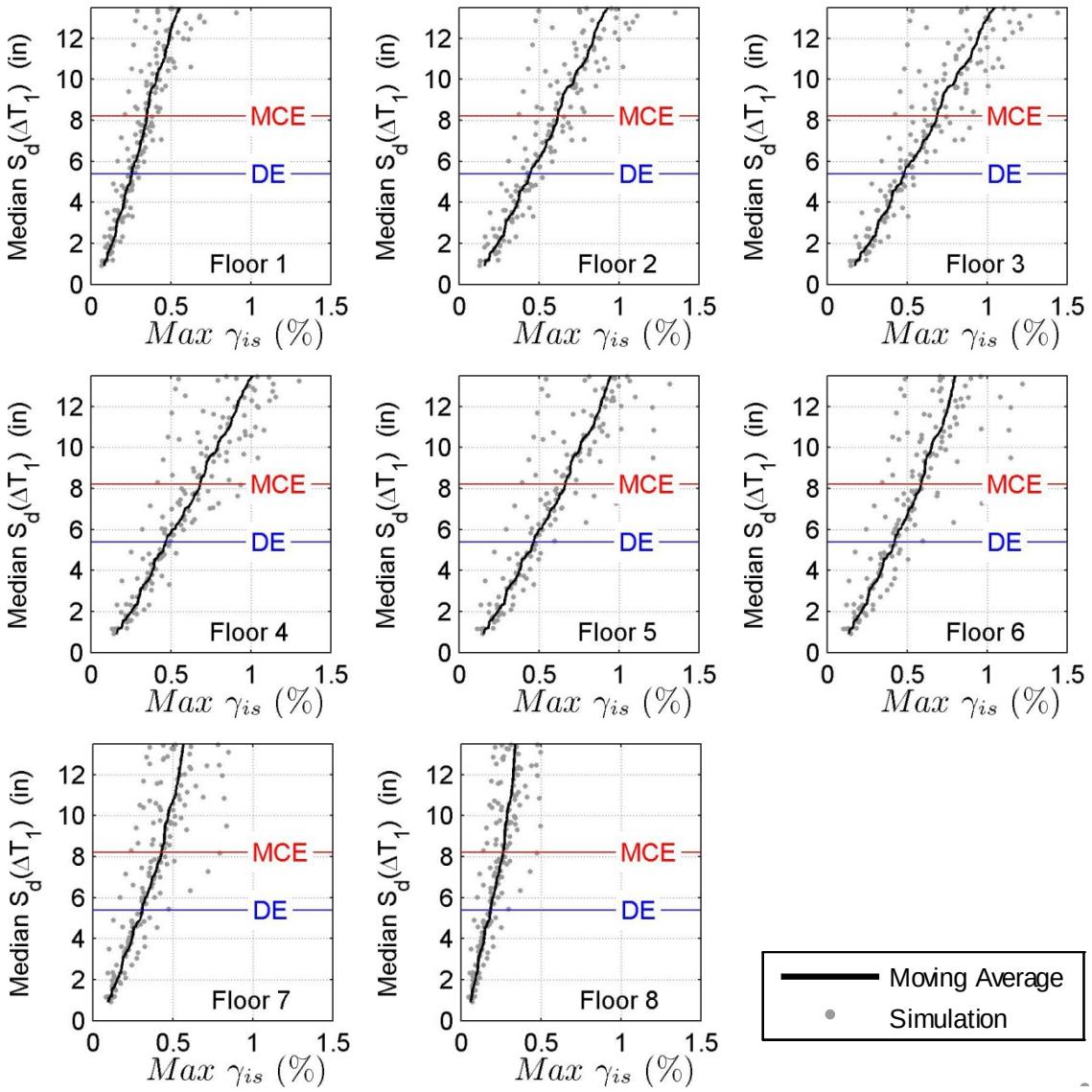

Figure B.34 IDA results for RC-8 ($L_{w,min}$ (μ–σ)): maximum interstory drift against median spectral displacement over the range of T_1.

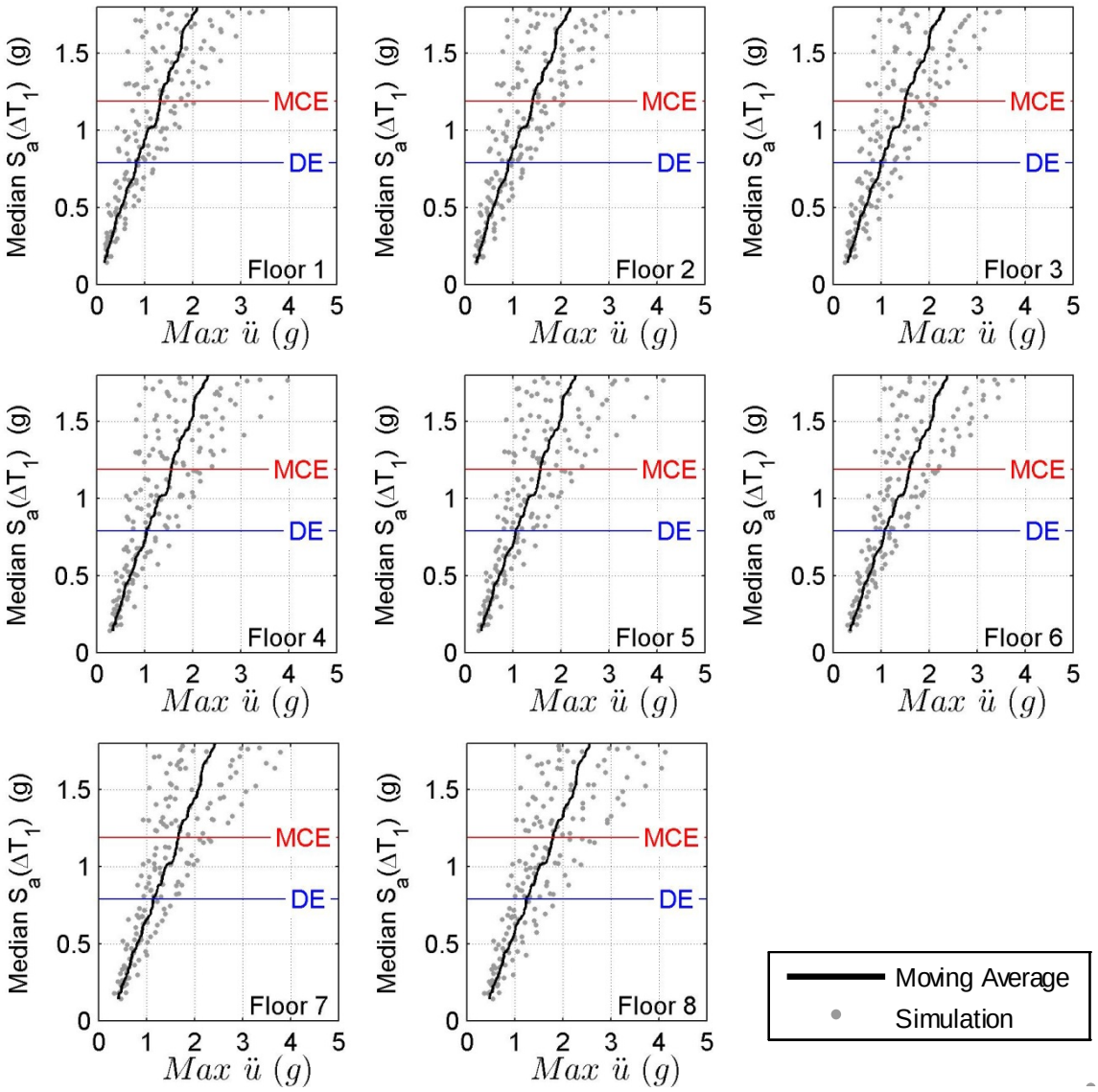

Figure B.35 IDA results for RC-8 ($L_{w,min}$ (μ–σ)): maximum floor level acceleration against median spectral acceleration over the range of T_1.

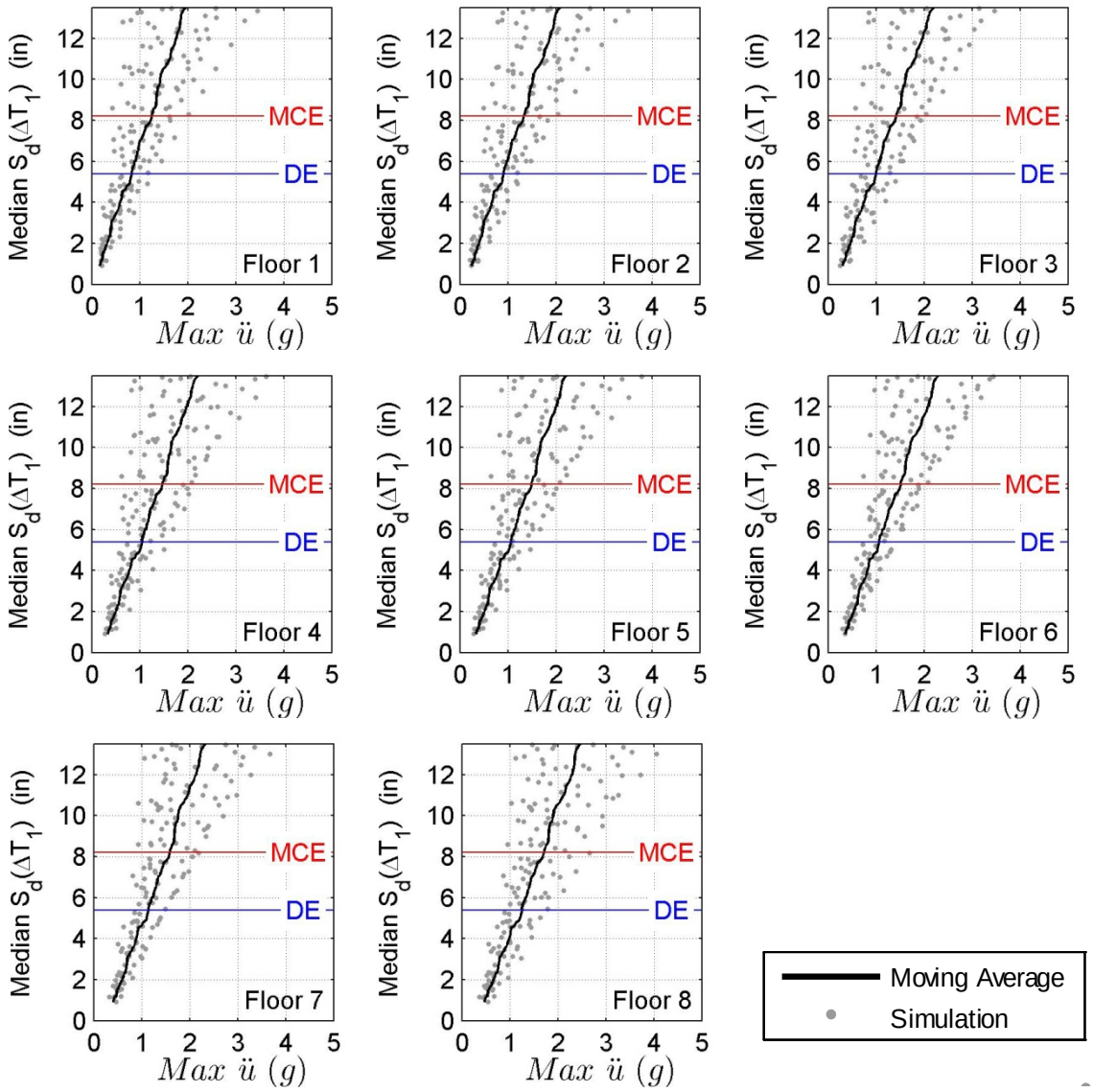

Figure B.36 IDA results for RC-8 ($L_{w,min}$ (μ–σ)): maximum floor level acceleration against median spectral displacement over the range of T_1.

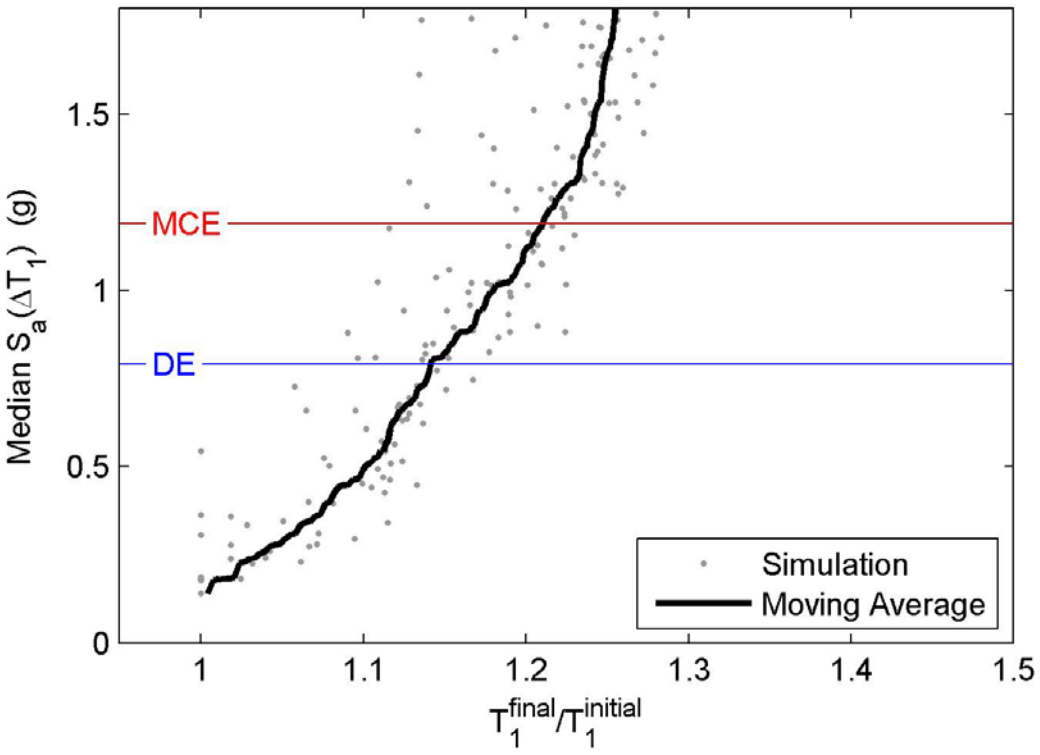

Figure B.37 IDA results for RC-8 ($L_{w,min}$ (μ–σ)): period elongation against median spectral acceleration over the range of T_1.

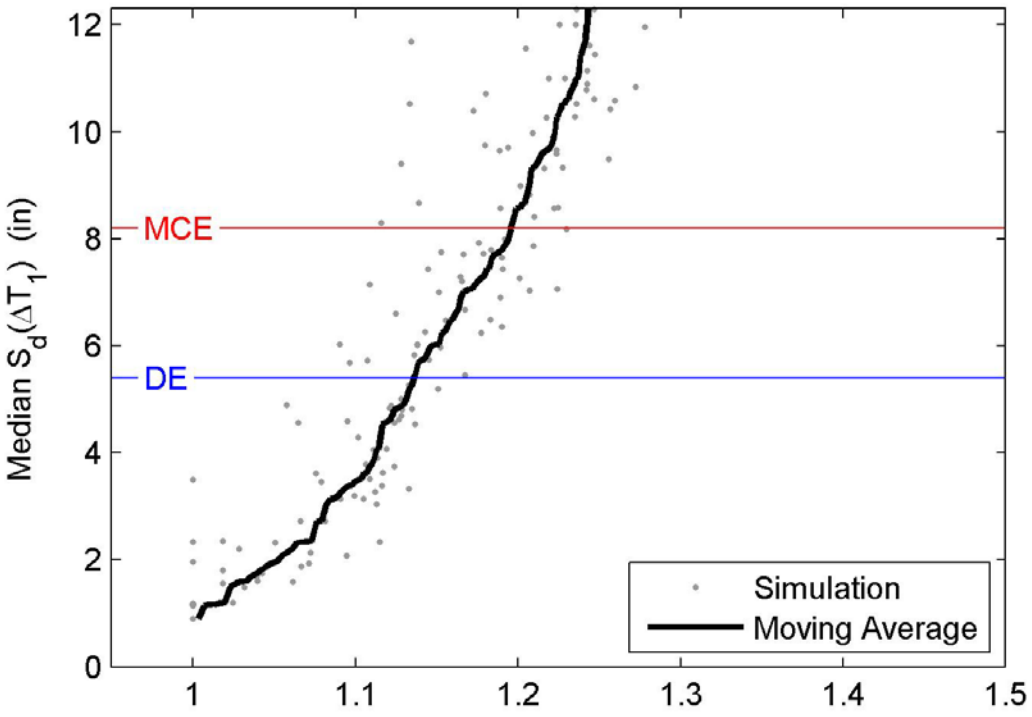

Figure B.38 IDA results for RC-8 ($L_{w,min}$ (μ–σ)): period elongation against median spectral displacement over the range of T_1.

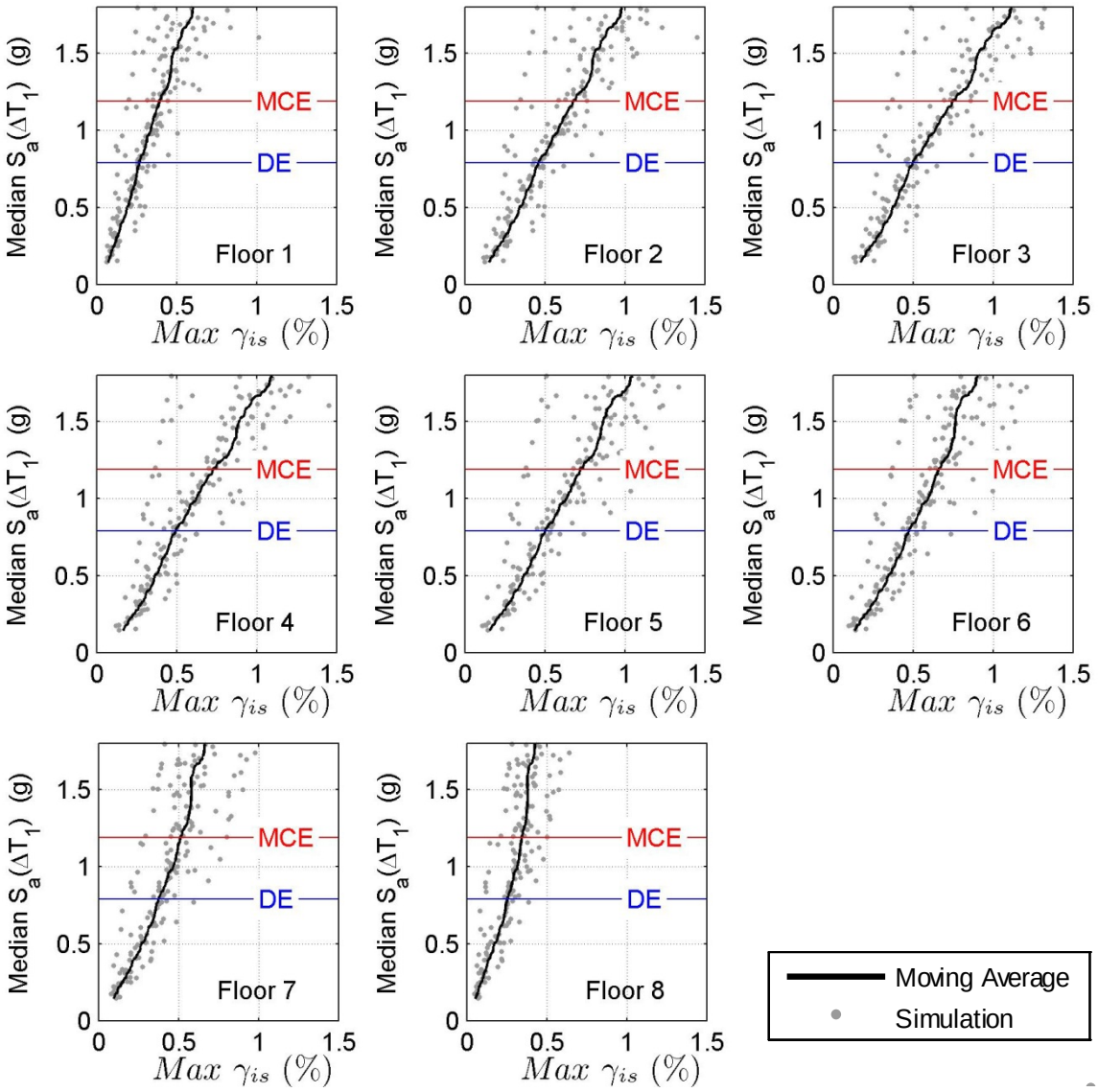

Figure B.39 IDA results for RC-8 ($L_{w,min}$ (μ+σ)): maximum interstory drift against median spectral acceleration over the range of T_1.

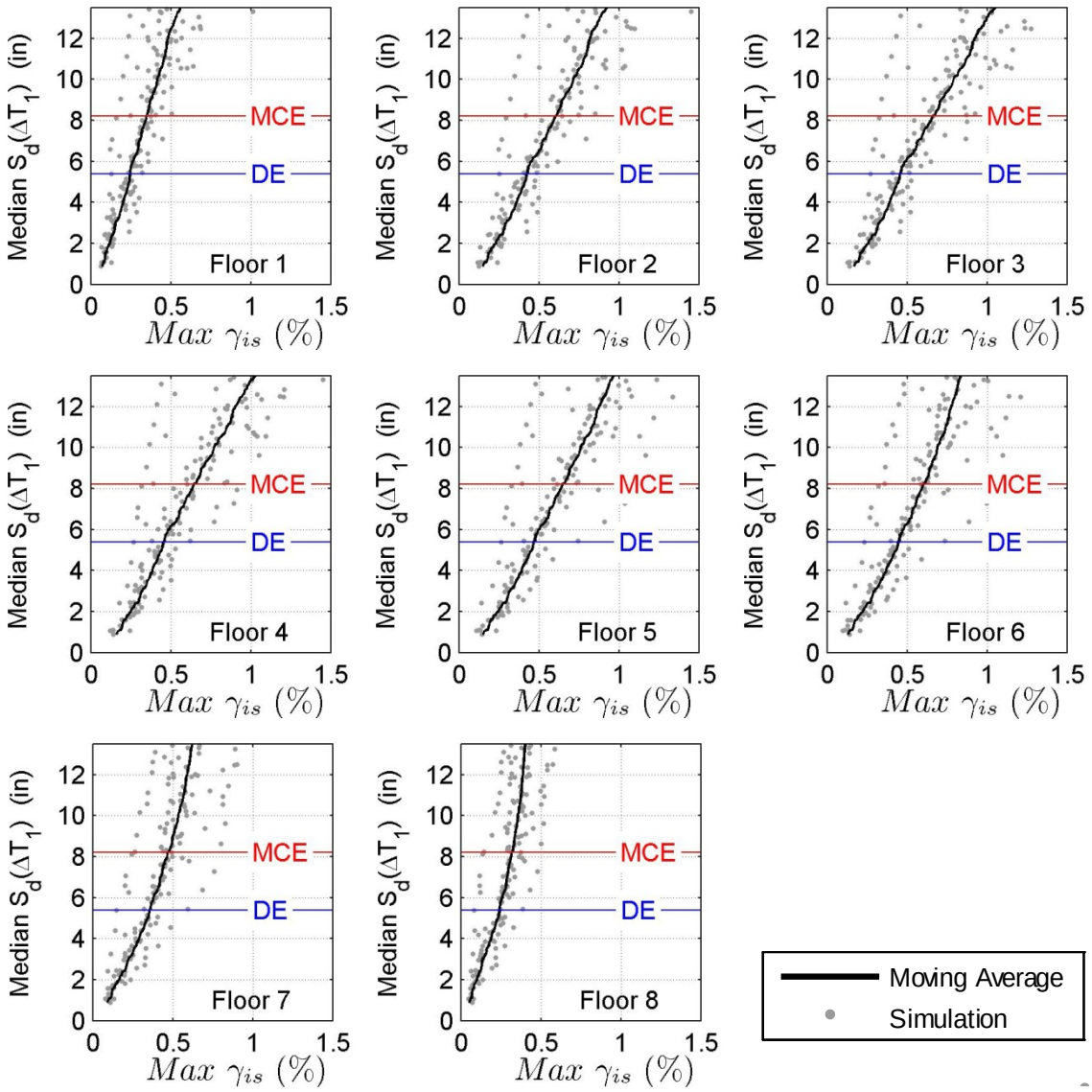

Figure B.40 IDA results for RC-8 ($L_{w,min}$ (μ+σ)): maximum interstory drift against median spectral displacement over the range of T_1.

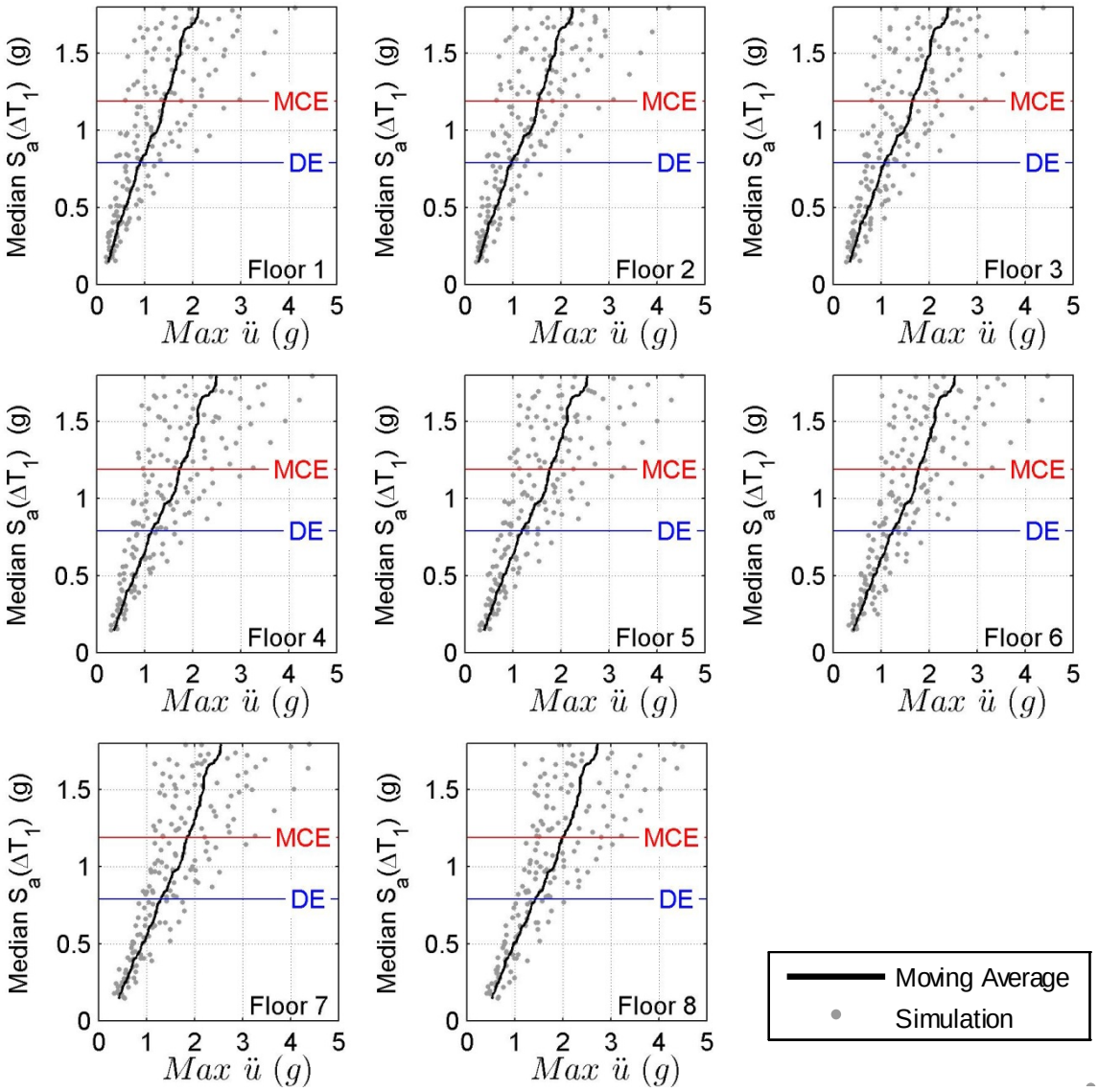

Figure B.41 IDA results for RC-8 ($L_{w,min}$ (μ+σ)): maximum floor level acceleration against median spectral acceleration over the range of T_1.

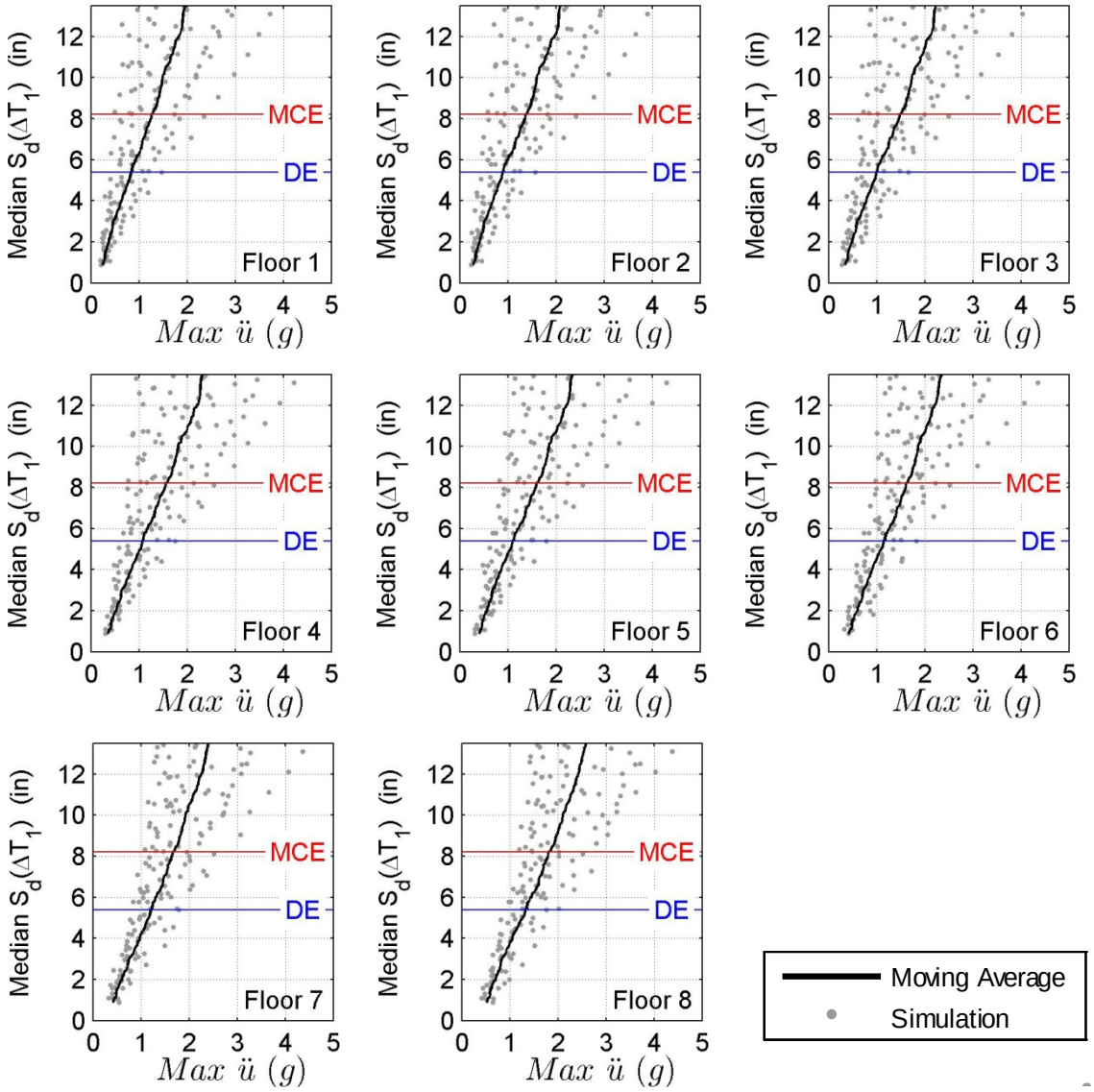

Figure B.42 IDA results for RC-8 ($L_{w,min}$ (μ+σ)): maximum floor level acceleration against median spectral displacement over the range of T_1.

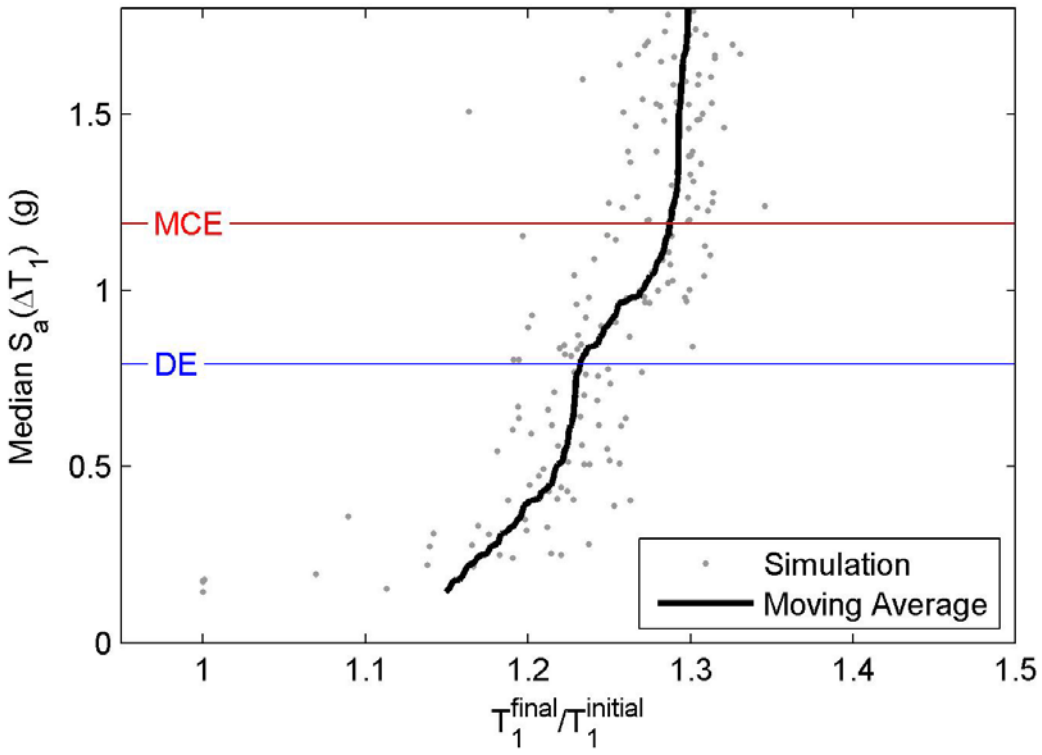

Figure B.43 IDA results for RC-8 ($L_{w,min}$ (μ+σ)): period elongation against median spectral acceleration over the range of T_1.

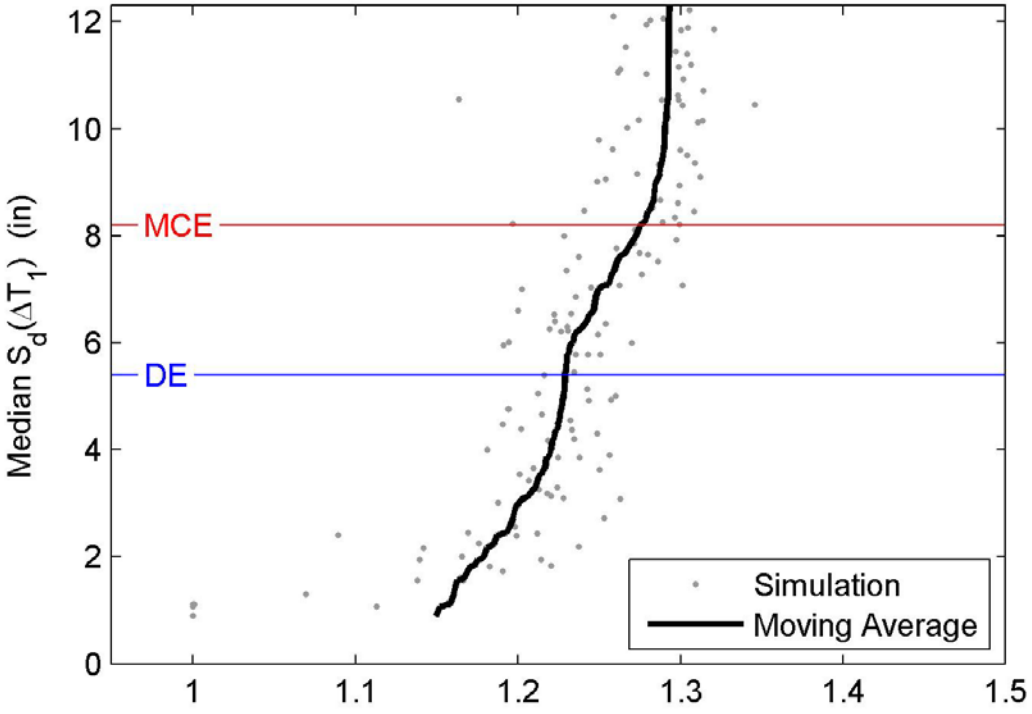

Figure B.44 IDA results for RC-8 ($L_{w,min}$ (μ+σ)): period elongation against median spectral displacement over the range of T_1.

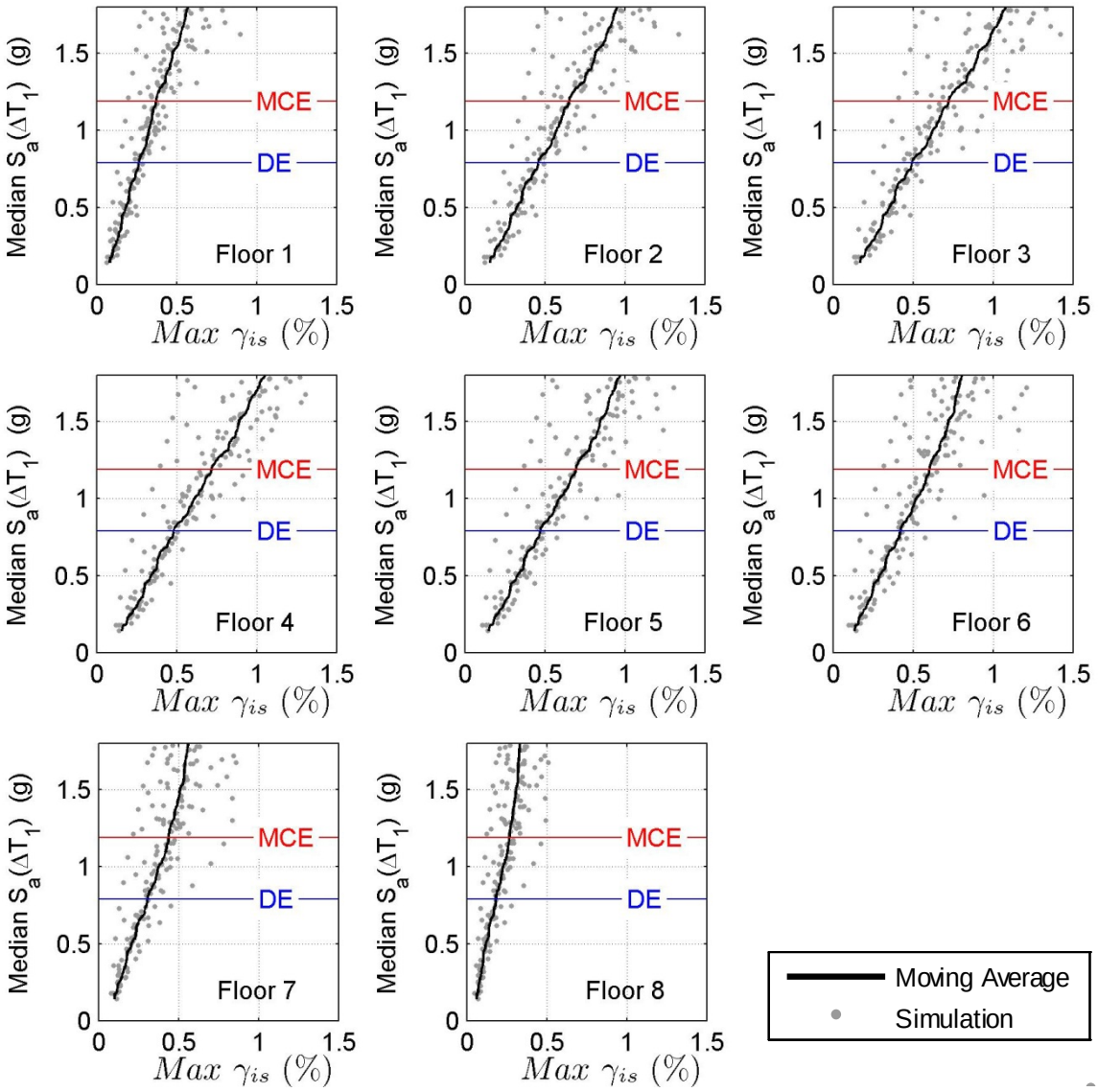

Figure B.45 IDA results for RC-8 ($L_{w,min}$ no post peak hardhening): maximum interstory drift against median spectral acceleration over the range of T_1.

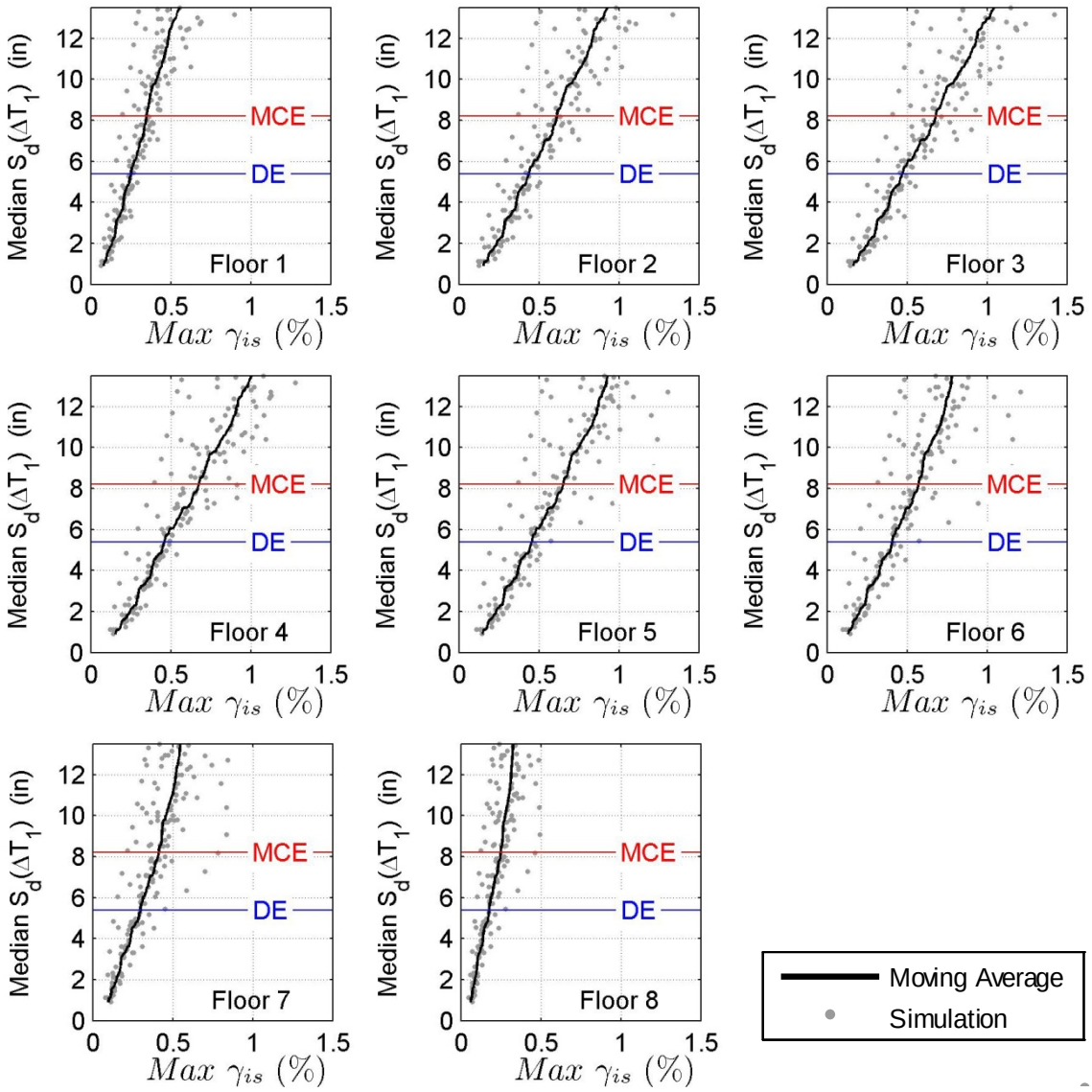

Figure B.46 IDA results for RC-8 ($L_{w,min}$ no post peak hardhening): maximum interstory drift against median spectral displacement over the range of T_1.

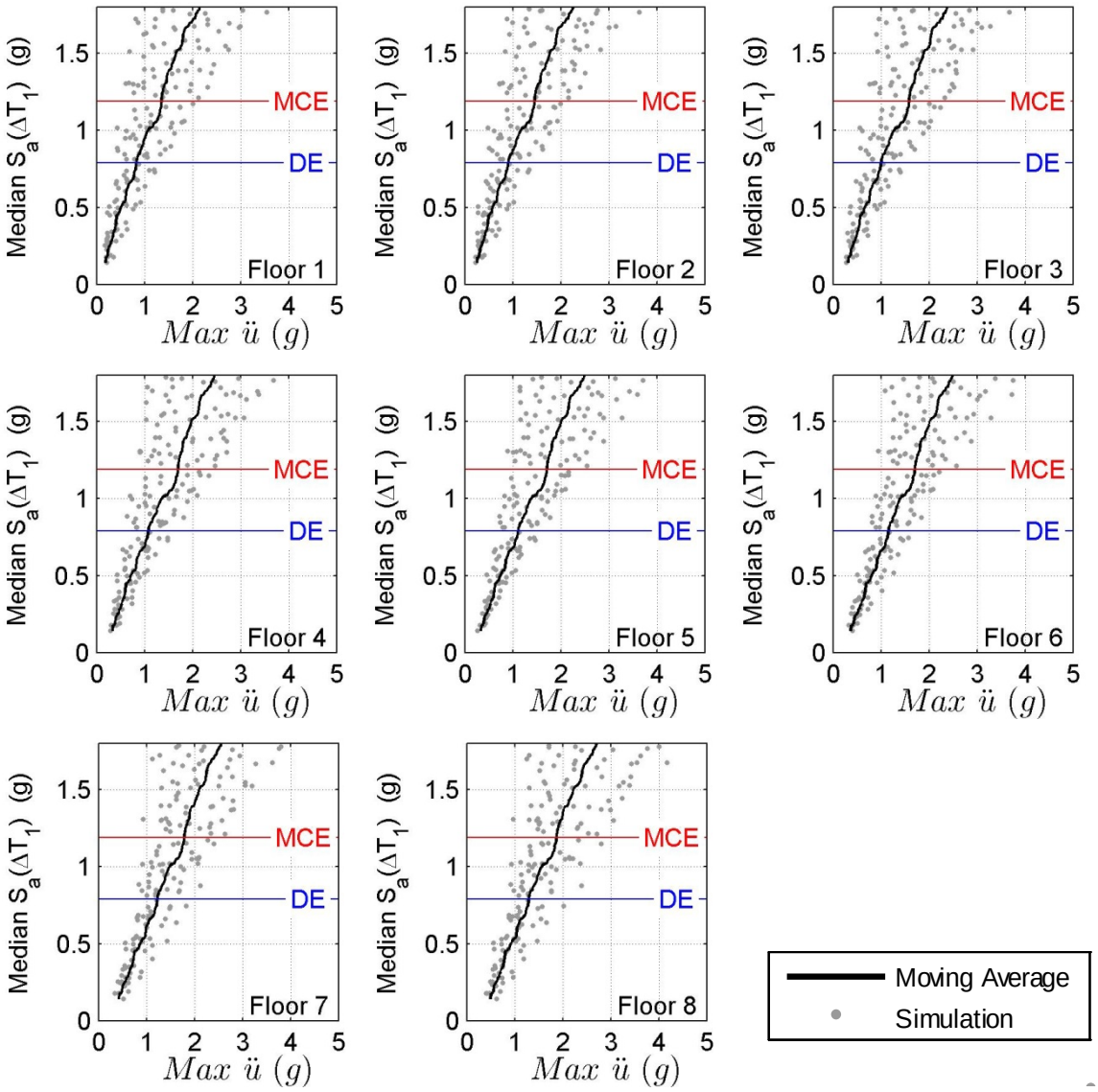

Figure B.47 IDA results for RC-8 ($L_{w,min}$ no post peak hardhening): maximum floor level acceleration against median spectral acceleration over the range of T_1.

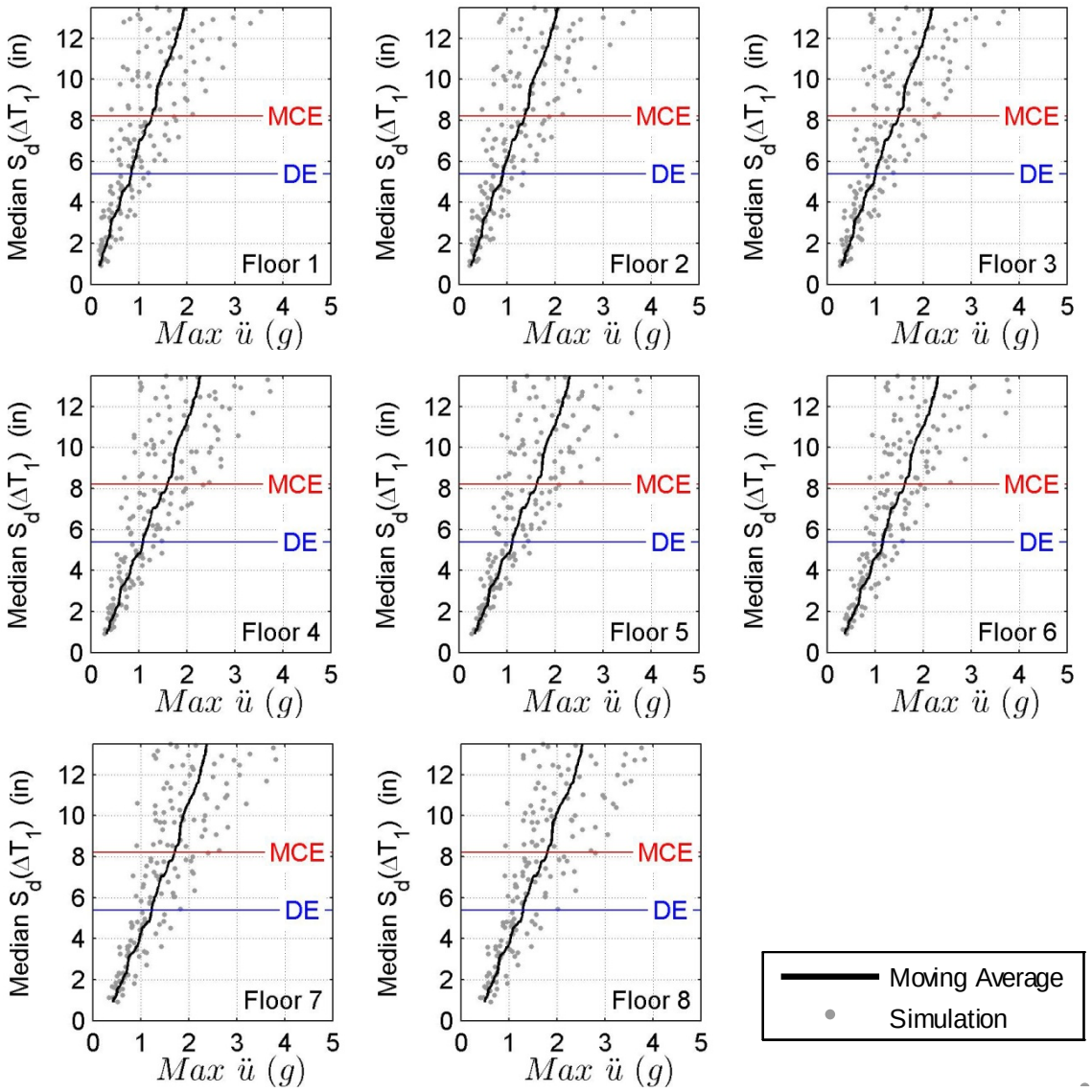

Figure B.48 IDA results for RC-8 ($L_{w,min}$ no post peak hardhening): maximum floor level acceleration against median spectral displacement over the range of T_1.

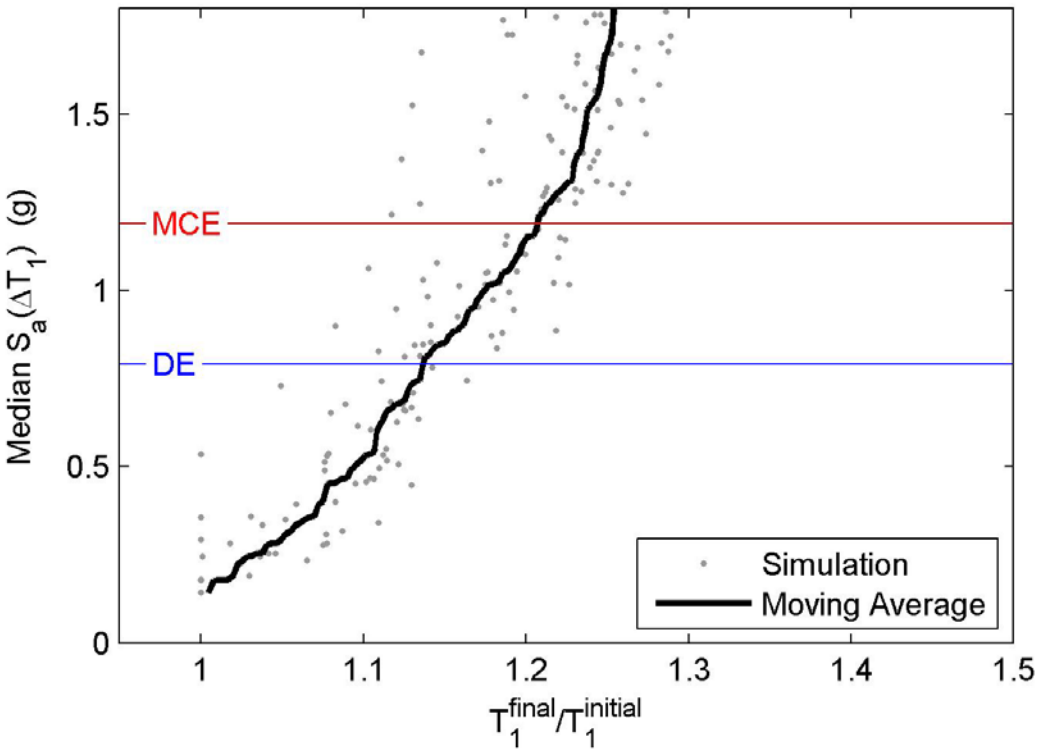

Figure B.49 IDA results for RC-8 ($L_{w,min}$ no post peak hardhening): period elongation against median spectral acceleration over the range of T_1.

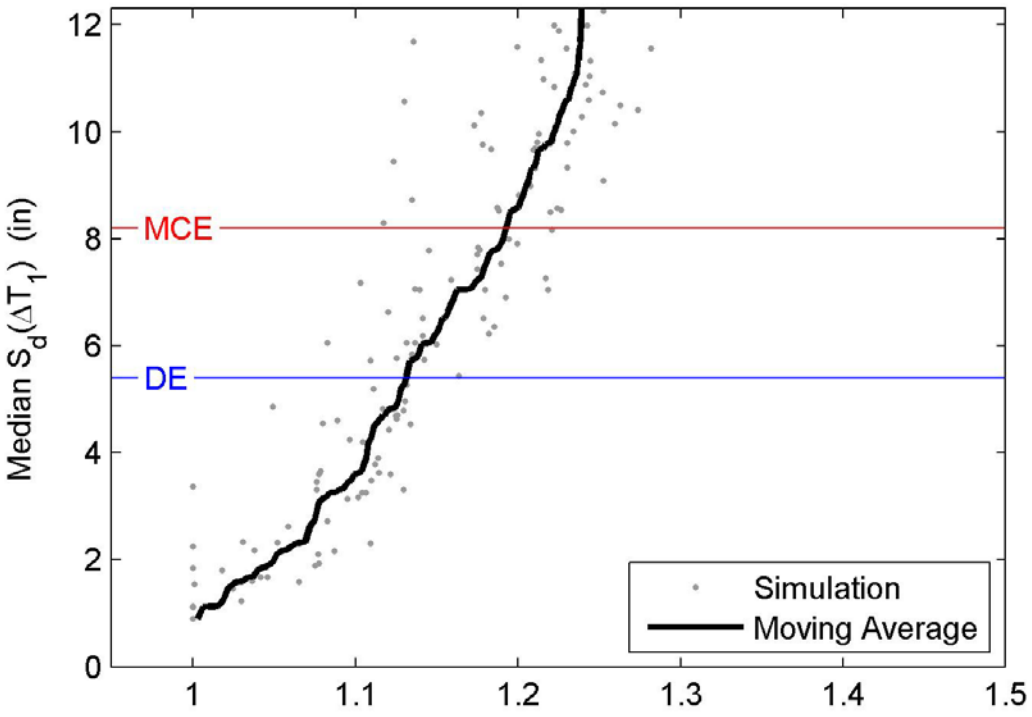

Figure B.50 IDA results for RC-8 ($L_{w,min}$ no post peak hardhening): period elongation against median spectral displacement over the range of T_1.

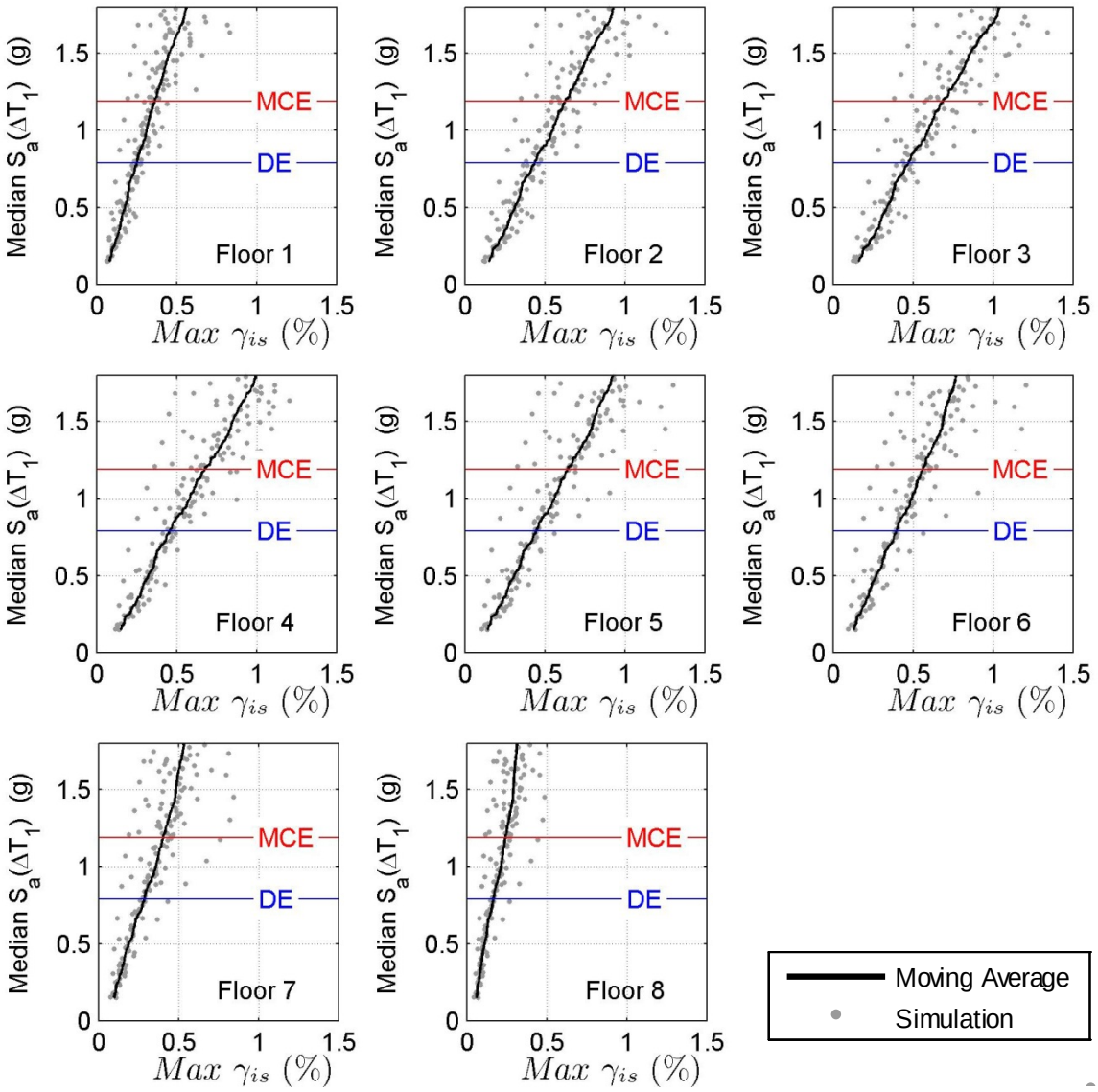

Figure B.51 IDA results for RC-8 ($L_{w,max}$ no post peak hardhening): maximum interstory drift against median spectral acceleration over the range of T_1.

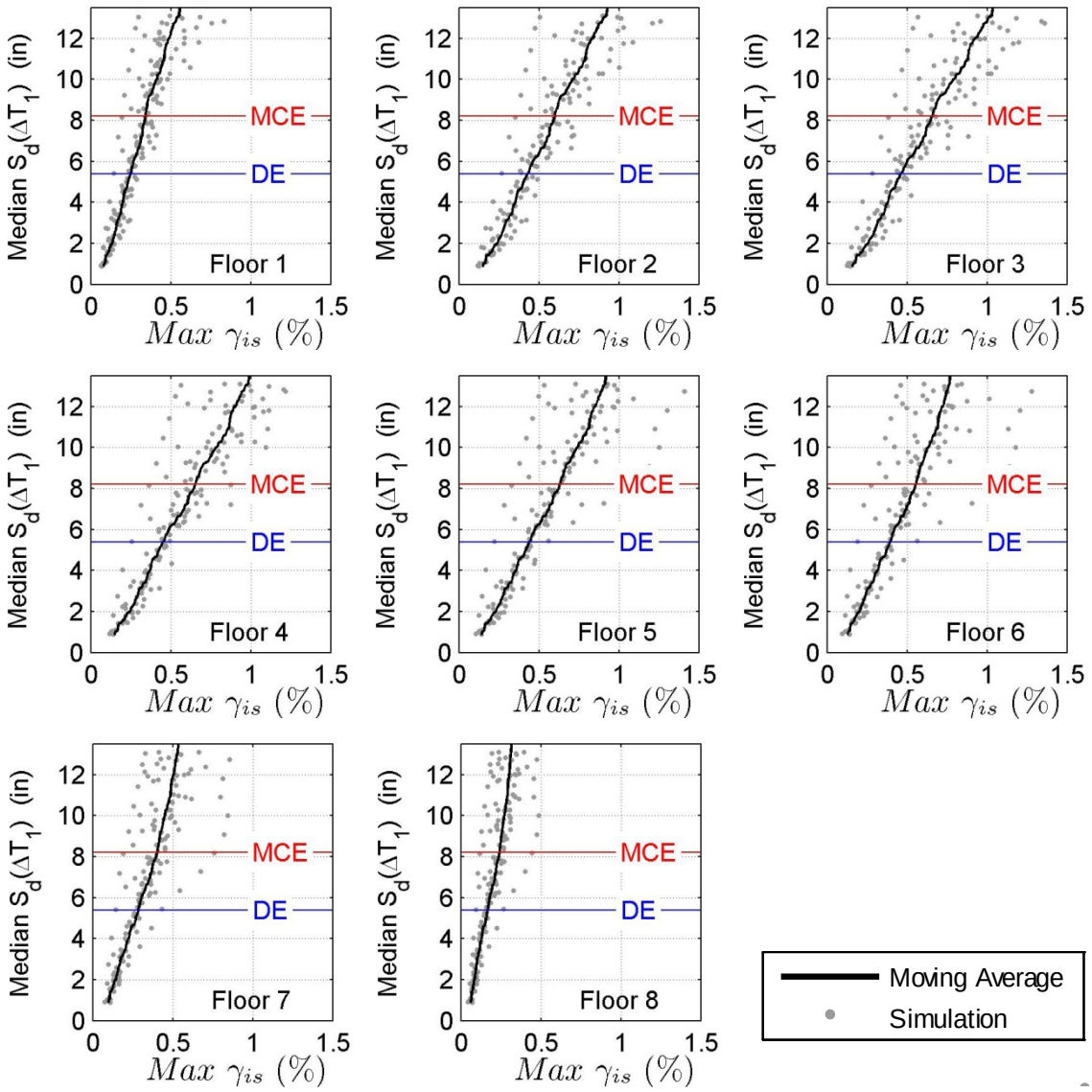

Figure B.52 IDA results for RC-8 ($L_{w,max}$ no post peak hardhening): maximum interstory drift against median spectral displacement over the range of T_1.

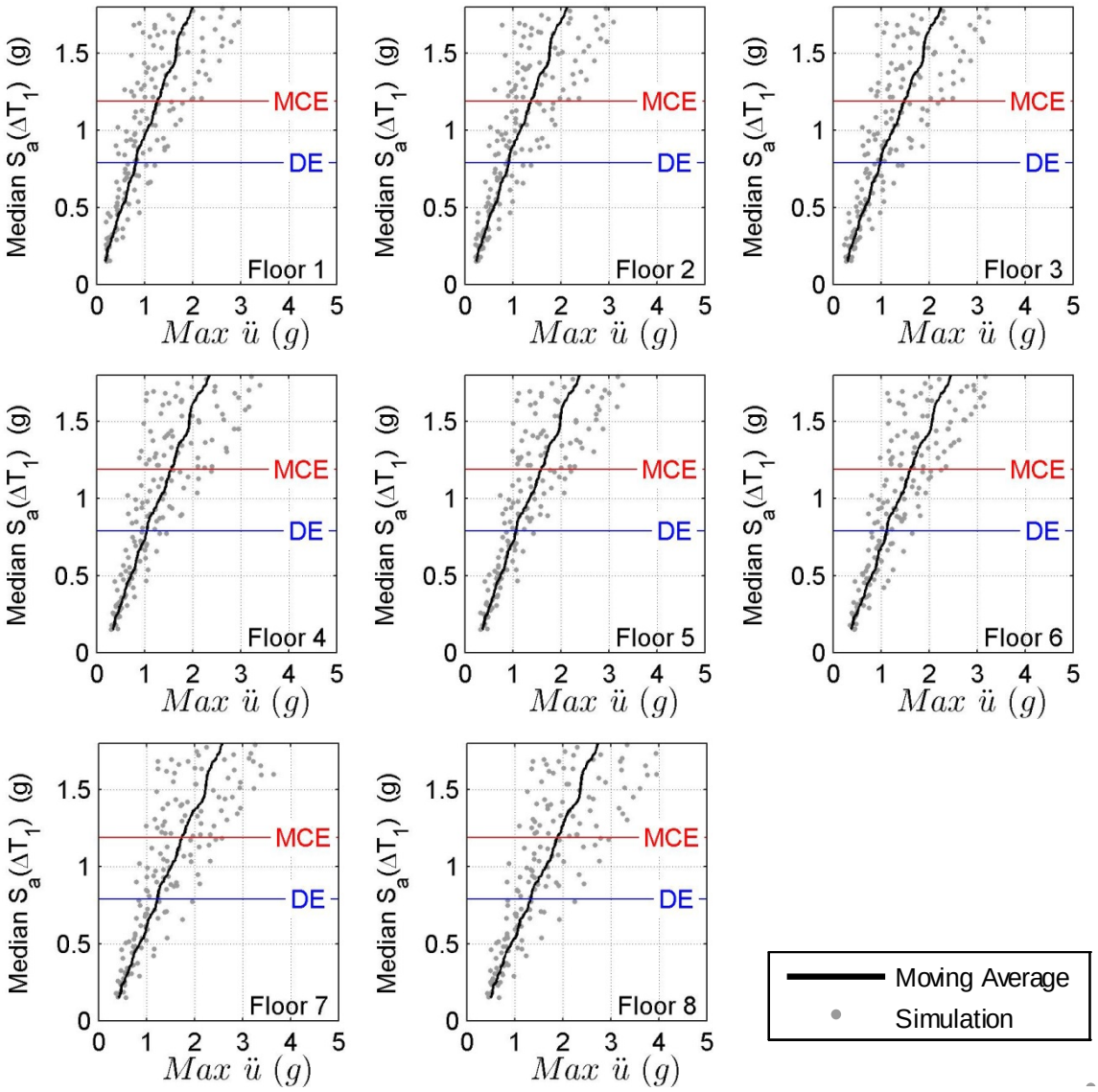

Figure B.53 IDA results for RC-8 ($L_{w,max}$ no post peak hardhening): maximum floor level acceleration against median spectral acceleration over the range of T_1.

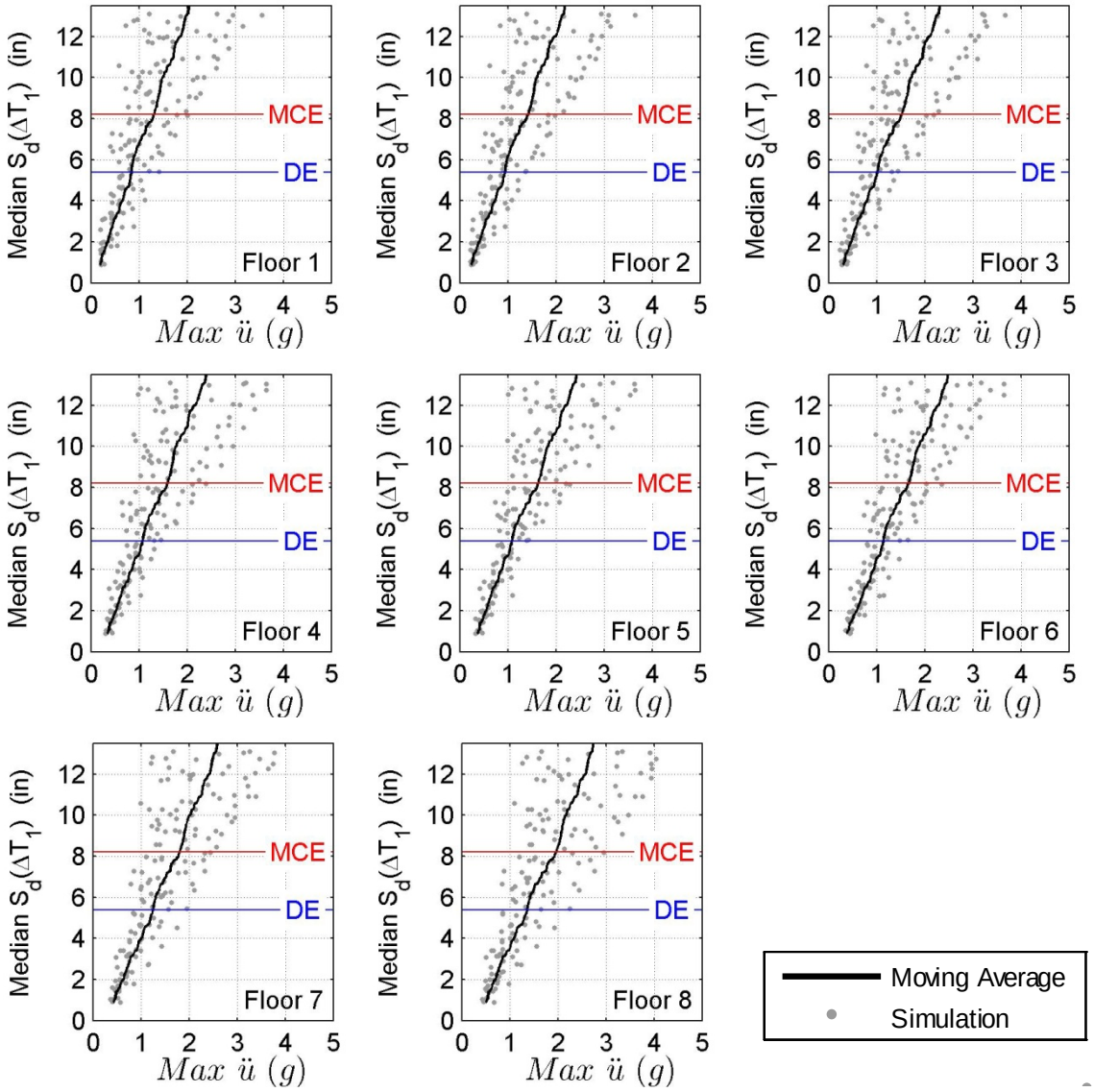

Figure B.54 IDA results for RC-8 ($L_{w,max}$ no post peak hardhening): maximum floor level acceleration against median spectral displacement over the range of T_1.

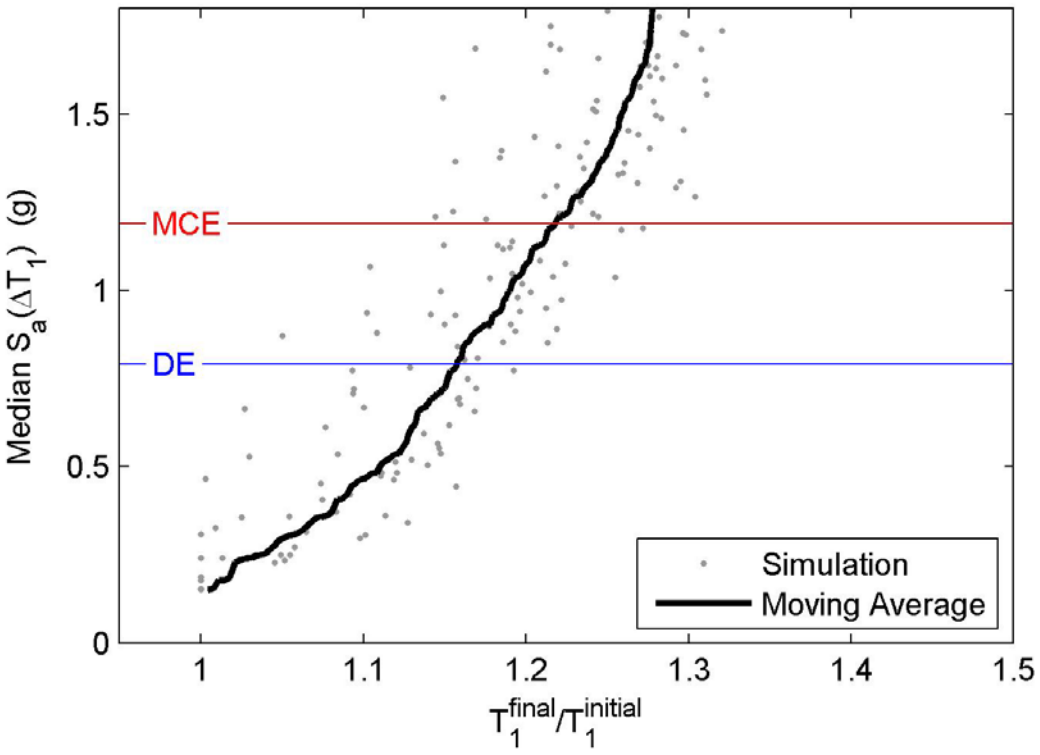

Figure B.55 IDA results for RC-8 ($L_{w,max}$ no post peak hardhening): period elongation against median spectral acceleration over the range of T_1.

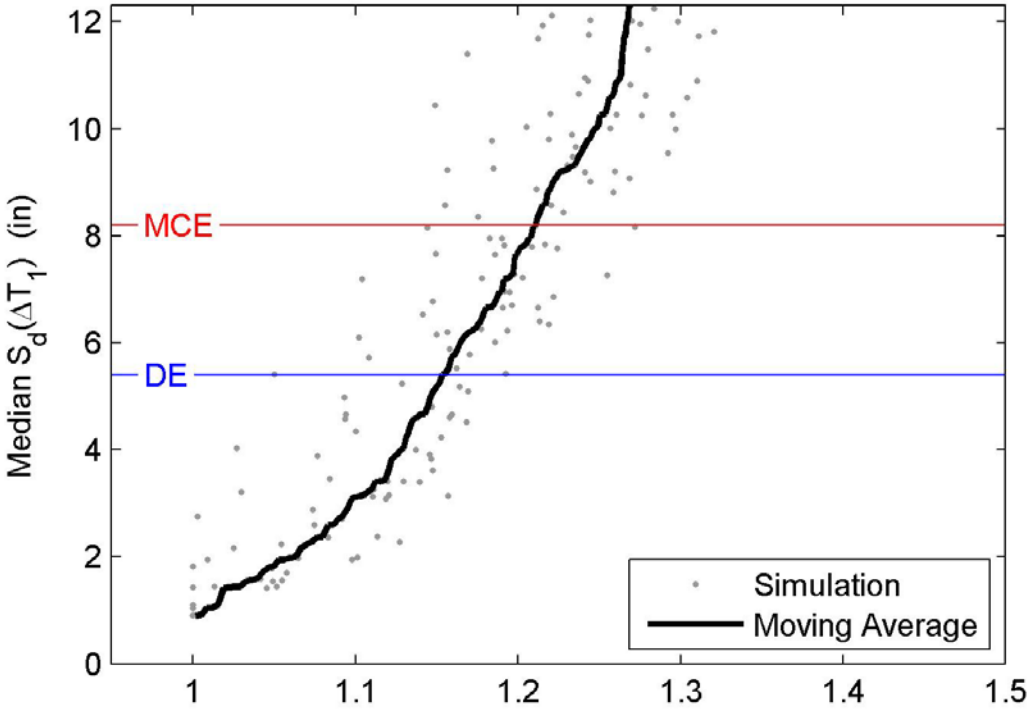

Figure B.56 IDA results for RC-8 ($L_{w,max}$ no post peak hardhening): period elongation against median spectral displacement over the range of T_1.

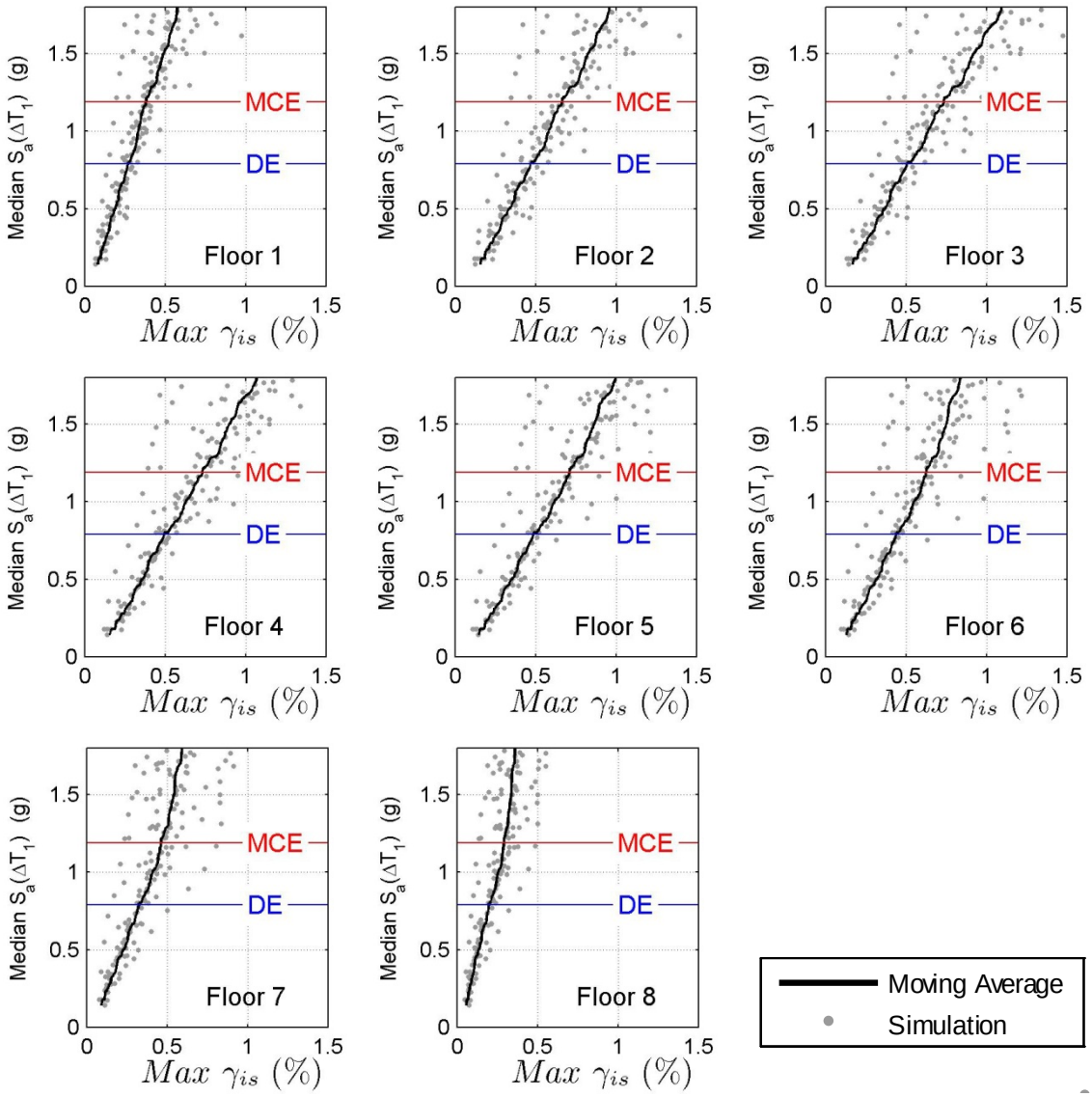

Figure B.57 IDA results for RC-8 ($L_{w,min}$ (μ) – no wall first floor): maximum interstory drift against median spectral acceleration over the range of T_1.

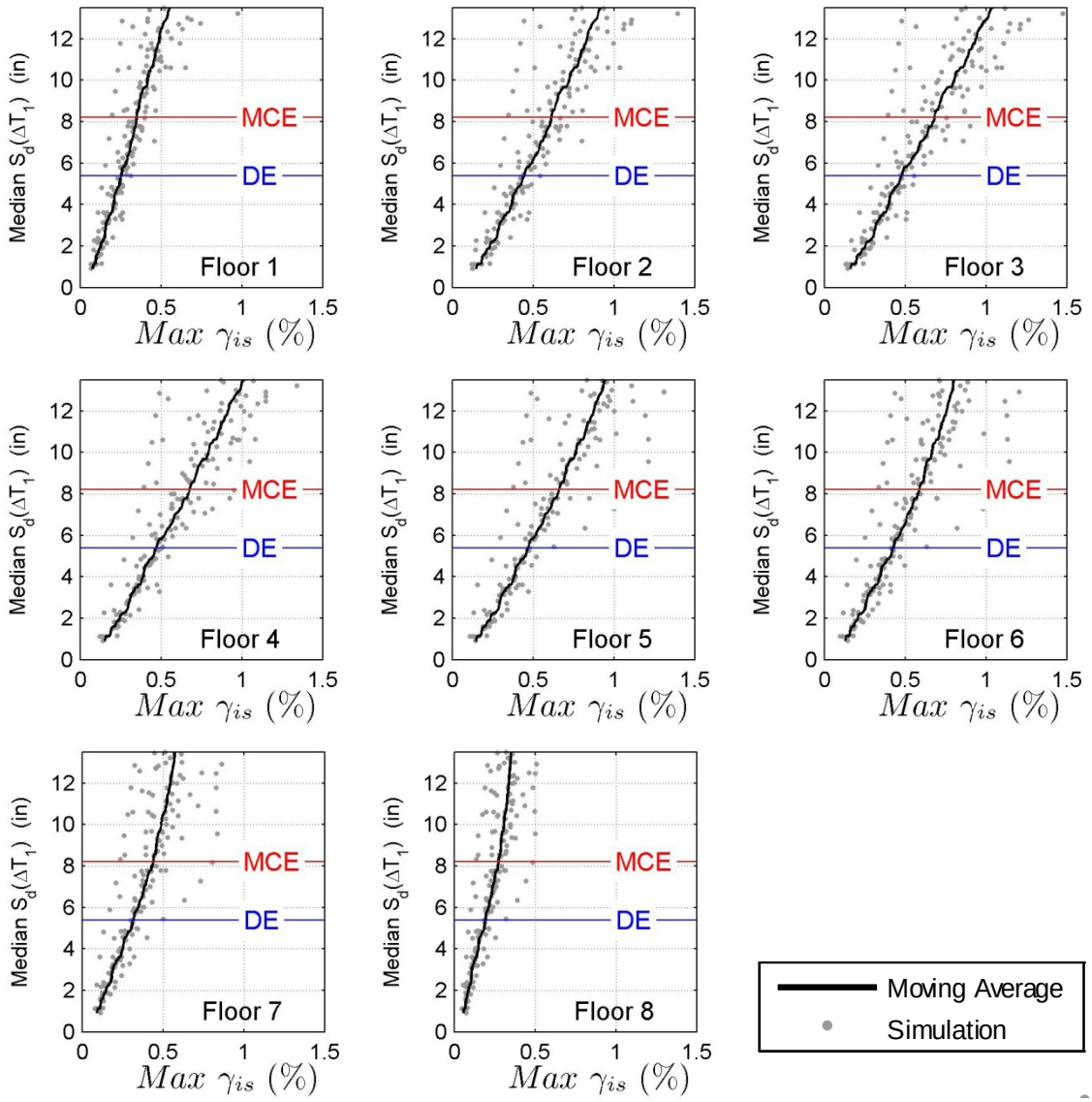

Figure B.58 IDA results for RC-8 ($L_{w,min}$ (μ)– no wall first floor): maximum interstory drift against median spectral displacement over the range of T_1.

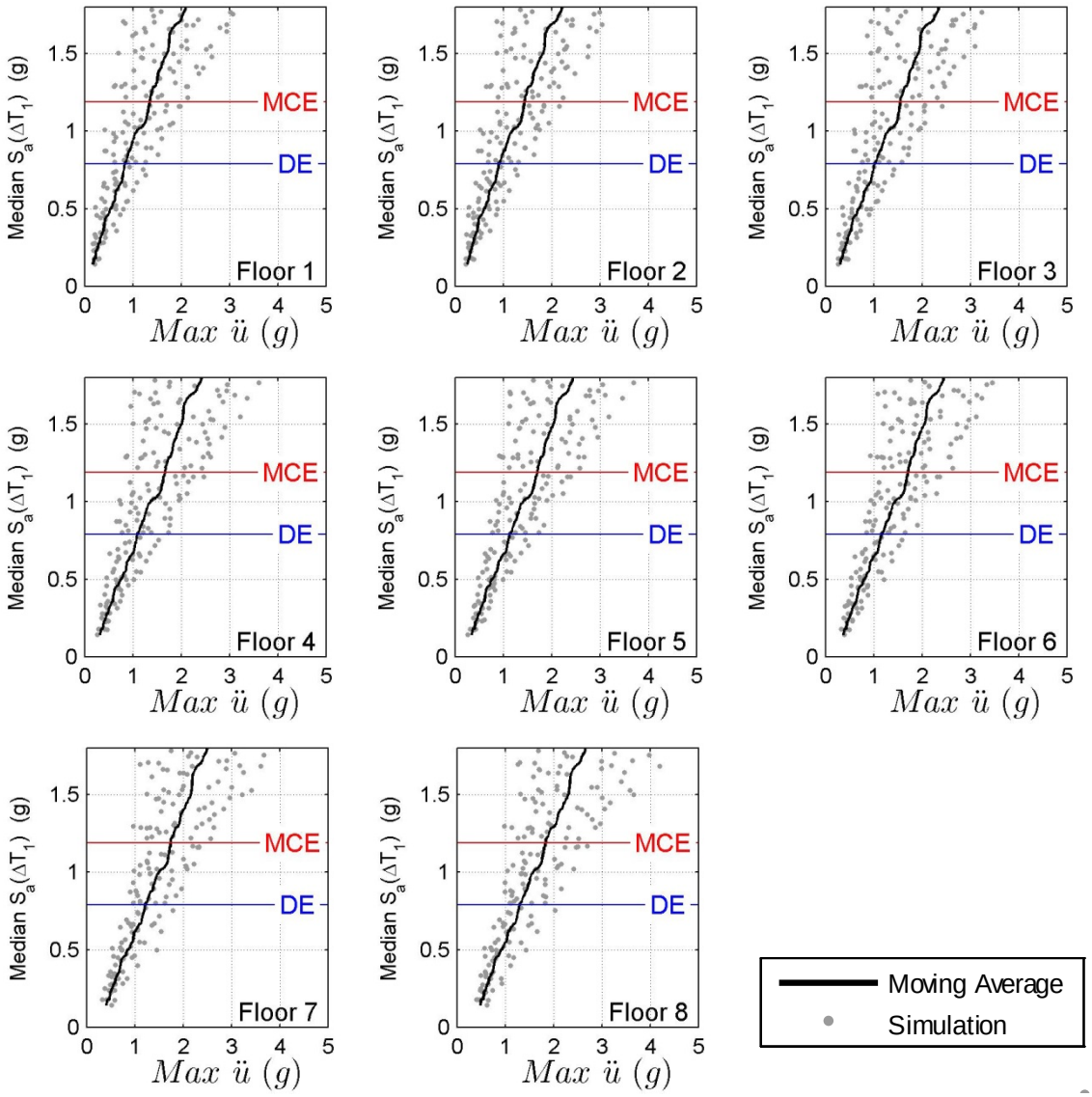

Figure B.59 IDA results for RC-8 ($L_{w,min}$ (μ) – no wall first floor): maximum floor level acceleration against median spectral acceleration over the range of T_1.

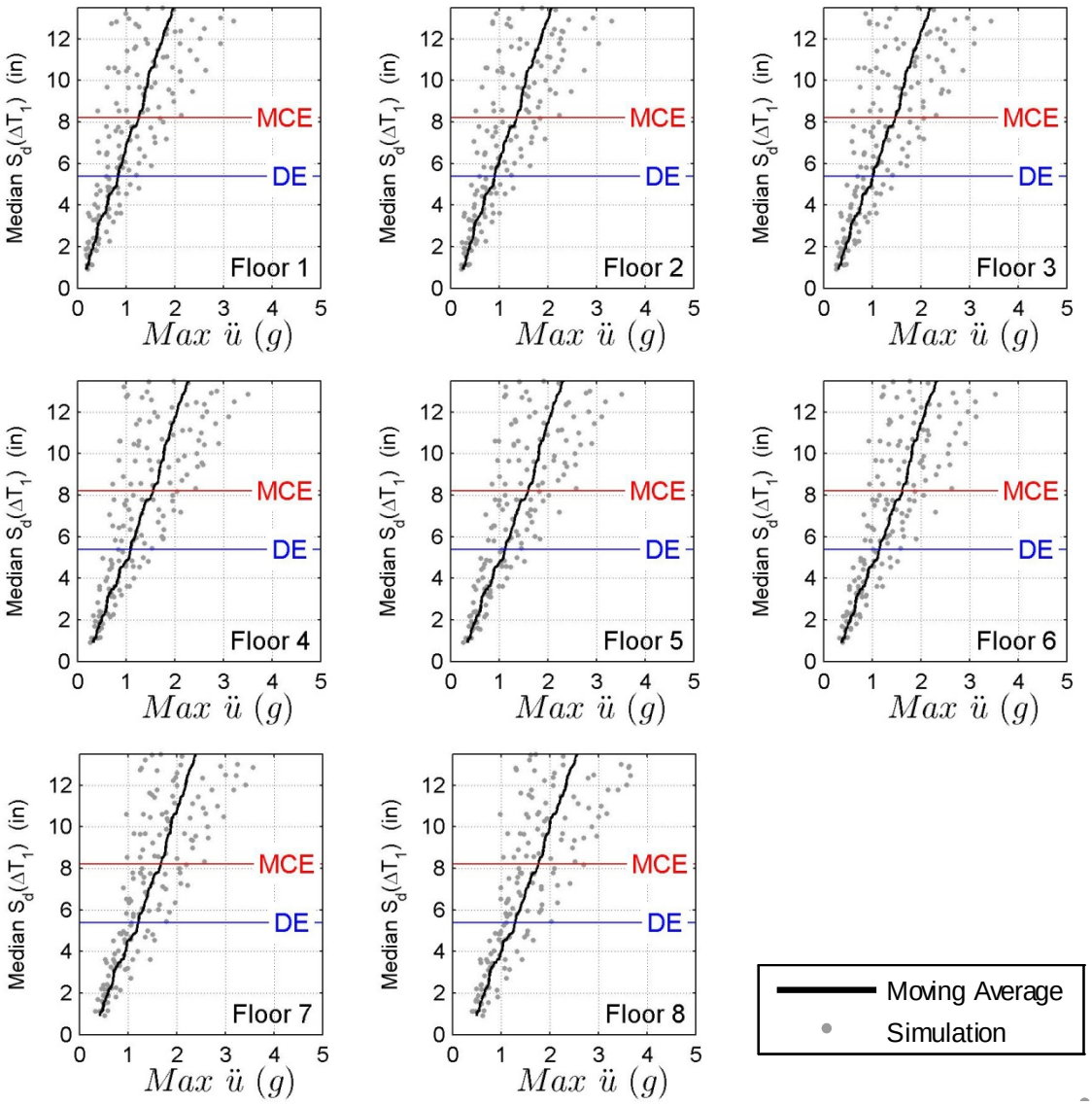

Figure B.60 IDA results for RC-8 ($L_{w,min}$ (μ)– no wall first floor): maximum floor level acceleration against median spectral displacement over the range of T_1.

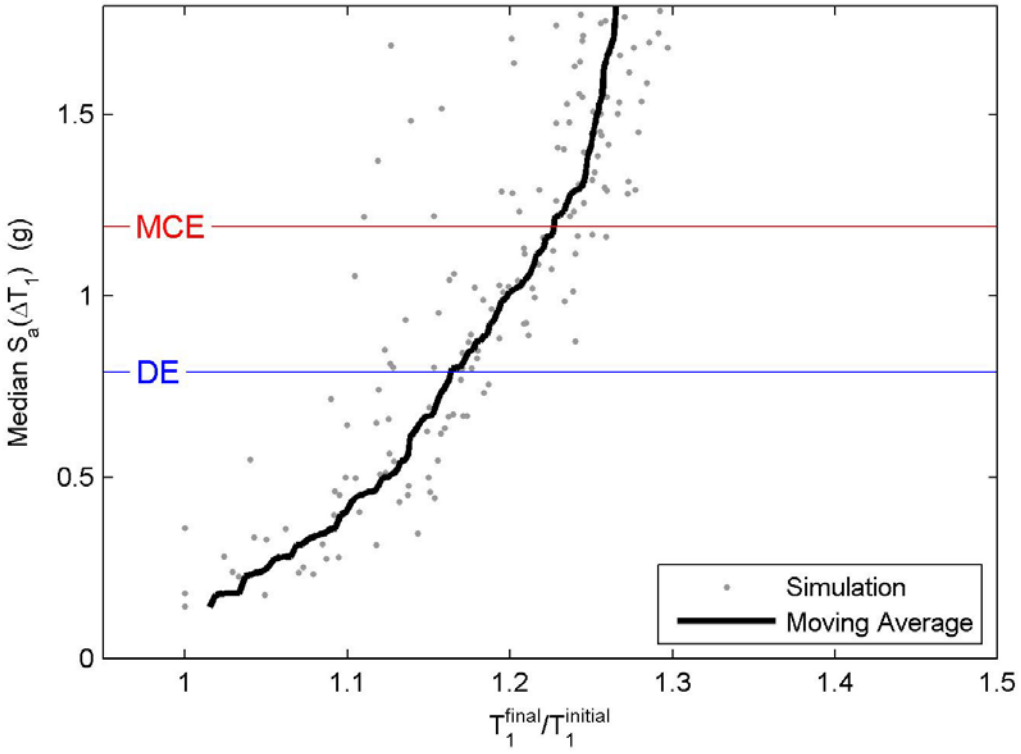

Figure B.61 IDA results for RC-8 ($L_{w,min}$ (μ)– no wall first floor): period elongation against median spectral acceleration over the range of T_1.

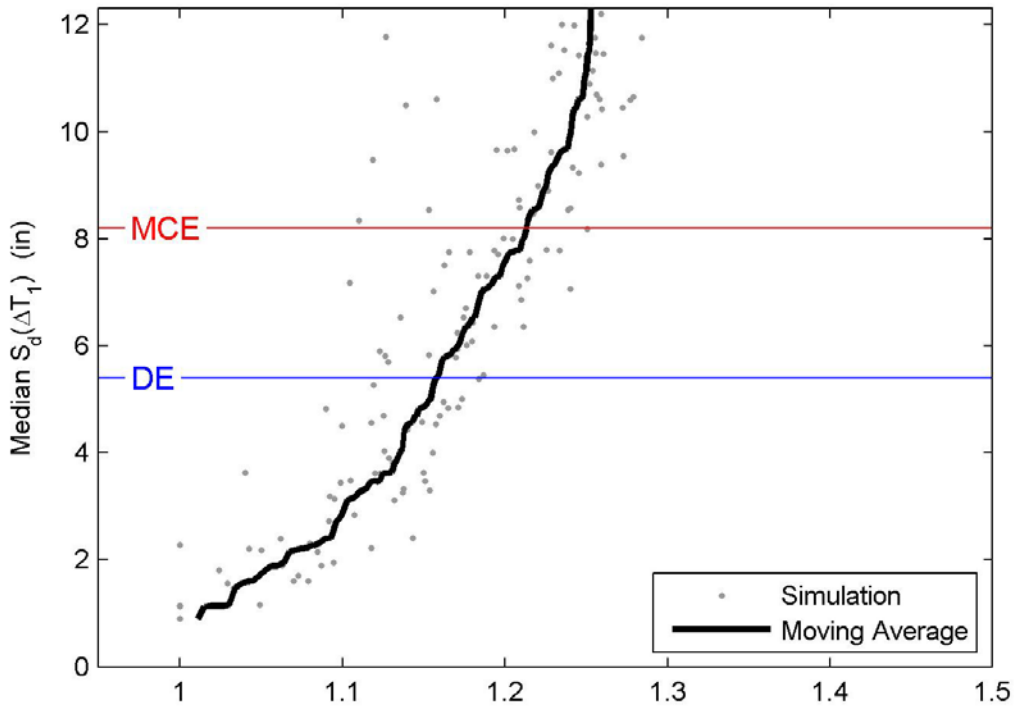

Figure B.62 IDA results for RC-8 ($L_{w,min}$ (μ) – no wall first floor): period elongation against median spectral displacement over the range of T_1.

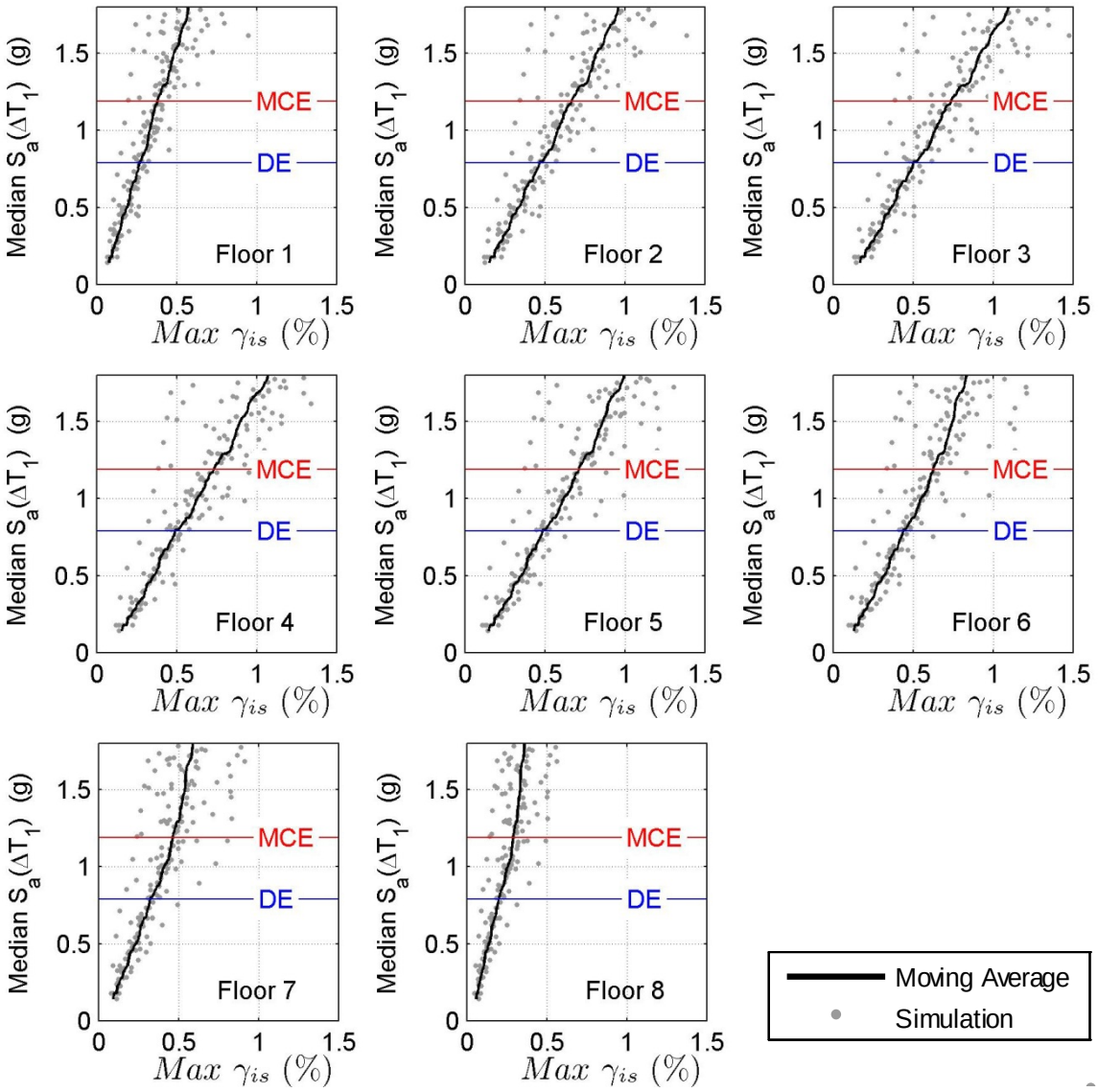

Figure B.63 IDA results for RC-8 ($L_{w,min}$ (μ) – no wall top level): maximum interstory drift against median spectral acceleration over the range of T_1.

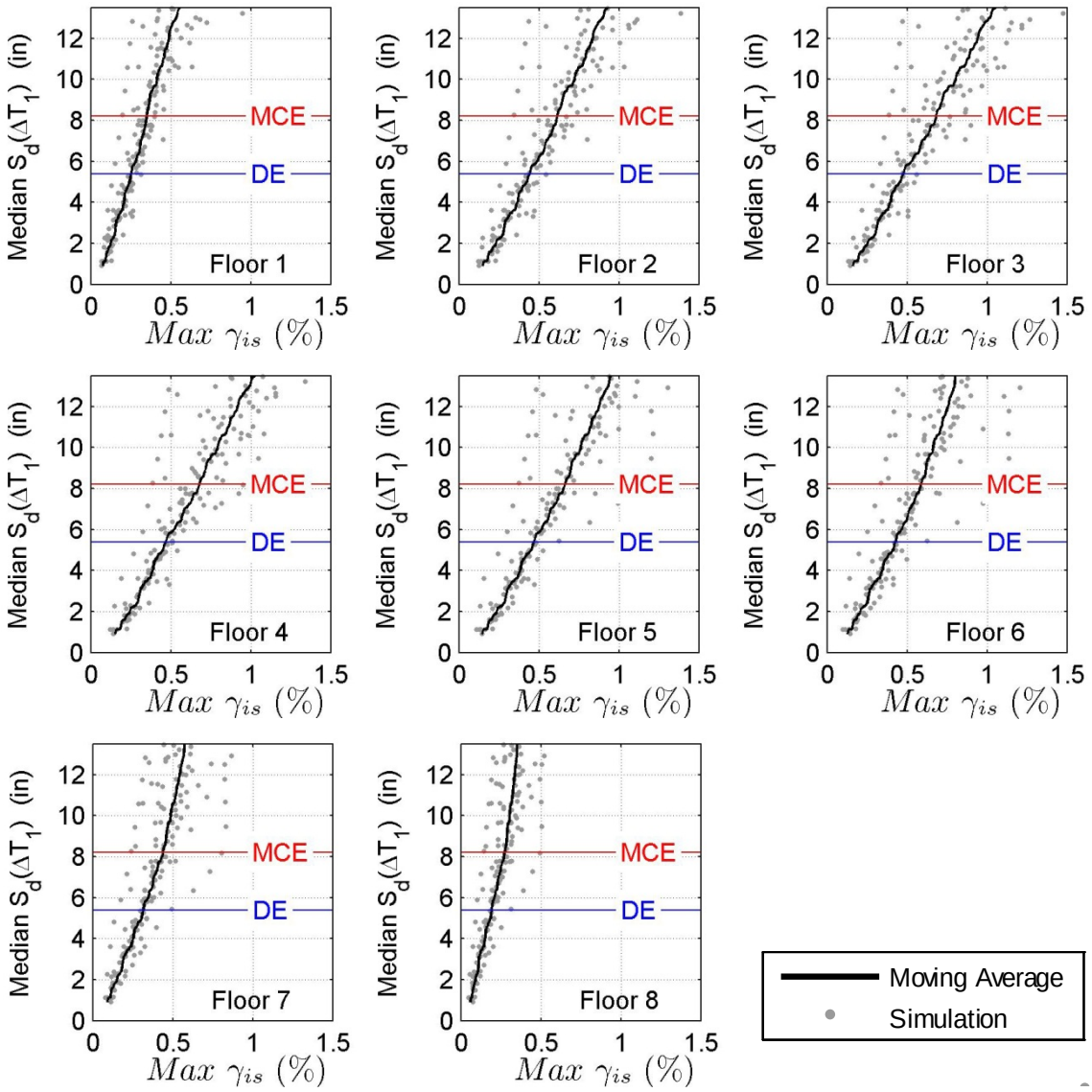

Figure B.64 IDA results for RC-8 ($L_{w,min}$ (μ) – no wall top level): maximum interstory drift against median spectral displacement over the range of T_1.

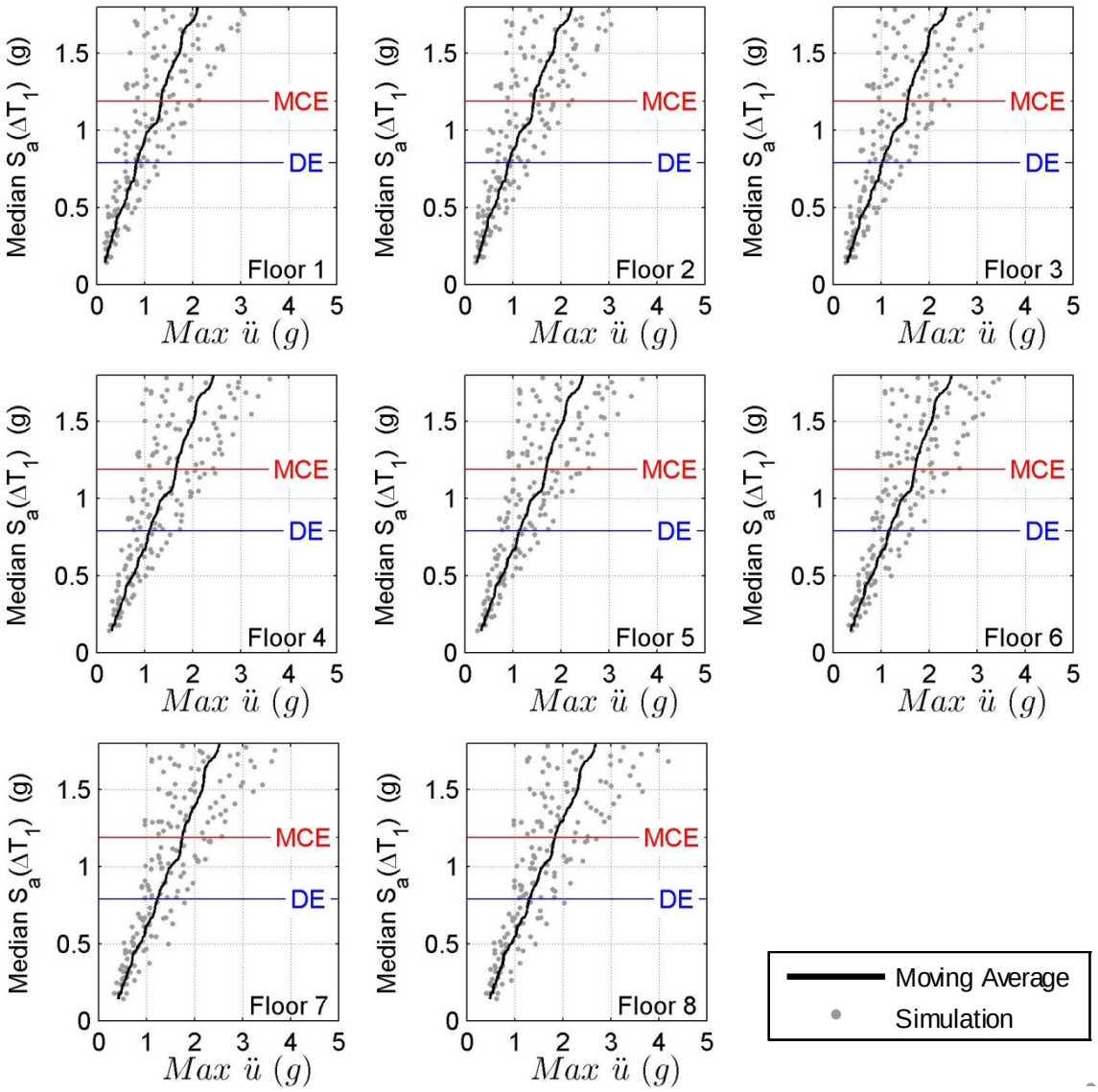

Figure B.65 IDA results for RC-8 ($L_{w,min}$ (μ) – no wall top level): maximum floor level acceleration against median spectral acceleration over the range of T_1.

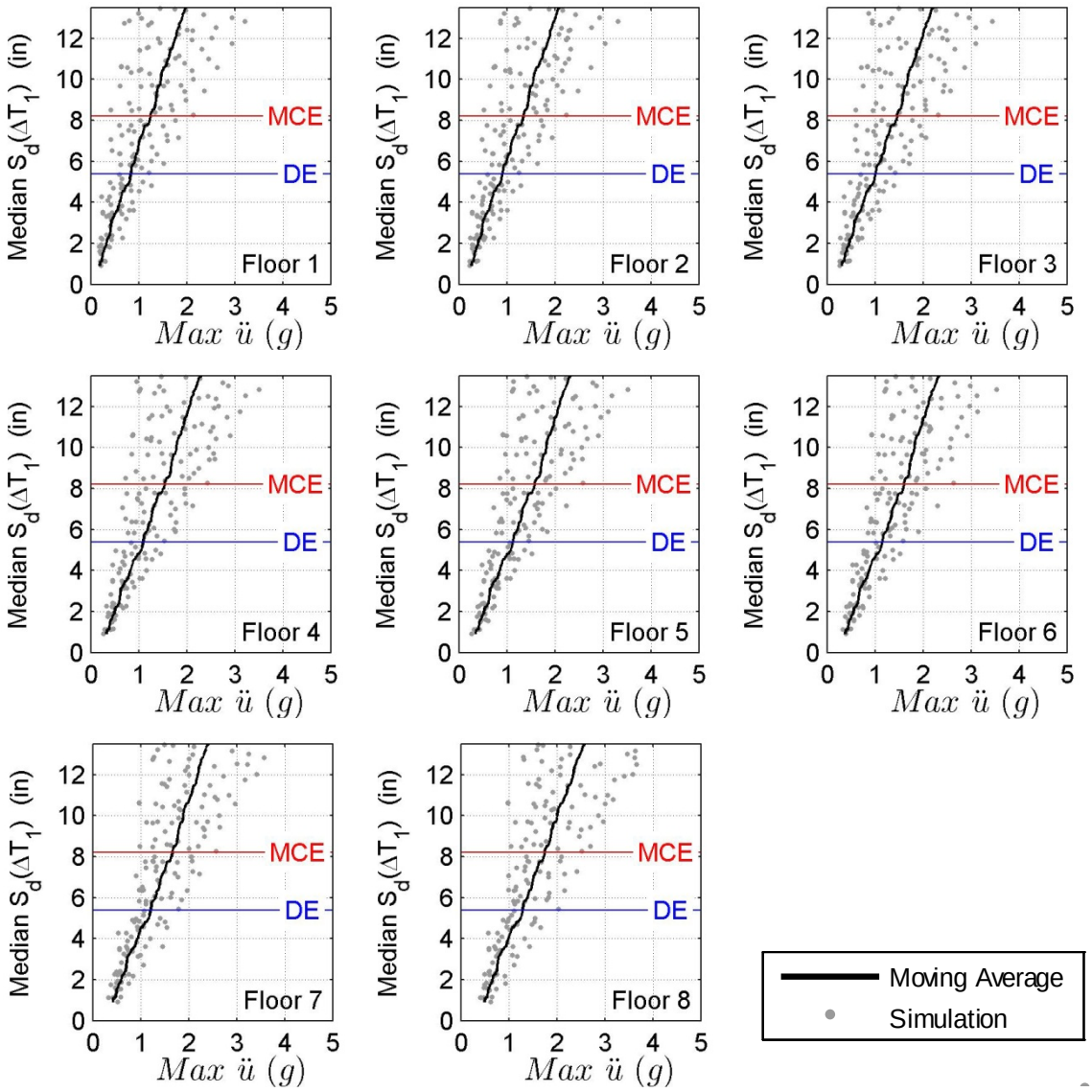

Figure B.66 IDA results for RC-8 ($L_{w,min}$ (μ) – no wall top level): maximum floor level acceleration against median spectral displacement over the range of T_1.

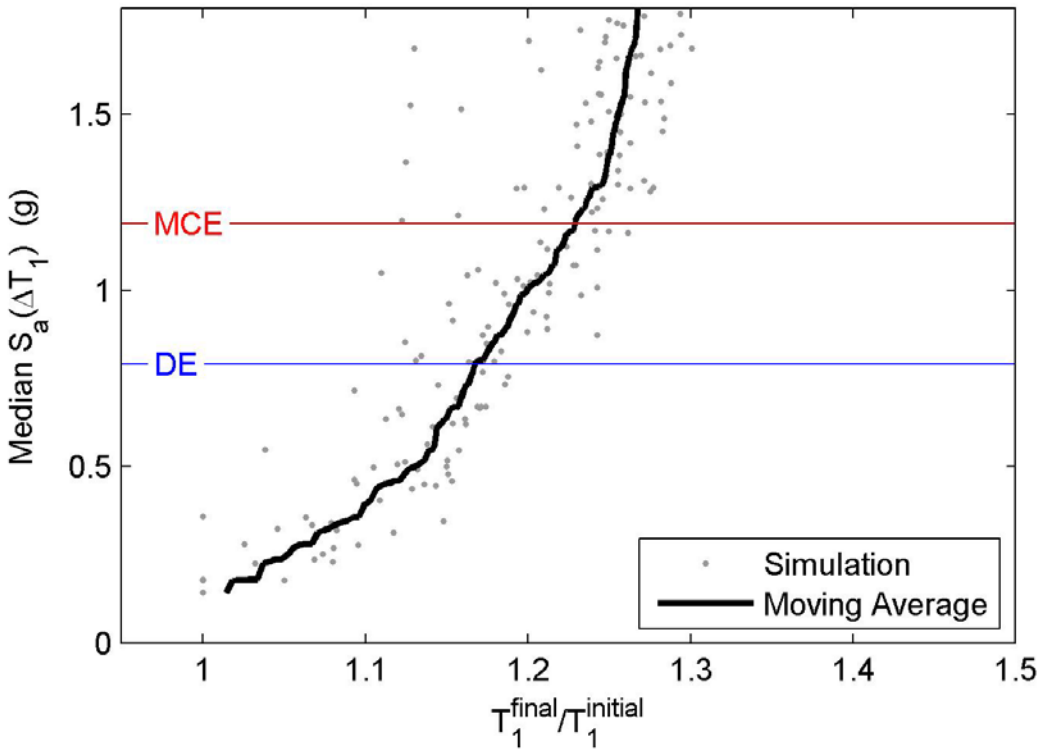

Figure B.67 IDA results for RC-8 ($L_{w,min}$ (μ) – no wall top level): period elongation against median spectral acceleration over the range of T_1.

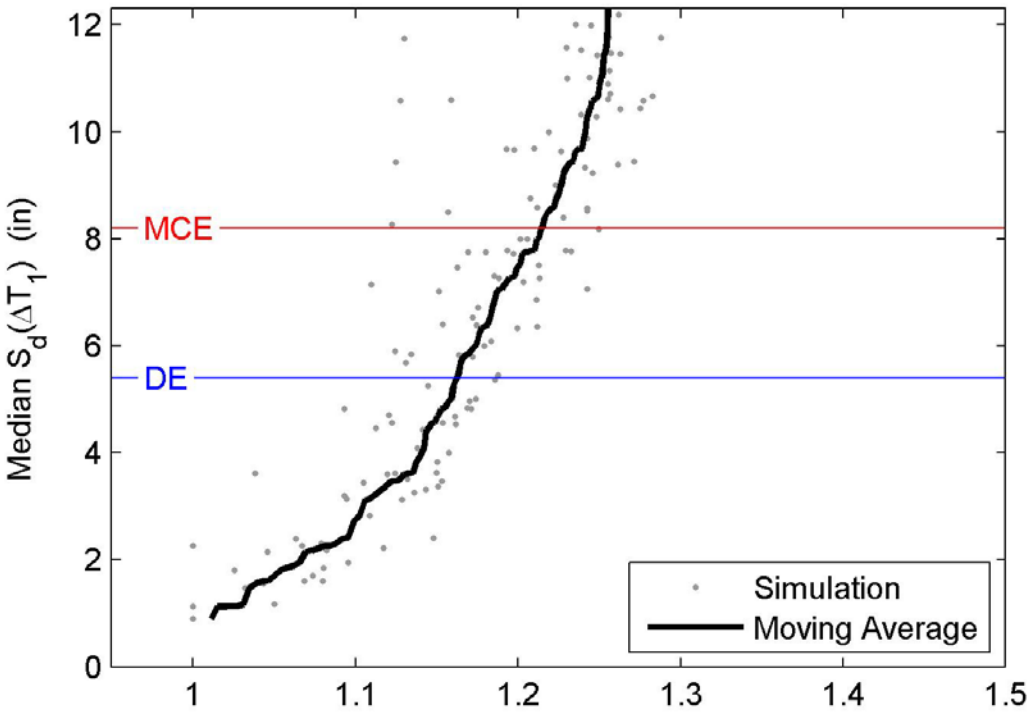

Figure B.68 IDA results for RC-8 ($L_{w,min}$ (μ) – no wall top level): period elongation against median spectral displacement over the range of T_1.

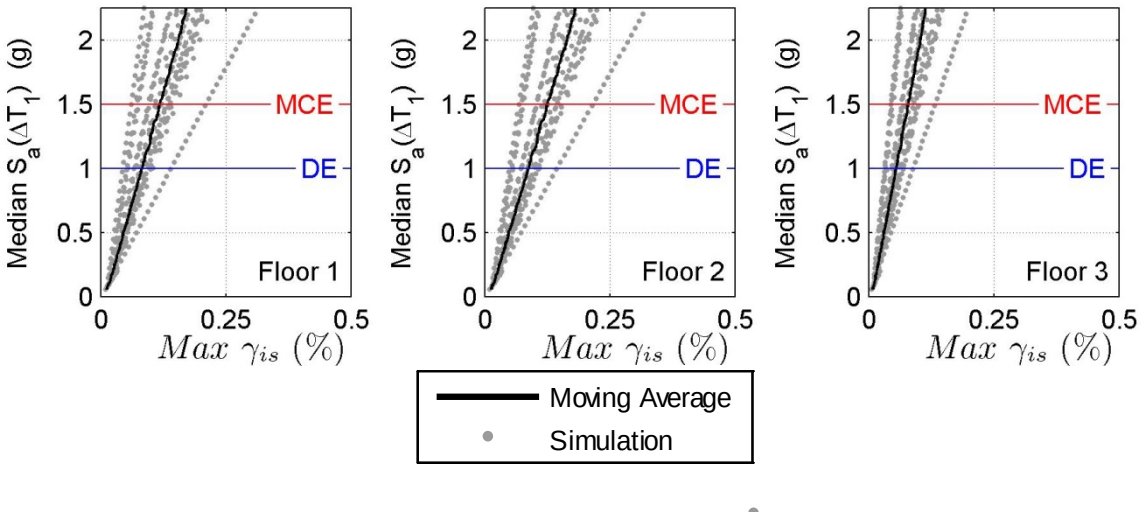

Figure B.69 IDA results for S-3H (no wall): maximum interstory drift against median spectral acceleration over the range of T_1.

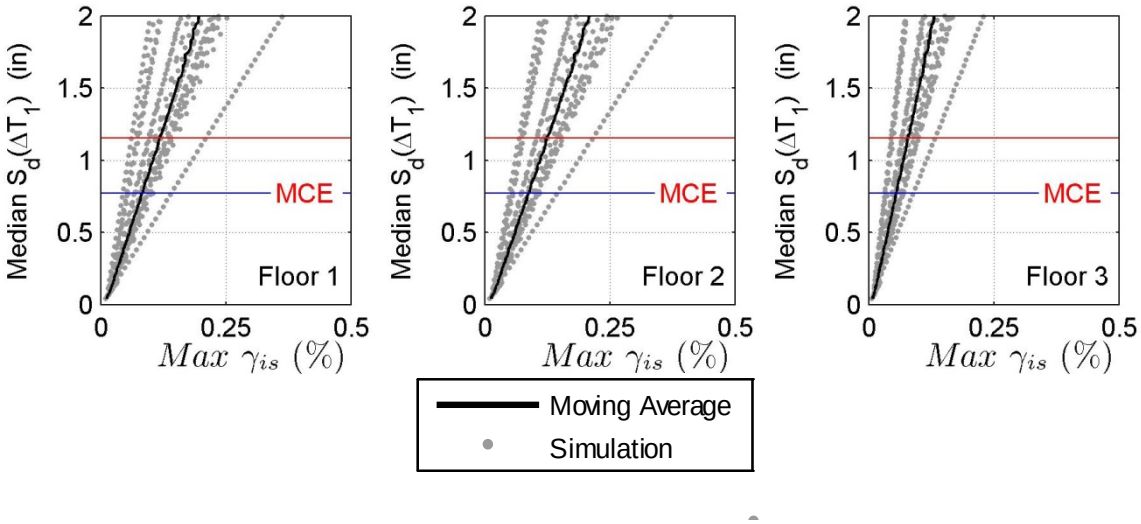

Figure B.70 IDA results for S-3H (no wall): maximum interstory drift against median spectral displacement over the range of T_1.

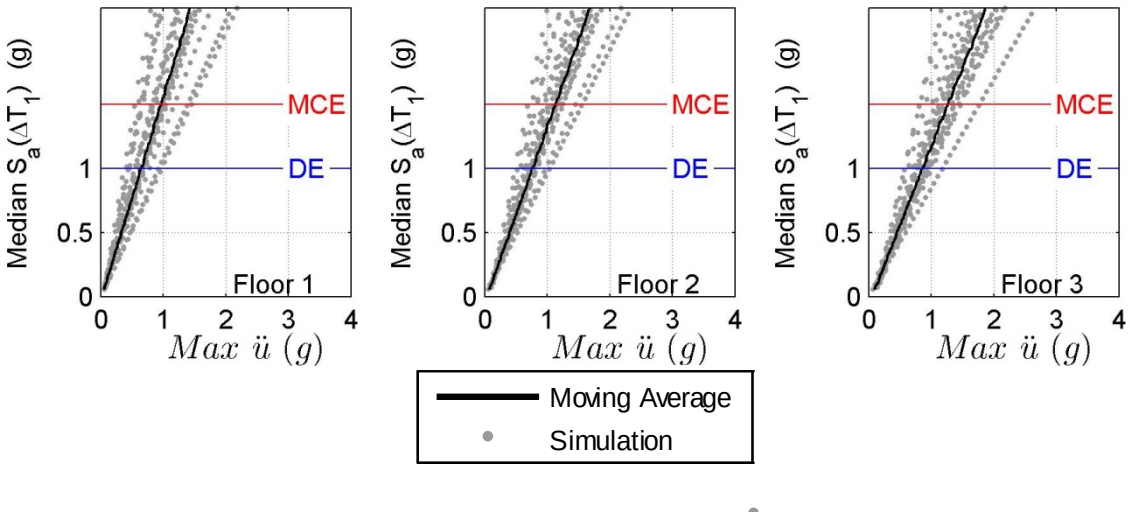

Figure B.71 IDA results for S-3H (no wall): maximum floor level acceleration against median spectral acceleration over the range of T_1.

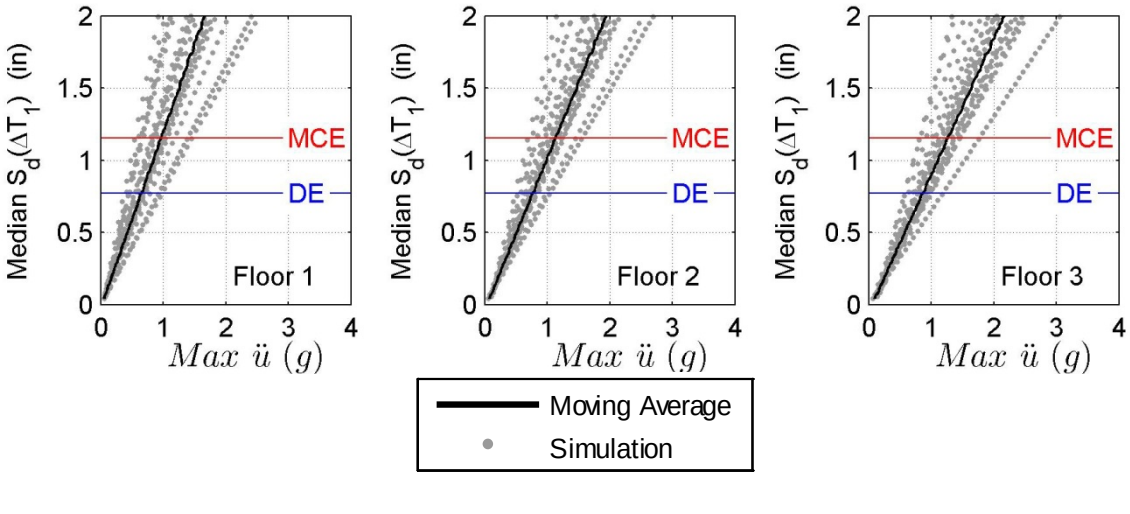

Figure B.72 IDA results for S-3H (no wall): maximum floor level acceleration against median spectral displacement over the range of T_1.

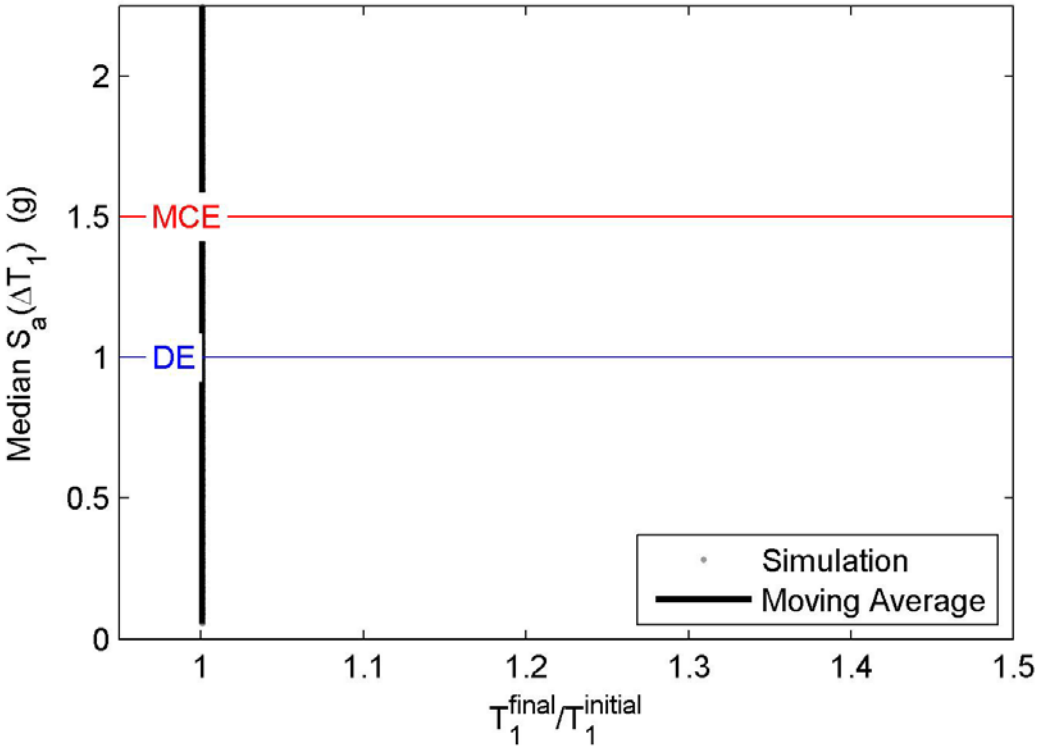

Figure B.73 IDA results for S-3H (no wall): period elongation against median spectral acceleration over the range of T_1.

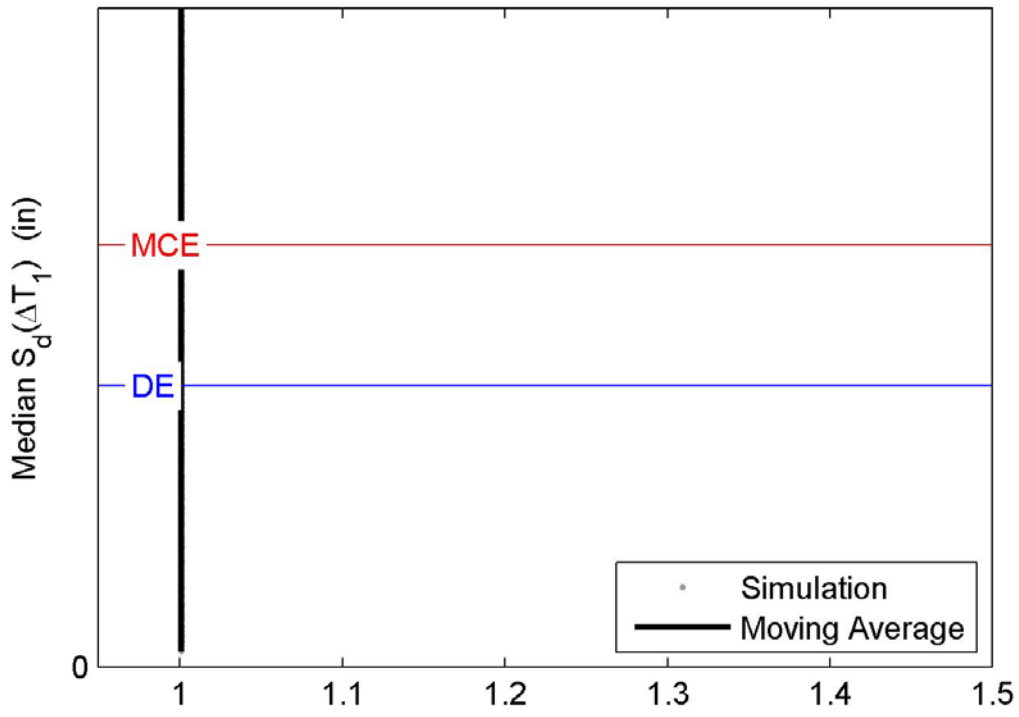

Figure B.74 IDA results for S-3H (no wall): period elongation against median spectral displacement over the range of T_1.

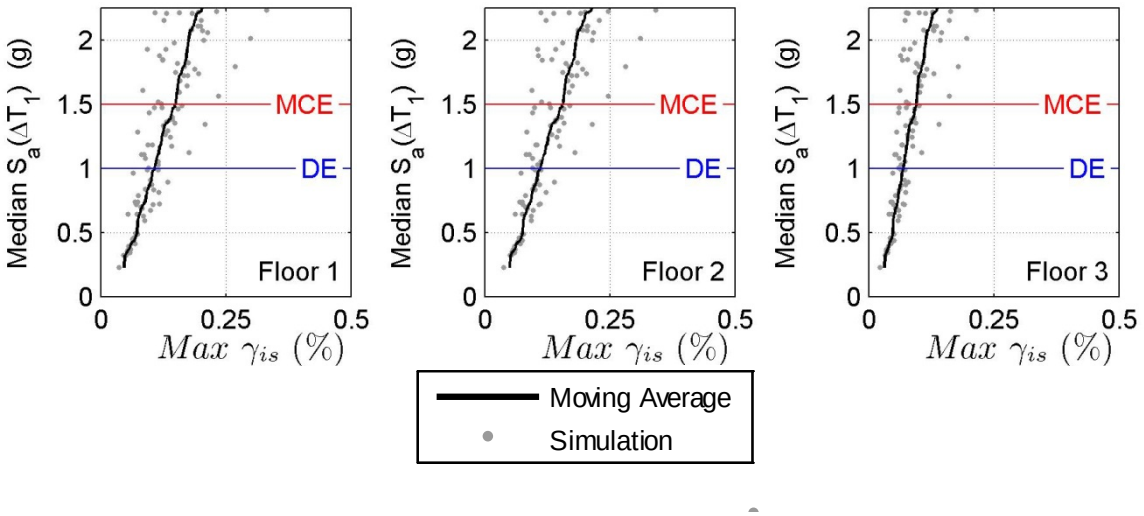

Figure B.75 IDA results for S-3H ($L_{w,min}$): maximum interstory drift against median spectral acceleration over the range of T_1.

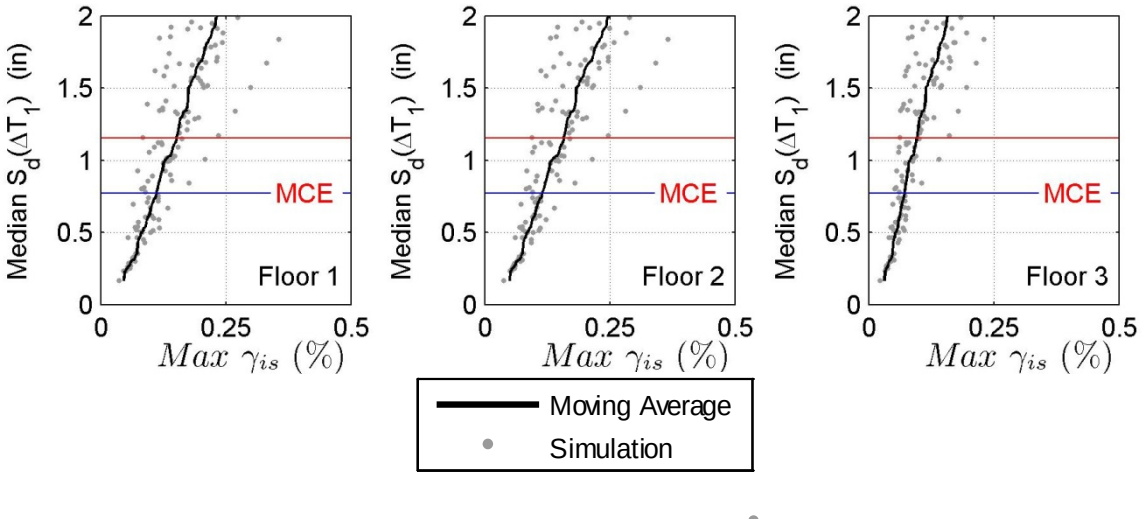

Figure B.76 IDA results for S-3H ($L_{w,min}$): maximum interstory drift against median spectral displacement over the range of T_1.

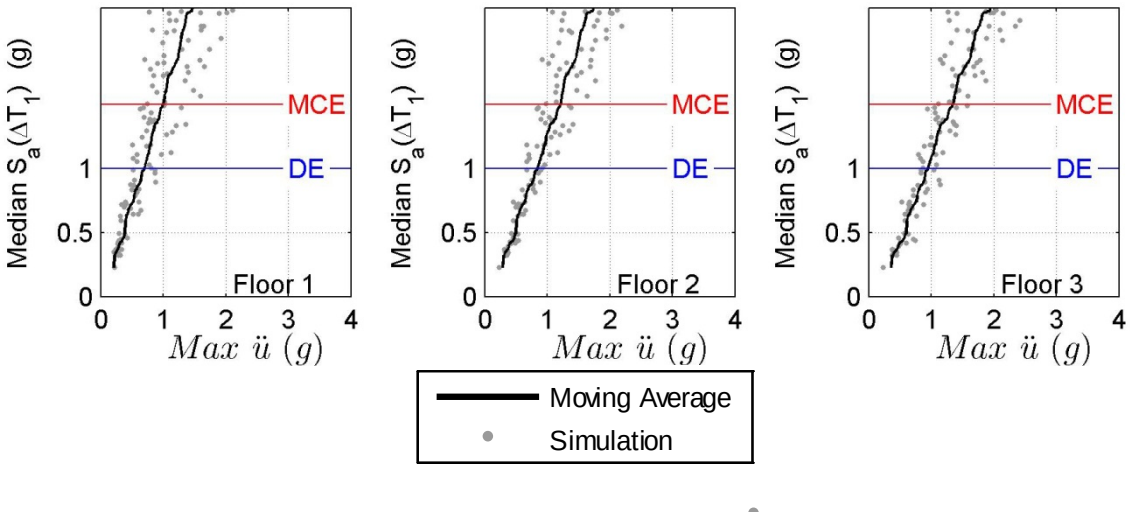

Figure B.77 IDA results for S-3H ($L_{w,min}$): maximum floor level acceleration against median spectral acceleration over the range of T_1.

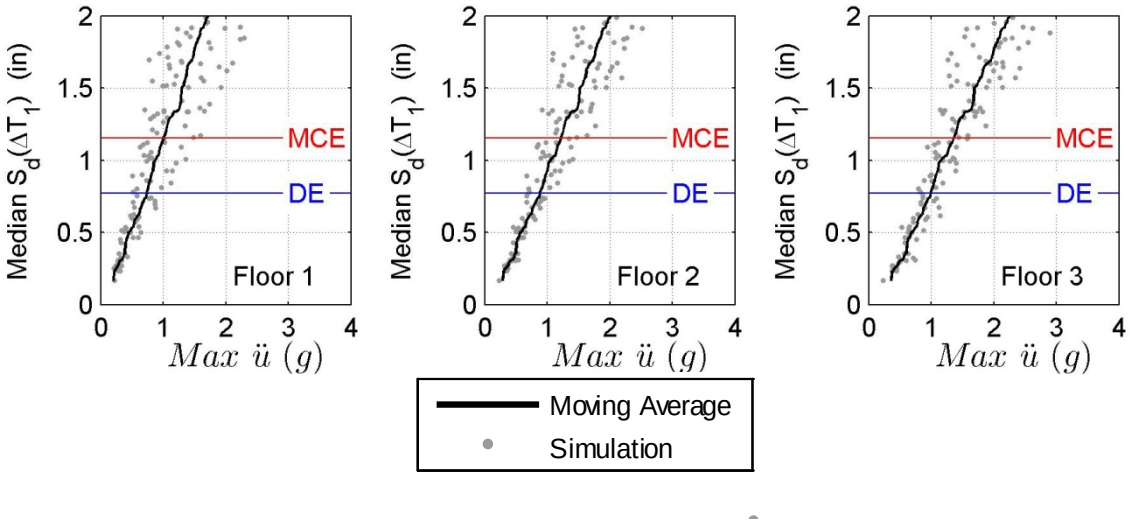

Figure B.78 IDA results for S-3H ($L_{w,min}$): maximum floor level acceleration against median spectral displacement over the range of T_1.

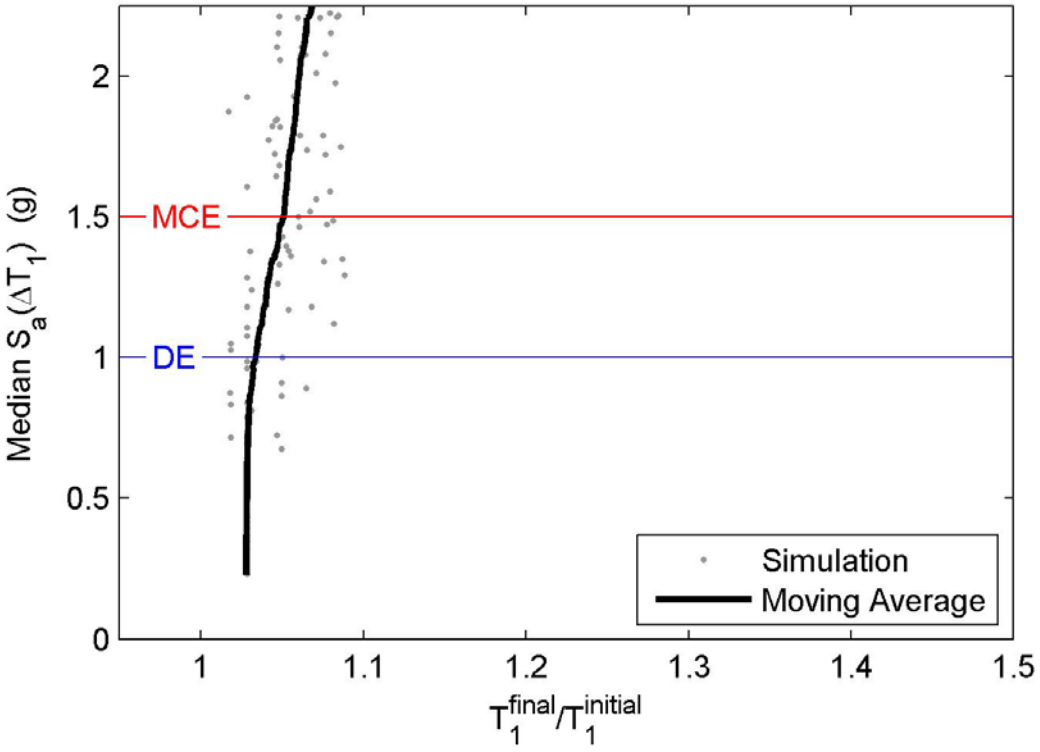

Figure B.79 IDA results for S-3H ($L_{w,min}$): period elongation against median spectral acceleration over the range of T_1.

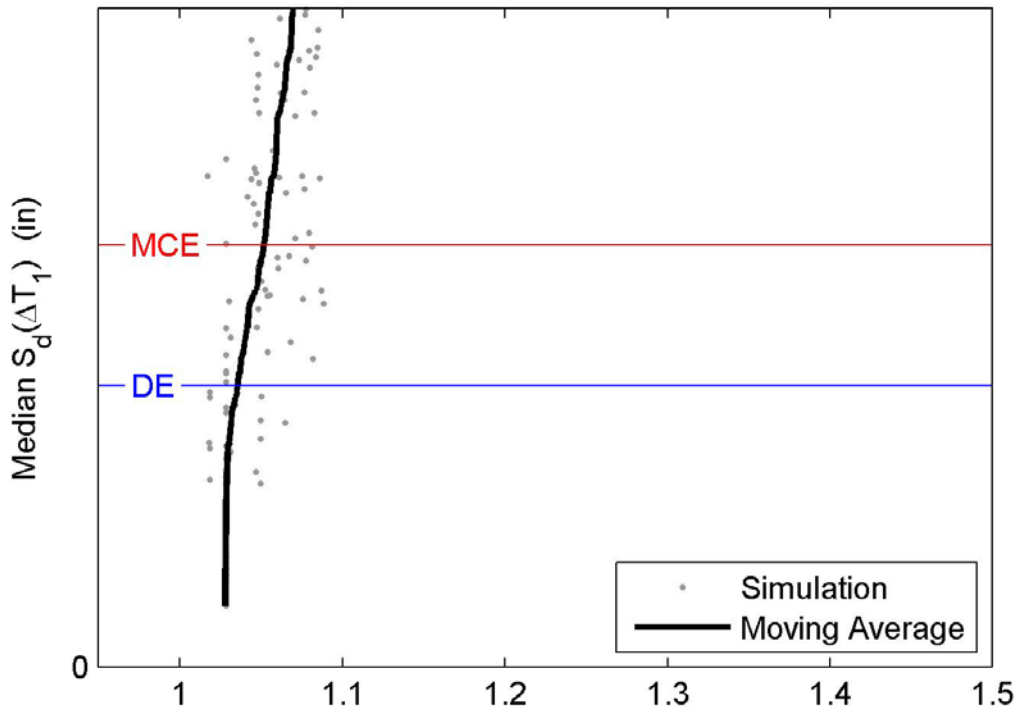

Figure B.80 IDA results for S-3H ($L_{w,min}$): period elongation against median spectral displacement over the range of T_1.

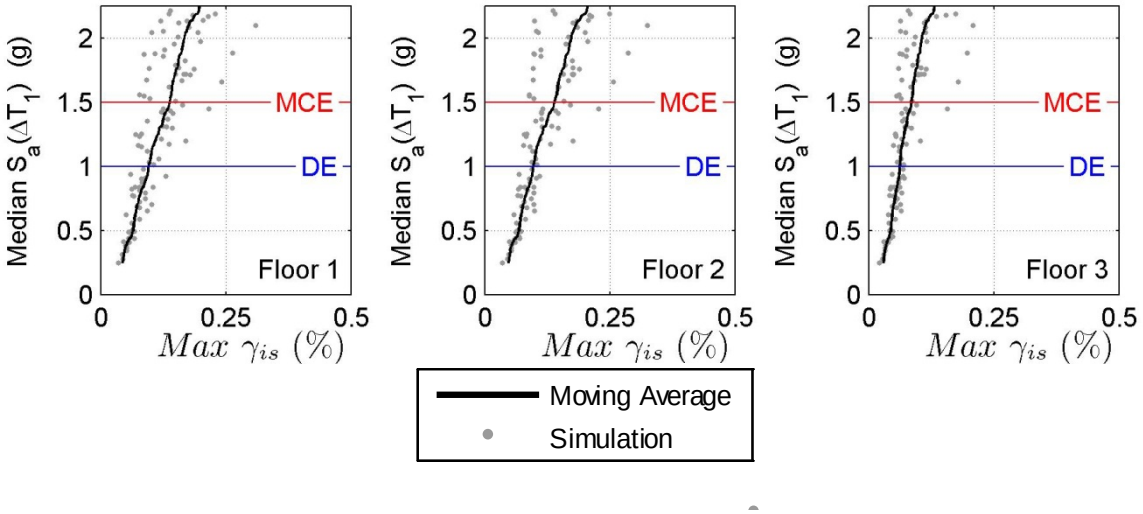

Figure B.81 IDA results for S-3H ($L_{w,max}$): maximum interstory drift against median spectral acceleration over the range of T_1.

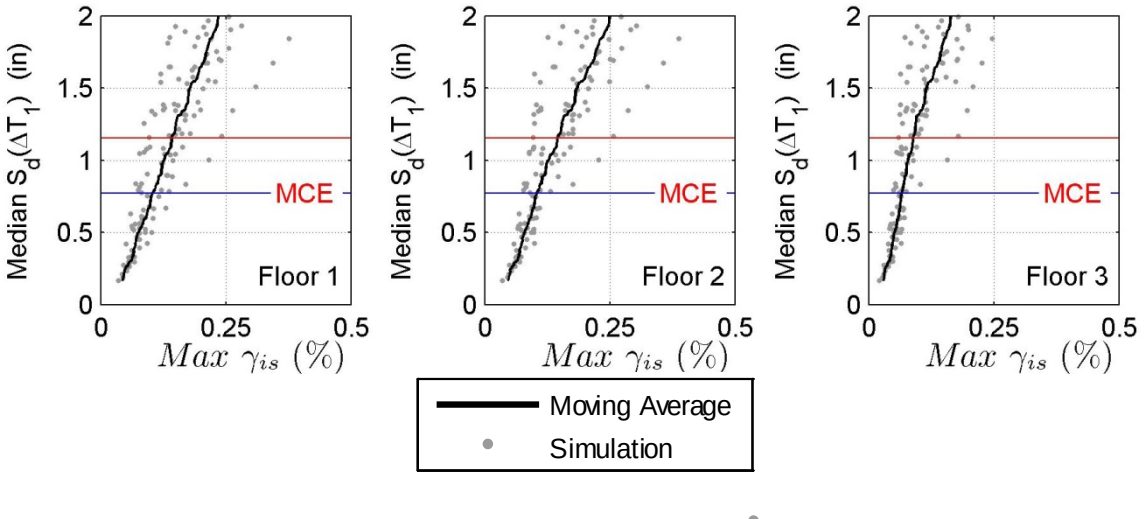

Figure B.82 IDA results for S-3H ($L_{w,max}$): maximum interstory drift against median spectral displacement over the range of T_1.

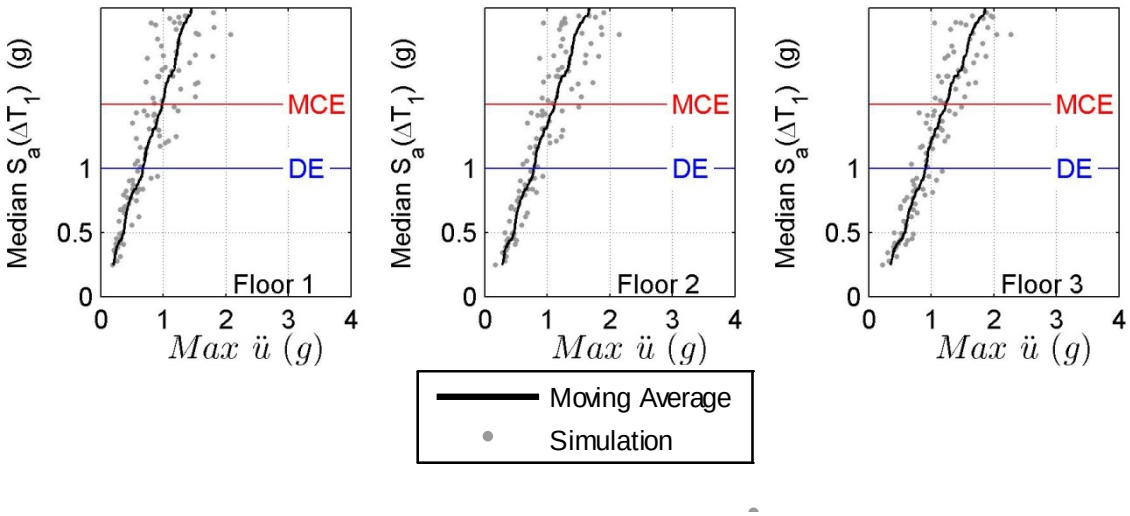

Figure B.83 IDA results for S-3H ($L_{w,max}$): maximum floor level acceleration against median spectral acceleration over the range of T_1.

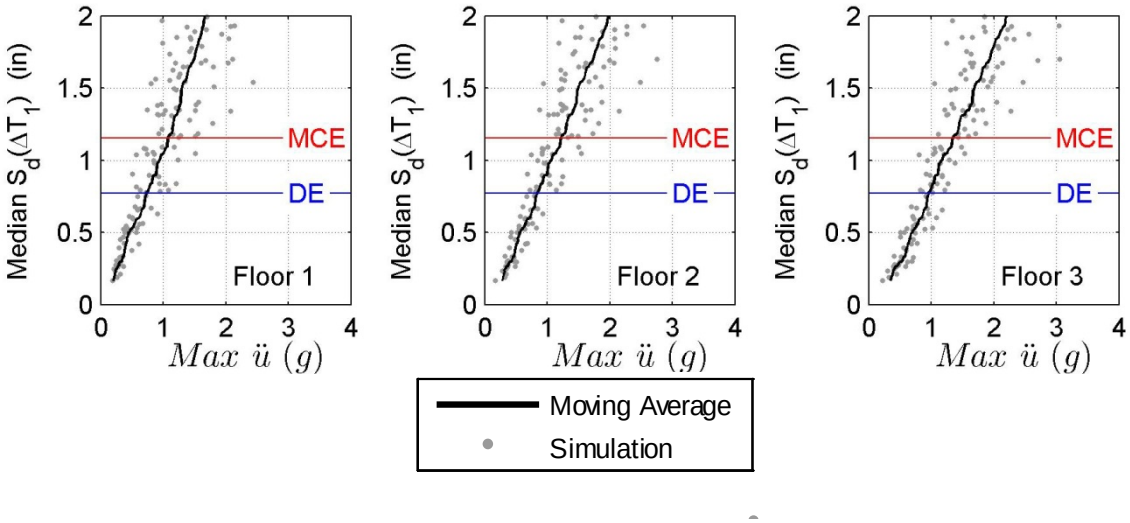

Figure B.84 IDA results for S-3H ($L_{w,max}$): maximum floor level acceleration against median spectral displacement over the range of T_1.

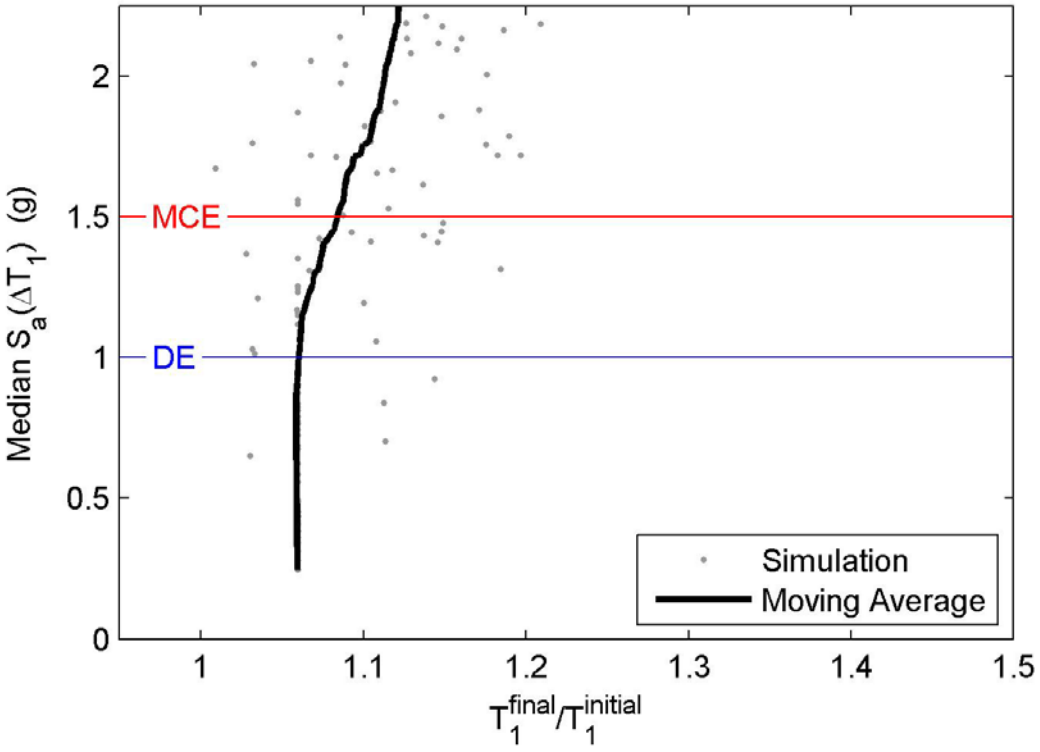

Figure B.85 IDA results for S-3H ($L_{w,max}$): period elongation against median spectral acceleration over the range of T_1.

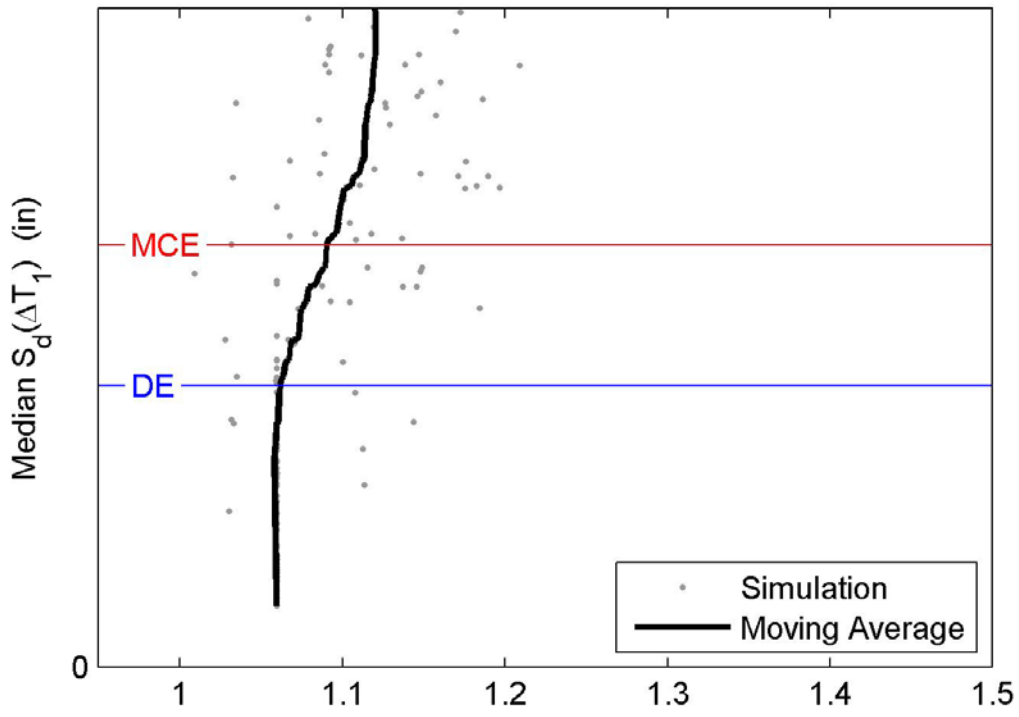

Figure B.86 IDA results for S-3H ($L_{w,max}$): period elongation against median spectral displacement over the range of T_1.

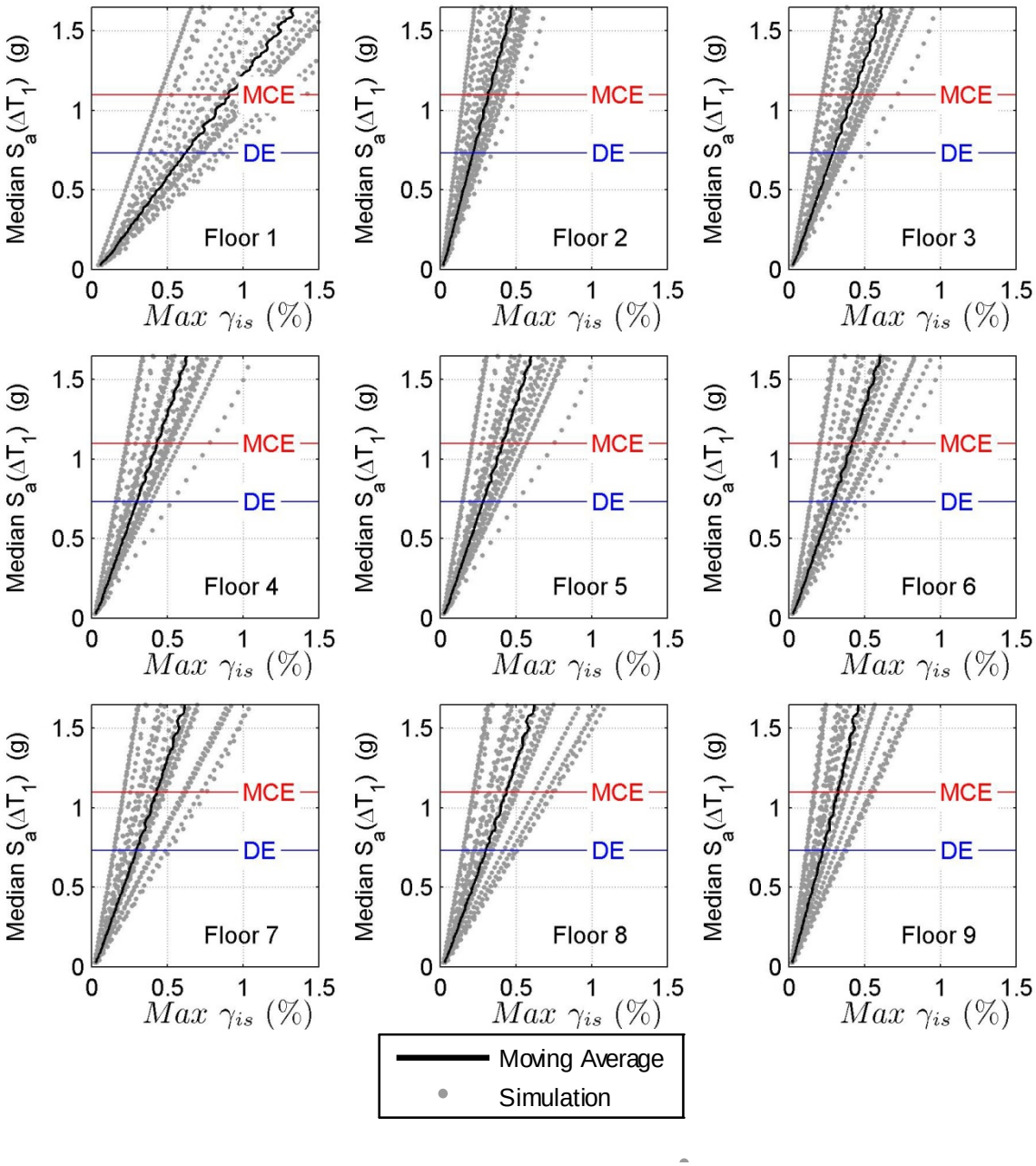

Figure B.87 IDA results for S-9 (no wall): maximum interstory drift against median spectral acceleration over the range of T_1.

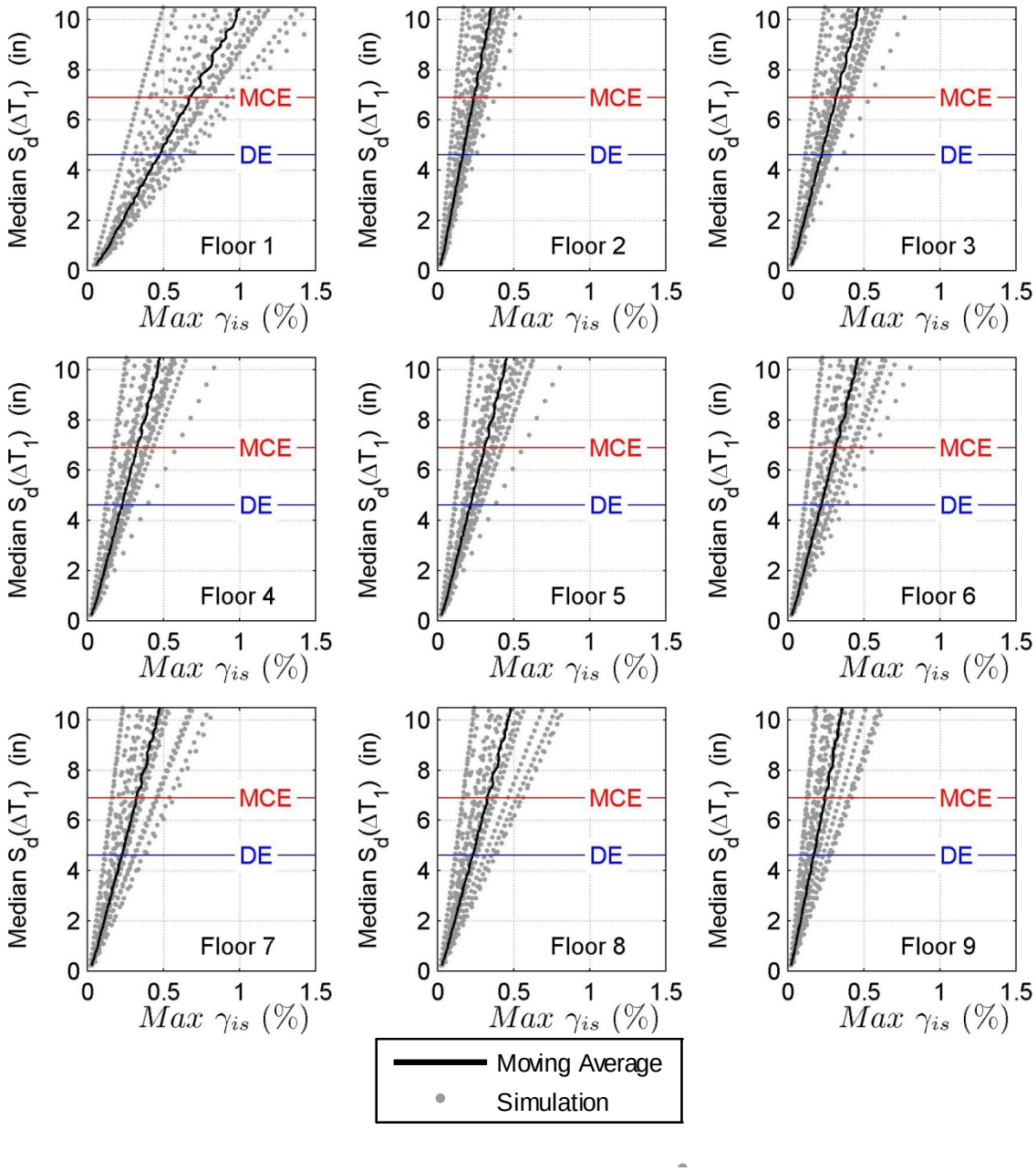

Figure B.88 IDA results for S-9 (no wall): maximum interstory drift against median spectral displacement over the range of T_1.

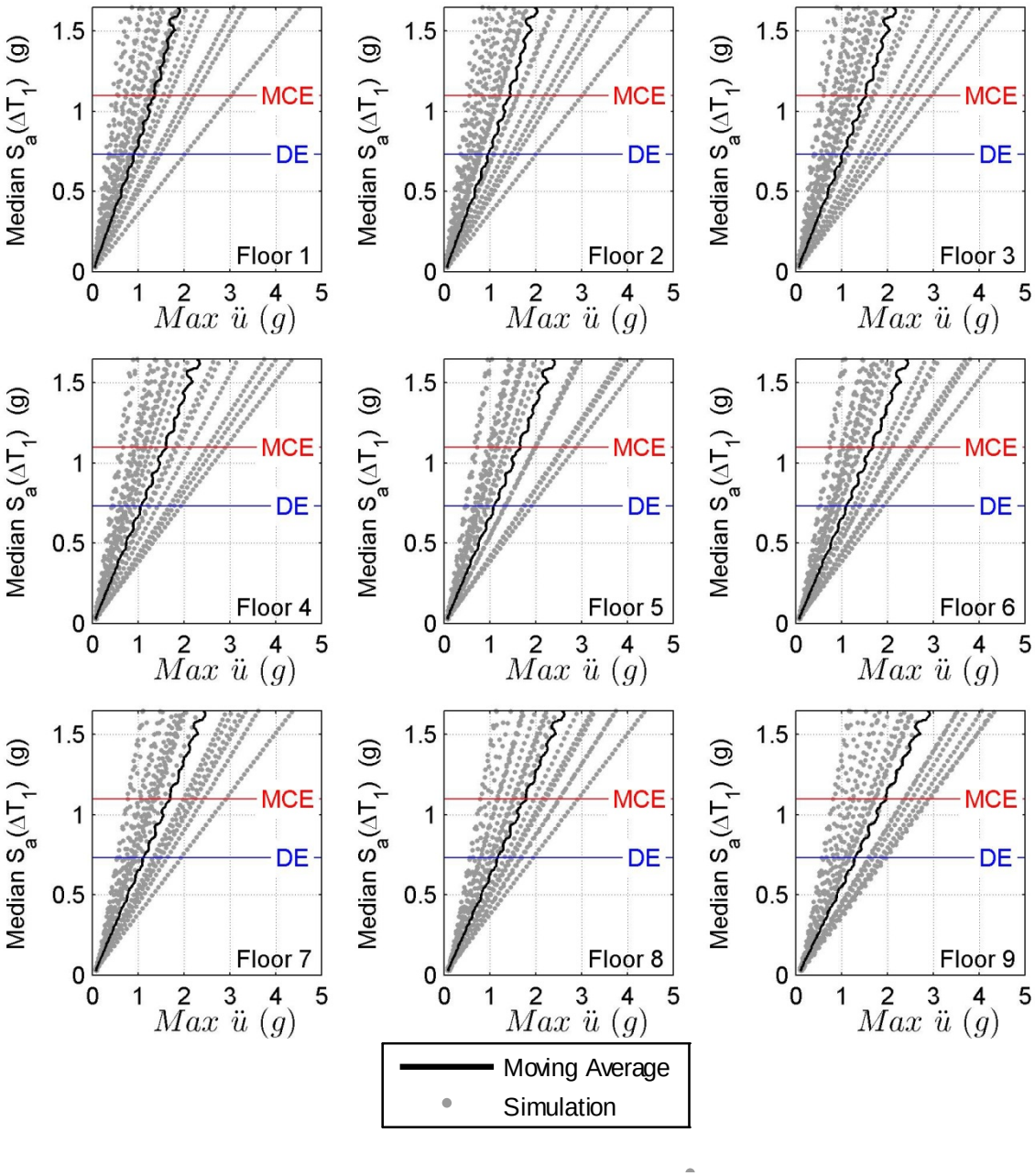

Figure B.89 IDA results for S-9 (no wall): maximum floor level acceleration against median spectral acceleration over the range of T_1.

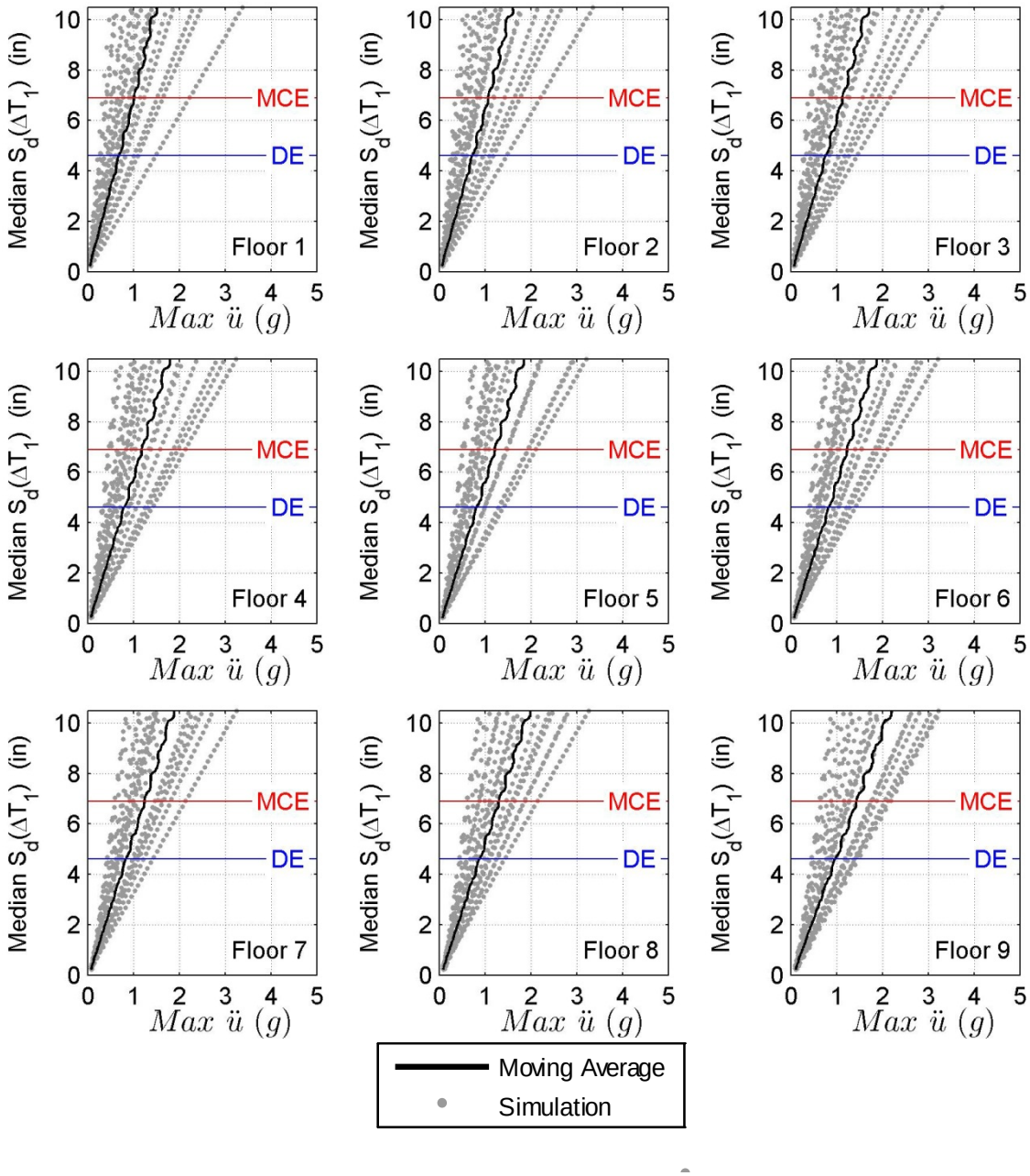

Figure B.90 IDA results for S-9 (no wall): maximum floor level acceleration against median spectral displacement over the range of T_1.

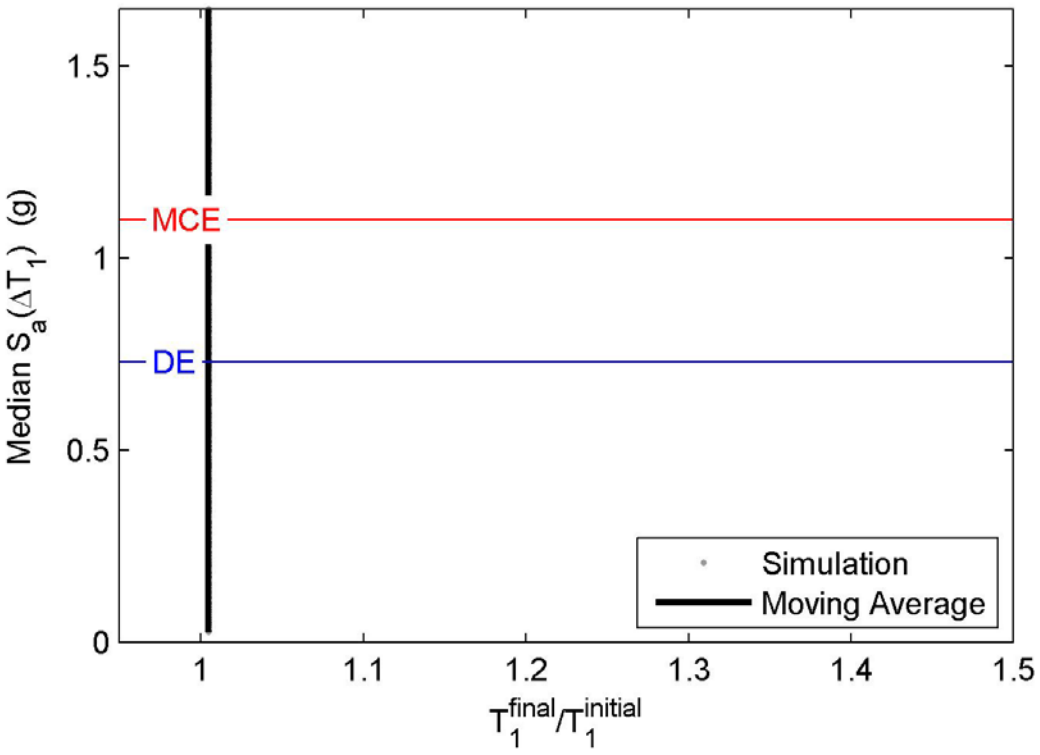

Figure B.91 IDA results for S-9 (no wall): period elongation against median spectral acceleration over the range of T_1.

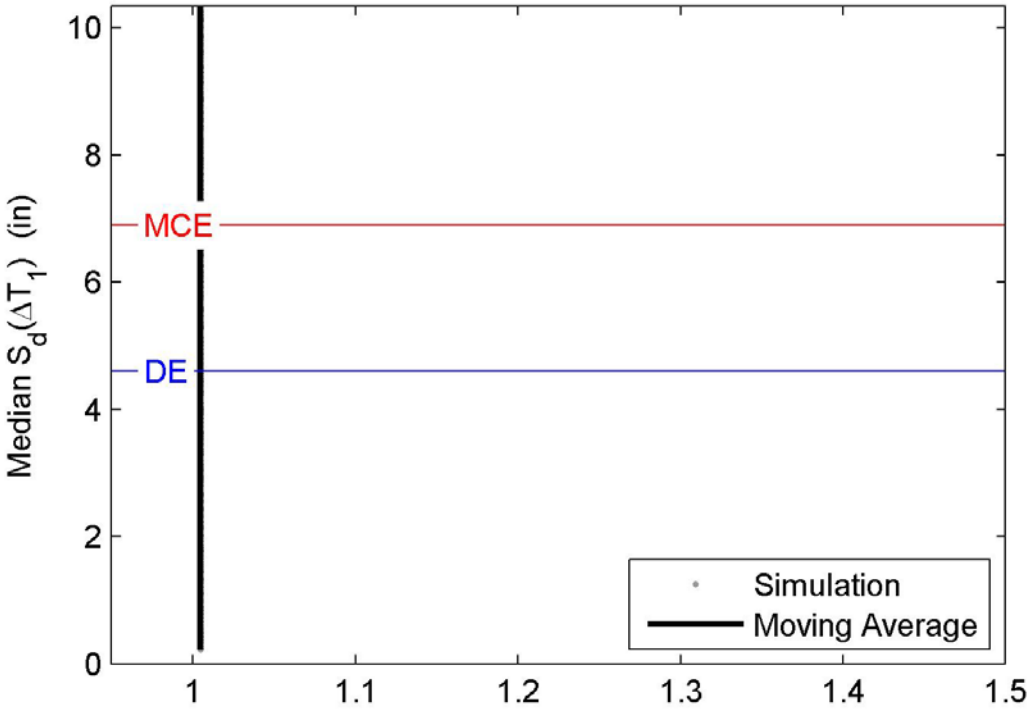

Figure B.92 IDA results for S-9 (no wall): period elongation against median spectral displacement over the range of T_1.

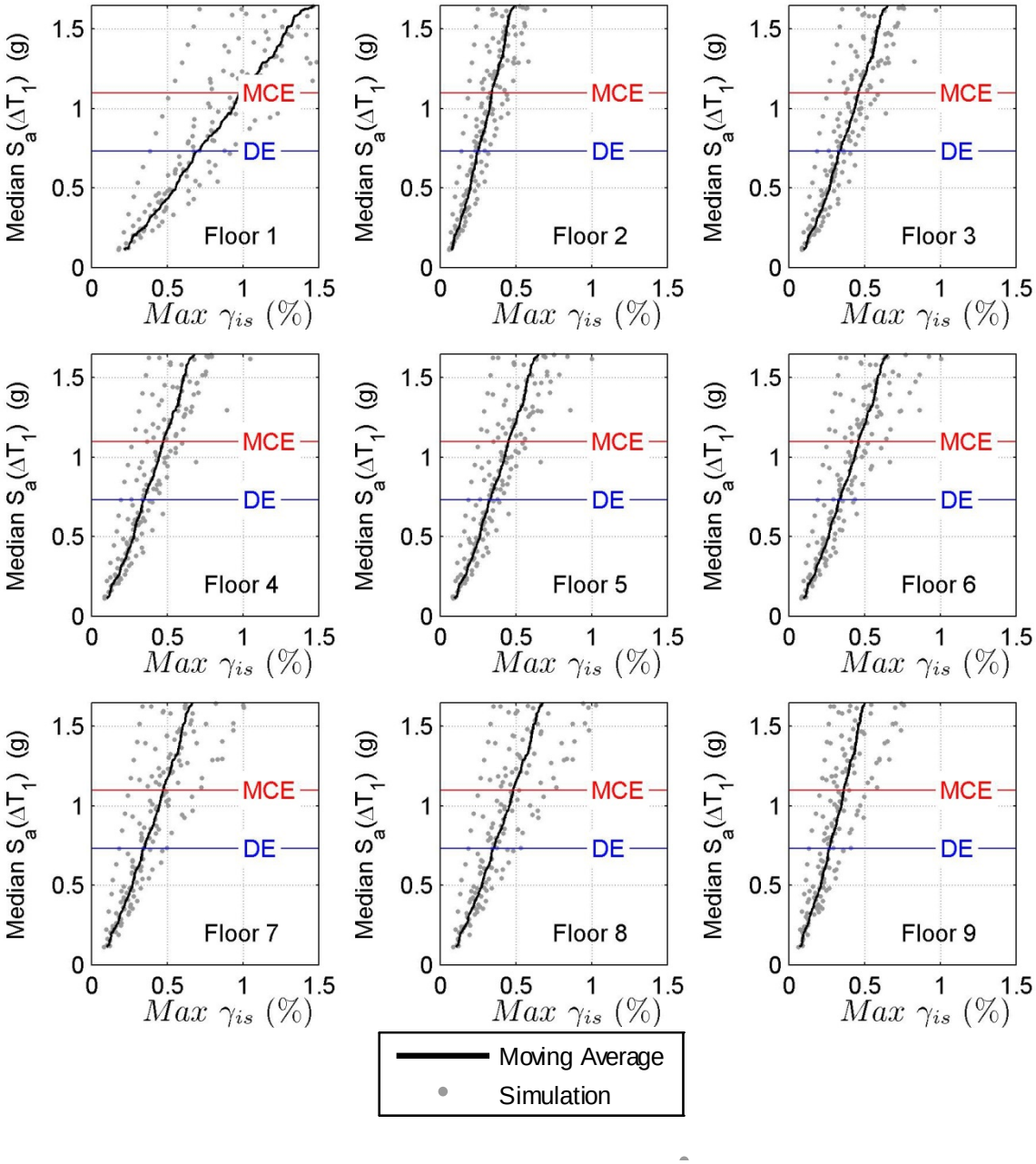

Figure B.93 IDA results for S-9 ($L_{w,min}$): maximum interstory drift against median spectral acceleration over the range of T_1.

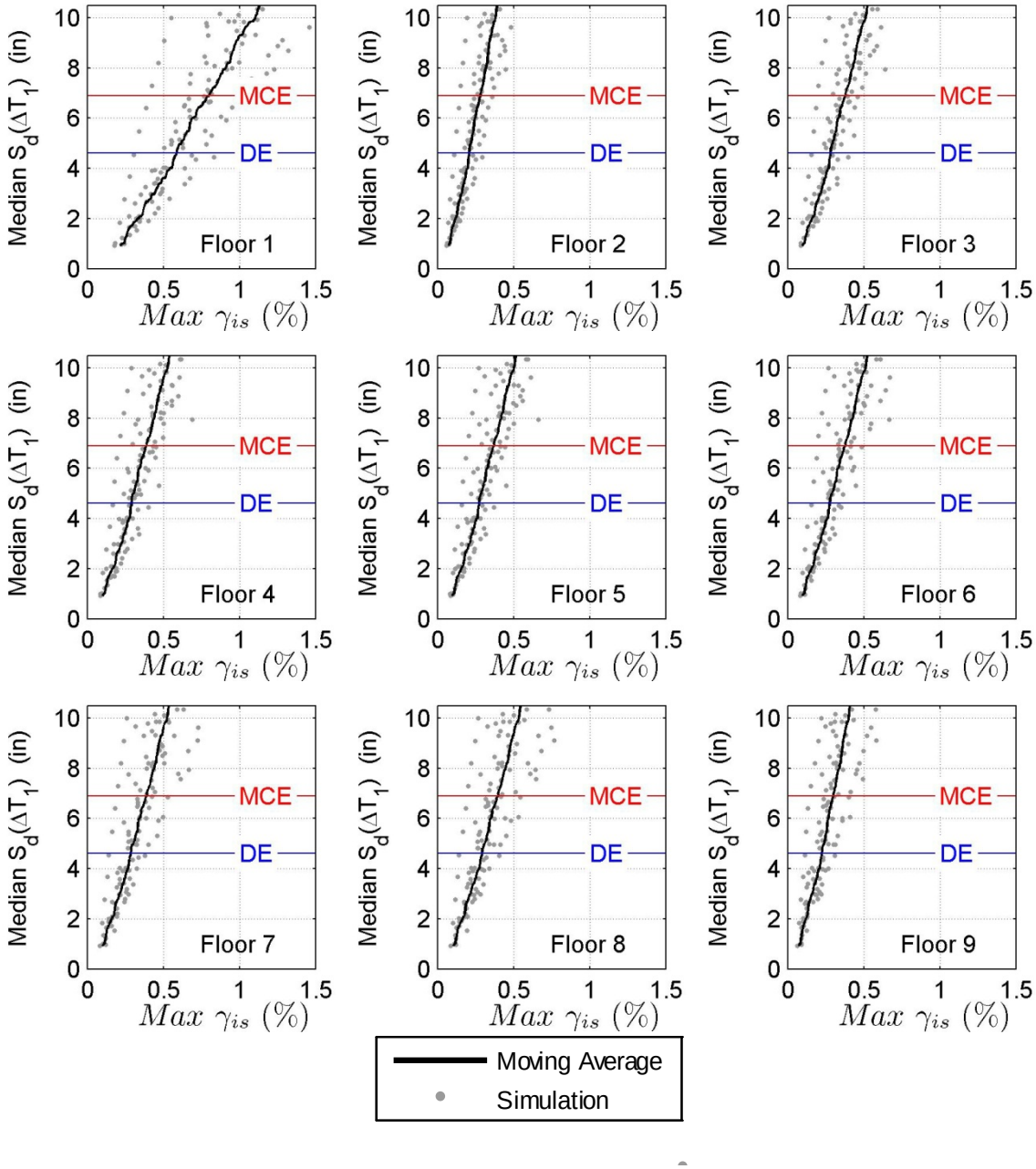

Figure B.94 IDA results for S-9 ($L_{w,min}$): maximum interstory drift against median spectral displacement over the range of T_1.

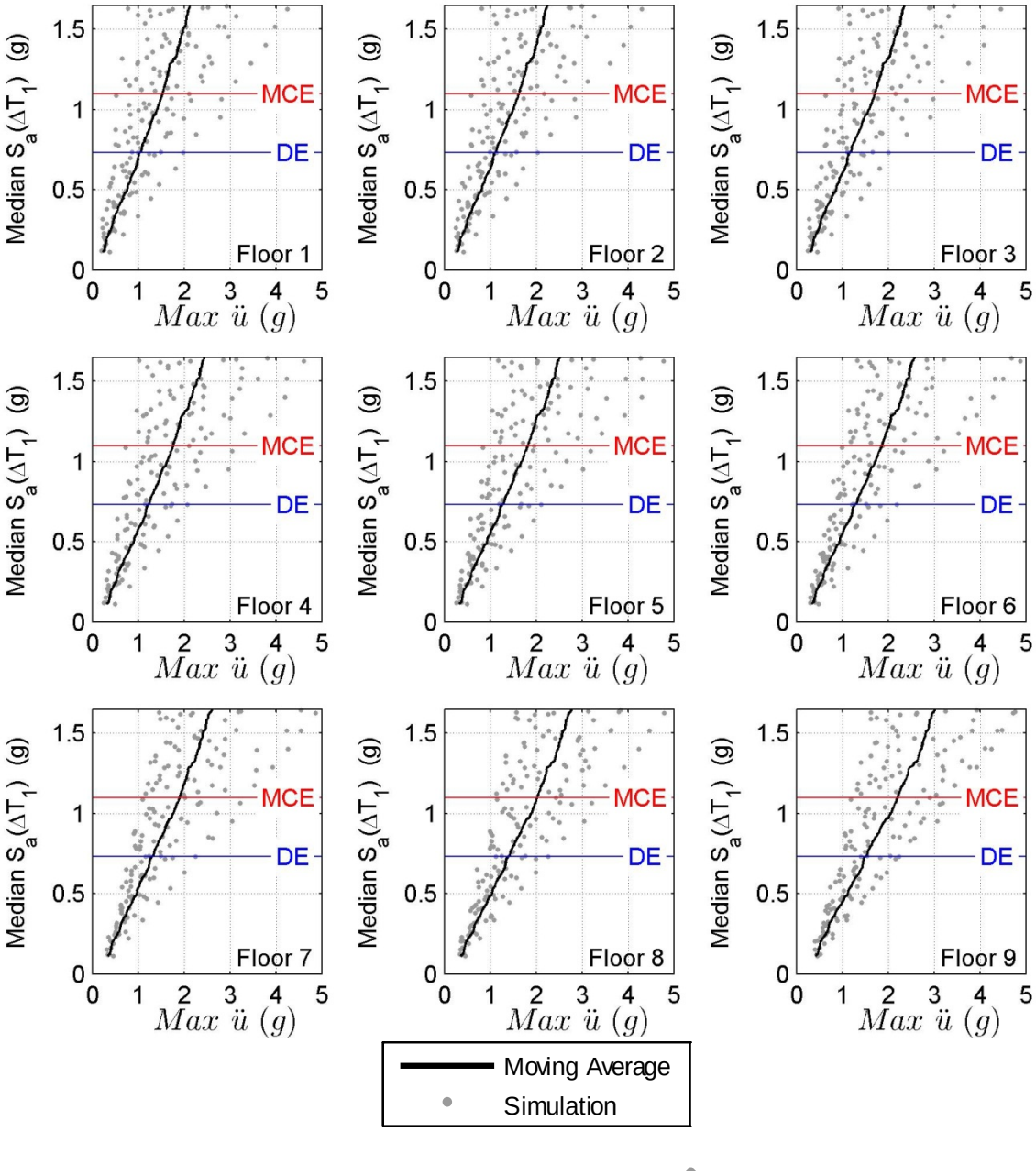

Figure B.95 IDA results for S-9 ($L_{w,min}$): maximum floor level acceleration against median spectral acceleration over the range of T_1.

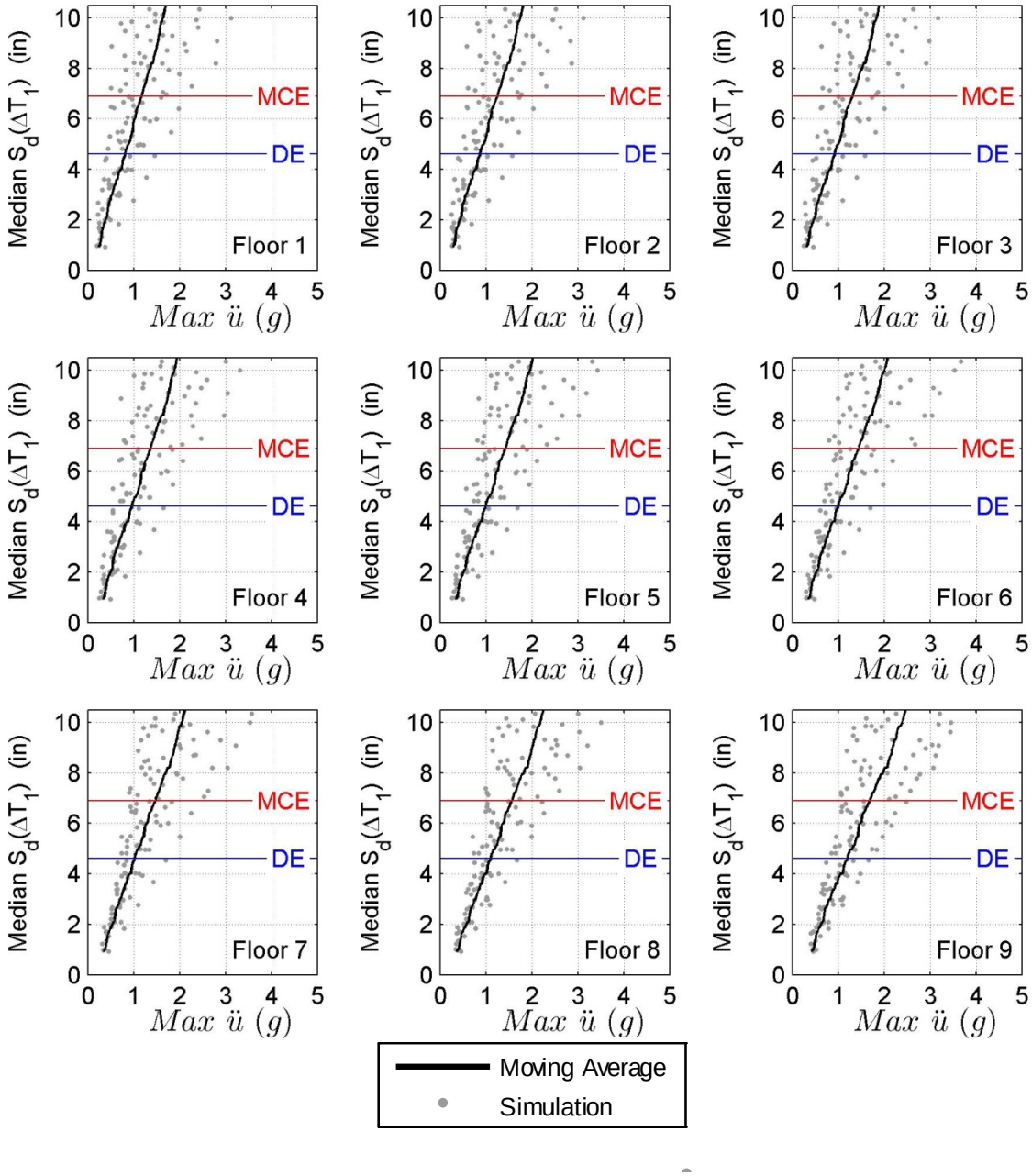

Figure B.96 IDA results for S-9 ($L_{w,min}$): maximum floor level acceleration against median spectral displacement over the range of T_1.

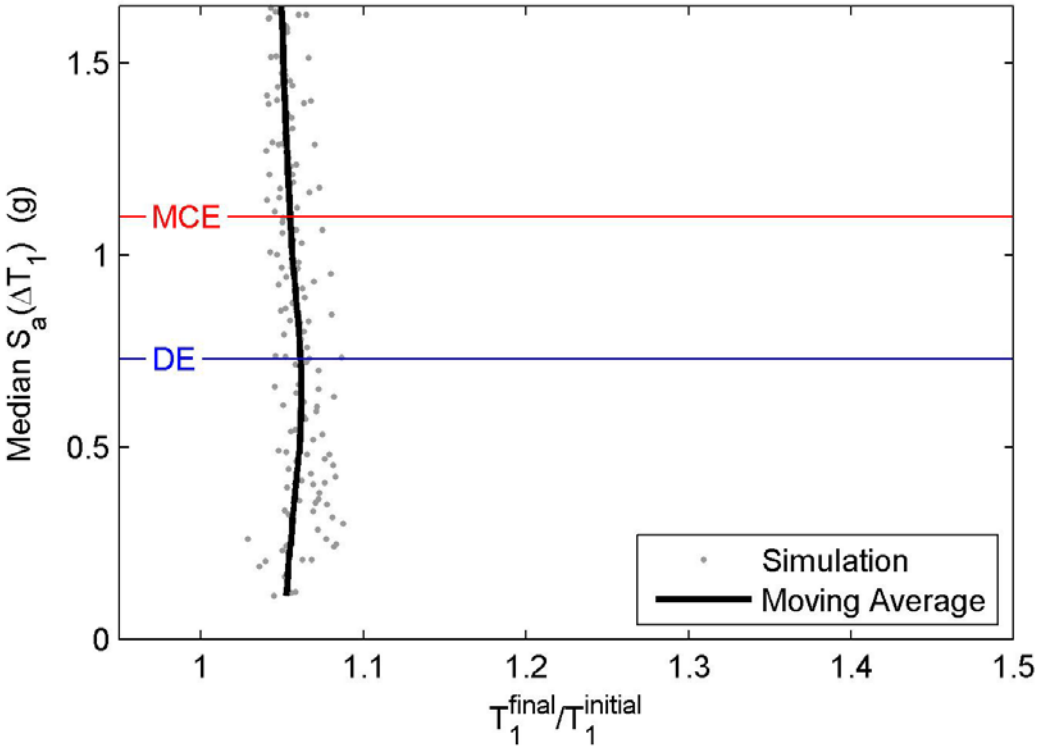

Figure B.97 IDA results for S-9 ($L_{w,min}$): period elongation against median spectral acceleration over the range of T_1.

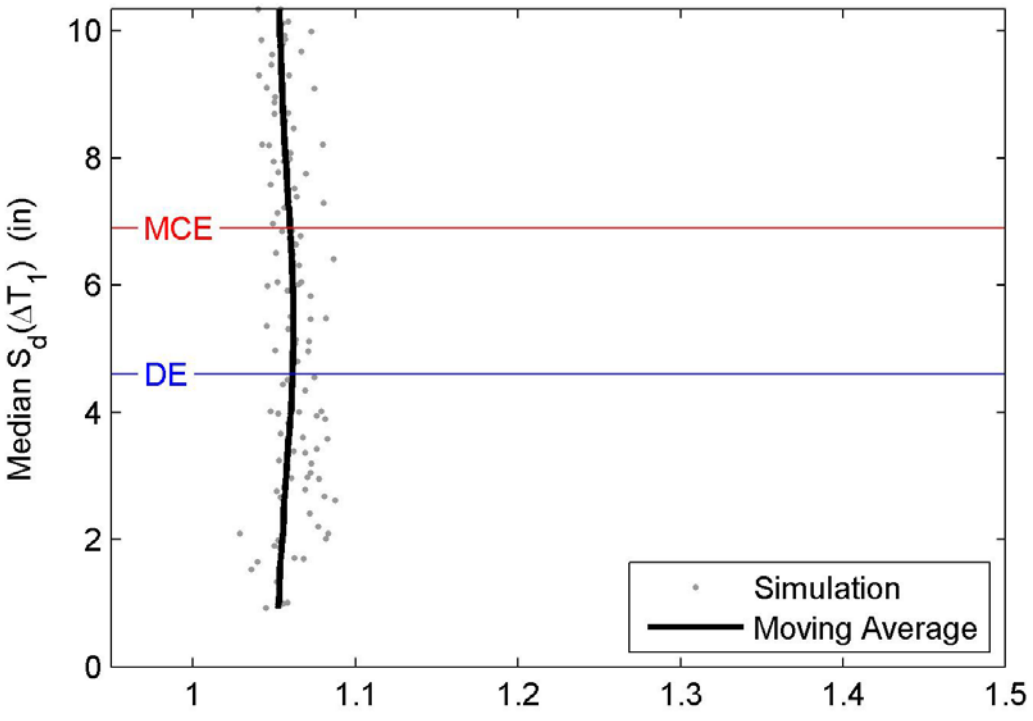

Figure B.98 IDA results for S-9 ($L_{w,min}$): period elongation against median spectral displacement over the range of T_1.

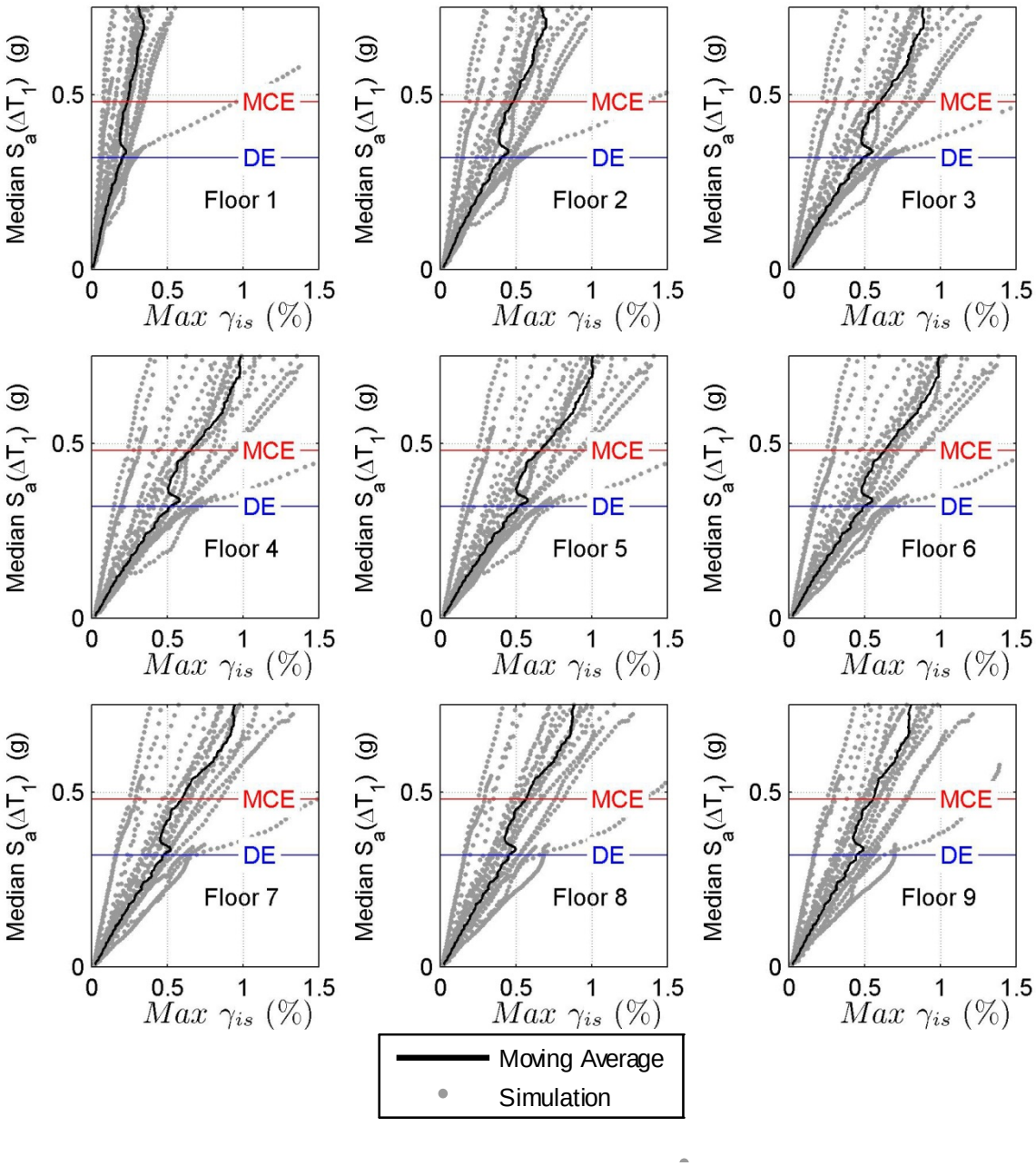

Figure B.99 IDA results for RC-20 (no wall): maximum interstory drift against median spectral acceleration over the range of T_1 for floors 1-9.

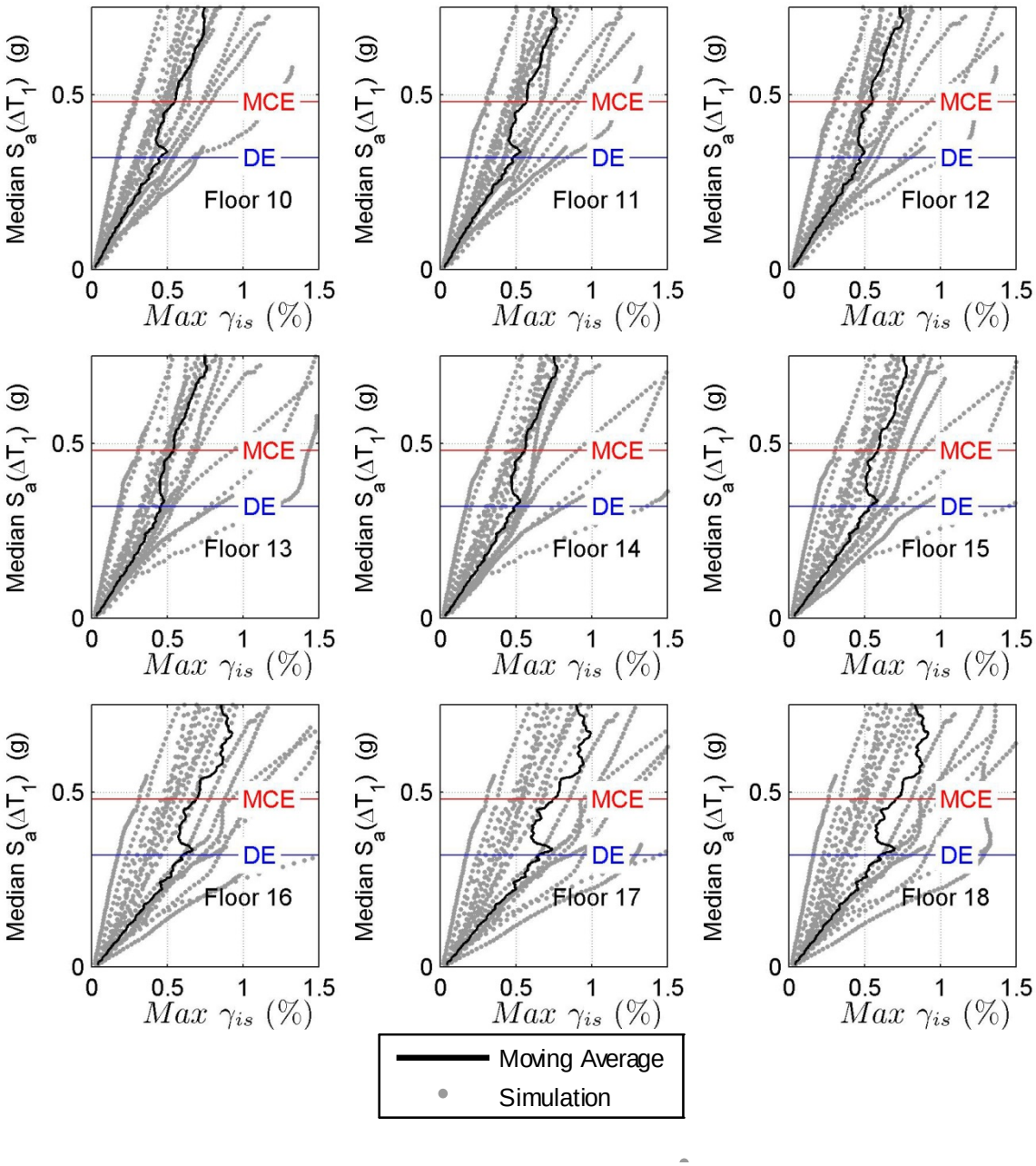

Figure B.100 IDA results for RC-20 (no wall): maximum interstory drift against median spectral acceleration over the range of T_1 for floors 10-18.

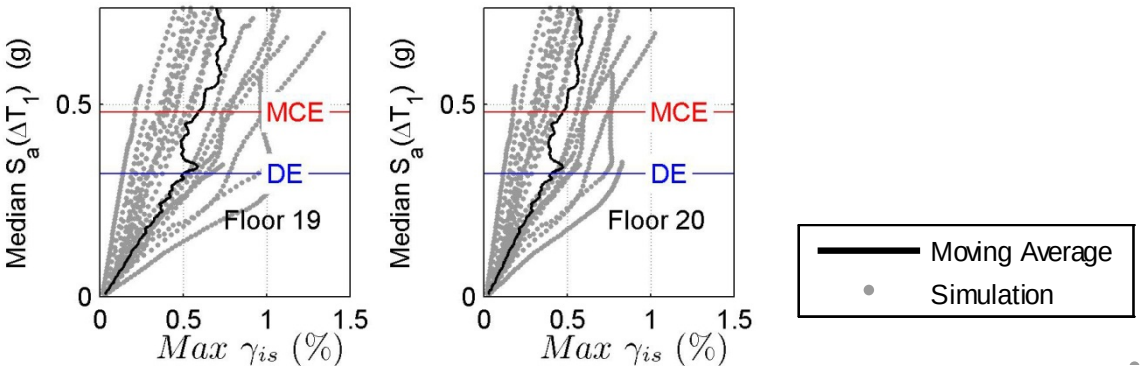

Figure B.101 IDA results for RC-20 (no wall): maximum interstory drift against median spectral acceleration over the range of T_1 for floors 19-20.

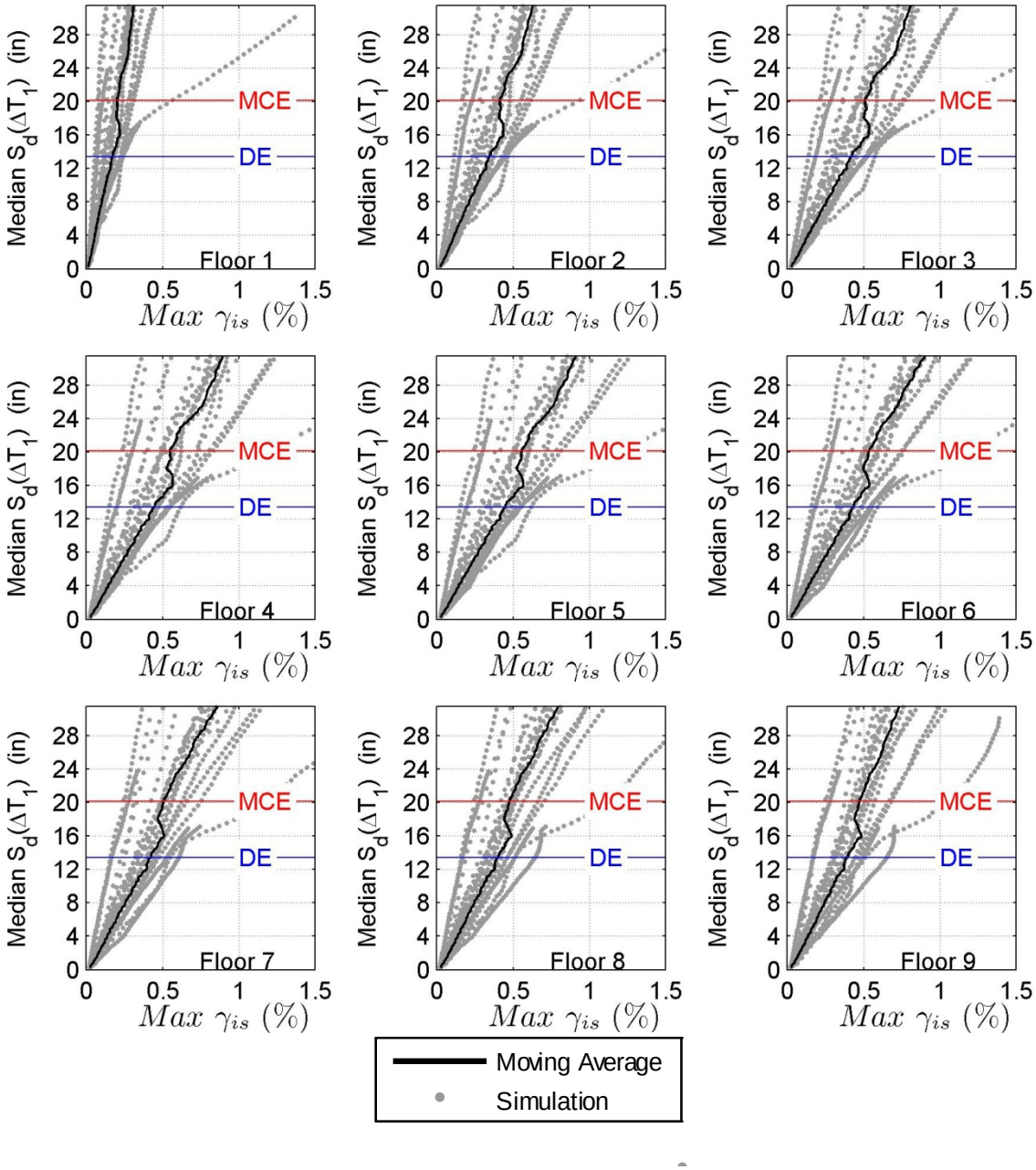

Figure B.102 IDA results for RC-20 (no wall): maximum interstory drift against median spectral displacement over the range of T_1 for floors 1-9.

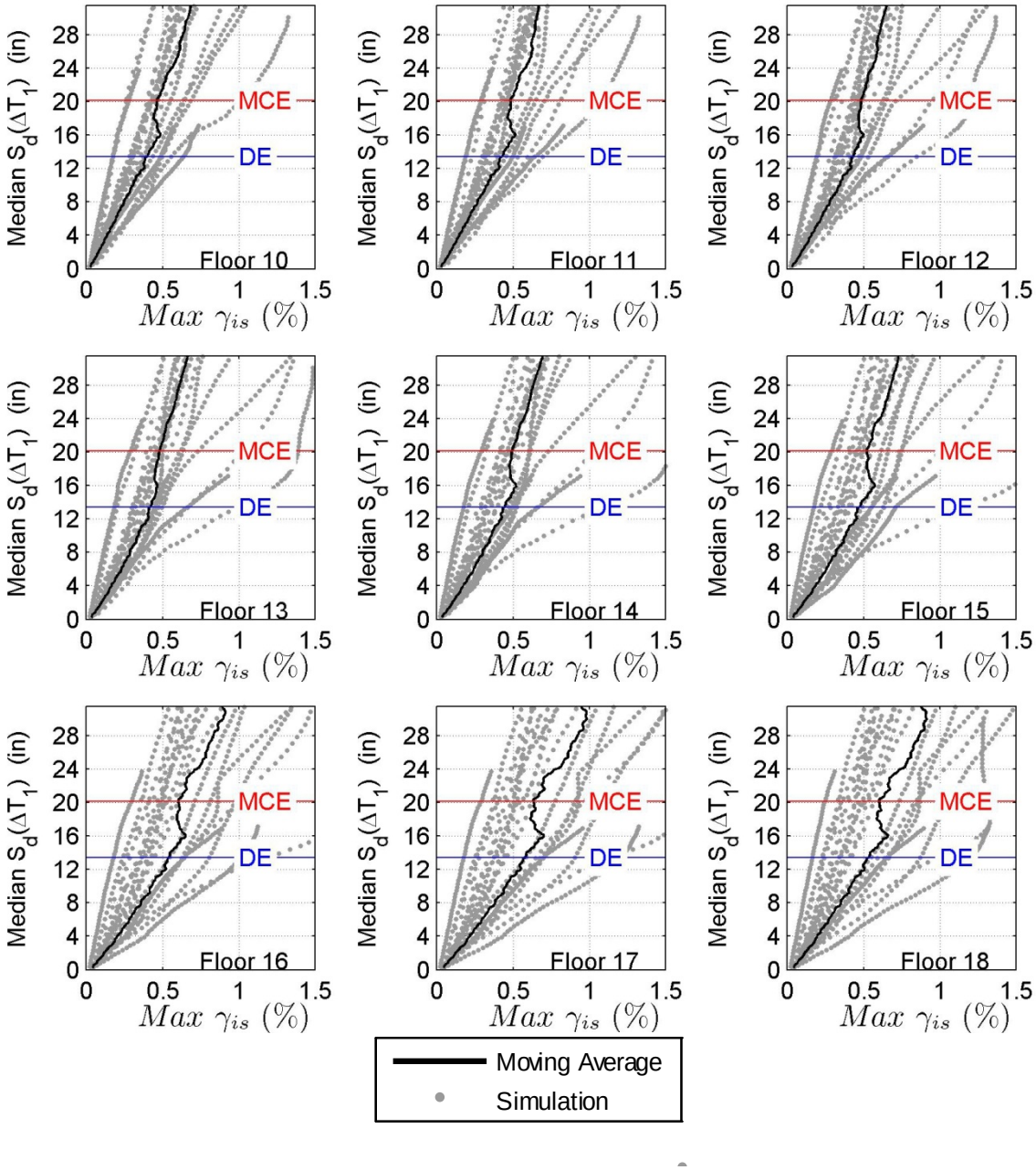

Figure B.103 IDA results for RC-20 (no wall): maximum interstory drift against median spectral displacement over the range of T_1 for floors 10-18.

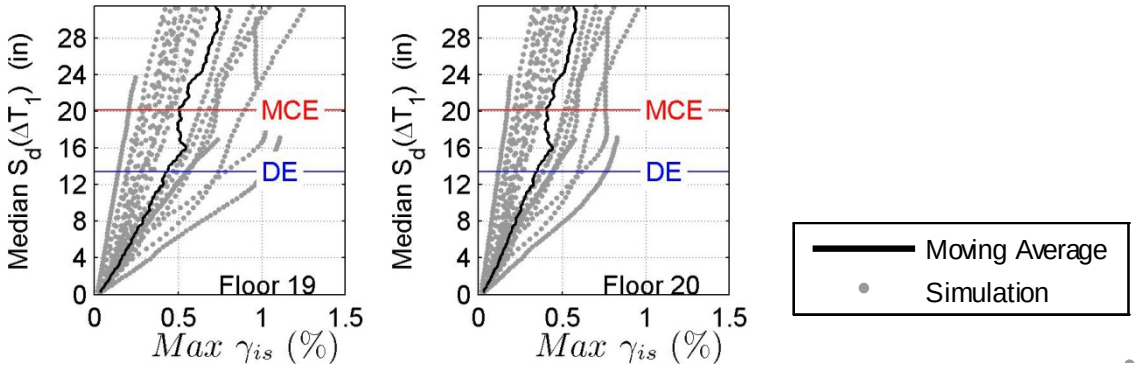

Figure B.104 IDA results for RC-20 (no wall): maximum interstory drift against median spectral displacement over the range of T_1 for floors 19-20.

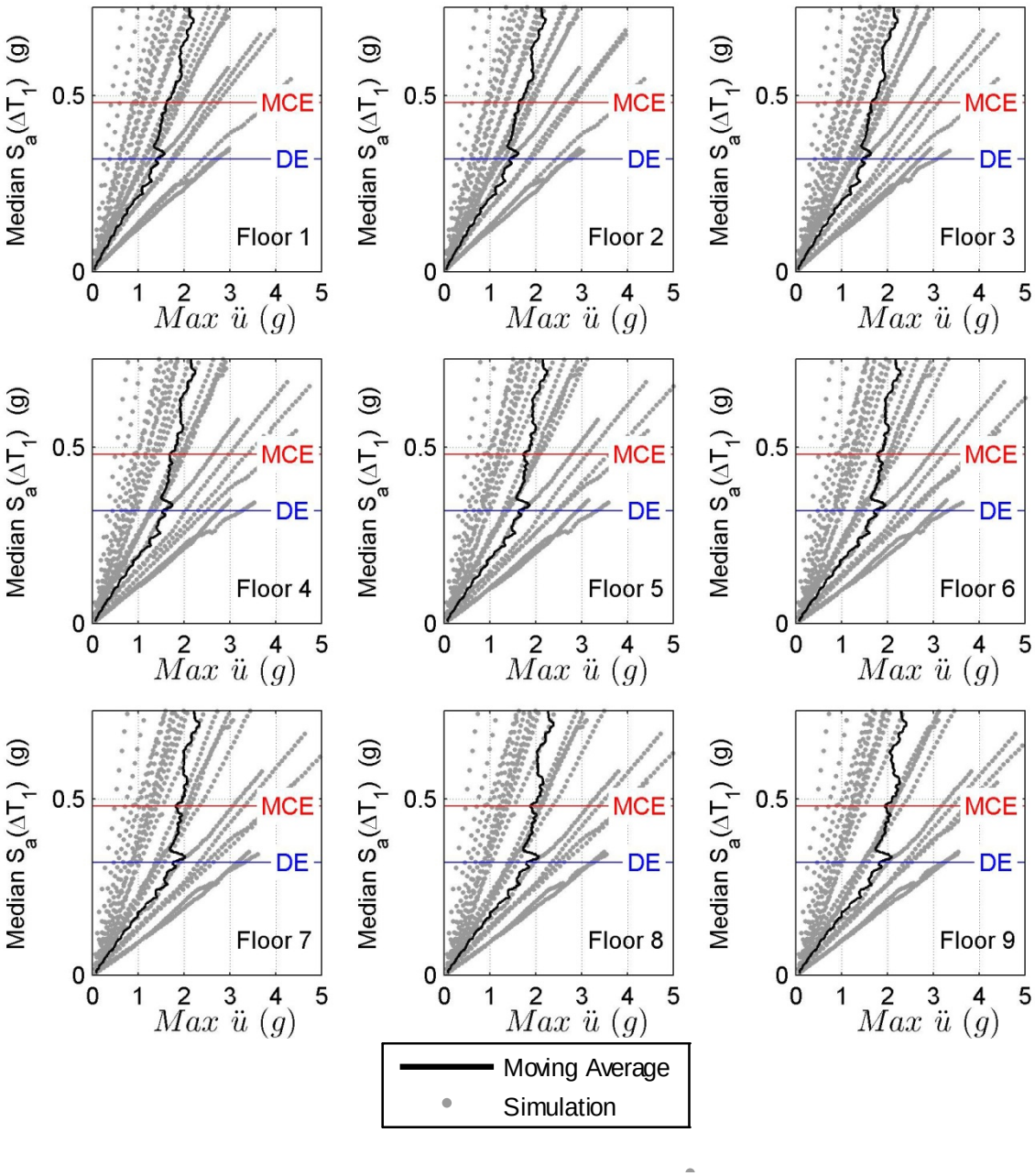

Figure B.105 IDA results for RC-20 (no wall): maximum floor level acceleration against median spectral acceleration over the range of T_1 for floors 1-9.

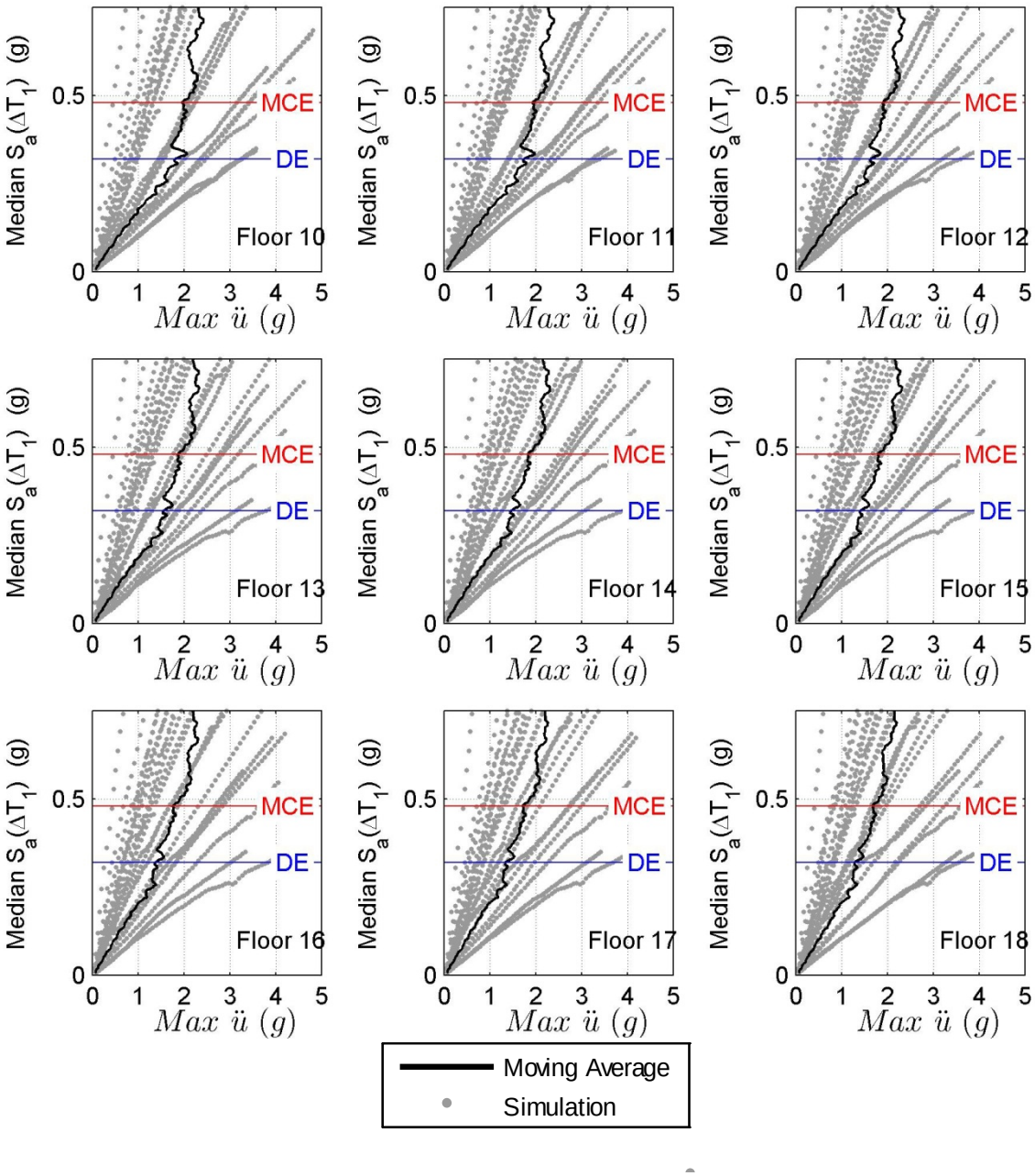

Figure B.106 IDA results for RC-20 (no wall): maximum floor level acceleration against median spectral acceleration over the range of T_1 for floors 10-18.

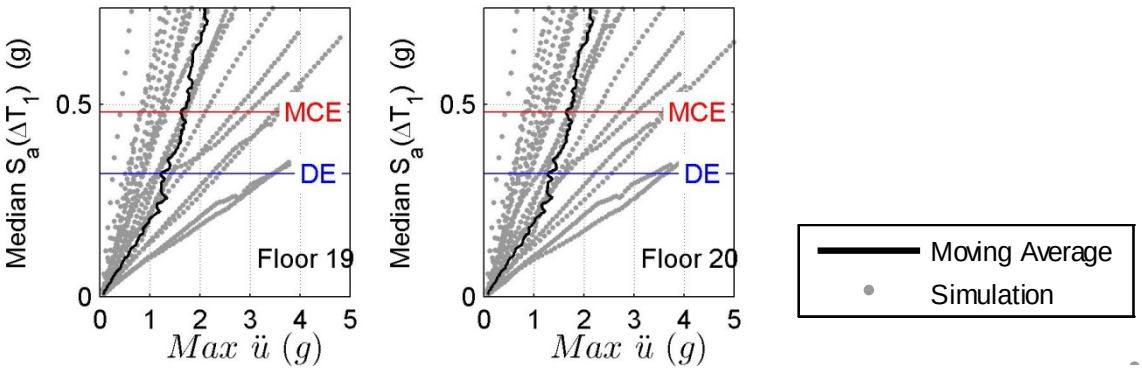

Figure B.107 IDA results for RC-20 (no wall): maximum floor level acceleration against median spectral acceleration over the range of T_1 for floors 19-20

.

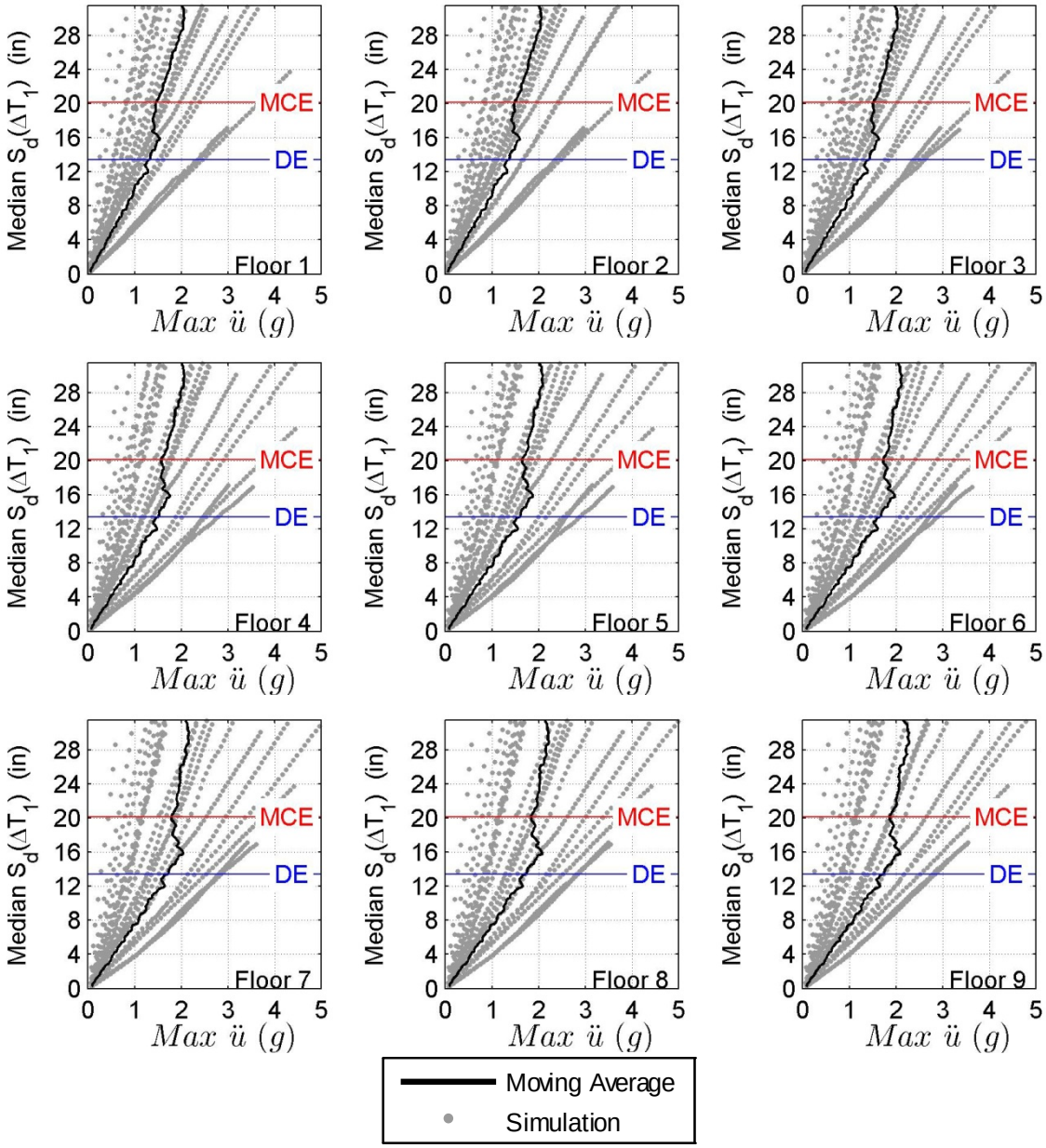

Figure B.108 IDA results for RC-20 (no wall): maximum floor level acceleration against median spectral displacement over the range of T_1 for floors 1-9.

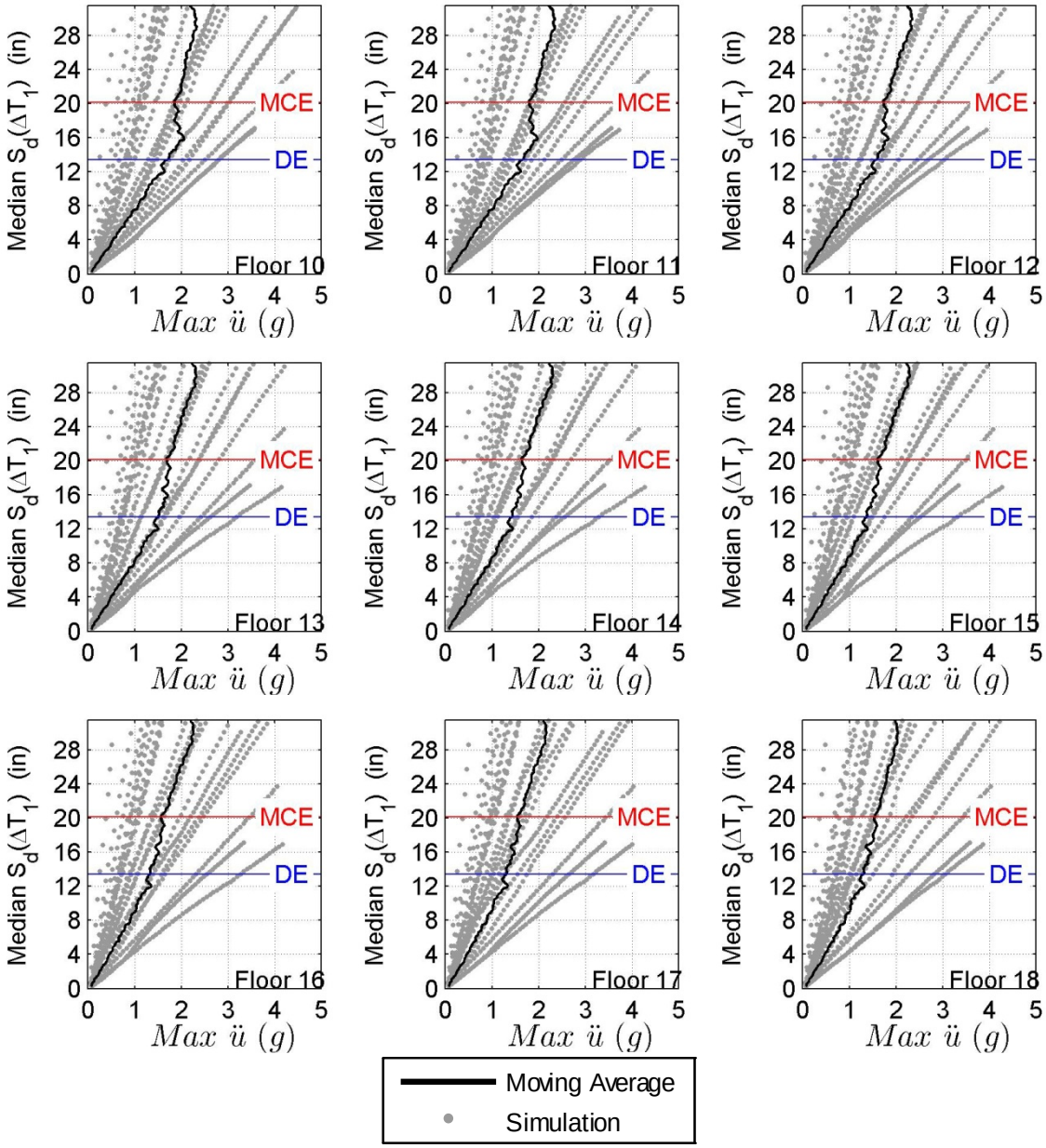

Figure B.109 IDA results for RC-20 (no wall): maximum floor level acceleration against median spectral displacement over the range of T_1 for floors 10-18.

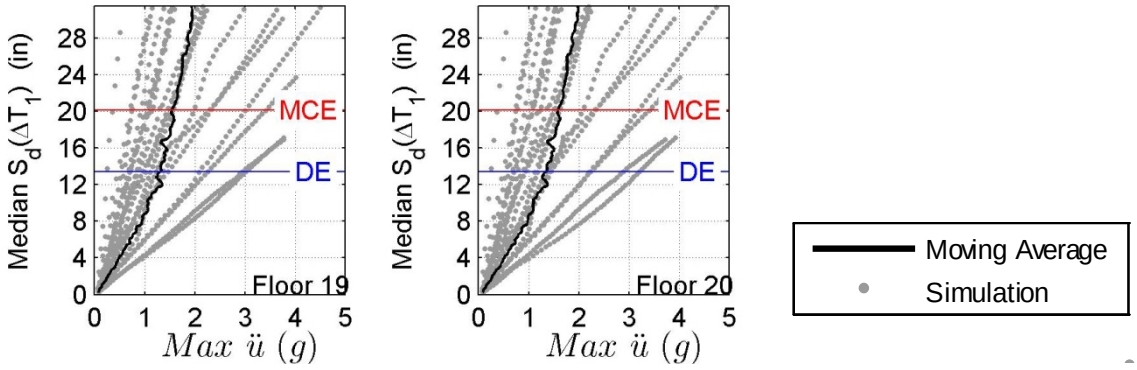

Figure B.110 IDA results for RC-20 (no wall): maximum floor level acceleration against median spectral displacement over the range of T_1 for floors 19-20.

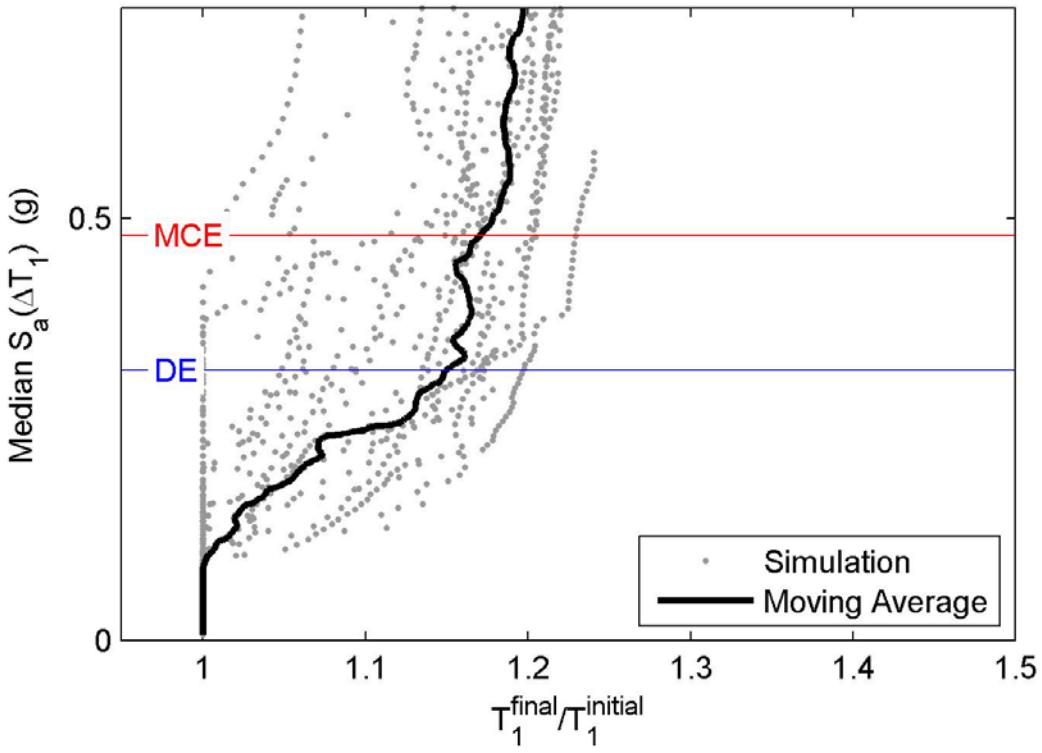

Figure B.111 IDA results for RC-20 (no wall): period elongation against median spectral acceleration over the range of T_1.

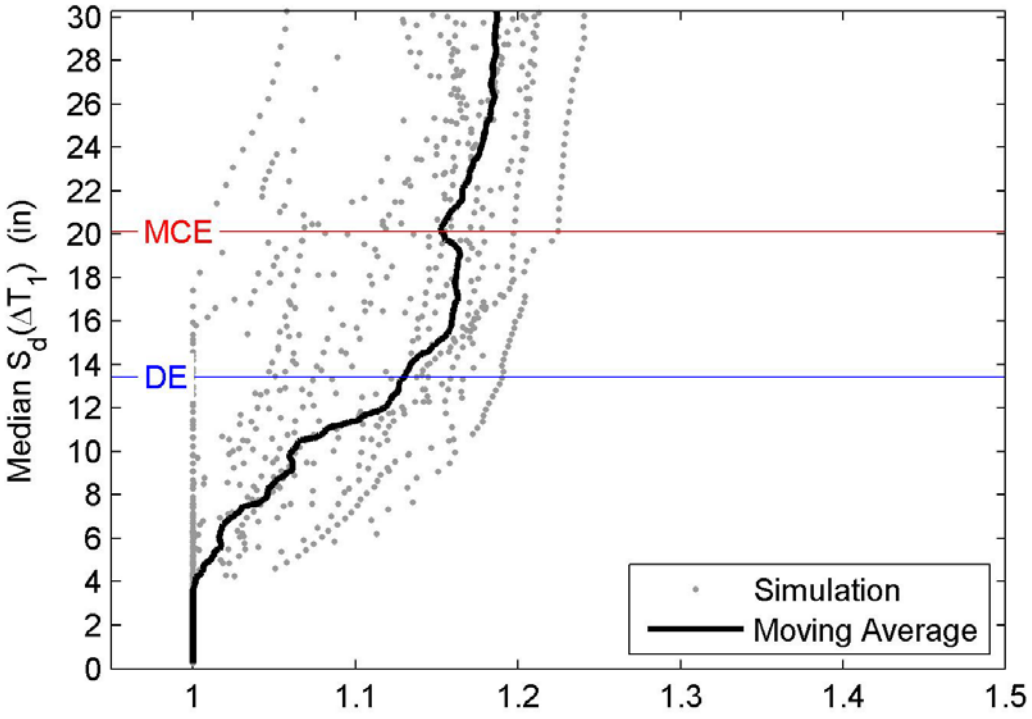

Figure B.112 IDA results for RC-20 (no wall): period elongation against median spectral displacement over the range of T_1.

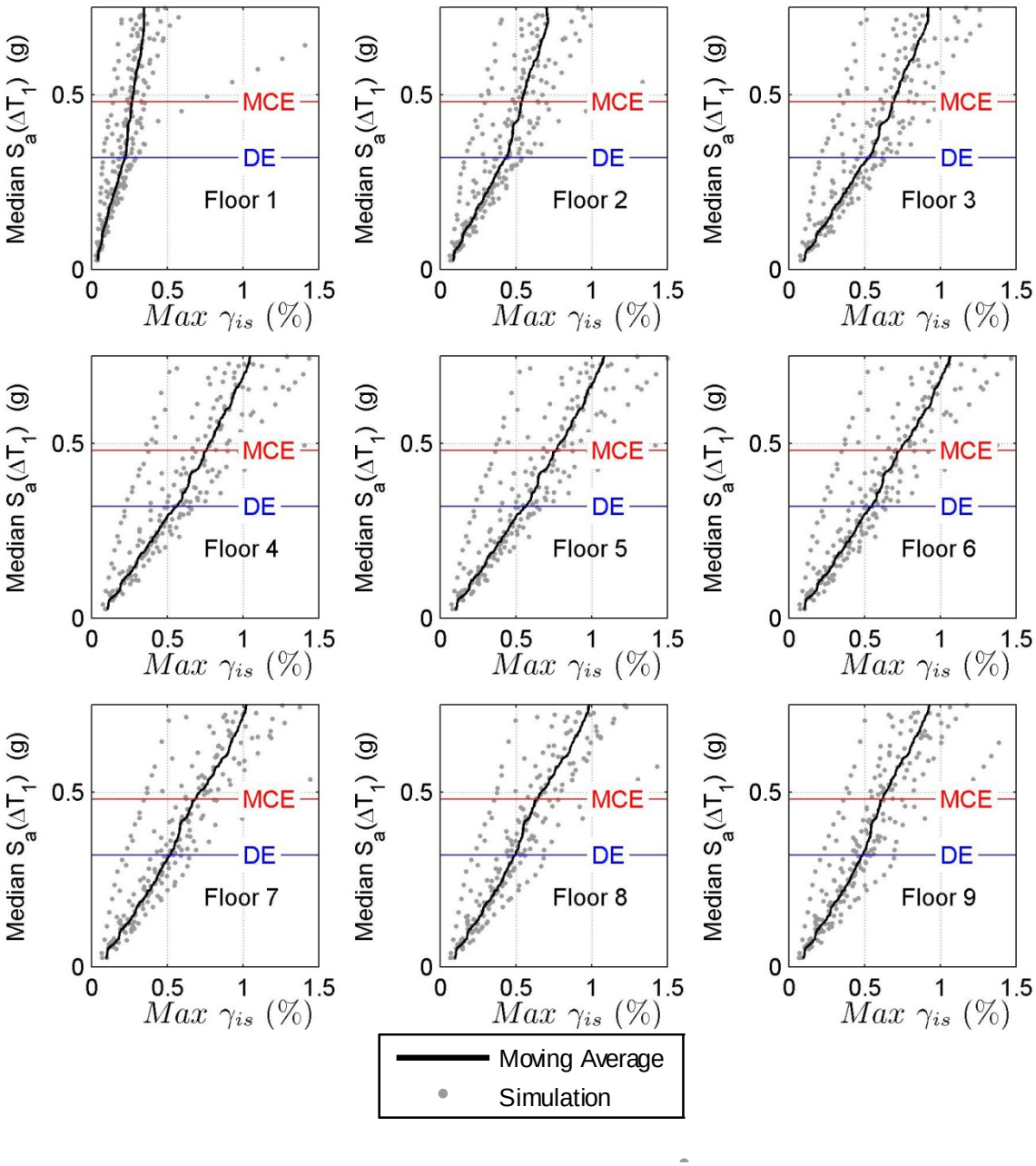

Figure B.113 IDA results for RC-20 ($L_{w,min}$): maximum interstory drift against median spectral acceleration over the range of T_1 for floors 1-9.

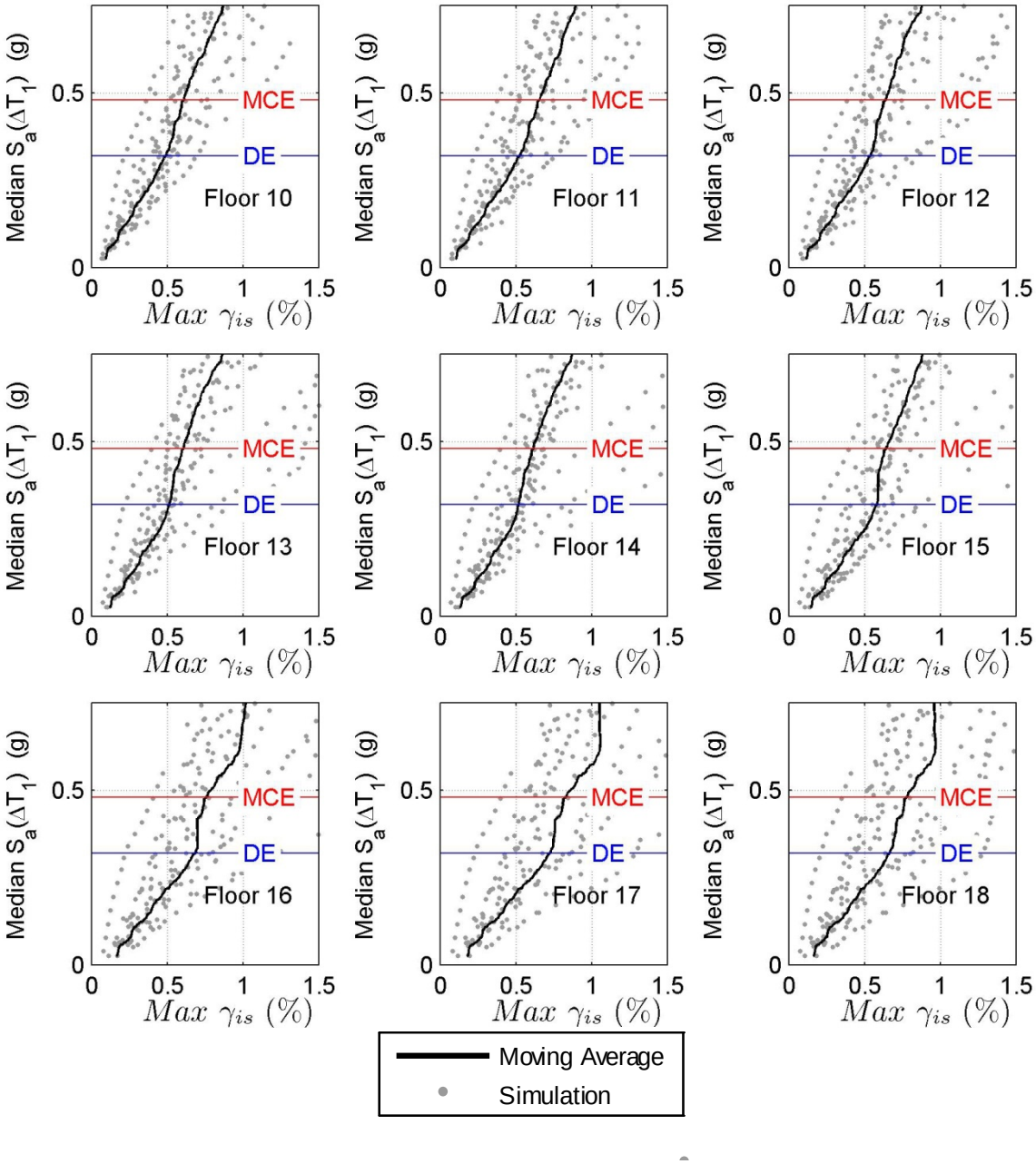

Figure B.114 IDA results for RC-20 ($L_{w,min}$): maximum interstory drift against median spectral acceleration over the range of T_1 for floors 10-18.

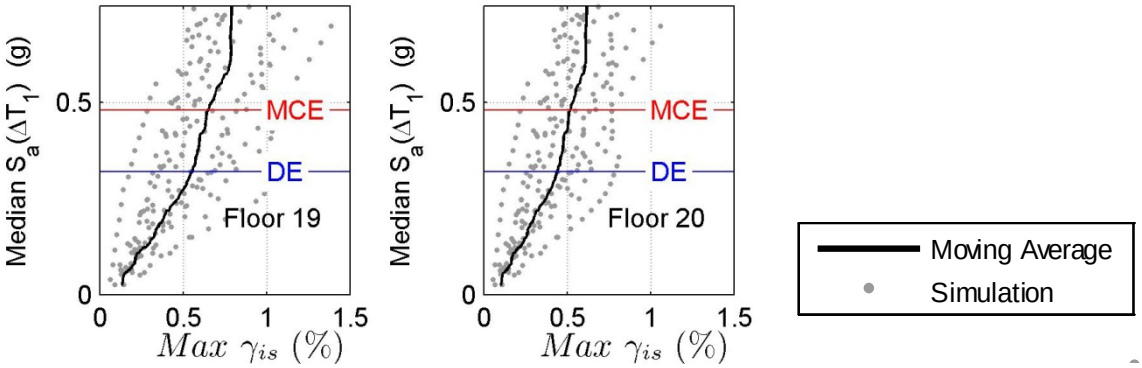

Figure B.115 IDA results for RC-20 ($L_{w,min}$): maximum interstory drift against median spectral acceleration over the range of T_1 for floors 19-20.

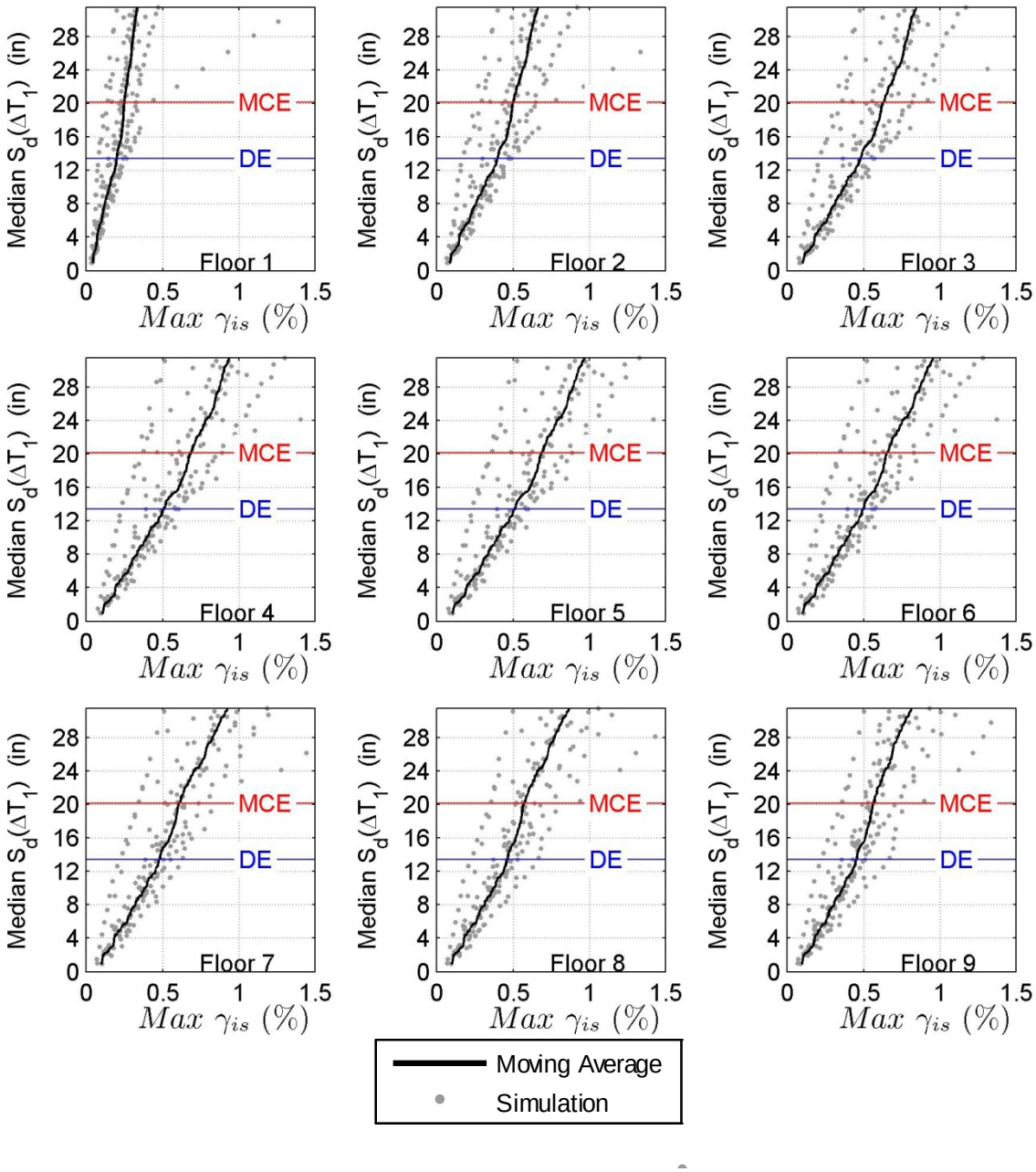

Figure B.116 IDA results for RC-20 ($L_{w,min}$): maximum interstory drift against median spectral displacement over the range of T_1 for floors 1-9.

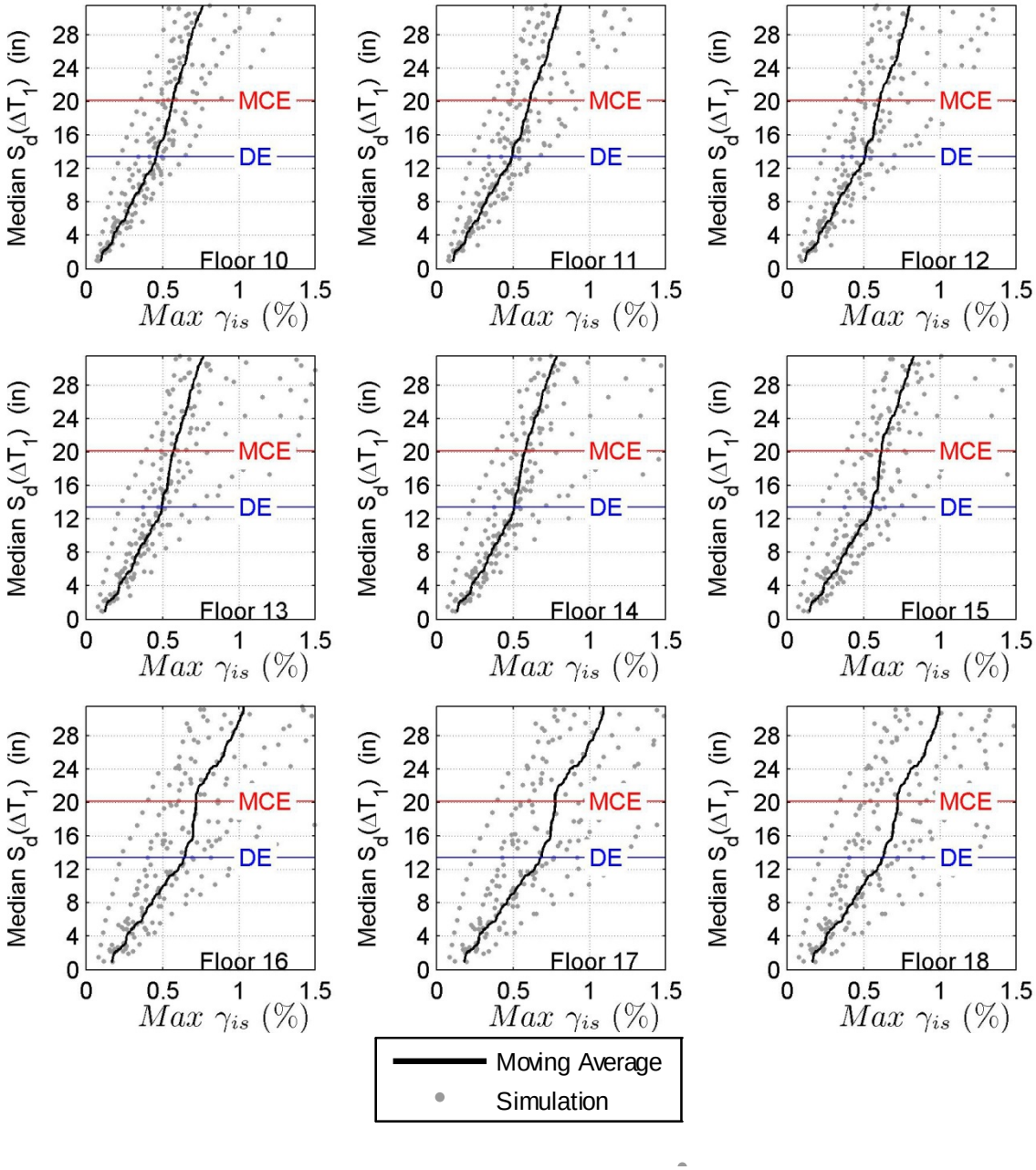

Figure B.117 IDA results for RC-20 ($L_{w,min}$): maximum interstory drift against median spectral displacement over the range of T_1 for floors 10-18.

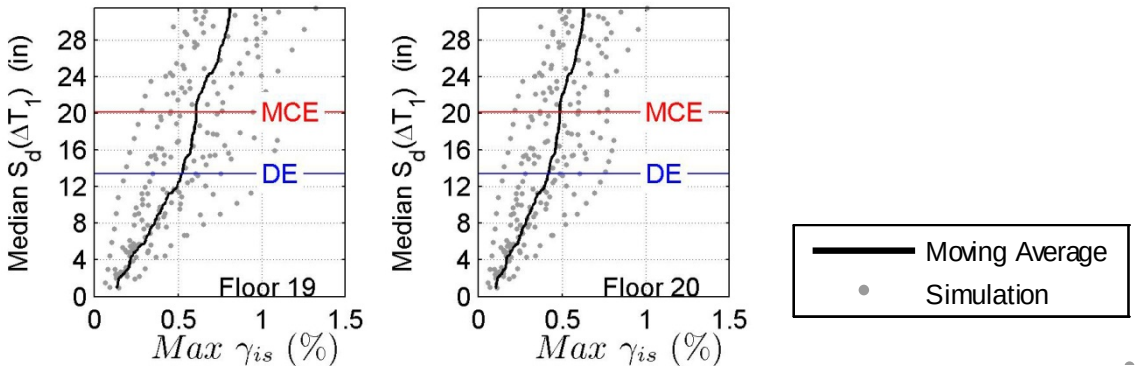

Figure B.118 IDA results for RC-20 ($L_{w,min}$): maximum interstory drift against median spectral displacement over the range of T_1 for floors 19-20.

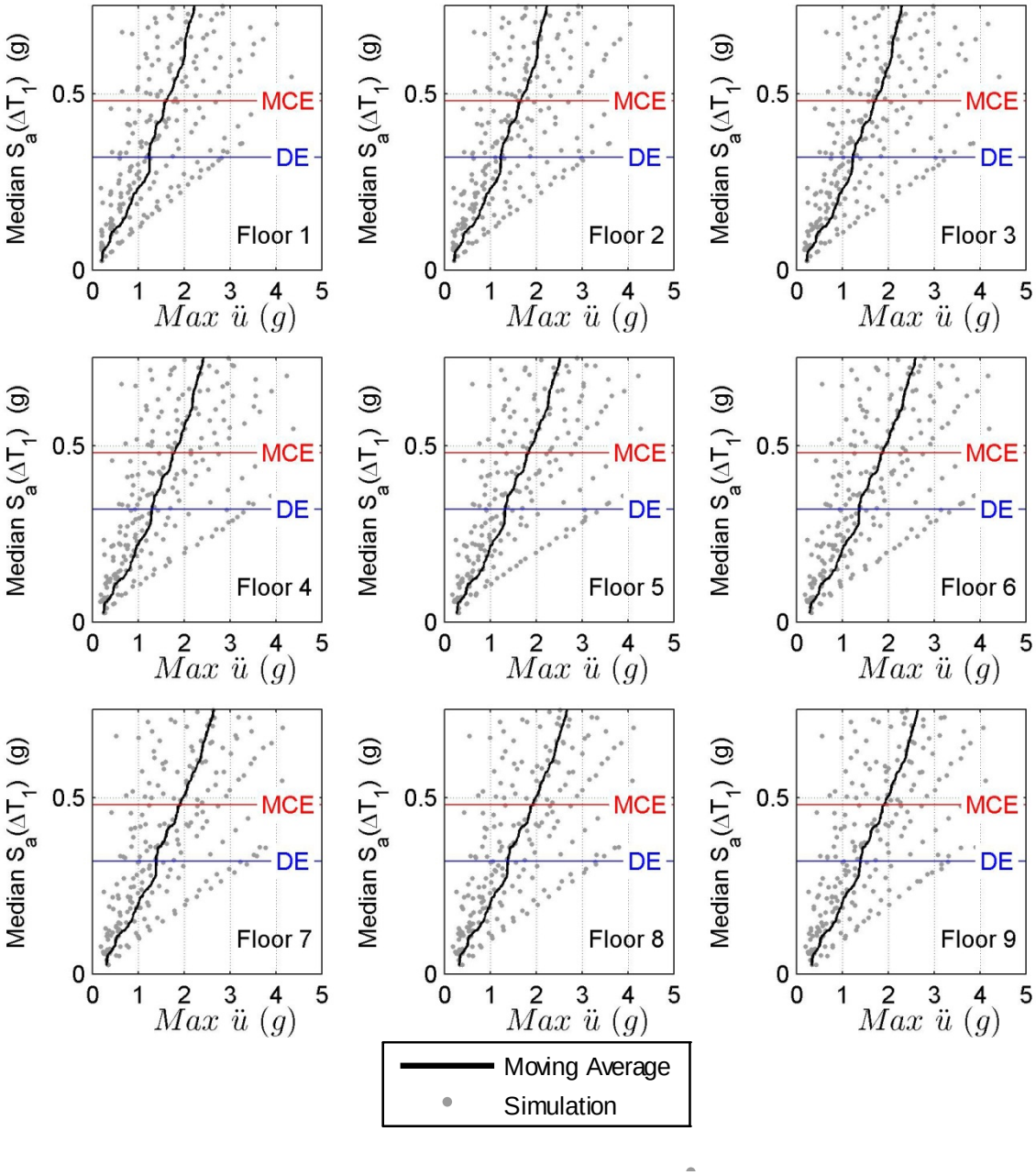

Figure B.119 IDA results for RC-20 ($L_{w,min}$): maximum floor level acceleration against median spectral acceleration over the range of T_1 for floors 1-9.

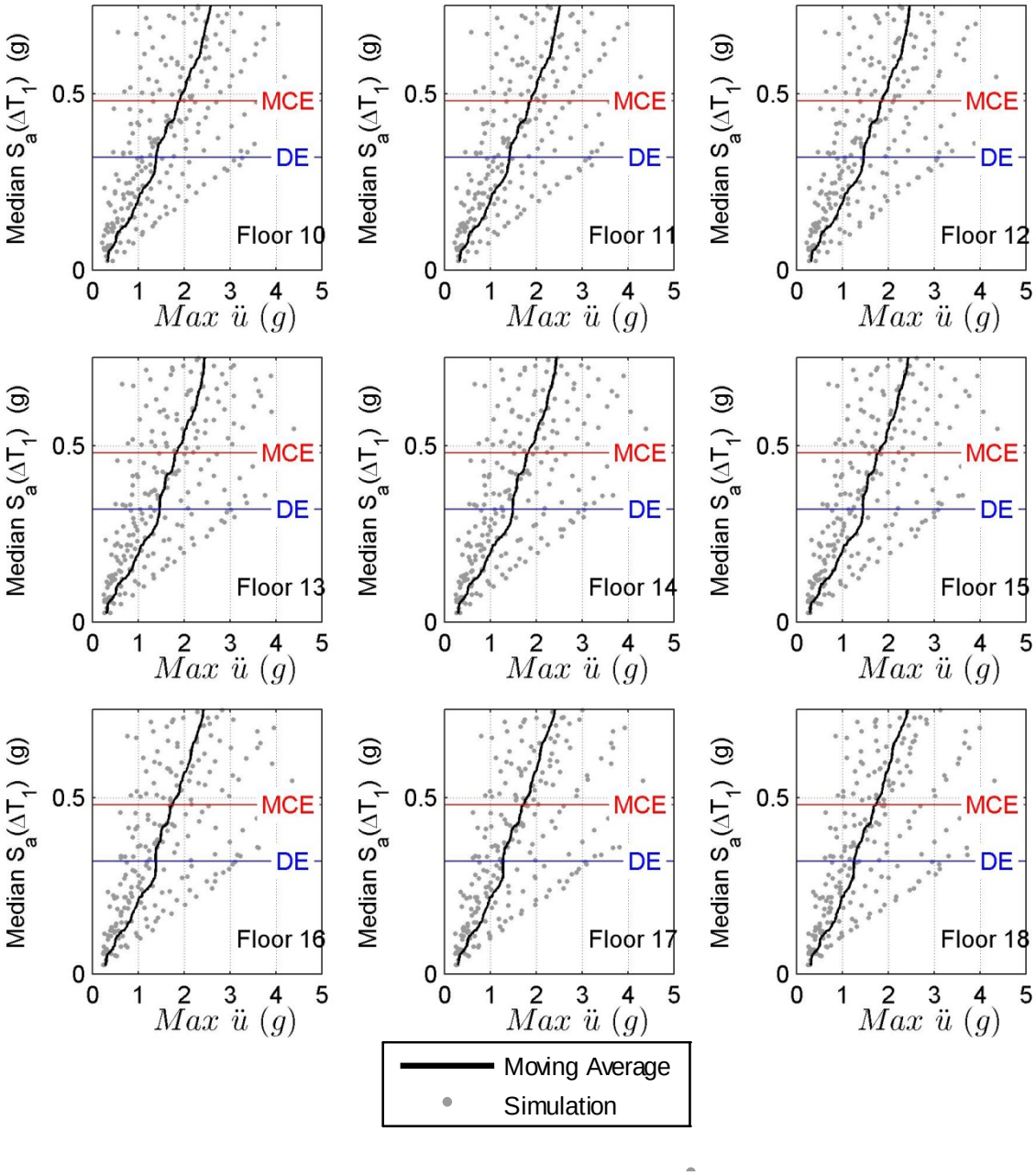

Figure B.120 IDA results for RC-20 ($L_{w,min}$): maximum floor level acceleration against median spectral acceleration over the range of T_1 for floors 10-18.

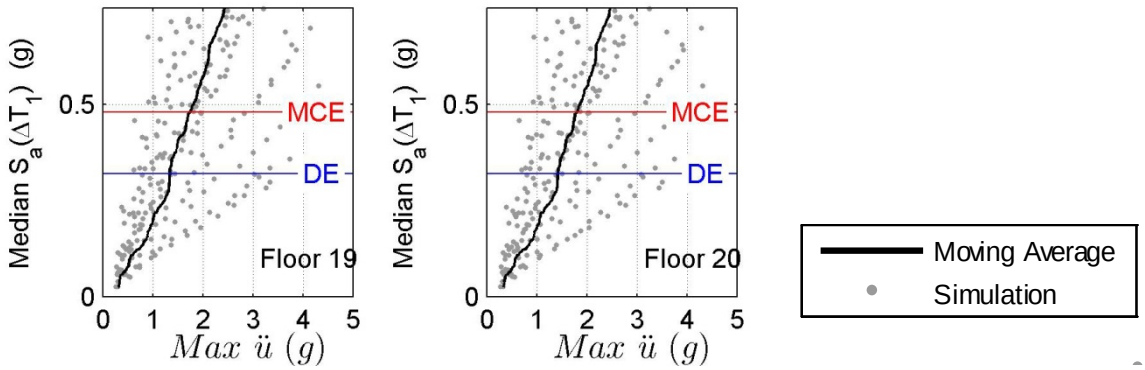

Figure B.121 IDA results for RC-20 ($L_{w,min}$): maximum floor level acceleration against median spectral acceleration over the range of T_1 for floors 19-20.

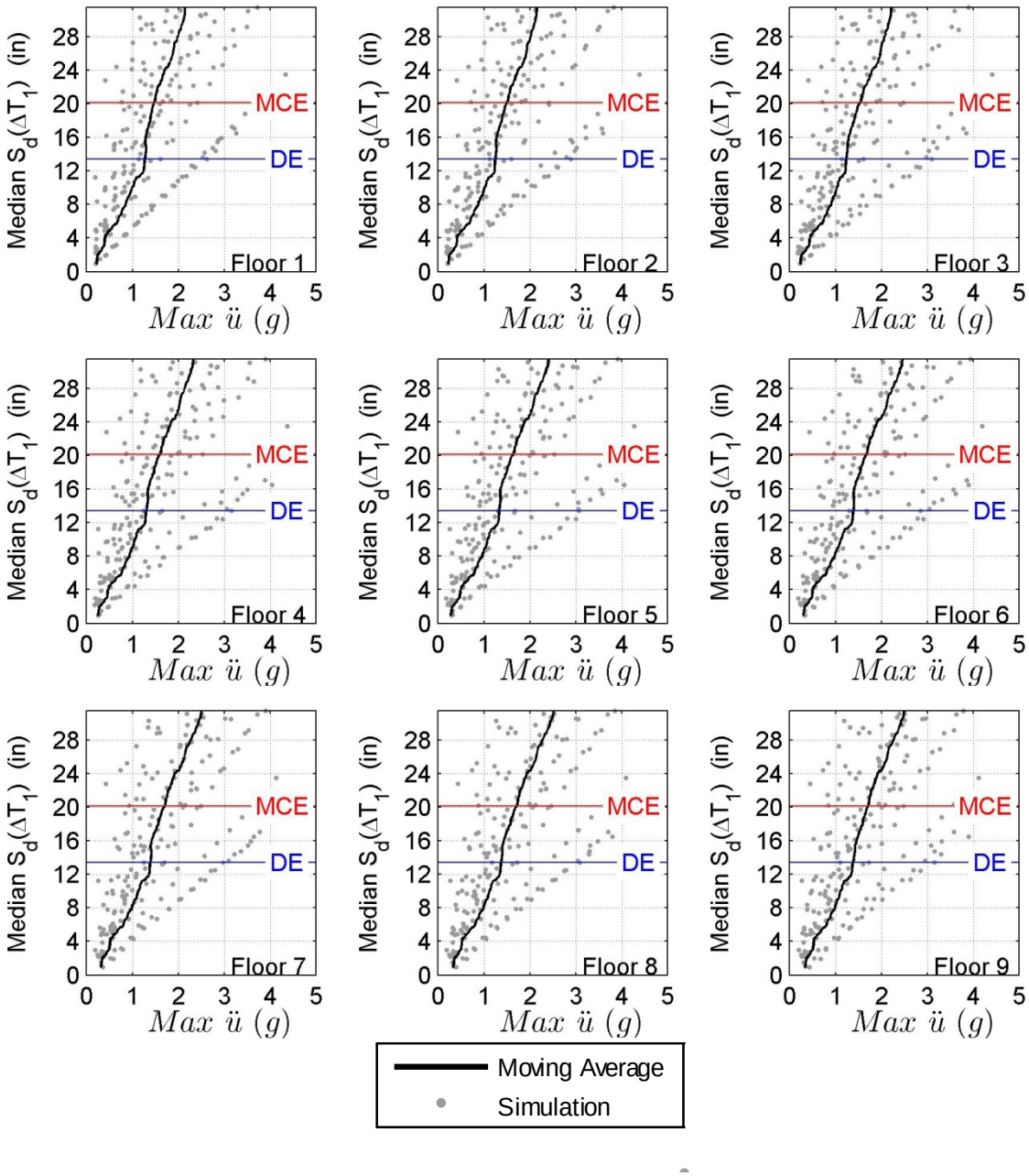

Figure B.122 IDA results for RC-20 ($L_{w,min}$): maximum floor level acceleration against median spectral displacement over the range of T_1 for floors 1-9.

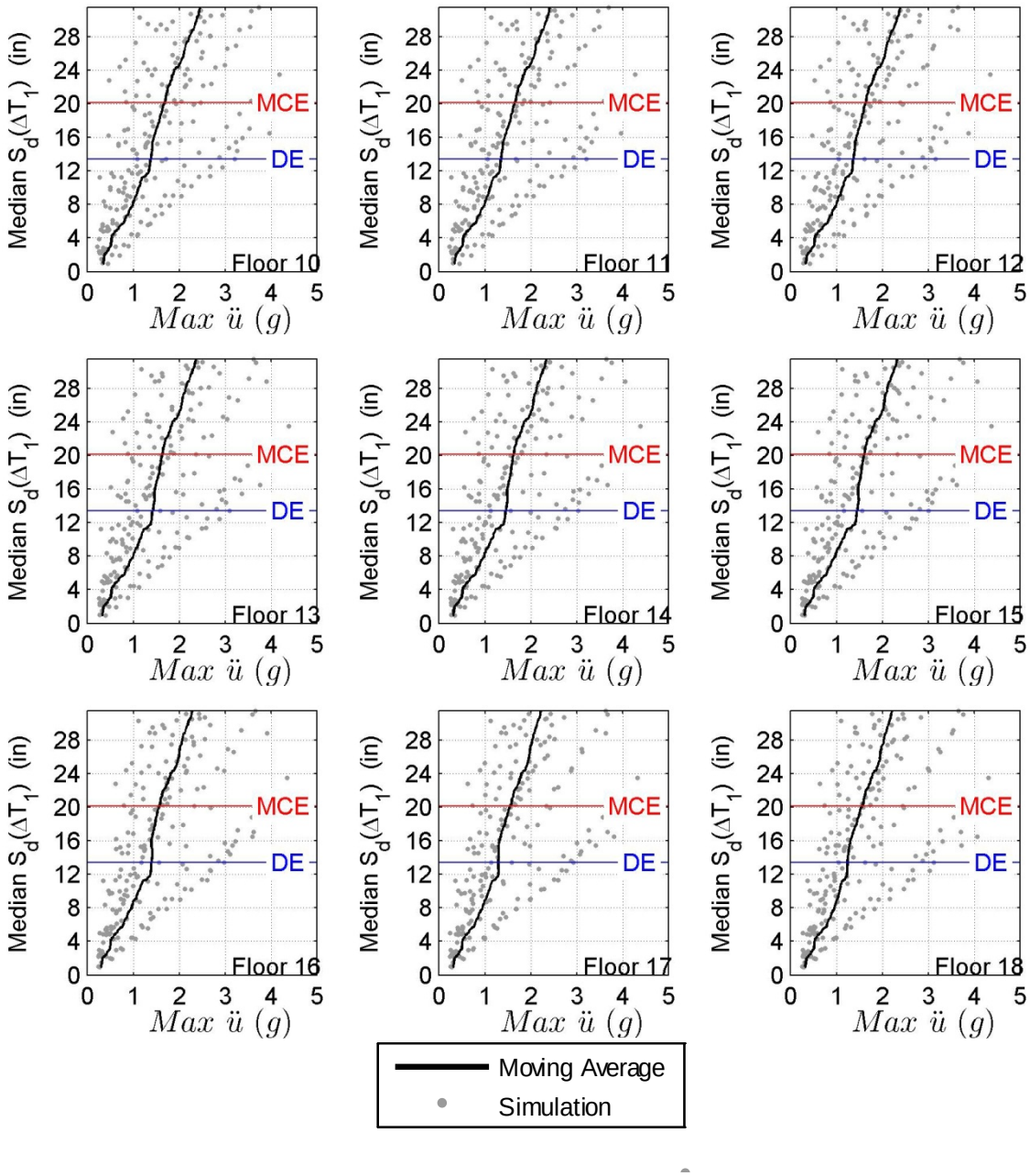

Figure B.123 IDA results for RC-20 ($L_{w,min}$): maximum floor level acceleration against median spectral displacement over the range of T_1 for floors 10-18.

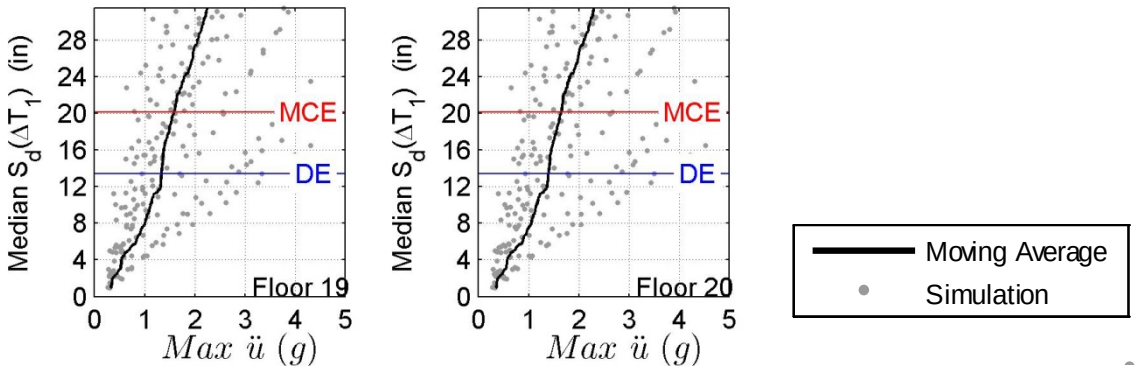

Figure B.124 IDA results for RC-20 ($L_{w,min}$): maximum floor level acceleration against median spectral displacement over the range of T_1 for floors 19-20.

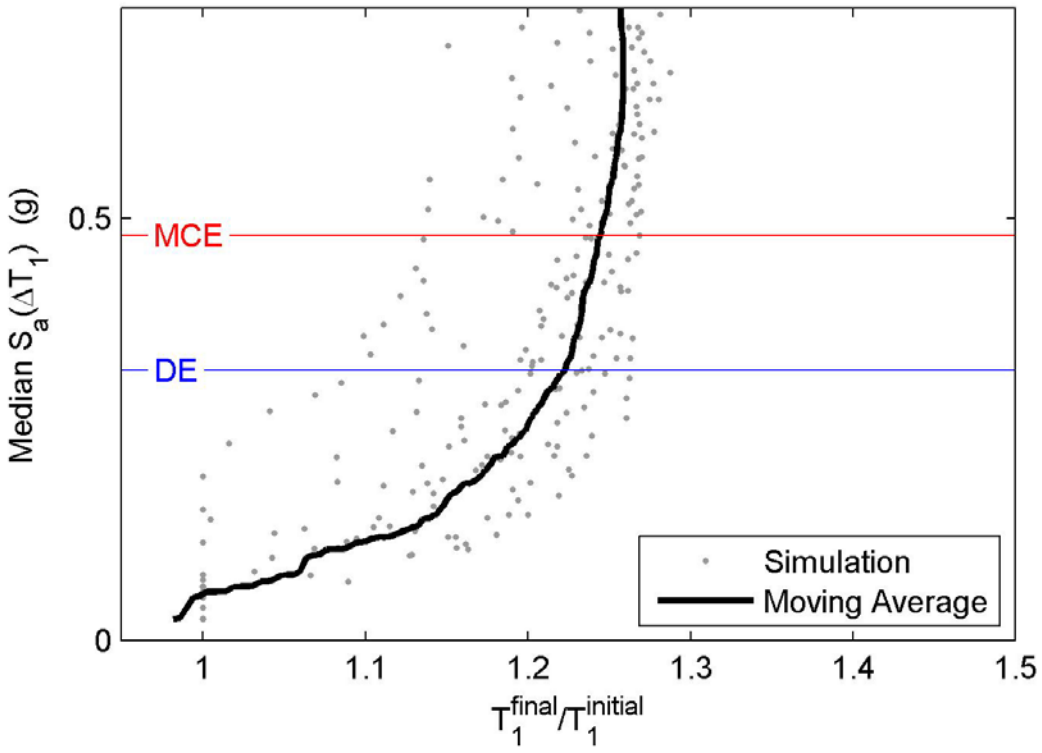

Figure B.125 IDA results for RC-20 ($L_{w,min}$): period elongation against median spectral acceleration over the range of T_1.

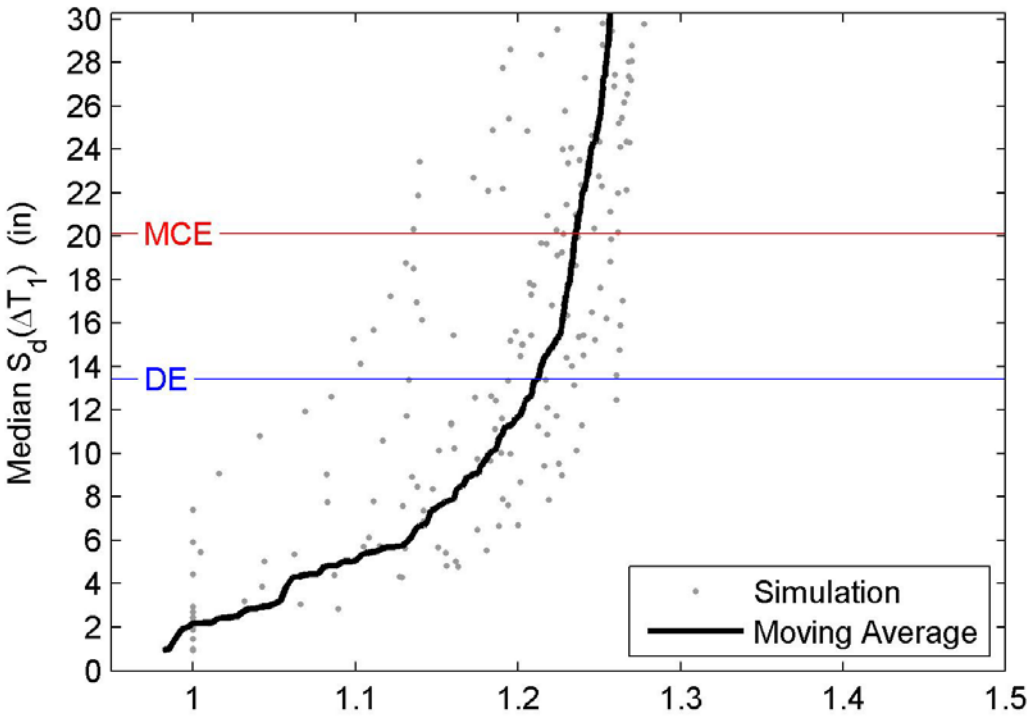

Figure B.126 IDA results for RC-20 ($L_{w,min}$): period elongation against median spectral displacement over the range of T_1.

Appendix C Summary of the Effect of Partition Walls

LIST OF FIGURES

Figure C.1 Maximum interstory drift moving average curves for RC-8 considering the cases of no wall, minimum wall length (mean) and maximum wall length against spectral acceleration at T_1 (uncracked). 429

Figure C.2 Maximum interstory drift moving average curves for RC-8 considering the cases of no wall, minimum wall length (mean) and maximum wall length against spectral displacement at T_1 (uncracked)..... 430

Figure C.3 Normalized maximum interstory drift moving average curves for RC-8 considering the cases of no wall, minimum wall length (mean) and maximum wall length against spectral acceleration at T_1 (uncracked)..... 431

Figure C.4 Normalized maximum interstory drift moving average curves for RC-8 considering the cases of no wall, minimum wall length (mean) and maximum wall length against displacment acceleration at T_1 (uncracked)..... 432

Figure C.5 Maximum interstory drift moving average curves for RC-8 considering the cases of no wall, minimum wall length (mean) and maximum wall length against median spectral acceleration over the range of T_1..... 433

Figure C.6 Maximum interstory drift moving average curves for RC-8 considering the cases of no wall, minimum wall length (mean) and maximum wall length against median spectral displacement over the range of T_1..... 434

Figure C.7 Normalized maximum interstory drift moving average curves for RC-8 considering the cases of no wall, minimum wall length (mean) and maximum wall length against median spectral acceleration over the range of T_1..... 435

Figure C.8 Normalized maximum interstory drift moving average curves for RC-8 considering the cases of no wall, minimum wall length (mean) and maximum wall length against median spectral displacement over the range of T_1..... 436

Figure C.9 Maximum interstory drift moving average curves for RC-8 considering the cases of no wall, minimum wall length (mean) and maximum wall length against mean spectral acceleration over the range of T_1..... 437

Figure C.10 Maximum interstory drift moving average curves for RC-8 considering the cases of no wall, minimum wall length (mean) and maximum wall length against mean spectral displacement over the range of T_1..... 438

Figure C.11 Normalized maximum interstory drift moving average curves for RC-8 considering the cases of no wall, minimum wall length (mean) and maximum wall length against mean spectral acceleration over the range of T_1..... 439

Figure C.12 Normalized maximum interstory drift moving average curves for RC-8 considering the cases of no wall, minimum wall length (mean) and maximum wall length against mean spectral displacement over the range of T_1..... 440

Figure C.13 Maximum interstory drift moving average curves for RC-8 considering the cases of no wall, minimum wall length (mean) and maximum wall length against maximum spectral acceleration over the range of T_1..... 441

Figure C.14 Maximum interstory drift moving average curves for RC-8 considering the cases of no wall, minimum wall length (mean) and maximum wall length against maximum spectral displacement over the range of T_1. 442

Figure C.15 Normalized maximum interstory drift moving average curves for RC-8 considering the cases of no wall, minimum wall length (mean) and maximum wall length against maximum spectral acceleration over the range of T_1. 443

Figure C.16 Normalized maximum interstory drift moving average curves for RC-8 considering the cases of no wall, minimum wall length (mean) and maximum wall length against maximum spectral acceleration over the range of T_1. 444

Figure C.17 Maximum floor level acceleration moving average curves for RC-8 considering the cases of no wall, minimum wall length (mean) and maximum wall length against spectral acceleration at T_1 (uncracked). 445

Figure C.18 Maximum floor level acceleration moving average curves for RC-8 considering the cases of no wall, minimum wall length (mean) and maximum wall length against spectral displacement at T_1 (uncracked). 446

Figure C.19 Normalized maximum floor level acceleration moving average curves for RC-8 considering the cases of no wall, minimum wall length (mean) and maximum wall length against spectral acceleration at T_1 (uncracked). 447

Figure C.20 Normalized maximum floor level acceleration moving average curves for RC-8 considering the cases of no wall, minimum wall length (mean) and maximum wall length against spectral displacement at T_1 (uncracked). 448

Figure C.21 Maximum floor level acceleration moving average curves for RC-8 considering the cases of no wall, minimum wall length (mean) and maximum wall length against median spectral acceleration over the range of T_1. 449

Figure C.22 Maximum floor level acceleration moving average curves for RC-8 considering the cases of no wall, minimum wall length (mean) and maximum wall length against median spectral displacement over the range of T_1. 450

Figure C.23 Normalized maximum floor level acceleration moving average curves for RC-8 considering the cases of no wall, minimum wall length (mean) and maximum wall length against median spectral acceleration over the range of T_1. 451

Figure C.24 Normalized maximum floor level acceleration moving average curves for RC-8 considering the cases of no wall, minimum wall length (mean) and maximum wall length against median spectral displacement over the range of T_1. 452

Figure C.25 Maximum floor level acceleration moving average curves for RC-8 considering the cases of no wall, minimum wall length (mean) and maximum wall length against mean spectral acceleration over the range of T_1. 453

Figure C.26 Maximum floor level acceleration moving average curves for RC-8 considering the cases of no wall, minimum wall length (mean) and maximum wall length against mean spectral displacement over the range of T_1. 454

Figure C.27 Normalized maximum floor level acceleration moving average curves for RC-8 considering the cases of no wall, minimum wall length (mean) and maximum wall length against mean spectral acceleration over the range of T_1. 455

Figure C.28 Normalized maximum floor level acceleration moving average curves for RC-8 considering the cases of no wall, minimum wall length (mean) and maximum wall length against mean spectral displacement over the range of T_1. 456

Figure C.29 Maximum floor level acceleration moving average curves for RC-8 considering the cases of no wall, minimum wall length (mean) and maximum wall length against maximum spectral acceleration over the range of T_1..... 457

Figure C.30 Maximum floor level acceleration moving average curves for RC-8 considering the cases of no wall, minimum wall length (mean) and maximum wall length against maximum spectral displacement over the range of T_1..... 458

Figure C.31 Normalized maximum floor level acceleration moving average curves for RC-8 considering the cases of no wall, minimum wall length (mean) and maximum wall length against maximum spectral acceleration over the range of T_1. 459

Figure C.32 Normalized maximum floor level acceleration moving average curves for RC-8 considering the cases of no wall, minimum wall length (mean) and maximum wall length against maximum spectral displacement over the range of T_1..... 460

Figure C.33 Period elongation moving average curves for RC-8 considering the cases of no wall, minimum wall length (mean) and maximum wall length against median spectral acceleration over the range of T_1..... 461

Figure C.34 Period elongation moving average curves for RC-8 considering the cases of no wall, minimum wall length (mean) and maximum wall length against median spectral displaccement over the range of T_1. 462

Figure C.35 Maximum interstory drift moving average curves for RC-8 considering the cases of wall variability: no wall, minimum wall length (mean), minimum wall length (mean-standard deviation), and minimum wall length (mean+standard deviation) against median spectral acceleration over the range of T_1..... 463

Figure C.36 Maximum interstory drift moving average curves for RC-8 considering the cases of wall variability: no wall, minimum wall length (mean), minimum wall length (mean-standard deviation), and minimum wall length (mean+standard deviation) against median spectral displacement over the range of T_1. 464

Figure C.37 Normalized maximum interstory drift moving average curves for RC-8 considering the cases of wall variability: no wall, minimum wall length (mean), minimum wall length (mean-standard deviation), and minimum wall length (mean+standard deviation) against median spectral acceleration over the range of T_1..... 465

Figure C.38 Normalized maximum interstory drift moving average curves for RC-8 considering the cases of wall variability: no wall, minimum wall length (mean), minimum wall length (mean-standard deviation), and minimum wall length (mean+standard deviation) against median spectral displacement over the range of T_1..... 466

Figure C.39 Maximum floor level acceleration moving average curves for RC-8 considering cases of the wall variability: no wall, minimum wall length (mean), minimum wall length (mean-standard deviation), and minimum wall length (mean+standard deviation) against median spectral acceleration over the range of T_1..... 467

Figure C.40 Maximum floor level acceleration moving average curves for RC-8 considering the cases of wall variability: no wall, minimum wall length (mean), minimum wall

length (mean-standard deviation), and minimum wall length (mean+standard deviation) against median spectral displacement over the range of T_1. 468

Figure C.41 Normalized maximum floor level acceleration moving average curves for RC-8 considering the cases of wall variability: no wall, minimum wall length (mean), minimum wall length (mean-standard deviation), and minimum wall length (mean+standard deviation) against median spectral acceleration over the range of T_1 469

Figure C.42 Normalized maximum floor level acceleration moving average curves for RC-8 considering the cases of wall variability: no wall, minimum wall length (mean), minimum wall length (mean-standard deviation), and minimum wall length (mean+standard deviation) against median spectral displacement over the range of T_1 470

Figure C.43 Period elongation moving average curves for RC-8 considering the cases of wall variability: no wall, minimum wall length (mean), minimum wall length (mean-standard deviation), and minimum wall length (mean+standard deviation) against median spectral acceleration over the range of T_1. 471

Figure C.44 Period elongation moving average curves for RC-8 considering the cases of wall variability: no wall, minimum wall length (mean), minimum wall length (mean-standard deviation), and minimum wall length (mean+standard deviation) against median spectral displacement over the range of T_1. 472

Figure C.45 Maximum interstory drift moving average curves for RC-8 considering the cases of effect of post-peak hardening: no wall, minimum wall length, and minimum wall length (no post-peak hardening) against median spectral acceleration over the range of T_1. 473

Figure C.46 Maximum interstory drift moving average curves for RC-8 considering the cases of effect of post-peak hardening: no wall, maximum wall length, and maximum wall length (no post-peak hardening) against median spectral acceleration over the range of T_1. 474

Figure C.47 Maximum interstory drift moving average curves for RC-8 considering the cases of effect of post-peak hardening: no wall, minimum wall length, and minimum wall length (no post-peak hardening) against median spectral displacement over the range of T_1. 475

Figure C.48 Maximum interstory drift moving average curves for RC-8 considering the cases of effect of post-peak hardening: no wall, maximum wall length, and maximum wall length (no post-peak hardening) against median spectral displacement over the range of T_1. 476

Figure C.49 Normalized interstory drift moving average curves for RC-8 considering the cases of effect of post-peak hardening: no wall, minimum wall length, and minimum wall length (no post-peak hardening) against median spectral acceleration over the range of T_1. 477

Figure C.50 Normalized interstory drift moving average curves for RC-8 considering the cases of effect of post-peak hardening: no wall, maximum wall length, and maximum wall length (no post-peak hardening) against median spectral acceleration over the range of T_1. 478

Figure C.51 Normalized interstory drift moving average curves for RC-8 considering the cases of effect of post-peak hardening: no wall, minimum wall length, and minimum wall length (no post-peak hardening) against median spectral displacement over the range of T_1. 479

Figure C.52 Normalized interstory drift moving average curves for RC-8 considering the cases of effect of post-peak hardening: no wall, maximum wall length, and maximum wall length (no post-peak hardening) against median spectral displacement over the range of T_1. 480

Figure C.53 Maximum floor level acceleration moving average curves for RC-8 considering the cases of effect of post-peak hardening: no wall, minimum wall length, and minimum wall length (no post-peak hardening) against median spectral acceleration over the range of T_1. 481

Figure C.54 Maximum floor level acceleration moving average curves for RC-8 considering the cases of effect of post-peak hardening: no wall, maximum wall length, and maximum wall length (no post-peak hardening) against median spectral acceleration over the range of T_1. 482

Figure C.55 Maximum floor level acceleration moving average curves for RC-8 considering the cases of effect of post-peak hardening: no wall, minimum wall length, and minimum wall length (no post-peak hardening) against median spectral displacement over the range of T_1. 483

Figure C.56 Maximum floor level acceleration moving average curves for RC-8 considering the cases of effect of post-peak hardening: no wall, maximum wall length, and maximum wall length (no post-peak hardening) against median spectral displacement over the range of T_1. 484

Figure C.57 Normalized maximum floor level acceleration moving average curves for RC-8 considering the cases of effect of post-peak hardening: no wall, minimum wall length, and minimum wall length (no post-peak hardening) against median spectral acceleration over the range of T_1. 485

Figure C.58 Normalized maximum floor level acceleration moving average curves for RC-8 considering the cases of effect of post-peak hardening: no wall, maximum wall length, and maximum wall length (no post-peak hardening) against median spectral acceleration over the range of T_1. 486

Figure C.59 Normalized maximum floor level acceleration moving average curves for RC-8 considering the cases of effect of post-peak hardening: no wall, minimum wall length, and minimum wall length (no post-peak hardening) against median spectral displacement over the range of T_1. 487

Figure C.60 Normalized maximum floor level acceleration moving average curves for RC-8 considering the cases of effect of post-peak hardening: no wall, maximum wall length, and maximum wall length (no post-peak hardening) against median spectral displacement over the range of T_1. 488

Figure C.61 Period elongation moving average curves for RC-8 considering the effect of post-peak hardening: no wall, minimum wall length, and minimum wall length (no post-peak hardening) against median spectral acceleration over the range of T_1. 489

Figure C.62 Period elongation moving average curves for RC-8 considering the effect of post-peak hardening: no wall, maximum wall length, and maximum wall length (no post-peak hardening) against median spectral acceleration over the range of T_1. . 490

Figure C.63 Period elongation moving average curves for RC-8 considering the effect of post-peak hardening: no wall, minimum wall length, and minimum wall length (no post-peak hardening) against median spectral displacement over the range of T_1. 491

Figure C.64 Period elongation moving average curves for RC-8 considering the effect of post-peak hardening: no wall, maximum wall length, and maximum wall length (no post-peak hardening) against median spectral displacement over the range of T_1. 492

Figure C.35 Maximum interstory drift moving average curves for RC-8 considering the cases of wall placement: no wall, minimum wall length (all floors), no wall first floor, and no wall on top level against median spectral acceleration over the range of T_1. ... 493

Figure C.36 Maximum interstory drift moving average curves RC-8 considering the cases of wall placement: no wall, minimum wall length (all floors), no wall first floor, and no wall on top level against median spectral displacement over the range of T_1. . 494

Figure C.37 Normalized maximum interstory drift moving average curves for RC-8 considering the cases of wall placement: no wall, minimum wall length (all floors), no wall first floor, and no wall on top level against median spectral acceleration over the range of T_1. 495

Figure C.38 Normalized maximum interstory drift moving average curves for RC-8 considering the cases of wall placement: no wall, minimum wall length (all floors), no wall first floor, and no wall on top level against median spectral displacement over the range of T_1. 496

Figure C.39 Maximum floor level acceleration moving average curves for RC-8 considering the cases of wall placement: no wall, minimum wall length (all floors), no wall first floor, and no wall on top level against median spectral acceleration over the range of T_1. 497

Figure C.40 Maximum floor level acceleration moving average curves for RC-8 considering the cases of wall placement: no wall, minimum wall length (all floors), no wall first floor, and no wall on top level against median spectral displacement over the range of T_1. 498

Figure C.41 Normalized maximum floor level acceleration moving average curves for RC-8 considering the cases of wall placement: no wall, minimum wall length (all floors), no wall first floor, and no wall on top level against median spectral acceleration over the range of T_1. 499

Figure C.42 Normalized maximum floor level acceleration moving average curves for RC-8 considering the cases of wall placement: no wall, minimum wall length (all floors), no wall first floor, and no wall on top level against median spectral displacement over the range of T_1. 500

Figure C.43 Period elongation moving average curves for RC-8 considering the cases of wall placement: no wall, minimum wall length (all floors), no wall first floor, and no wall on top level against median spectral acceleration over the range of T_1. 501

Figure C.44 Period elongation moving average curves for RC-8 considering the cases of wall placement: no wall, minimum wall length (all floors), no wall first floor, and no wall on top level against median spectral displacement over the range of T_1. 502

Figure C.65 Maximum interstory drift moving average curves for S-3H considering the cases of various wall length: no wall, minimum wall length, and minimum wall length against median spectral acceleration over the range of T_1. 503

Figure C.66 Maximum interstory drift moving average curves for S-3H considering the cases of various wall length: no wall, minimum wall length, and minimum wall length against median spectral displacement over the range of T_1. 503

Figure C.67 Normalized maximum interstory drift moving average curves for S-3H considering cases of various wall length: no wall, minimum wall length, and minimum wall length against median spectral acceleration over the range of T_1. 504

Figure C.68 Normalized maximum interstory drift moving average curves for S-3H considering cases of various wall length: no wall, minimum wall length, and minimum wall length against median spectral displacement over the range of T_1. 504

Figure C.69 Maximum floor level acceleration moving average curves for S-3H considering the cases of various wall length: no wall, minimum wall length, and minimum wall length against median spectral acceleration over the range of T_1. 505

Figure C.70 Maximum floor level acceleration moving average curves for S-3H considering the cases of various wall length: no wall, minimum wall length, and minimum wall length against median spectral displacement over the range of T_1. 505

Figure C.71 Normalized maximum floor level acceleration moving average curves for S-3H considering the cases of various wall length: no wall, minimum wall length, and minimum wall length against median spectral acceleration over the range of T_1. 506

Figure C.72 Normalized maximum floor level acceleration moving average curves for S-3H considering the cases of various wall length: no wall, minimum wall length, and minimum wall length against median spectral displacement over the range of T_1. 506

Figure C.73 Period elongation moving average curves for S-3H considering the cases of various wall length: no wall, minimum wall length, and minimum wall length against median spectral acceleration over the range of T_1. 507

Figure C.74 Period elongation moving average curves for S-3H considering cases of various wall length: no wall, minimum wall length, and minimum wall length against median spectral displacement over the range of T_1. 508

Figure C.75 Maximum interstory drift moving average curves for S-9 considering the cases of no wall and minimum wall length against median spectral acceleration over the range of T_1. 509

Figure C.76 Maximum interstory drift moving average curves for S-9 considering the cases of no wall and minimum wall length against median spectral displacement over the range of T_1. 510

Figure C.77 Normalized maximum interstory drift moving average curves for S-9 considering the cases of no wall and minimum wall length against median spectral acceleration over the range of T_1. 511

Figure C.78 Normalized maximum interstory drift moving average curves for S-9 considering the cases of no wall and minimum wall length against median spectral displacement over the range of T_1. 512

Figure C.79 Maximum floor level acceleration moving average curves for S-9 considering the cases of no wall and minimum wall length against median spectral acceleration over the range of T_1 513

Figure C.80 Maximum floor level acceleration moving average curves for S-9 considering the cases of no wall and minimum wall length against median spectral acceleration over the range of T_1 514

Figure C.81 Normalized maximum floor level acceleration moving average curves for S-9 considering the cases of no wall and minimum wall length against median spectral acceleration over the range of T_1. 515

Figure C.82 Normalized maximum floor level acceleration moving average curves for S-9 considering the cases of no wall and minimum wall length against median spectral displacement over the range of T_1. 516

Figure C.83 Period elongation moving average curves for S-9 considering the cases of no wall and minimum wall length against median spectral acceleration over the range of T_1. 517

Figure C.84 Period elongation moving average curves for S-9 considering the cases of no wall and minimum wall length against median spectral displacement over the range of T_1 518

Figure C.75 Maximum interstory drift moving average curves for RC-20 considering the cases of no wall and minimum wall length against median spectral acceleration over the range of T_1 for floors 1-9. 519

Figure C.75 Maximum interstory drift moving average curves for RC-20 considering the cases of no wall and minimum wall length against median spectral acceleration over the range of T_1 for floors 10-18 520

Figure C.75 Maximum interstory drift moving average curves for RC-20 considering the cases of no wall and minimum wall length against median spectral acceleration over the range of T_1 for floors 19-20. 521

Figure C.76 Maximum interstory drift moving average curves for RC-20 considering the cases of no wall and minimum wall length against median spectral displacement over the range of T_1 for floors 1-9. 522

Figure C.76 Maximum interstory drift moving average curves for RC-20 considering the cases of no wall and minimum wall length against median spectral displacement over the range of T_1 for floors 10-18 523

Figure C.76 Maximum interstory drift moving average curves for RC-20 considering the cases of no wall and minimum wall length against median spectral displacement over the range of T_1 for floors 19-20. 524

Figure C.77 Normalized maximum interstory drift moving average curves for RC-20 considering the cases of no wall and minimum wall length against median spectral acceleration over the range of T_1 for floors 1-9. 525

Figure C.77 Normalized maximum interstory drift moving average curves for RC-20 considering the cases of no wall and minimum wall length against median spectral acceleration over the range of T_1 for floors 10-18. 526

Figure C.77 Normalized maximum interstory drift moving average curves for RC-20 considering the cases of no wall and minimum wall length against median spectral acceleration over the range of T_1 for floors 19-20. 527

Figure C.78 Normalized maximum interstory drift moving average curves for RC-20 considering the cases of no wall and minimum wall length against median spectral displacement over the range of T_1 for floors 1-9. 528

Figure C.78 Normalized maximum interstory drift moving average curves for RC-20 considering the cases of no wall and minimum wall length against median spectral displacement over the range of T_1 for floors 10-18. 529

Figure C.78 Normalized maximum interstory drift moving average curves for RC-20 considering the cases of no wall and minimum wall length against median spectral displacement over the range of T_1 for floors 19-20. 530

Figure C.79 Maximum floor level acceleration moving average curves for RC-20 considering the cases of no wall and minimum wall length against median spectral acceleration over the range of T_1 for floors 1-9. 531

Figure C.79 Maximum floor level acceleration moving average curves for RC-20 considering the cases of no wall and minimum wall length against median spectral acceleration over the range of T_1 for floors 10-18. 532

Figure C.79 Maximum floor level acceleration moving average curves for RC-20 considering the cases of no wall and minimum wall length against median spectral acceleration over the range of T_1 for floors 19-20. 533

Figure C.80 Maximum floor level acceleration moving average curves for RC-20 considering the cases of no wall and minimum wall length against median spectral acceleration over the range of T_1 for floors 1-9. 534

Figure C.80 Maximum floor level acceleration moving average curves for RC-20 considering the cases of no wall and minimum wall length against median spectral acceleration over the range of T_1 for floors 10-18. 535

Figure C.80 Maximum floor level acceleration moving average curves for RC-20 considering the cases of no wall and minimum wall length against median spectral acceleration over the range of T_1 for floors 19-20. 536

Figure C.81 Normalized maximum floor level acceleration moving average curves for RC-20 considering the cases of no wall and minimum wall length against median spectral acceleration over the range of T_1 for floors 1-9. 537

Figure C.81 Normalized maximum floor level acceleration moving average curves for RC-20 considering the cases of no wall and minimum wall length against median spectral acceleration over the range of T_1 for floors 10-18. 538

Figure C.81 Normalized maximum floor level acceleration moving average curves for RC-20 considering the cases of no wall and minimum wall length against median spectral acceleration over the range of T_1 for floors 19-20. 539

Figure C.82 Normalized maximum floor level acceleration moving average curves for RC-20 considering the cases of no wall and minimum wall length against median spectral displacement over the range of T_1 for floors 1-9. 540

Figure C.82 Normalized maximum floor level acceleration moving average curves for RC-20 considering the cases of no wall and minimum wall length against median spectral displacement over the range of T_1 for floors 10-18. 541

Figure C.82 Normalized maximum floor level acceleration moving average curves for RC-20 considering the cases of no wall and minimum wall length against median spectral displacement over the range of T_1 for floors 19-20. 542

Figure C.83 Period elongation moving average curves for RC-20 considering the cases of no wall and minimum wall length against median spectral acceleration over the range of T_1. 542

Figure C.84 Period elongation moving average curves for RC-20 considering the cases of no wall and minimum wall length against median spectral displacement over the range of T_1. 543

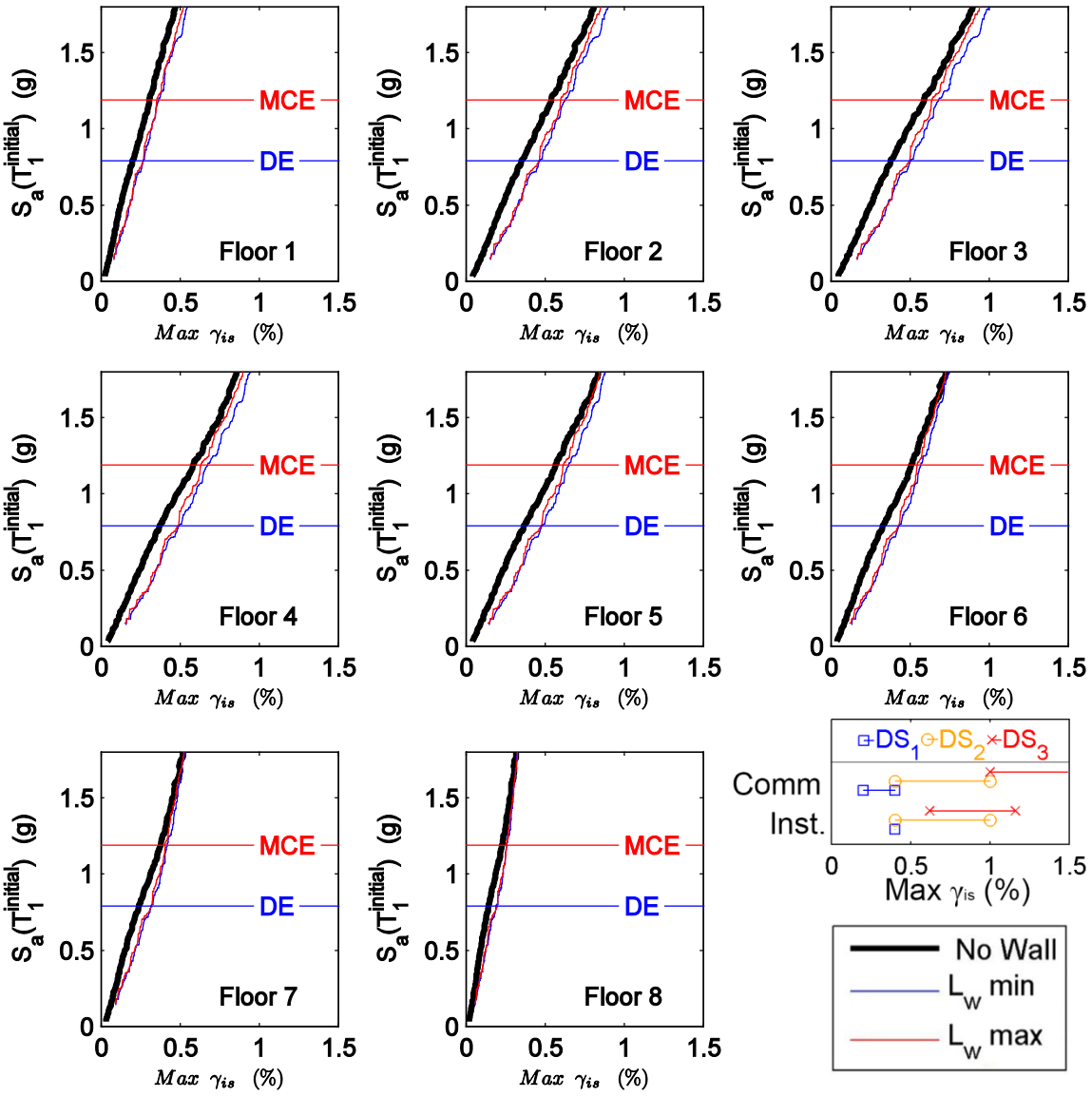

Figure C.1 Maximum interstory drift moving average curves for RC-8 considering the cases of no wall, minimum wall length (mean) and maximum wall length against spectral acceleration at T_1 (uncracked).

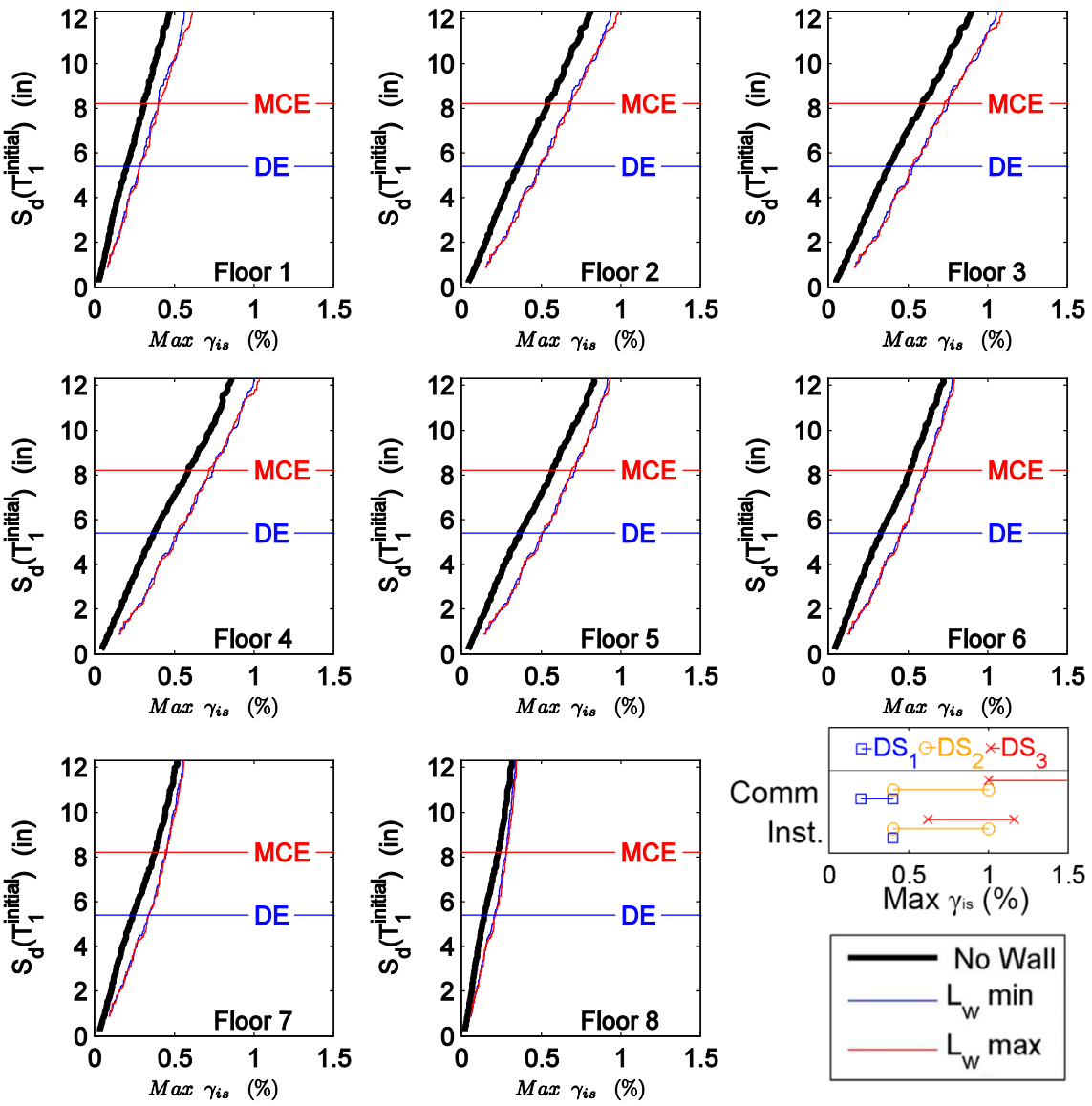

Figure C.2 Maximum interstory drift moving average curves for RC-8 considering the cases of no wall, minimum wall length (mean) and maximum wall length against spectral displacement at T_1 (uncracked).

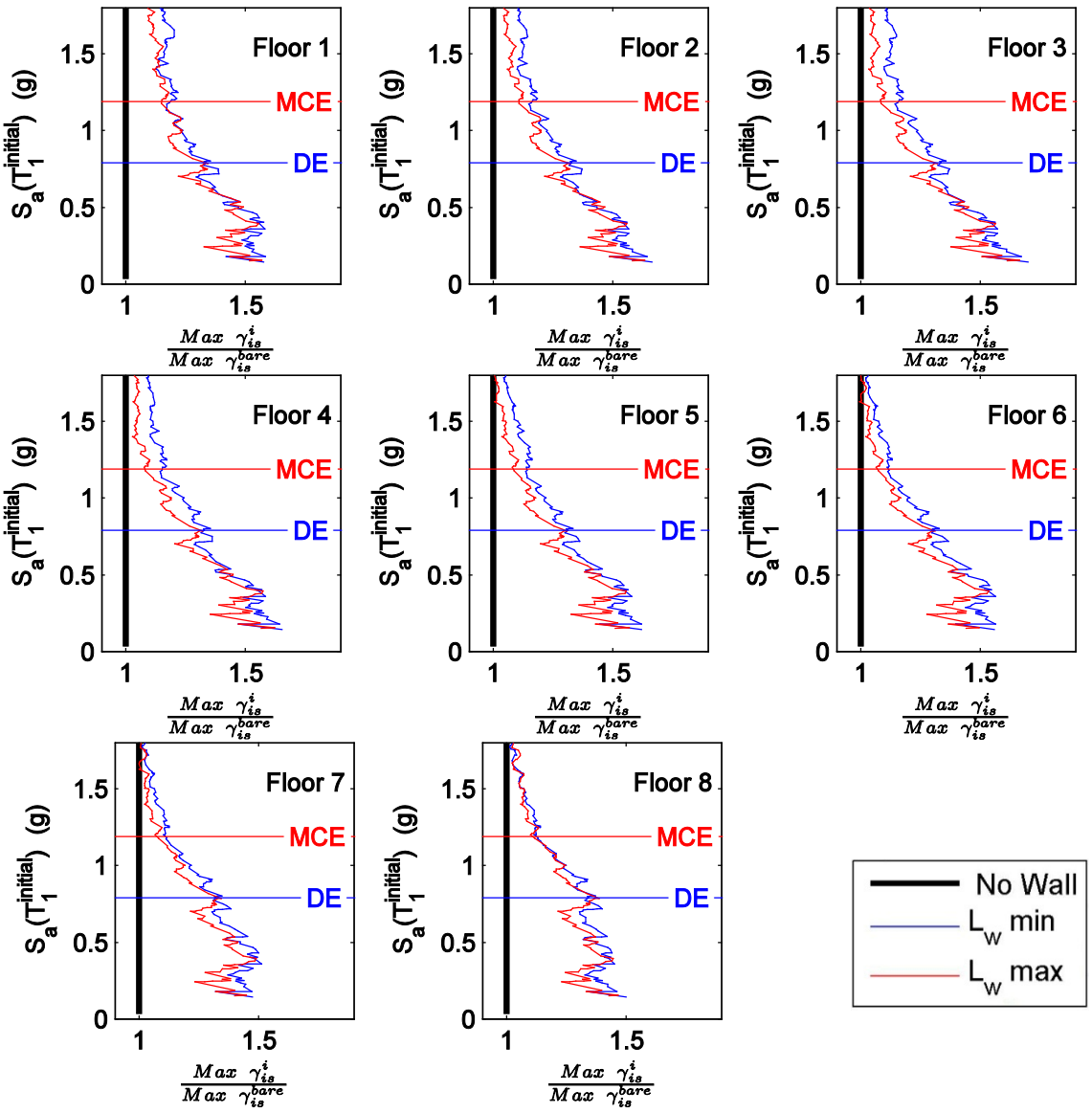

Figure C.3 Normalized maximum interstory drift moving average curves for RC-8 considering the cases of no wall, minimum wall length (mean) and maximum wall length against spectral acceleration at T_1 (uncracked).

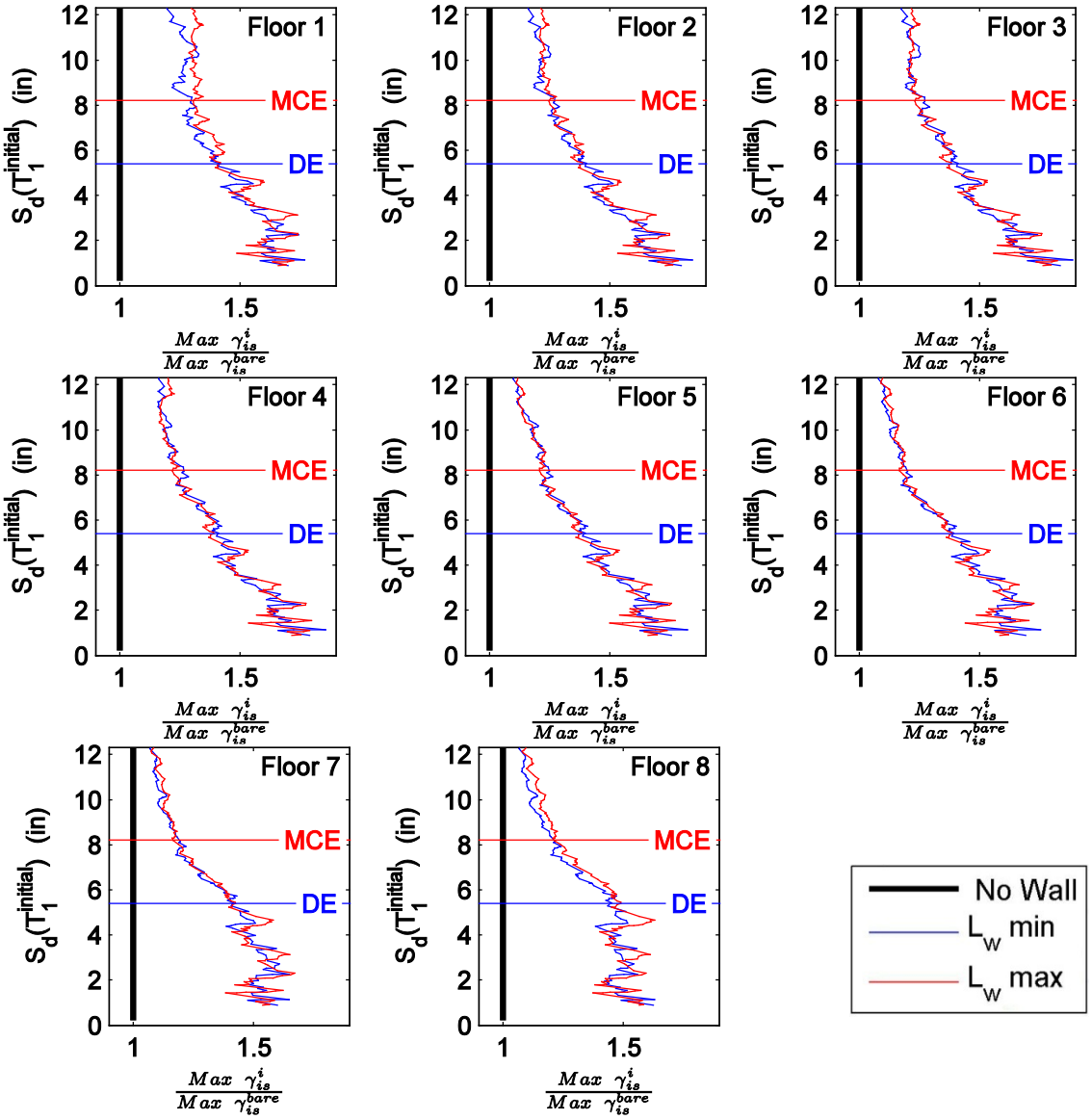

Figure C.4 Normalized maximum interstory drift moving average curves for RC-8 considering the cases of no wall, minimum wall length (mean) and maximum wall length against displacment acceleration at T_1 (uncracked).

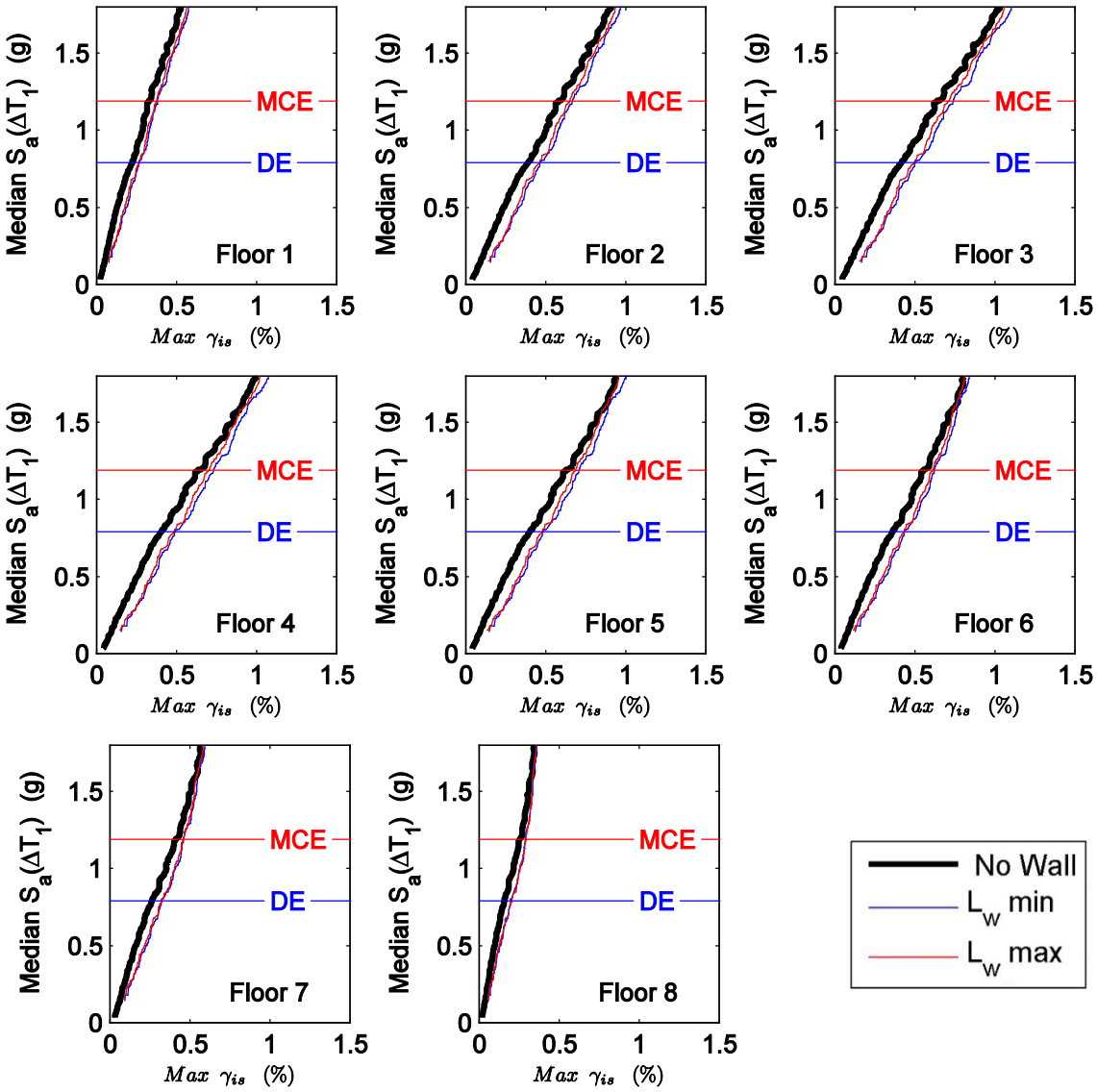

Figure C.5 Maximum interstory drift moving average curves for RC-8 considering the cases of no wall, minimum wall length (mean) and maximum wall length against median spectral acceleration over the range of T_1.

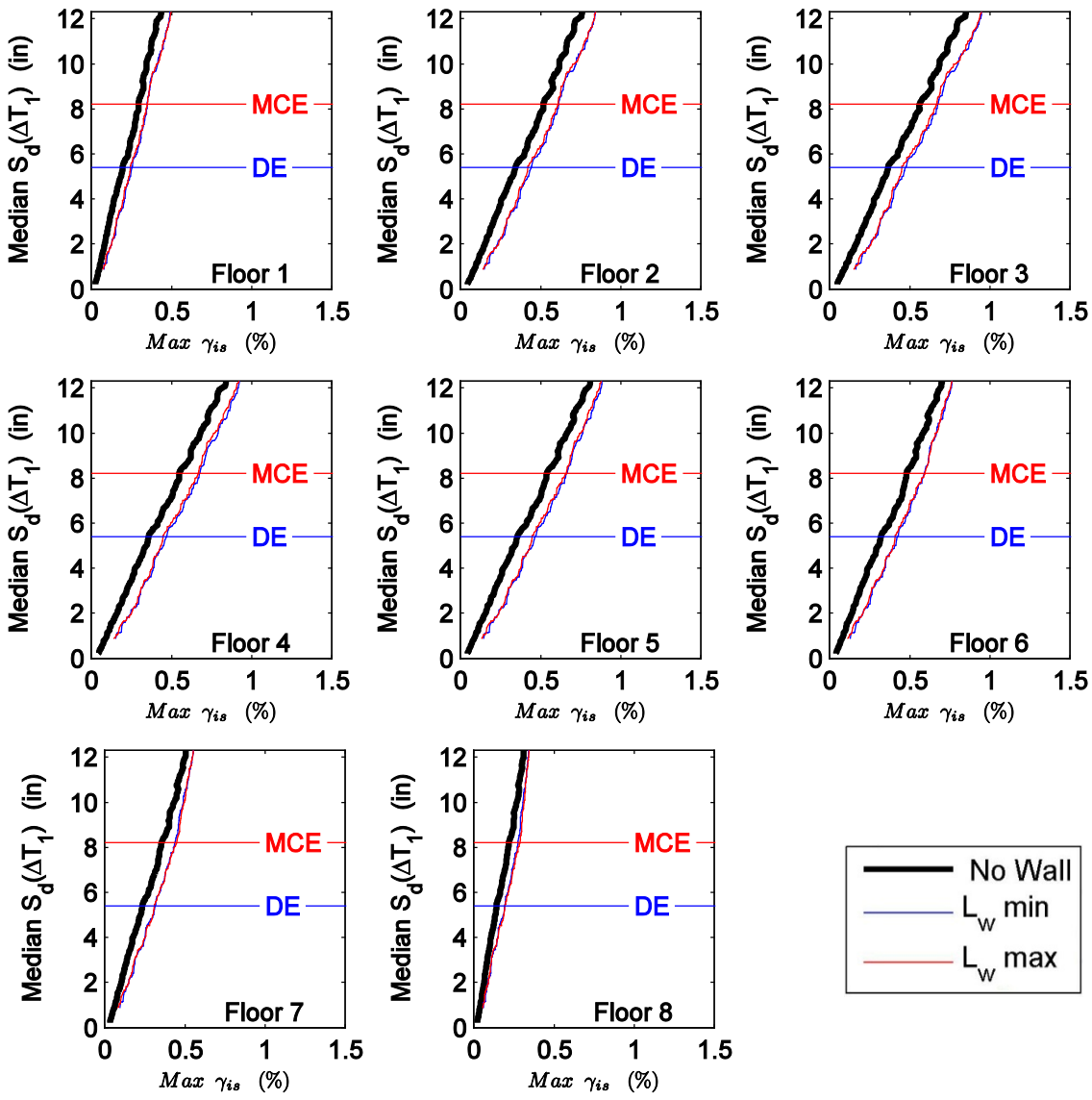

Figure C.6 Maximum interstory drift moving average curves for RC-8 considering the cases of no wall, minimum wall length (mean) and maximum wall length against median spectral displacement over the range of T_1.

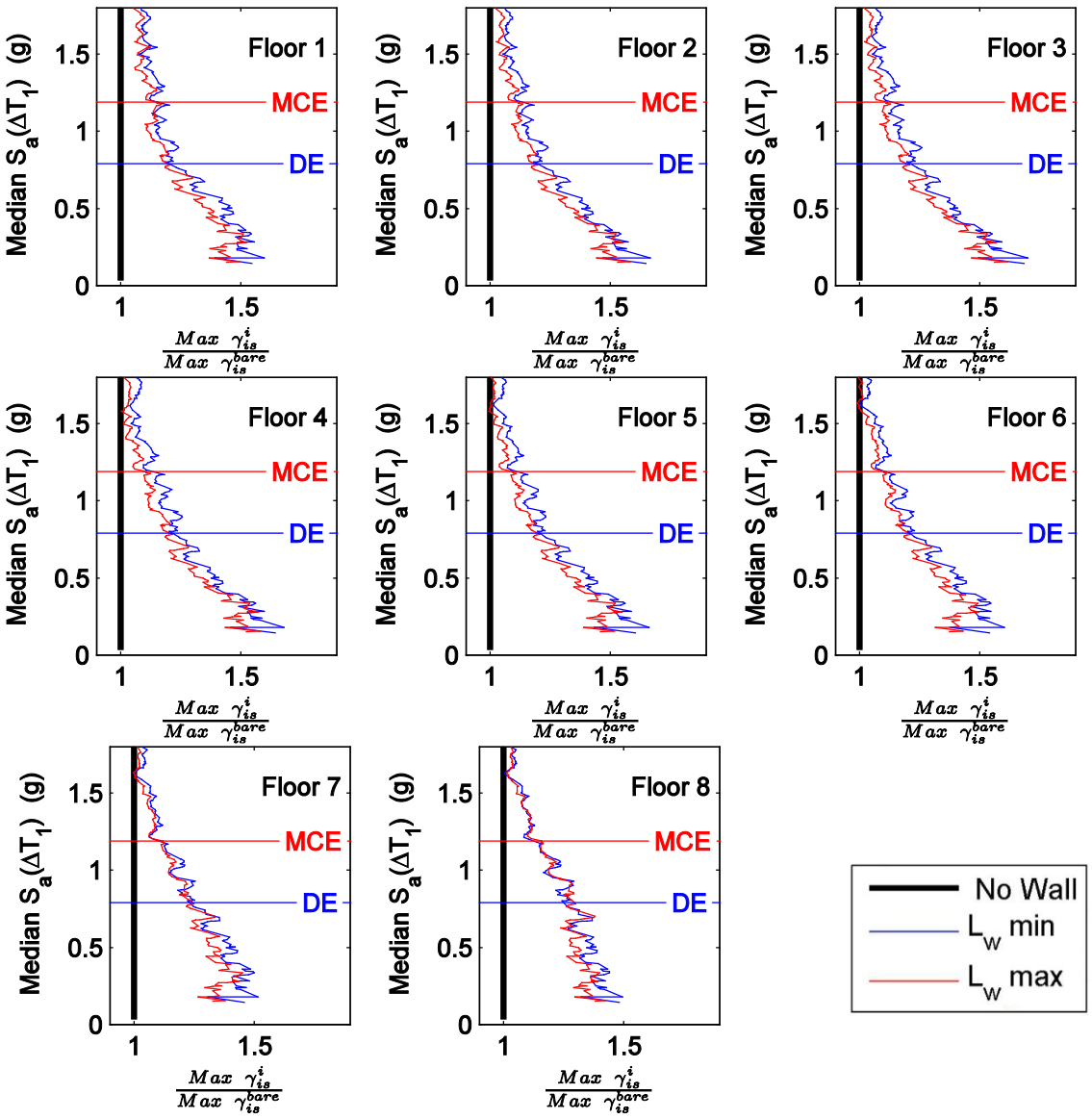

Figure C.7 Normalized maximum interstory drift moving average curves for RC-8 considering the cases of no wall, minimum wall length (mean) and maximum wall length against median spectral acceleration over the range of T_1.

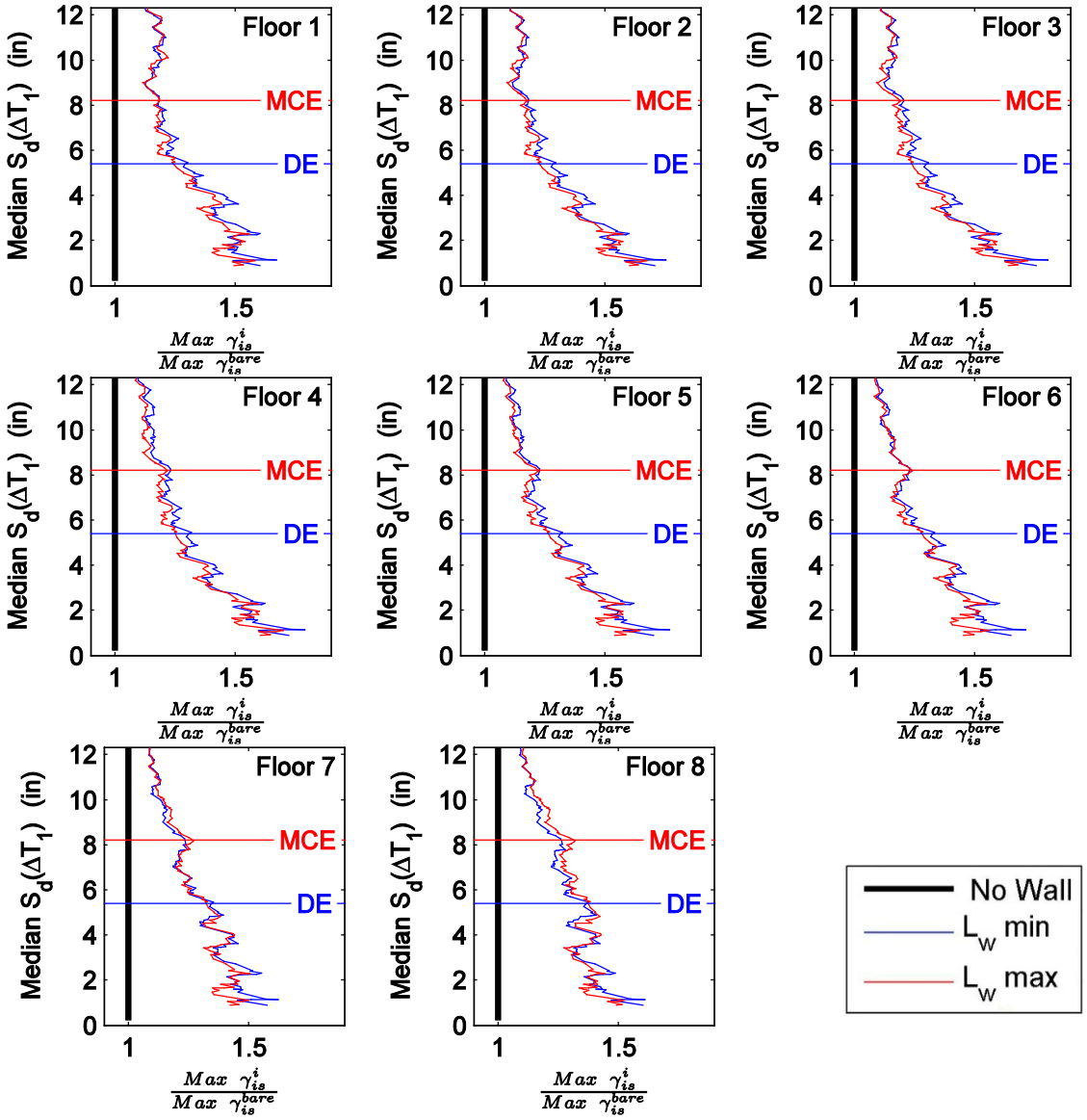

Figure C.8 Normalized maximum interstory drift moving average curves for RC-8 considering the cases of no wall, minimum wall length (mean) and maximum wall length against median spectral displacement over the range of T_1.

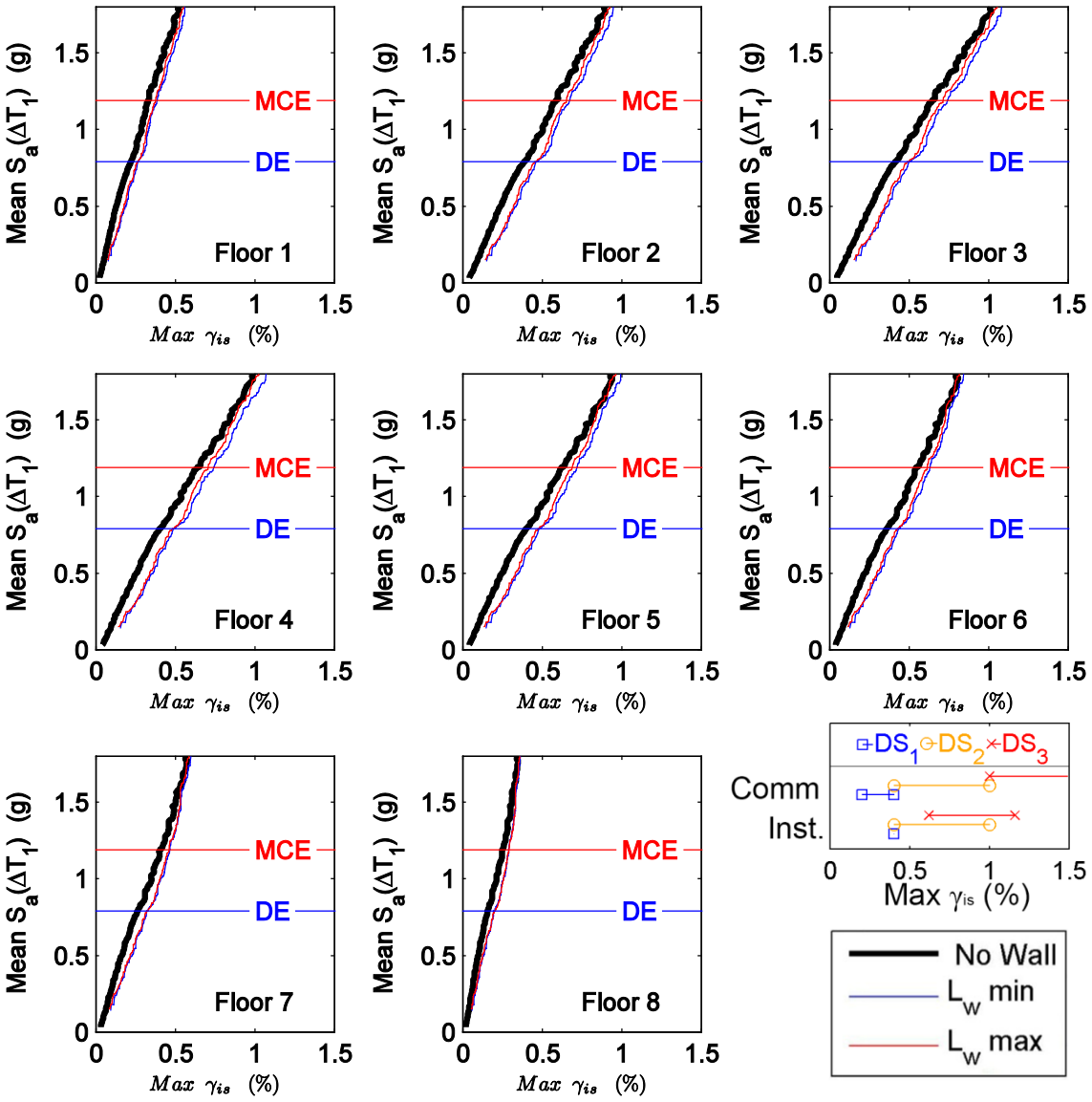

Figure C.9 Maximum interstory drift moving average curves for RC-8 considering the cases of no wall, minimum wall length (mean) and maximum wall length against mean spectral acceleration over the range of T_1.

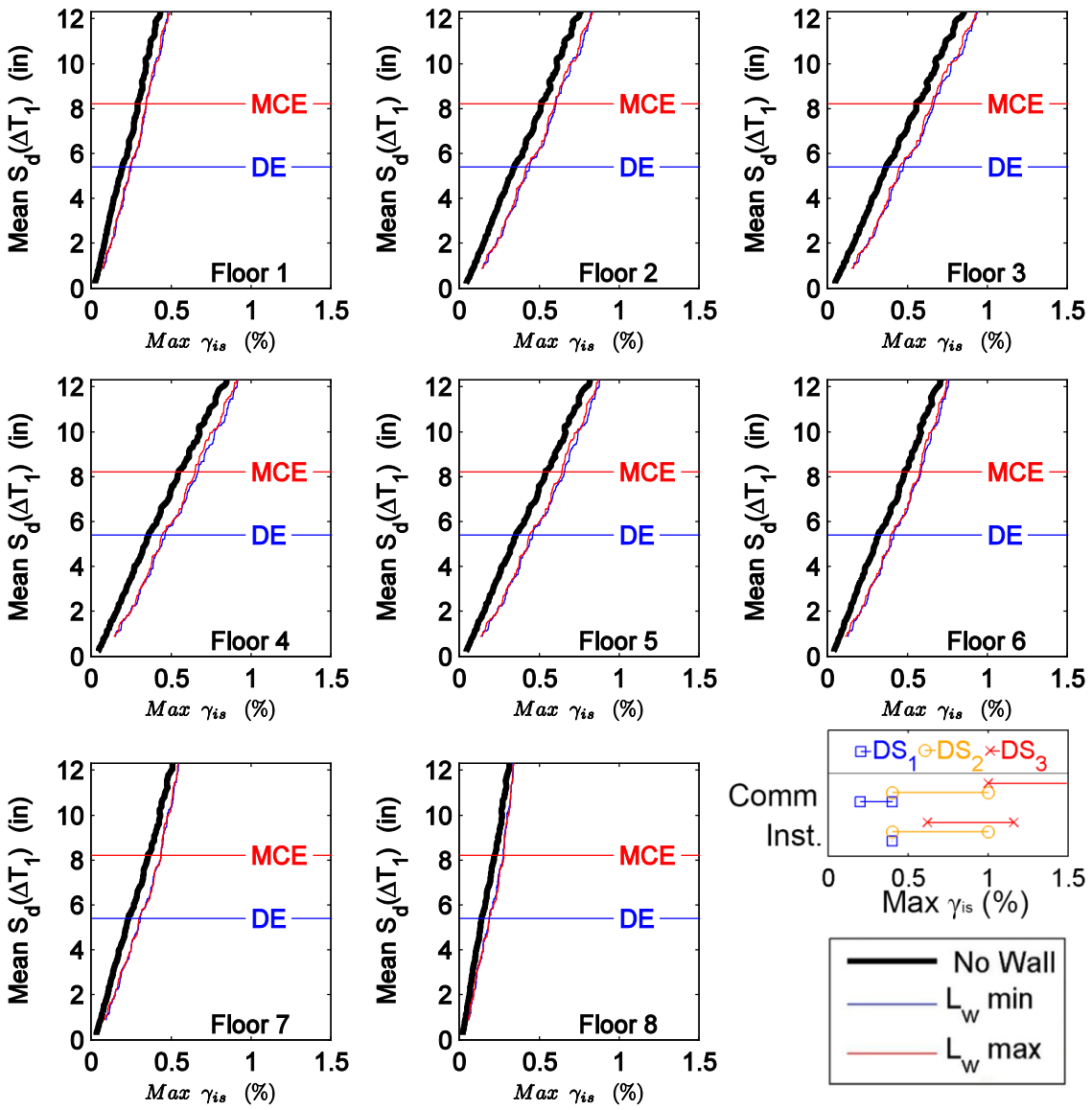

Figure C.10 Maximum interstory drift moving average curves for RC-8 considering the cases of no wall, minimum wall length (mean) and maximum wall length against mean spectral displacement over the range of T_1.

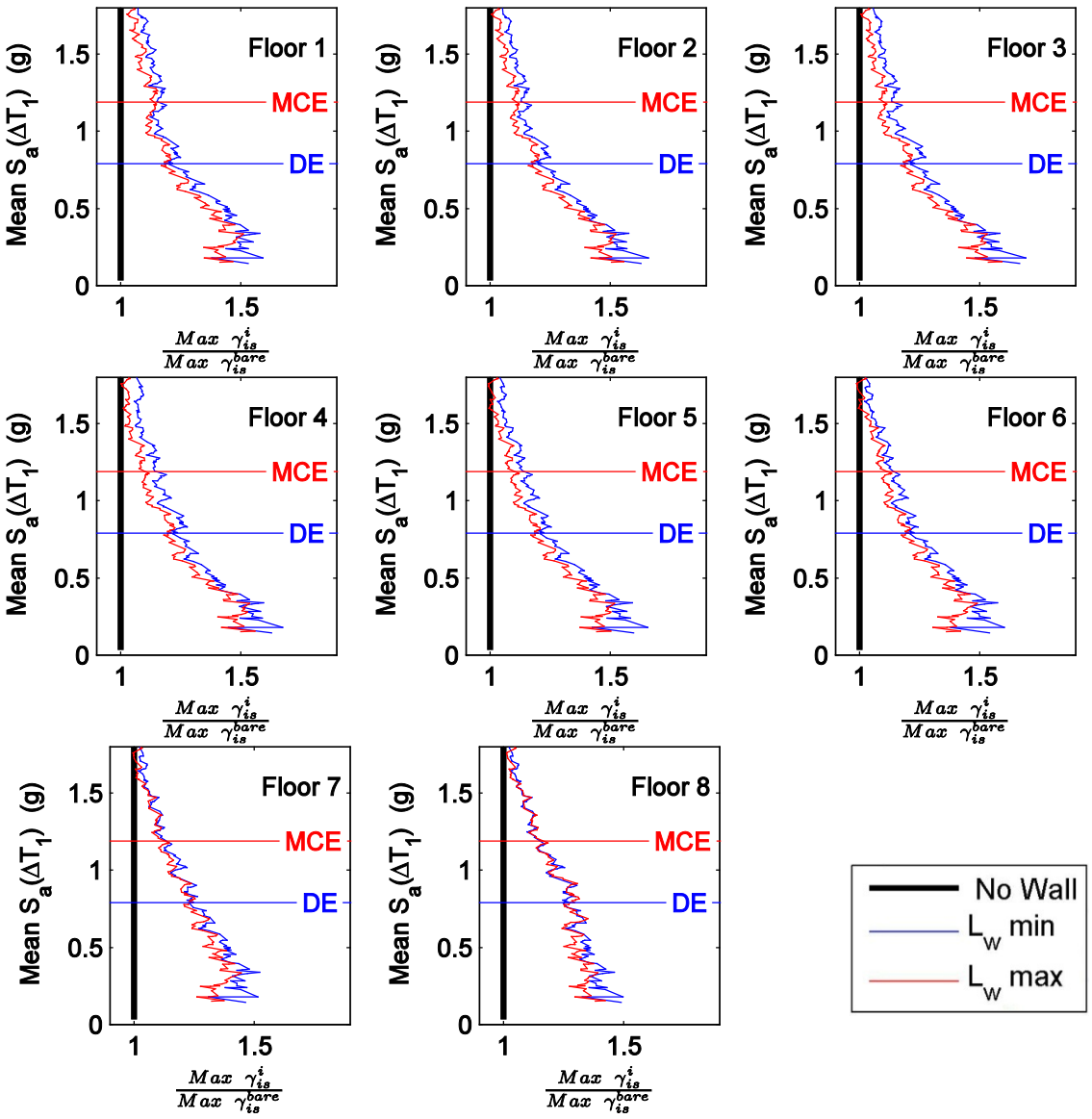

Figure C.11 Normalized maximum interstory drift moving average curves for RC-8 considering the cases of no wall, minimum wall length (mean) and maximum wall length against mean spectral acceleration over the range of T_1.

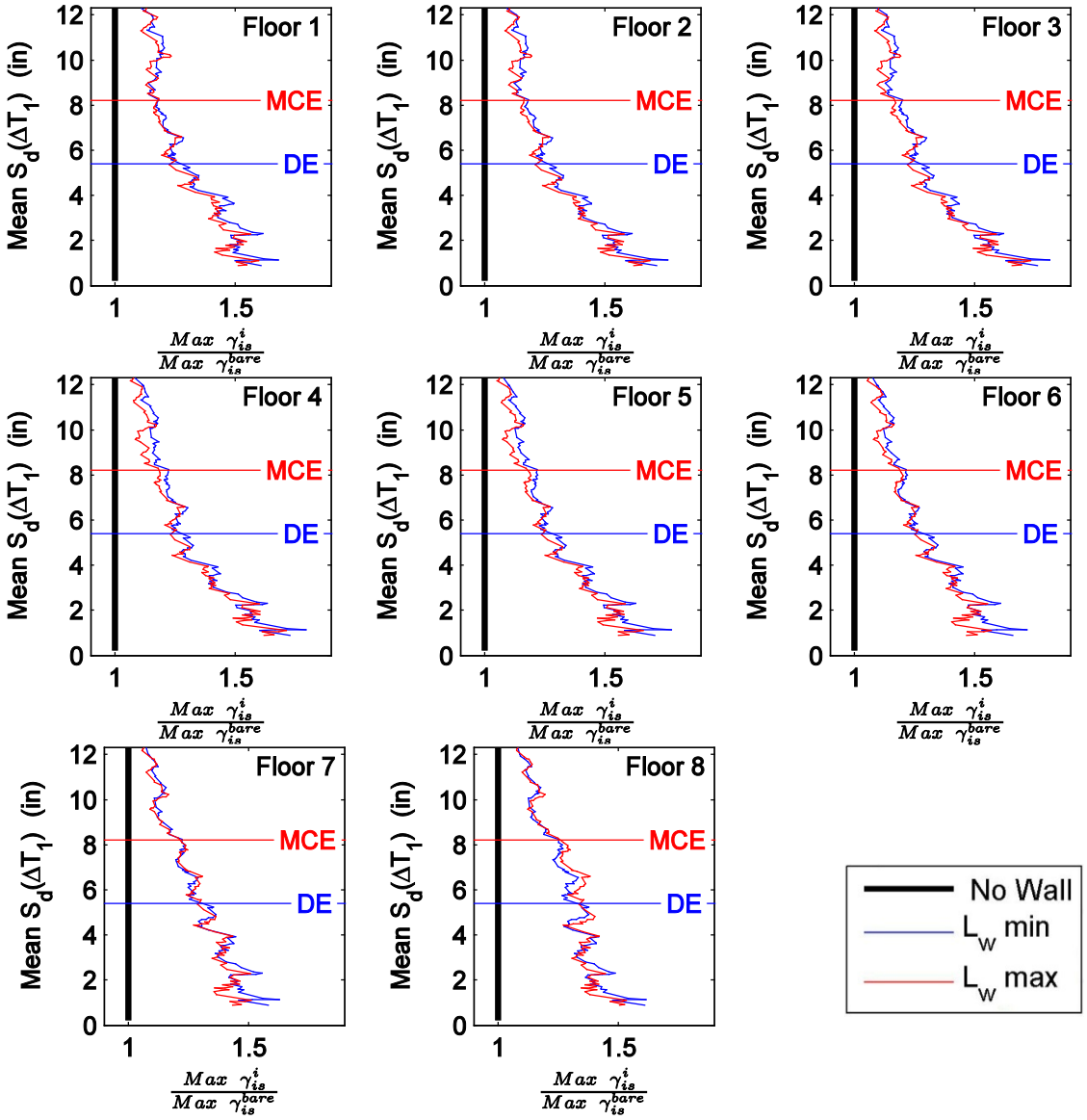

Figure C.12 Normalized maximum interstory drift moving average curves for RC-8 considering the cases of no wall, minimum wall length (mean) and maximum wall length against mean spectral displacement over the range of T_1.

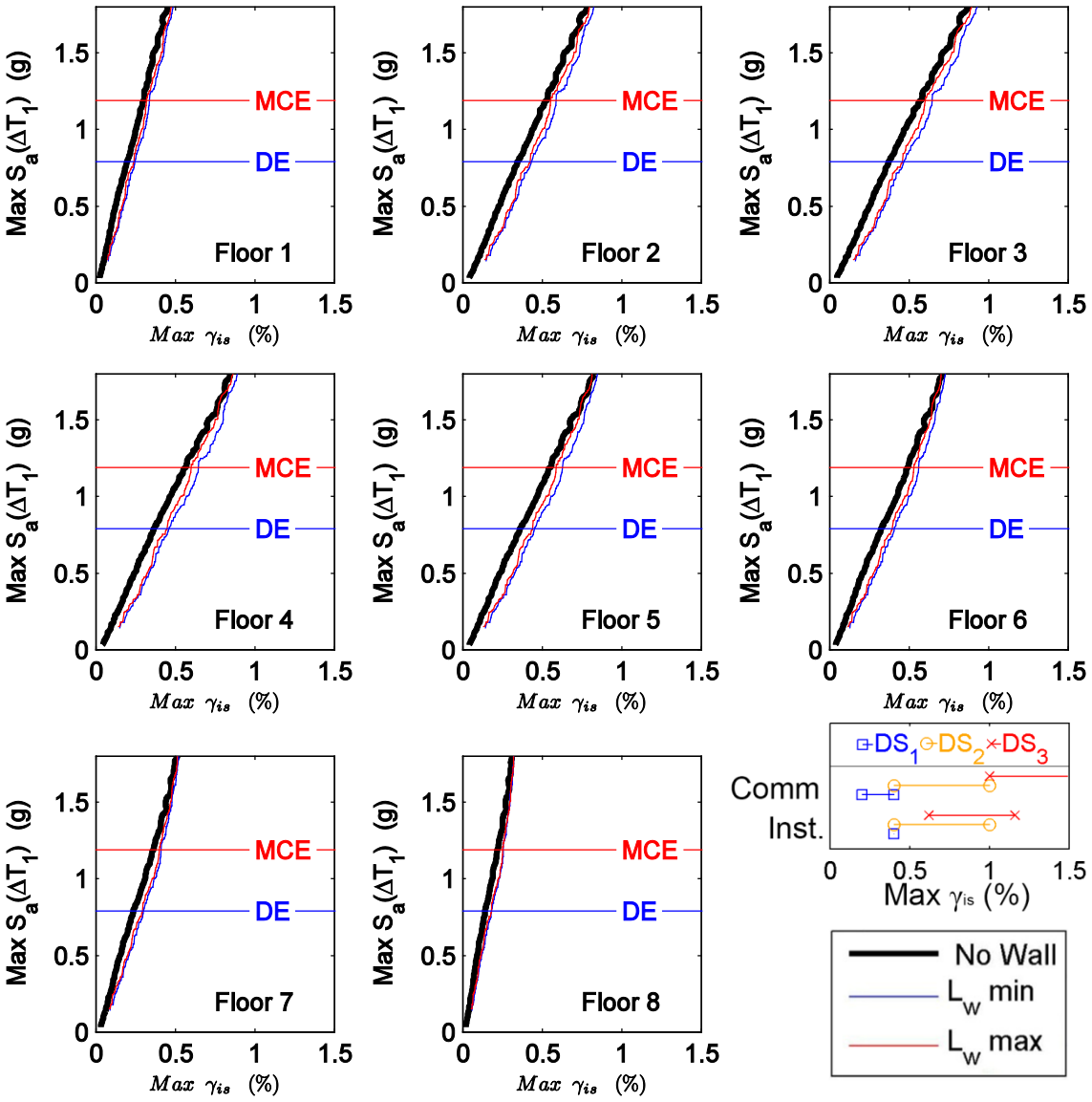

Figure C.13 Maximum interstory drift moving average curves for RC-8 considering the cases of no wall, minimum wall length (mean) and maximum wall length against maximum spectral acceleration over the range of T_1.

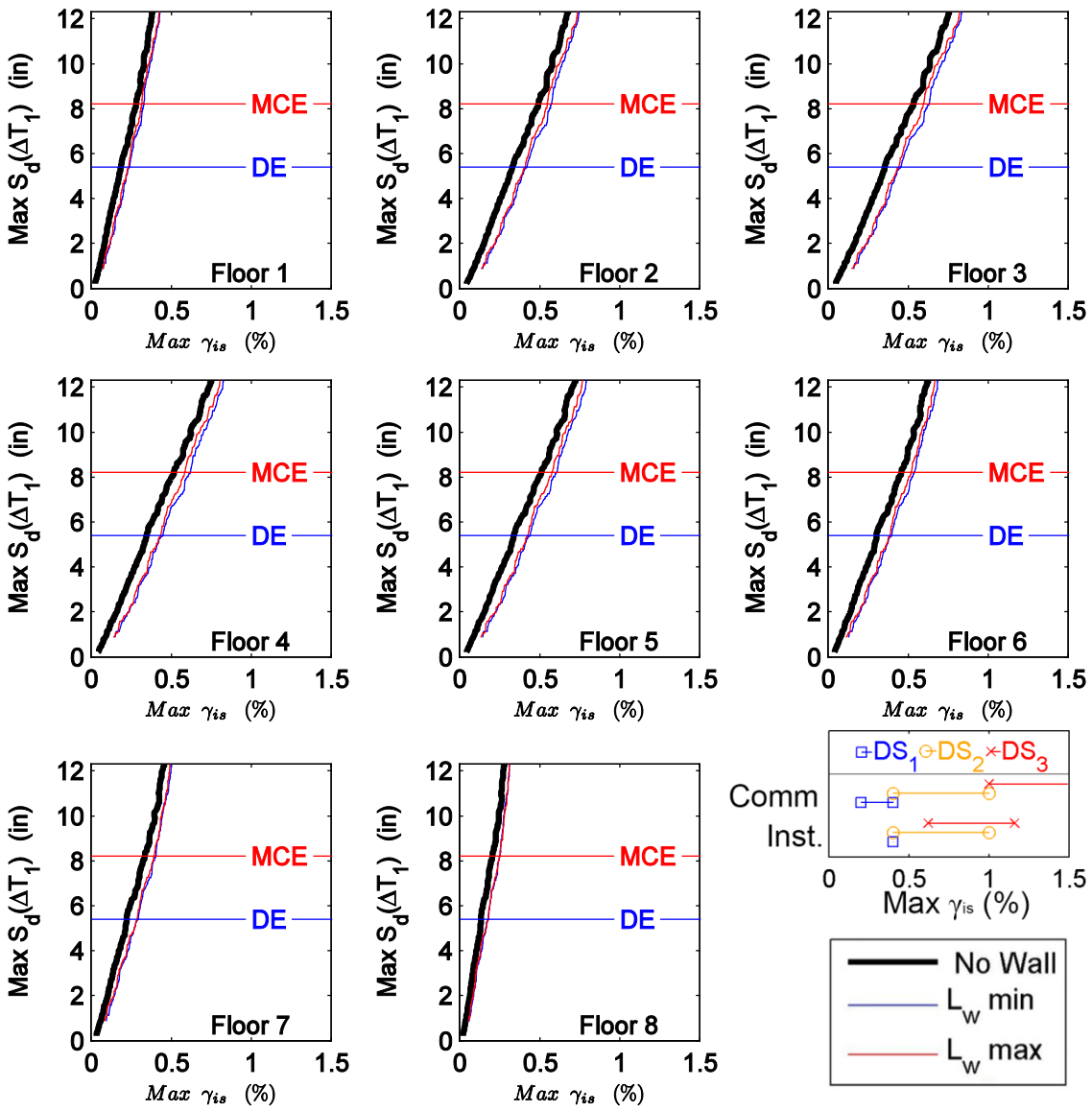

Figure C.14 Maximum interstory drift moving average curves for RC-8 considering the cases of no wall, minimum wall length (mean) and maximum wall length against maximum spectral displacement over the range of T_1.

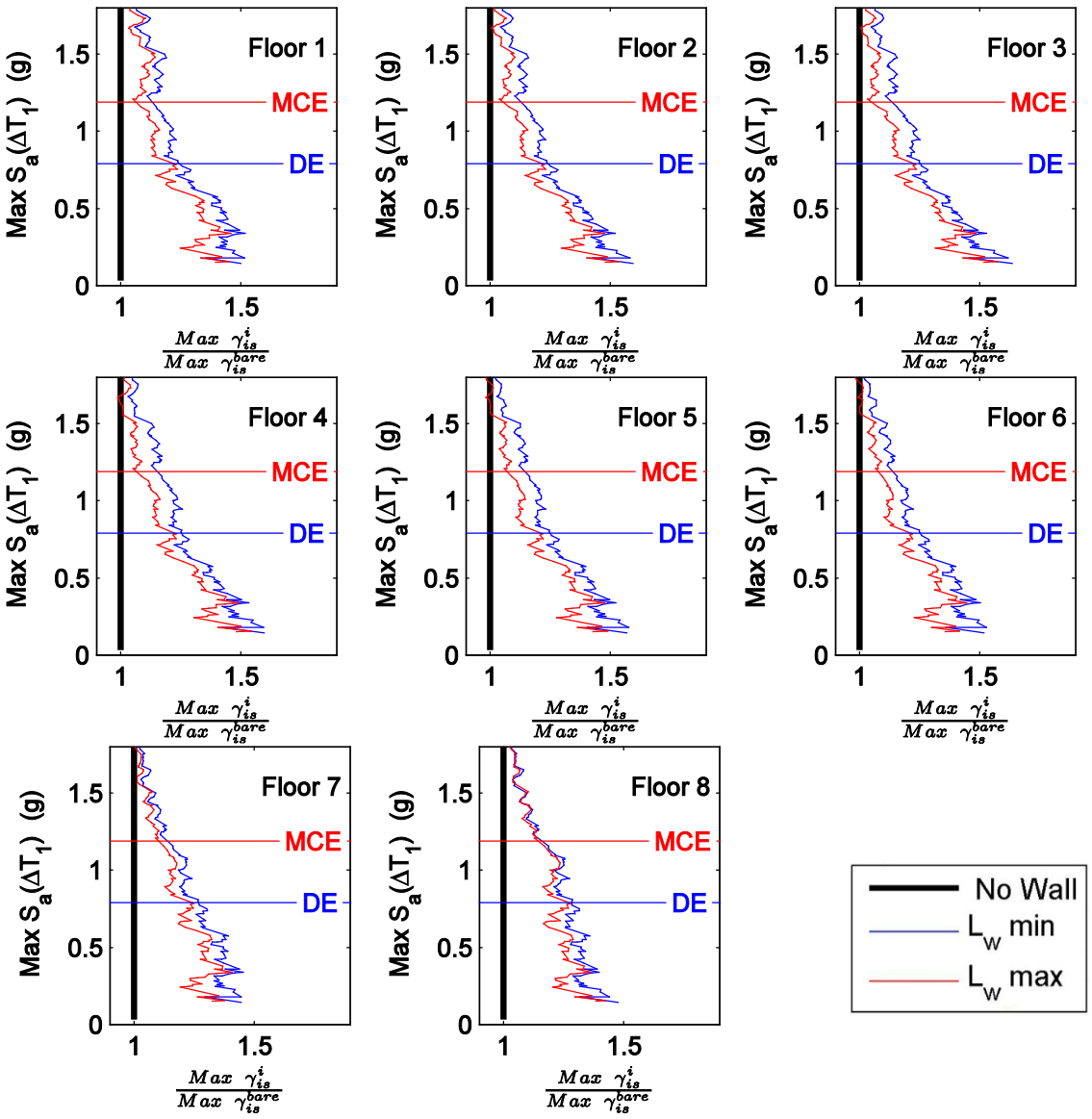

Figure C.15 Normalized maximum interstory drift moving average curves for RC-8 considering the cases of no wall, minimum wall length (mean) and maximum wall length against maximum spectral acceleration over the range of T_1.

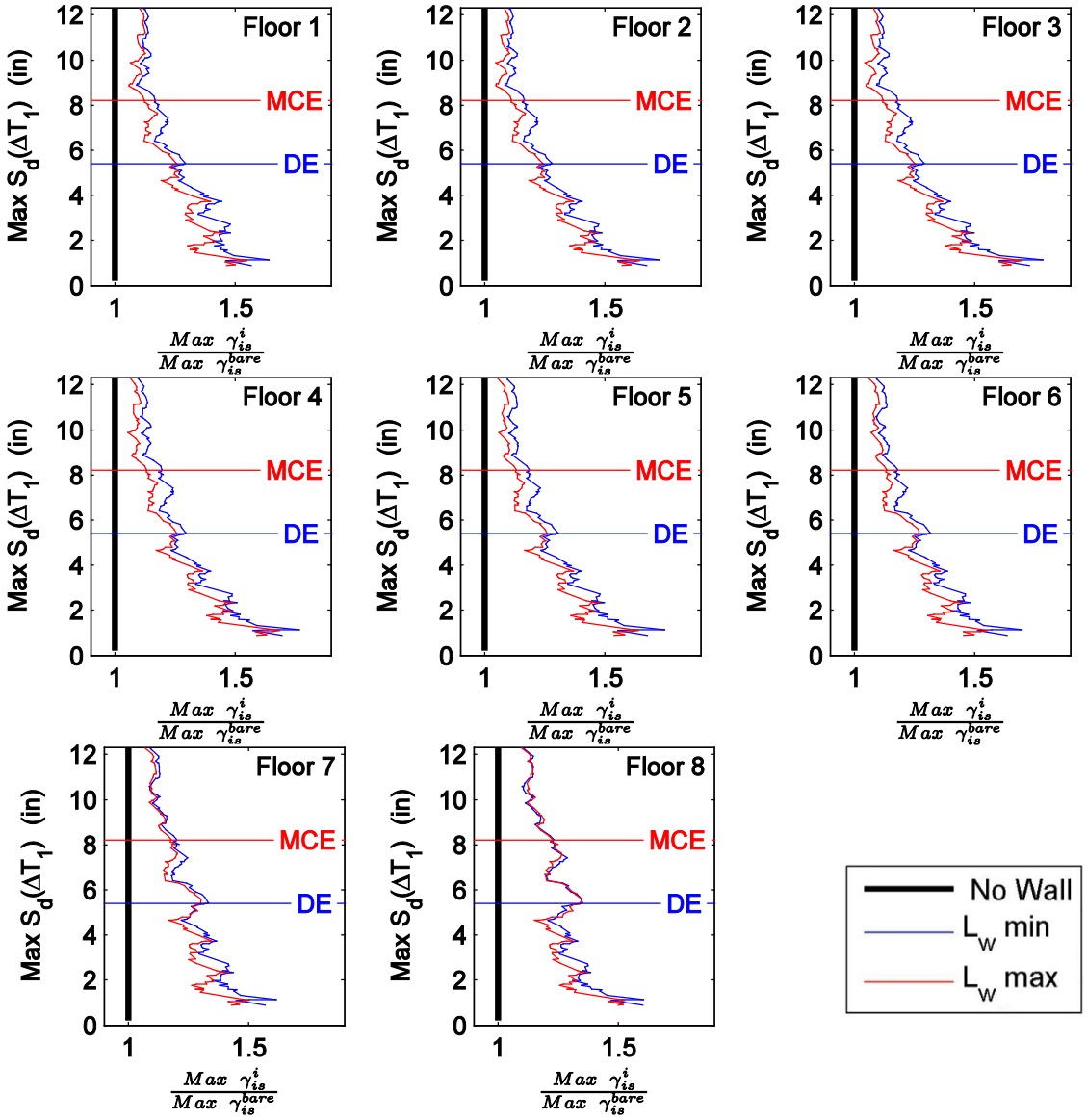

Figure C.16 Normalized maximum interstory drift moving average curves for RC-8 considering the cases of no wall, minimum wall length (mean) and maximum wall length against maximum spectral acceleration over the range of T_1.

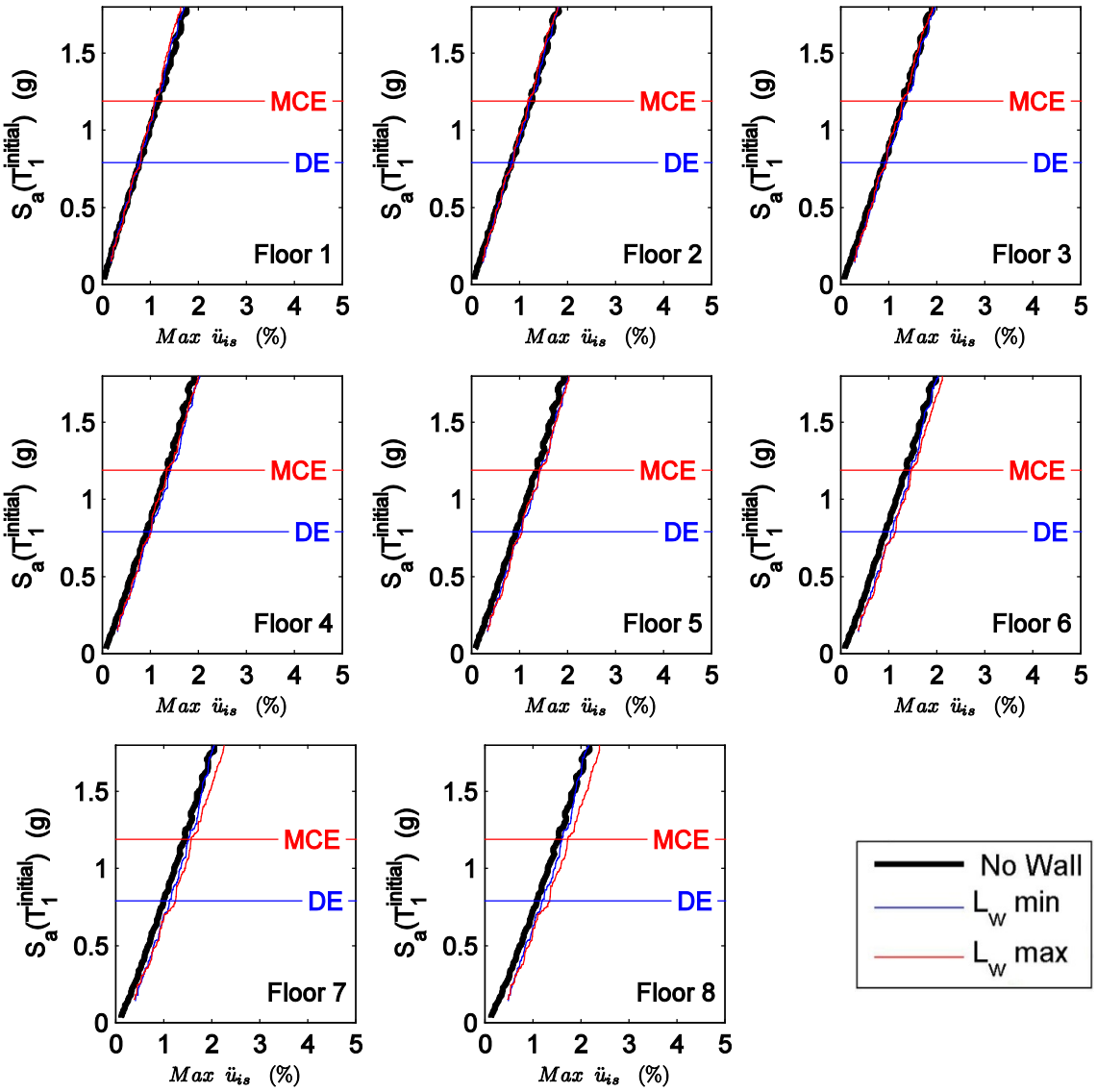

Figure C.17 Maximum floor level acceleration moving average curves for RC-8 considering the cases of no wall, minimum wall length (mean) and maximum wall length against spectral acceleration at T_1 (uncracked).

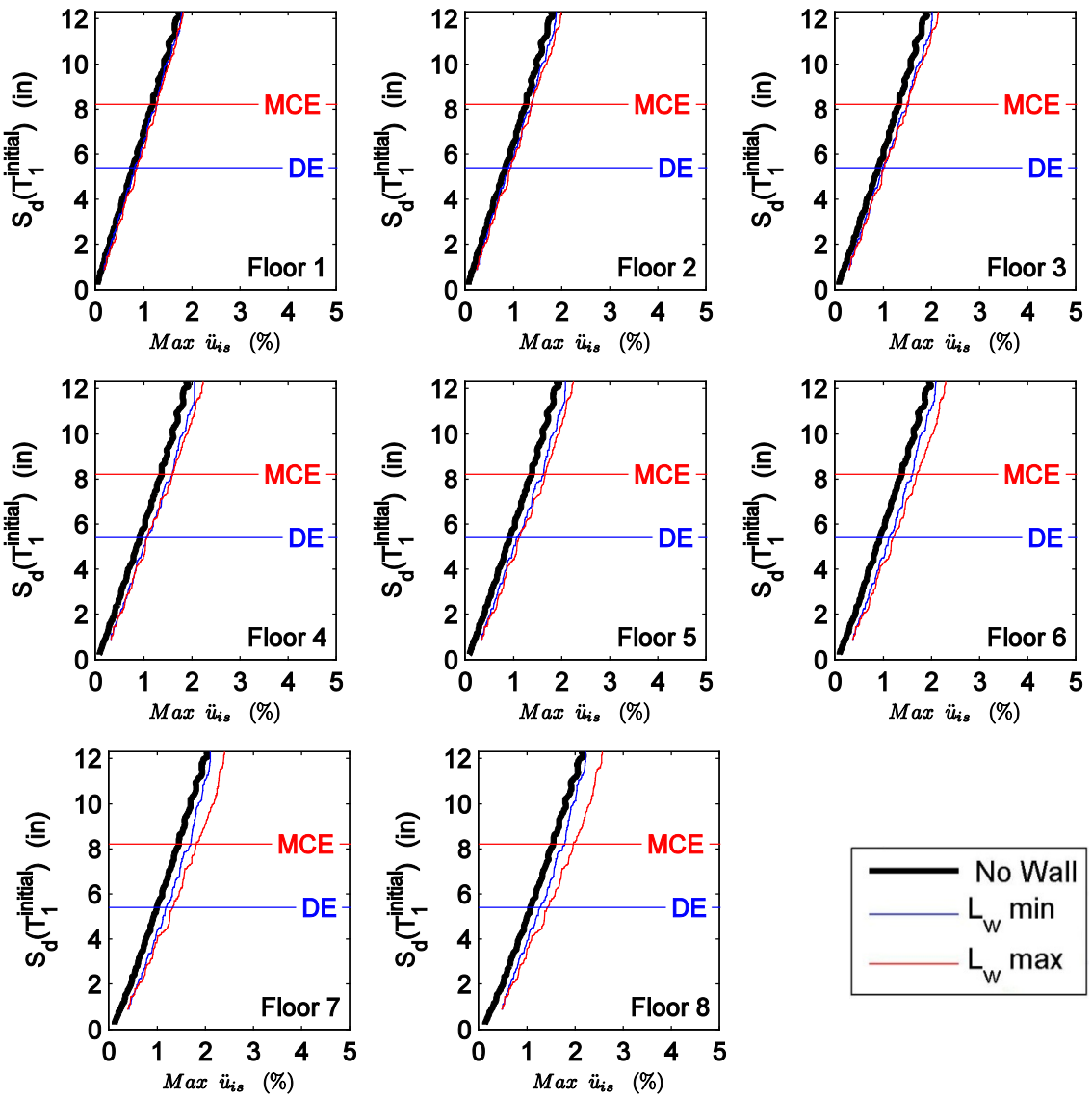

Figure C.18 Maximum floor level acceleration moving average curves for RC-8 considering the cases of no wall, minimum wall length (mean) and maximum wall length against spectral displacement at T_1 (uncracked).

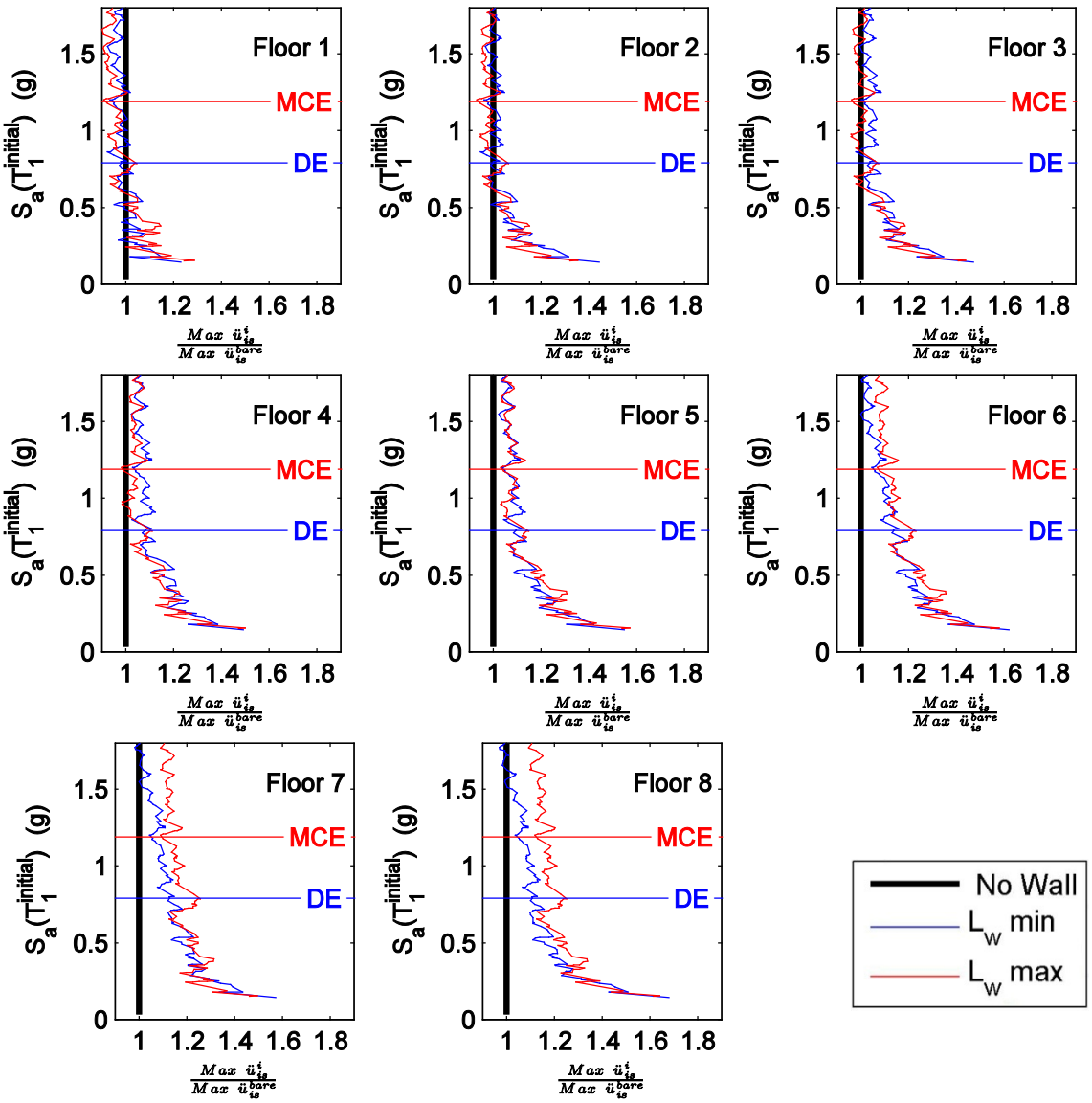

Figure C.19 Normalized maximum floor level acceleration moving average curves for RC-8 considering the cases of no wall, minimum wall length (mean) and maximum wall length against spectral acceleration at T_1 (uncracked).

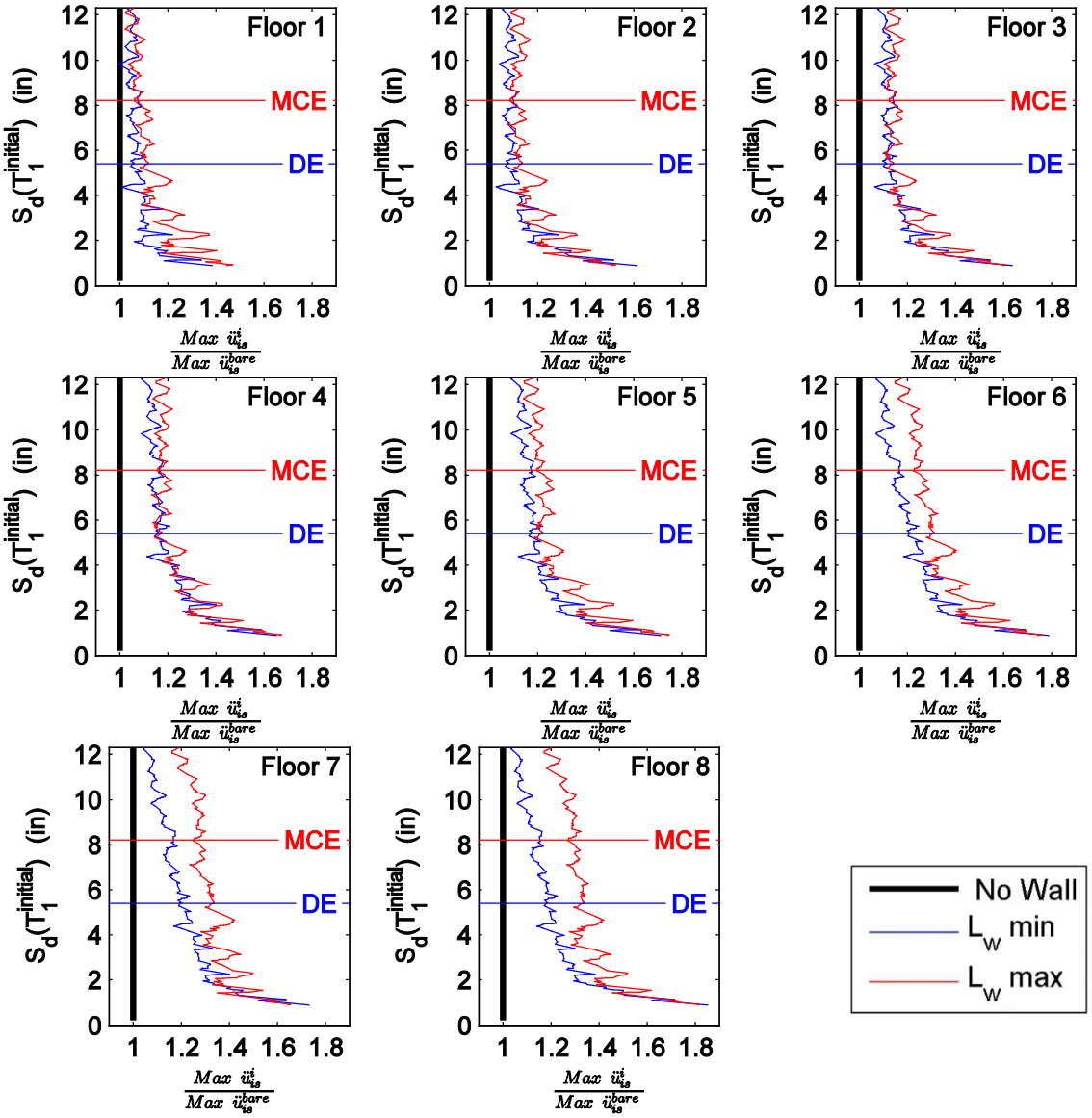

Figure C.20 Normalized maximum floor level acceleration moving average curves for RC-8 considering the cases of no wall, minimum wall length (mean) and maximum wall length against spectral displacement at T_1 (uncracked).

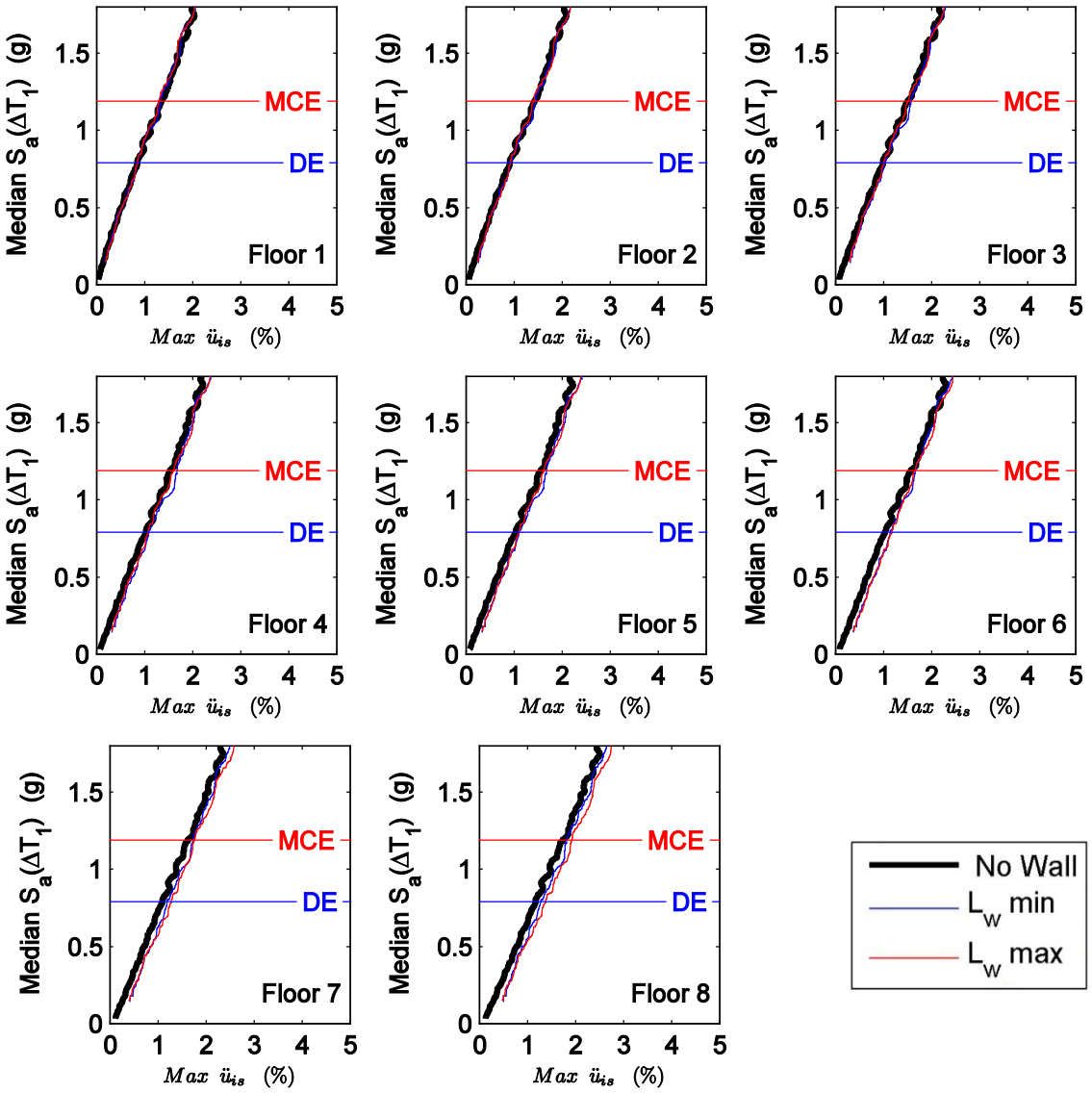

Figure C.21 Maximum floor level acceleration moving average curves for RC-8 considering the cases of no wall, minimum wall length (mean) and maximum wall length against median spectral acceleration over the range of T_1.

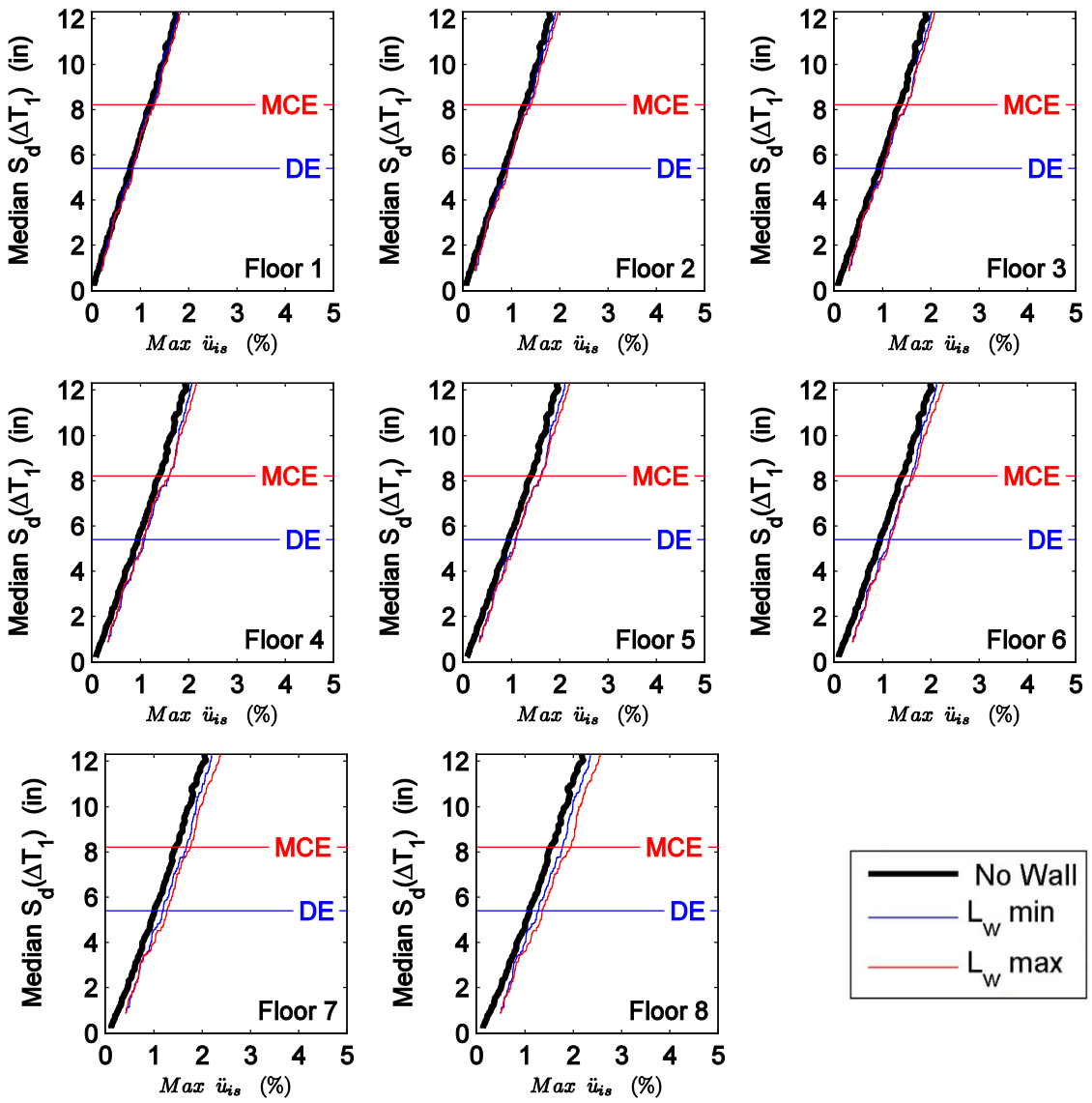

Figure C.22 Maximum floor level acceleration moving average curves for RC-8 considering the cases of no wall, minimum wall length (mean) and maximum wall length against median spectral displacement over the range of T_1.

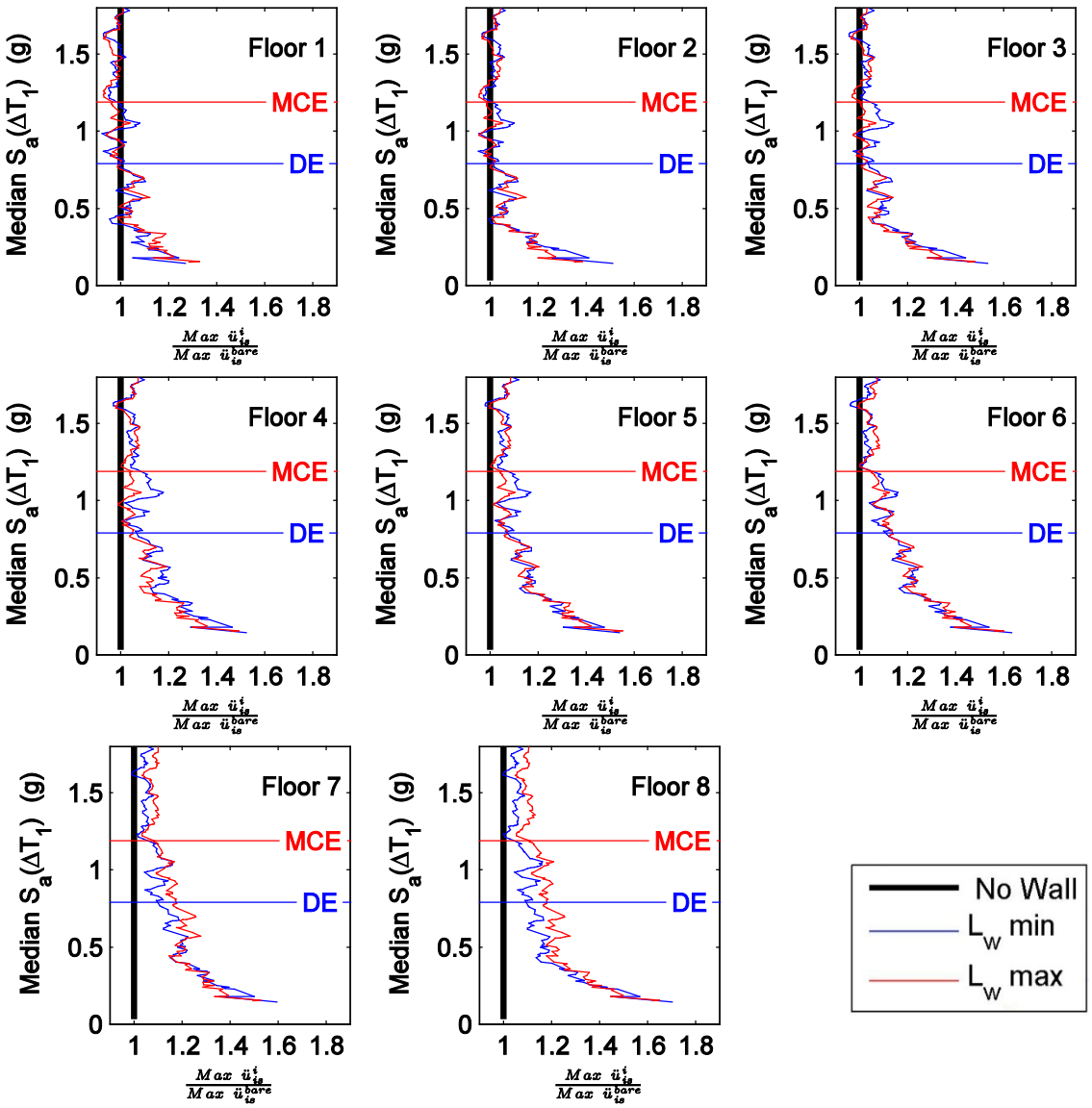

Figure C.23 Normalized maximum floor level acceleration moving average curves for RC-8 considering the cases of no wall, minimum wall length (mean) and maximum wall length against median spectral acceleration over the range of T_1.

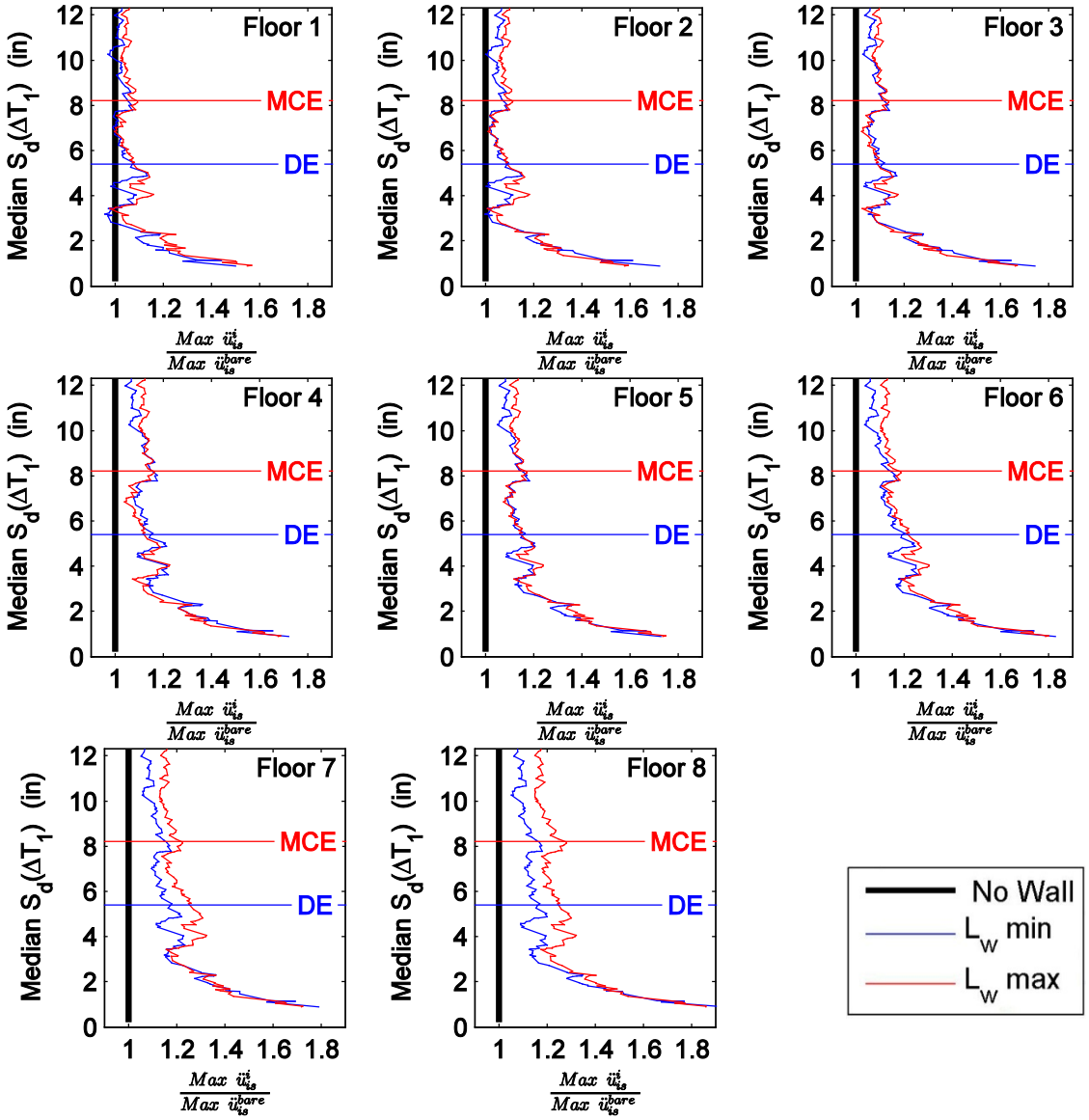

Figure C.24 Normalized maximum floor level acceleration moving average curves for RC-8 considering the cases of no wall, minimum wall length (mean) and maximum wall length against median spectral displacement over the range of T_1.

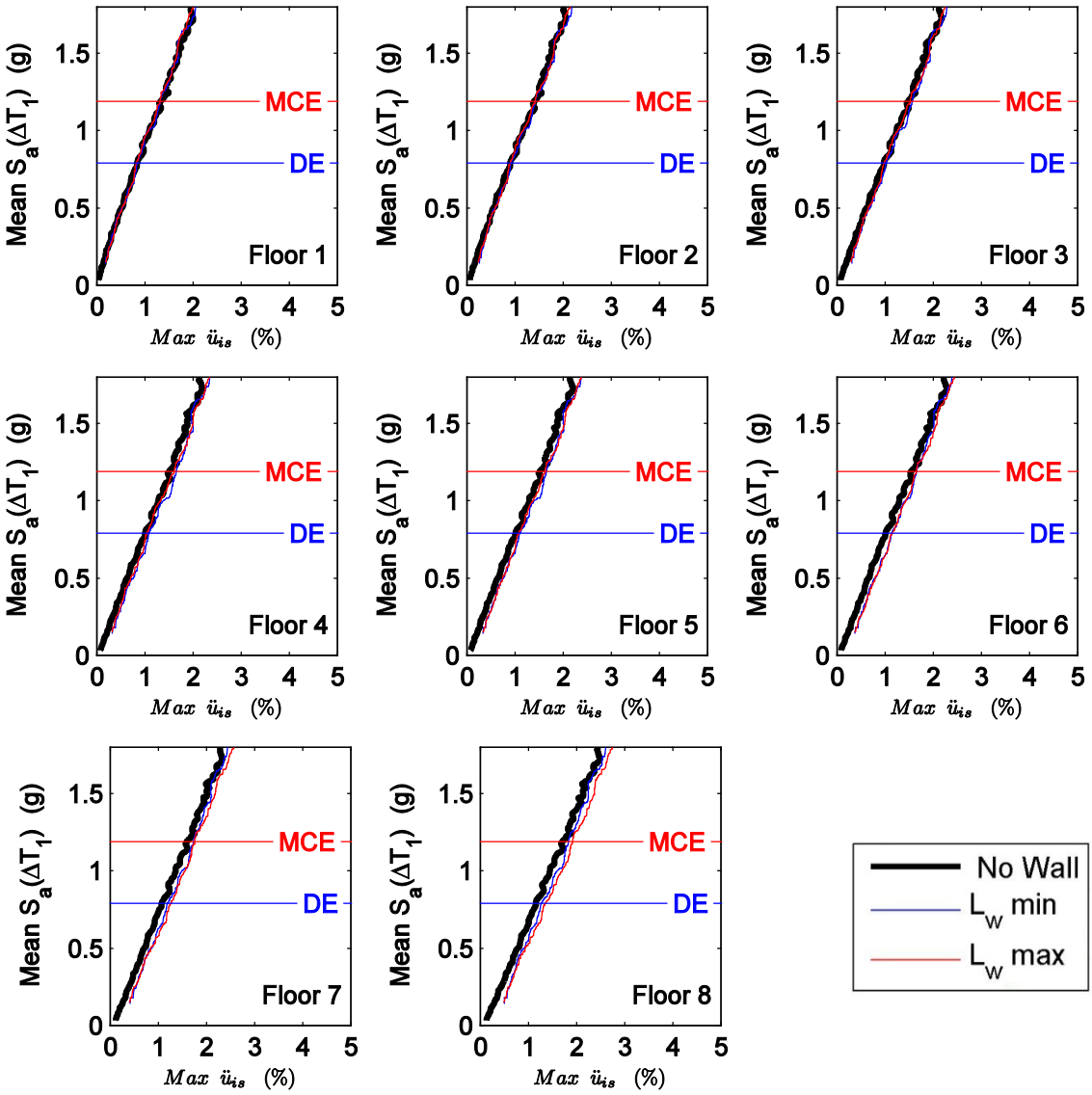

Figure C.25 Maximum floor level acceleration moving average curves for RC-8 considering the cases of no wall, minimum wall length (mean) and maximum wall length against mean spectral acceleration over the range of T_1.

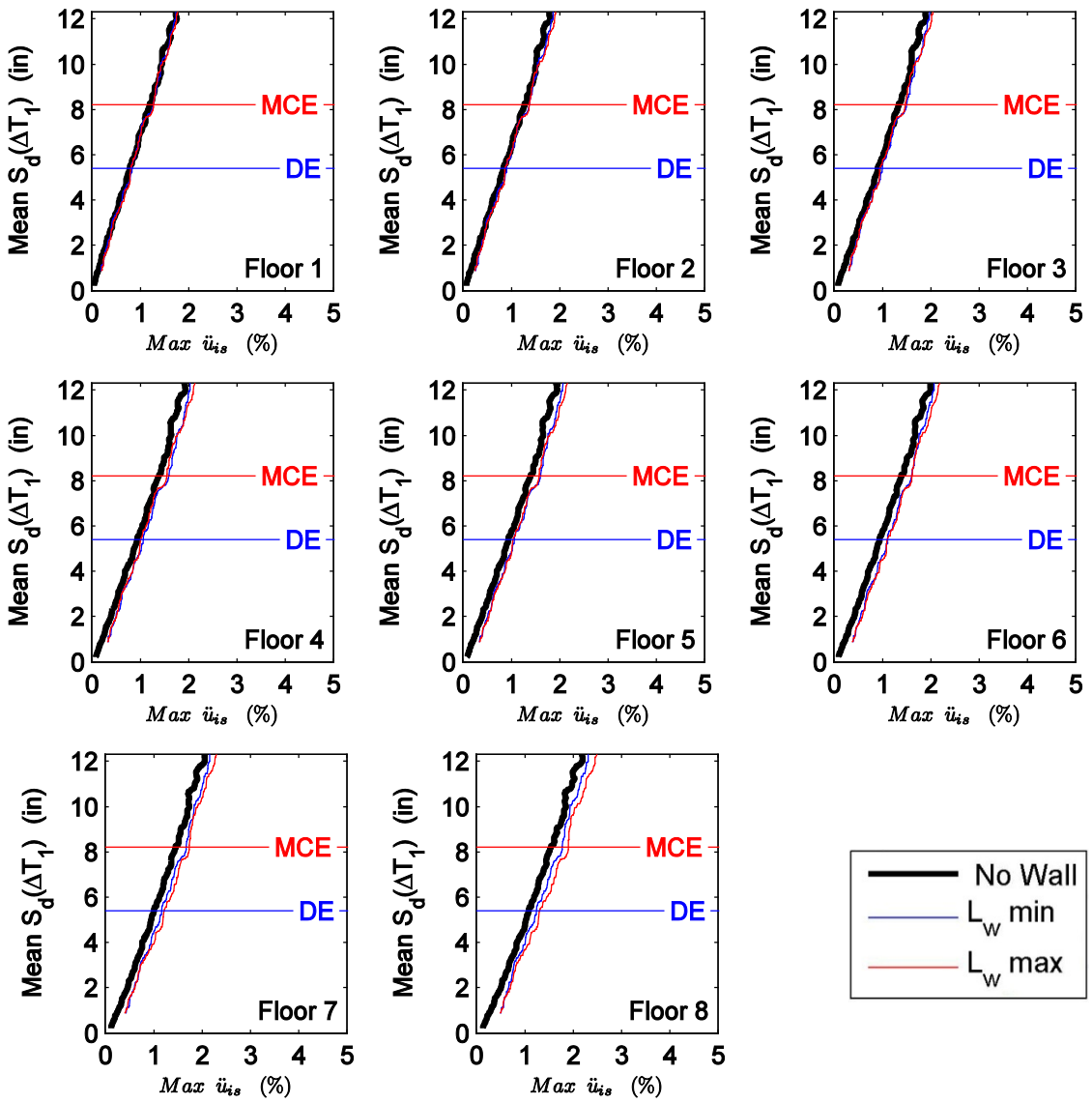

Figure C.26 Maximum floor level acceleration moving average curves for RC-8 considering the cases of no wall, minimum wall length (mean) and maximum wall length against mean spectral displacement over the range of T_1.

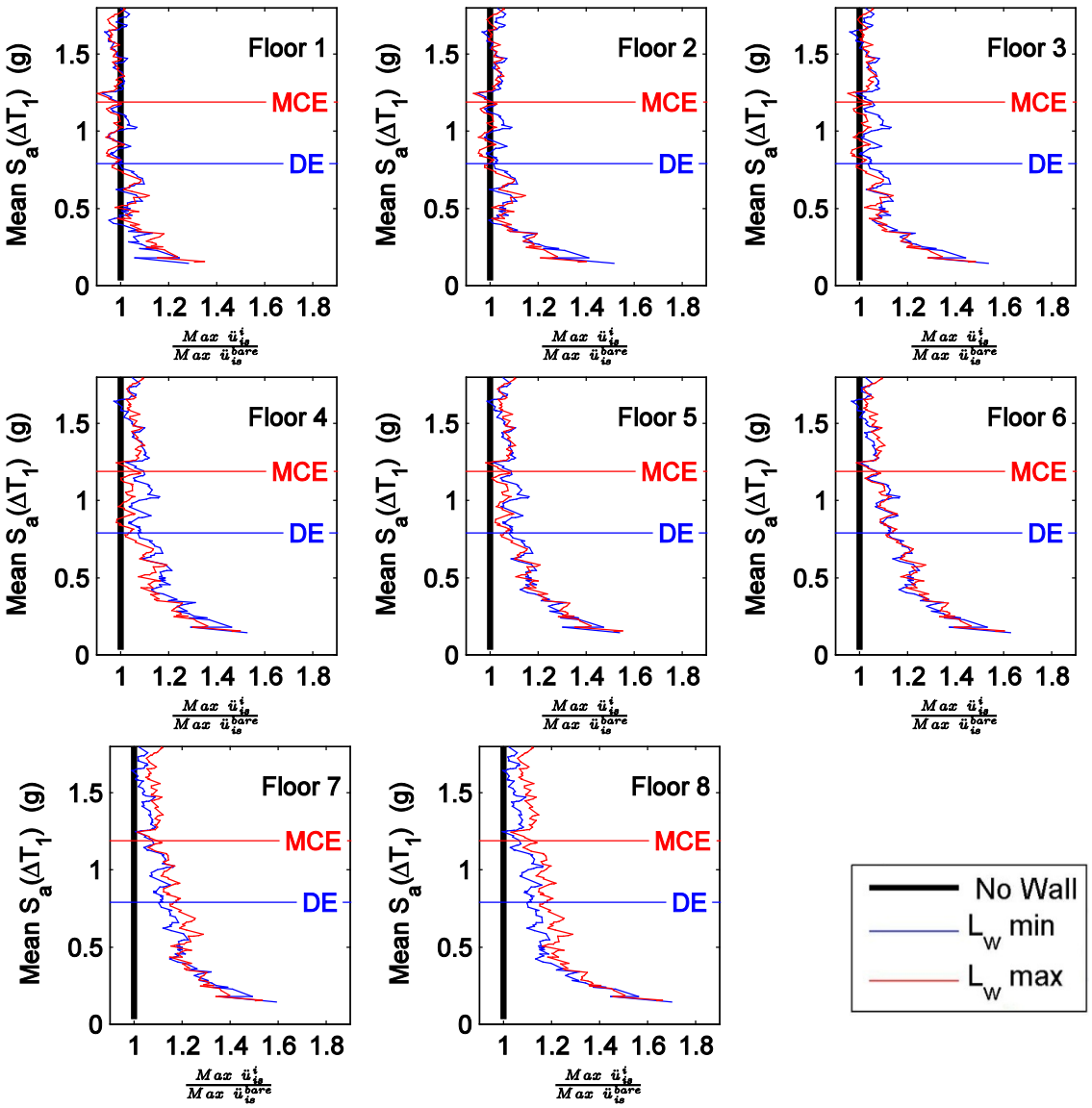

Figure C.27 Normalized maximum floor level acceleration moving average curves for RC-8 considering the cases of no wall, minimum wall length (mean) and maximum wall length against mean spectral acceleration over the range of T_1.

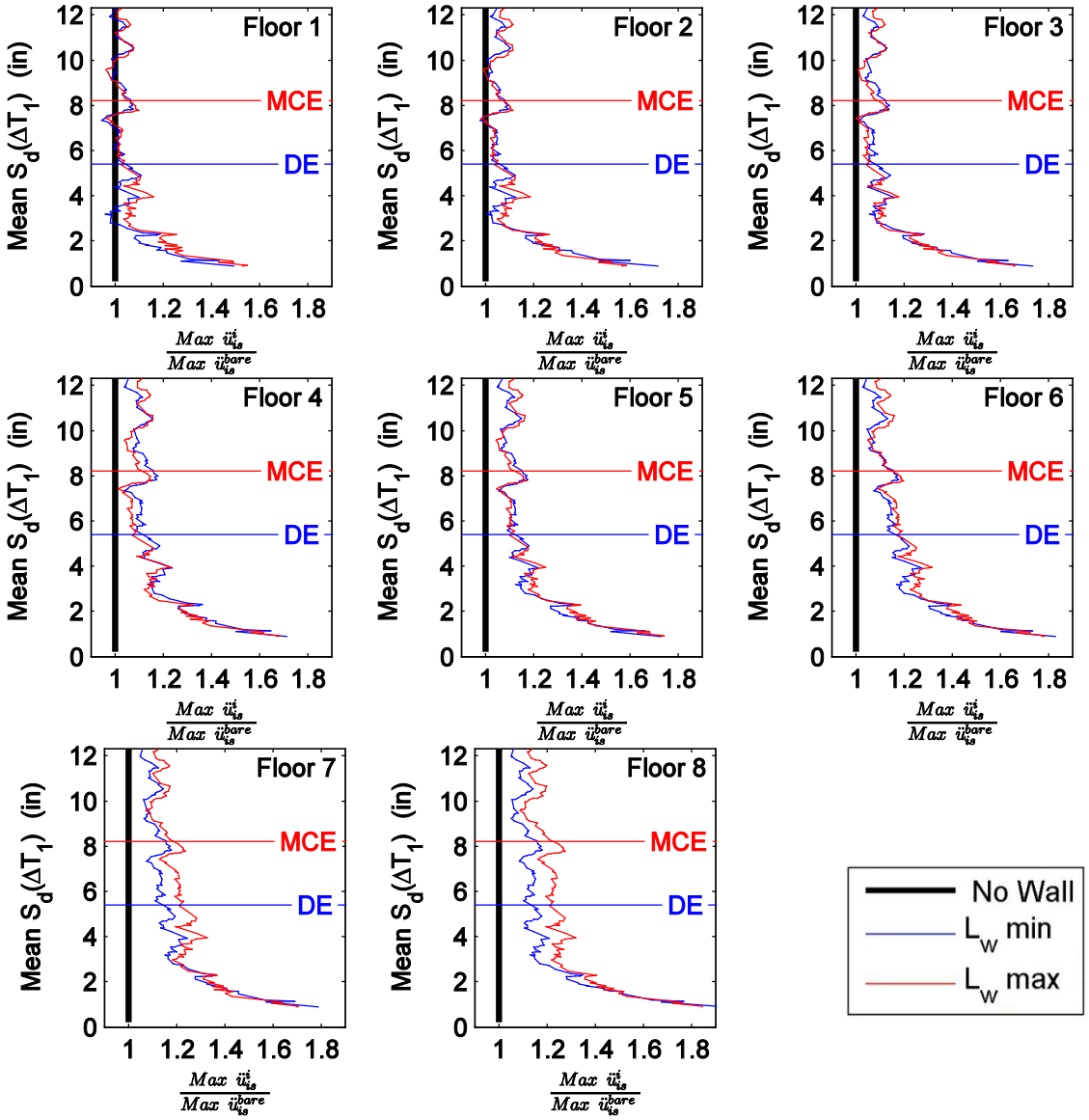

Figure C.28 Normalized maximum floor level acceleration moving average curves for RC-8 considering the cases of no wall, minimum wall length (mean) and maximum wall length against mean spectral displacement over the range of T_1.

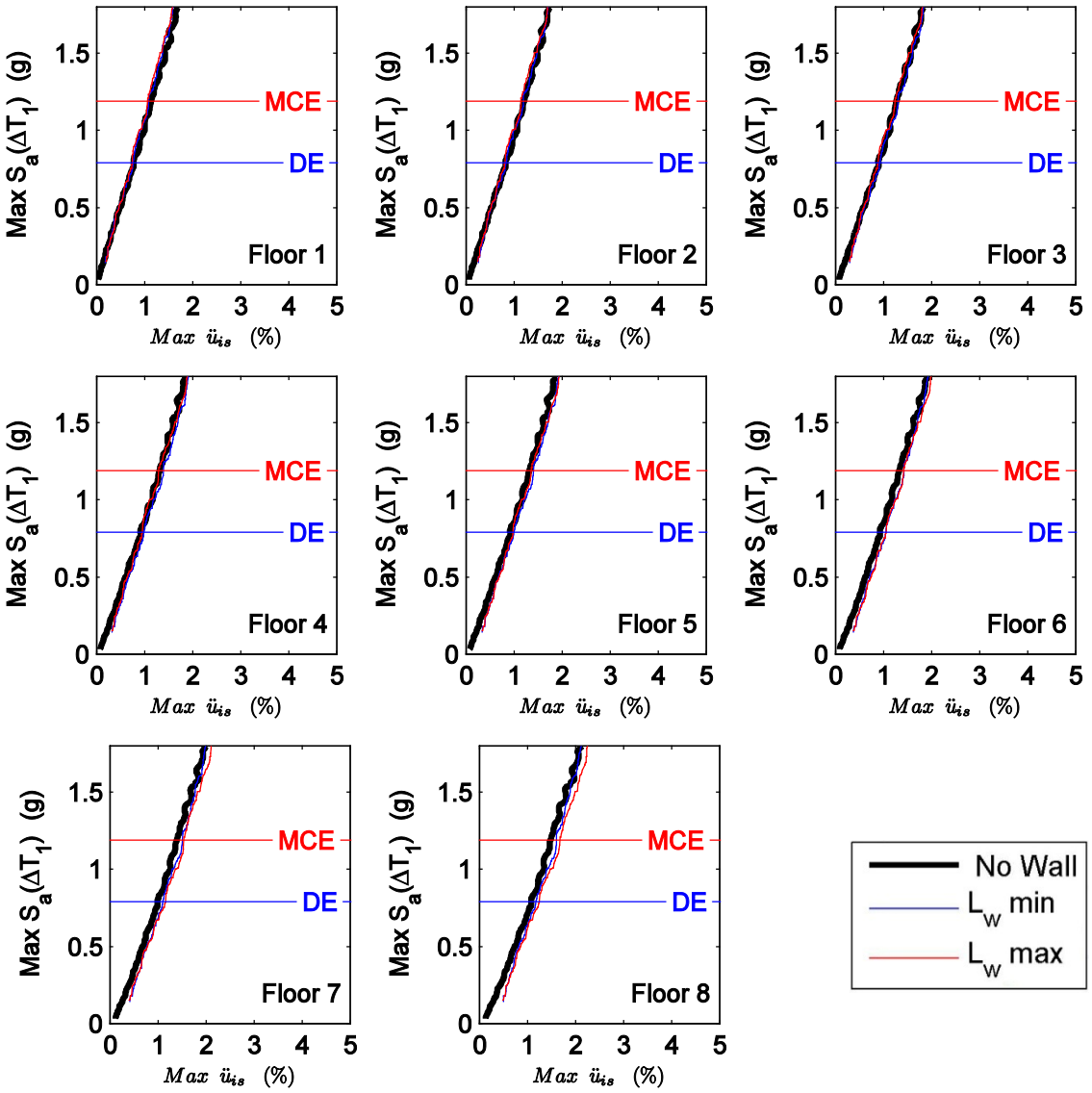

Figure C.29 Maximum floor level acceleration moving average curves for RC-8 considering the cases of no wall, minimum wall length (mean) and maximum wall length against maximum spectral acceleration over the range of T_1.

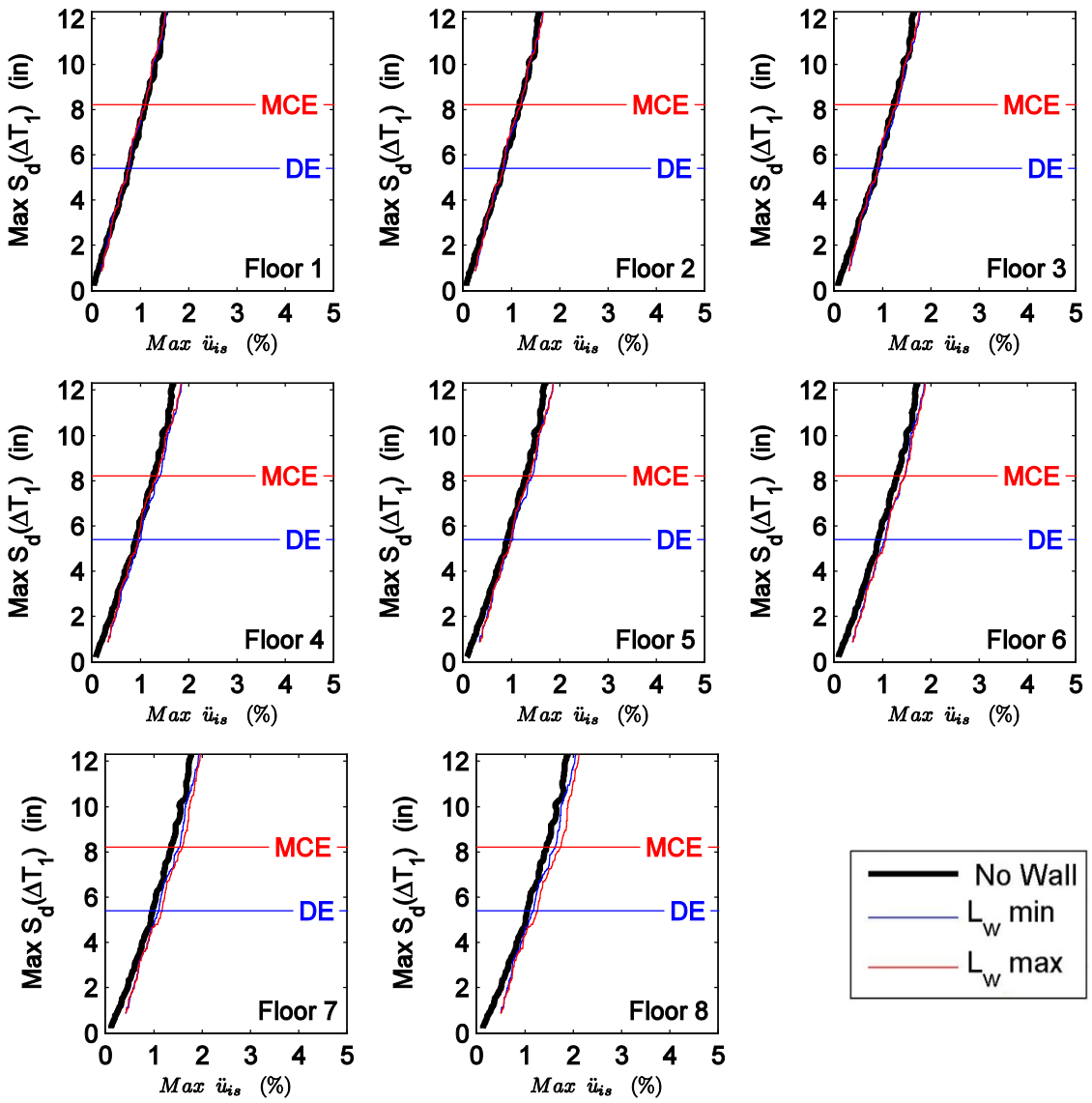

Figure C.30 Maximum floor level acceleration moving average curves for RC-8 considering the cases of no wall, minimum wall length (mean) and maximum wall length against maximum spectral displacement over the range of T_1.

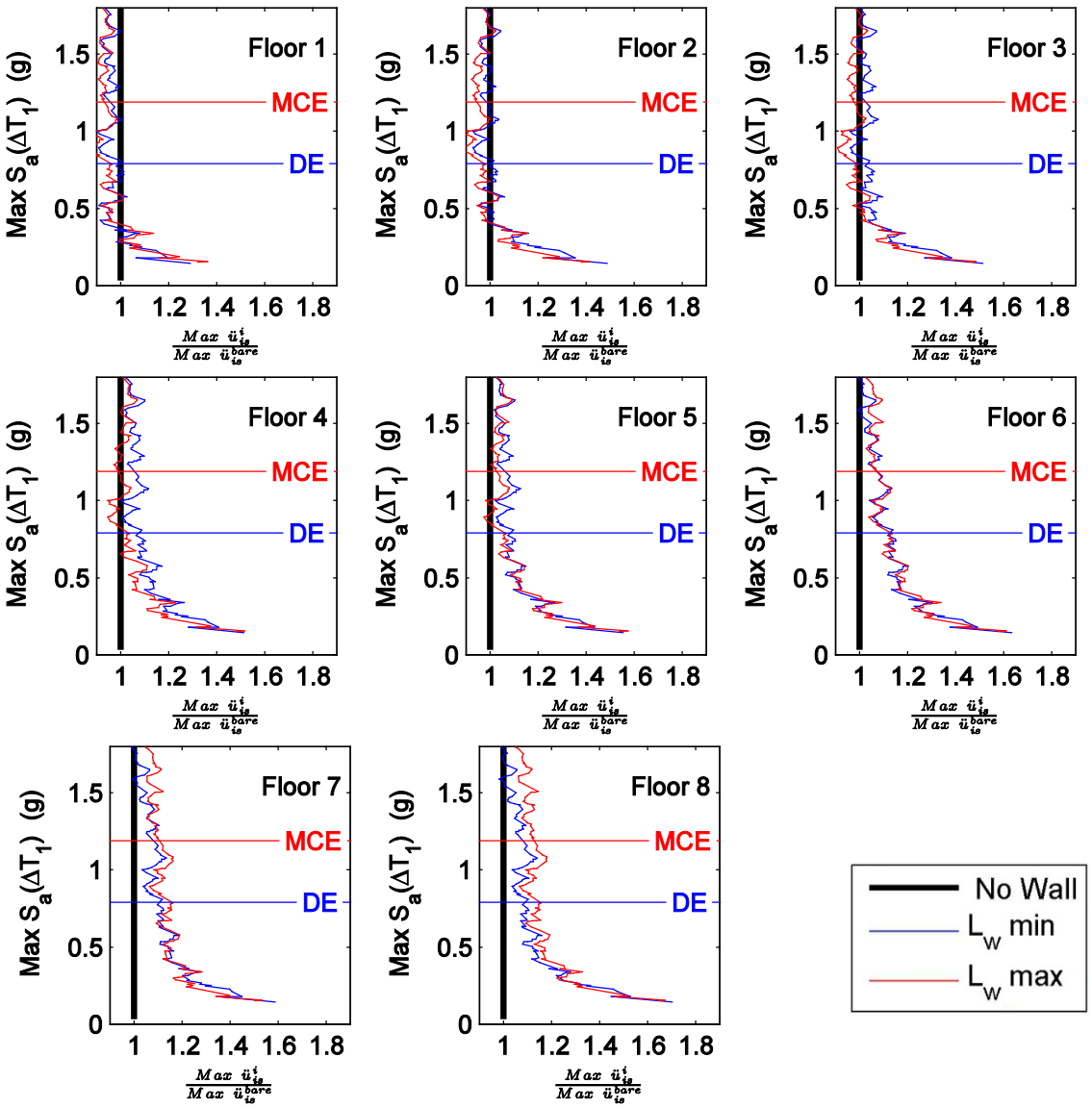

Figure C.31 Normalized maximum floor level acceleration moving average curves for RC-8 considering the cases of no wall, minimum wall length (mean) and maximum wall length against maximum spectral acceleration over the range of T_1.

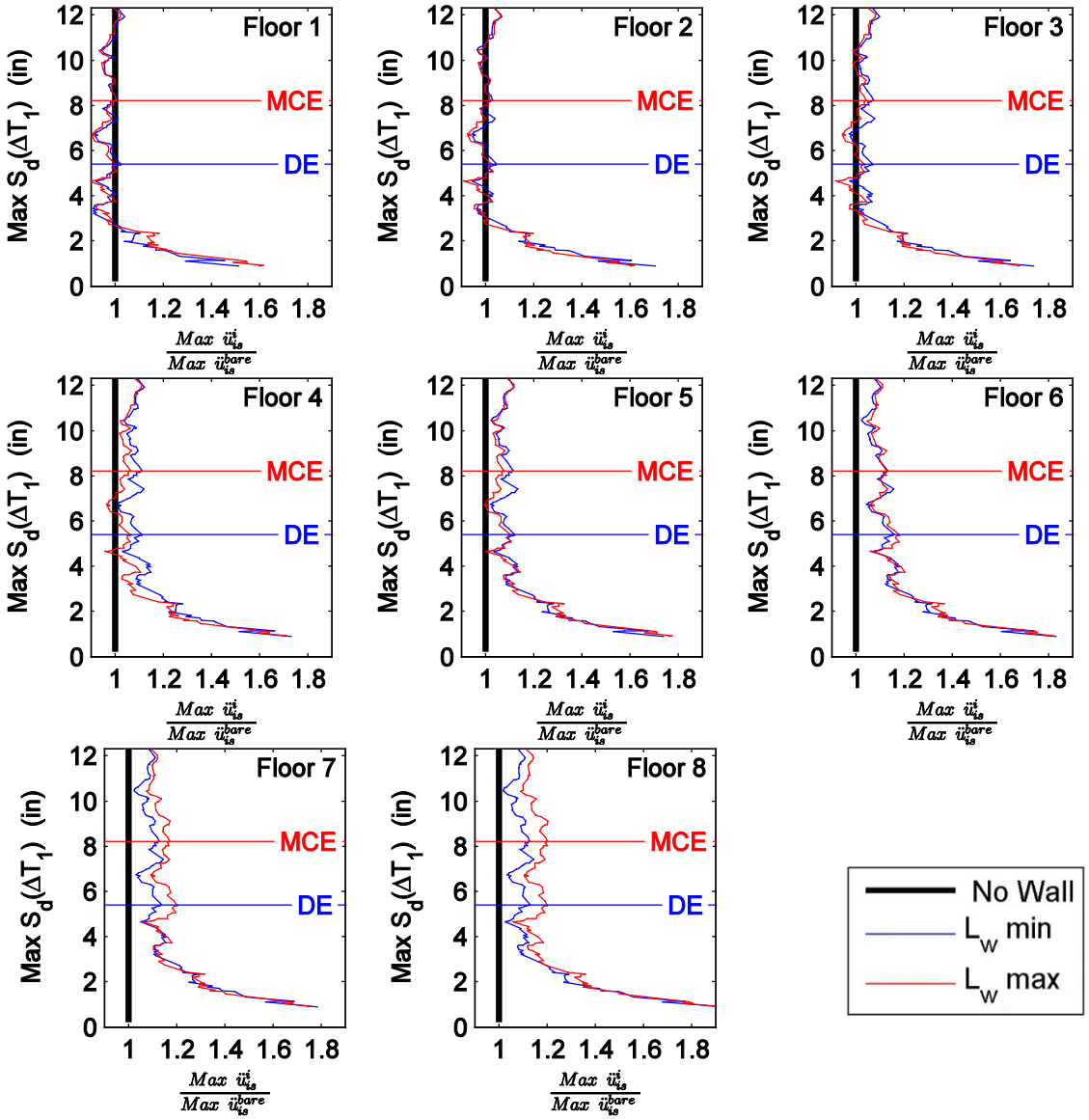

Figure C.32 Normalized maximum floor level acceleration moving average curves for RC-8 considering the cases of no wall, minimum wall length (mean) and maximum wall length against maximum spectral displacement over the range of T_1.

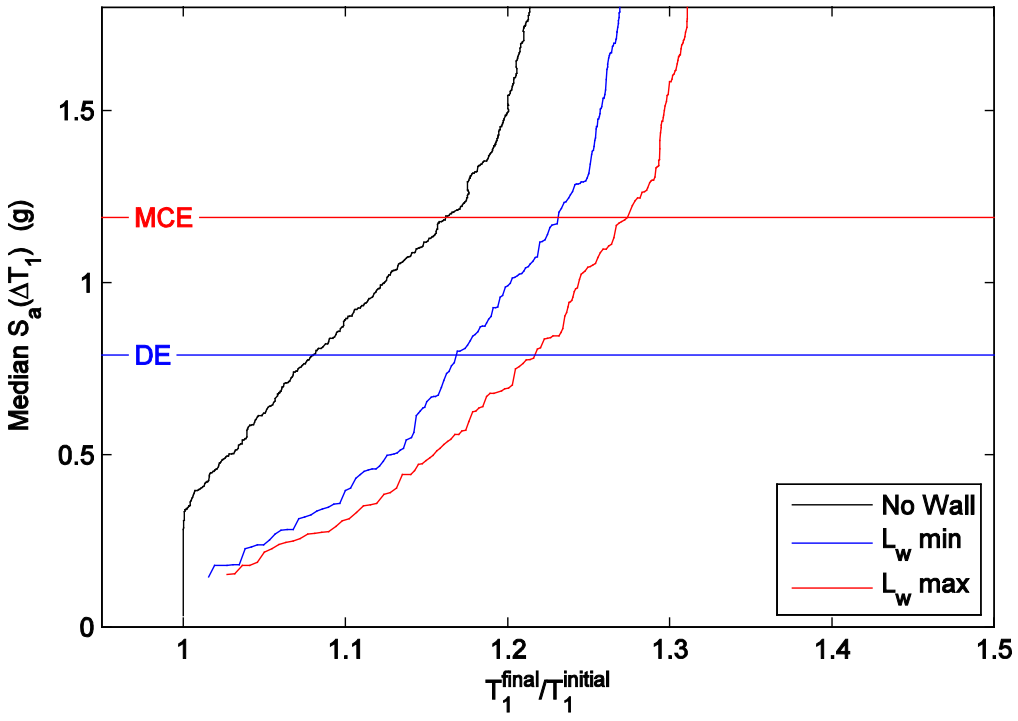

Figure C.33 Period elongation moving average curves for RC-8 considering the cases of no wall, minimum wall length (mean) and maximum wall length against median spectral acceleration over the range of T_1.

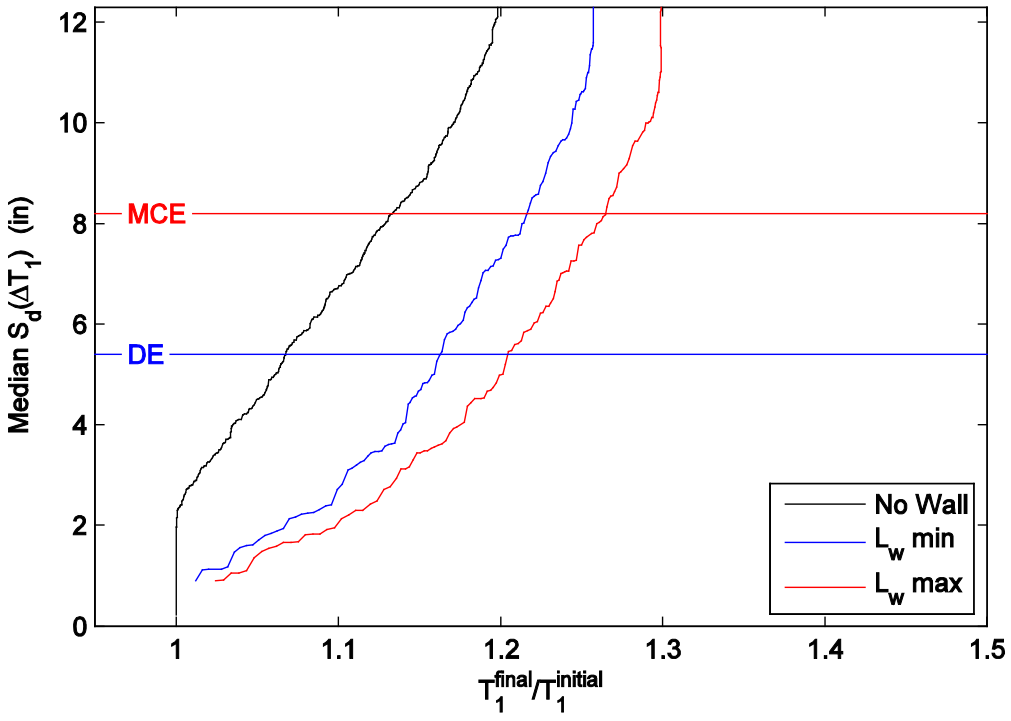

Figure C.34 Period elongation moving average curves for RC-8 considering the cases of no wall, minimum wall length (mean) and maximum wall length against median spectral displaccement over the range of T_1.

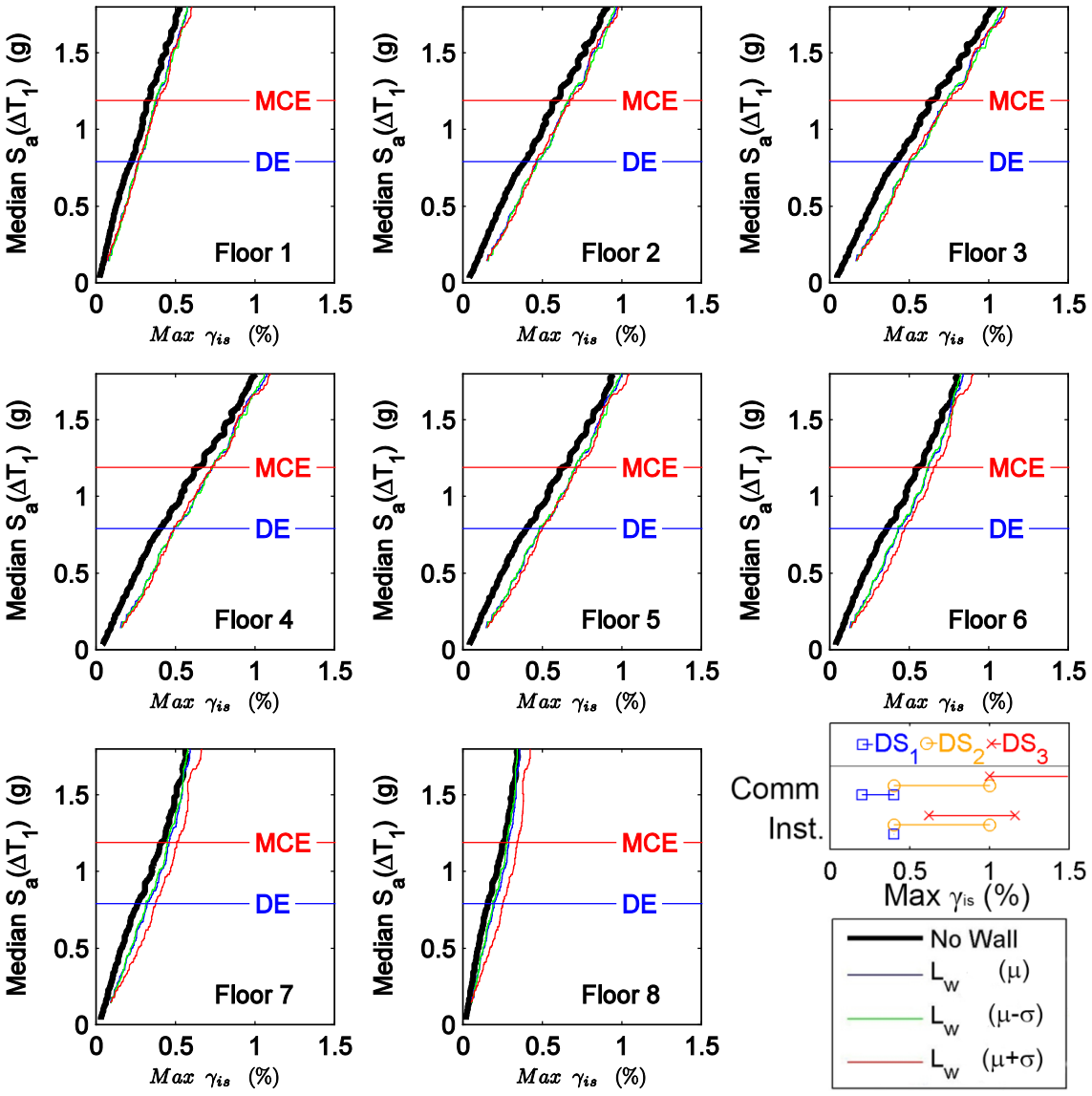

Figure C.35 Maximum interstory drift moving average curves for RC-8 considering the cases of wall variability: no wall, minimum wall length (mean), minimum wall length (mean-standard deviation), and minimum wall length (mean+standard deviation) against median spectral acceleration over the range of T_1.

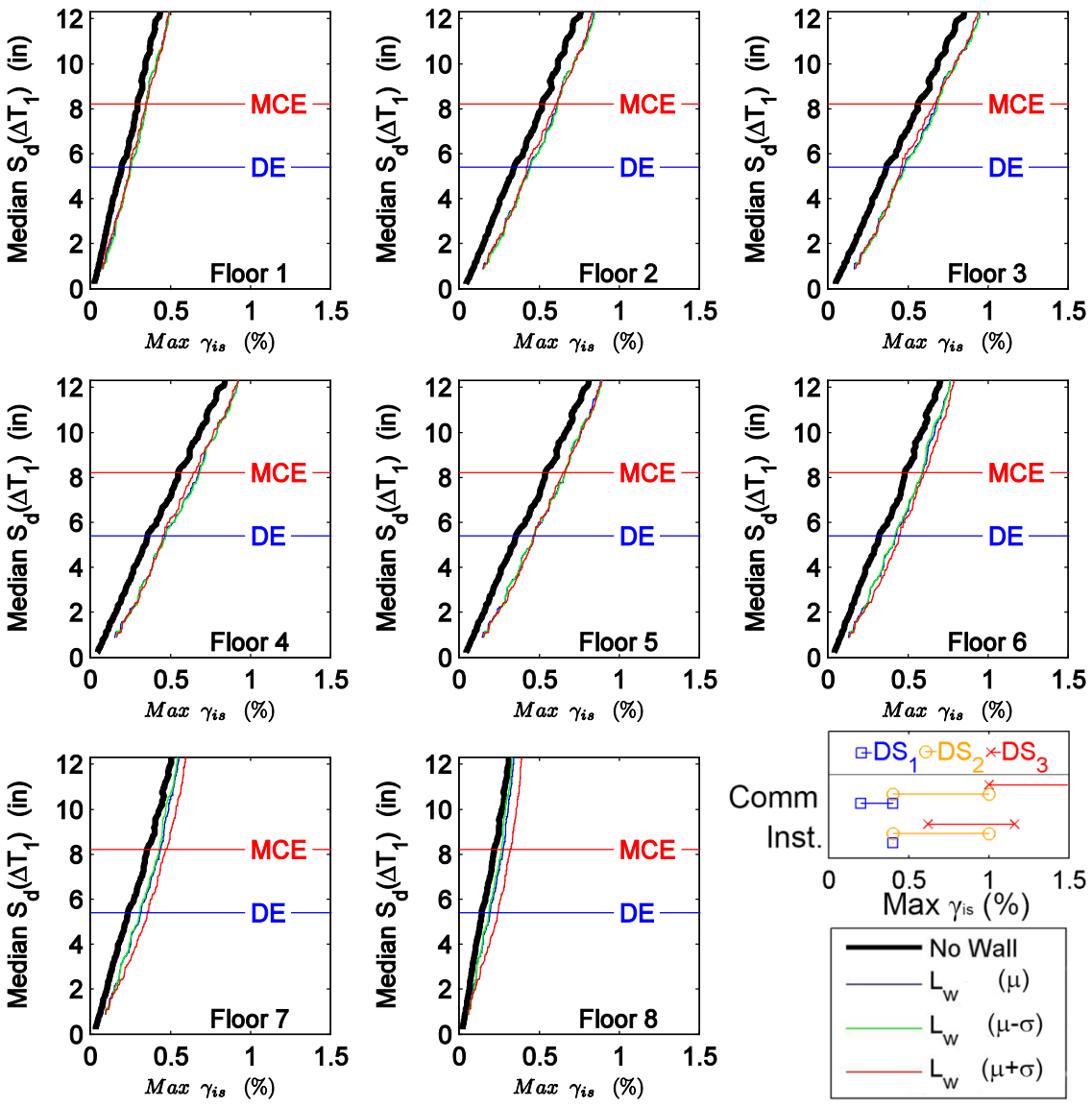

Figure C.36 Maximum interstory drift moving average curves for RC-8 considering the cases of wall variability: no wall, minimum wall length (mean), minimum wall length (mean-standard deviation), and minimum wall length (mean+standard deviation) against median spectral displacement over the range of T_1.

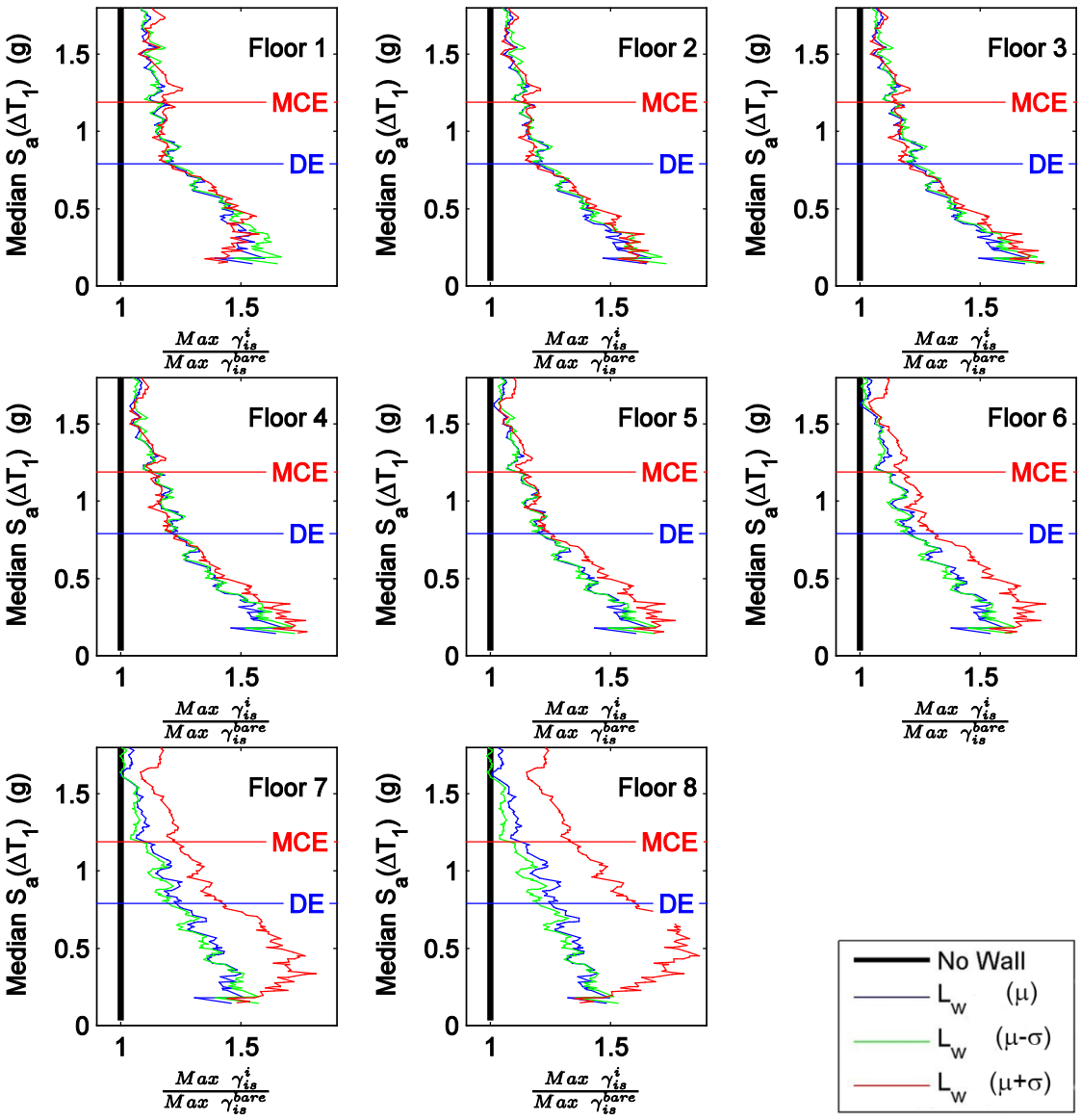

Figure C.37 Normalized maximum interstory drift moving average curves for RC-8 considering the cases of wall variability: no wall, minimum wall length (mean), minimum wall length (mean-standard deviation), and minimum wall length (mean+standard deviation) against median spectral acceleration over the range of T_1.

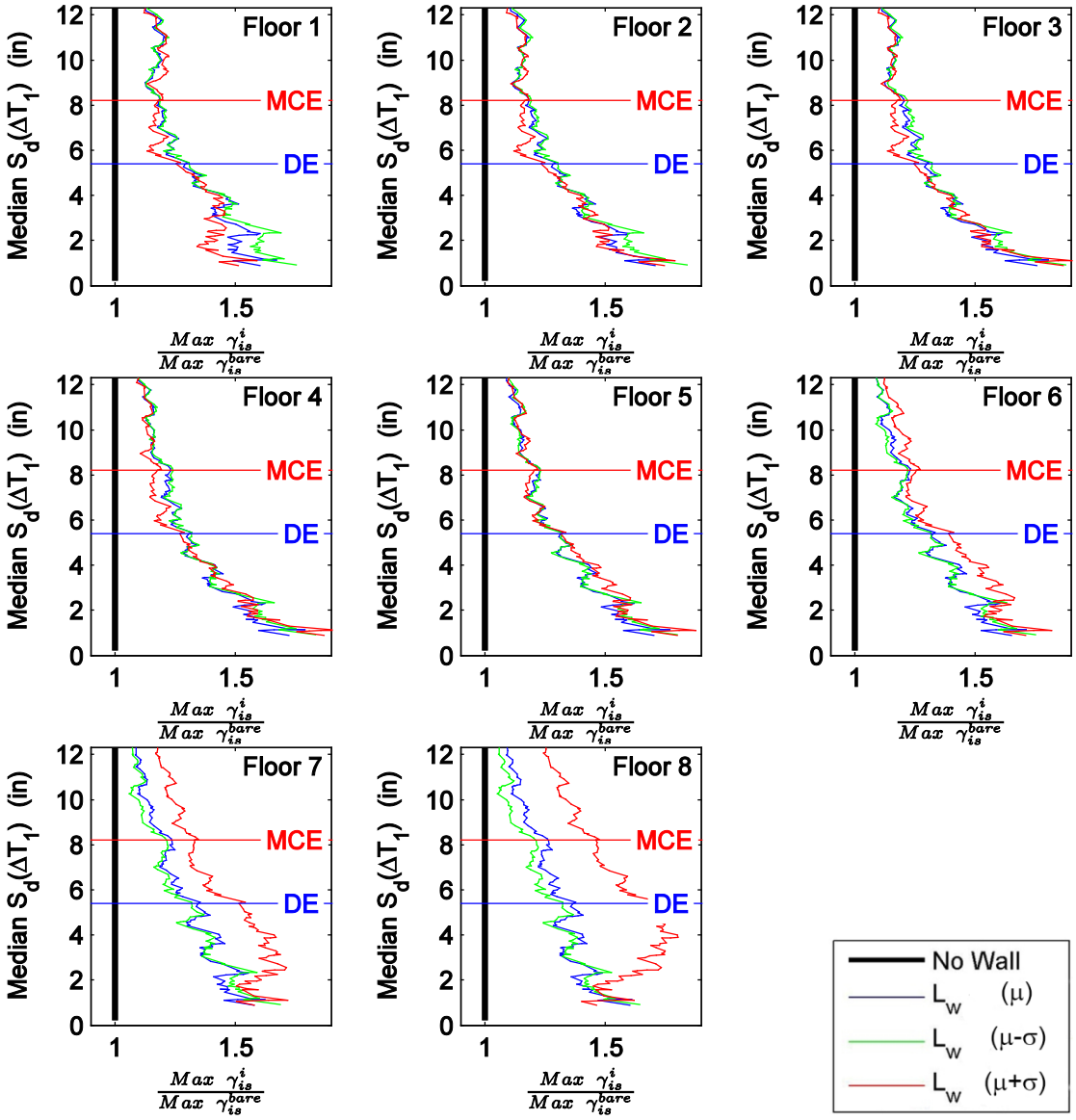

Figure C.38 Normalized maximum interstory drift moving average curves for RC-8 considering the cases of wall variability: no wall, minimum wall length (mean), minimum wall length (mean-standard deviation), and minimum wall length (mean+standard deviation) against median spectral displacement over the range of T_1.

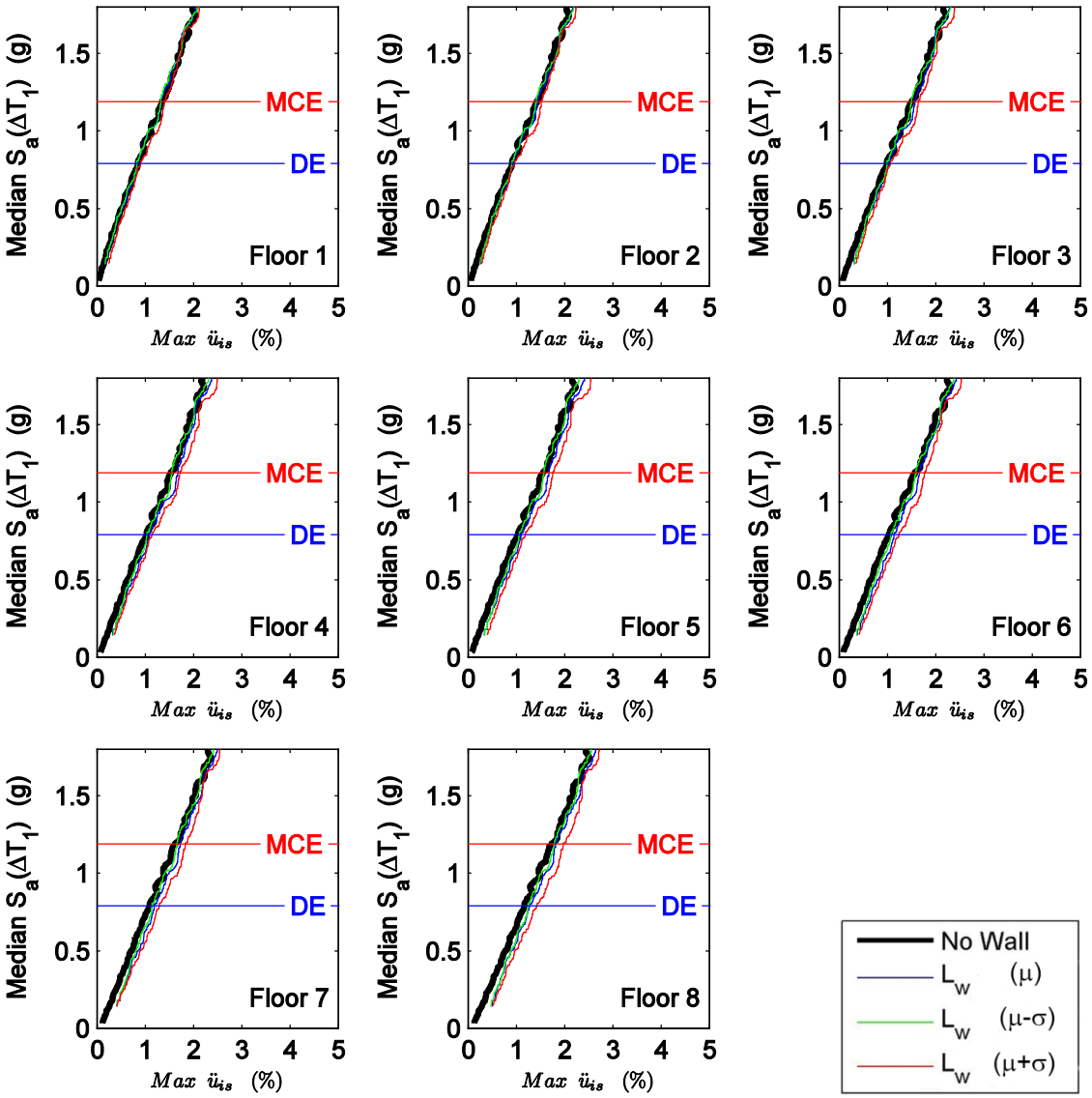

Figure C.39 Maximum floor level acceleration moving average curves for RC-8 considering cases of the wall variability: no wall, minimum wall length (mean), minimum wall length (mean-standard deviation), and minimum wall length (mean+standard deviation) against median spectral acceleration over the range of T_1.

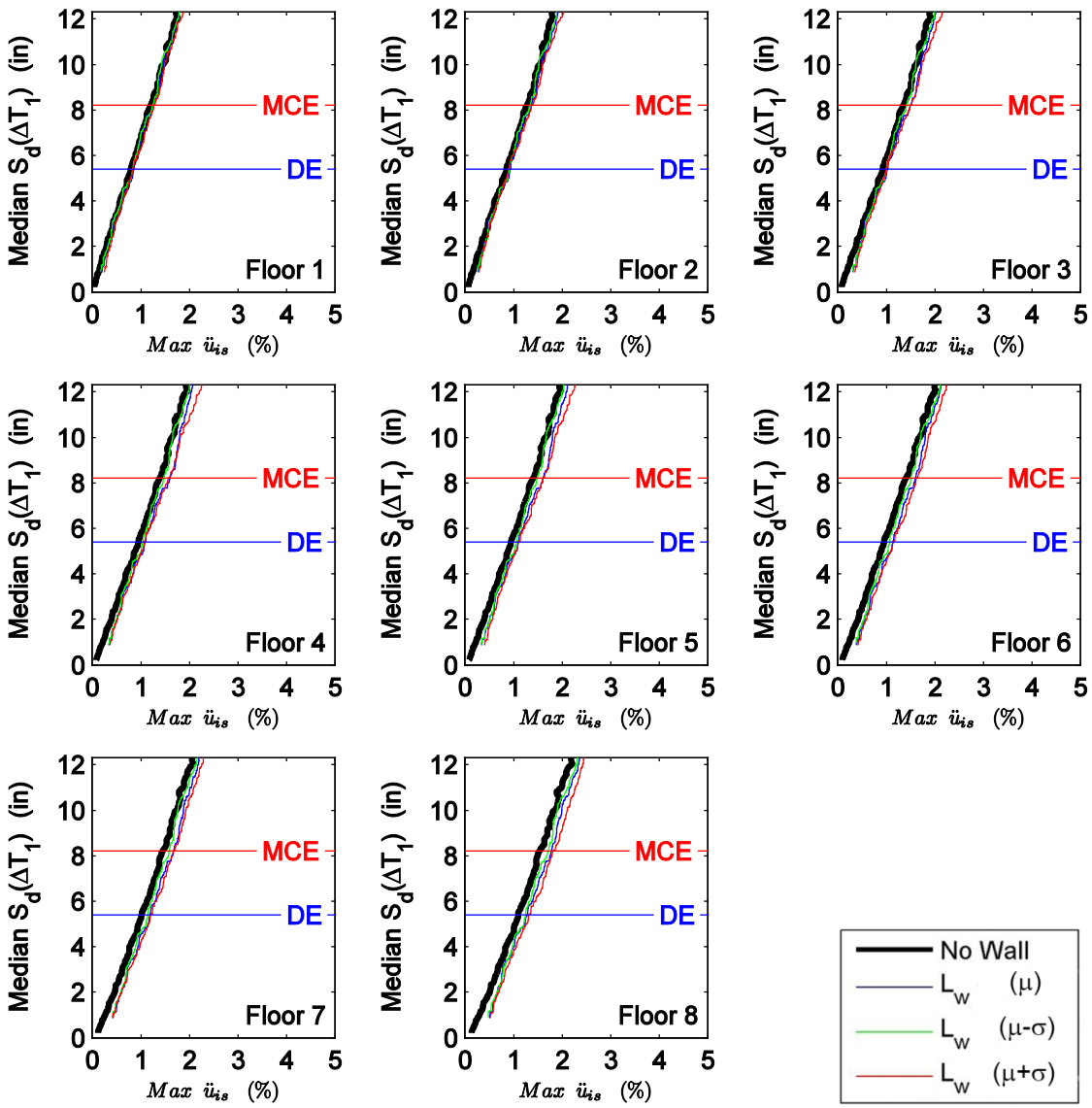

Figure C.40 Maximum floor level acceleration moving average curves for RC-8 considering the cases of wall variability: no wall, minimum wall length (mean), minimum wall length (mean-standard deviation), and minimum wall length (mean+standard deviation) against median spectral displacement over the range of T_1.

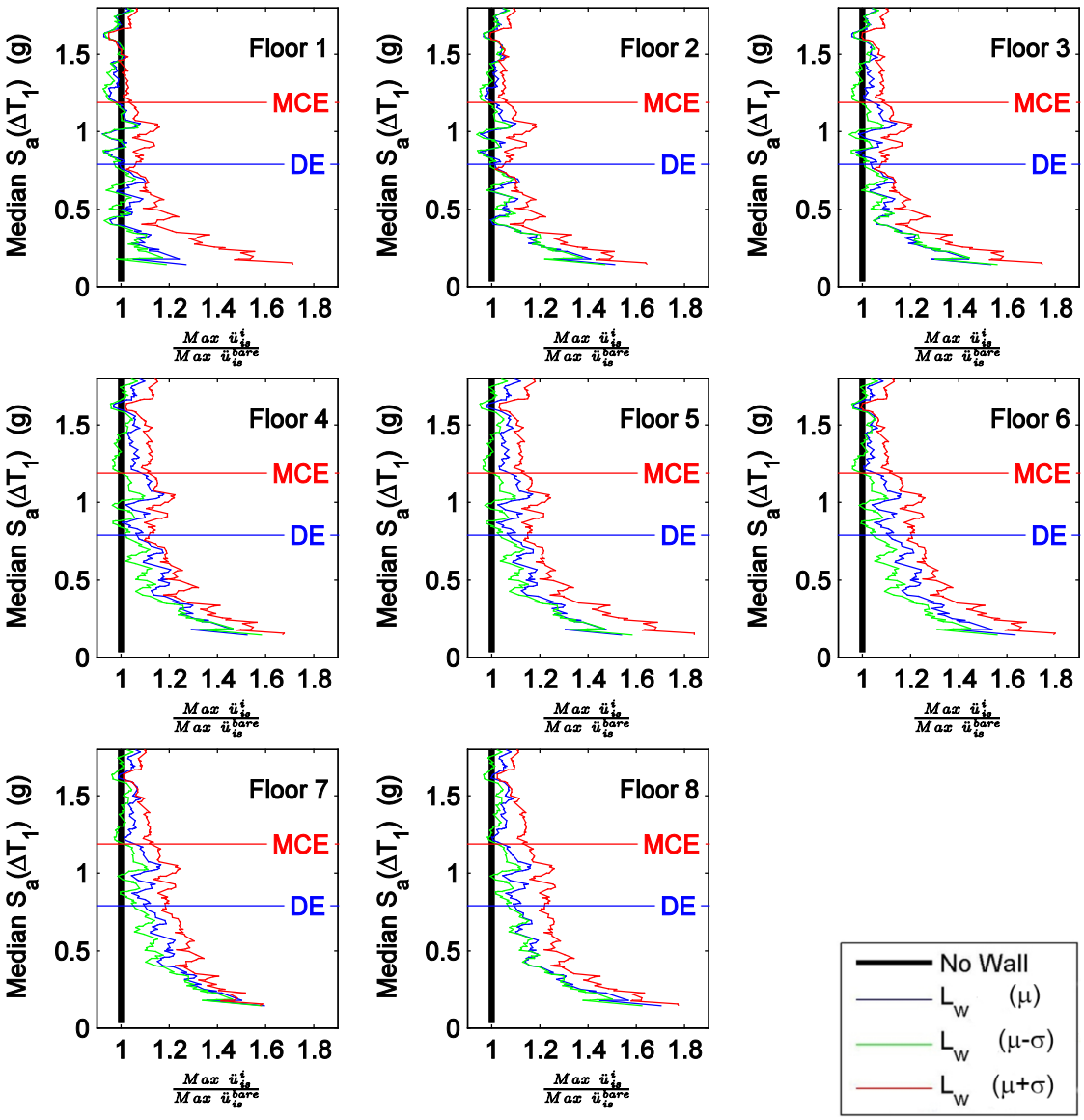

Figure C.41 Normalized maximum floor level acceleration moving average curves for RC-8 considering the cases of wall variability: no wall, minimum wall length (mean), minimum wall length (mean-standard deviation), and minimum wall length (mean+standard deviation) against median spectral acceleration over the range of T_1.

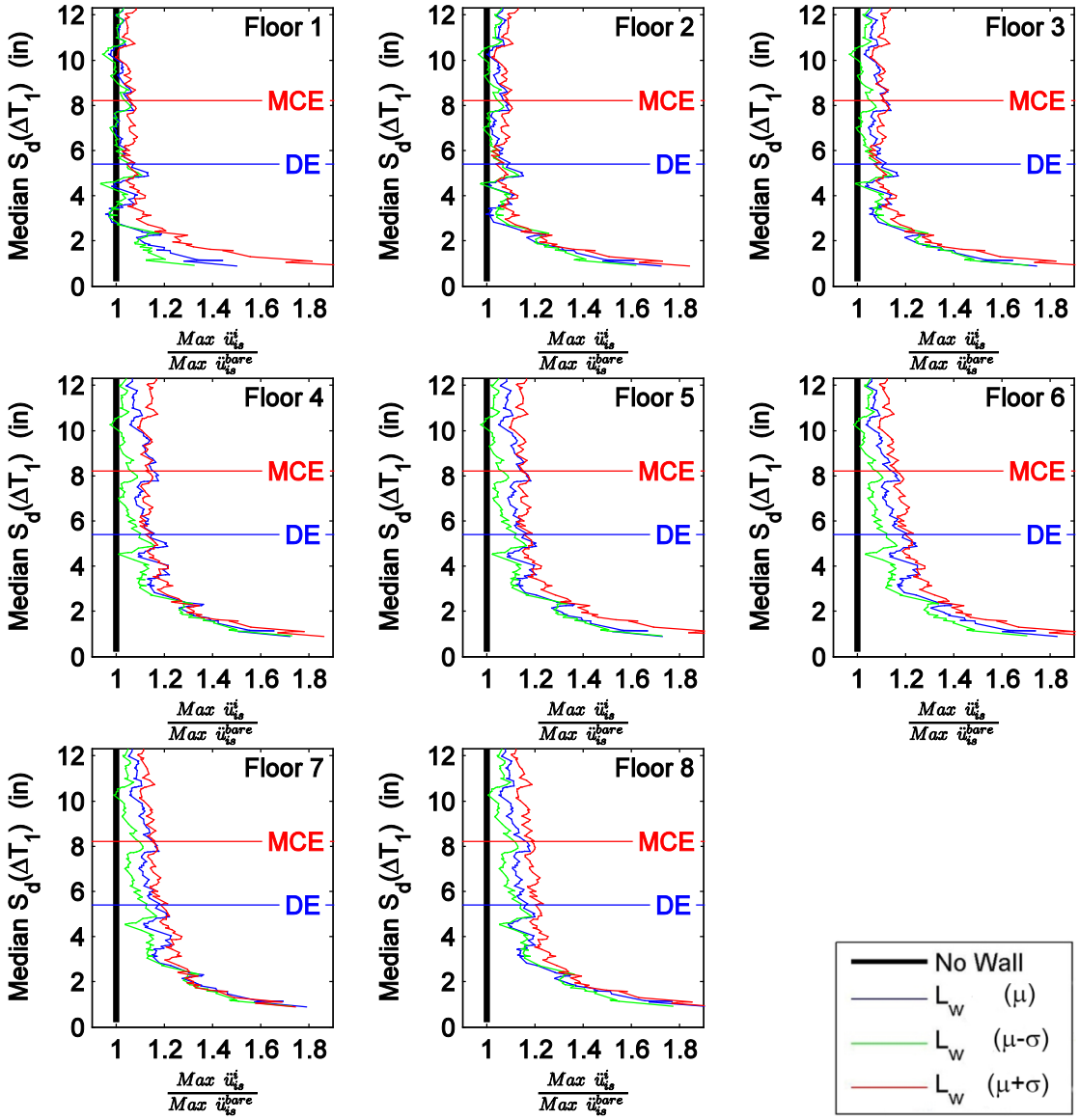

Figure C.42 Normalized maximum floor level acceleration moving average curves for RC-8 considering the cases of wall variability: no wall, minimum wall length (mean), minimum wall length (mean-standard deviation), and minimum wall length (mean+standard deviation) against median spectral displacement over the range of T_1.

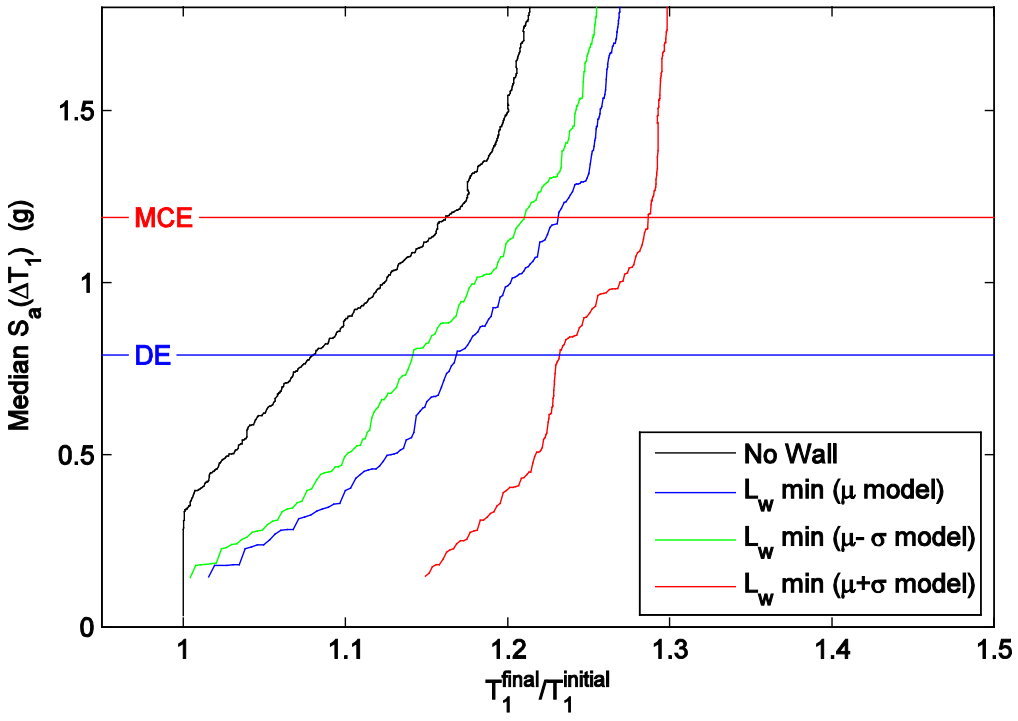

Figure C.43 Period elongation moving average curves for RC-8 considering the cases of wall variability: no wall, minimum wall length (mean), minimum wall length (mean-standard deviation), and minimum wall length (mean+standard deviation) against median spectral acceleration over the range of T_1.

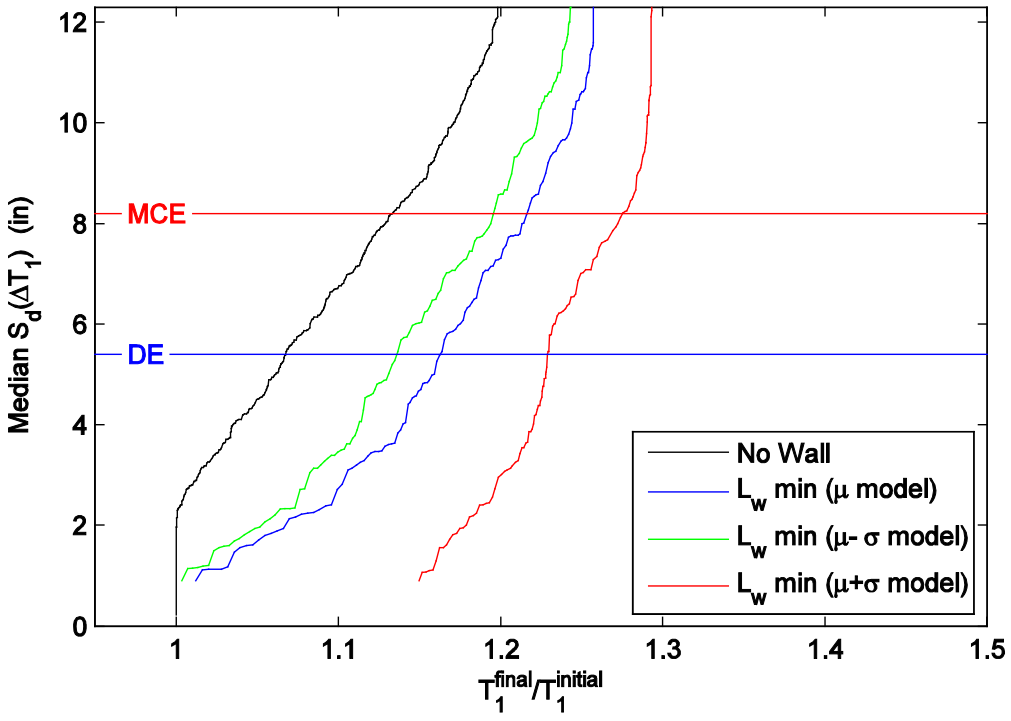

Figure C.44 Period elongation moving average curves for RC-8 considering the cases of wall variability: no wall, minimum wall length (mean), minimum wall length (mean-standard deviation), and minimum wall length (mean+standard deviation) against median spectral displacement over the range of T_1.

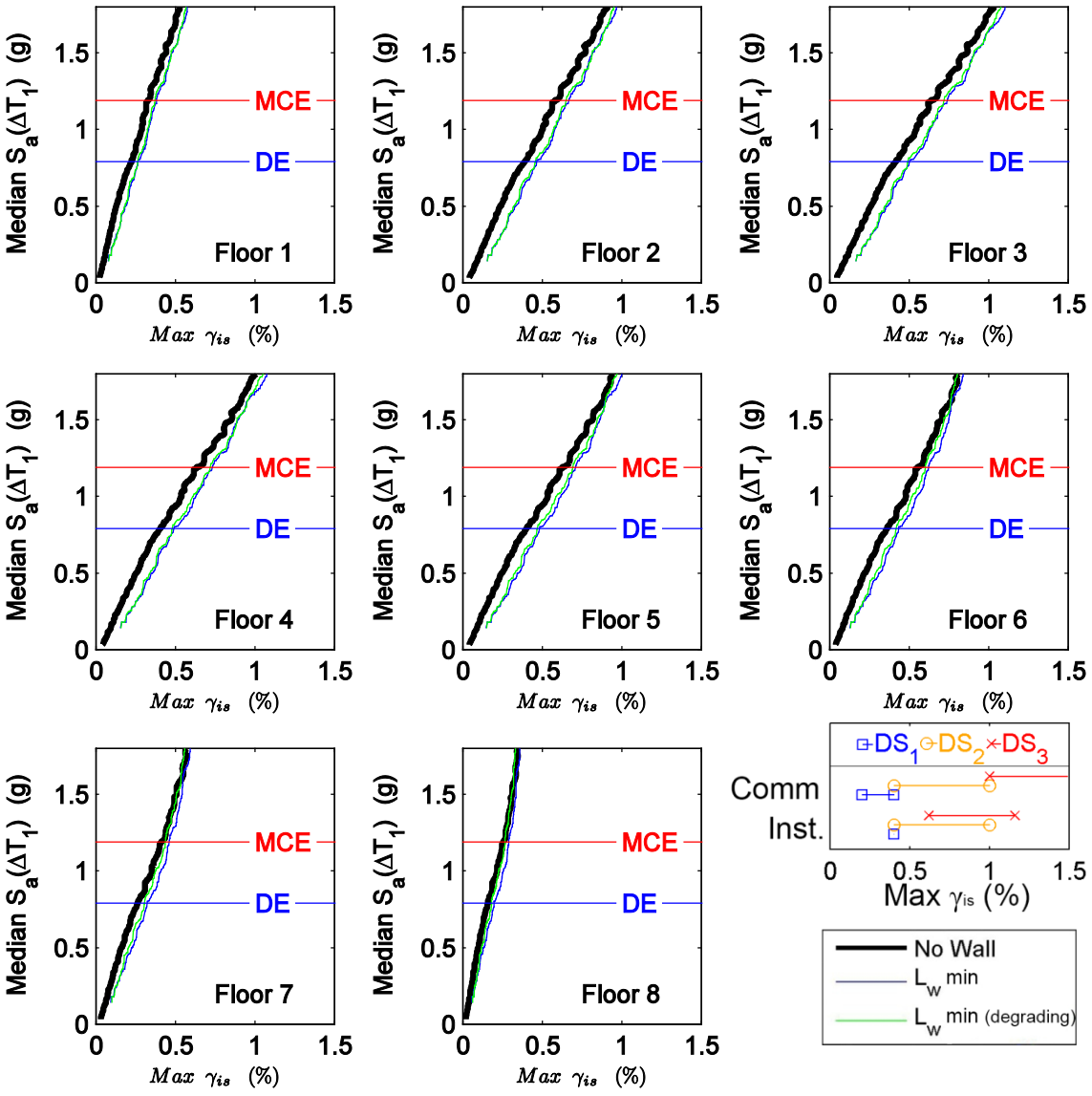

Figure C.45 Maximum interstory drift moving average curves for RC-8 considering the cases of effect of post-peak hardening: no wall, minimum wall length, and minimum wall length (no post-peak hardening) against median spectral acceleration over the range of T_1.

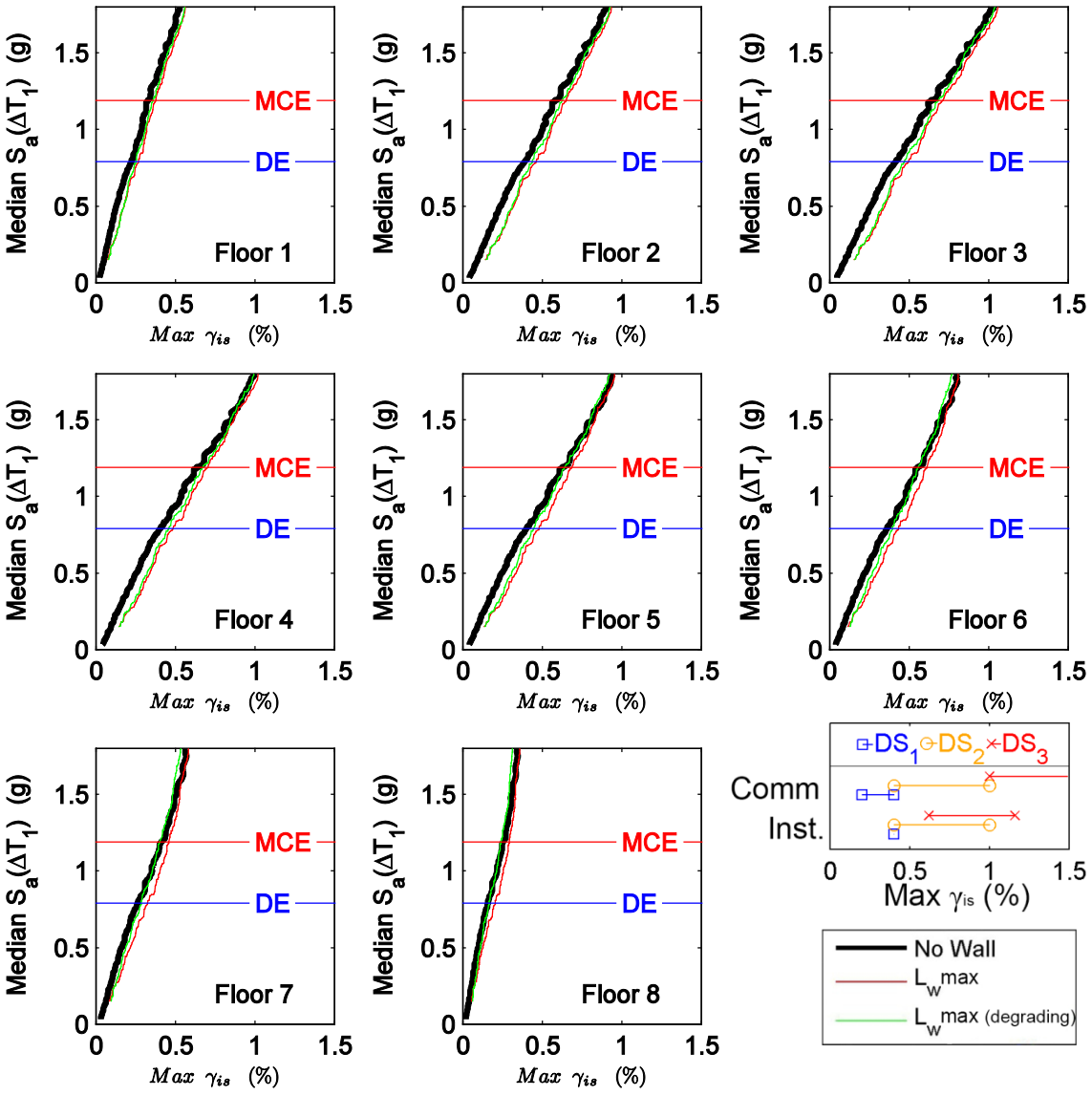

Figure C.46 Maximum interstory drift moving average curves for RC-8 considering the cases of effect of post-peak hardening: no wall, maximum wall length, and maximum wall length (no post-peak hardening) against median spectral acceleration over the range of T_1.

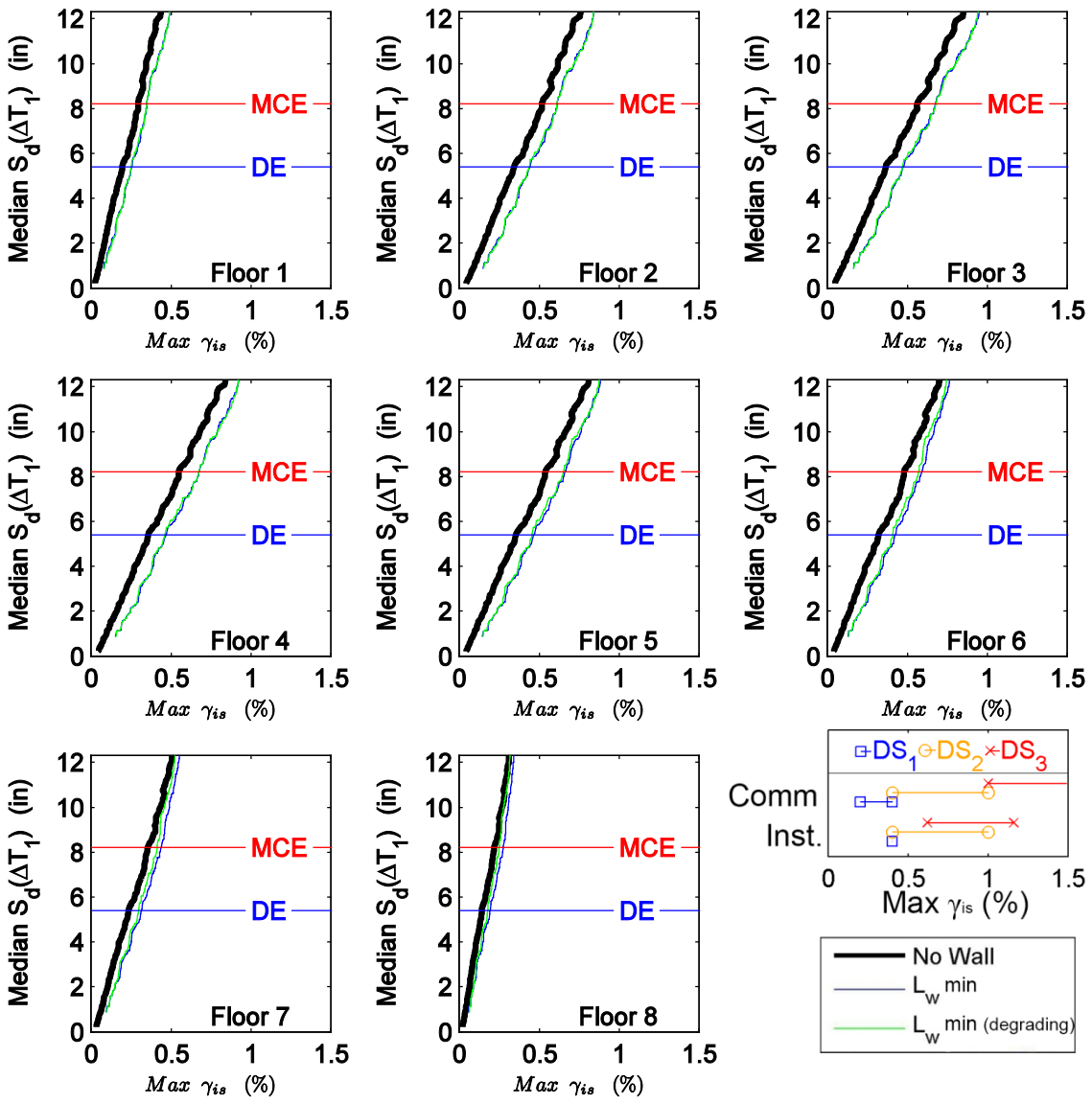

Figure C.47 Maximum interstory drift moving average curves for RC-8 considering the cases of effect of post-peak hardening: no wall, minimum wall length, and minimum wall length (no post-peak hardening) against median spectral displacement over the range of T_1.

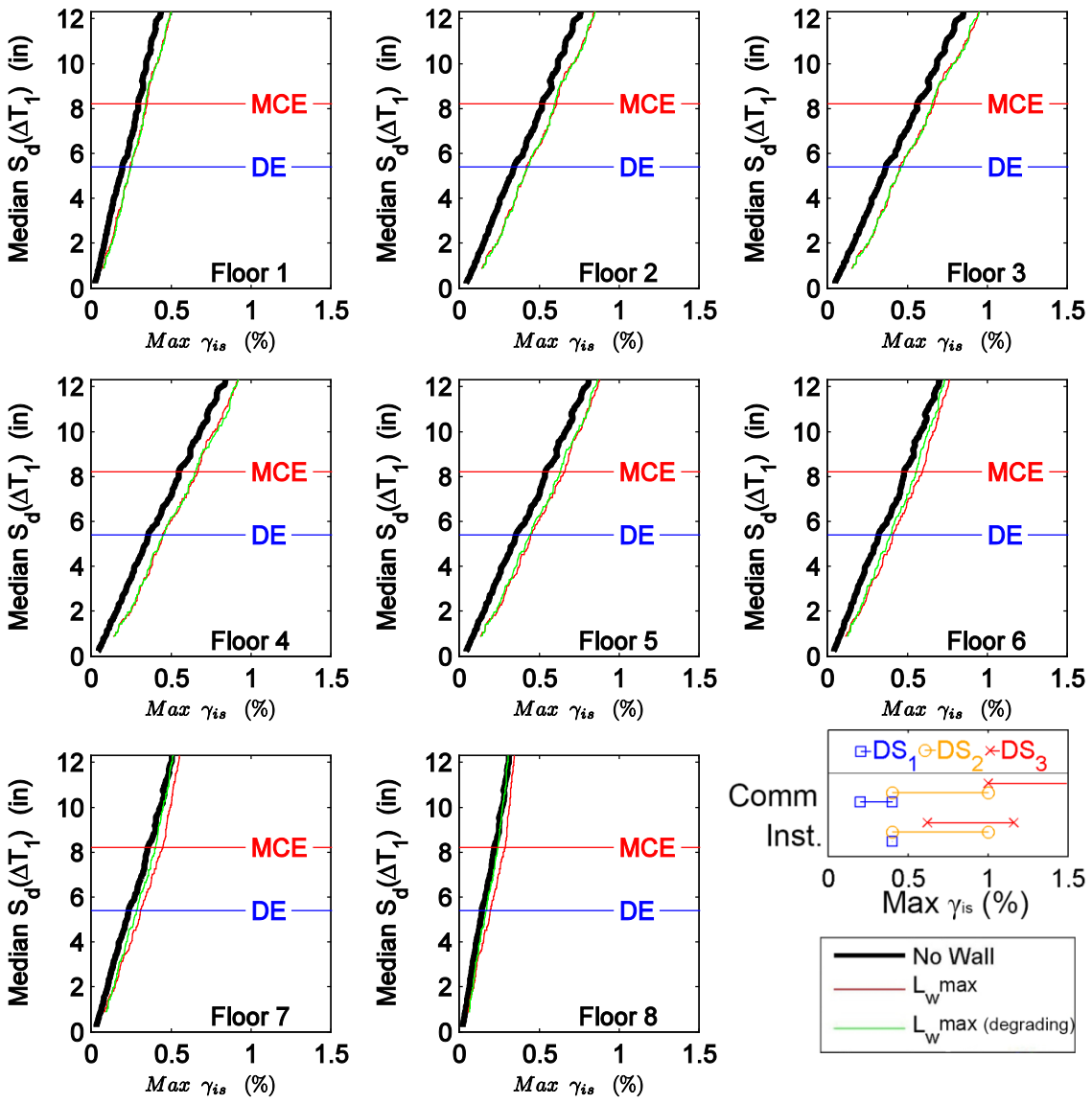

Figure C.48 Maximum interstory drift moving average curves for RC-8 considering the cases of effect of post-peak hardening: no wall, maximum wall length, and maximum wall length (no post-peak hardening) against median spectral displacement over the range of T_1.

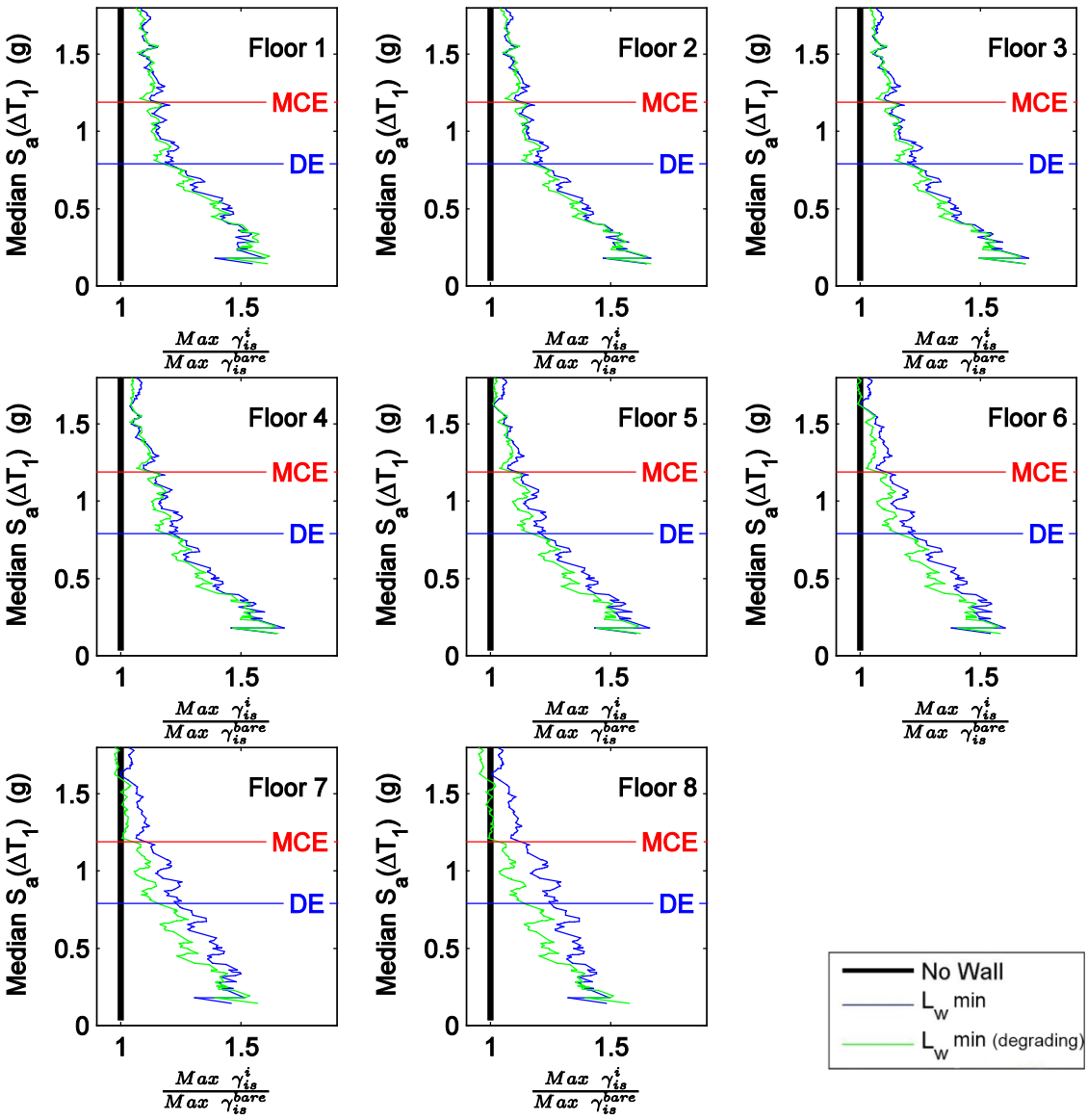

Figure C.49 Normalized interstory drift moving average curves for RC-8 considering the cases of effect of post-peak hardening: no wall, minimum wall length, and minimum wall length (no post-peak hardening) against median spectral acceleration over the range of T_1.

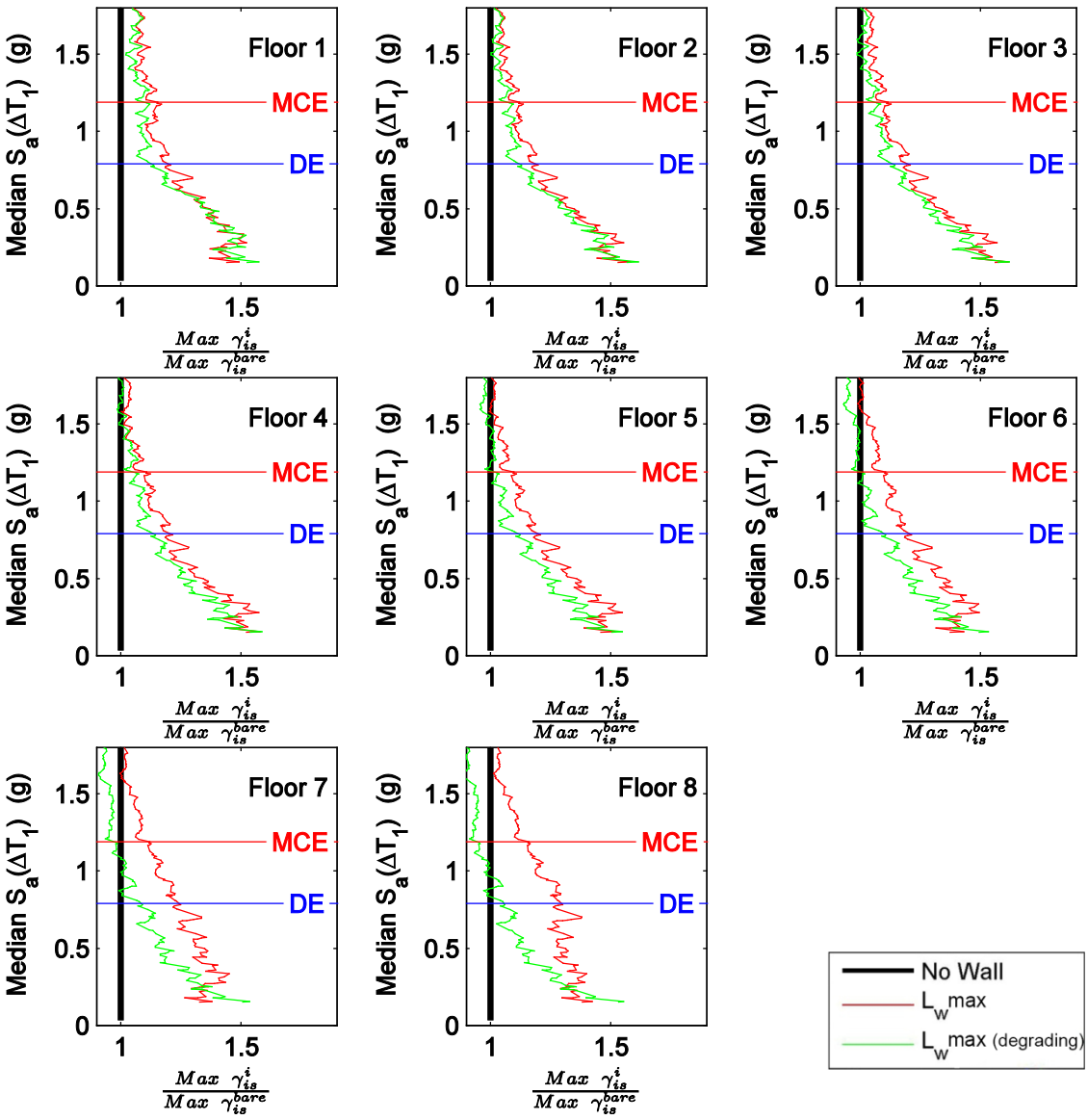

Figure C.50 Normalized interstory drift moving average curves for RC-8 considering the cases of effect of post-peak hardening: no wall, maximum wall length, and maximum wall length (no post-peak hardening) against median spectral acceleration over the range of T_1.

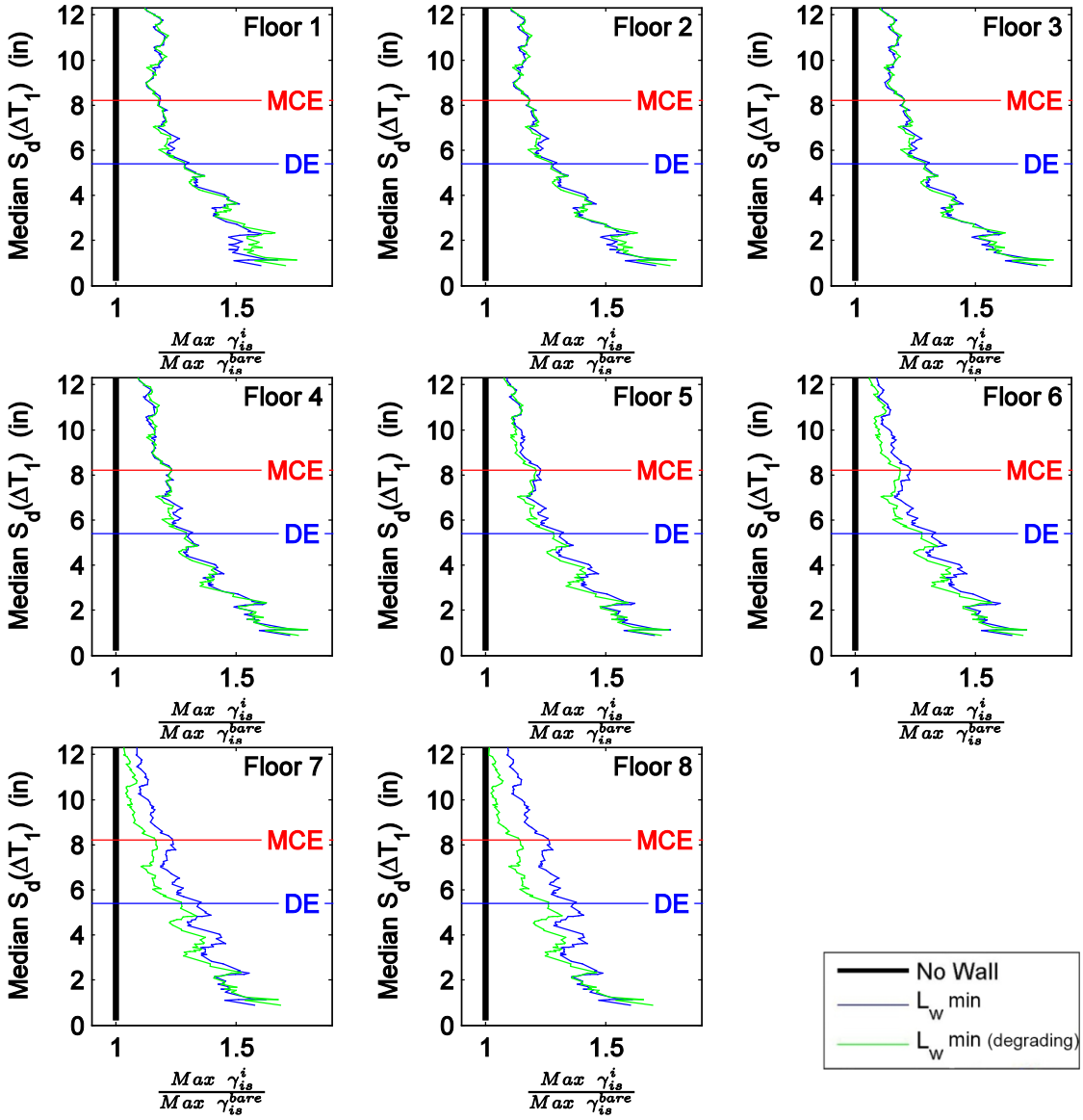

Figure C.51 Normalized interstory drift moving average curves for RC-8 considering the cases of effect of post-peak hardening: no wall, minimum wall length, and minimum wall length (no post-peak hardening) against median spectral displacement over the range of T_1.

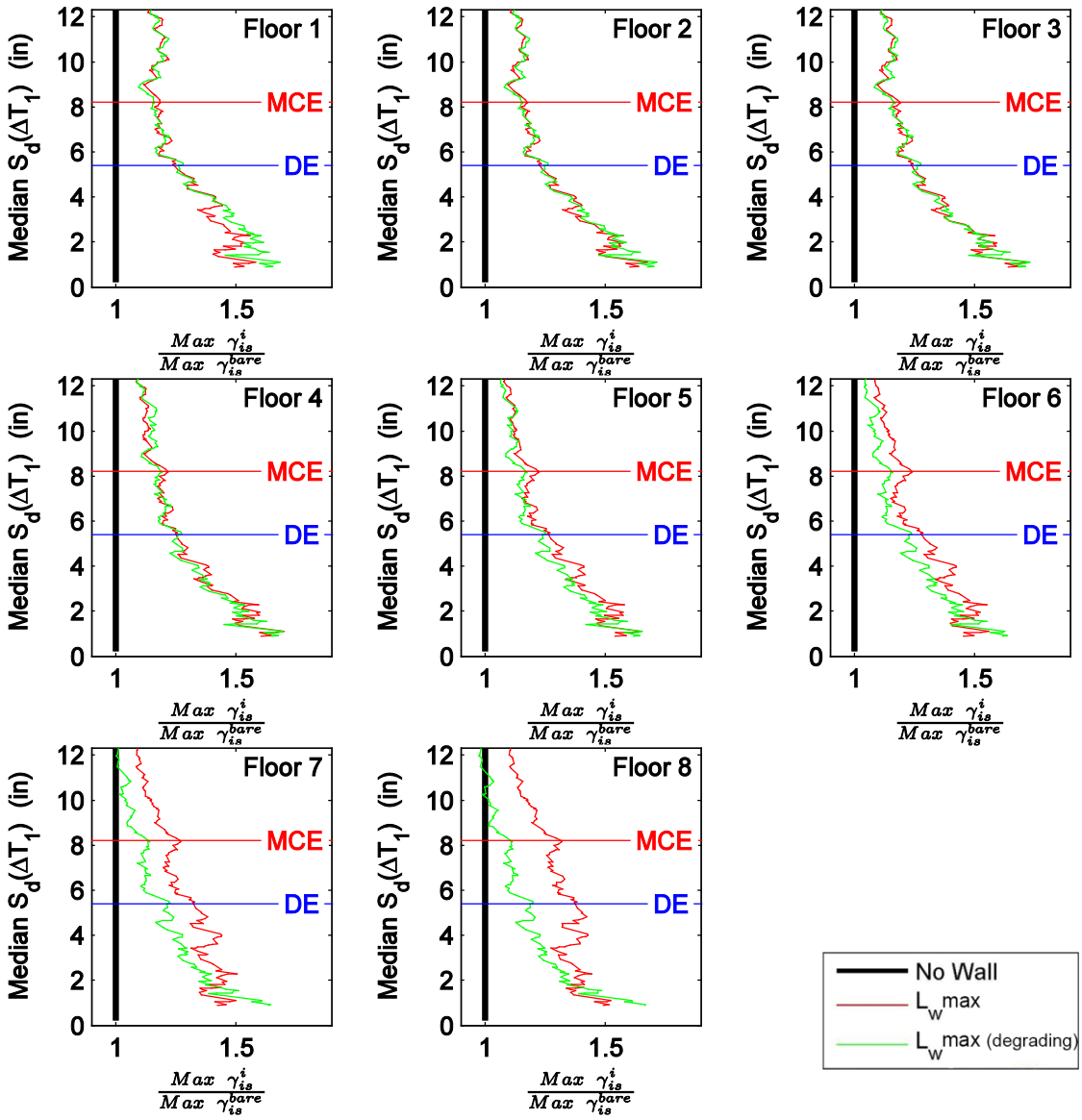

Figure C.52 Normalized interstory drift moving average curves for RC-8 considering the cases of effect of post-peak hardening: no wall, maximum wall length, and maximum wall length (no post-peak hardening) against median spectral displacement over the range of T_1.

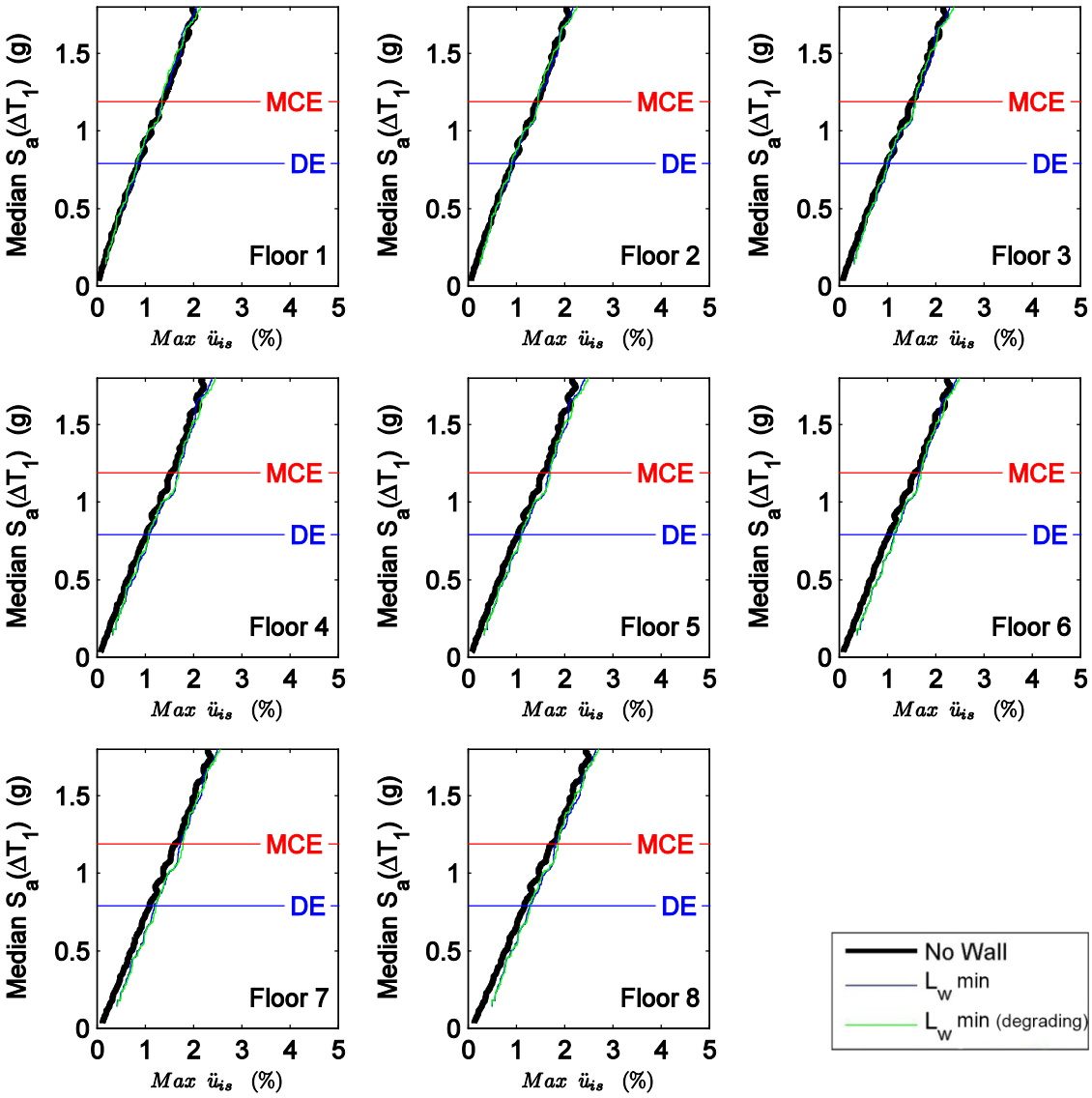

Figure C.53 Maximum floor level acceleration moving average curves for RC-8 considering the cases of effect of post-peak hardening: no wall, minimum wall length, and minimum wall length (no post-peak hardening) against median spectral acceleration over the range of T_1.

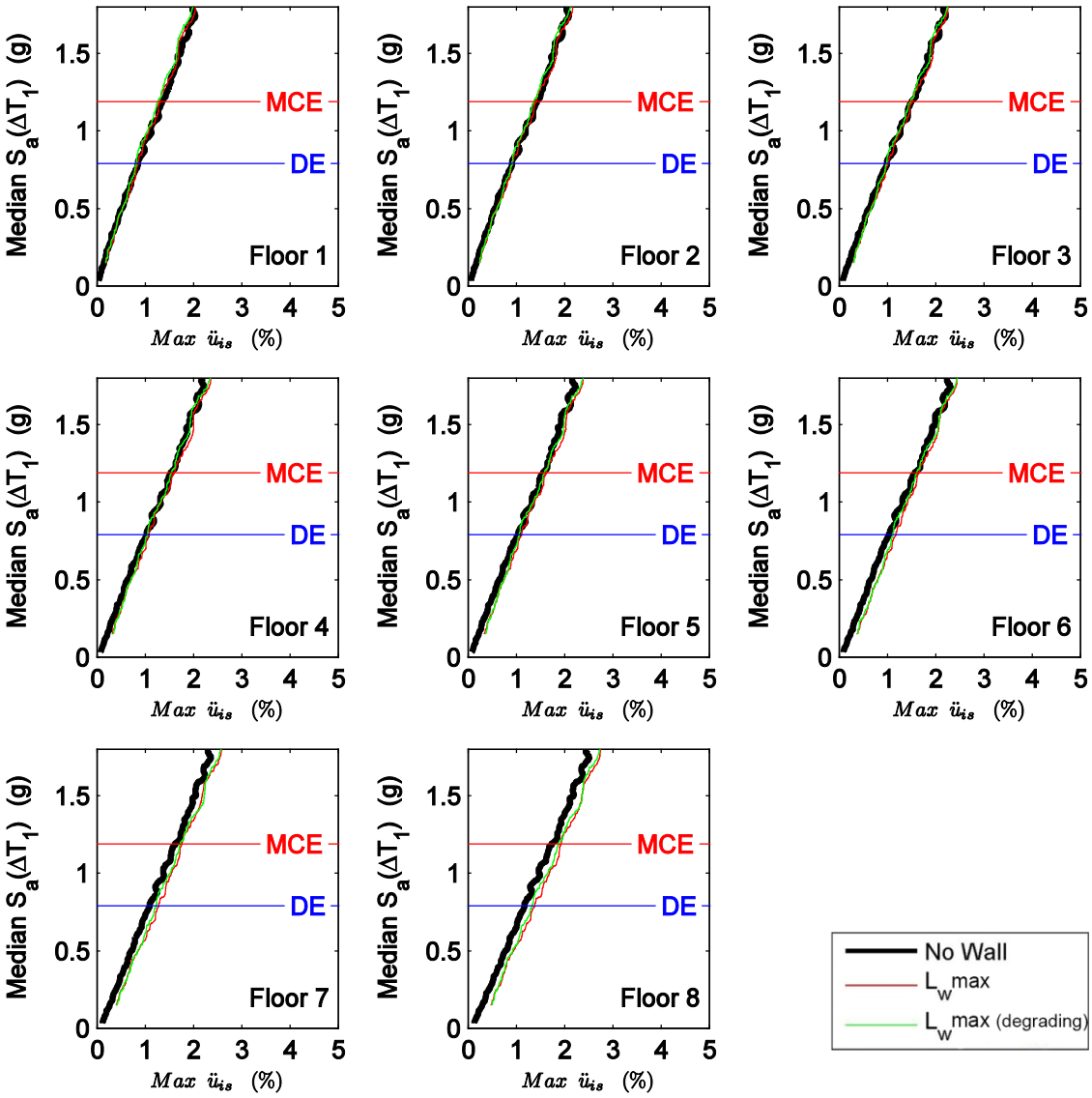

Figure C.54 Maximum floor level acceleration moving average curves for RC-8 considering the cases of effect of post-peak hardening: no wall, maximum wall length, and maximum wall length (no post-peak hardening) against median spectral acceleration over the range of T_1.

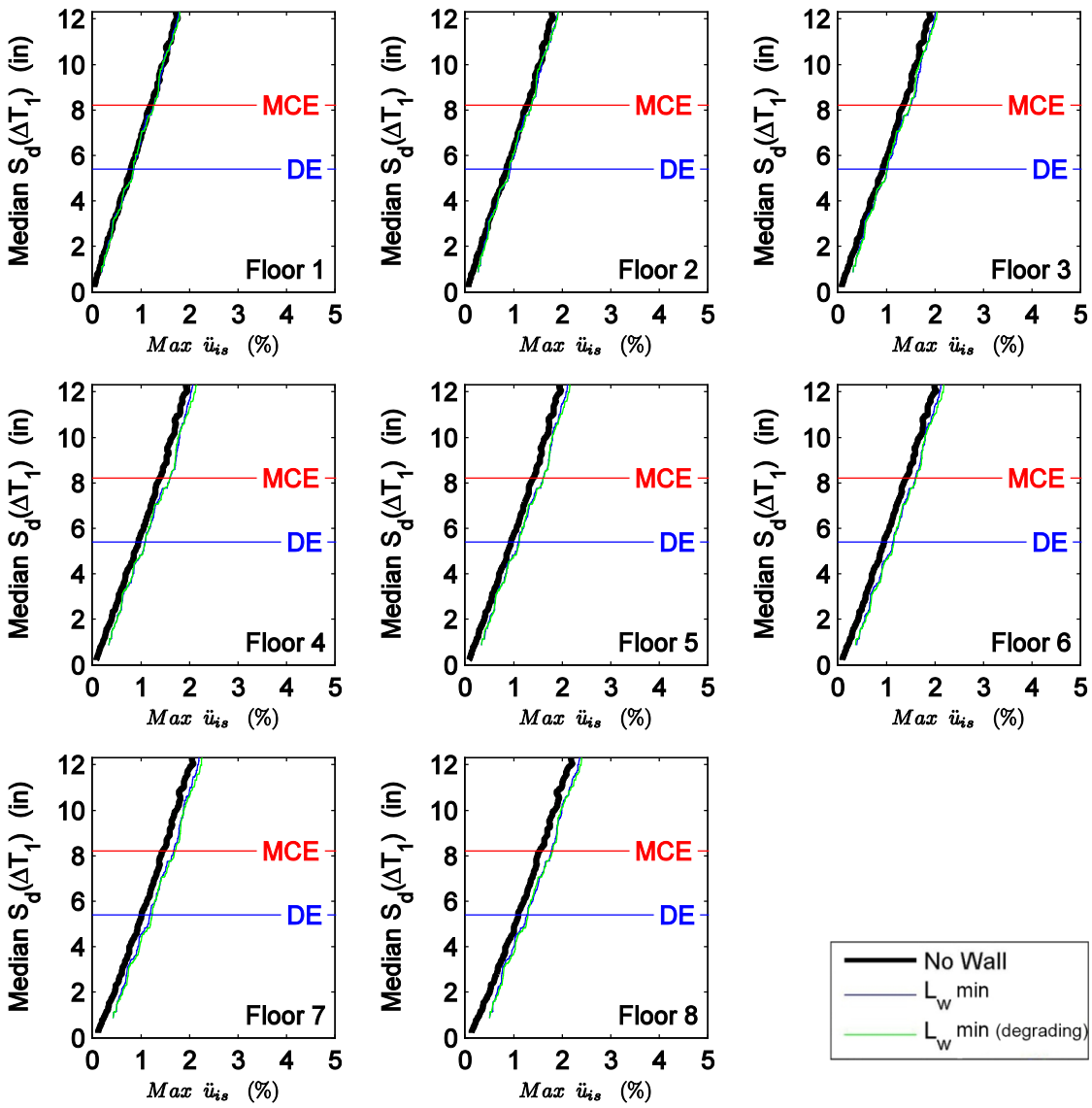

Figure C.55 Maximum floor level acceleration moving average curves for RC-8 considering the cases of effect of post-peak hardening: no wall, minimum wall length, and minimum wall length (no post-peak hardening) against median spectral displacement over the range of T_1.

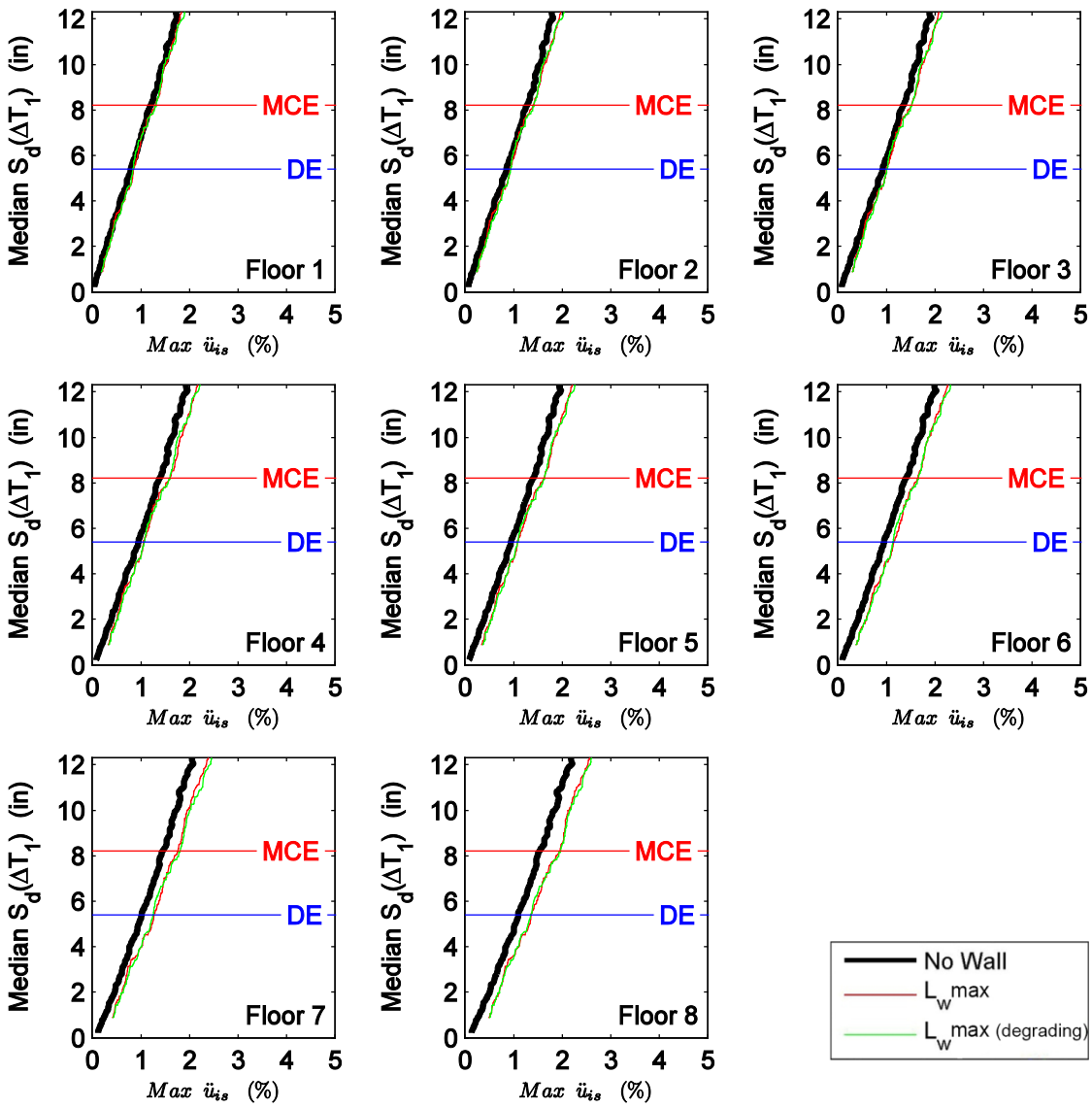

Figure C.56 Maximum floor level acceleration moving average curves for RC-8 considering the cases of effect of post-peak hardening: no wall, maximum wall length, and maximum wall length (no post-peak hardening) against median spectral displacement over the range of T_1.

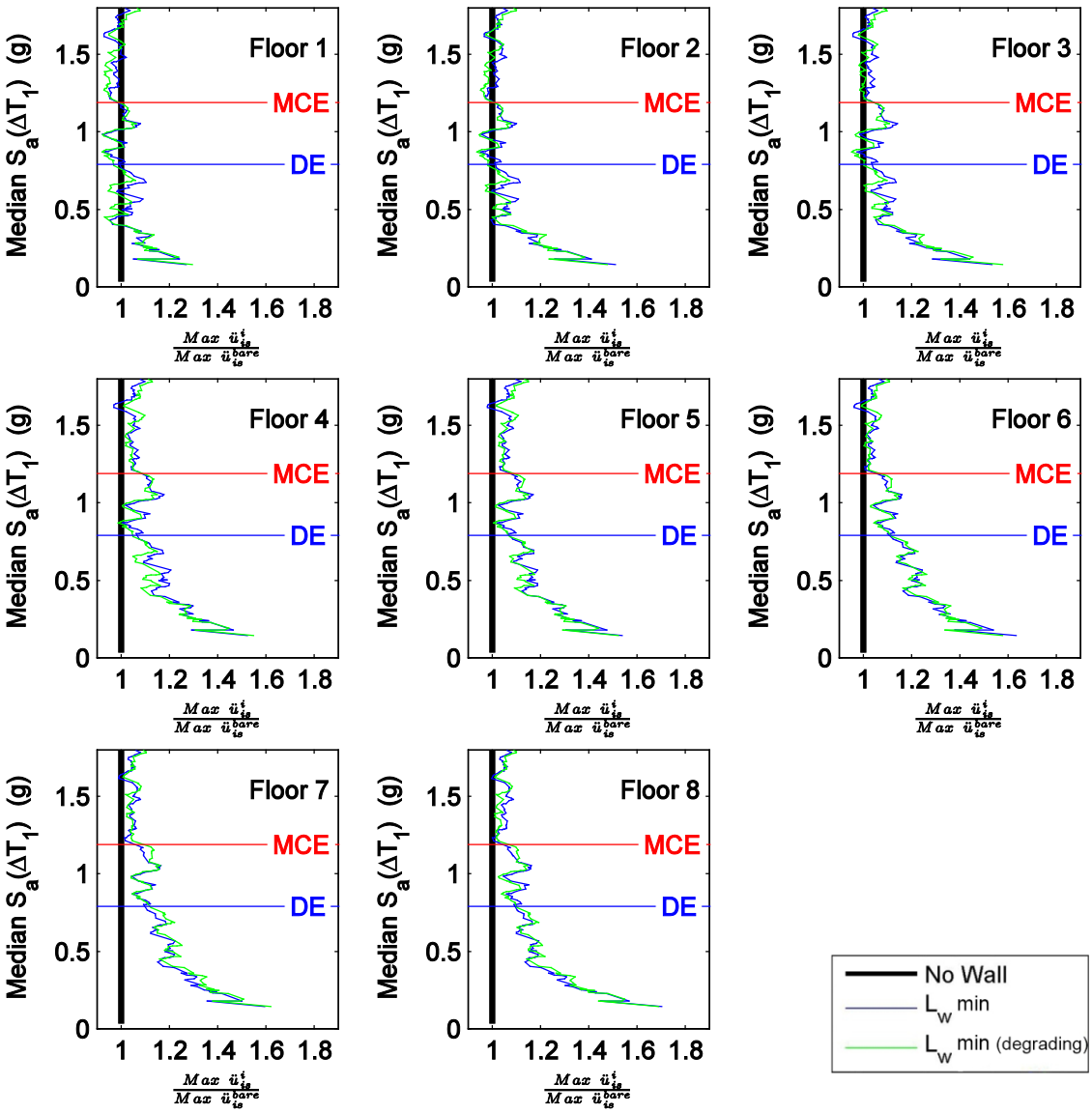

Figure C.57 Normalized maximum floor level acceleration moving average curves for RC-8 considering the cases of effect of post-peak hardening: no wall, minimum wall length, and minimum wall length (no post-peak hardening) against median spectral acceleration over the range of T_1.

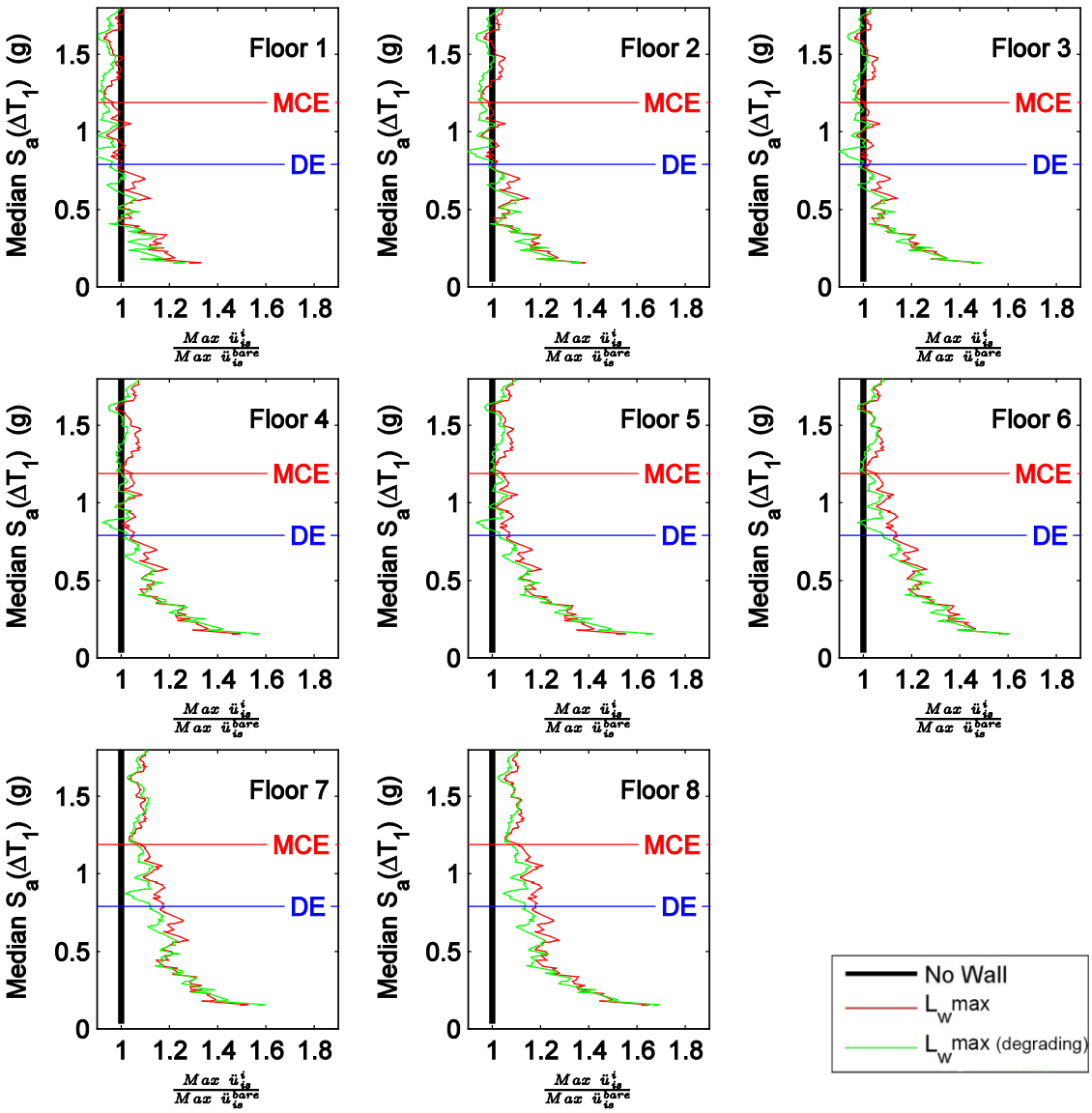

Figure C.58 Normalized maximum floor level acceleration moving average curves for RC-8 considering the cases of effect of post-peak hardening: no wall, maximum wall length, and maximum wall length (no post-peak hardening) against median spectral acceleration over the range of T_1.

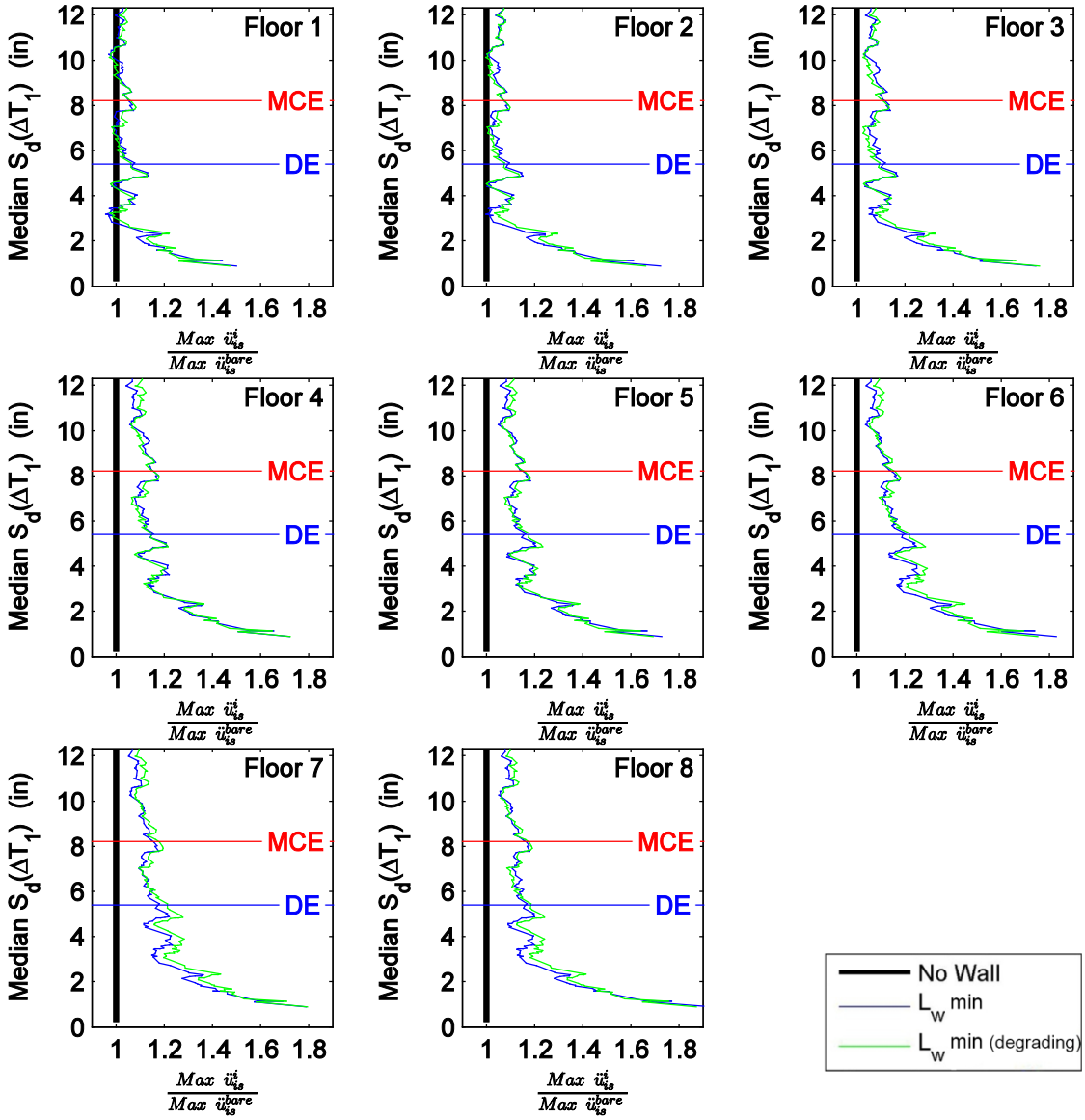

Figure C.59 Normalized maximum floor level acceleration moving average curves for RC-8 considering the cases of effect of post-peak hardening: no wall, minimum wall length, and minimum wall length (no post-peak hardening) against median spectral displacement over the range of T_1.

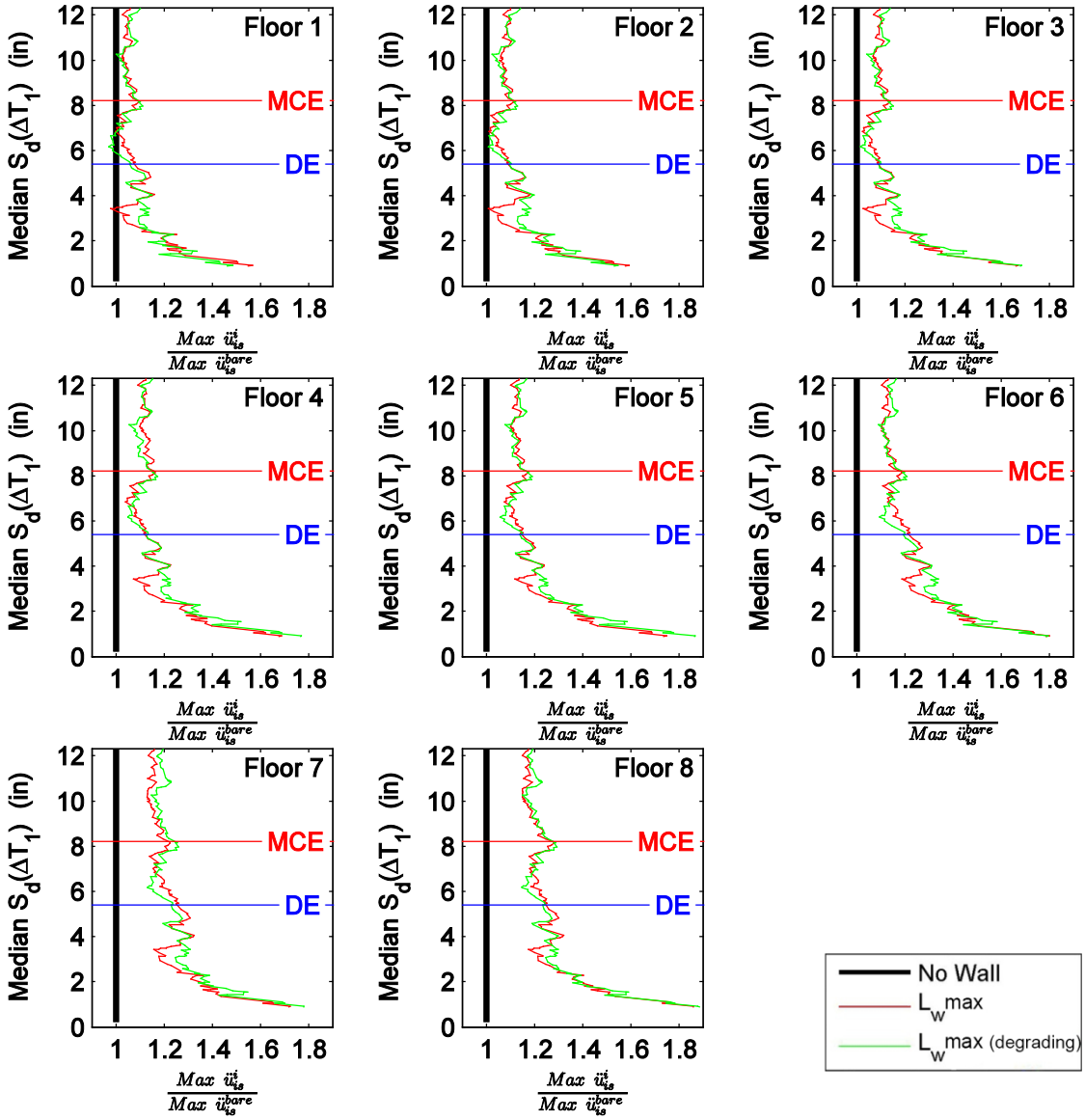

Figure C.60 Normalized maximum floor level acceleration moving average curves for RC-8 considering the cases of effect of post-peak hardening: no wall, maximum wall length, and maximum wall length (no post-peak hardening) against median spectral displacement over the range of T_1.

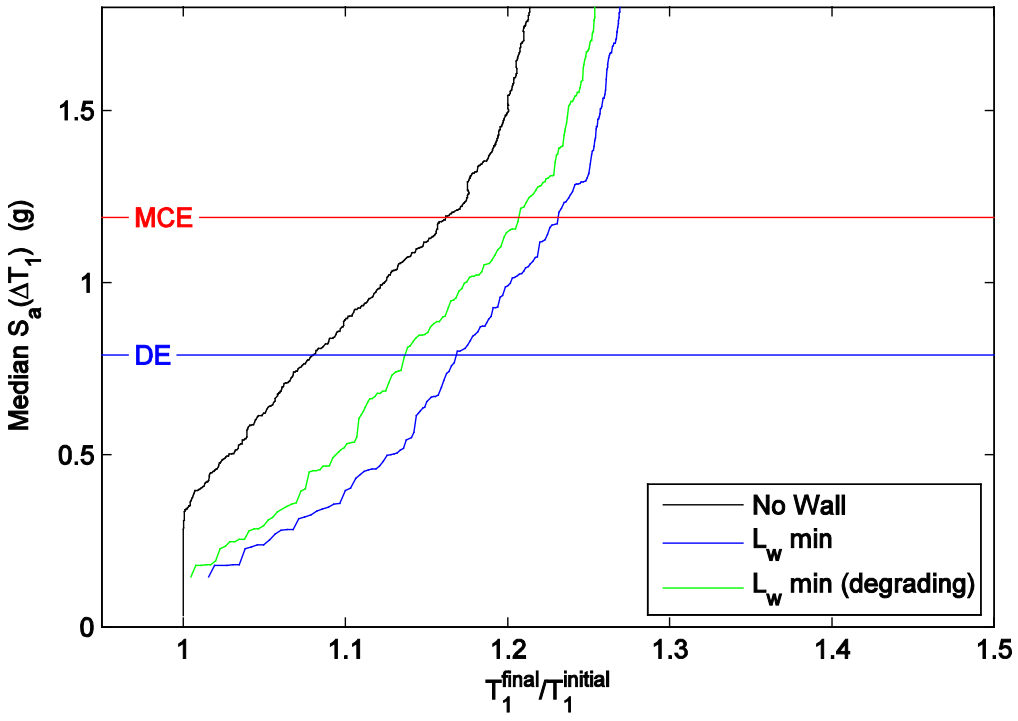

Figure C.61 Period elongation moving average curves for RC-8 considering the effect of post-peak hardening: no wall, minimum wall length, and minimum wall length (no post-peak hardening) against median spectral acceleration over the range of T_1.

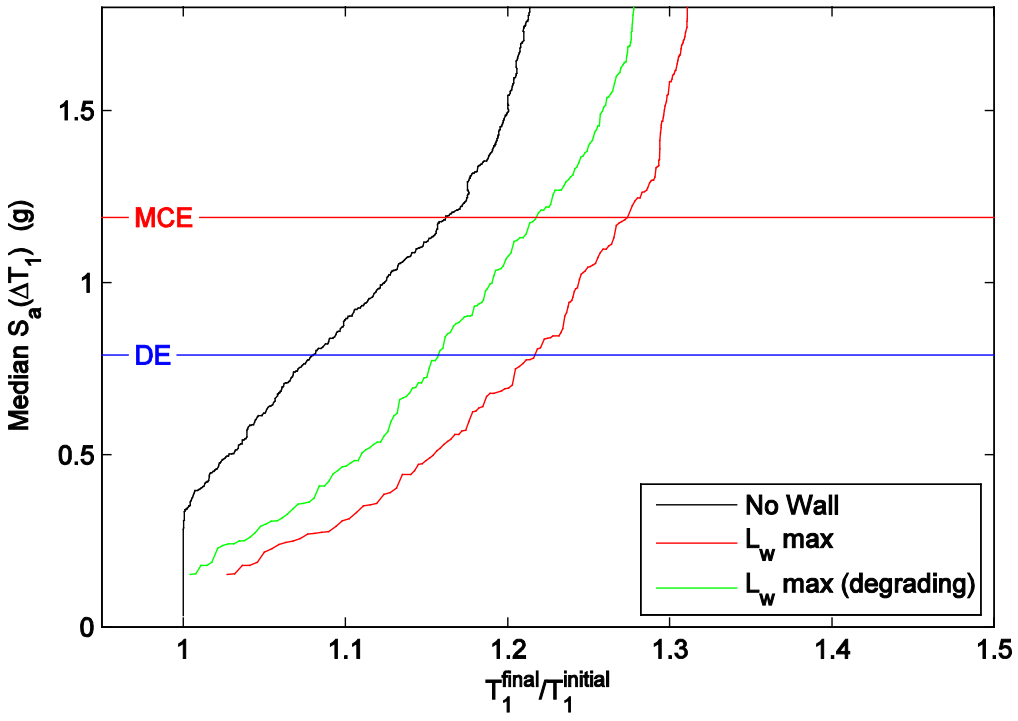

Figure C.62 Period elongation moving average curves for RC-8 considering the effect of post-peak hardening: no wall, maximum wall length, and maximum wall length (no post-peak hardening) against median spectral acceleration over the range of T_1.

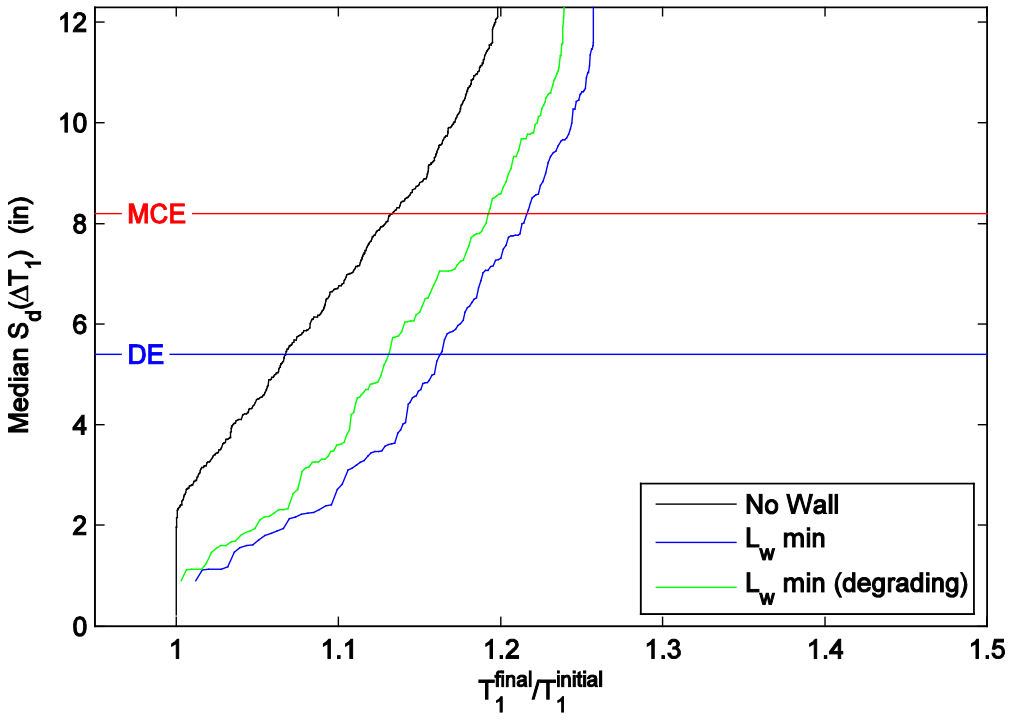

Figure C.63 Period elongation moving average curves for RC-8 considering the effect of post-peak hardening: no wall, minimum wall length, and minimum wall length (no post-peak hardening) against median spectral displacement over the range of T_1.

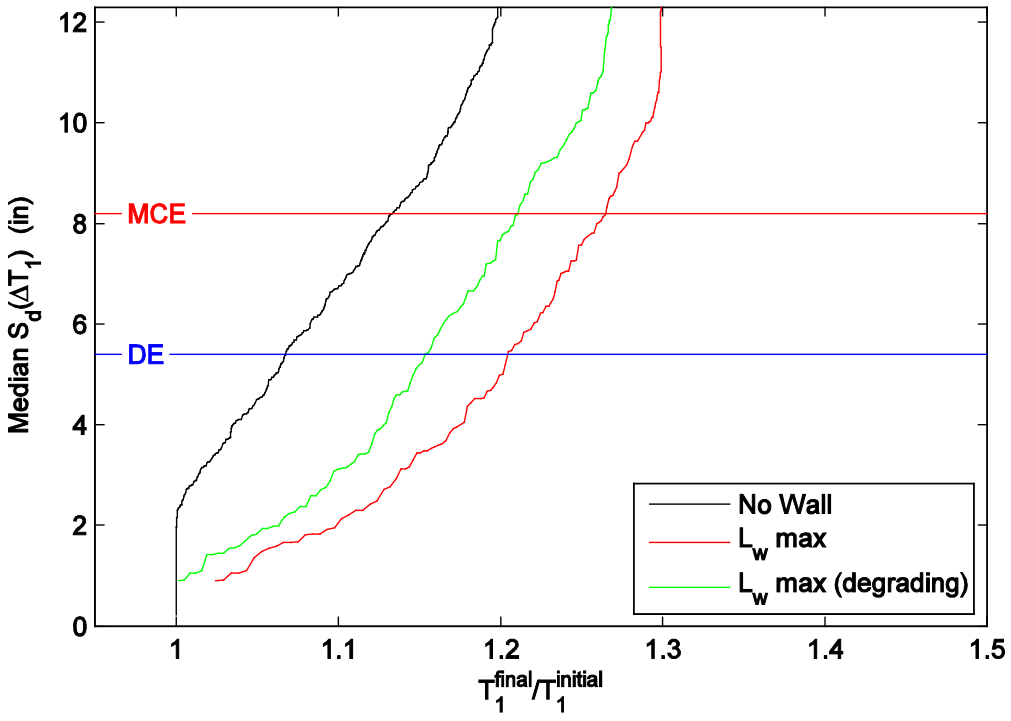

Figure C.64 Period elongation moving average curves for RC-8 considering the effect of post-peak hardening: no wall, maximum wall length, and maximum wall length (no post-peak hardening) against median spectral displacement over the range of T_1.

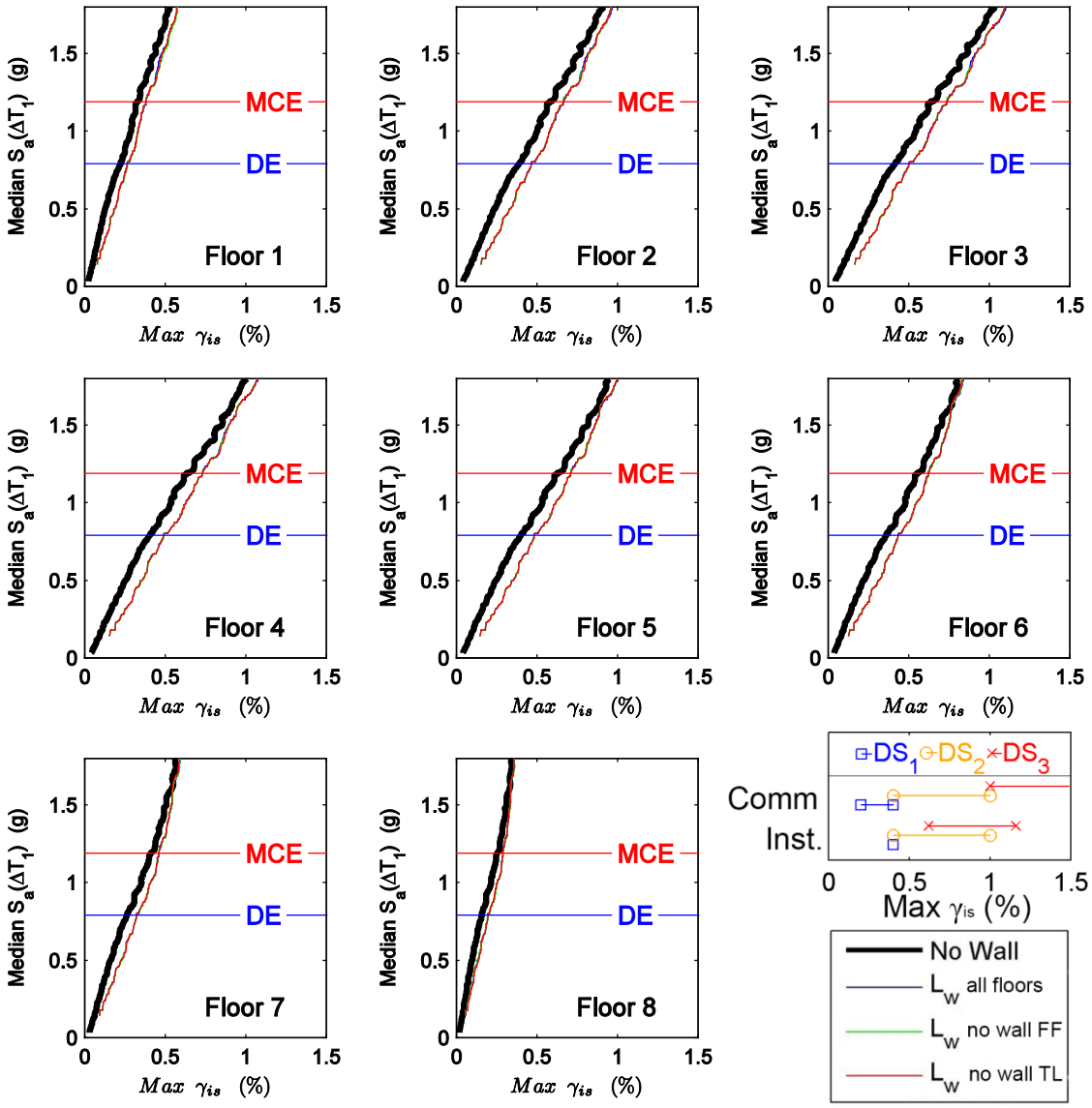

Figure C.65 Maximum interstory drift moving average curves for RC-8 considering the cases of wall placement: no wall, minimum wall length (all floors), no wall first floor, and no wall on top level against median spectral acceleration over the range of T_1.

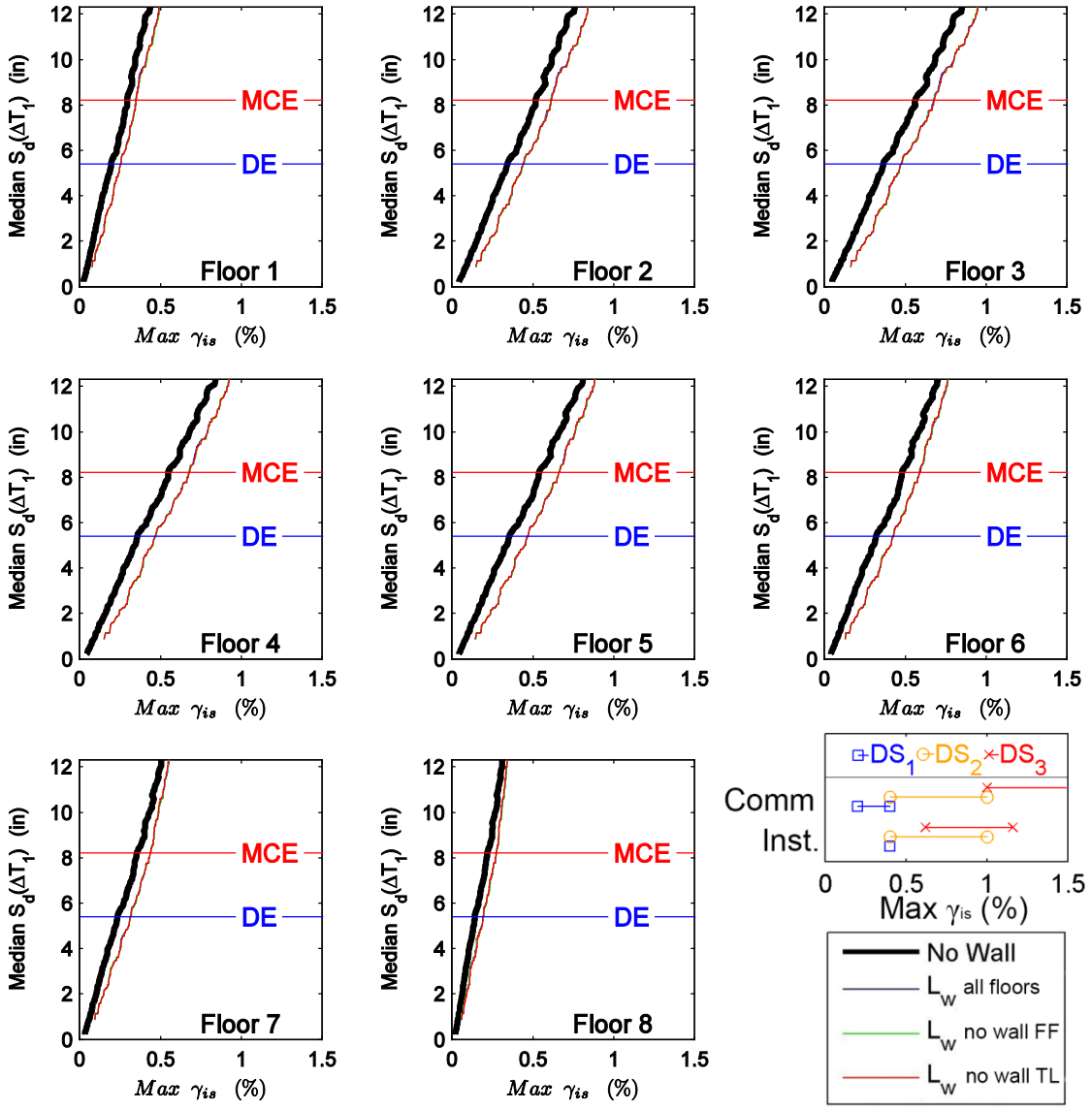

Figure C.66 Maximum interstory drift moving average curves RC-8 considering the cases of wall placement: no wall, minimum wall length (all floors), no wall first floor, and no wall on top level against median spectral displacement over the range of T_1.

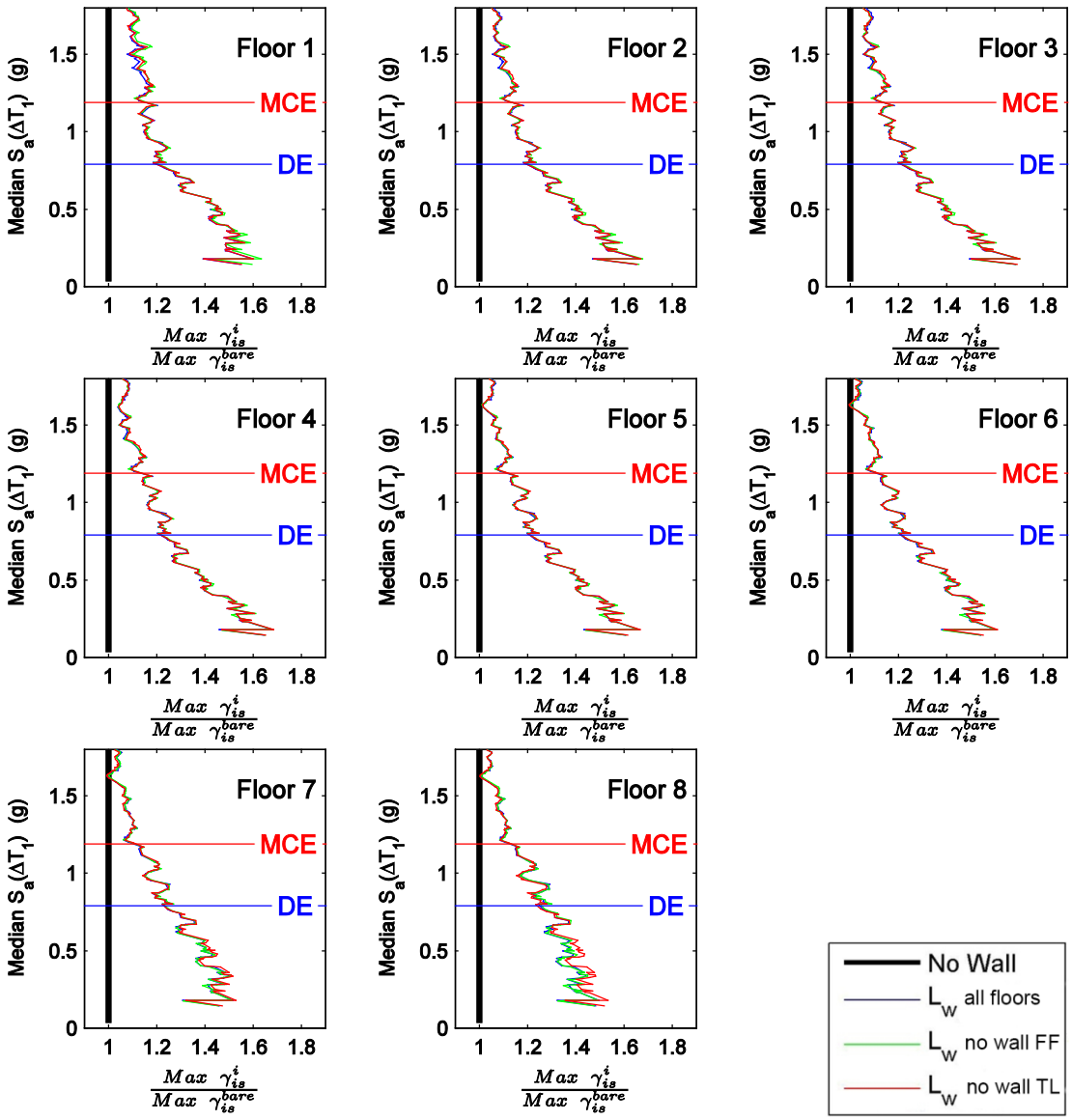

Figure C.67 Normalized maximum interstory drift moving average curves for RC-8 considering the cases of wall placement: no wall, minimum wall length (all floors), no wall first floor, and no wall on top level against median spectral acceleration over the range of T_1.

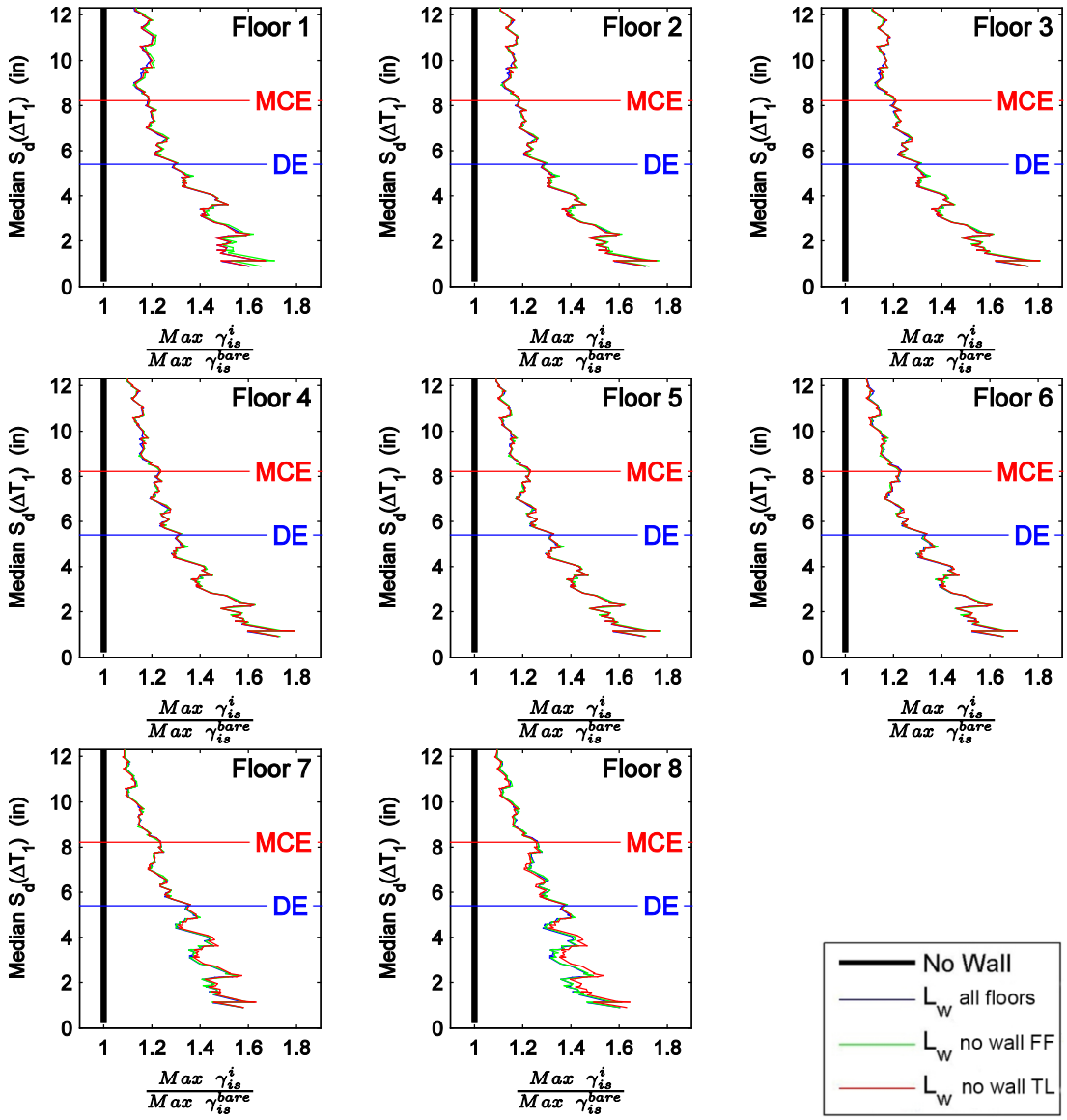

Figure C.68 Normalized maximum interstory drift moving average curves for RC-8 considering the cases of wall placement: no wall, minimum wall length (all floors), no wall first floor, and no wall on top level against median spectral displacement over the range of T_1.

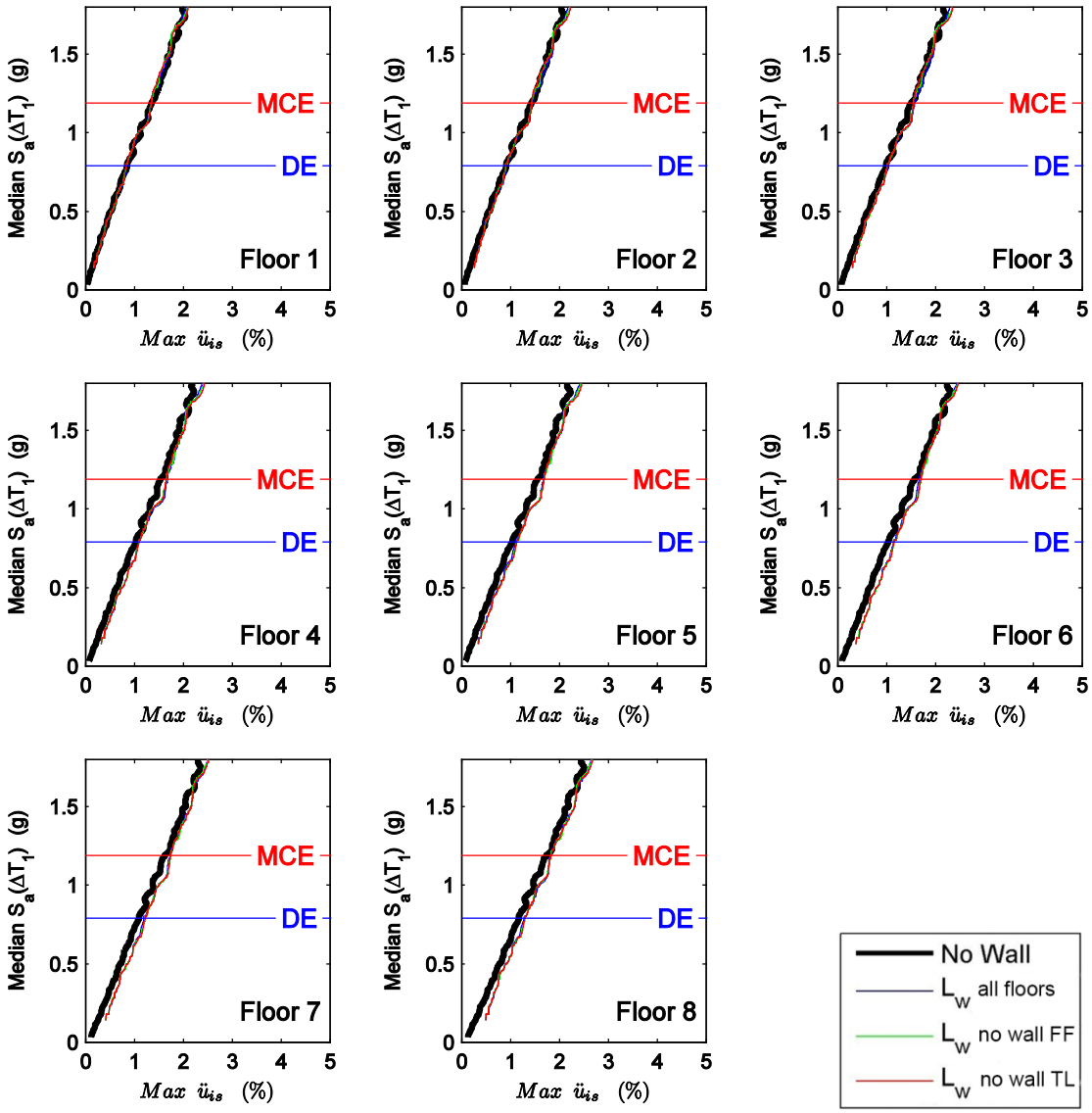

Figure C.69 Maximum floor level acceleration moving average curves for RC-8 considering the cases of wall placement: no wall, minimum wall length (all floors), no wall first floor, and no wall on top level against median spectral acceleration over the range of T_1.

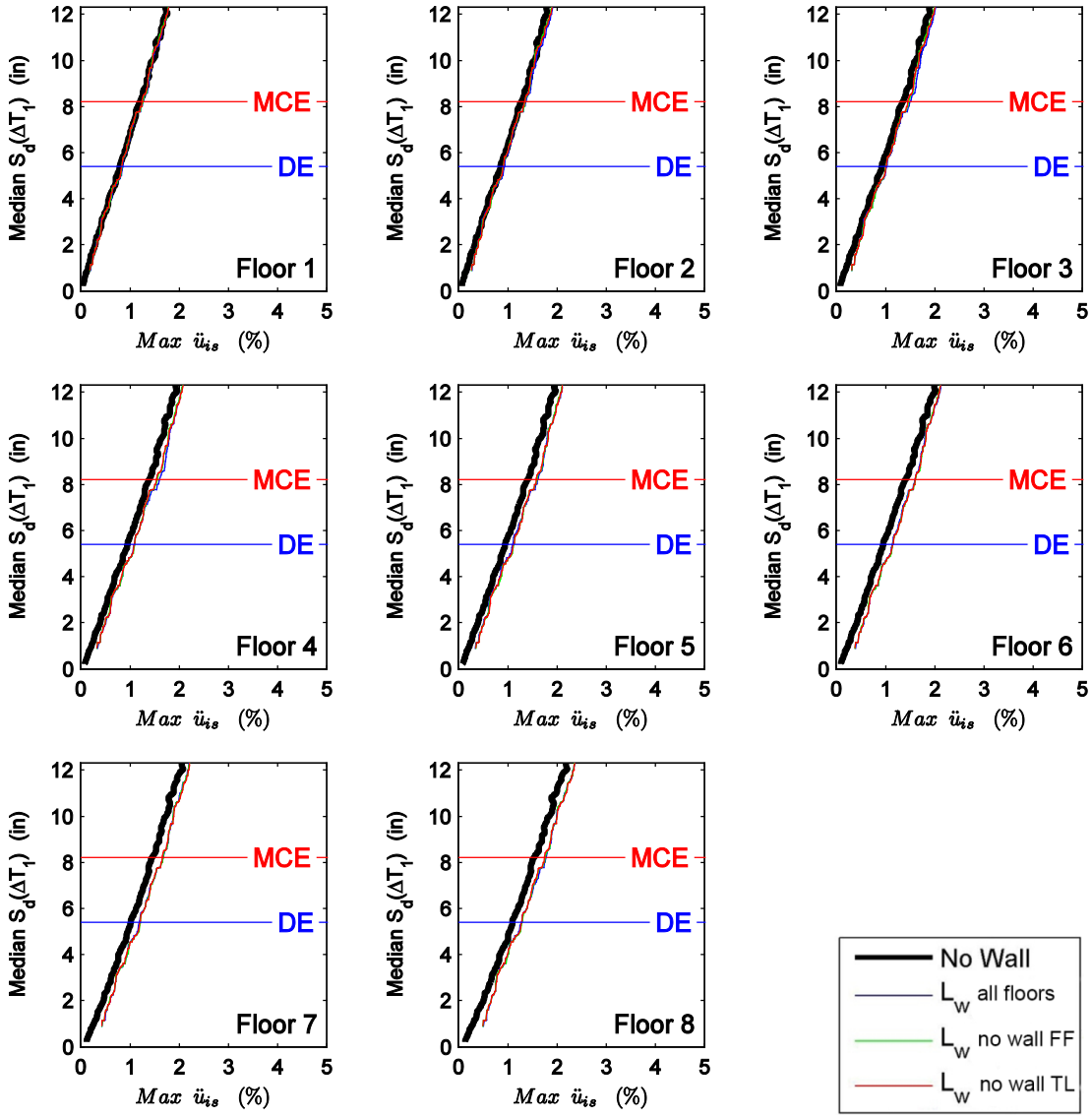

Figure C.70 Maximum floor level acceleration moving average curves for RC-8 considering the cases of wall placement: no wall, minimum wall length (all floors), no wall first floor, and no wall on top level against median spectral displacement over the range of T_1.

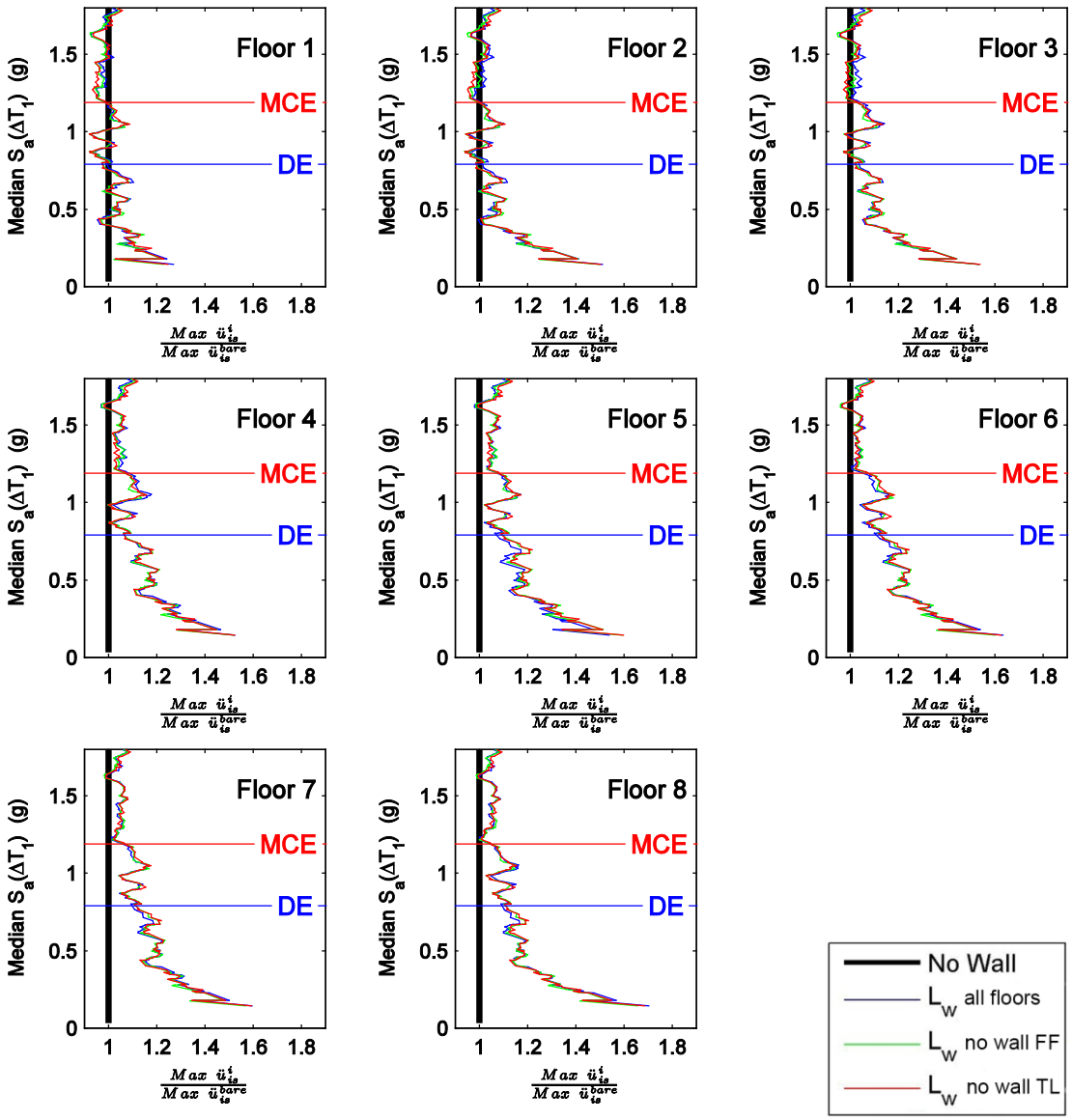

Figure C.71 Normalized maximum floor level acceleration moving average curves for RC-8 considering the cases of wall placement: no wall, minimum wall length (all floors), no wall first floor, and no wall on top level against median spectral acceleration over the range of T_1.

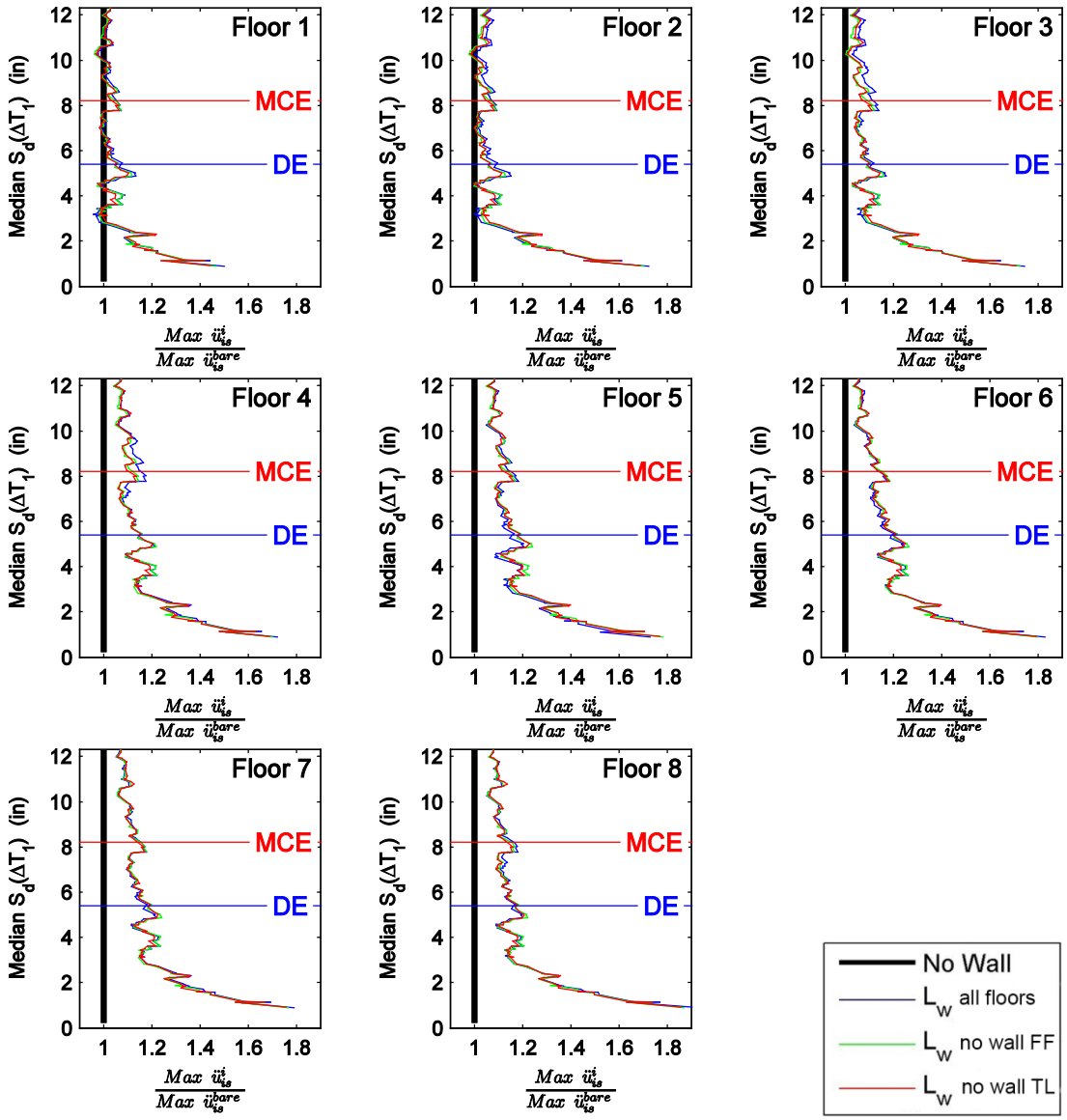

Figure C.72 Normalized maximum floor level acceleration moving average curves for RC-8 considering the cases of wall placement: no wall, minimum wall length (all floors), no wall first floor, and no wall on top level against median spectral displacement over the range of T_1.

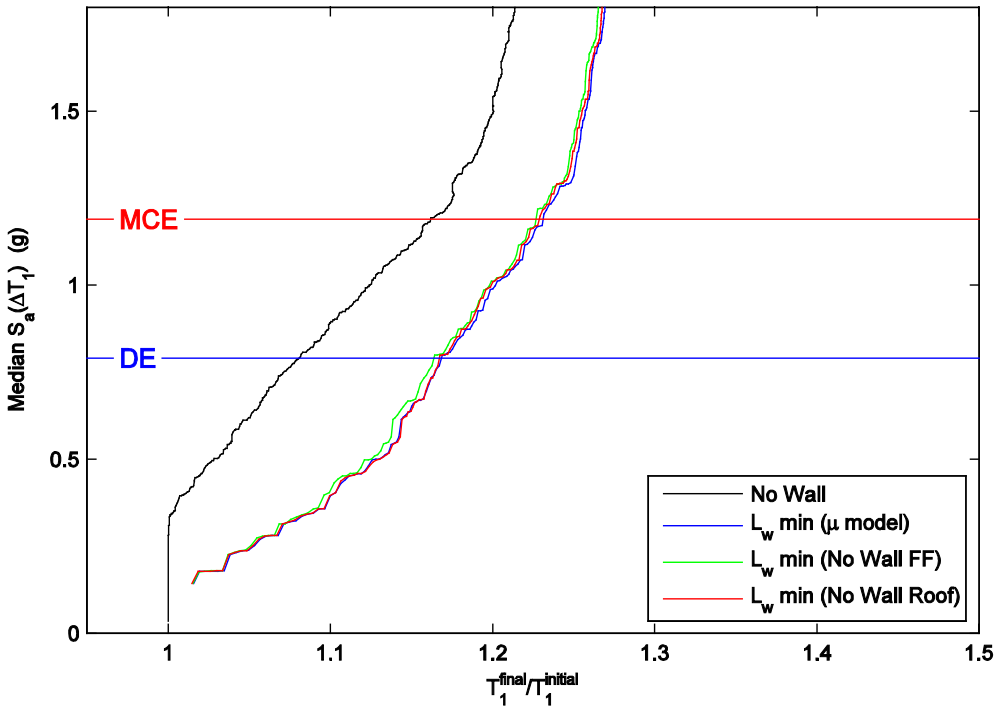

Figure C.73 Period elongation moving average curves for RC-8 considering the cases of wall placement: no wall, minimum wall length (all floors), no wall first floor, and no wall on top level against median spectral acceleration over the range of T_1.

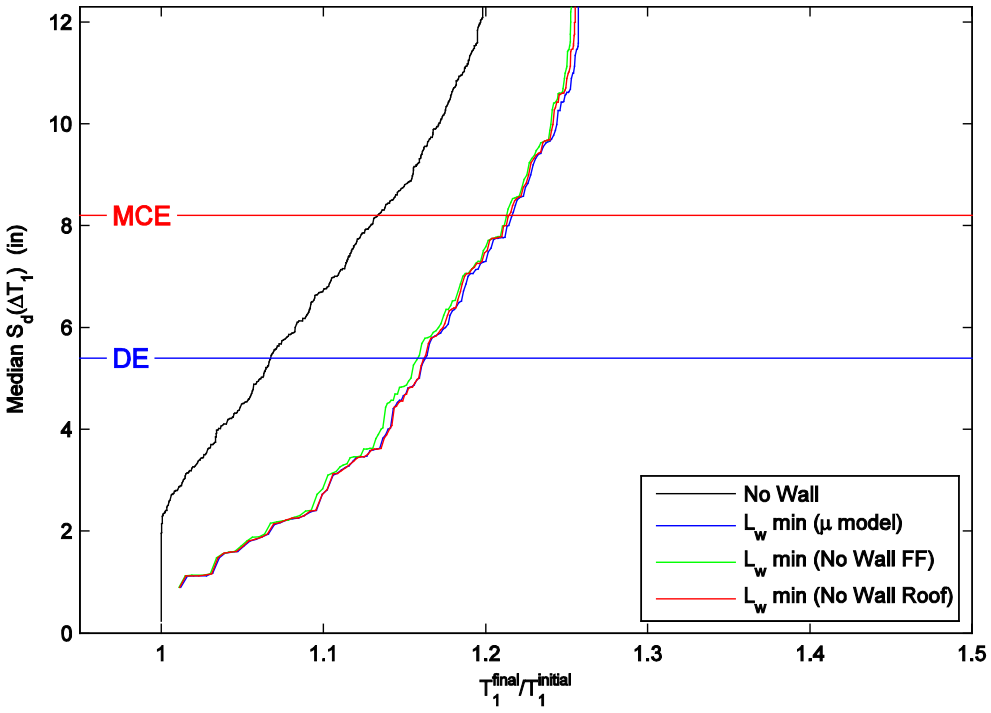

Figure C.74 Period elongation moving average curves for RC-8 considering the cases of wall placement: no wall, minimum wall length (all floors), no wall first floor, and no wall on top level against median spectral displacement over the range of T_1.

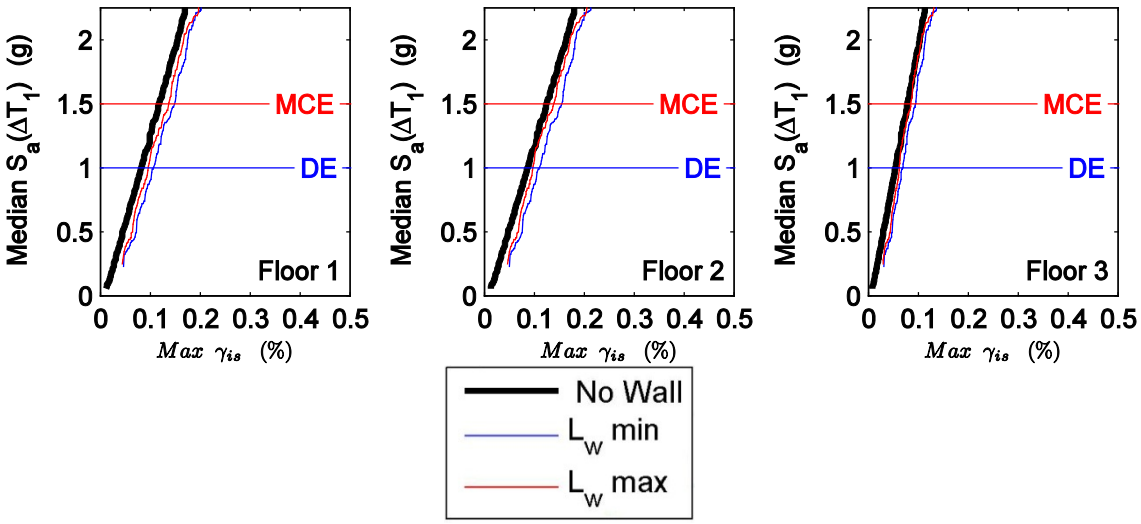

Figure C.75 Maximum interstory drift moving average curves for S-3H considering the cases of various wall length: no wall, minimum wall length, and minimum wall length against median spectral acceleration over the range of T_1.

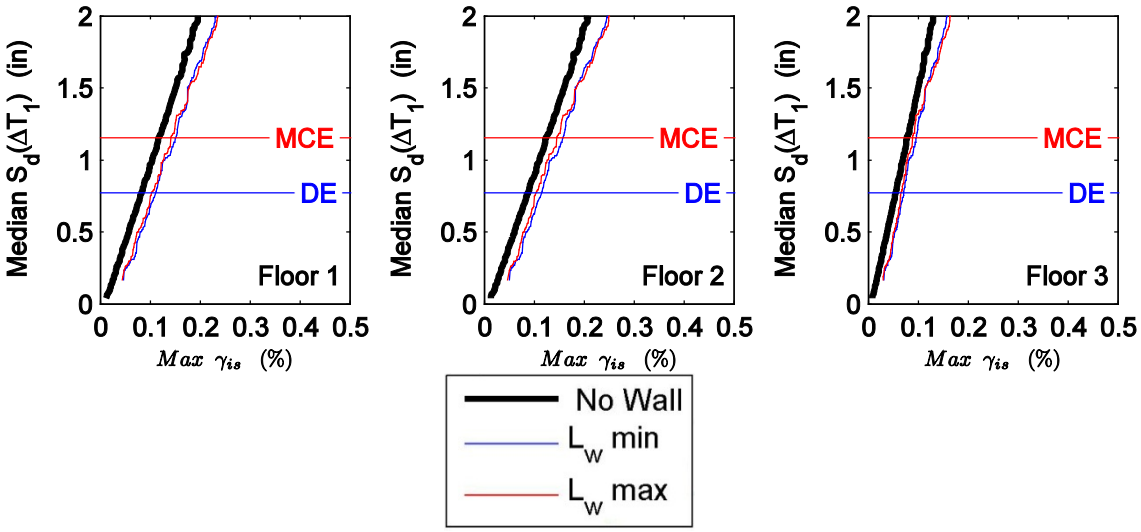

Figure C.76 Maximum interstory drift moving average curves for S-3H considering the cases of various wall length: no wall, minimum wall length, and minimum wall length against median spectral displacement over the range of T_1.

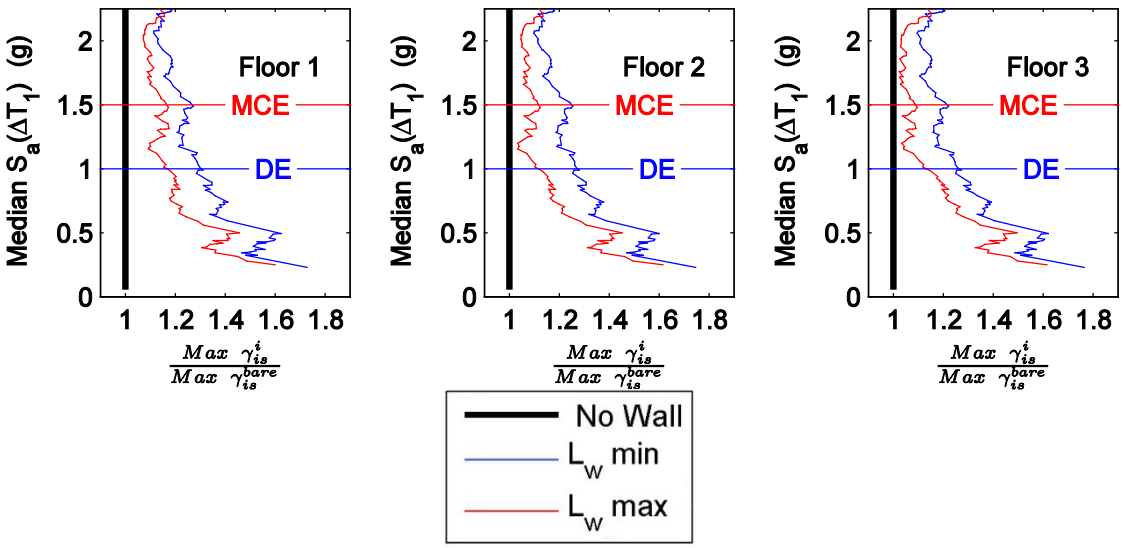

Figure C.77 Normalized maximum interstory drift moving average curves for S-3H considering cases of various wall length: no wall, minimum wall length, and minimum wall length against median spectral acceleration over the range of T_1.

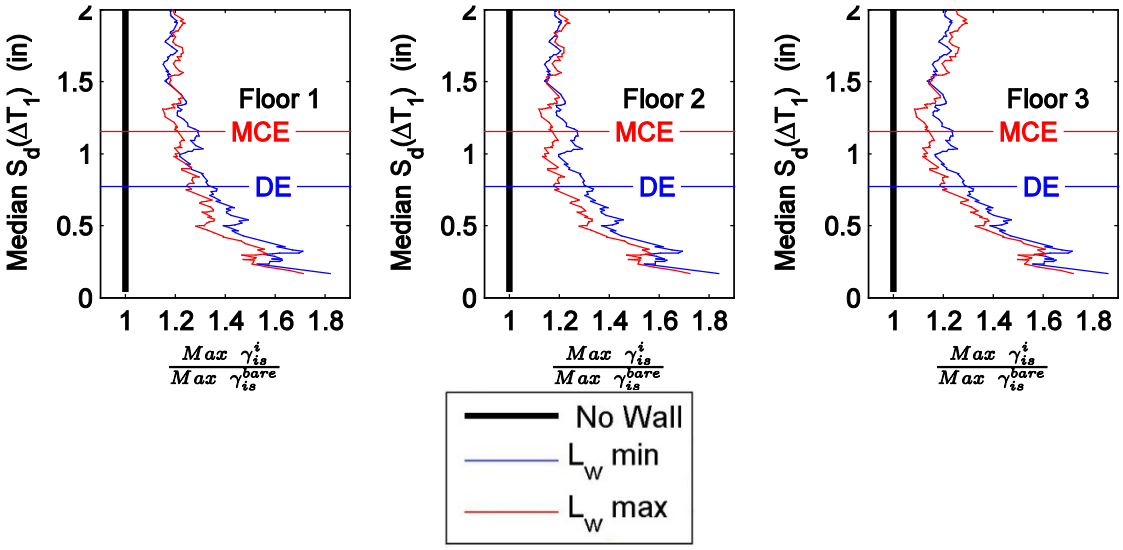

Figure C.78 Normalized maximum interstory drift moving average curves for S-3H considering cases of various wall length: no wall, minimum wall length, and minimum wall length against median spectral displacement over the range of T_1.

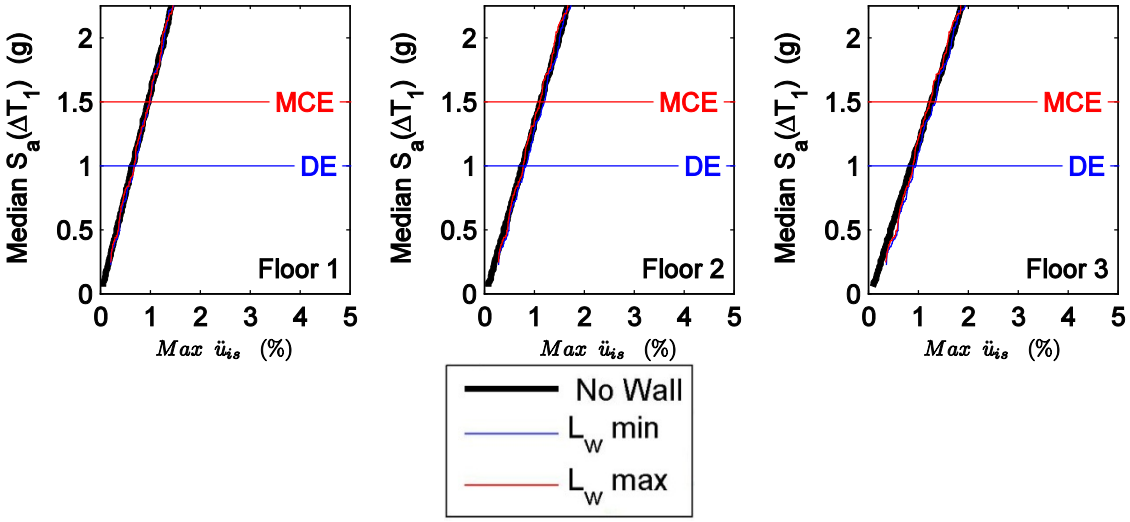

Figure C.79 Maximum floor level acceleration moving average curves for S-3H considering the cases of various wall length: no wall, minimum wall length, and minimum wall length against median spectral acceleration over the range of T_1.

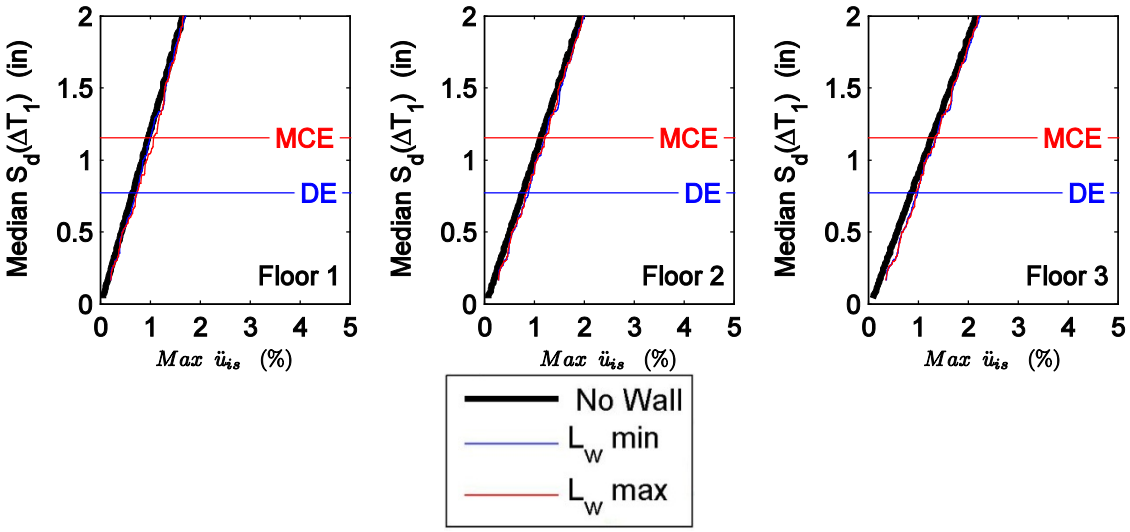

Figure C.80 Maximum floor level acceleration moving average curves for S-3H considering the cases of various wall length: no wall, minimum wall length, and minimum wall length against median spectral displacement over the range of T_1.

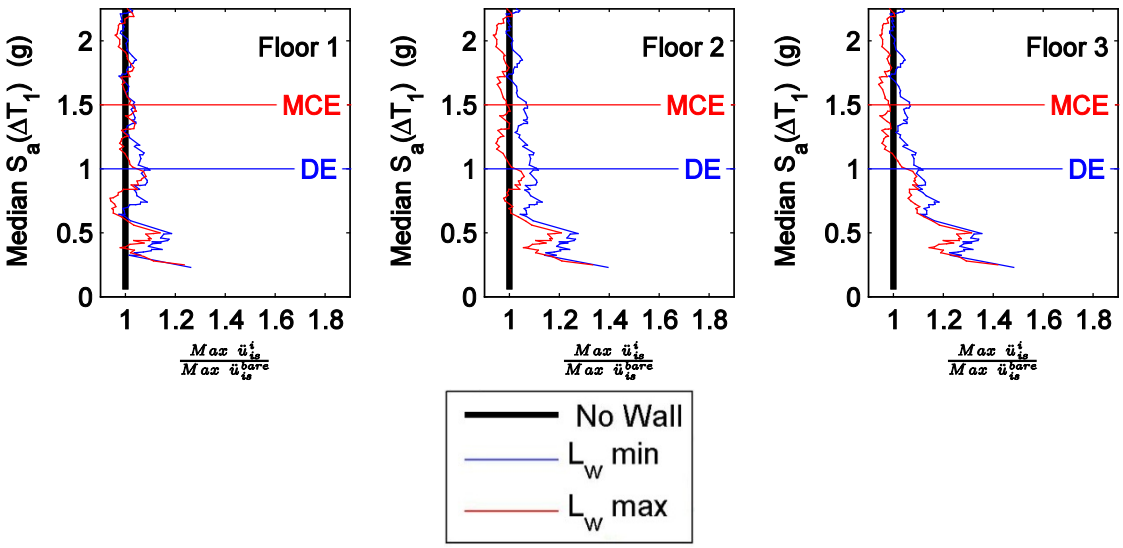

Figure C.81 Normalized maximum floor level acceleration moving average curves for S-3H considering the cases of various wall length: no wall, minimum wall length, and minimum wall length against median spectral acceleration over the range of T_1.

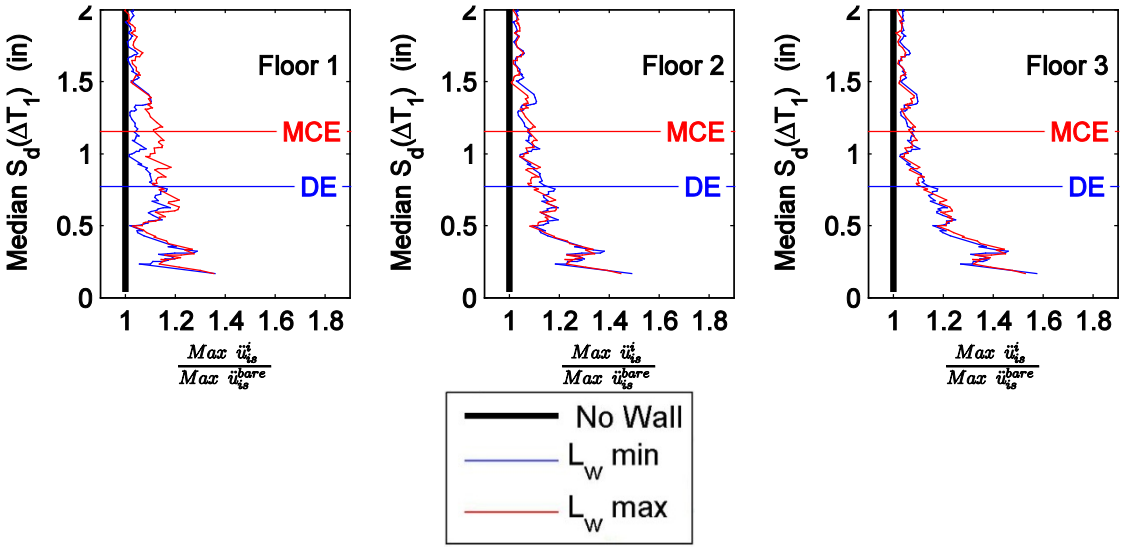

Figure C.82 Normalized maximum floor level acceleration moving average curves for S-3H considering the cases of various wall length: no wall, minimum wall length, and minimum wall length against median spectral displacement over the range of T_1.

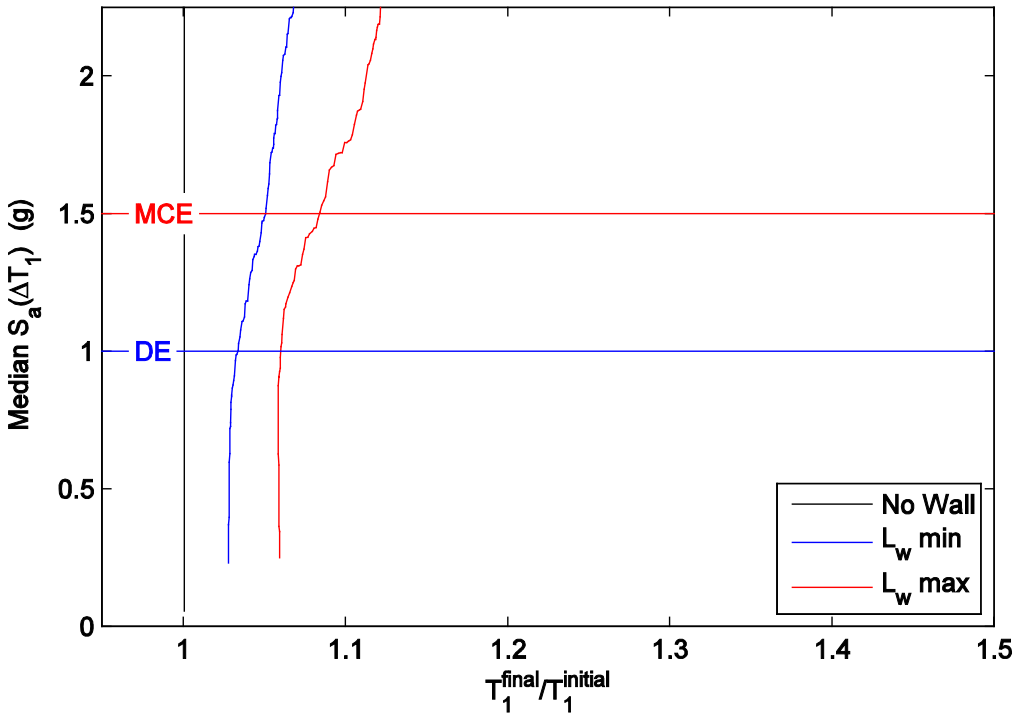

Figure C.83 Period elongation moving average curves for S-3H considering the cases of various wall length: no wall, minimum wall length, and minimum wall length against median spectral acceleration over the range of T_1.

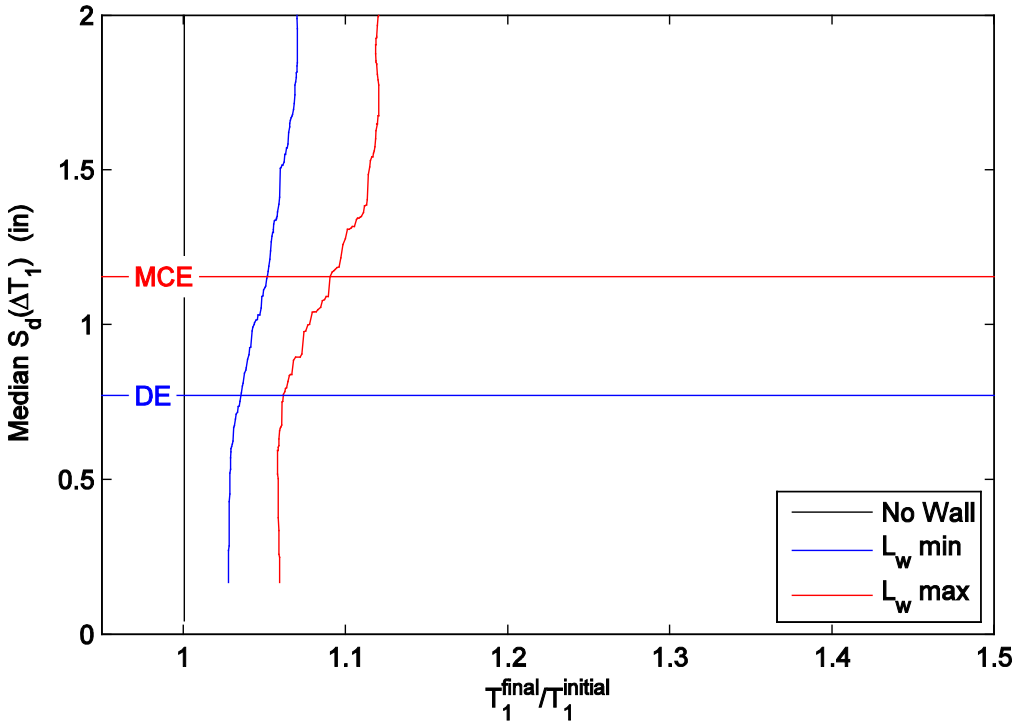

Figure C.84 Period elongation moving average curves for S-3H considering cases of various wall length: no wall, minimum wall length, and minimum wall length against median spectral displacement over the range of T_1.

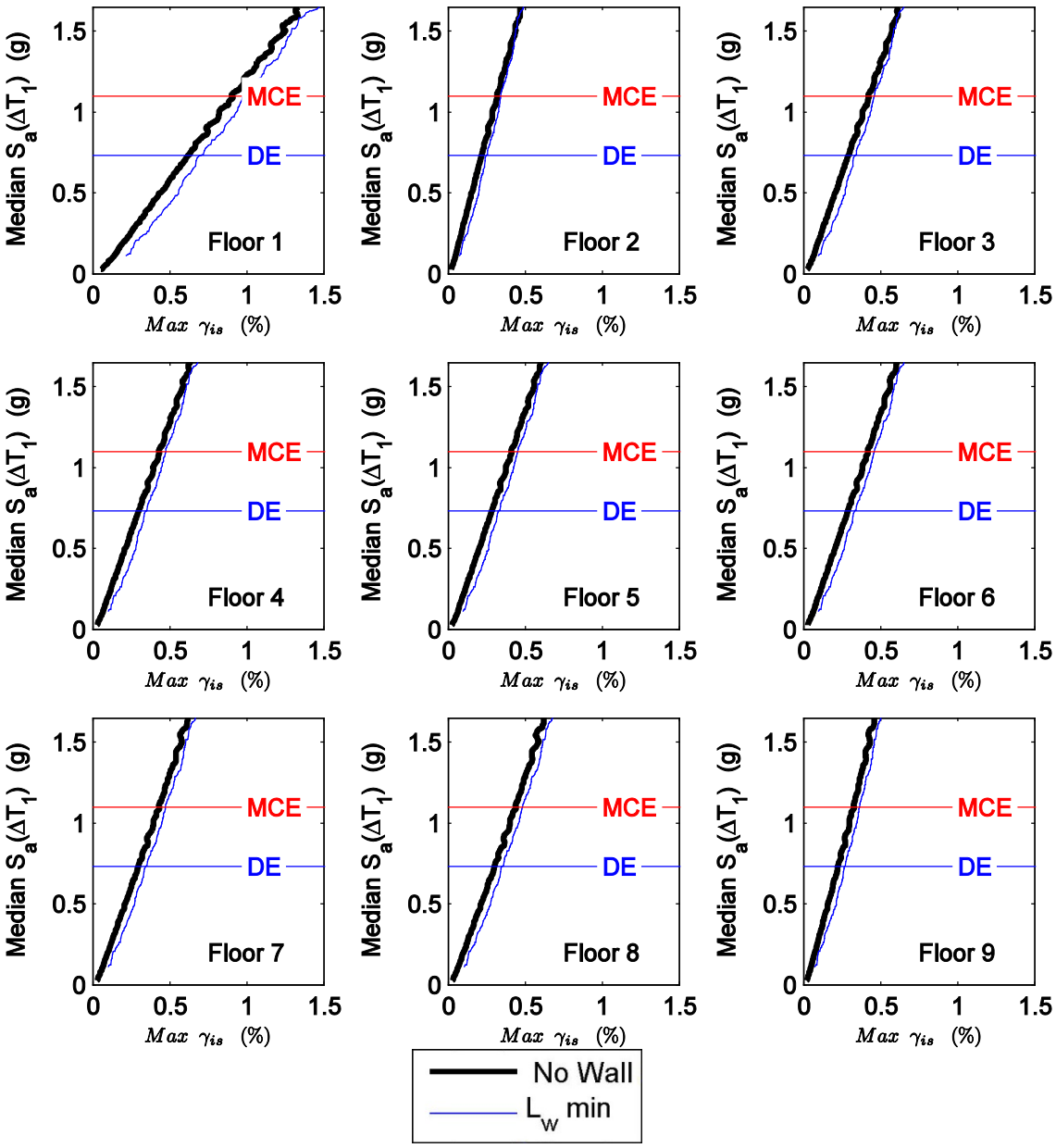

Figure C.85 Maximum interstory drift moving average curves for S-9 considering the cases of no wall and minimum wall length against median spectral acceleration over the range of T_1.

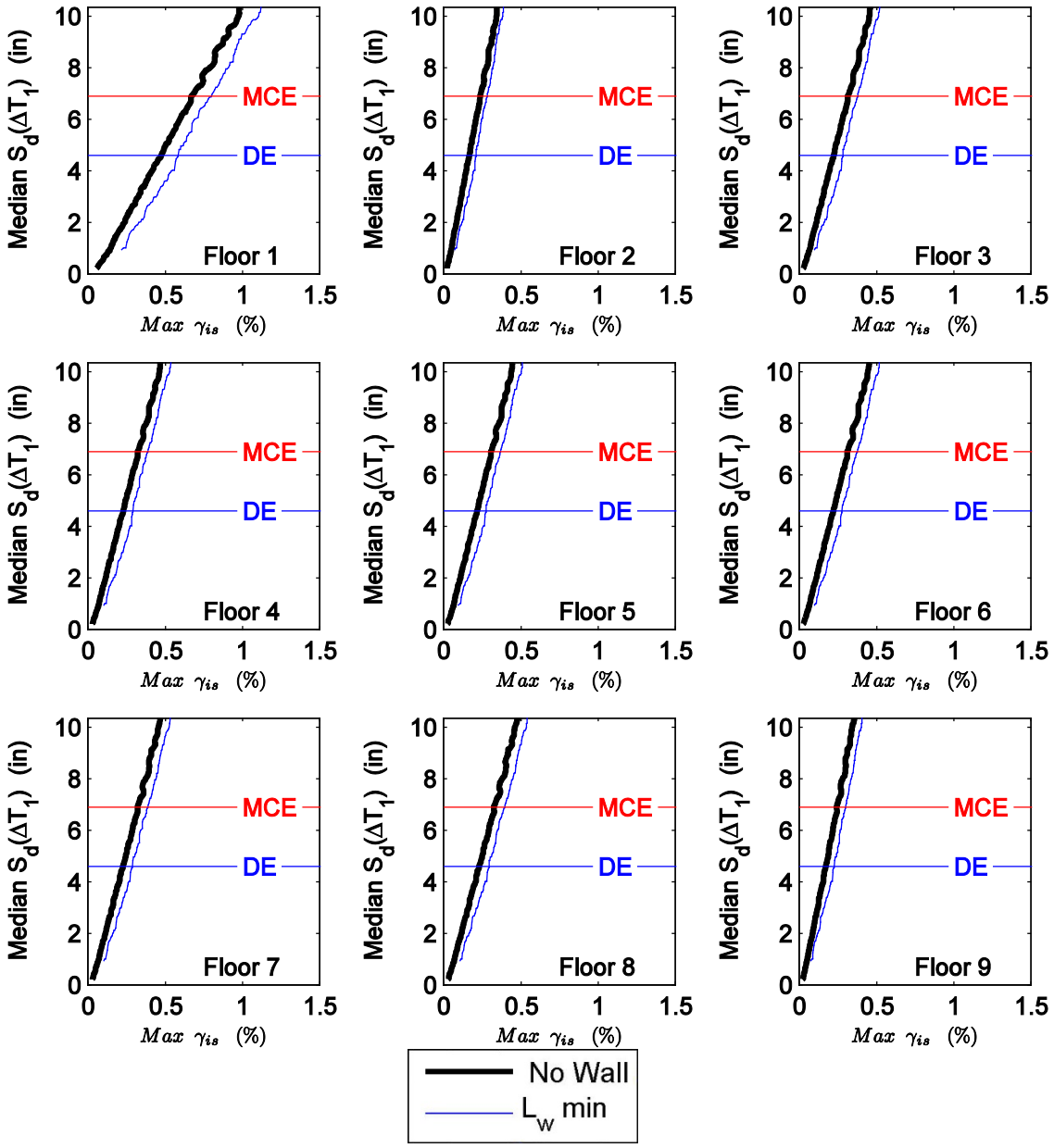

Figure C.86 Maximum interstory drift moving average curves for S-9 considering the cases of no wall and minimum wall length against median spectral displacement over the range of T_1.

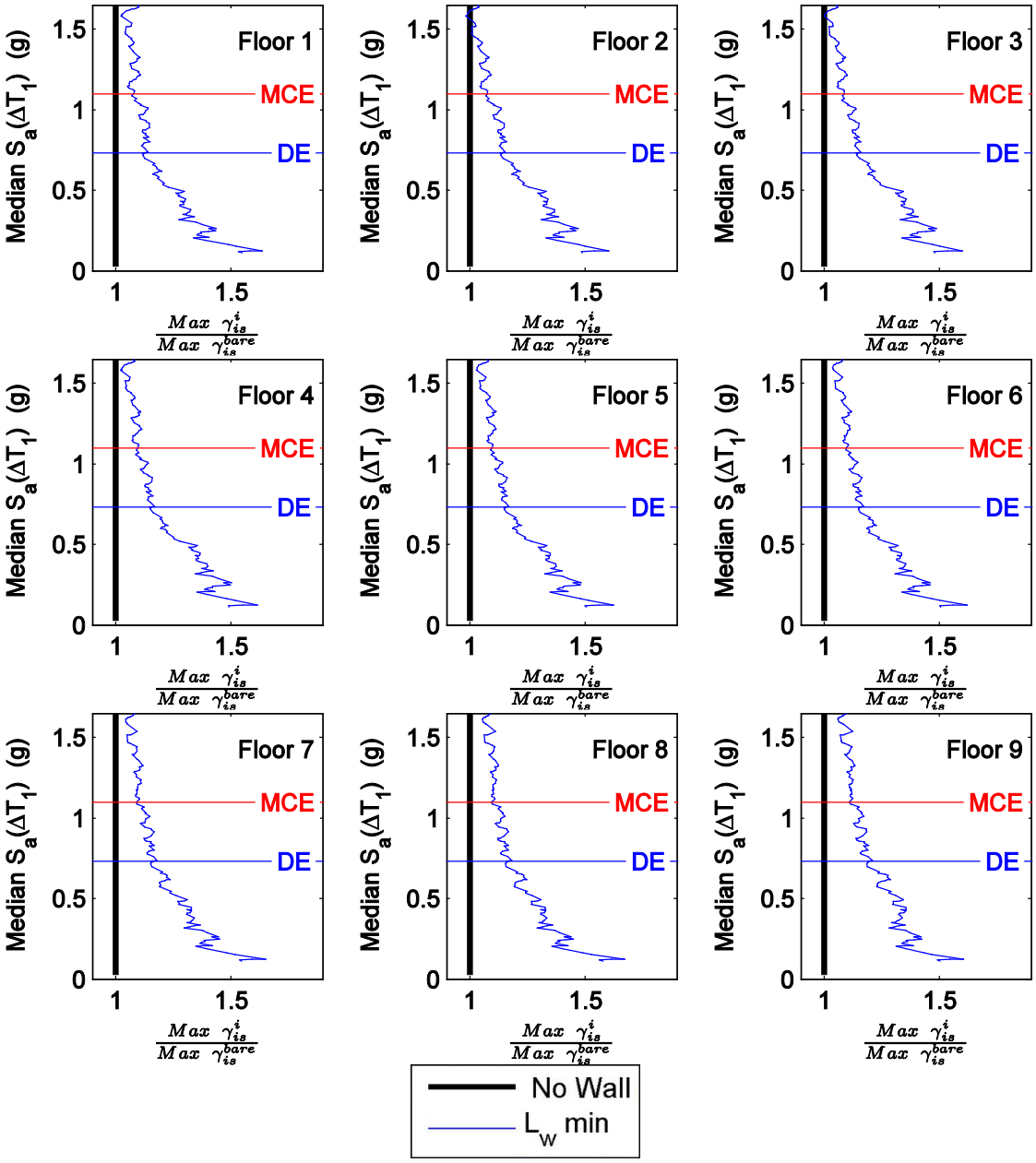

Figure C.87 Normalized maximum interstory drift moving average curves for S-9 considering the cases of no wall and minimum wall length against median spectral acceleration over the range of T_1.

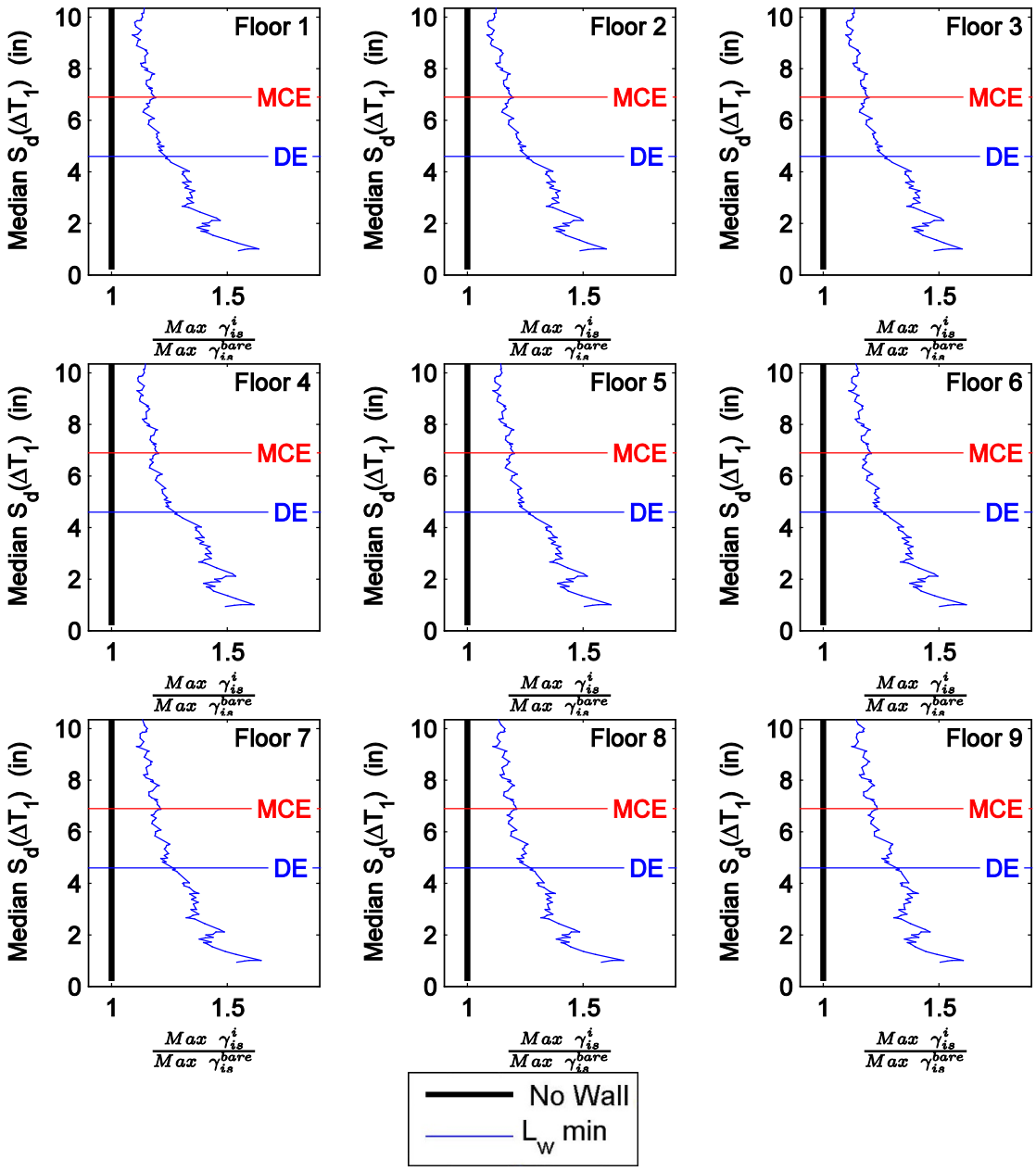

Figure C.88 Normalized maximum interstory drift moving average curves for S-9 considering the cases of no wall and minimum wall length against median spectral displacement over the range of T_1.

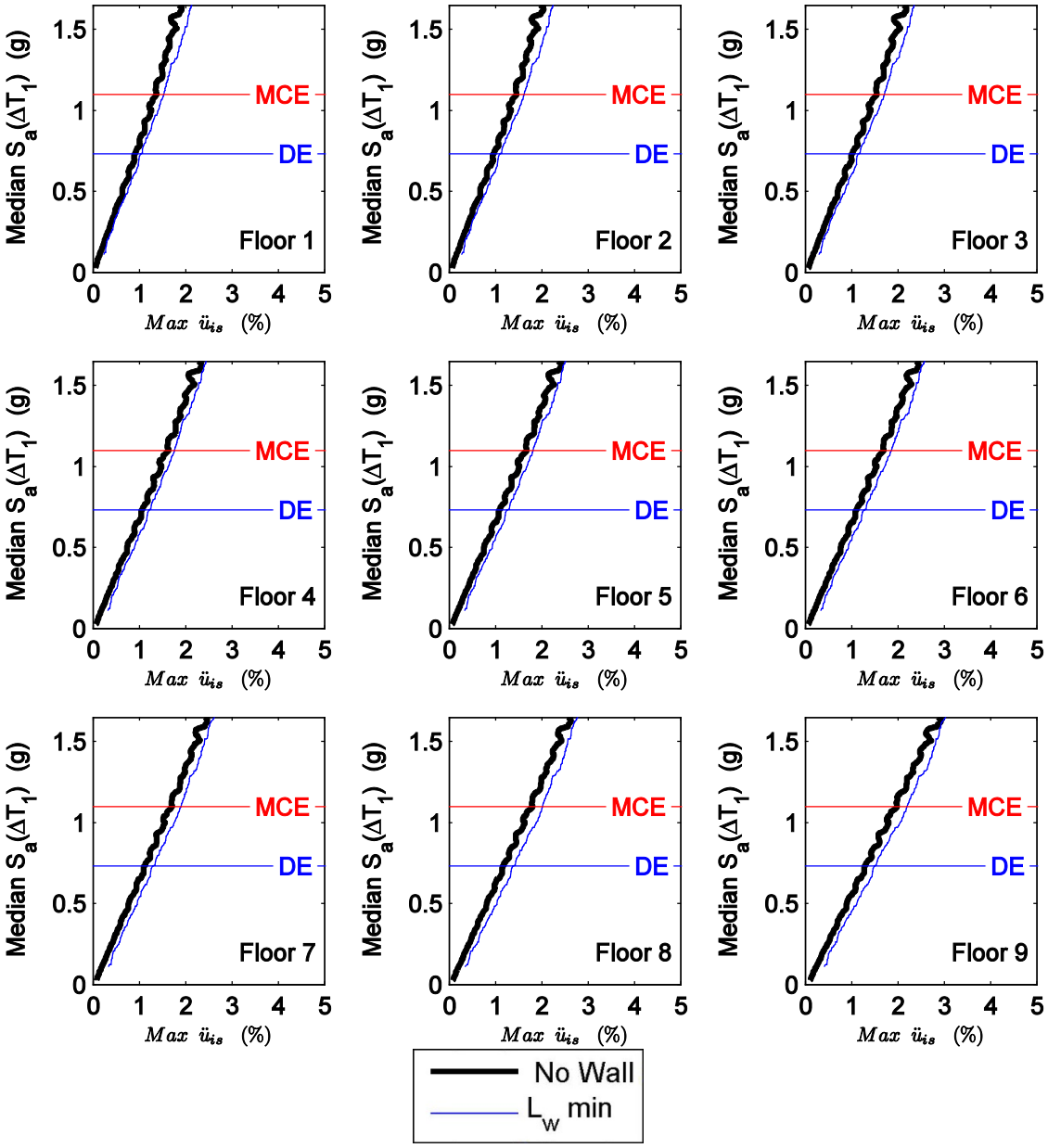

Figure C.89 Maximum floor level acceleration moving average curves for S-9 considering the cases of no wall and minimum wall length against median spectral acceleration over the range of T_1.

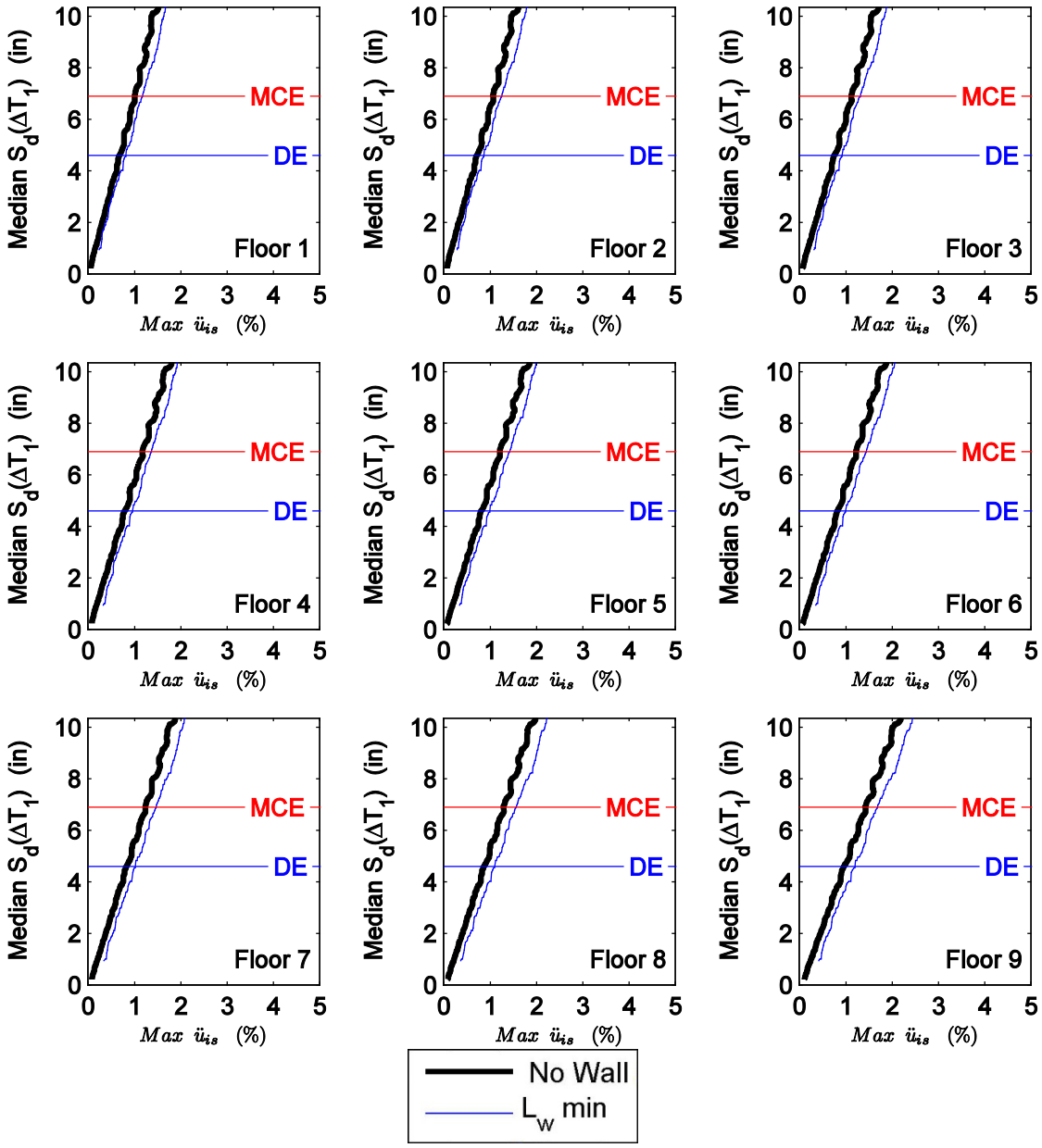

Figure C.90 Maximum floor level acceleration moving average curves for S-9 considering the cases of no wall and minimum wall length against median spectral acceleration over the range of T_1.

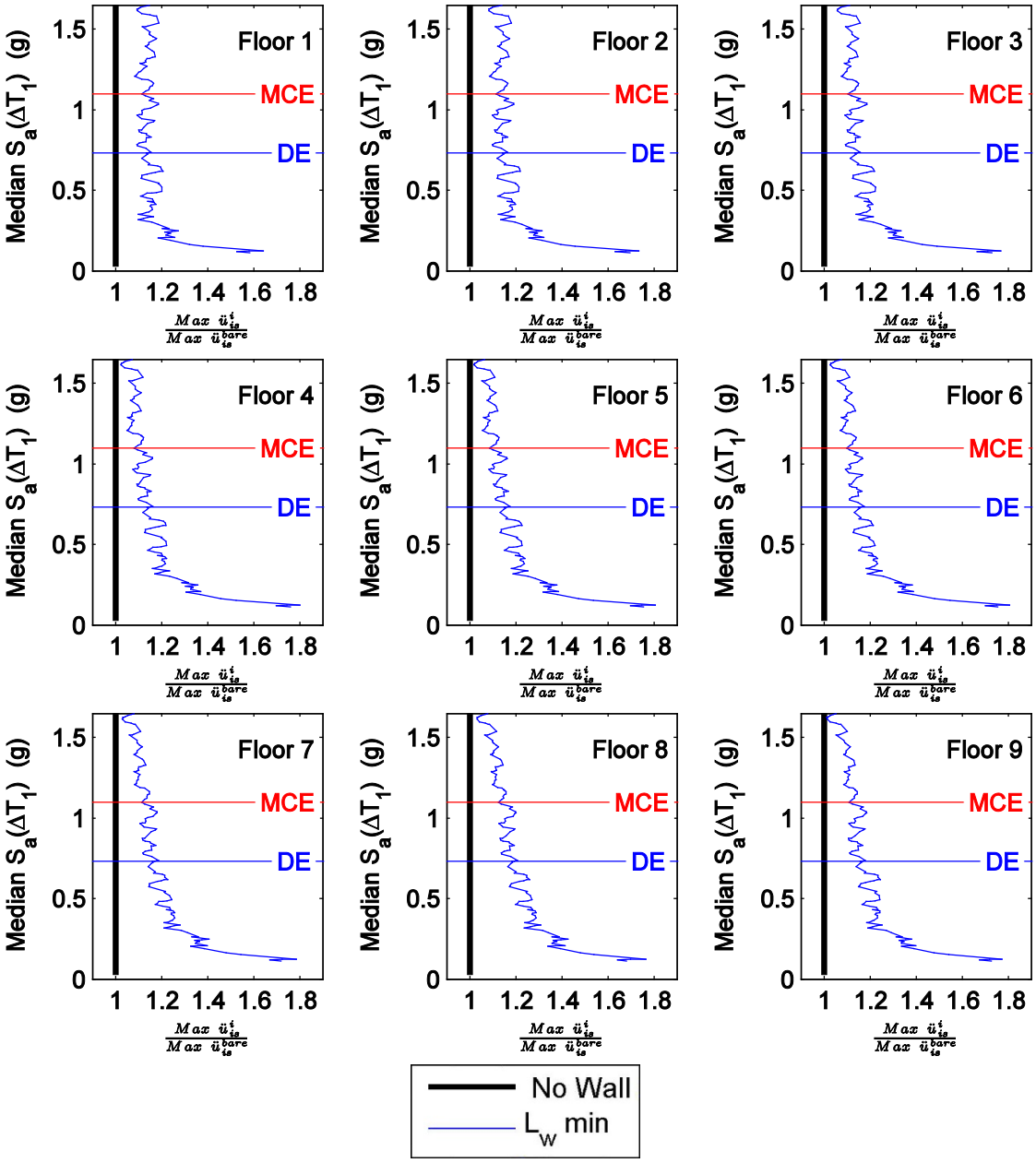

Figure C.91 Normalized maximum floor level acceleration moving average curves for S-9 considering the cases of no wall and minimum wall length against median spectral acceleration over the range of T_1.

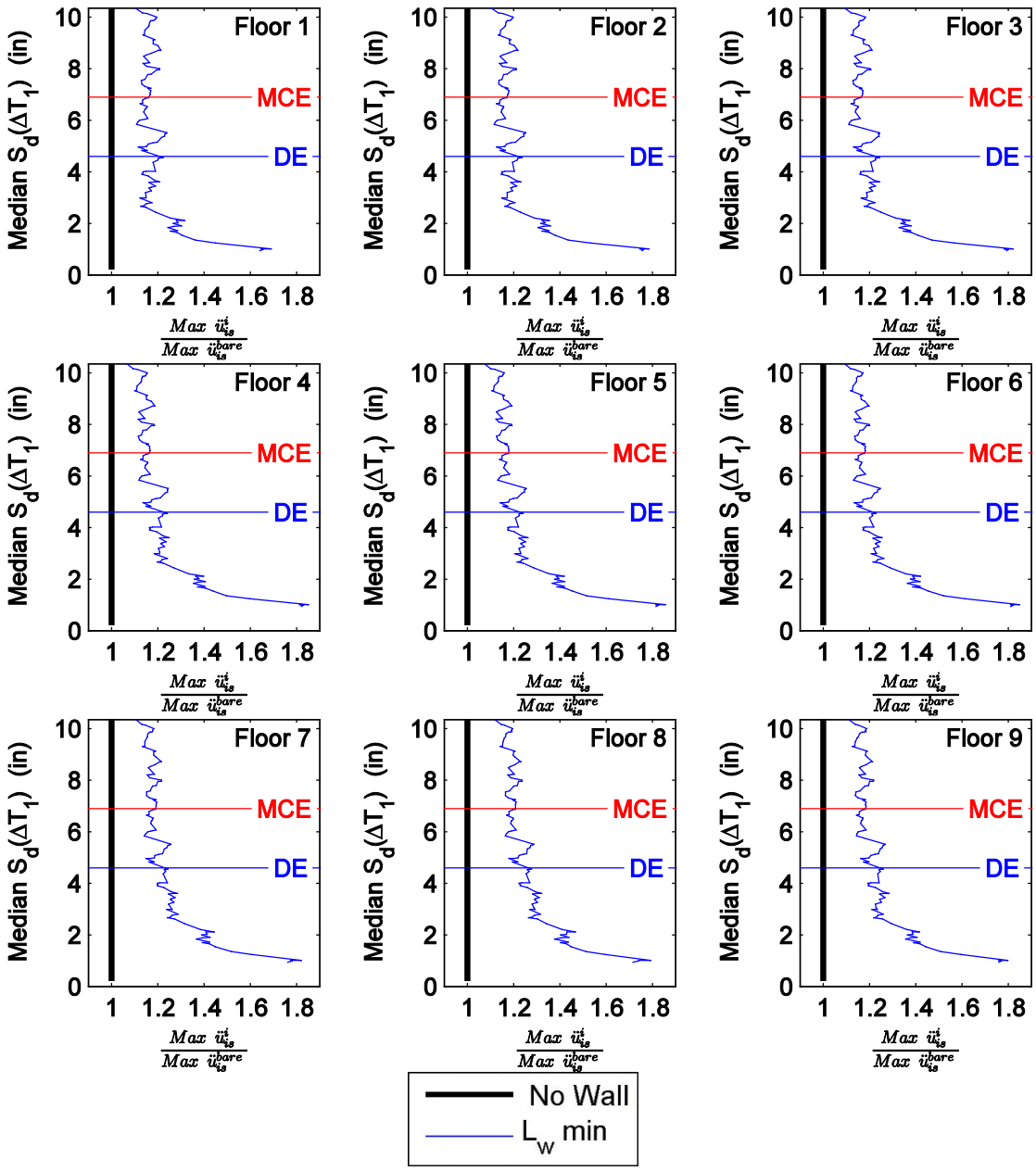

Figure C.92 Normalized maximum floor level acceleration moving average curves for S-9 considering the cases of no wall and minimum wall length against median spectral displacement over the range of T_1.

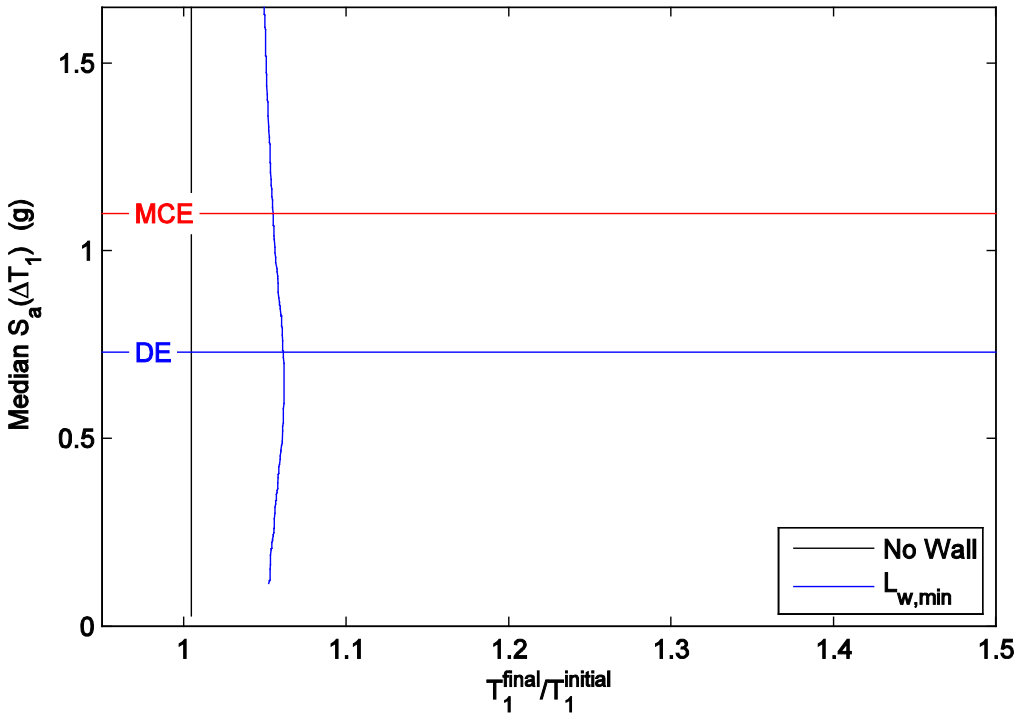

Figure C.93 Period elongation moving average curves for S-9 considering the cases of no wall and minimum wall length against median spectral acceleration over the range of T_1.

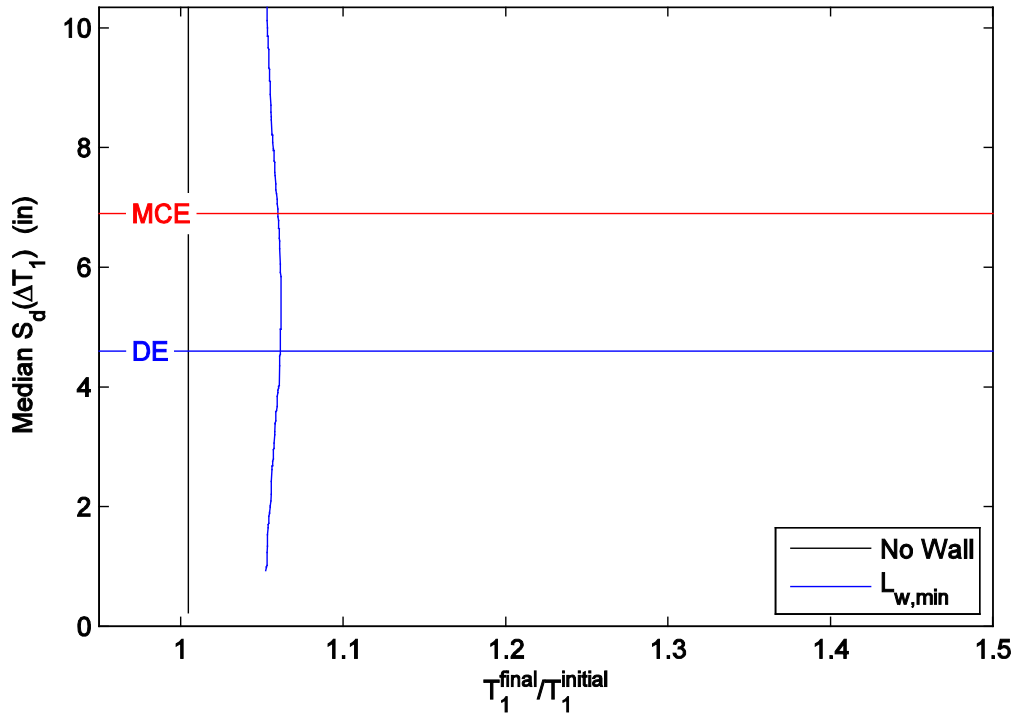

Figure C.94 Period elongation moving average curves for S-9 considering the cases of no wall and minimum wall length against median spectral displacement over the range of T_1.

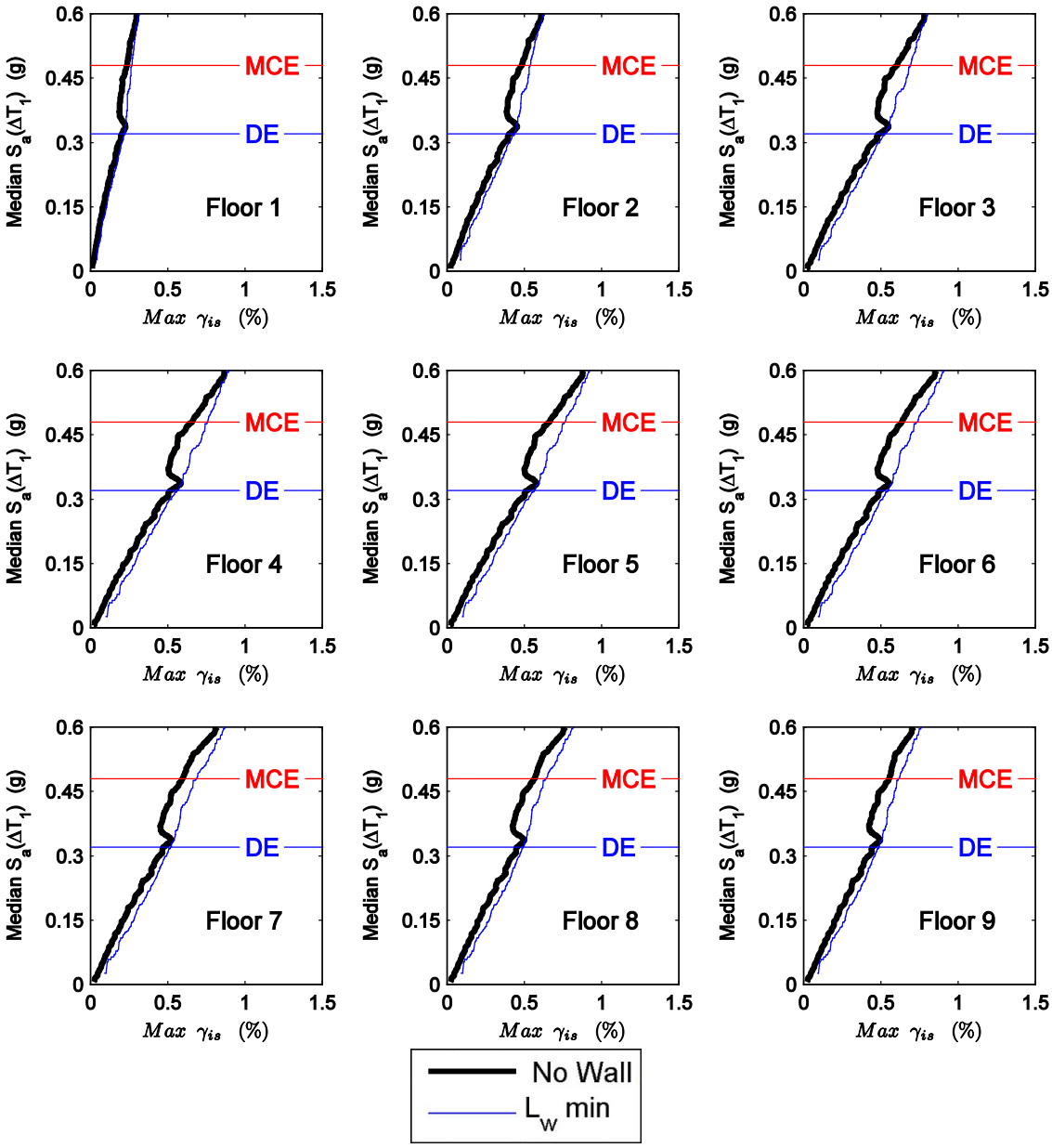

Figure C.95 Maximum interstory drift moving average curves for RC-20 considering the cases of no wall and minimum wall length against median spectral acceleration over the range of T_1 for floors 1-9.

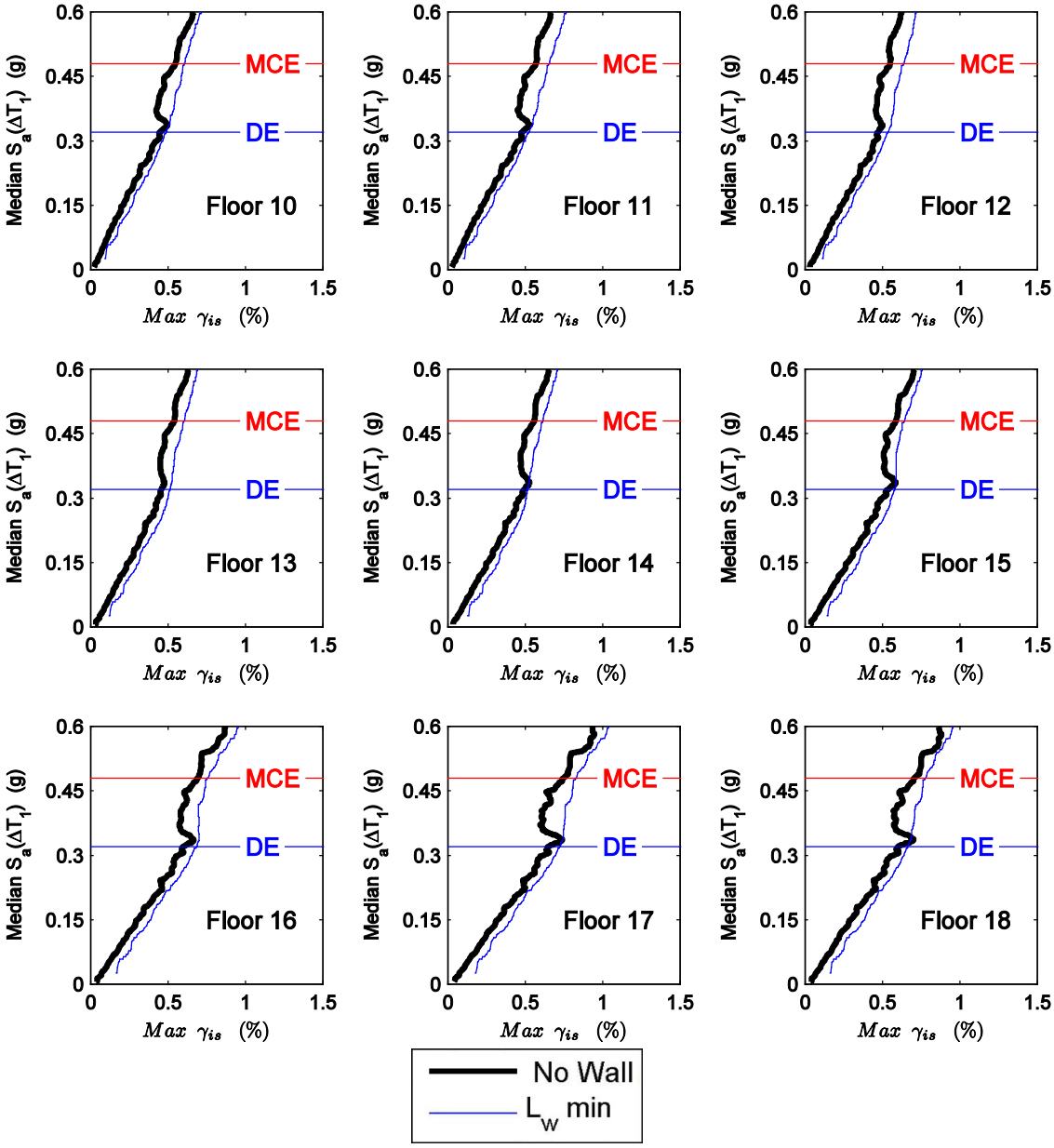

Figure C.96 Maximum interstory drift moving average curves for RC-20 considering the cases of no wall and minimum wall length against median spectral acceleration over the range of T_1 for floors 10-18

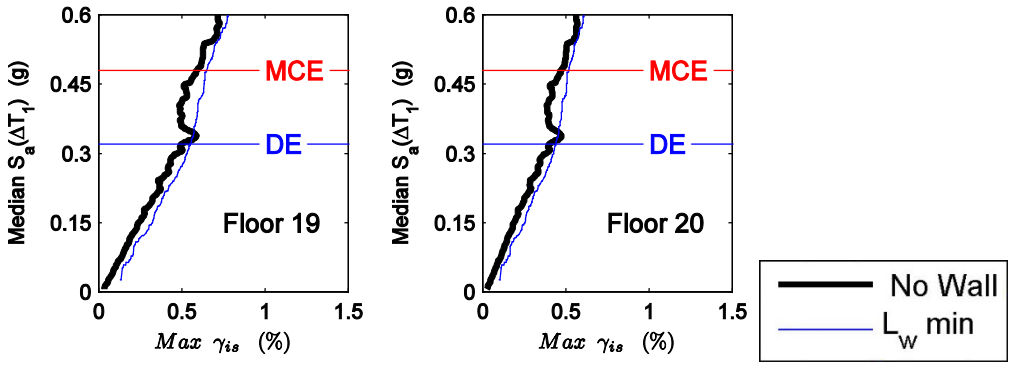

Figure C.97 Maximum interstory drift moving average curves for RC-20 considering the cases of no wall and minimum wall length against median spectral acceleration over the range of T_1 for floors 19-20.

.

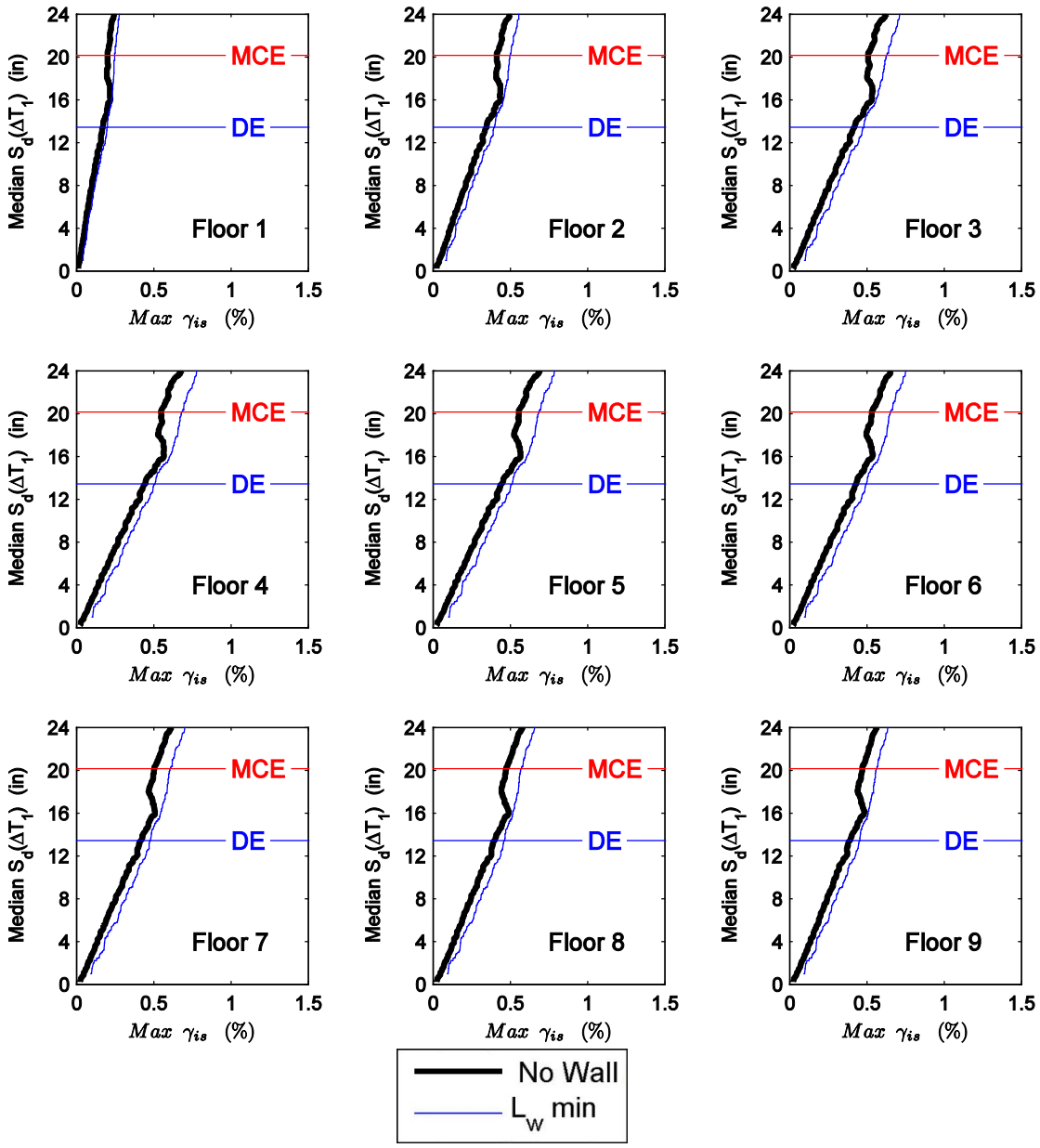

Figure C.98 Maximum interstory drift moving average curves for RC-20 considering the cases of no wall and minimum wall length against median spectral displacement over the range of T_1 for floors 1-9.

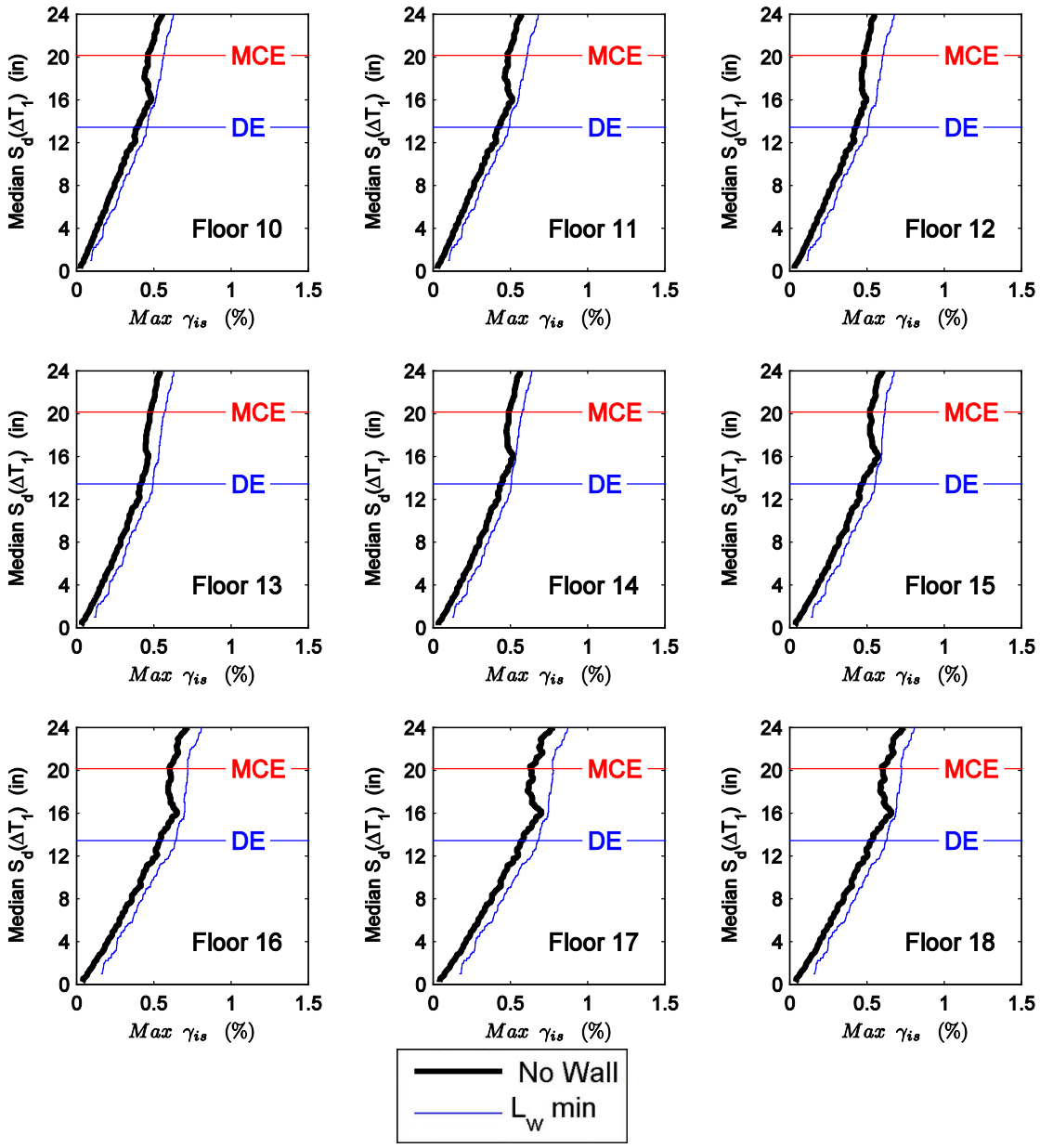

Figure C.99 Maximum interstory drift moving average curves for RC-20 considering the cases of no wall and minimum wall length against median spectral displacement over the range of T_1 for floors 10-18

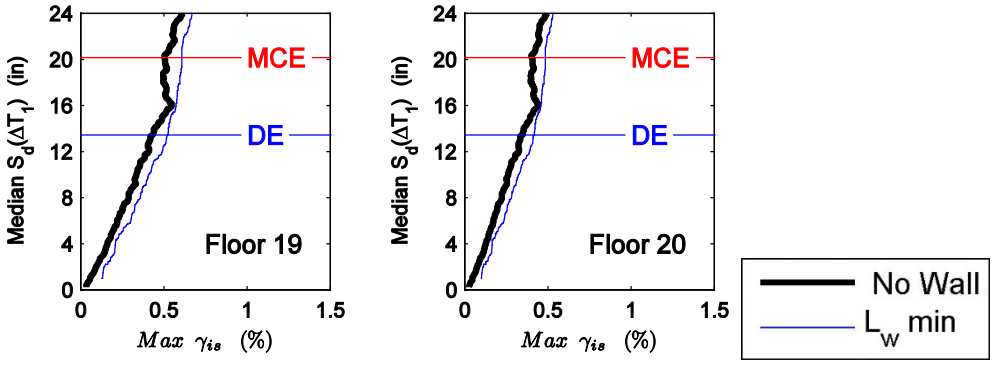

Figure C.100 Maximum interstory drift moving average curves for RC-20 considering the cases of no wall and minimum wall length against median spectral displacement over the range of T_1 for floors 19-20.

.

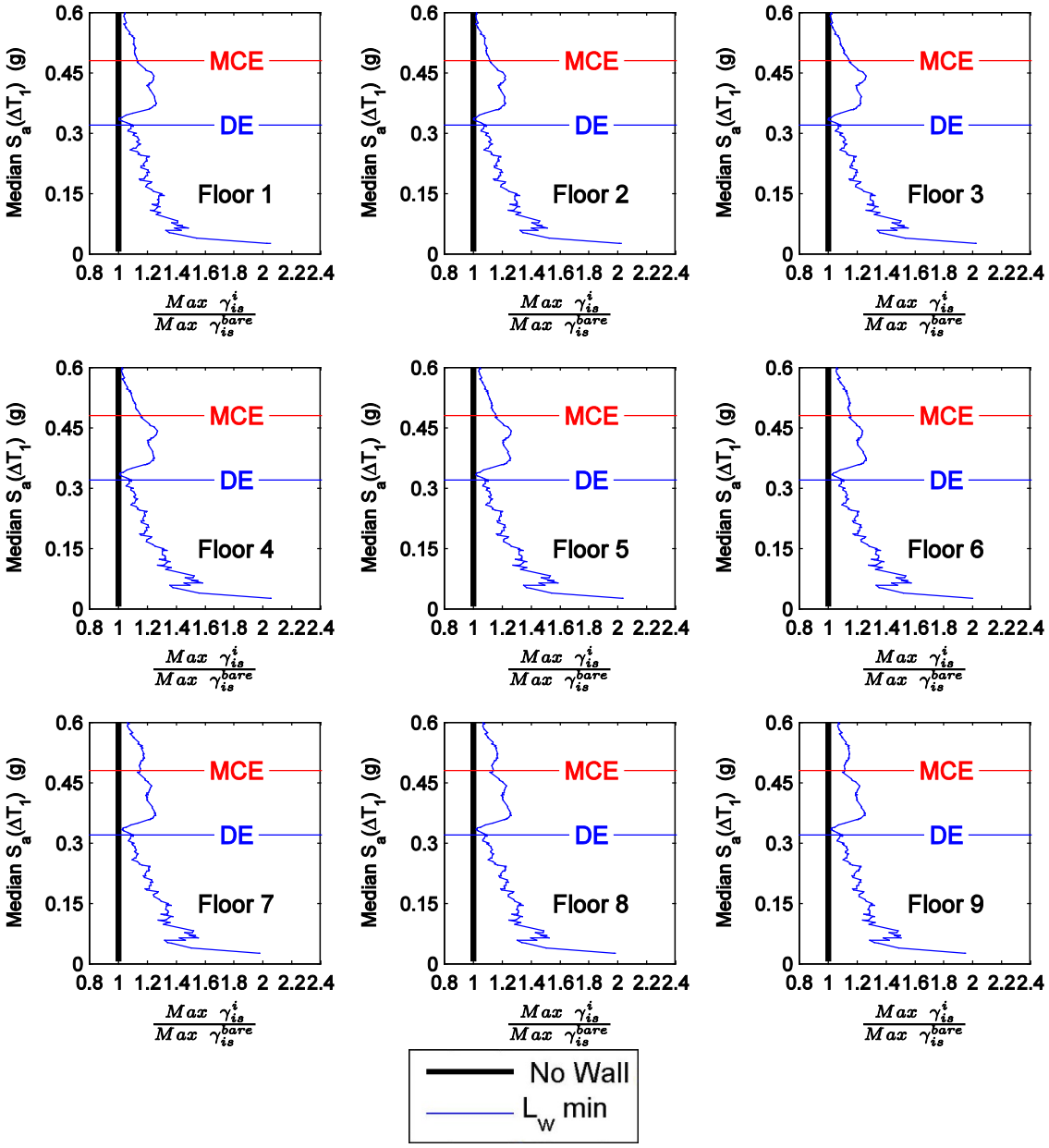

Figure C.101 Normalized maximum interstory drift moving average curves for RC-20 considering the cases of no wall and minimum wall length against median spectral acceleration over the range of T_1 for floors 1-9.

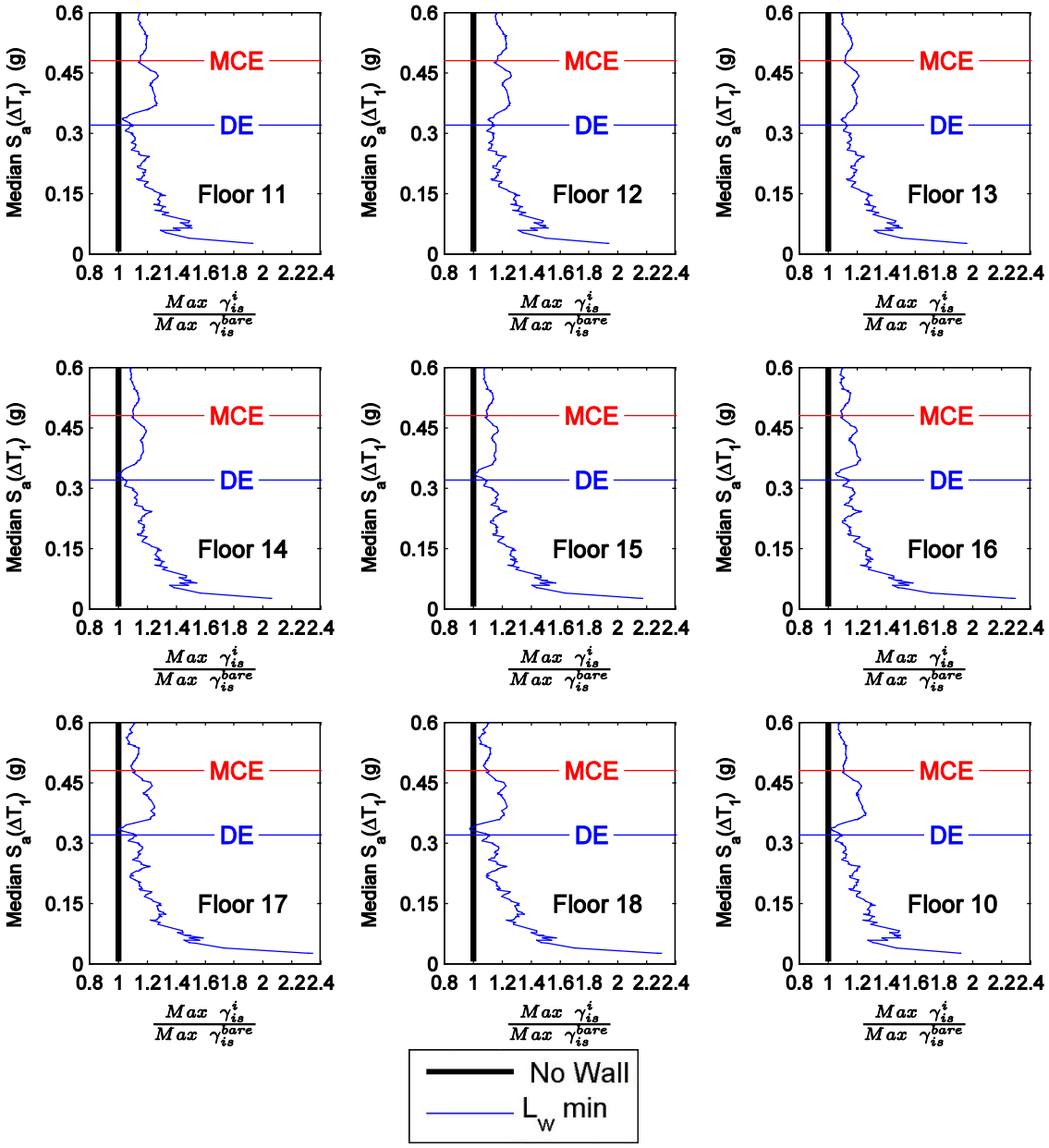

Figure C.102 Normalized maximum interstory drift moving average curves for RC-20 considering the cases of no wall and minimum wall length against median spectral acceleration over the range of T_1 for floors 10-18.

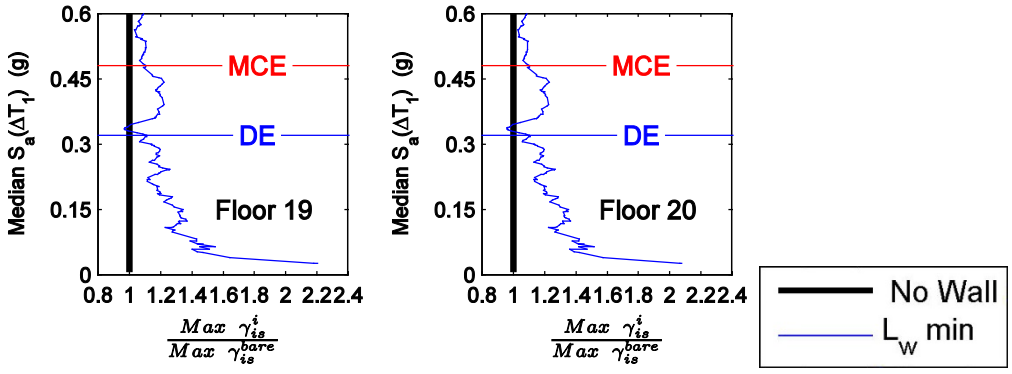

Figure C.103 Normalized maximum interstory drift moving average curves for RC-20 considering the cases of no wall and minimum wall length against median spectral acceleration over the range of T_1 for floors 19-20.

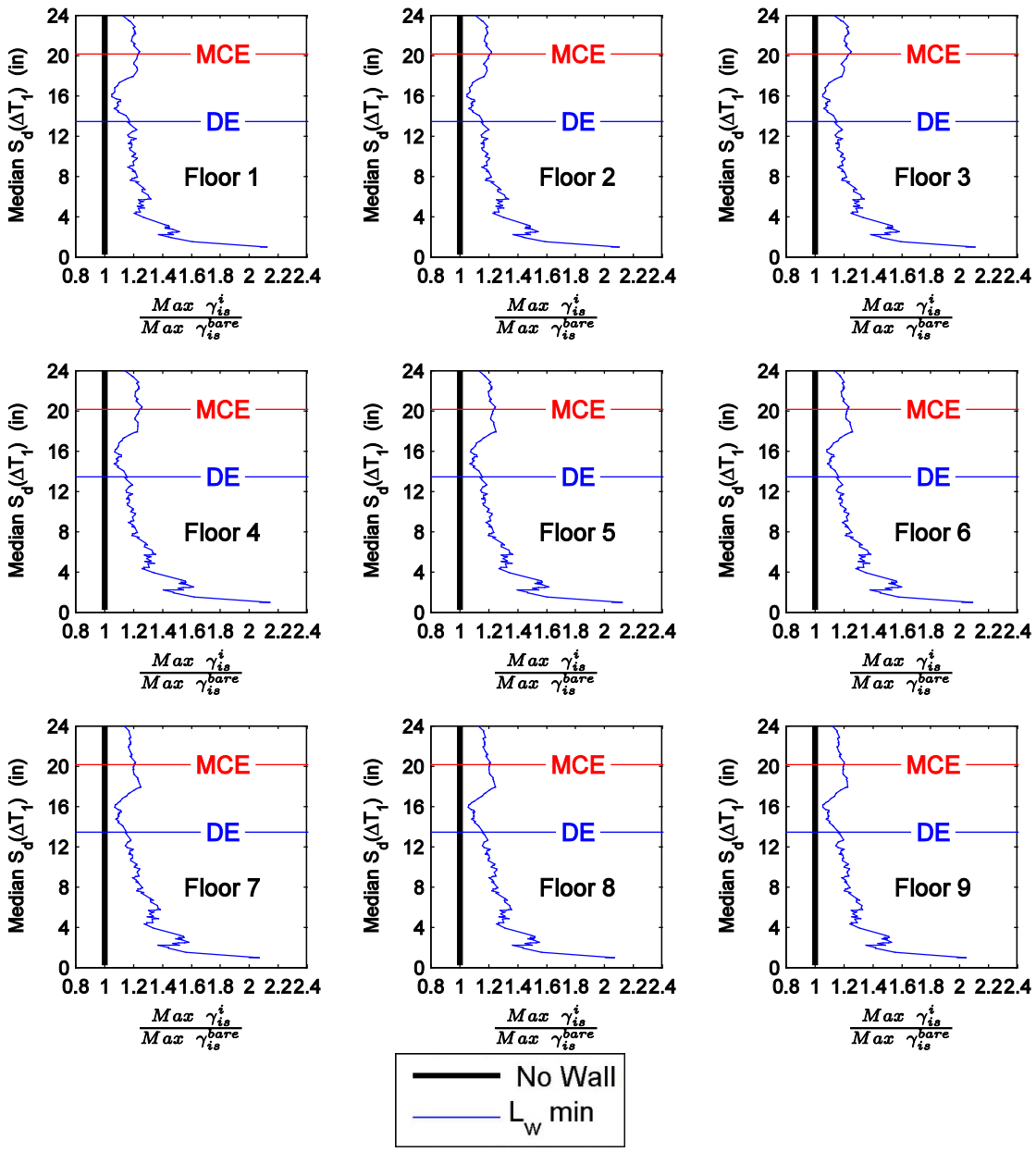

Figure C.104 Normalized maximum interstory drift moving average curves for RC-20 considering the cases of no wall and minimum wall length against median spectral displacement over the range of T_1 for floors 1-9.

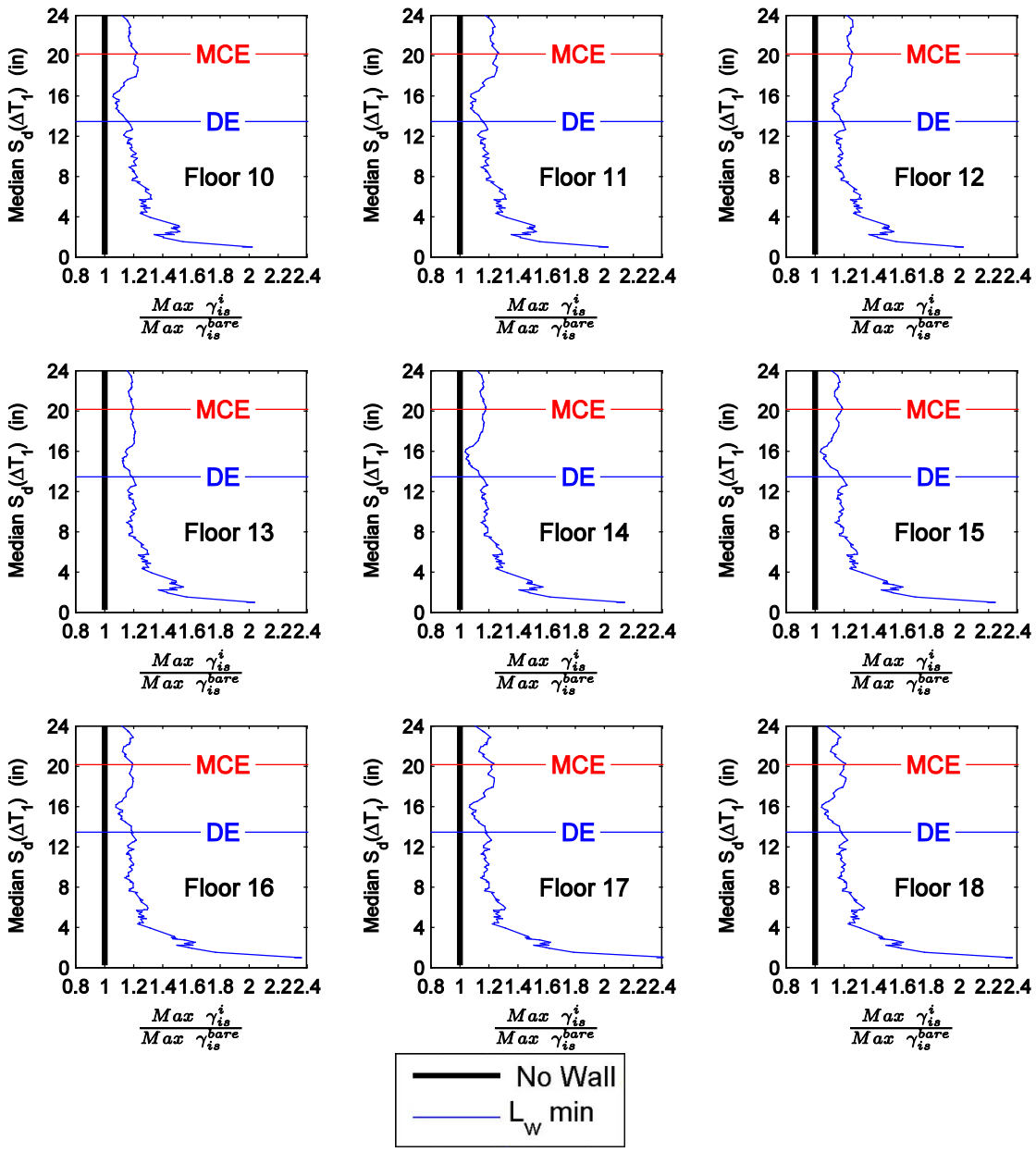

Figure C.105 Normalized maximum interstory drift moving average curves for RC-20 considering the cases of no wall and minimum wall length against median spectral displacement over the range of T_1 for floors 10-18.

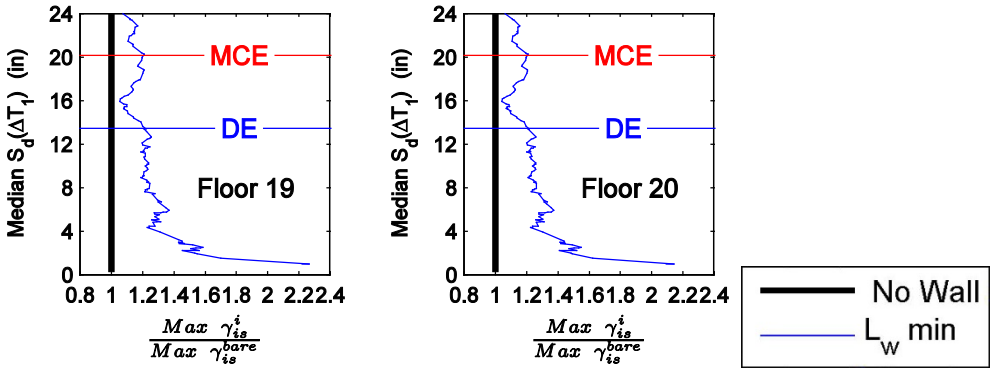

Figure C.106 Normalized maximum interstory drift moving average curves for RC-20 considering the cases of no wall and minimum wall length against median spectral displacement over the range of T_1 for floors 19-20.

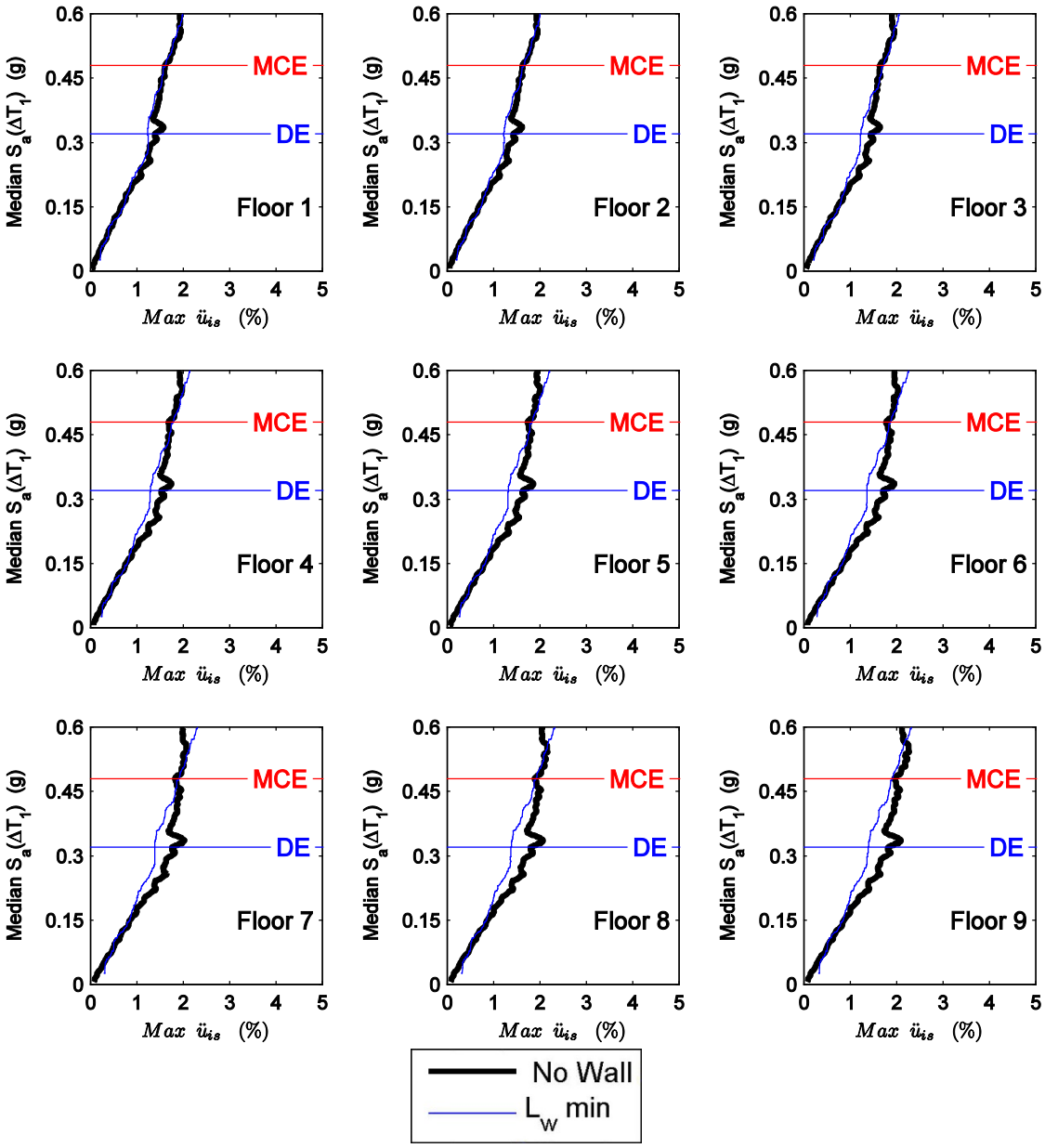

Figure C.107 Maximum floor level acceleration moving average curves for RC-20 considering the cases of no wall and minimum wall length against median spectral acceleration over the range of T_1 for floors 1-9.

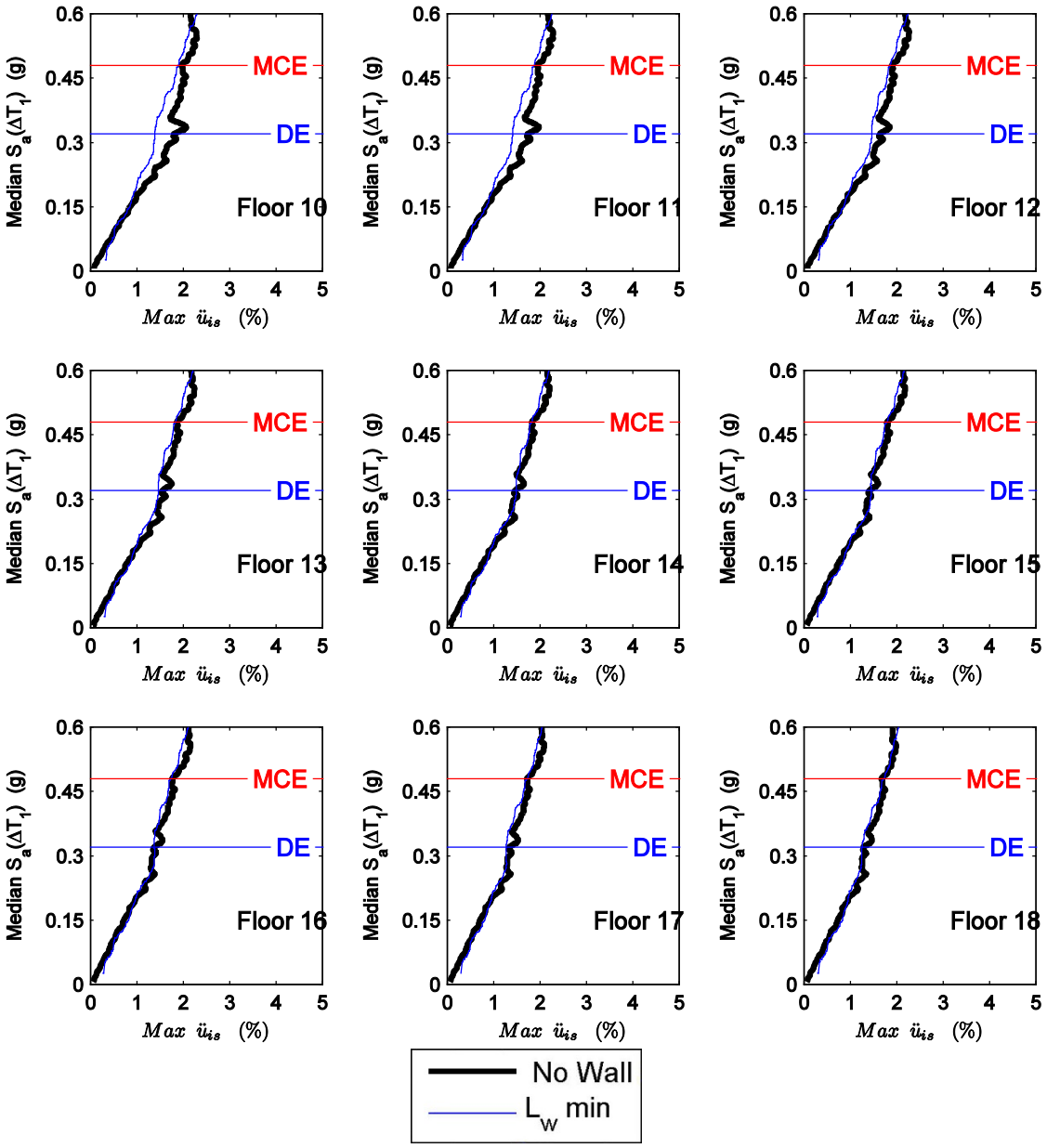

Figure C.108 Maximum floor level acceleration moving average curves for RC-20 considering the cases of no wall and minimum wall length against median spectral acceleration over the range of T_1 for floors 10-18.

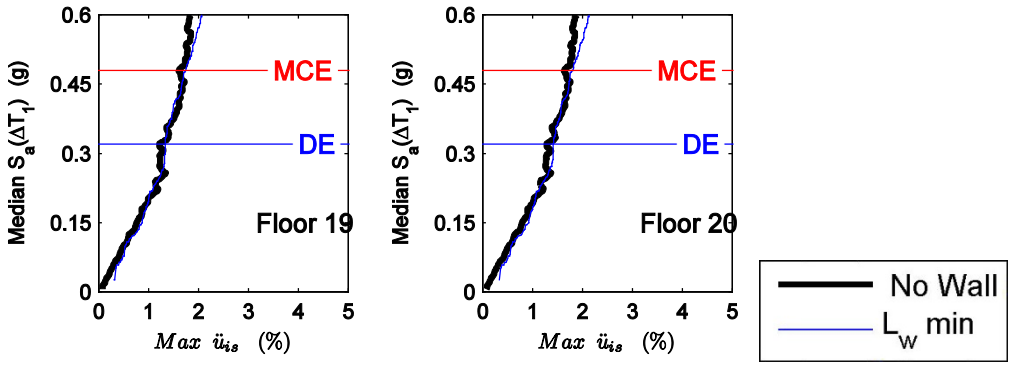

Figure C.109 Maximum floor level acceleration moving average curves for RC-20 considering the cases of no wall and minimum wall length against median spectral acceleration over the range of T_1 for floors 19-20.

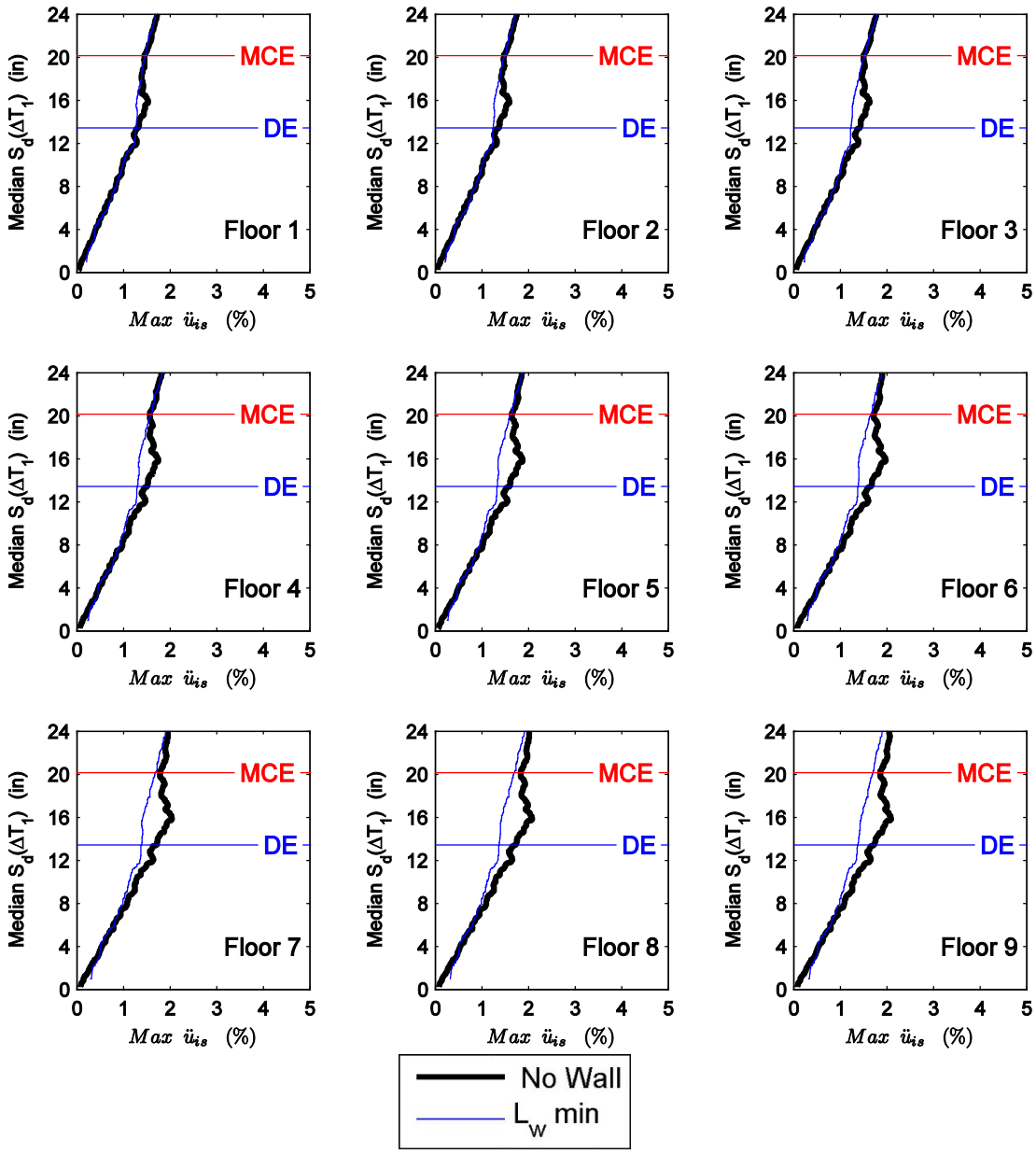

Figure C.110 Maximum floor level acceleration moving average curves for RC-20 considering the cases of no wall and minimum wall length against median spectral acceleration over the range of T_1 for floors 1-9.

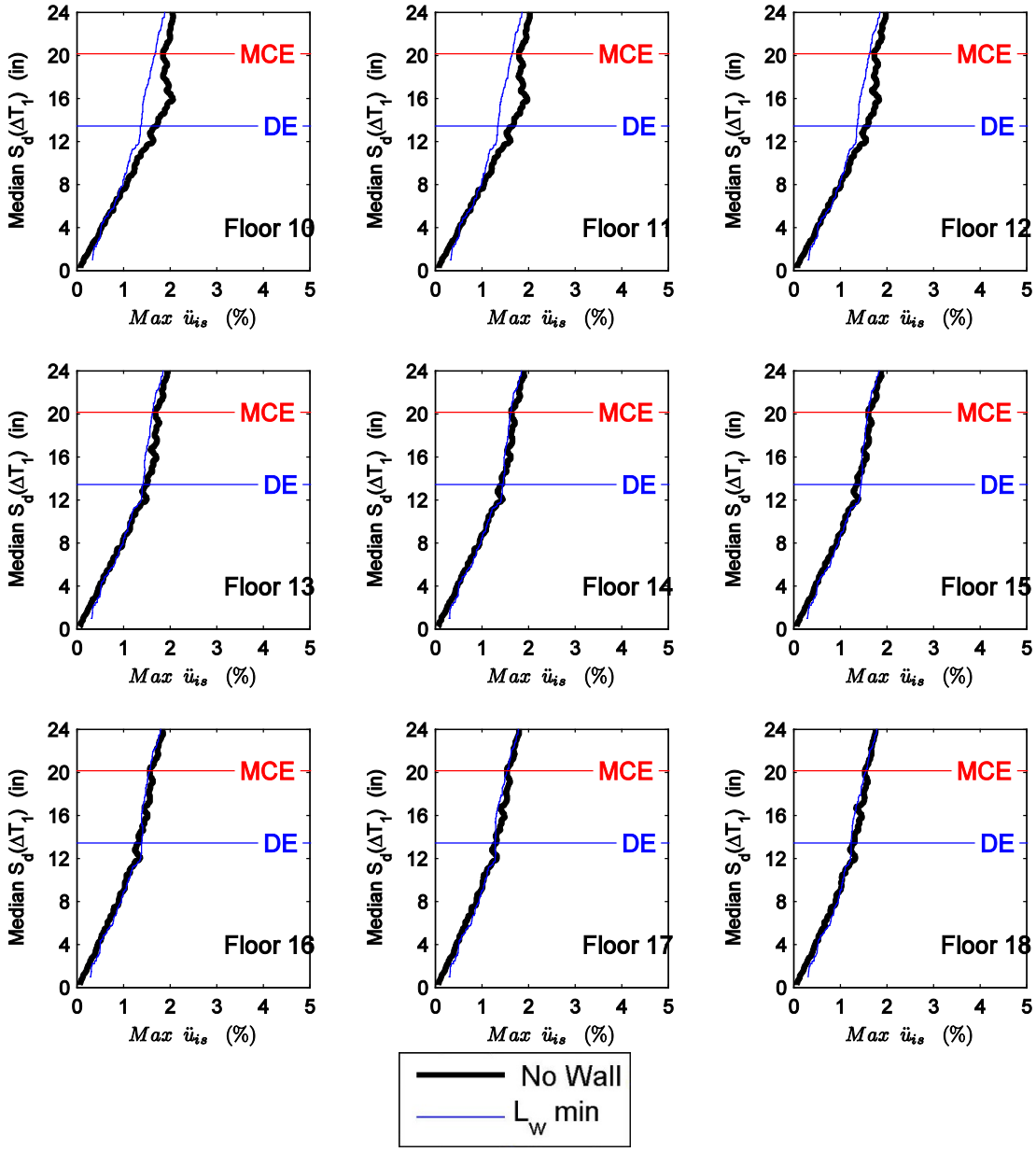

Figure C.111 Maximum floor level acceleration moving average curves for RC-20 considering the cases of no wall and minimum wall length against median spectral acceleration over the range of T_1 for floors 10-18.

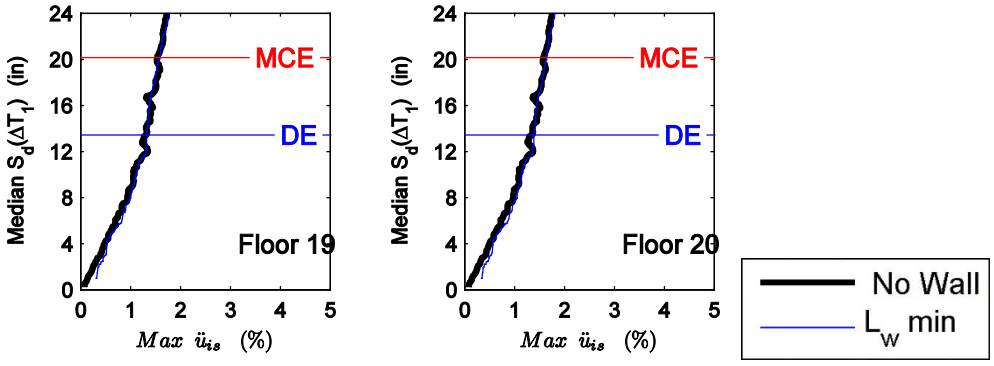

Figure C.112 Maximum floor level acceleration moving average curves for RC-20 considering the cases of no wall and minimum wall length against median spectral acceleration over the range of T_1 for floors 19-20.

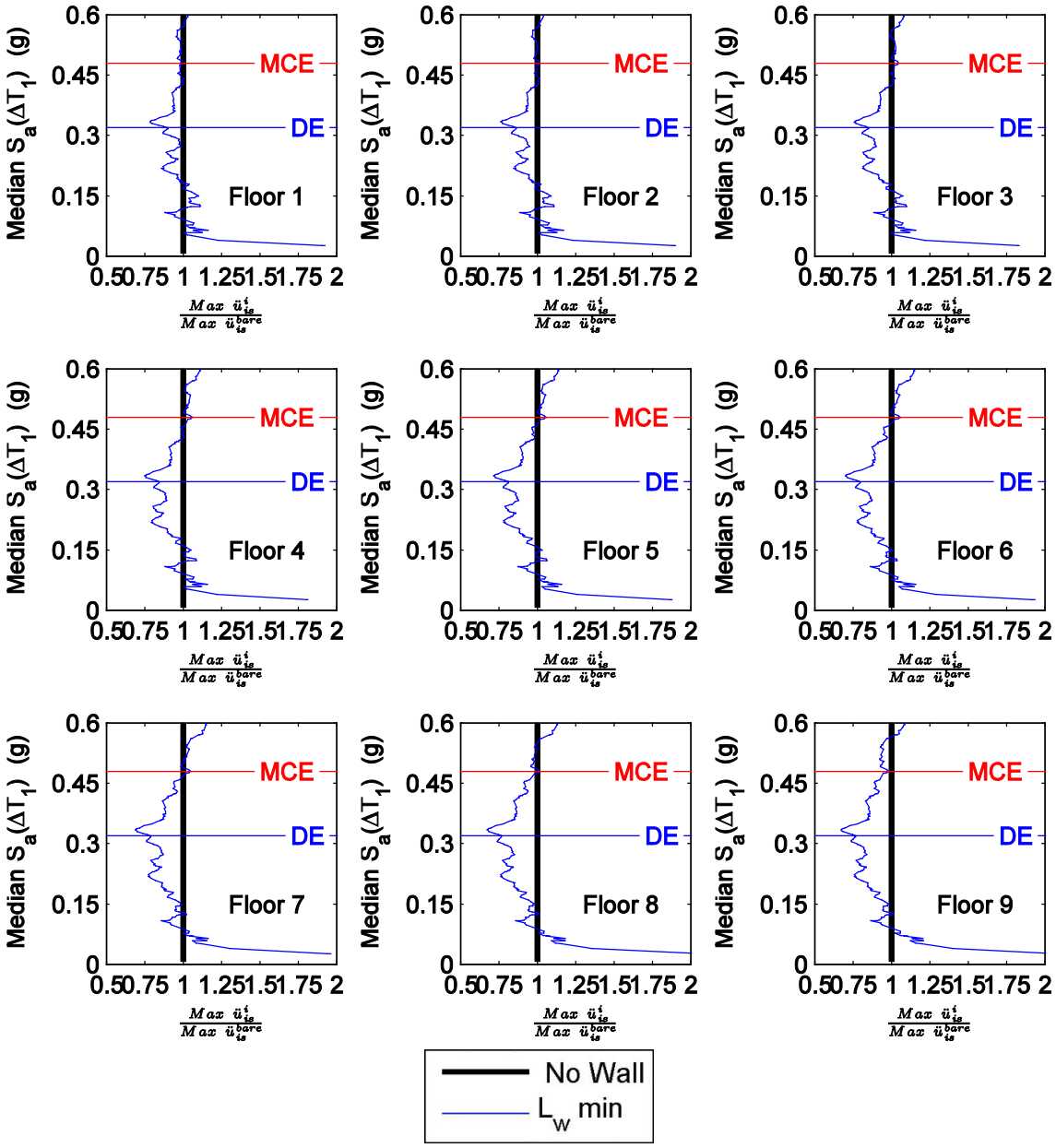

Figure C.113 Normalized maximum floor level acceleration moving average curves for RC-20 considering the cases of no wall and minimum wall length against median spectral acceleration over the range of T_1 for floors 1-9.

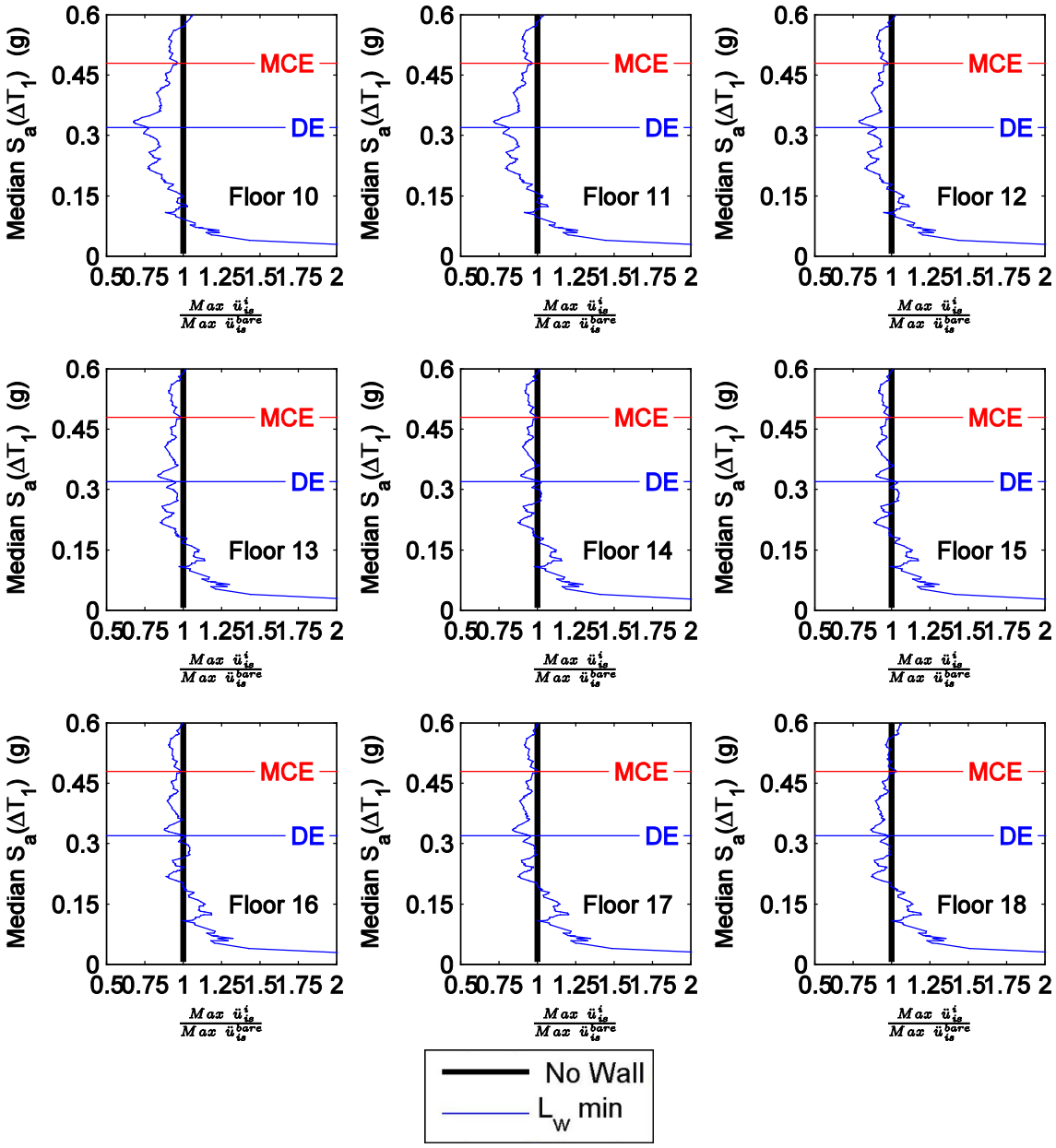

Figure C.114 Normalized maximum floor level acceleration moving average curves for RC-20 considering the cases of no wall and minimum wall length against median spectral acceleration over the range of T_1 for floors 10-18.

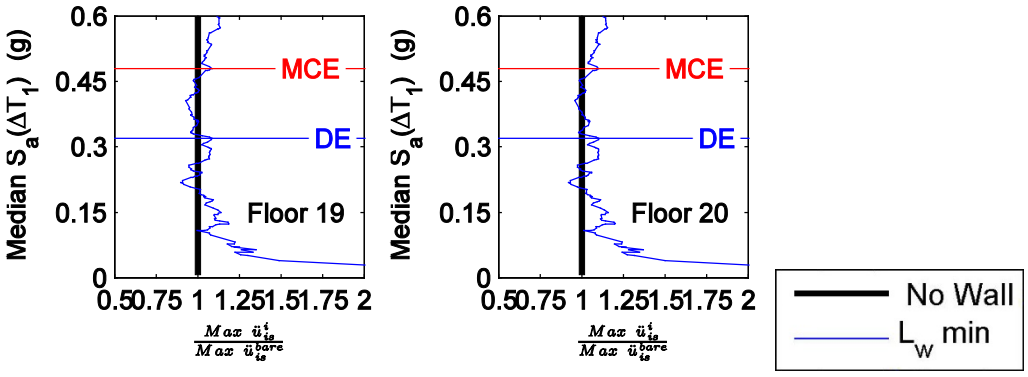

Figure C.115 Normalized maximum floor level acceleration moving average curves for RC-20 considering the cases of no wall and minimum wall length against median spectral acceleration over the range of T_1 for floors 19-20.

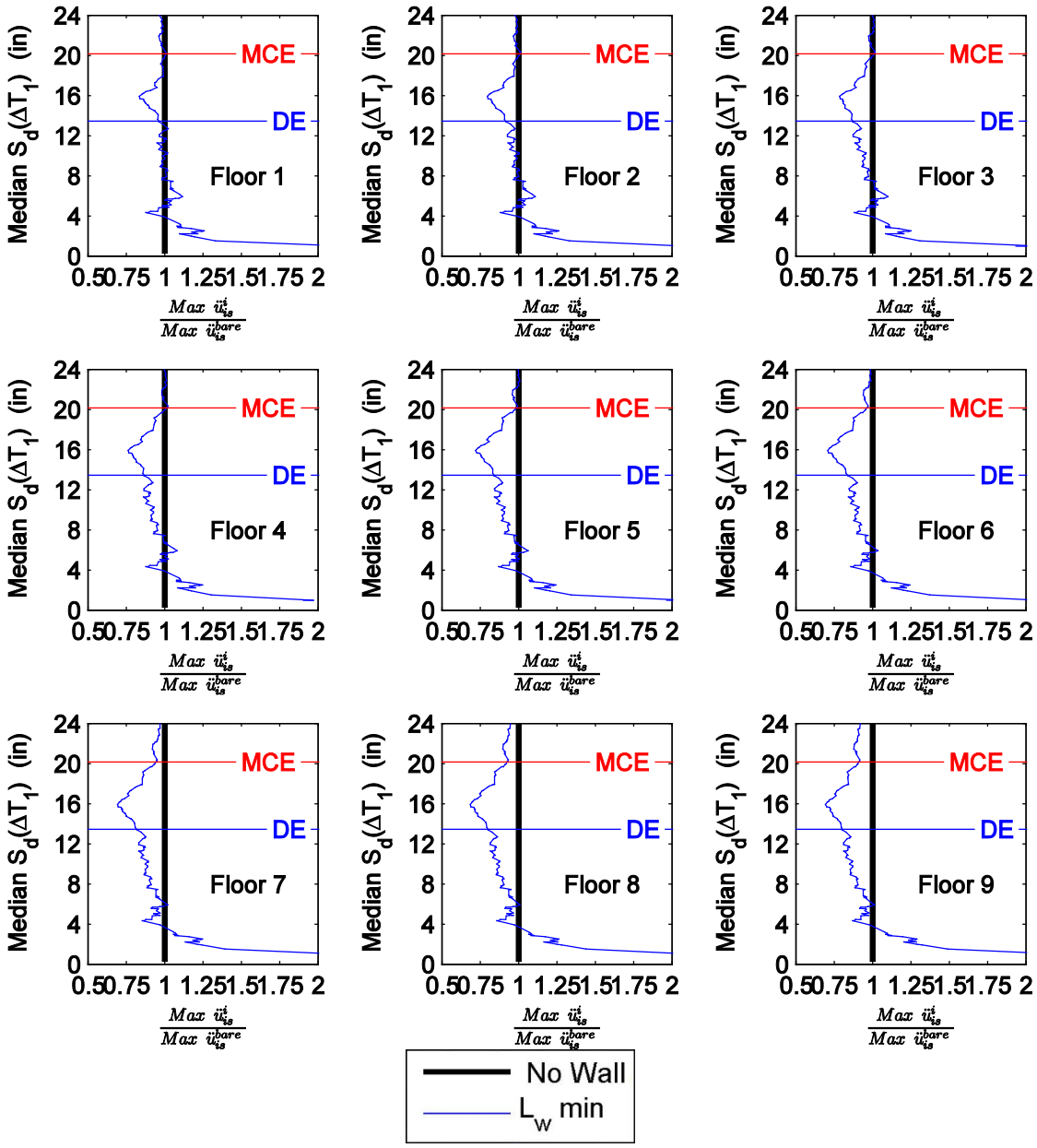

Figure C.116 Normalized maximum floor level acceleration moving average curves for RC-20 considering the cases of no wall and minimum wall length against median spectral displacement over the range of T_1 for floors 1-9.

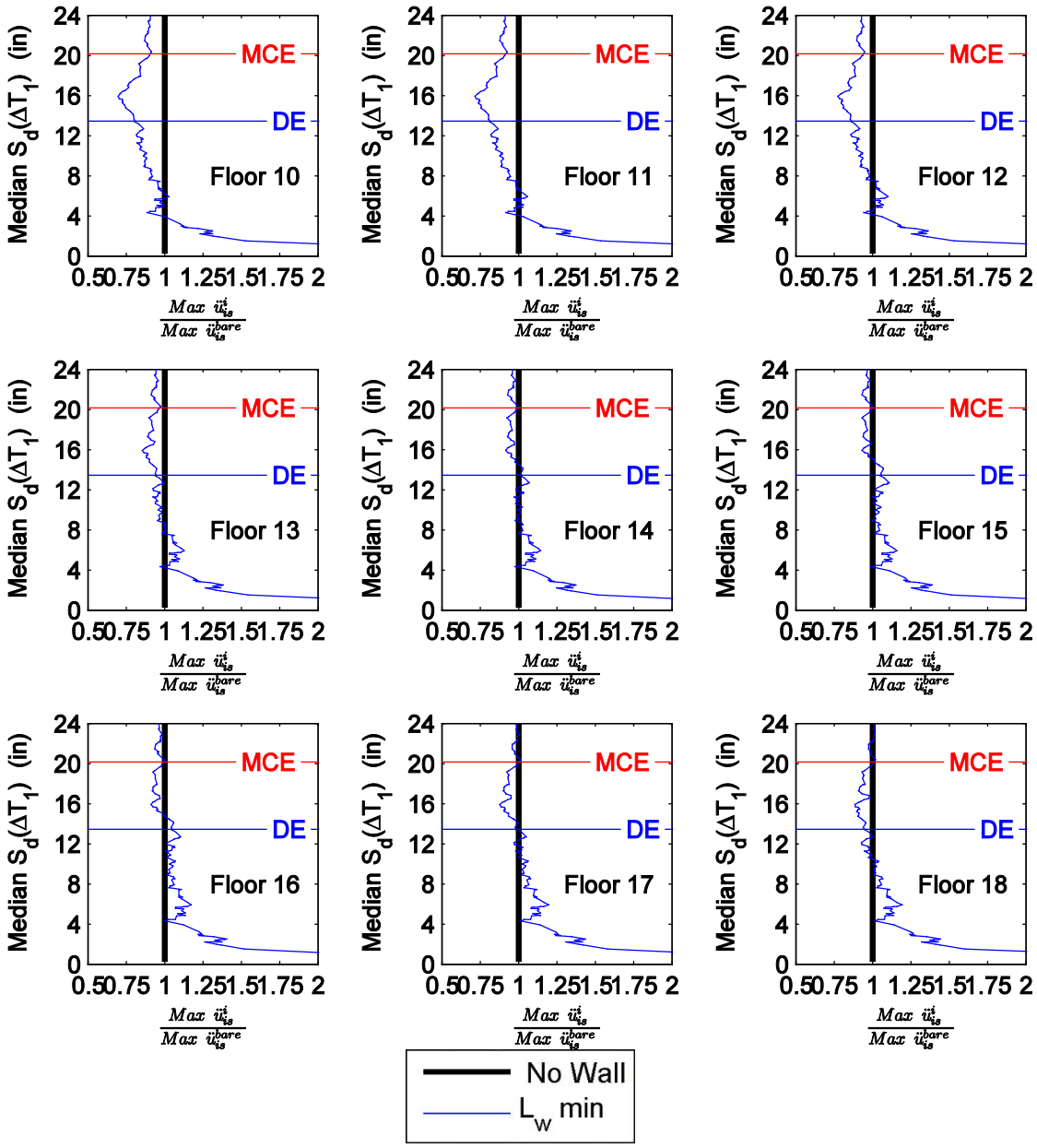

Figure C.117 Normalized maximum floor level acceleration moving average curves for RC-20 considering the cases of no wall and minimum wall length against median spectral displacement over the range of T_1 for floors 10-18.

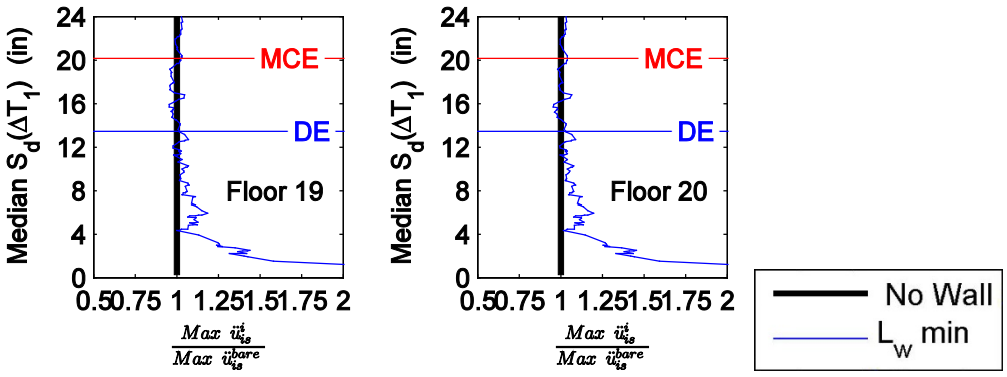

Figure C.118 Normalized maximum floor level acceleration moving average curves for RC-20 considering the cases of no wall and minimum wall length against median spectral displacement over the range of T_1 for floors 19-20.

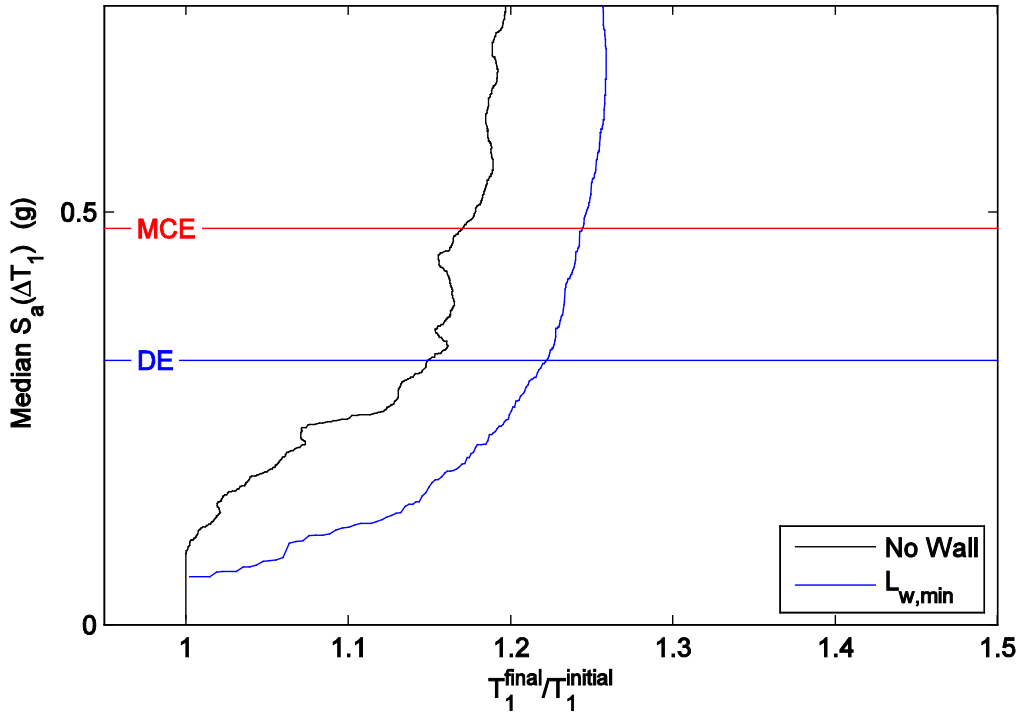

Figure C.119 Period elongation moving average curves for RC-20 considering the cases of no wall and minimum wall length against median spectral acceleration over the range of T_1.

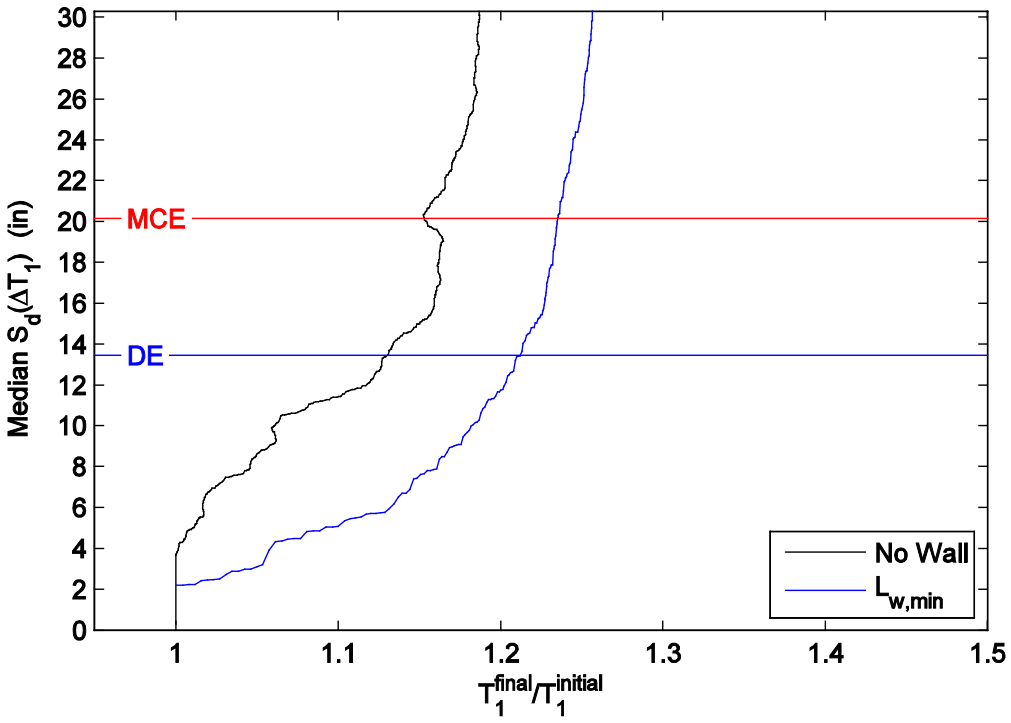

Figure C.120 Period elongation moving average curves for RC-20 considering the cases of no wall and minimum wall length against median spectral displacement over the range of T_1.